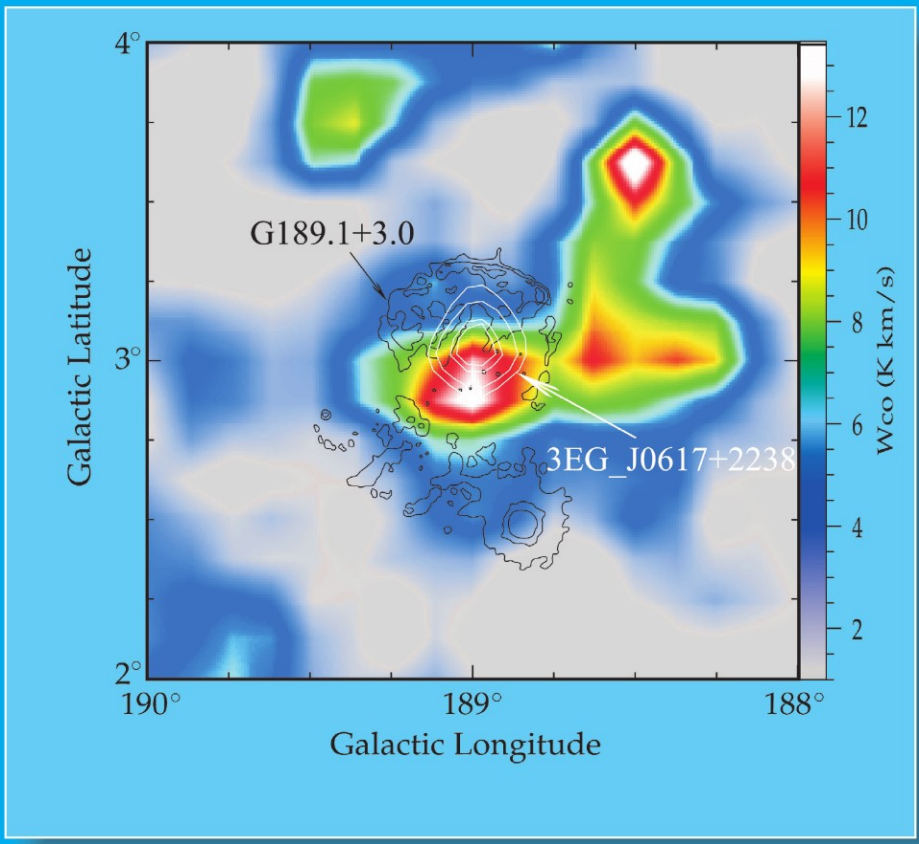
Multiwavelength Approach to Unidentified Gamma-Ray Sources

K.S. Cheng and G.E. Romero (Eds.)



Springer

MULTIWAVELENGTH APPROACH TO UNIDENTIFIED GAMMA-RAY SOURCES

A Second Workshop on the Nature of the High-Energy Unidentified Sources

MULTIWAVELENGTH APPROACH TO UNIDENTIFIED GAMMA-RAY SOURCES

A Second Workshop on the Nature of the High-Energy Unidentified Sources

Edited by:

K.S. CHENG
University of Hong Kong, China

G.E. ROMERO
Instituto Argentino de Radioastronomia, Buenos Aires, Argentina

Reprinted from *Astrophysics and Space Science*
Volume 297, Nos. 1–4, 2005

Springer

Library of Congress Cataloging-in-Publication Data is available

ISBN 1-4020-3214-5

2003055495

Published by Springer,
P.O. Box 17, 3300 AA Dordrecht, The Netherlands.

Cover figure: Multiwavelength image of the supernova remnant IC 443.

Credit: Supernova Remnants and Gamma-Ray Sources, by D.F. Torres, G.E. Romero, T. Dame, J.A. Combi and Y.M. Butt: 2003, Physics Reports, 382, 303

Printed on acid-free paper

All Rights Reserved
© Springer 2005
No part of the material protected by this copyright notice may be reproduced or utilized in any form or by any means, electronic or mechanical, including photocopying, recording or by any information storage and retrieval system, without written permission from the copyright owner.

Printed in the Netherlands

TABLE OF CONTENTS

Preface ix–x

List of Participants xi–xvi

D.J. THOMPSON / The Multiwavelength Approach to Unidentified Gamma-Ray Sources 1–7

G. BISNOVATYI-KOGAN / Regular Particle Acceleration in Relativistic Jets 9–20

E.V. DERISHEV, F.A. AHARONIAN, V.V. KOCHAROVSKY and Vl.V. KOCHAROVSKY / The Converter Mechanism of Particle Acceleration and its Applications to the Unidentified EGRET Sources 21–30

P.G. EDWARDS / An Examination of Candidate AGN Counterparts to Unidentified EGRET Sources 31–41

E. HAYS / A Search for TeV Emission from X-ray Selected AGN with Milagro 43–52

Y.F. HUANG, T. LU and K.S. CHENG / Beaming Effects in GRBs and Orphan Afterglows 53–61

A. HARDING and A. MUSLIMOV / Pulsar Slot Gaps and Unidentified EGRET Sources 63–70

P.L. GONTHIER, R. VAN GUILDER, A.K. HARDING, I.A. GRENIER and C.A. PERROT / Radio-Loud and Radio-Quiet Gamma-Ray Pulsars from the Galaxy and the Gould Belt 71–80

K. HIROTANI / Gamma-Ray Emission from Pulsar Outer Magnetospheres 81–91

M.S.E. ROBERTS, C.L. BROGAN, B.M. GAENSLER, J.W.T. HESSELS, C.-Y. NG and R.W. ROMANI / Pulsar Wind Nebulae in EGRET Error Boxes 93–100

R.N. MANCHESTER / Pulsar Radio and Gamma-Ray Emission 101–108

I.A. GRENIER, M.M. KAUFMAN BERNADÓ and G.E. ROMERO / Unidentified γ-Ray Sources off the Galactic Plane as Low-Mass Microquasars? 109–118

V. BOSCH-RAMON, G.E. ROMERO and J.M. PAREDES / On the Nature of the Variable Gamma-Ray Sources at Low Galactic Latitudes 119–129

S.K. CHAKRABARTI / Spectral Properties of Black Holes in Gamma Rays 131–142

M. RIBÓ, J.A. COMBI and I.F. MIRABEL / Towards a Population of HMXB/NS Microquasars as Counterparts of Low-Latitude Unidentified EGRET Sources 143–154

X.Y. WANG, Z.G. DAI and T. LU / The Large-Scale, Decelerating X-ray Jets from the Microquasar XTE J1550−564: Evidence for External Shocks Caused by the Jet-Ism Interaction? 155–166

M. ORELLANA and G.E. ROMERO / Gamma-Ray Emission from Be/X-ray Binaries 167–178

R. XU / Low-Mass Quark Stars 179–190

T. MIYAGI, D. BHATTACHARYA and A.D. ZYCH / The Spiral ARM Connection of EGRET Unidentified Sources 191–199

V.A. DOGIEL, A.V. GUREVICH, YA.N. ISTOMIN and K.P. ZYBIN / Cosmic Ray Acceleration Inside Molecular Clouds 201–211

M. HOLLERAN and O.C. DE JAGER / Methanol Masers as Precursors of Gamma-Ray Sources 213–221

J.M. PAREDES, J. MARTÍ, D.F. TORRES, G.E. ROMERO, J.A. COMBI, V. BOSCH-RAMON and J. GARCÍA-SÁNCHEZ / Identifying Variable γ-Ray Sources Through Radio Observations 223–233

S. CHATY and P. FILLIATRE / Revealing the Nature of the Obscured High Mass X-ray Binary IGR J16318-4848 235–244

J. CORTINA / Status and First Results of the Magic Telescope 245–255

J.J. HERNÁNDEZ-REY / The Neutrino Telescope Antares 257–267

S. MANDAL and S.K. CHAKRABARTI / Identification of Shocks in the Spectra from Black Holes 269–274

P. COGAN / An Overview of the Veritas Prototype Telescope and Camera 275–281

S. ZHANG, W. COLLMAR and V. SCHÖNFELDER / Comptel Constraints on Unidentified EGRET Sources 283–290

M. DE BECKER, G. RAUW and J.-P. SWINGS / On the Multiplicity of the O-Star Cyg OB2 #8A and its Contribution to the γ-Ray Source 3EG J2033+4118 291–298

J. FLIX, J.E. TAYLOR, M. MARTÍNEZ, F. PRADA, J. SILK and J. CORTINA / Do the Unidentified EGRET Sources Trace Annihilating Dark Matter in the Local Group? 299–308

K.G. GAINULLIN and A.M. ZLOBIN / Coherent Synchrotron Radiation of Gamma-Ray Bursts 309–318

T. HARKO and K.S. CHENG / Constraints on Extra-Dimensions and Variable Constants from Cosmological Gamma-Ray Bursts 319–326

T. HATTORI and K. NISHIJIMA / Search for TeV Gamma-Rays from 3EG J1234-1318 with the Cangaroo-II Telescope 327–334

N. LA PALOMBARA, P. CARAVEO, R. MIGNANI, E. HATZIMINAOGLOU, G.F. BIGNAMI and M. SCHIRMER / Multiwavelength Study of Two Unidentified γ-Ray Sources 335–344

M.J. LANG, D.A. CARTER-LEWIS, D.J. FEGAN, S.J. FEGAN, A.M. HILLAS, R.C. LAMB, M. PUNCH, P.T. REYNOLDS and T.C. WEEKES / A New TeV Source Confirmed in Whipple Archival Data: TeV J2032+41 345–351

Z. LI and L.-M. SONG / The Prompt Ultraviolet/Soft X-Ray Emission of GRBs 353–360

L.C.-C. LIN and H.-K. CHANG / Periodicity Search in the X-ray Data of RX J0007.0+7302 361–367

R. MODERSKI and M. SIKORA / The Klein–Nishina Effects in Blazar Jets 369–376

R. ORDUÑA, C. BAIXERAS, A. CARRAMIÑANA and V. FONSECA / Detectivity of Unidentified EGRET Sources as Gamma-Ray Pulsars with the Magic Telescope 377–383

J.A. COMBI, M. RIBÓ and I.F. MIRABEL / On the Nature of the Unidentified X-ray/γ-Ray Sources IGR J18027–1455 and IGR J21247+5058 385–391

D.F. TORRES, T.M. DAME and G.E. ROMERO / Status of the Connection Between Unidentified EGRET Sources and Supernova Remnants: The Case of CTA 1 393–398

C. VENTER and O.C. DE JAGER / Spectral Constraints for Millisecond Pulsars Due to General Relativistic Frame Dragging 399–407

P. WALLACE, S. BLOOM and M. LEWIS / A Multiwavelength Investigation of Unidentified EGRET Sources 409–414

W. WANG / X-ray Lines in Gamma-Ray Bursts and Cerenkov Line Mechanism 415–422

Y.-F. YUAN, B. LI and J.-M. WANG / Line Emission from Conical Jets Around Rotating Black Holes 423–430

S.J. FEGAN and T.C. WEEKES / A Survey of Unidentified EGRET Sources at TeV Energies 431–438

PREFACE

After a tremendous development during the 1990s, gamma-ray astronomy appears now as a field plenty of sources. Unfortunately, most of these sources, especially those detected in the MeV–GeV range, remain unidentified. Large error boxes in their location and the plurality of potential counterparts have prevented, up till now, unequivocal and positive identification in most cases.

Since gamma-rays are produced by relativistic particles V through interaction with matter or electromagnetic fields – which can also produce additional radiation at lower energies – multiwavelength studies of unidentified gamma-ray sources and their environments seem to be the most powerful tool at our disposal to elucidate the nature of these objects.

This volume contains the contributing papers to the first meeting completely devoted solely to the multiwavelength approach for the identification of high-energy sources. The conference was held in the Department of Physics of the University of Hong Kong, from 1 to 4 June 2004. All contributions are full-length papers that were subject to the usual peer reviewing process. Hence, this issue of *Astrophysics and Space Science* can be considered as a thematic volume providing the most updated information currently available on the topic.

While working on this project, from the organization of the meeting to the editorial work on this volume, we benefited from the support of the following organizations: K.C. Wong Education Foundation, Lee Hysan Foundation Ltd., The Astrophysical Society of Hong Kong, The University of Hong Kong, the Agencia Nacional para la Promoción de la Ciencia y la Tecnología (Argentina) and the Fundación Antorchas.

We are very grateful to the other members of the Scientific Organizing Committee (Felix Aharonian, Alberto Carramiñana, O. de Jager, Isabelle Grenier, Dick Manchester, Sandro Mereghetti, Dave Thompson and Heinz Voelk) for their valuable suggestions and also to the other members of the Local Organizing Committee (H.F. Chau, Jason Pun, K.L. Chan and M.C. Chu), as well as to the staff of the Physics Department of the University of Hong Kong, for their help and support.

Finally, we wish to specially thank Ms. Anisia Tang for her excellent work on most of the aspects of the organization of the meeting and for her invaluable assistance with the editorial work.

This volume represents a step forward in our understanding of the physical processes of cosmic gamma-ray sources. Hopefully, very soon, new instruments



© Springer 2005

will provide us with a fuller view of the depths we can now glimpse through the papers presented here.

K.S. CHENG
GUSTAVO E. ROMERO

LIST OF PARTICIPANTS

Dr. Felix Aharonian
Max-Planck-Institut fur Kernphysik, Saupfercheckweg 1, D-69117 Heidelberg, Germany

Dr. Dipen Bhattacharya
IGPP, UCR, Riverside, CA 92521, USA

Prof. Gennady Bisnovatyi-Kogan
Space Research Institute RAS, Profsoyuznaya 84/32, Moscow 117997, Russia

Dr. Valenti Bosch-Ramon
Universitat de Barcelona, Av. Diagonal 647, E-08028 Barcelona, Catalonia, Spain

Prof. Sandip K. Chakrabarti
S.N. Bose National Centre for Basic Sciences, JD-Block, Salt Lake, Kolkota 700098, India

Prof. Hsiang-Kuang Chang
Department of Physic, National Tsing Hua University, Hsinchu 30013, Taiwan

Dr. Sylvain Chaty
DSM/DAPNIA/SAp, CEA-Saclay, Bat. 709, L'Orme des Merisiers, F-91 191 Gif-sur-Yvette Cedex, France

Prof. K.S. Cheng
Department of Physics, The University of Hong Kong, Pokfulam Road, Hong Kong, China

Prof. Ming-chung Chu
Department of Physics, The Chinese University of Hong Kong, Shatin, New Territories, Hong Kong, China

Mr. Peter Cogan
Department of Experimental Physics, University College Dublin, Belfield, Dublin 4, Ireland

Astrophysics and Space Science **297:** xi–xvi, 2005.
© Springer 2005

Dr. Werner Collmar
Max-Planck-Institut fuer extraterrestrische Physik (MPE), P.O. Box 1312, 85741 Garching, Germany

Dr. Juan Cortina
IFAE, Edifici Cn, Campus Bellaterra UAB, 08193 Spain

Dr. Michaël De Becker
Institut d'astrophysique et de géophysique, Allée du 6 Août, 17, Bât. B5c, 4000 Liège, Belgium

Prof. Okkie de Jager
Unit for Space Physics, Potchefstroom Campus, Northwest University, Potchefstroom 2520, South Africa

Mr. Peter R. den Hartog
Sorbonnelaan 2, 3584 CA UTRECHT, The Netherlands

Dr. Evgeny Derishev
Institute of Applied Physics, 46 Ulyanov St., 603950 Nizhny Novgorod, Russia

Dr. Guido Di Cocco
via P. Gobetti 101, 40129 Bologna, Italy

Dr. Vladimir Dogiel
Leninskii pr. 53, 119991 Moscow, Russia

Dr. Philippe Durouchoux
CE Saclay, DSM, DAPNIA, Service d'Astrophysique, 91191 Gif sur Yvette Cedex, France

Dr. Philip Edwards
ISAS, Yoshinodai 3-1-1, Sagamihara, Kanagawa 229-8510, Japan

Prof. Rob Fender
Kruislaan 403, 1098 SJ Amsterdam, The Netherlands

Dr. Kamil Gainullin
607190, Sarov Nizhni Novgorod Region, Mira Ave. 37, Russia

Prof. Peter Gonthier
Hope College, Department of Physics and Engineering, 27 Graves Place, MI 49423, The Netherlands

Prof. Isabelle Grenier
Université Paris VII & Service d'Astrophysique, CEA Saclay, 91191 Gif/Yvette, France

Dr. Alice K. Harding
Code 661, NASA Goddard Space Flight Center, Greenbelt, MD 20771, USA

Dr. Tiberiu Harko
Department of Physics, The University of Hong Kong, Pokfulam Road, Hong Kong, China

Prof. Takahiro Hattori
Katou Haitsu 101, Minamiyana 2007, Hadano, Kanagawa, Japan

Dr. Elizabeth Hays
Physics Box 77, 82 Regents Drive, College Park, MD 20742, USA

Prof. Willem Hermsen
SRON National Institute for Space Research, Sorbonnelaan 2, 3584 CA Utrecht, The Netherlands

Dr. Juan-Jose Hernandez-Rey
Instituto de Fisica Corpuscular, Ed. Investigacion Paterna, Universidad de Valencia, apdo. 22085, E-46071 Valencia, Spain

Dr. Kouichi Hirotani
MPI fuer Kernphysik, Postfach 103980, D-69029 Heidelberg, Germany

Mr. M. Holleran
Unit for Space Physics, School of Physics, North-West University, Potchefstroom Campus 2520, South Africa

Dr. Yong-Feng Huang
Department of Astronomy, Nanjing University, Nanjing 210093, P.R. China

Dr. Nicola La Palombara
IASF-CNR, Via E. Bassini 15, I-20133 Milan, Italy

Ms. Kuen Lee
Department of Physics, Washington University, One Brookings Drive, St. Louis, MO 63130-4899, USA

Dr. Zhuo Li
Particle Astrophysics Center, Institute of High Energy Physics, Chinese Academy of Sciences, Beijing 100039, P.R. China

Dr. Chun-Che Lin
National Tsing-Huan University, 30013 Taiwan

Mr. Jinrong Lin
Tsinghua Center for Astrophysics, Tsinghua University, Beijing 100084, P.R. China

Prof. Tan Lu
Department of Astronomy, Nanjing University, Nanjing 210093, P.R. China

Prof. Kam-Biu Luk
Department of Physics, University of California, Berkeley, CA 94720, USA

Prof. Richard Manchester
ATNF-CSIRO, P.O. Box 76, Epping, NSW 1710, Australia

Dr. Julie McEnery
NASA/GSFC (mail code 661), Greenbelt, MD 20771, USA

Ms. Nestor Mirabal
ALTSCHUL 506, MS 4-5101, USA

Dr. Felix Mirabel
Service d'Astrophysique, Centre d'Etudes de Saclay, 91191 Gif-sur-Yvette, France

Dr. Rafal Moderski
Copernicus Astronomical Center, Bartycka 18, 00-716 Warszawa, Poland

Dr. Igor Moskalenko
Max-Planck-Institut fuer extraterrestrische Physik , Postfach 1312, 85741 Garching, Germany

Prof. Kyoshi Nishijima
Tokai University, 1117 Kitakaname, Hiratsuka, Kanagawa 259-1292, Japan

Dr. Raul Ordua
Departament de fisica, Facultat de Ciencies, Universitat Autonoma de Barcelona, Edifici CC, 08193 Bellaterra, Barcelona, Spain

Dr. Josep M. Paredes
Departament d'Astronomia i Meteorologia, Universitat de Barcelona, Av. Diagonal 647, 08028 Barcelona, Spain

Dr. Leonardo Javier Pellizza Gonzalez
CEA-Saclay, Bat. 709, L' Orme des Merisiers, 91191 Gif-sur-Yvette, France

Dr. Gregor Rauw
Institut d'Astrophysique, Allee du 6 Aout 17, Bat. B5c, B-4000 Liege, Belgium

Dr. Olaf Reimer
Institut für Theoretische Physik, Lehrstuhl IV, NB 7/68, Ruhr-Universität Bochum, 44780 Bochum, Germany

Dr. Marc Ribo
Service d'Astrophysique, CEA Saclay, Bat. 709, L'Orme des Merisiers, F-91191 Gif-sur-Yvette Cedex, France

Dr. George Ricker
MIT, Room 37-535, 77 Massachusetts Avenue, Cambridge, MA 02139, USA

Dr. Mallory Roberts
McGill University/Eureka Scientific, 3600 University Street, USA

Prof. Gustavo E. Romero
Instituto Argentino de Radioastronomia-CONICET, CC 5, 1894 Villa Elisa, Buenos Aires, Argentina

Prof. Bronislaw Rudak
Copernicus Astronomical Center, Rabianska 8, 87-100 Torun, Poland

Dr. Ming Sun
Harvard CFA, MS10, cfa, 60 Garden Street, Cambridge, MA 02138, USA

Mr. Pak Hin Tam
Department of Physics, The University of Hong Kong, Pokfulam Road, Hong Kong, China

Dr. Dave Thompson
Code 661, NASA Goddard Space Flight Center, Greenbelt, MD 20771, USA

Dr. Diego Torres
Lawrence Livermore National Laboratory, 7000 East Ave. L-413, Livermore, CA 94550, USA

Ms. Ka Yee Tso
Department of Physics, The Chinese University of Hong Kong, Shatin, New Territories, Hong Kong, China

Prof. Heinz Voelk
Max-Planck-Institut fuer Kernphysik, Postfach 103980, 69029 Heidelberg, Germany

Prof. Paul Wallace
Berry College, Campus Box 5004, Mt. Berry, GA 30149-5004, USA

Dr. Wei Wang
Department of Physics, The University of Hong Kong, Pokfulam Road, Hong Kong, China

Dr. Xiangyu Wang
Department of Astronomy, Nanjing University, Nanjing 210093, P.R. China

Prof. Trevor C. Weekes
Harvard-Smithsonian Center for Astrophysics, Amado, AZ 85645-0097, USA

Dr. Renxin Xu
School of Physics, Peking University, Beijing 100871, P.R. China

Dr. Ye-Fei Yuan
Center for Astrophysics, University of Science and Technology of China, Hefei, Anhui 230026, P.R. China

Dr. Anatoly Zlobin
607190, Sarov Nizhni Novgorod Region, Mira Ave. 37, Russia

THE MULTIWAVELENGTH APPROACH TO UNIDENTIFIED GAMMA-RAY SOURCES

DAVID J. THOMPSON

Laboratory for High Energy Astrophysics, NASA Goddard Space Flight Center, Greenbelt, MD, U.S.A.; E-mail: djt@egret.gsfc.nasa.gov

(Received 23 June 2004; accepted 3 July 2004)

Abstract. As the highest-energy photons, gamma rays have an inherent interest to astrophysicists and particle physicists studying high-energy, nonthermal processes. Gamma-ray telescopes complement those at other wavelengths, especially radio, optical, and X-ray, providing the broad, mutiwavelength coverage that has become such a powerful aspect of modern astrophysics. Multiwavelength techniques of various types have been developed to help identify and explore unidentified gamma-ray sources. This overview summarizes the ideas behind several of these methods.

Keywords: gamma rays, sources, multiwavelength

1. Introduction: Gamma-Ray Sources as Multiwavelength Objects

In the MeV range and above, astrophysical sources are almost exclusively nonthermal, i.e., produced by interactions of energetic particles, through such processes as bremsstrahlung, synchrotron radiation, Compton scattering, and neutral pion production. High-energy, nonthermal sources are inherently multiwavelength objects, for several reasons:

1. Nature rarely produces monoenergetic particle beams. The cosmic ray spectrum, for example, covers a huge expanse of energies. A broad range of particle energies naturally leads to a broad range of photon energies.
2. Charged particles rarely interact by only one process. Different processes radiate in different energy bands. Blazars, for example, shine by synchotron radiation (electrons in magnetic fields) for radio through soft X-ray energies, while the same electrons Compton scatter low-energy photons to produce hard X-ray and gamma-ray emission.
3. High-energy particles, as they lose energy, can radiate in lower-energy bands. The afterglows seen in gamma-ray bursts illustrate this effect.

Results from the four instruments on the Compton Gamma Ray Observatory revealed a large number of sources, including gamma-ray bursts, pulsars, blazars, interstellar clouds, and a sizeable number that remained unidentified. In the third EGRET catalog, for example, over half the sources were considered unidentified



Astrophysics and Space Science **297:** 1–7, 2005.
© Springer 2005

(Hartman et al., 1999). Except for gamma-ray bursts, which are self-identifying, the other sources were identified by association with objects at other wavelengths. The new knowledge of the Universe that came from exploring these sources usually involved combining the gamma-ray data with those from other parts of the electromagnetic spectrum. Multiwavelength studies are therefore both expected and essential for gamma-ray astrophysics.

The following sections will describe some of the methods used for identification of unidentified gamma-ray sources. In addition, some comments are included about how multiwavelength studies are used to move beyond identification to exploration of sources once they are identified. This paper is intended as a broad overview of the many facets of the multiwavelength approach, not an in-depth review. Many of the latest results appear in other contributions to these proceedings.

2. X-Rays: Searches for Counterparts from the Highest Energies Down

As the nearest neighbors to gamma rays in the electromignetic spectrum, X-rays are a logical starting point for gamma-ray source identification. The basic concept of starting with X-rays is that, at some level, gamma-ray sources will all have X-ray counterparts. If the X-ray counterpart can be found, the excellent X-ray position information allows deep searches at still longer wavelengths. The way this approach is applied is as follows: using an X-ray image of a gamma-ray source error box, eliminate most of the X-ray sources from consideration based on their X-ray, optical, and radio properties. Look for a nonthermal source with a plausible mechanism to produce gamma rays. The classic example is Geminga. Bignami et al. (1983) started this search in 1983. The final result appeared in 1992 with the detection of pulsations from this isolated neutron star in X-rays (Halpern and Holt, 1992) and then in gamma rays (Bertsch et al., 1992).

A more recent example is the work on 3EG J1835 + 5918. Parallel effort by two groups, Mirabal et al. (2000) and Reimer et al. (2001), used the same approach and reached the same conclusion. Steps in the process were:

- A long ROSAT exposure was used to find candidate X-ray counterparts.
- Optical observations were made of the X-ray counterparts.
- All but one of the candidates were found to be unlikely gamma-ray emitting objects such as stars and QSOs.
- The remaining candidate, RX J1836.2 + 5925, had no optical counterpart, suggesting an isolated neutron star.
- A radio search of the error box revealed no radio pulsar counterpart (Nice and Sayer, 1997).
- A deep Chandra observation found a two-component spectrum, a thermal plus power-law combination.
- The full multiwavelength spectral energy distribution (SED) resembles that of Geminga.

– Despite the absence of pulsations, this object appears to be an isolated neutron star, possibly a radio-quiet pulsar that will be seen in X-rays and gamma-rays with deeper exposures.

Other examples of the use of X-rays for "top down" gamma-ray source identification include:

– ASCA observations of unidentified Galactic gamma-ray sources that show evidence of pulsar wind nebulae (Roberts et al., 2001).
– Identification of a blazar near the Galactic Plane (Mukherjee et al., 2001).
– XMM Newton observations of intermediate-latitude sources, with the analysis still in progress (La Palombara et al., 2004).

3. Radio: Searches for Counterparts from the Lowest Energies Up

The largest class of identified gamma-ray sources is blazars, all of which have radio emission characterized by a bright compact source and a flat radio spectrum. If a flat-spectrum radio source with strong ($\sim$1 Jy), compact emission at 5 GHz or above is found in a gamma-ray source error box, it becomes a blazar candidate. The approach is then to use radio catalogs to search for flat-spectrum radio sources. If a candidate is found, follow-up observations can be made to locate other blazar characteristics such as polarization, time variability and a Spectral Energy Distribution with a synchrotron plus a Compton component. The EGRET team used this approach in compiling the EGRET catalogs. Mattox et al. (2001) quantified the method based on proximity and radio intensity. Sowards-Emmerd et al. (2003) have expanded the number of known blazars with this approach.

One example of this type of identification is described by Foreman et al. (2001) for 3EG JJ0433 + 2908:

– From radio catalogs, a flat-spectrum source with 5GHz flux of 475 mJy was found.
– Optical and X-ray catalogs showed a counterpart for this source.
– Infrared observations also found a counterpart.
– Follow-on radio and X-ray observations indicated likely variability.
– Follow-on optical observations found a featureless spectrum.
– The full multiwavelength spectral energy distribution (SED) resembles that of blazars, with a synchrotron and a Compton component.
– This appears to be a BL Lac object.

Radio observations have also been used to search "bottom up" for

– Extended gamma-ray sources related to molecular clouds (Digel et al., 1999)
– Microquasars in gamma-ray source error boxes (Paredes et al., 2000)
– Possible supernova remnants with nearby molecular clouds (Combi et al., 1998; Torres et al., 2003).

4. Periodicity as a Multiwavelength Tool

Finding a high-significance common periodic variability, either rotational or orbital, at multiple wavelengths is a definitive identifier for a source. Pulsars (rotating neutron stars) are the prototype of this method, dating back to balloon and early satellite observations of gamma rays from the Crab and Vela pulsars. The approach is to search out a periodic signal at one wavelength, then fold data from other wavelength bands at the expected period. For a summary of observations of gamma-ray pulsars, see Thompson (2004). Thus, all gamma-ray pulsars were first found at other wavelengths, where the higher density of photons made periodicity searches easier. The GLAST large area telescope (LAT) will have the capability for independent period searches for some gamma-ray sources. The deepest searches for pulsation will still require contemporaneous radio or X-ray observations.

Recent TeV observations with H.E.S.S. have indicated a source with orbital periodicity. The binary system consisting of PSR B1259–63 and a Be star shows gamma-ray emission near periastron (Beilicke et al., 2004).

In addition to identification, periodic sources facilitate exploration of physical processes in the region of the neutron star. The light curves provide information about the physics and geometry of particle acceleration and interaction. The broadband energy spectra show multiple components, produced by different physical processes.

5. Flaring: Other Types of Varaibility

The basic concept for using nonperiodic variability is that transient or long-term variability helps to identify sources and to understand their physics. Variability studies have shown that gamma-ray pulsars have low variability (except for their pulsations), while blazars typically show substantial variability. The approach is to use degree of variability as a guide to source identification, then examine variability correlations at different wavelengths as a diagnostic of emission processes. Transients, including gamma-ray bursts, require fast response in order to obtain multiwavelength data.

An example of using flaring as a multiwavelength tool to identify a blazar was given by Wallace et al. (2002) as follows:

- In a study of short-term variability of EGRET sources, 3EG J2006−2321 was seen to be variable.
- From radio catalogs, two flat-spectrum sources with modest 5 GHz flux were found.
- Optical observations showed one of these to be a normal galaxy (unlikely to be the gamma-ray source) and the other to have a redshift $z = 0.83$.
- Observations of optical polarization from the distant object showed significant polarization, with variability.

– X-ray observations showed only an upper limit.
– The full multiwavelength spectral energy distribution resembles that of blazars, with a synchrotron and a Compton component.
– This appears to be a flat-spectrum radio quasar.

Blazars are characterized by both short-term and long-term variability at essentially all wavelengths. The relationship between changes at different wavelengths is a powerful tool for studying the jets in these sources. This multiwavelength variability is an example of moving from identification to study of the detailed astrophysics of objects.

6. Population Studies: Collective Properties of Sources

Because gamma-ray source error boxes are typically large by standards of other branches of astronomy, positional agreement with a candidate object is rarely a strong argument by itself for physical association. Even if individual gamma-ray source identifications are not possible, however, statistical analysis may show a pattern of correlation with a given type of object. The approach is to compare a gamma-ray source catalog (or subset of a catalog) with known classes of objects, using some statistical measure of correlation. If an association can be found, then it is valuable to study the implications of this source class.

Some examples of population studies are

– Kaaret and Cottam (1996) found a correlation between EGRET unidentified low-latitude sources and OB associations.
– Yadigaroglu and Romani (1997) also found evidence of gamma-ray sources near OB associations, as well as pulsars and supernova remnants.
– Romero et al. (1999) also related EGRET sources to supernova remants and OB associations in a statistical sense.
– At intermediate Galactic latitudes Grenier (2000) and Gehrels et al. (2000) found that steady gamma-ray sources appear to represent a new population, distinct from the sources along the Galactic Plane. These sources may be associated with the Gould Belt. If so, they would be nearby, low luminosity objects, possibly pulsars or microquasars. No individual candidate objects have yet been identified at other wavelengths.

7. Theory and Modeling: 'Glue' that Connects the Various Observations

Although multiwavelength observations are critical, theory and modeling are the means to link the different observations and construct a physical picture of a source. Three broad areas show the importance of this work as

– Theoretical work provides explanation and understanding of what has already been seen. These calculations help move science from "What is there?" to "How

do they work?" Gamma-ray pulsar modeling, for example, has evolved rapidly with the Compton observatory pulsar observations. Numerous detailed calculations have offered several possibilities for explaining the observations. For a recent summary, see Cheng (2004). Similarly, the discovery of gamma-ray emission from blazars stimulated an explosive growth of blazar modeling.

– Theory gives observations more predictive power. For known sources, theory predicts what should be seen (or not seen) at wavelengths not yet explored. An example is the study of the region of the sky containing 3EG J1714−3857/SNR RXJ1713−3946. CANGAROO TeV observations appeared to be consistent with a simple model of proton acceleration and interaction (Enomoto et al., 2002), but the theory showed that emission would then have been expected in the EGRET band. The EGRET upper limits indicate that the simplest model is insufficient (Reimer and Pohl, 2002; Butt et al., 2002).
– For the future, theory predicts what new sources should be expected. Different pulsar models, for example, make dramatically different predictions of which radio pulsars should be seen with the next generation of gamma-ray telescopes (Thompson, 2004).

8. Conclusions

The value of multiwavelength studies for both identification and exploration of gamma-ray sources has been clearly established. The identifications of pulsars and blazars as classes of gamma-ray emitters depended on observations at other wavelengths, and a number of other likely identifications have been directly enabled by multiwavelength observations. The extensive theoretical work on pulsars and blazars in particular has utilized observations at many wavelengths to investigate the implications of these sources for astrophysics.

Despite substantial efforts, however, these techniques have not solved all the mysteries of the unidentified EGRET sources. A majority of the unidentified sources from the EGRET catalog remain in that category. The population studies have offered tantalizing prospects, but not definitive solutions.

Probably the greatest advance resulting from the multiwavelength approach is the recognition of its importance and the preparation for the future. Using a variety of methods, the multiwavelength community will be well prepared for the new generation, already in operation or planned for the near future, of satellite and ground-based gamma-ray telescopes: INTEGRAL, Swift, AGILE, GLAST, HESS, MAGIC, CANGAROO-3, VERITAS, MILAGRO.

References

Beilicke, M. et al.: 2004, *Astronomer's Telegram*, ATEL No. 250.
Bertsch, D.L. et al.: 1992, *Nature* **357**, 306.
Bignami, G.F., Caraveo, P.A. and Lamb, R.C.: 1983, *ApJ* **272**, L9.

Butt, Y.M., Torres, D.F., Romero, G.E., Dame, T.M. and Combi, J.A.: 2002, *Nature* **418**, 499.
Cheng, K.S.: 2004, in: K.S. Cheng and G.E. Romero (eds.), *Cosmic Gamma Ray Sources*, Kluwer, Dordrecht, pp. 169–204.
Combi, J.A., Romero, G.E. and Benaglia, P.: 1998, *A&A* **333**, L91.
Digel, S.W., Aprile, E., Hunter, S.D., Mukherjee, R. and Xu, F.: 1998, *A&A* **333**, L91.
Enomoto, R. et al.: 2002, *Nature* **416**, 823.
Foreman, J.V., Eracleous, M., Halpern, J.P., Thompson, D.J. and Wallace, P.M.: 2001, *BAAS* **33**, 1453.
Gehrels, N., Macomb, D.J., Bertsch, D.L., Thompson, D.J. and Hartman, R.C.: 2000, *Nature* **404**, 363.
Grenier, I.A.: 2000, *A&A* **364**, L93.
Halpern, J.P. and Holt, S.S.: 1992, *Nature* **357**, 222.
Hartman, R.C. et al.: *ApJS* **123**, 79.
Kaaret, P. and Cottam, J.: 1996, *ApJ* **462**, L35.
La Palombara, N., Bignami, G.F., Caraveo, P., De Luca, A., Mereghetti, S. and Mignani, R.: 2004, *Memorie della Societa Astronomica Italiana* **75**, 476.
Mattox, J.R., Hartman, R.C. and Reimer, O.: 2001, *ApJS* **135**, 155.
Mirabal, N., Halpern, J.P., Eracleous, M. and Becker, R.H.: 2000, *ApJ* **541**, 180.
Mukherjee, R., Gotthelf, E.V., Halpern, J. and Tavani, M.: 2001, *ApJ* **542**, 740.
Nice, D.J. and Sayer, R.W.: 1997, *ApJ* **476**, 261.
Paredes, J.M. et al.: 2000, *Science* **288**, 2340.
Reimer, O. and Pohl, M.: 2002, *A&A* **390**, L43.
Reimer, O. et al.: 2001, *MNRAS* **324**, 772.
Roberts, Mallory S.E., Romani, Roger W. and Kawai, Nobuyuki: 2001, *ApJS* **133**, 451.
Romero, G.E., Benaglia, P. and Torres, D.F.: 1999, *A&A* **348**, 868.
Sowards-Emmerd, D., Romani, R.W. and Michelson, P.F.: 2003, The Gamma-Ray Blazar Content of the Northern Sky. *ApJ* **590**, 109.
Thompson, D.J.: 2004, in: K.S. Cheng and G.E. Romero (eds.), *Cosmic Gamma Ray Sources*, Kluwer, Dordrecht, pp. 149–168.
Torres, D.F., Romero, G.E., Dame, T.M., Combi, J.A. and Butt, Y.M.: 2003, *Phys. Rep.* **382**, 303.
Wallace, P.M., Halpern, J.P., Magalhães, A.M. and Thompson, D.J.: 2002, *ApJ* **569**, 36.
Yadigaroglu, I.A. and Romani, R.W.: 1997, *ApJ* **476**, 347.

REGULAR PARTICLE ACCELERATION IN RELATIVISTIC JETS

GENNADY BISNOVATYI-KOGAN

Space Research Institute RAN, Moscow, Russia and Joint Institute of Nuclear Researches, Dubna, Russia; E-mail: gkogan@mr.iki.rssi.ru

(Received 11 June 2004; accepted 22 July 2004)

Abstract. An exact solution is obtained for the electromagnetic field around a conducting cylinder of infinite length and finite radius, with a periodical axial current, when the wavelength is much larger than the radius of the cylinder. The solution describes simultaneously the fields in the near zone close to the cylinder, and transition to the wave zone. Proper long-wave oscillations of such cylinder are studied. The electromagnetic energy flux from the cylinder is calculated. These solutions could be applied for description of the electromagnetic field around relativistic jets from active galactic nuclei and quasars and particle acceleration inside jets.

Keywords: accretion disk, X-ray source, jet

1. Introduction

Objects of different scale and nature in the universe – from both young and very old stars to active galactic nuclei (AGN) (Bridle, 1984; Eilek, 1984; Eilek and Hughes, 1990) – show the existence of collimated outbursts or jets. The geometrical sizes of these jets lay between parsecs and megaparsecs. The origin of astrophysical jets is not well understood and only several qualitative mechanisms are proposed. A theory of jets should answer to the question of the origin of relativistic particles in the outbursts from AGN, where synchrotron emission is observed. Relativistic particles, ejected from the central engine, rapidly loose their energy so the problem arises of the particle acceleration inside the jet, see reviews (Begelman et al., 1984; Bisnovatyi-Kogan, 1993).

It is convenient sometimes to investigate jets in a simple model of infinitely long circular cylinder (Chandrasekhar and Fermi, 1953). The magnetic field in collimated jets determines its direction, and the axial current stabilizes the jet's elongated form at large distances from the source (e.g., in AGNs) (Bisnovatyi-Kogan et al., 1969). When observed with high angular resolution these jets show a structure with bright knots separated by relatively dark regions (Bridle, 1984; Eilek, 1984; Thomson et al., 1993). High percentages of polarization, sometimes exceeding 50% in some objects, indicate the nonthermal nature of the radiation, which is well explained as synchrotron emission of the relativistic electrons in a weak but ordered magnetic field. Estimates of the lifetime of these electrons, based on the observed luminosities



Astrophysics and Space Science **297:** 9–20, 2005.
© Springer 2005

and spectra, often give values much less than the kinematic ages t_k/c, where d is the distance of the emitting point from the central source. Because the jet flow is most likely originated from an outburst or continuous outflow from the central source, there is a necessity of continuous re-acceleration of the electrons in the jets in order to explain the observations. The acceleration mechanism for electrons in extragalactic jets proposed in Bisnovatyi-Kogan and Lovelace (1995) considers that intense long-wavelength electromagnetic oscillations accompany a relativistic jet as a result of the non-steady mechanism of the jet's generation in the nucleus of the source. The electromagnetic wave amplitudes envisioned are sufficient to give *in situ* acceleration of electrons to the very high energies observed $>10^{13}$ eV. It was assumed that jets are formed by a sequence of outbursts from the nucleus with considerable charge separation at the moment of the outburst (Bisnovatyi-Kogan et al., 1969). The direction of motion of the outbursts is determined by the large-scale magnetic field. The outbursts are accompanied by an intense electromagnetic disturbance which propagates outward moving with the jet material in the direction of the large scale magnetic field. It was suggested in Bisnovatyi-Kogan et al. (1969) that a toroidal magnetic field, generated during the outbursts is important for the lateral confinement of the jet.

When the plasma density in the surrounding medium is small, the electromagnetic wave generated by the non-potential plasma oscillations of the confined body is emitted outside and can accelerate particles. When the emitted wave is strong enough it washes out the medium around and the density can become very small, consisting only of the accelerated particles. The action of the oscillating knot is similar to the action of a pulsar, considered as an inclined magnetic rotator. Both emit strong electromagnetic waves, which could effectively accelerate particles (Pacini, 1967; Gunn and Ostriker, 1970). Long-periodic proper oscillations in the plasma cylinder with a finite radius, and emission of electromagnetic waves had been studied in Bisnovatyi-Kogan and Lovelace (1995), and in a simpler model in Bisnovatyi-Kogan (1996). Enhanced oscillations in such cylinder have been studied in Bisnovatyi-Kogan (2004). Both models are represented below.

2. Cylinder with Oscillating Current

Consider an infinitely conducting circular cylinder in vacuum. This model is valid at low density in surrounding plasma, which cannot screen the emitting electromagnetic wave. The Maxwell equations are (Landau and Lifshits, 1982)

$$\operatorname{div}\mathbf{B} = 0, \quad \operatorname{rot}\mathbf{B} = \frac{1}{c}\frac{\partial \mathbf{E}}{\partial t} + \frac{4\pi}{c}\mathbf{j}, \tag{1}$$

$$\operatorname{rot}\mathbf{E} = -\frac{1}{c}\frac{\partial \mathbf{B}}{\partial t}, \quad \operatorname{div}\mathbf{E} = 4\pi\rho_e. \tag{2}$$

For periodic oscillations with all values $\sim \exp(-i\omega t)$ they read

$$\operatorname{div}\mathbf{B} = 0, \quad \operatorname{rot}\mathbf{B} = -\frac{i\omega}{c}\mathbf{E} + \frac{4\pi}{c}\mathbf{j}, \quad \operatorname{rot}\mathbf{E} = \frac{i\omega}{c}\mathbf{B}, \quad \operatorname{div}\mathbf{E} = 0. \tag{3}$$

We use the same definitions for all complex values depending on coordinates. Consider an infinitely long cylinder with zero charge density, where in the cylinder coordinate system (r, ϕ, z) the only nonzero components are E_z, B_ϕ, j_z, and $\partial/\partial\phi = \partial/\partial z = 0$. Only two valid equations remain from the system (3):

$$\frac{dE_z}{dr} + \frac{i\omega}{c}B_\phi = 0, \quad \frac{1}{r}\frac{d(rB_\phi)}{dr} + \frac{i\omega}{c}E_z - \frac{4\pi}{c}j_z = 0; \tag{4}$$

from which, we obtain the equation for E_z:

$$\frac{1}{r}\frac{d}{dr}\left(r\frac{dE_z}{dr}\right) + \frac{\omega^2}{c^2}E_z + \frac{4\pi i\omega}{c^2}j_z = 0. \tag{5}$$

3. Vacuum Solution

In the vacuum, $j_z = 0$. Using the non-dimensional variable $x = r\omega/c$, we obtain from (4) and (5)

$$x^2E_z'' + xE_z' + x^2E_z = 0, \quad B_\phi = iE_z'. \tag{6}$$

Here $'$ denotes differentiation over x. Equation (6) belongs to the Bessel type and has a solution

$$E_z = C_1J_0(x) + C_2Y_0(x), \quad B_\phi = -i[C_1J_1(x) + C_2Y_1(x)]. \tag{7}$$

Relations for Bessel functions are (Gradshtein and Ryzhik, 1964)

$$J_0'(x) = -J_1(x), \quad Y_0'(x) = -Y_1(x). \tag{8}$$

The general solution for the physical values, accounting for the time dependence, is obtained from the real part of the complex solution at

$$\exp(-i\omega t) = \cos\omega t - i\sin\omega t, \quad C_1 = C_1^{(r)} + iC_1^{(i)}, \quad C_2 = C_2^{(r)} + iC_2^{(i)}. \tag{9}$$

The general solution in the vacuum is

$$E_z = \left[C_1^{(r)}J_0(x) + C_2^{(r)}Y_0(x)\right]\cos\omega t + \left[C_1^{(i)}J_0(x) + C_2^{(i)}Y_0(x)\right]\sin\omega t, \tag{10}$$

$$B_\phi = -\left[C_1^{(r)}J_1(x) + C_2^{(r)}Y_1(x)\right]\sin\omega t + \left[C_1^{(i)}J_1(x) + C_2^{(i)}Y_1(x)\right]\cos\omega t. \tag{11}$$

The boundary condition far from the cylinder follows from the demand that there exists only an expanding wave. This means that only functions depending on the combination $(x - \omega t)$ survive. Using the asymptotic of Bessel functions at large arguments (Gradshtein and Ryzhik, 1964)

$$J_0(x) \approx \sqrt{\frac{2}{\pi x}} \cos\left(x - \frac{\pi}{4}\right), \quad J_1(x) \approx \sqrt{\frac{2}{\pi x}} \sin\left(x - \frac{\pi}{4}\right),$$
$$Y_0(x) \approx \sqrt{\frac{2}{\pi x}} \sin\left(x - \frac{\pi}{4}\right), \quad Y_1(x) \approx -\sqrt{\frac{2}{\pi x}} \cos\left(x - \frac{\pi}{4}\right), \quad \text{at} \quad x \gg 1. \tag{12}$$

we obtain for the expanding wave $C_1^{(i)} = -C_2^{(r)}$, $C_2^{(i)} = C_1^{(r)}$, leading to the following solution at large distances

$$E_z \approx \sqrt{\frac{2}{\pi x}}\left[C_1^{(r)} \cos\left(x - \frac{\pi}{4} - \omega t\right) + C_2^{(r)} \sin\left(x - \frac{\pi}{4} - \omega t\right)\right],$$
$$B_\phi = -E_z. \tag{13}$$

The general vacuum solution, satisfying conditions at infinity reads as

$$E_z = \left[C_1^{(r)} J_0(x) + C_2^{(r)} Y_0(x)\right] \cos \omega t + \left[-C_2^{(r)} J_0(x) + C_1^{(r)} Y_0(x)\right] \sin \omega t, \tag{14}$$
$$B_\phi = -\left[C_1^{(r)} J_1(x) + C_2^{(r)} Y_1(x)\right] \sin \omega t + \left[-C_2^{(r)} J_1(x) + C_1^{(r)} Y_1(x)\right] \cos \omega t. \tag{15}$$

4. Solution Inside the Cylinder

The equations in the matter are

$$x^2 E_z'' + x E_z' + x^2 E_z + \frac{4\pi i}{\omega} x^2 j_z = 0, \quad B_\phi = i E_z'. \tag{16}$$

A solution of the non-uniform linear equation (16) is a sum of a general solution of the uniform equation, and a particular solution of the non-uniform one $\mathcal{E}_0(x)$.

$$E_z = \mathcal{E}_1 J_0(x) + \mathcal{E}_2 Y_0(x) + \mathcal{E}_0(x). \tag{17}$$

The function $Y_0(x)$ is singular at $x = 0$, so for a finite solution $\mathcal{E}_2 = 0$. We look for a particular solution in the form $E_z = \mathcal{E}(x) J_0(x)$. A first order equation with

respect to $F = \mathcal{E}'$ follows from (16)

$$x^2(F'J_0 + 2FJ_0') + xFJ_0 + \frac{4\pi i}{\omega}x^2 j_z = 0. \tag{18}$$

From this equation we obtain the general solution for the amplitude of the electric field in the matter, in presence of periodic EEF:

$$E_z = -\frac{4\pi i}{\omega}J_0(x)\int_0^x \frac{dy}{yJ_0^2(y)}\int_0^y zJ_0(z)j_z(z)\,dz + \mathcal{E}_1 J_0(x). \tag{19}$$

Consider waves much longer than the radius of the cylinder r_0

$$x_0 = \frac{\omega r_0}{c} \ll 1. \tag{20}$$

Then use the expansion at $x \ll 1$ (Gradshtein and Ryzhik, 1964),

$$J_0 \approx 1 - \frac{x^2}{4}, \quad J_1 \approx \frac{x}{2}, \quad Y_0 \approx \frac{2}{\pi}\ln\frac{x}{2}, \quad Y_1 \approx -\frac{2}{\pi x}. \tag{21}$$

Using (21) we obtain from (19) the solution for long waves

$$E_z = -\frac{2i\omega}{c^2}\int_0^x I_z(y)\frac{dy}{y} + \mathcal{E}_1, \tag{22}$$

where $I_z(r) \equiv I_z(y)$ is the complex amplitude of the electrical current inside a cylindrical radius $r = cy/\omega$

$$I_z = 2\pi\int_0^r j_z r\,dr = 2\pi\frac{c^2}{\omega^2}\int_0^x j_z x\,dx \tag{23}$$

The complex values – the function $I_z(r)$ and the constant $\mathcal{E}_1$ – are

$$I_z = I_z^{(r)} + iI_z^{(i)}, \quad \mathcal{E}_1 = \mathcal{E}_1^{(r)} + i\mathcal{E}_1^{(i)}. \tag{24}$$

5. Matching of Solutions and Long-Wave Limit

The total electrical current through the cylinder $I_0 = I_z(r_0)$, and the fields on its surface (inside) $E_0 = E_z(r_0)$, $B_0 = B_\phi(r_0)$ (real parts of complex relations) are defined as

$$I_0 = I_0^{(r)} \cos\omega t + I_0^{(i)} \sin\omega t,$$
$$E_0 = \left[\frac{2\omega}{c^2}\int_0^{x_0} I_z^{(i)}(y)\frac{dy}{y} + \mathcal{E}_1^{(r)}\right]\cos\omega t + \left[-\frac{2\omega}{c^2}\int_0^{x_0} I_z^{(r)}(y)\frac{dy}{y} + \mathcal{E}_1^{(i)}\right]\sin\omega t,$$
$$B_0 = \left[\frac{2\omega}{c^2}\frac{I_0^{(r)}}{x_0} + \frac{x_0}{2}\mathcal{E}_1^{(i)}\right]\cos\omega t + \left[\frac{2\omega}{c^2}\frac{I_0^{(i)}}{x_0} - \frac{x_0}{2}\mathcal{E}_1^{(r)}\right]\sin\omega t. \tag{25}$$

At small x_0 the external solution on the surface of the cylinder can be written as

$$E_{z0} = \left[C_1^{(r)} + C_2^{(r)}\frac{2}{\pi}\ln\frac{x_0}{2}\right]\cos\omega t + \left[-C_2^{(r)} + C_1^{(r)}\frac{2}{\pi}\ln\frac{x_0}{2}\right]\sin\omega t,$$
$$B_{\phi 0} = -\left[C_1^{(r)}\frac{x_0}{2} - C_2^{(r)}\frac{2}{\pi x_0}\right]\sin\omega t + \left[-C_2^{(r)}\frac{x_0}{2} - C_1^{(r)}\frac{2}{\pi x_0}\right]\cos\omega t. \tag{26}$$

All field components are continuous at the cylinder surface in absence of the surface charges and currents. Matching magnetic and electrical fields (Figure 1) we obtain, using (25) and (26), the coefficients in the solution of the external electromagnetic field, which are determined by the periodic electrical current in the cylinder:

$$C_1^{(r)}\left(\frac{2}{\pi x_0} + \frac{x_0}{\pi}\ln\frac{x_0}{2}\right) = -\frac{2\omega}{c^2}\frac{I_0^{(r)}}{x_0} - \frac{x_0\omega}{c^2}\int_0^{x_0} I_z^{(r)}(y)\frac{dy}{y}, \tag{27}$$
$$C_2^{(r)}\left(\frac{2}{\pi x_0} + \frac{x_0}{\pi}\ln\frac{x_0}{2}\right) = \frac{2\omega}{c^2}\frac{I_0^{(i)}}{x_0} + \frac{x_0\omega}{c^2}\int_0^{x_0} I_z^{(i)}(y)\frac{dy}{y}. \tag{28}$$

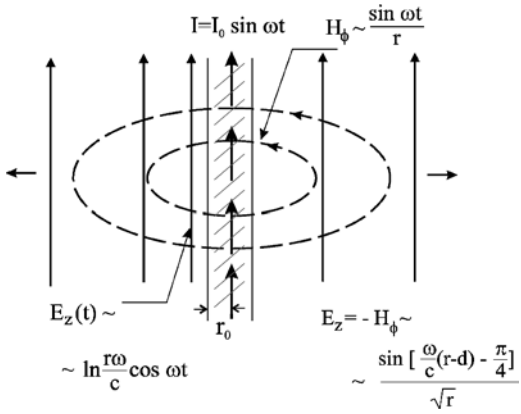


Figure 1. Magnetic and electrical fields around the infinite cylinder with the radius r_0, and low-frequency $\omega \ll c/r_0$, sinusoidal electrical current along the cylinder axis. In the near zone electrical and magnetic fields are varying in antiphase, and far from the cylinder $r \gg c/\omega$ the expanding cylindrical electromagnetic wave is formed, with $E_z = -B_\phi$.

$$\mathcal{E}_1^{(r)} = C_1^{(r)} + C_2^{(r)} \frac{2}{\pi} \ln \frac{x_0}{2} - \frac{2\omega}{c^2} \int_0^{x_0} I_z^{(i)}(y) \frac{dy}{y}, \tag{29}$$

$$\mathcal{E}_1^{(i)} = -C_2^{(r)} + C_1^{(r)} \frac{2}{\pi} \ln \frac{x_0}{2} + \frac{2\omega}{c^2} \int_0^{x_0} I_z^{(r)}(y) \frac{dy}{y}. \tag{30}$$

Consider a case when the resulting electrical current produced by the external EEF is purely sinusoidal, $I_z^{(r)} = 0$. Than it follows from (27) and (30)

$$C_1^{(r)} = 0, \quad \mathcal{E}_1^{(i)} = -C_2^{(r)}. \tag{31}$$

At $x_0 \ll 1$ we neglect the logarithmic terms in (27)–(28), and terms with the integrals in (27)–(30), so the details of the current distribution over the cylinder radius are of a little importance. In this approximation

$$C_2^{(r)} = \frac{\pi\omega}{c^2} I_0^{(i)}, \quad \mathcal{E}_1^{(r)} = \frac{2\omega}{c^2} \ln \frac{x_0}{2} I_0^{(i)}. \tag{32}$$

The solution for the electromagnetic field of the long wave emitted by the cylinder with the sinusoidal electric current, starting from the surface of the cylinder until the wave zone, follows from (14):

$$\begin{aligned} E_z &= \frac{\pi\omega}{c^2} I_0^{(i)} [Y_0(x) \cos\omega t - J_0(x) \sin\omega t], \\ B_\phi &= -\frac{\pi\omega}{c^2} I_0^{(i)} [Y_1(x) \sin\omega t + J_1(x) \cos\omega t]. \end{aligned} \tag{33}$$

Near the cylinder we have, with the account of the expansions (21)

$$\begin{aligned} E_z &= \frac{\pi\omega}{c^2} I_0^{(i)} \left(\frac{2}{\pi} \ln \frac{x}{2} \cos\omega t - \sin\omega t \right) \\ &\approx \frac{2\omega}{c^2} I_0^{(i)} \ln \frac{x}{2} \cos\omega t = \frac{2\omega}{c^2} I_0^{(i)} \ln \frac{r\omega}{2c} \cos\omega t, \end{aligned} \tag{34}$$

$$B_\phi = -\frac{\pi\omega}{c^2} I_0^{(i)} \left(-\frac{2}{\pi x} \sin\omega t + \frac{x}{2} \cos\omega t \right) \approx \frac{2\omega}{c^2 x} I_0^{(i)} \sin\omega t = \frac{2I_0^{(i)}}{cr} \sin\omega t. \tag{35}$$

Note, that in the near zone of the long wave the magnetic field adiabatically follows the current through the cylinder (Landau and Lifshits, 1982). The distribution of the electrical field is similar to the one of the linearly growing current in the cylinder (Bisnovatyi-Kogan, 2003). At large r we obtain from (33), (12) the expanding cylindrical wave

$$\begin{aligned} B_\phi = -E_z &= -\frac{\pi\omega}{c^2} \sqrt{\frac{2}{\pi x}} I_0^{(i)} \sin\left(x - \frac{\pi}{4} - \omega t \right) \\ &= -\frac{1}{c} \sqrt{\frac{2\pi\omega}{cr}} I_0^{(i)} \sin\left[\frac{\omega}{c}(r - ct) - \frac{\pi}{4} \right]. \end{aligned} \tag{36}$$

6. Electromagnetic Energy Flux from Jet

A strong electromagnetic wave generated by oscillations may accelerate effectively particles at large distances from the nucleus near the jet, as well as at larger radii (Bisnovatyi-Kogan and Lovelace, 1995). Let us estimate the energy flux in the electromagnetic wave radiated by the jet of length l, and radius r_0. If n_e is the electron density producing the electrical current, then, the Pointing flux $P = \frac{c}{4\pi}[\mathbf{EB}]$ through the cylinder surface is

$$F = 2\pi r_0 l P = \frac{\pi l \omega}{2c^2} I_0^2. \tag{37}$$

For the amplitude of the electrical current along the cylinder radius $I_0 = \pi r_0^2 n_e c e$, we obtain the energy flux from the jet in the form:

$$F = \frac{\pi^3}{2} e^2 l r_0^4 \omega n_e^2 \approx 2 \times 10^{49} \text{ erg s}^{-1} \frac{l}{1 \text{ kpc}} \left(\frac{r_0}{1 \text{ pc}} \right)^4 \frac{100 \text{ years}}{T} \left(\frac{n_e}{10^{-10} \text{ cm}^{-3}} \right)^2. \tag{38}$$

Here $T = \frac{2\pi}{\omega}$ is the period of the electromagnetic wave. Part of the radiated energy is used for particle acceleration up to very large energies (Bisnovatyi-Kogan and Lovelace, 1995), and support the jet radiation at different energy regions of the electromagnetic spectrum.

7. Generation of Strong Electromagnetic Wave by Proper Oscillations in a Separate Blob.

The mechanism of shock acceleration of particles, often considered (Eilek and Hughes, 1990), is not certain. Actually, it is unlikely that shock acceleration can give a fairly uniform brightness jet as observed in some cases. The mechanisms of magnetic field reconnection (Romanova and Lovelace, 1992) and plasma turbulence acceleration (Eilek and Hughes, 1990) are also highly uncertain. When the plasma density in the surrounding medium is small, the electromagnetic wave generated by the non-potential plasma oscillations of the confined body is emitted outside and can accelerate particles. When the emitted wave is strong enough it washes out the medium around and the density may become very small, consisting only of the accelerated particles. The solution of the whole problem of the dynamical behavior of the confined knots embedded into the large-scale elongated magnetic field and producing the toroidal field can be solved by self-consistent calculations of the knot oscillations, using together the hydrodynamical and complete Maxwell equations. In order to estimate the properties of a long wave radiation by an oscillating knot we solve instead the idealized problem having the analytical solution. Consider

linear plasma oscillations of the infinitely long uniform cylinder. Problems of such kind have been intensively studied for plasma wave-guides (Kondratenko, 1976). The main difference in this problem are the different boundary conditions which suggest a vacuum state around the cylinder. When considering linear electromagnetic oscillations in the static plasma cylinder, only Maxwell equations (3) with time dependence in the form $\sim \exp(-i\omega t)$ are needed. The background constant field $B_z = B_0$ is adopted. The dependence of j on $\mathbf{E}$, $\mathbf{B}$ and B_0 can be obtained, using the expression for the dielectric permeability

$$\epsilon_{ij} = \delta_{ij} + \frac{4\pi i}{\omega}\left[\sigma_{ij}(e) + \sigma_{ij}(p)\right], \quad j_i = \left[\sigma_{ij}(e) + \sigma_{ij}(p)\right] E_j \tag{39}$$

Here we consider for simplicity pure hydrogen plasma. The components for $\sigma_{ij}(\alpha)$ in the case of perfect conductivity are (Kondratenko, 1976)

$$\begin{aligned} \sigma_{11}(\alpha) &= \sigma_{22}(\alpha) = \frac{i}{4\pi}\frac{\omega_{p\alpha}^2\,\omega}{\omega^2 - \omega_{B\alpha}^2}, \\ \sigma_{12}(\alpha) &= -\sigma_{21}(\alpha) = -\frac{1}{4\pi}\frac{\omega_{p\alpha}^2\,\omega_{B\alpha}}{\omega^2 - \omega_{B\alpha}^2}, \quad \sigma_{33}(\alpha) = \frac{i}{4\pi}\frac{\omega_{p\alpha}^2}{\omega} \end{aligned} \tag{40}$$

where $\omega_{p\alpha}$ and $\omega_{B\alpha}$ are the plasma and Larmor frequencies of electrons (e) and protons (p): $\omega_{p\alpha} = \frac{4\pi n_0 e_\alpha^2}{m_\alpha}$, $\omega_{B\alpha} = \frac{e_\alpha B_0}{m_\alpha c}$. In the cylindrical coordinates $(r,\ \phi,\ z)$ with $\frac{\partial}{\partial\phi} = 0$, $\frac{\partial}{\partial z} = ik$ we have from (3) and (39)

$$-ikB_\phi = \frac{4\pi}{c}\,j_r - \frac{i\omega}{c}E_r, \tag{41}$$

$$\begin{aligned} ikB_r - \frac{dB_r}{dr} &= \frac{4\pi}{c}\,j_\phi - \frac{i\omega}{c}E_\phi, \quad \frac{1}{r}\frac{d}{dr}(rB_\phi) = \frac{4\pi}{c}\,j_z - \frac{i\omega}{c}E_z, \\ -ikE_\phi &= \frac{i\omega}{c}B_r, \quad ikE_r - \frac{dE_z}{dr} = \frac{i\omega}{c}B_\phi, \quad \frac{1}{r}\frac{d}{dr}(rE_\phi) = \frac{i\omega}{c}B_z. \end{aligned} \tag{42}$$

We are interested in long wave oscillations with $\omega \ll \omega_{pe}, \omega_{pp}, \omega_{Be}, \omega_{Bp}$, so approximately

$$j_r = -\frac{i}{4\pi}\frac{\omega_{pp}^2\omega}{\omega_{Bp}^2}E_r, \quad j_\phi = -\frac{i}{4\pi}\frac{\omega_{pp}^2\omega}{\omega_{Bp}^2}E_\phi, \quad j_z = -\frac{i}{4\pi}\frac{\omega_{pe}^2}{\omega}E_z. \tag{43}$$

Substituting (43) into (41), (42) we can see that two types of long waves, corresponding to different polarizations, exist independently: electric-type (E) waves

with $B_z = 0$ and nonzero $(E_r,\ E_z,\ B_\phi)$, and magnetic-type (B) waves with $E_z = 0$ and nonzero $(B_r,\ B_z,\ E_\phi)$. The equations for E-wave has a form

$$\frac{d}{dr}\left[\frac{1}{r}\frac{d}{dr}(rZ_E)\right] + \left(\frac{\omega_{pe}^2}{\omega^2} - 1\right)\left(\frac{k^2c_A^2}{c^2} - \frac{\omega^2}{c^2}\right)Z_E = 0, \tag{44}$$

$$\frac{1}{r}\frac{d}{dr}\left(r\frac{dE_z}{dr}\right) + \left(\frac{\omega_{pe}^2}{\omega^2} - 1\right)\left(\frac{k^2c_A^2}{c^2} - \frac{\omega^2}{c^2}\right)E_z = 0, \tag{45}$$

where $Z_E = E_r$ or B_ϕ, and

$$c_A^2 = c^2\left(1 + \frac{\omega_{pp}^2}{\omega_{Bp}^2}\right)^{-1} = c^2\left(1 + \frac{4\pi\rho c^2}{B^2}\right)^{-1} \tag{46}$$

is a speed of the Alfven waves. The equations for a B-wave have the form

$$\frac{d}{dr}\left[\frac{1}{r}\frac{d}{dr}(rZ_B)\right] + \left(\frac{\omega^2}{c_A^2} - k^2\right)Z_B = 0, \tag{47}$$

$$\frac{1}{r}\frac{d}{dr}\left(r\frac{dB_z}{dr}\right) + \left(\frac{\omega^2}{c_A^2} - k^2\right)B_z = 0, \tag{48}$$

where $Z_B = B_r$ or E_ϕ, Outside the cylinder Equations (44), (45), (47), (48) retain their form after substituting c everywhere instead of c_A. Solutions of these equations are given by Bessel functions:

$$Z_{B,E} = Z_{B0,E0}J_1(\kappa_{B,E}r),\ B_Z = B_{Z0}J_0(\kappa_B r),\ E_Z = E_{Z0}J_0(\kappa_E r), \tag{49}$$

where $\kappa_B^2 = \frac{\omega^2}{c_A^2} - k^2$, $\kappa_E^2 = (\frac{\omega_{pe}^2}{\omega^2} - 1)(\frac{k^2c_A^2}{c^2} - \frac{\omega^2}{c^2})$ inside the cylinder. Outside the same solutions (49) are valid with $\kappa^2 = \frac{\omega^2}{c^2} - k^2$, instead of κ_E^2 or κ_B^2. Discrete values of κ_B and κ_E are determined by the dispersion equation, obtained from the boundary conditions on the surface of the cylinder. For B-wave the components B_r and E_ϕ are continuous on the boundary and $B_z = 0$ is taken at the boundary $r = r_0 - 0$. That leads to the relations

$$\kappa_{Bn}r_0 = \lambda_{0n},\quad \omega_n^2 = c_A^2\left(k^2 + \frac{\lambda_{0n}^2}{r_0^2}\right). \tag{50}$$

For E-wave E_z is continuous and $E_r = 0$ at $r = r_0 - 0$, so we have

$$\kappa_{Ei}r_0 = \lambda_{1i},\quad \omega_i^2 = c_A^2k^2\left(1 + \frac{\lambda_{1i}^2c^2}{r_0^2\omega_{pe}^2}\right)^{-1}, \tag{51}$$

where λ_{0n} and λ_{1i} are zero's of the Bessel functions $J_o(x)$ and $J_1(x)$. We have then for the wave vectors outside the cylinder

$$\kappa_n^2 = \frac{c_A^2}{c^2}\frac{\lambda_{0n}^2}{r_0^2} - k^2\left(1 - \frac{c_A^2}{c^2}\right) \ (B), \quad \kappa_i^2 = -k^2\left(1 - \frac{c_A^2/c^2}{1 + \frac{\lambda_{1i}^2 c^2}{r_0^2\omega_{pe}^2}}\right) \ (E). \quad (52)$$

It is clear from (46) that $\kappa_i^2 < 0$ for E-waves, but for each k there is n_* such that $\kappa_n^2 > 0$ for $n > n_*$ and Alfven B-wave is transforming into electromagnetic one. The vacuum values of $B_r(r_0+0)$ and $E_\phi(r_0+0)$ at the boundary are obtained from the continuity conditions, and the outer value of $B_z(r_0+0)$ is found from the last Equation in (42). The jump $\Delta B_z = B_z(r_0+0)$ on the boundary determines the induced surface current i_ϕ. The very long electromagnetic wave emitted with the amplitude E_ϕ could accelerate particles up to energies $\epsilon \approx e\,E\,r_0 \approx \alpha 10^3$ ergs for $r_0 = 1$ pc and $E = \alpha \times 10^{-6}$ in CGS. The real energy of the accelerated particles could be much less due to the radiation losses.

8. Conclusion

The similarity of the acceleration mechanisms of the particles in both pulsars and relativistic jets could be a reason for the similarity of the high-energy radiation around 100 Mev observed by EGRET in number of radiopulsars (Thompson et al., (1992); quasars and AGN (Thompson et al., 1993).

Acknowledgement

The author is grateful to the organizers for support and hospitality. Partial funding provided by RFBR grant 02-02-16900, INTAS grant 00491, and Astronomy Programm "Nonstationary phenomena in astrophysics".

References

Begelman, M.C., Blandford, R.D. and Rees, M.J.: 1984, *Rev. Mod. Phys.* **56**, 255.

Bisnovatyi-Kogan, G.S.: 1993, in: L. Errico and A.A. Vittone (eds.), *Stellar Jets and Bipolar Outflows*, Kluwer.

Bisnovatyi-Kogan, G.S.: 1996, *Formation of Extragalactic Jets and Particle Acceleration. Proceedings of the First International Meeting on Kosmomicrophysics "Kosmion"*, Moscow. Edition Frontiers, p. 333.

Bisnovatyi-Kogan, G.S.: 2003, *Month. Not. R. Astronom. Soc.* **343**, 771.

Bisnovatyi-Kogan, G.S.: 2004, *Astrofizika* **47**, 473.

Bisnovatyi-Kogan, G.S., Komberg, B.V. and Fridman, A.M.: 1969, *Astron. Zh.* **46**, 465.

Bisnovatyi-Kogan, G.S. and Lovelace R.V.E.: 1995, *Astron. Ap.* **296**, L17.
Bridle, A.H.: 1984, *Phenomenology of Extragalactic Radio Jets. Proceedings of NRAO Workshop No. 9 "Physics of Energy Transport in Extragalactic Radio Sources"*. (Greenbank: NRAO), p. 1.
Chandrasekhar, S. and Fermi, E.: 1953, *Astrophys. J.* **118**, 116.
Eilek, J.A.: 1984, *The Physics of Particle Acceleration in Radio Galaxies. Proceedings of NRAO Workshop No. 9 "Physics of Energy Transport in Extragalactic Radio Sources"*. (Greenbank: NRAO), p. 216.
Eilek, J.A. and Hughes, P.E.: 1991, in: P.E. Hughes (ed.), *Beams and Jets in Astrophysics*, Cambridge University Press, p. 428.
Gradshtein, I.S. and Ryzhik, I.M.: 1964, *Tables of Integrals, Sums and Products*. Nauka, Moscow.
Gunn, J. and Ostriker, J.: 1971, *Astrophys. J.* **165**, 523.
Kondratenko, A.N.: 1976, *Plasma Waveguides*. Atomizdat, Moscow.
Landau, L.D. and Lifshits, E.M.: 1982, *Electrodynamics of Continuous Media*. Nauka, Moscow.
Pacini, F.: 1967, *Nature* **216**, 567.
Romanova, M.M. and Lovelace, R.V.E.: 1992, *Astron. Ap.* **262**, 26.
Thompson, D.J., Arzoumanian, Z., Bertsch, D.L. et al.: 1992, *Nature* **359**, 615.
Thompson, D.J., Bertsch, D.L., Dingus, B.L. et al.: 1993, *Astrophys. J. Lett.* **415**, L13.
Thomson, R.C., Mackay, C.D. and Wright, A.E.: 1993, *Nature* **365**, 133.

THE CONVERTER MECHANISM OF PARTICLE ACCELERATION AND ITS APPLICATIONS TO THE UNIDENTIFIED EGRET SOURCES

E.V. DERISHEV[1], F.A. AHARONIAN[2], V.V. KOCHAROVSKY[1] and Vl.V. KOCHAROVSKY[1]

[1]*Institute of Applied Physics, 46 Ulyanov st., Nizhny Novgorod, Russia; E-mail: derishev@appl.sci-nnov.ru*

[2]*Max-Planck-Institut für Kernphysik, Saupfercheckweg 1, Heidelberg, Germany*

(Received 22 June 2004; accepted 14 July 2004)

Abstract. We discuss the properties of gamma-ray radiation accompanying the acceleration of cosmic rays via the converter mechanism. The mechanism exploits multiple photon-induced conversions of high-energy particles from charged into neutral state (namely, protons to neutrons and electrons to photons) and back. Because a particle in the neutral state can freely cross the magnetic field lines, this allows to avoid both particle losses downstream and reduction in the energy gain factor, which normally takes place due to highly collimated distribution of accelerated particles. The converter mechanism efficiently operates in relativistic outflows under the conditions typical for Active Galactic Nuclei, Gamma-Ray Bursts, and microquasars, where it outperforms the standard diffusive shock acceleration.

The accompanying radiation has a number of distinctive features, such as an increase of the maximum energy of synchrotron photons and peculiar radiation beam-pattern, whose opening angle is much wider at larger photon energies. This provides an opportunity to observe off-axis relativistic jets in GeV–TeV energy range. One of the implications is the possibility to explain high-latitude unidentified EGRET sources as off-axis but otherwise typical relativistic-jet sources, such as blazars.

Keywords: unidentified sources, gamma-ray emission, cosmic rays

1. Introduction

The production of highest-energy (10^{20} eV) cosmic rays is possible only for a limited class of astrophysical objects, most likely those with relativistic outflows (Aharonian et al., 2002). The widely accepted view holds that the acceleration of high-energy cosmic rays proceeds through multiple reflections from inhomogeneities of magnetic field in the environments where large velocity gradients are present, e.g., (Malkov and Drury, 2001; Berezhko, 1981; Ostrowski, 1998). This mechanism works equally well for shocks and shear flows, and the emerging spectra of accelerated particles are such, that only a small fraction (of the order of few per cent) of the total energy budget is contained in the most energetic particles. Ultrarelativistic shocks are usually regarded as especially promising: the energy gain at each particle-shock encounter can approach the factor of $\sim\Gamma^2$, where Γ is the Lorentz factor of the shock. Such a scenario was suggested as the dominant



Astrophysics and Space Science **297:** 21–30, 2005.
© Springer 2005

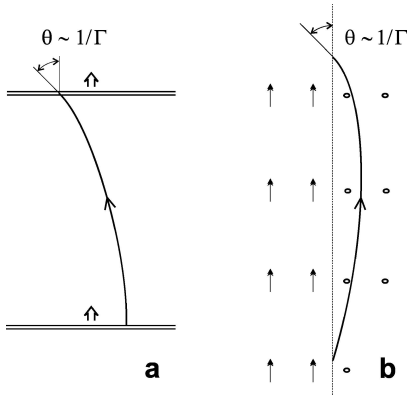


Figure 1. The acceleration cycle in the standard mechanism for a shock (a) and for a shear flow (b). The thick solid line shows the particle's trajectory. The magnetic field is perpendicular to the picture plane. The locations of the shock at the moments of particle escape from the shock and subsequent catch-up are shown as double lines. The shear flow boundary is shown by thin dotted line.

acceleration mechanism for relativistic outflows, e.g., in Gamma-Ray Bursts (GRBs) (Levinson and Eichler, 1993; Vietri, 1995; Waxman, 1995).

However, in the standard acceleration theory, the energy gain of $\sim\Gamma^2$ occurs only at the first cycle, while the subsequent ones result in energy gain of ~ 2 each (Bednarz and Ostrowski, 1998; Achterberg et al., 2001). The reason is that the shock catches up to the reflected particle (or the particle crosses the boundary of the shear flow) when its trajectory makes an angle of $\simeq 2/\Gamma$ to the shock normal (or bulk velocity vector), while keeping the Γ^2 energy gain would require isotropization. The smallness of this angle is apparent for the case of shear flow (see Figure 1b). For shocks it is a consequence of relativistic motion (Figure 1a). Indeed, the component of particle velocity along the shock normal becomes smaller than the velocity of the shock itself as soon as the angle between the particle's momentum and the shock normal grows larger than $1/\Gamma$.

So, there are concerns about the standard mechanism with its relatively small acceleration rate, causing leakage of accelerated particles and making it sensitive to the magnetic field geometry. To reduce these difficulties and to make the acceleration process more robust, we proposed the converter acceleration mechanism (Derishev et al., 2003), which efficiently operates in relativistic outflows under the conditions typical for Active Galactic Nuclei (AGNs), GRBs, and microquasars.

Paradoxically, interactions with photons, which have been always treated as dissipative processes leading to degradation of particle energy, in this scenario play positive role: they allow (through the charge-changing particle conversion) to keep the Γ^2 energy gain up to the largest particle energies. Indeed, a particle in the neutral state can freely cross the magnetic field lines, that allows to avoid both particle losses downstream and reduction in the energy gain factor, which normally takes place due to highly collimated distribution of accelerated particles.

2. The Converter Acceleration Mechanism

The photopionic reactions have a threshold $\Delta \simeq 150$ MeV in the nucleon comoving frame. At energies well above the threshold, they convert proton into neutron (and vice versa) with the probability of $\sim 1/2$. One can consider an accelerated proton as a particle (nucleon), which has both charged and neutral states and spends roughly equal time in each state. In a similar way, one can consider the electron cycle, where the electron(positron)/photon particle, which exists through a sequence of alternating inverse Compton scattering and pair production events, is accelerated.

The deviation from the standard acceleration mechanism occurs when the particle leaves the shock front in the neutral state and, its trajectory being not affected by the magnetic field, outruns the shock by a large distance. When a transition from neutral to charged state occurs (it may be the spontaneous decay of a neutron), the charged particle has a handicap which allows it to be deflected by an angle much larger than $2/\Gamma$ before the encounter with the shock (see Figure 2). Thus, the energy gain much larger than 2 becomes possible; it amounts to Γ^2 in the case of full isotropization.

We expect that the converter mechanism never operates alone and the standard Fermi-type mechanism competes with it. The new (converter) mechanism has smaller acceleration rate at low energies, but just the same (with one exception, see below) absolute, i.e., ignoring radiative losses, energy limit for the accelerated particles. However, in the converter mechanism, this energy is attained in much fewer steps, with potentially much more particles survived. Moreover, the particles – when converted into neutral state – can escape from regions located deep inside the relativistic flow, which further reduces irreversible particle losses in the

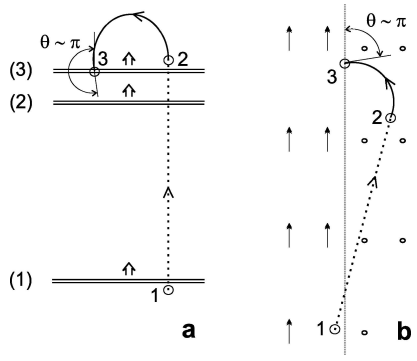


Figure 2. The acceleration cycle in the converter mechanism for a shock (a) and for a shear flow (b). The particle's trajectory is shown by thick dotted line (neutral state) and thick solid line (charged state). The magnetic field is perpendicular to the picture plane. Numbered are the moments of particle conversion into neutral state, transition from neutral to charged state, and subsequent return to the flow. The locations of the shock at the corresponding moments are shown by double lines. The shear flow boundary is shown by thin dotted line.

downstream. So, at the highest energy part of the distribution almost all particles are produced by the converter mechanism, regardless of its performance at low energies.

The main parameter, characterizing the converter acceleration mechanism, is the optical depth for charge-changing reactions, i.e., the ratio of the light-crossing time to the timescale of the particle-photon interactions. Because of relatively large cross-section, the optical depth for photon-induced reactions is not a problem for the electron cycle, but it could be a limiting factor for the proton cycle. Let us estimate the optical depth for photopionic reactions in three cases. For inner jets in AGNs we obtain (taking into account only comoving photon fields)

$$\tau \simeq 0.1\left(\frac{L(\varepsilon_*)}{10^{45}\,\mathrm{erg\,s^{-1}}}\right)\left(\frac{\varepsilon}{10^{18}\,\mathrm{eV}}\right)\left(\frac{10}{\Gamma}\right)^4\left(\frac{10^{15}\,\mathrm{cm}}{R}\right). \tag{1}$$

Here $L(\varepsilon_*)$ is the apparent luminosity per logarithmic frequency interval at photon energy $\varepsilon_* = 2mc^2\Delta/(\varepsilon\Theta^2)$, where the interaction with target photons is the most efficient, ε the energy of accelerated particle, R the distance from the central engine, Θ the beaming angle of target radiation field ($\Theta \sim 1/\Gamma$ for comoving photon field), Δ and m are the threshold and the mass of the particle for one of the possible cycles.

The radiation from AGN broad-line regions creates the optical depth

$$\tau \sim 5 \times 10^{-2}\left(\frac{L}{10^{44}\,\mathrm{erg\,s^{-1}}}\right)\left(\frac{10\,\mathrm{eV}}{\bar{\varepsilon}}\right)\left(\frac{10^{17}\,\mathrm{cm}}{R}\right), \tag{2}$$

which does not depend on the particle's energy: for all particles with energy $\varepsilon > 2mc^2\Delta/\bar{\varepsilon} \simeq 5 \times 10^{16}$ eV the number of target photons is essentially constant because of their relatively narrow spectral distribution, where the majority of photons have energies around $\bar{\varepsilon}$.

In GRBs, the optical depth due to comoving photons is

$$\tau \simeq 3 \times 10^{-3} \times \left(\frac{E(\varepsilon_*)}{10^{52}\,\mathrm{erg}}\right)\left(\frac{\varepsilon}{10^{16}\,\mathrm{eV}}\right)\left(\frac{100}{\Gamma}\right)^2\left(\frac{10^{16}\,\mathrm{cm}}{R}\right)^2. \tag{3}$$

The conversion probability $p_{\mathrm{cn}} = [1-\exp(-p_c\tau)]$ in the proton cycle is usually, though not always, much smaller than unity. Here $p_c = 0.3 \div 0.5$ is the probability of charge change in photopionic reactions.

3. Energy Gain

Assuming that momenta of particles are isotropized in the comoving frame upon their encounter with the relativistic flow, one gets the average energy gain per cycle

$$g \simeq \frac{(\Gamma\theta)^2}{2}, \tag{4}$$

where θ is the angle between the particle's momentum and the flow's velocity (deflection angle) at the moment of encounter. If the deflection angle is small, $\theta \ll 1$, then it grows linearly with distance ℓ (travelled by the particle in the charged state) $\theta = \theta_0 + \ell/r_g$ in uniform magnetic field, while in chaotic field it behaves as $\langle\theta\rangle = \sqrt{\theta_0^2 + \ell\ell_c/r_g^2}$ on average. Here θ_0 is the initial deflection angle, measured at the time of conversion from neutral to charged state, $\ell_c < \ell$ the turbulence scale of the magnetic field, and r_g the gyroradius of the particle, calculated as if the field were uniform.

In the case of acceleration at the shock front, the shock catches up to the particle when the displacement of the particle along the shock normal, after it crossed the shock, becomes equal to the distance travelled by the shock front, i.e.,

$$\frac{\sqrt{\Gamma^2 - 1}}{\Gamma}(\ell_0 + \ell) = \ell_0 \cos\theta_0 + \int_0^{\ell} \cos\theta \, d\ell', \tag{5}$$

where ℓ_0 is the distance travelled by the particle in the neutral state after it left the relativistic flow, and we neglected the difference between particle's velocity and the velocity of light.

In the uniform magnetic field, the deflection angle is

$$\theta \simeq \left\{\frac{3\,\ell_0}{r_g\Gamma^2}\left(1 - \Gamma^2\theta_0^2\right)\right\}^{1/3} \sim \left(\frac{3\,\ell_0}{r_g\Gamma^2}\right)^{1/3}, \tag{6}$$

provided $r_g/\Gamma \ll \ell_0 \ll r_g\Gamma^2$. For smaller initial displacement, one arrives to the result of standard theory $\theta \simeq 1/\Gamma$, whereas for larger displacement the deflection angle is $\theta \sim 1$. If one substitutes ℓ_0 by R, then the applicability limits give two critical energies (both measured at the end of acceleration cycle – point 3 in Figure 2):

$$\varepsilon_1 = \Gamma eBR \quad \text{and} \quad \varepsilon_2 = eBR, \tag{7}$$

where e is the charge of the accelerated particle and B the magnetic field strength. The acceleration proceeds with the maximum energy gain of $\sim \Gamma^2$ up to the energy ε_2, whereas above the energy ε_1 there is no advantage over the standard mechanism

in the energy gain. At the same time, ε_1 is equal to the maximum energy, achievable in the standard mechanism.

In the chaotic magnetic field

$$\langle\theta\rangle \simeq \left\{\frac{2\,\ell_c\ell_0}{r_g^2\Gamma^2}\left(1-\Gamma^2\theta_0^2\right)\right\}^{1/4} \sim \left(\frac{2\,\ell_c\ell_0}{r_g^2\Gamma^2}\right)^{1/4} \tag{8}$$

for $r_g^2/\,\Gamma^2 \ll \ell_c\ell_0 \ll \Gamma^2 r_g^2$, and the critical energies are equal,

$$\varepsilon_1 = \varepsilon_2 = \Gamma eB\sqrt{R\ell_c}\,. \tag{9}$$

In the case of shear flow, the catch-up condition reads

$$\ell_0 \sin\theta_0 = \int_0^{\ell} \sin\theta\, d\ell'\,. \tag{10}$$

The deflection angle is

$$\theta \simeq \left(2\frac{\ell_0\theta_0}{r_g}\right)^{1/2} \sim \left(\frac{2\,\ell_0}{r_g\Gamma}\right)^{1/2} \tag{11}$$

for uniform field ($r_g/\,\Gamma \ll \ell_0 \ll r_g\Gamma$) and

$$\langle\theta\rangle \simeq \left(\frac{3}{2}\frac{\ell_0\ell_c\theta_0}{r_g^2}\right)^{1/3} \sim \left(\frac{3}{2}\frac{\ell_0\ell_c}{r_g^2\Gamma}\right)^{1/3} \tag{12}$$

for chaotic field ($r_g^2/\,\Gamma^2 \ll \ell_0\ell_c \ll r_g^2\Gamma$).

The critical energies in the case of acceleration by a shear flow are

$$\varepsilon_1 = \varepsilon_2 = \Gamma eBR \tag{13}$$

for uniform magnetic field and

$$\varepsilon_1 = \Gamma eB\sqrt{R\ell_c} \quad \text{and} \quad \varepsilon_2 = \Gamma^{\frac{3}{2}} eB\sqrt{R\ell_c} \tag{14}$$

for chaotic field. It is interesting to note, that in the latter case the maximum energy achievable in the converter mechanism appears to be $\Gamma^{1/2}$ times larger than that in the standard mechanism.

4. Spectrum of the Accompanying Emission and Beam-Pattern Broadening

The synchrotron emission of the accelerated particles has two distinctive features. First, the maximum energy of synchrotron photons for the converter mechanism is Γ^2 times larger than for the standard one. Indeed, the acceleration cycle in the standard mechanism lasts $\sim r_g/c$ and the energy increment is $\sim\varepsilon$, which gives the acceleration rate $\dot{\varepsilon}\sim\varepsilon c/r_g$. The maximum admissible rate of synchrotron losses is just the same, so that the particle's energy is limited to

$$\varepsilon_{\rm cr} = \frac{3}{2}\frac{(mc^2)^2}{\sqrt{e^3 B}} \tag{15}$$

and so is the cut-off frequency of their synchrotron emission:

$$\nu_{\rm cr} \simeq \frac{0.5}{\pi}\frac{eB}{mc}\left(\frac{\varepsilon_{\rm cr}}{mc^2}\right)^2, \qquad h\nu_{\rm cr} \simeq 270\, mc^2\,. \tag{16}$$

Doppler boosting gives additional factor Γ. The definition of critical energy is easily generalized for the case of predominantly inverse Compton losses, or the case of chaotic magnetic field, or both.

The same reasoning is valid for the converter mechanism, in which the cycle duration is $\geq r_g/c$ and the energy increment is $\leq\Gamma^2\varepsilon$. This gives Γ^2 times larger limit for the energy of accelerated particle, which translates into factor Γ^4 in Eq. (16). When the accelerated particle enters the relativistic flow having an energy larger than $\varepsilon_{\rm cr}$, the synchrotron emission is so efficient, that the particle looses most of its energy before it is deflected by an angle ~ 1. Thus, the resulting synchrotron emission is beamed backwards in the flow comoving frame. The beaming angle is of $\sim 1/\Gamma$ for the most energetic particles with $\varepsilon\sim\Gamma^2\varepsilon_{\rm cr}$, and such an emission appears redshifted by the factor Γ in the laboratory frame, in contrast to the standard mechanism, in which the synchrotron emission is blueshifted by the same factor Γ.

Taking into account all factors, we find that for an observer resting in the laboratory frame, the maximum frequency of synchrotron photons accompanying the converter-acceleration is $\Gamma^3\nu_{\rm cr}$, that is by the factor of $\sim\Gamma^2$ larger than in the standard mechanism. Moreover, this highest-frequency synchrotron radiation is quasi-isotropic in the laboratory frame, which is another distinctive feature of the converter mechanism.

Generally speaking, the converter mechanism makes neutral beams of all kinds (photon, neutrino and neutron beams) broader than $1/\Gamma$, so that they can be seen even if the jet that produced them is not pointing towards the observer. The jet sources, which are observed off-axis owing to the effect of beam pattern broadening should exhibit very hard spectra. Indeed, the emission with broadened beam pattern is produced by high-energy particles which cool radiatively over a distance smaller than their gyroradius. For such particles the deflection angle (and hence the width

of the beam pattern) is a function of their energy. An observer situated at a large angle to the jet axis effectively sees the particle distribution devoid of its low-energy part, whose emission can only be seen at smaller viewing angles. Therefore, the off-axis emission is the hardest possible – it is essentially as hard as the spectrum of an individual particle.

Let us consider a quantitative example. Assume a continuous jet and a power-law injection of relativistic particles $d\dot{N}/d\varepsilon \propto \varepsilon^{-s}$, where $s > 1$. The majority of injected particles penetrate deep into downstream, loose energy through synchrotron and other types of radiation, and form a cooling distribution $dN/d\varepsilon = \dot{N}/\dot{\varepsilon} \propto t_c \varepsilon^{-s}$. The cooling timescale $t_c = \varepsilon/\dot{\varepsilon}$ is inversely proportional to the particle's energy ($t_c \propto \varepsilon^{-1}$) in the case of synchrotron losses or inverse Compton losses in the Thomson regime, but it can be nearly energy-independent if the dominant loss mechanism is inverse Compton in the Klein–Nishina regime.

Define brightness as $B = \nu\, dL_\nu/d\Omega$, where $d\Omega$ is the solid angle element, and $\phi'(\varepsilon)$ as the maximum deflection angle of an injected particle (measured at the time when it looses half of its energy) with respect to the axis directed counter to the jet's velocity. Here and below the prime denotes the jet comoving frame for angles, frequencies, and brightness.

The angle-averaged brightness in the comoving frame can be derived in a straightforward way. Then we take into account that emission at frequencies above ν_{cr} is produced by particles with energies larger than ε_{cr} and therefore is concentrated within a cone with opening angle $\phi'(\varepsilon)$. So, the brightness at small angles $1/\Gamma \ll \phi' \ll 1$ is given by

$$B'(\nu') \propto \begin{cases} t_c \nu'^{\frac{-s+3}{2}} & \nu' < \nu_{cr} \\ \dfrac{t_c}{\phi'^2} \nu'^{\frac{-s+3}{2}} & \nu_{cr} < \nu' < \nu'_{max} = \left(\dfrac{\varepsilon(\phi')}{\varepsilon_{cr}}\right)^2 \nu_{cr}, \end{cases} \tag{17}$$

where we assumed that the spectrum of an individual particle is monochromatic with frequency $\nu' \propto \varepsilon^2$. The spectrum (17) cuts off above ν'_{max}, except for small angles $\phi' < 1/\Gamma$.

The maximum deflection angle can be found from the following equations:

$$\phi'^2 \simeq \frac{\varepsilon_{cr}^2}{t_c(\varepsilon_{cr})} \frac{t_c(\varepsilon)}{\varepsilon^2} \tag{18}$$

for chaotic magnetic field and

$$\phi' \simeq \frac{\varepsilon_{cr}}{t_c(\varepsilon_{cr})} \frac{t_c(\varepsilon)}{\varepsilon} \tag{19}$$

for quasi-uniform magnetic field. In the case where $t_c \propto \varepsilon^{-1}$, the spectral index between ν_{cr} and ν'_{max} increases by 1.5 and 2 for chaotic and quasi-uniform magnetic

field, respectively. For an injected particle distribution with indices s smaller than 10/3 or 13/3 (chaotic or quasi-uniform magnetic field, respectively), that includes the typical assumption $s \simeq 2$, the resulting spectrum formally appears to be harder than the low-frequency asymptotic for the synchrotron emission of an individual particle. This means that in the above frequency range, as well as immediately below $\nu_{\rm cr}$, the spectrum is determined by the low-frequency emission of the most energetic particles.

The angle (with respect to the jet's velocity), frequency, and brightness in the laboratory frame are related to the comoving-frame values as follows:

$$\cos\phi = \frac{\beta - \cos\phi'}{1 - \beta\cos\phi'}, \tag{20}$$

where $\beta = \sqrt{1 - \Gamma^{-2}}$, and

$$B(\nu) = \delta^3 B'(\nu'), \tag{21}$$

$$\nu = \delta\nu', \tag{22}$$

where $\delta = \Gamma(1 - \beta\cos\phi')$ is the Doppler factor. For angles $1/\Gamma \ll \phi' \ll 1$ one can use approximate relations: $\phi \simeq 2(\Gamma\phi')^{-1}$ and $\delta \simeq \Gamma\phi'^2/2$.

It is noteworthy that the cut-off frequency of the emission observed at an angle $1/\Gamma \ll \phi \ll 1$ to the jet's axis can be expressed via the cooling timescale

$$\nu_{\rm max}(\phi) \simeq \frac{\Gamma}{2}\nu_{\rm cr} \times \begin{cases} t_{\rm c}(\varepsilon)/t_{\rm c}(\varepsilon_{\rm cr}) & \text{for the chaotic field} \\ \left(t_{\rm c}(\varepsilon)/t_{\rm c}(\varepsilon_{\rm cr})\right)^2 & \text{for the quasi-uniform field.} \end{cases} \tag{23}$$

Here $\varepsilon(\phi)$ is the energy of particles whose beam-pattern width is equal to ϕ. In the case of synchrotron losses, where $t_{\rm c} \propto \varepsilon^{-1}$, the dependencies of the observed cut-off frequency on the viewing angle are $\nu_{\rm max} \propto \phi^{-2/3}$ for the chaotic field and $\nu_{\rm max} \propto \phi^{-1}$ for the quasi-uniform field. They are much weaker than the relation $\nu_{\rm max} \propto \phi^{-2}$, which stems from the Doppler factor alone. Moreover, prevalence of the inverse Compton losses may cancel out or even reverse the above dependencies.

5. Conclusions and Implications

The proposed converter mechanism, which operates via continuous conversion of accelerated particles from charged into neutral state and back, is efficient for acceleration of both protons and electrons/positrons. It is capable of producing the highest-energy ($>10^{20}$ eV) cosmic rays in either GRB or AGN environments. With a much lower energy limit, the mechanism works in microquasars as well.

Despite certain similarity to the standard acceleration mechanism, the converter mechanism violates some of its inherent relations. For example, the maximum attainable particle energy is $\Gamma^{1/2}$ times larger than in the standard mechanism, if the acceleration occurs in a shear flow with chaotic ambient magnetic field.

Some peculiarities of the accompanying emission can be a tell-tale sign of the converter mechanism. The maximum energy of accompanying synchrotron photons appears to be Γ^2 times larger than in the standard acceleration mechanism. A beam pattern wider than $1/\Gamma$ is characteristic for any type of accompanying emission (synchrotron radiation at highest energies, neutrino emission or photons from pion decay), as well as for the escaping neutrons. This distinctive feature of the converter mechanism opens an interesting possibility for observation of the off-axis blazars and GRBs. The harder spectrum at large viewing angles can explain the phenomenon of unidentified gamma-ray sources. In addition, a population-synthesis survey of off-axis sources will be able to reveal the details and relative importance of the electron cooling processes.

Acknowledgements

E.V. Derishev acknowledges the support from the Russian Science Support Foundation. This work was also supported by the RFBR Grant No. 02-02-16236, the President of the Russian Federation Program (Grant No. NSh-1744.2003.2), and the program "Nonstationary Phenomena in Astronomy" of the Presidium of the Russian Academy of Science.

References

Aharonian, F.A., Belyanin, A.A., Derishev, E.V., Kocharovsky, V.V. and Kocharovsky, Vl.V.: 2002, *Phys. Rev. D* **66**, 023005.
Malkov, M.A. and Drury, L.O'C.: 2001, *Rep. Prog. Phys.* **64**(4), 429.
Berezhko, E.G.: 1981, *JETP Lett.* **33**(8), 399.
Ostrowski, M.: 1998, *A&A* **335**, 134.
Levinson, A. and Eichler, D.: 1993, *ApJ* **418**, 386.
Vietri, M.: 1995, *ApJ* **453**, 883.
Waxman, E.: 1995, *Phys. Rev. Lett.* **75**, 386.
Bednarz, J. and Ostrowski, M.: 1998, *Phys. Rev. Lett.* **80**, 3911.
Achterberg, A., Gallant, Y.A., Kirk, J.G. and Guthmann, A.W.: 2001, *MNRAS* **328**, 393.
Derishev, E.V., Aharonian, F.A., Kocharovsky, V.V. and Kocharovsky, Vl.V.: 2003, *Phys. Rev. D* **68**, 043003.

AN EXAMINATION OF CANDIDATE AGN COUNTERPARTS TO UNIDENTIFIED EGRET SOURCES

PHILIP G. EDWARDS

Institute of Space and Astronautical Science, Japan Aerospace Exploration Agency, Sagamihara, Kanagawa, Japan; E-mail: pge@vsop.isas.jaxa.jp

(Received 6 July 2004; accepted 2 August 2004)

Abstract. Radio observations of candidate active galactic nucleus counterparts to eight EGRET sources with $|b| > 9^\circ$ are examined, and several new identifications suggested. Preference is given to the use of all-sky, flux-density limited surveys in searching for counterparts and attention is drawn to the importance of not relying exclusively on spectral indices inferred from single-dish observations.

Keywords: radio surveys, VLBI, AGN

1. Introduction

The third EGRET catalog (Hartman et al., 1999) contains 271 sources detected at energies greater than 100 MeV. Excluding the 1991 solar flare and eight sources noted as being possible artifacts, there are 185 sources with $|b| > 10^\circ$ and 77 sources with $|b| < 10^\circ$. The latter contains a significant galactic population of sources, likely to contain pulsars, pulsar wind nebulae, supernova remnants and other sources (Hartman et al., 1999; Gehrels et al., 2000).

Mattox et al. (1997) demonstrated that EGRET was clearly detecting the blazar class of active galactic nuclei (AGN) and Hartman et al. (1999) and Mattox et al. (2001), among others, have suggested counterparts for a number of EGRET sources. More recently, Sowards-Emmerd et al. (2003, 2004) have identified blazar counterparts for $\sim$70% of sources with $|b| > 10^\circ$. Their inability to find candidate counterparts for the remaining $\sim$30% led them to posit the existence of a new extragalactic population or a population of Galactic objects with a large scale height.

Sowards-Emmerd et al. (2003, 2004) used the Cosmic Lens All-Sky Survey (CLASS) (Myers et al., 2003) as the primary catalog for their northern survey. Although this survey contains valuable information on many potential counterparts, its selection criteria are biased against compact nuclei embedded in more extended radio structure. For this reason, candidate counterparts are found here by reference to all-sky surveys: both single dish, such as GB6 (Gregory et al., 1996) and PMN (Griffith et al., 1994; Wright et al., 1994; Griffith et al., 1995; Wright et al., 1996) and interferometric, such as NVSS (Condon et al., 1998).



Astrophysics and Space Science **297:** 31–41, 2005.
© Springer 2005

TABLE I

Characteristics of the gamma-ray sources examined in this paper

Source	l	b	TS	γ	δ	3EG	MHR	SE
3EG J0118+0248	136.23	−59.36	4.5	2.63	1.18	a	a	Aaa
3EG J0416+3650	162.22	−9.97	5.3	2.59	0.59	a	U	N
3EG J1308+8744	122.74	29.38	4.9	3.17	0	U	U	N
3EG J1607−1101	0.91	29.05	4.1	–	1.45	U	U	Aaa
3EG J1735−1500	10.73	9.22	5.4	3.24	0.87	U	U	A
3EG J1813−6419	330.04	−20.32	4.2	2.85	0	U	a	–
3EG J1935−4022	358.65	−25.23	5.2	2.86	1.34	A	aa	–
3EG J1959+6342	96.61	17.10	4.9	2.45	0	U	a	A

The significance, TS, and photon spectral index, γ, are from the third EGRET catalog, 3EG (Hartman et al., 1999). The variability index, δ, is from Nolan et al. (2003). MHR refers to Mattox et al. (2001) and SE to Sowards-Emmerd et al. (2003, 2004). A high confidence identification is given by 'A' and a lower confidence association by 'a'. Two plausible lower confidence associations for a given source are denoted by 'aa', etc. 'U' denotes unidentified, and 'N' non-blazar.

It is generally accepted that extra-galactic counterparts, particularly for variable EGRET sources, will be active galactic nuclei (AGN) containing compact component(s) near the core. Thus, bright radio sources with flat radio spectra, pronounced radio variability, and/or milli-arcsecond (mas) scale structure are good candidates for counterparts to an EGRET source. Searches for counterparts are often limited to the 95% confidence contour, despite the fact this confidence level only reflects the statistical uncertainty in position. Systematic uncertainties can also affect the position determination (Hartman et al., 1999): as noted by Sowards-Emmerd et al. (2003) considerably fewer than half of the detections of bright 3EG blazars lie within the 50% contour, and several lie outside the 99% contour. It seems reasonable then, to extend the search beyond the 95% contour, particularly when previous searches have not yielded likely counterparts (although see Punsly, 1997 for a dissenting view).

In Section 2, possible counterparts for the eight sources in Table I are considered. The radio spectral index, α, is defined such that $S \propto \nu^{+\alpha}$, although for gamma-ray photon spectral indices we follow the third EGRET catalog (hereafter 3EG) convention of $F(E) \propto E^{-\gamma}$.

2. Selected Sources

2.1. 3EG J0118+0248

As shown in Table II and Figure 1, there is no shortage of potential counterparts to 3EG J0118+0248! The 3EG notes J0121+0422 (0119+041) as a lower confidence

TABLE II

Candidate counterparts to 3EG J0118+0248, compiled from NVSS and PMN data. The angular separation from the 3EG position is given by r. The comments refer to the identifications ('A' for high confidence, 'a' for lower confidence) described in Table I

Source	$S_{1.4}$ [mJy]	$S_{4.8}$ [mJy]	α	r [°]	Comments
J0113+0222	490.5	654.0	0.23	1.25	A (SE)
J0114+0208	148.4	144.0	−0.02	1.26	
J0118+0258 (3C 37)	1521.8	409.0	−1.06	0.16	a (MHR)
J0121+0422	1065.6	1942.0	0.48	1.80	a (3EG), a (SE)
J0122+0310	98.4	126.0	0.20	0.97	a (SE)

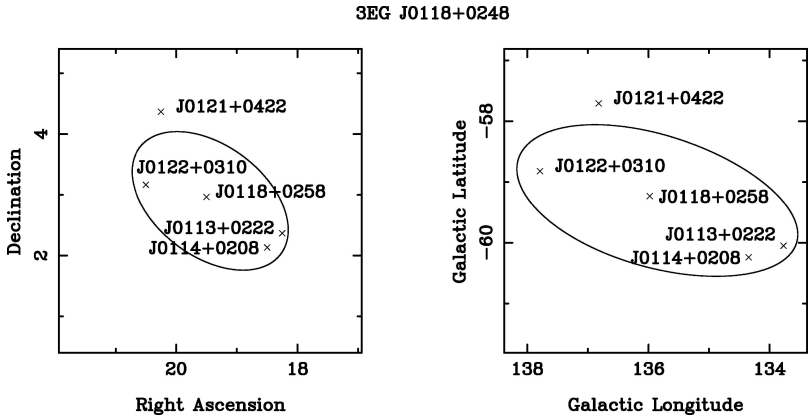


Figure 1. Location of candidate counterparts to 3EG J0118+0248 with respect to the parametrization of the 95% confidence contour of Mattox et al. (2001). As the actual contours are given in 3EG in equatorial coordinates for some sources and galactic coordinates for others, both are plotted here. The units for both axes are degrees.

identification, however Mattox et al. (2001) suggest a plausible association with J0118+0258 (B0115+027, 3C 37) although note the spectral index is −0.7.

As the spectral index of 3C 37 is less than −0.5, it was not included in the CLASS survey and so was not considered by Sowards-Emmerd et al. (2003); in any case the steep spectral index would have resulted in this source being accorded a low Figure of Merit (FoM). They find J0113+0222 is a high confidence association, with J0121+0422 and J0122+0310 both lower confidence associations (see their Figure 3).

However, the 4.8 GHz total flux density of 3C 37 has varied from 614 mJy in GB6 to 409 mJy in PMN suggesting there is a compact, variable core. This is confirmed by the fact that Morabito et al. (1986) detected 3C 37 on VLBI baselines with correlated flux densities of 60 mJy at 2.3 GHz and 150 Jy at 8.4 GHz. These suggest a very inverted spectrum for the mas-scale structure, although further

multi-frequency VLBI observations are needed to confirm these single baseline snapshot measurements. In any case, it is apparent that sources with steep spectra based on single-dish, or short-baseline, data can host flat-spectrum cores, i.e., that compact components may exist in extended radio structure.

2.2. 3EG J0416+3650

3EG J0416+3650 was identified at low confidence with B0415+379 (J0418+3801, 3C 111) in 3EG but the association not considered likely by Mattox et al. (2001). 3C 111, a broad-line radio galaxy at $z = 0.0485$, is strong but quite extended, being catalogued as three sources in NVSS – J0418+3800, J0418+3801 and J0418+3802 – with a total 1.4 GHz flux density of ∼15 Jy. Combining this with the GB6 flux density of 5.2 Jy yields a spectral index of $\alpha = -0.86$, which would have precluded inclusion of the source in the JVAS and CLASS surveys and hence the source was not considered by Sowards-Emmerd et al. (2003), who assigned the ($b = -9.97^\circ$) EGRET source a "likely galactic" classification.

However, the 4.8 GHz VLBA survey of Fomalont et al. (2000) reveals that 3C111 does have a compact core with a correlated flux density of 0.9 Jy measured on 100 Mλ baselines, and so this association does bear further investigation, with the relatively faint J0417+3631 the most likely alternative identification (see Table III and Figure 2).

2.3. 3EG J1308+8744

Due to the polar mount of the Green Bank telescope used for the 87GB/GB6 survey, these catalogs do not extend to declinations above 75°. Consequently, the CLASS catalog, which was based predominantly on these surveys, has very little coverage above this declination. This being the case, the 'non-blazar' classification for 3EG J1308+8744 of Sowards-Emmerd et al. (2003) seems somewhat premature.

In Table IV (see also Figure 3) we list several potential counterparts, selected on the basis of the their Westerbork Northern Sky Survey (WENSS) 352 MHz data (Rengelink et al., 1997) and NVSS 1.4 GHz flux densities. None have a particularly flat spectral index, but higher frequency data or VLBI observations are required to determine which, if any, hosts a compact core.

TABLE III

NVSS and GB6 data for candidate counterparts to 3EG J0416+3650

Source	$S_{1.4}$ [mJy]	$S_{4.8}$ [mJy]	α	r [°]	Comments
J0417+3631	96.9	123.0	0.19	0.39	
J0418+3801 (3C 111)	14960.0	5168.0	−0.86	1.26	a (3EG)
J0422+3716	92.9	74.0	−0.18	1.29	

TABLE IV

Candidate counterparts to 3EG J1308+8744, compiled from 325 MHz WENSS and 1.4 GHz NVSS data, and corresponding spectral index

Source	$S_{0.325}$ [mJy]	$S_{1.4}$ [mJy]	α	r [°]
J1137+8728	525	167.8	−0.83	0.99
J1148+8742	789	163.7	−1.14	0.79
J1244+8755	933	371.0	−0.67	0.29
J1314+8712	280	119.1	−0.62	0.53

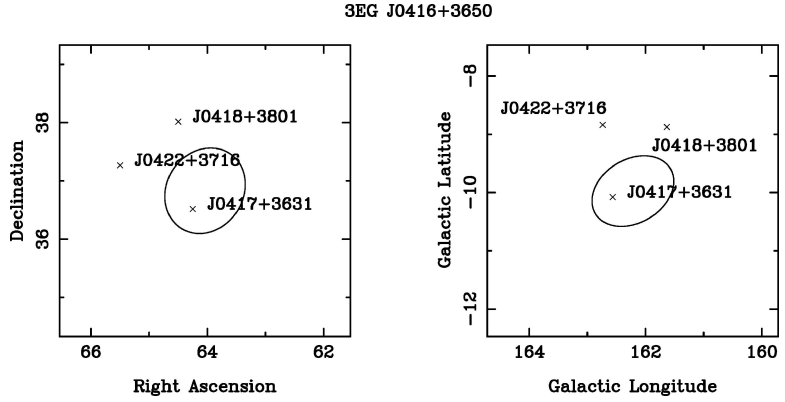


Figure 2. Location of candidate counterparts to 3EG J0416+3650. See Figure 1 for details.

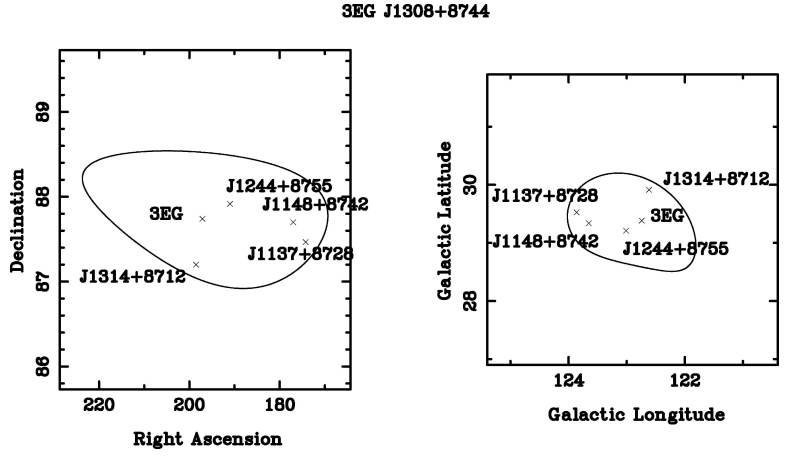


Figure 3. Location of candidate counterparts to 3EG J1308+8744. See Figure 1 for details. The ellipses appear misshapen on these plots as the source is very close to the north celestial pole. The 3EG position is also shown for reference.

TABLE V
Candidate counterparts to 3EG J1607–1101 compiled from NVSS and PMN data

Source	$S_{1.4}$ [mJy]	$S_{4.8}$ [mJy]	α	r [°]	Comments
J1603−1007	151.9	153.0	0.01	1.38	a (SE)
J1605−1139	258.0	371.0	0.29	0.85	Tornikoski et al. (2002)
J1605−0926	1200.9	998.0	−0.15	1.67	see text
J1605−1012	79.8	109.0	0.25	0.97	a (SE)
J1612−1133	60.8	123.0	0.57	1.27	A (SE)

2.4. 3EG J1607–1101

Sowards-Emmerd et al. (2004) find one high confidence association (J1612−1133) and two lower confidence counterparts (J1603−1007 and J1605−1012) for this EGRET source. As noted in Table IV (and Figure 4), Tornikoski et al. (2002) suggest J1605−1139 as a possible counterpart based on a 90 GHz flux density of 530 mJy. Sowards-Emmerd et al. (2004) acknowledge this suggestion but comment that the source does not match their survey criteria. These authors favour J1612−1133 based on an extrapolated 8.4 GHz flux density due the very inverted spectral index between the NVSS and PMN flux densities. However, the proximity of J1605–1139 to the EGRET position and the inverted spectrum, continuing to mm-wavelengths, would appear to lend support for this being the more likely counterpart to the EGRET source.

Of other possible counterparts, J1605–0926 is a compact NVSS source, with two extended sources, J1605–0927 and J1605–0928, within 4 arcmin: the summed flux density for the three is 3.5 Jy. The PMN source (which is noted as being extended) will include contributions from all three sources and has an overall spectral index

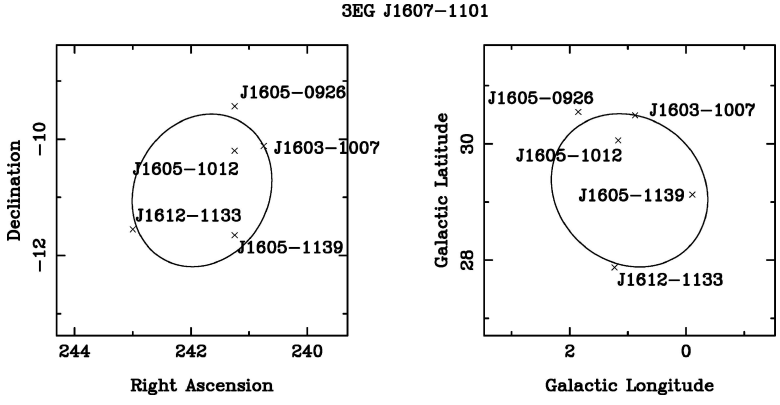


Figure 4. Candidate counterparts to 3EG J1607–1101. See Figure 1 for details.

TABLE VI
Candidate counterparts to 3EG J1735–1500, compiled from NVSS and PMN catalogs

Source	$S_{1.4}$ [mJy]	$S_{4.8}$ [mJy]	α	r [°]	Comments
J1737−1511	55.6	$\lesssim$18	< -0.9	0.42	Combi et al. (2003)
J1738−1503	330.1	268.0	−0.17	0.56	A (SE), Combi et al.
J1740−1515	122.9	1128.0	0.03	0.03	
J1742−1517	246.2	188.0	−0.22	1.55	

of −1.0. Higher frequency and/or VLBI observations are required to assess whether it is a more likely counterpart than J1605–1139.

2.5. 3EG J1735–1500

Sources within the 95% confidence contour of this source have been examined in detail by Combi et al. (2003), who favour the radio galaxy J1737–1511 as the counterpart, though note that the brighter and flatter spectrum source PMN J1738–1503 is also a potential association (see Table VI and Figure 5).

3EG J1735–1500, $(l, b) = (10.73, 9.22)$, lies relatively close to the galactic centre, and near the Gould belt. It is not, however, a member of the population characterized by Gehrels et al. (2000) as it is significantly variable (Torres et al., 2001; Nolan et al., 2003).

Sowards-Emmerd et al. (2004) find Combi et al.'s alternative candidate, J1738–1503, is a high confidence association, and, given the significant gamma-ray variability, this does appear the more likely counterpart. The radio galaxies detected by EGRET, Cen A and NGC 6251, both have most probable variability indices, δ, of 0, with upper limits of 0.49 and 0.52, respectively (Nolan et al., 2003), suggesting that radio galaxies may not be as variable at GeV energies as blazars.

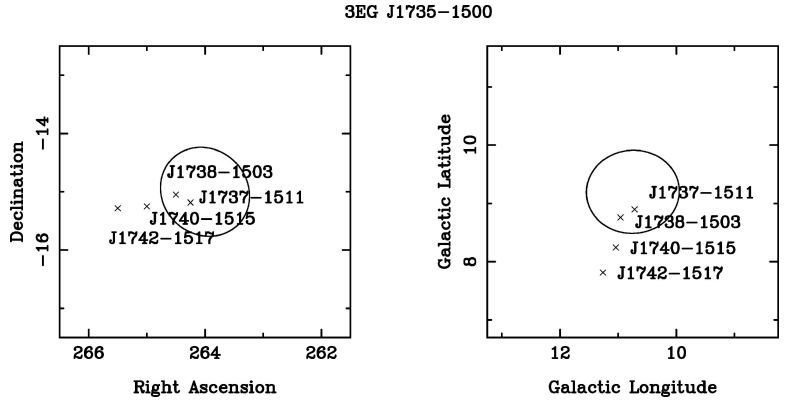


Figure 5. Candidate counterparts to 3EG J1735–1500. See Figure 1 for details.

TABLE VII

Candidate counterparts to 3EG J1813–6419 from the PMN 4.8 GHz and ATCA 8.4 GHz observations. The highly inverted spectrum implied for J1807–6413 reflects the fact these observations were not made contemporaneously

Source	$S_{4.8}$ [mJy]	$S_{8.6}$ [mJy]	α	r [°]	Comments
J1803–6507	780	577	−0.52	1.33	
J1807–6413	171	331	1.14	0.60	
J1819–6345 (B1814–637)	4506	2090	−1.33	0.89	a (MHR)

2.6. 3EG J1813–6419

Mattox et al. (2001) find B1814–637 (J1819–6345) to be a plausible counterpart to 3EG J1813–6419, in part as it is a bright radio source at 4.8 GHz (see Table VII and Figure 6). However, PKS 1814–637 is a steep spectrum source and previous VLBI observations have revealed it is not detectable on intercontinental baselines (Shen et al., 1997). Furthermore, PKS 1814–637 is classified optically as a Seyfert 2 galaxy, and as a Compact Steep Spectrum source (Tzioumis et al., 2002).

A pilot 18 GHz survey has been performed on a strip of southern sky between $\delta = -59$ and $-71°$, in part to characterize the radio source population and to test observing strategies for a future all southern sky survey (Ricci et al., 2004). The survey utilized a novel wide-band (4 GHz) analogue correlator on a 30 m baseline of the Australia Telescope Compact Array (ATCA). Besides J1819–6345 (1.44 ± 0.29 Jy at 18 GHz), the survey detected the 428 mJy source, PMN J1807–6413.

This source has a (June 1990) PMN flux density of 171 mJy (Wright et al., 1994), however follow-up ATCA observations made by Tasker (2000) several years later measured a 4.8 GHz flux density of 331

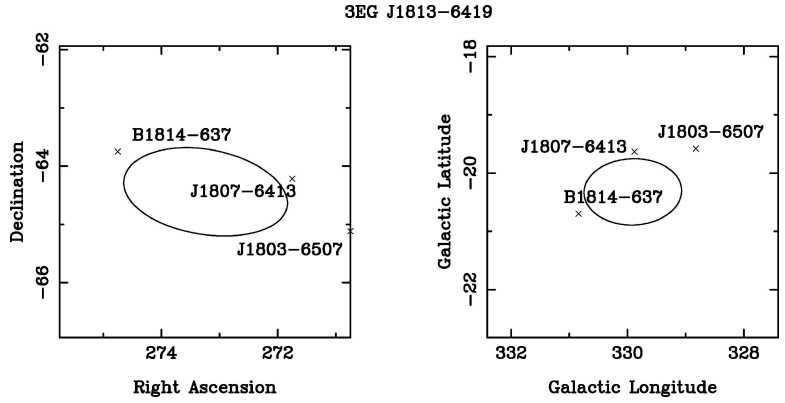


Figure 6. Candidate counterparts to 3EG J1813–6419. See Figure 1 for details.

mJy, yielding a spectral index of −0.2. The source is clearly variable and has a flat spectrum so is a candidate counterpart to the EGRET source.

However, J1819–6345, and another candidate with a larger angular separation from the nominal EGRET position, J1803–6507, were both detected at higher frequencies as WMAP foreground sources (Bennett et al., 2003), and so these cannot yet be categorically ruled out as the counterpart(s). J1819–6345 may well be another steep-spectrum source with a flat-spectrum core.

2.7. 3EG J1935–4022

The 3EG lists B1933–400 (J1937–3957) as a high confidence identification with 3EG J1935–4022, however, Mattox et al. (2001) find two plausible counterparts to this EGRET source; the blazar 1933–400 (J1937–3957) and 1930−397 (J1933–3940), a galaxy pair (see Table VIII and Figure 7). The gamma-ray source is quite variable (see Table I), suggesting the blazar is the more likely counterpart.

The spectral index between the PKSCAT90 2.7 GHz (Wright and Otrupcek, 1990) and PMN 4.8 GHz flux densities for J1933–3940 is −0.6, and a similar value is obtained by summing the the close and extended NVSS sources J1933–3940, J1933–3940, and J1933–3941 and calculating the spectral index with the PMN flux

TABLE VIII

Candidate counterparts to 3EG J1935–4022 compiled from PMN 4.8 GHz and ATCA 8.6 GHz data

Source	$S_{4.8}$ [mJy]	$S_{8.6}$ [mJy]	α	r [°]	Comments
J1926–3917	847.8	318	−0.79	2.04	
J1933–3940	1250.0	1097	−0.11	0.86	a (MHR)
J1937–3957	1001.6	1129	0.10	0.49	A (3EG), a (MHR)

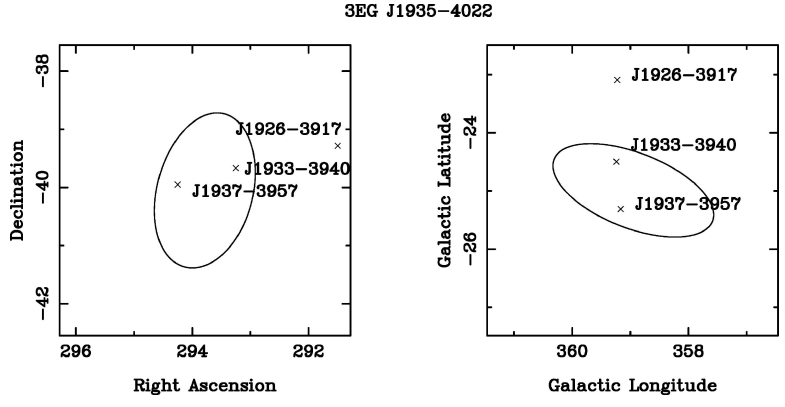


Figure 7. Candidate counterparts to 3EG J1935–4022. See Figure 1 for details.

density. J1937–3957 has a flatter spectrum: the 2.7 GHz PKSCAT90 and 4.8 GHz PMN flux densities yield −0.3, however the more contemporaneous NVSS and PMN values give 0.1. Again, J1937–3957 appears the more likely identification.

This is further supported by the ATCA observations of Tasker (2000). J1933–3940 was found to be very extended, with an integrated flux density of 601 mJy at 4.8 GHz, but a peak flux density of only 1 mJy. (Peak flux densities are commonly given in mJy/beam, but the table at http://www.atnf.csiro.au/resources/catalogues/pmn_atca gives these in mJy: in any case, the source is clearly very resolved on the ATCA baselines.) In contrast, PMN J1937–3957 had a peak flux density of 1000 mJy at 4.8 GHz. At 8.6 GHz the source was unresolved with the integrated and peak flux densities both equal to 747 mJy. The source was also found to be only slightly resolved at 2.3 GHz on the 275 km baseline of the Parkes–Tidbinbilla Interferometer (Duncan et al., 1993) and has been detected at 90 GHz (Tornikoski et al., 2002).

The NVSS survey ends a fraction of a degree below −40°, precluding a detailed study of the full area around the EGRET source, however J1937–3957 is a strong candidate for the counterpart.

2.8. 3EG J1959+6342

Mattox et al. (2001) considered J2006+6424 to be a plausible association for 3EG J1959+6342, and Sowards-Emmerd et al. (2003) consider it a high confidence association. However, the TeV gamma-ray source J1959+6508 (Holder et al., 2003) is also relatively close. Sowards-Emmerd et al. (2003) gave added weight to sources detected at X-ray energies in their FoM: although an X-ray detection does not guarantee a GeV detection, a GeV detection does make an X-ray detection more likely. In the same manner, at current sensitivities, a TeV detection makes a GeV detection more likely. The association of J1959+6508 with 3EG J1959+6342 will be considered in detail elsewhere (Edwards et al., in preparation).

3. Discussion

Candidate counterparts to eight EGRET sources have been studied. It is noteworthy that steep single-dish spectra, indicative of extended radio structure, do not rule out the possibility of a compact core. Teräsranta et al. (2001) have also noted that extended sources should not be excluded as potential counterparts to EGRET sources.

The degree of variability, and galactic latitude, of an EGRET source are at present the most reliable indicators for an AGN counterpart, although not all EGRET sources identified with AGN are variable, and conversely not all variable sources have suggested AGN counterparts (yet!). EGRET has opened a new window on the universe, allowing a significant number of sources to be identified, and providing indications as to which populations of sources include gamma-ray emitters. The

launch of AGILE and GLAST are eagerly anticipated, as their improved angular resolutions should make the job of identifying counterparts much easier. The multi-wavelength approach will continue to play a key role in understanding the processes at work in these sources.

Acknowledgements

Bob Hartman, Jun Kataoka, Jim Lovell, John Mattox, Glenn Piner, and Elaine Sadler are thanked for helpful discussions, and the referee is acknowledged for comments which resulted in an improved paper.

References

Bennett, C.L., Hill, R.S., Hinshaw, G. et al.: 2003, *ApJS* **148**, 97.
Combi, J.A., Romero, G.E., Paredes, J.M., Torres, D.F. and Ribó, M.: 2003, *ApJ* **588**, 731.
Condon, J.J., Cotton, W.D., Greisen, E.W. et al.: 1998, *AJ* **115**, 1693.
Duncan, R.A., White, G.L., Wark, R. et al.: 1993, *PASAu* **10**, 310.
Fomalont, E.B., Frey, S., Paragi, Z. et al.: 2000, *ApJS* **131**, 95.
Gehrels, N., Macomb, D.J., Bertsch, D.L., Thompson, D.J. and Hartman, R.C.: 2000, *Nature* **404**, 363.
Gregory, P.C., Scott, W.K., Douglas, K. and Condon, J.J.: 1996, *ApJS* **103**, 427.
Griffith, M.R., Wright, A.E., Burke, B.F. and Ekers, R.D.: 1994, *ApJS* **90**, 179.
Griffith, M.R., Wright, A.E., Burke, B.F. and Ekers, R.D.: 1995, *ApJS* **97**, 347.
Hartman, R.C., Bertsch, D.L., Bloom, S.D. et al.: 1999, *ApJS* **123**, 79.
Holder, J., Bond, I.H., Boyle, P.J. et al.: 2003, *ApJ* **583**, L9.
Mattox, J.R., Schachter, J., Molnar, L., Hartman, R.C. and Patnaik, A.R.: 1997, *ApJ* **481**, 95.
Mattox, J.R., Hartman, R.C. and Reimer, O.: 2001, *ApJS* **135**, 155.
Morabito, D.D., Niell, A.E., Preston, R.A., Linfield, R.P., Wehrle, A.E. and Faulkner, J.: 1986, *AJ* **91**, 1038.
Myers, S.T. et al.: 2003, *MNRAS* **341** 1.
Nolan, P.L., Tompkins, W.F., Grenier, I.A. and Michelson, P.F.: 2003, *ApJ* **597**, 615.
Punsly, B.: 1997, *AJ* **114**, 544.
Rengelink, R.B., Tang, Y., de Bruyn, A.G. et al.: 1997, *A&AS* **124**, 259.
Ricci, R., Sadler, E.M., Ekers, R.D. et al.: 2004, *MNRAS* **354**, 305.
Shen, Z.-Q., Wan, T.-S., Moran, J.M. et al.: 1997, *AJ* **114**, 1999.
Sowards-Emmerd, D., Romani, R.W. and Michelson, P.F.: 2003, *ApJ* **590**, 109.
Sowards-Emmerd, D., Romani, R.W., Michelson, P.F. and Ulvestad, J.S.: 2004, *ApJ* **604**, 564.
Tasker, N.: 2000, Ph.D. Thesis, Macquarie University.
Teräsranta, H., Urpo, S., Wiren, S. and Valtonen, M.: 2001, *A&A* **368**, 431.
Tornikoski, M., Lähteenmäki, A., Lainela, M. and Valtaoja, E.: 2002, *ApJ* **579**, 136.
Torres, D.F., Romero, G.E., Combi, J.A., Benaglia, P., Andernach, H. and Punsley, B.: 2001, *A&A* **370**, 468.
Tzioumis, A., King, E., Morganti, R. et al.: 2002, *A&A*, **392**, 841.
Wright, A. and Otrupcek, R.: 1990, Parkes Catalogue 1990, (Australia Telescope National Facility).
Wright, A.E., Griffith, M.R., Burke, B.F. and Ekers, R.D.: 1994, *ApJS* **91**, 111.
Wright, A.E., Griffith, M.R., Hunt, A.J., Troup, E., Burke, B.F. and Ekers, R.D.: 1996, *ApJS* **103**, 145.

A SEARCH FOR TeV EMISSION FROM X-RAY SELECTED AGN WITH MILAGRO

ELIZABETH HAYS*

University of Maryland, MD, USA; E-mail: ehays@umdgrb.umd.edu

(Received 2 July 2004; accepted 1 September 2004)

Abstract. A TeV emission component has been detected from several active galactic nuclei (AGN). The majority of TeV detections of AGN are for nearby ($z < 0.13$) X-ray selected BL Lacs in flaring states. The variability of these sources makes continuous monitoring necessary to detect flaring activity.

The Milagro gamma-ray observatory is a wide-field ($\sim$2 sr) instrument that operates continuously allowing daily observations of the Northern hemisphere. No significant detections of unidentified sources have been made to date. The observations are used to set limits on the time-integrated behavior of a set of X-ray selected BL Lacs. Costamante and Ghisellini [A&A 384 (2002) 56] present a selection of BL Lacs with X-ray and radio flux levels favorable for TeV emission and make predictions for the TeV flux levels. Twenty-seven objects selected from this sample are the subjects of a search for TeV emission on time scales from 8 days to 2.8 years in data taken between December 15, 2000, and September 8, 2003. None of the selected BL Lacs are detected on any of the time scales. Flux limits will be presented for each galaxy and time scale and comparisons will be made with the predicted emission.

Keywords: Milagro, AGN

1. Introduction

There has been a notable lack of overlap between the AGN detected by EGRET (30 MeV–20 GeV) and those detected by ground-based gamma-ray detectors, which are sensitive to higher energies ($E > 100$ GeV). Many of the blazar type AGN detected with EGRET are classified as low-frequency peaked BL Lacs (LBLs), also known as radio-selected, which are observed to have spectral components peaking in the IR/optical band and in the lower portion of the gamma-ray waveband. Only high-frequency peaked BL Lacs (HBLs), also known as X-ray-selected, in which the first spectral component peaks instead in the UV/X-ray band, currently have confirmed detections at TeV energies (Horan and Weekes, 2004). The BL Lacs that are bright at TeV energies have been absent or weak detections in the EGRET catalog. This has been interpreted as an indication the spectral component occurring at MeV energies for LBLs is shifted to higher energies in HBLs, moving the dominant emission peak out of the EGRET waveband (Padovani and Giommi, 1995).

HBLs are highly variable sources and have been observed to undergo flaring states at TeV energies with short-term behavior on time scales less than an hour

*For the Milagro Collaboration.

Astrophysics and Space Science **297:** 43–52, 2005.
© Springer 2005

and long-term behavior lasting for months. The variability of these objects is not yet understood. Correlations have been predicted and observed between X-ray and TeV emission (Krawczynski et al., 2004). For the HBL, Mrk 421, increases in X-ray activity have been a good indication of TeV high states. Not all TeV flaring, however, has been associated with a simultaneous increase in the X-ray flux (Krawczynski et al., 2004). Candidate sources require frequent monitoring by TeV instruments to detect outbursts and further establish a connection between the X-ray and TeV emission in HBLs.

Searches for TeV emission from X-ray-selected BL Lacs have had some success. Repeated observations of 1ES 1959+650 by the Whipple air Čerenkov telescope, for example, produced a confirmed detection of flaring activity (Holder et al., 2003) following a tentative detection by the Seven Telescope Array (Nishiyama et al., 1999). The strong flaring that followed was observed as part of a multi-wavelength campaign and enabled simultaneous measurements of the broadband spectral energy distribution (SED) (Krawczynski et al., 2004). Another X-ray-selected BL Lac, H 1426+428, was observed as part of an AGN campaign in Whipple and eventually was detected in a high state (Horan et al., 2002). The study presented here focuses specifically on X-ray selected BL Lacs because of the potential for TeV emission and the availability of predictive models that may be constrained.

The Milagro detector is well-suited to searches for variable emission from objects of this type. The search described in this paper is a subset of an all-sky analysis that exploits Milagro's ability to observe the overhead sky. The locations of a set of X-ray selected BL Lacs taken from Costamante and Ghisellini (2002) are observed over 2.8 years for TeV emission on time scales extending from 8 days to the length of the data set. In the absence of significant detections, upper limits on the flux are provided for each object and time scale searched. The limits are compared with the predicted TeV fluxes from Costamante and Ghisellini (2002). The flux predictions made using a single-zone synchrotron self-Compton (SSC) model fall below the sensitivity of the Milagro observations, but some predictions made using an empirical blazar parametrization (Fossati et al., 1998) modified by Costamante and Ghisellini (2002) are constrained. Although the BL Lacs examined here are relatively close in redshift, the TeV emission is affected by absorption through pair production on the extragalactic background light (EBL) (Primack et al., 1999; Vassiliev, 2000; de Jager and Stecker, 2002). Additional calculations of the Milagro flux are made assuming absorption, but do not entirely explain the difference between the flux limit and predicted flux for two of the BL Lacs.

2. Milagro's All-Sky Capability

The large field of view and high duty cycle of Milagro provide observations of the Northern sky at TeV energies (100 GeV–100 TeV) on a daily basis. All locations

above the zenith angle horizon, $\theta < 45^\circ$, are observed at any given time. Over a sidereal day, all but the highest latitude locations in the Northern hemisphere pass through the field of view. The all-sky capability enables searches for TeV emission in the overhead sky from very short time scales (μs) to long time integrations that include daily and multi-day observations of the Northern hemisphere. The Milagro detector runs 90% of the time providing hours of observations of the Northern sky each day for most of the year. Results for specific locations are presented here, but all locations within the field of view have been and continue to be monitored for significant emission. The all-sky searches have not yet detected any new variable TeV sources. However, the transient nature of the objects and continuing improvements in source sensitivity do not exclude the possibility of future detections.

The qualities that make Milagro a good instrument for all-sky searches apply to monitoring specific sources for transient emission as well. The available range of time integrations allows a comprehensive search to be made for flaring activity in selected sources. As an extension of the all-sky search, a sample of potential TeV emitters are monitored for flaring behavior that may not have been considered significant in searches of the entire field of view.

3. TeV Candidate BL Lacs

In Costamante and Ghisellini (2002) a sample of BL Lacs are selected as favorable sources of TeV emission based on brightness in X-ray and radio surveys. The appeal of this sample lies in the similarity between the selected BL Lacs and detected TeV sources. The BL Lacs with confirmed detections at TeV energies, Mrk 501, Mrk 421, H 1426+428, 1ES 2344+514 and PKS 2155–304, fall within the selection criteria, and one of the BL Lacs included in the sample, 1ES 1959+650, has since been detected by imaging air Čerenkov telescopes (IACTs) (Nishiyama et al., 1999; Holder et al., 2003).

In Costamante and Ghisellini (2002) 32 BL Lacs are selected from X-ray and radio surveys as the best TeV candidates. Twenty-seven of these fall within the field of view of Milagro, which extends from approximately 0° to 80° in declination. Table I lists the BL Lacs included in the search with their equatorial coordinates and redshift. Three of the objects lack a measured redshift and are given the mean value for the sample, $z = 0.2$. Additionally, RGB 1725+118 has a marginally measured redshift value determined from one absorption line.

Costamante and Ghisellini (2002) use optical, radio, and X-ray data for each candidate to fit the SED using both the blazar parametrization (Fossati et al., 1998) and a SSC model. The blazar parameterization is based on an apparent sequence of peak frequency and luminosity when blazar observations are averaged based on classes of radio luminosity. The SED peaks are fit using parabolic forms with

TABLE I

BL Lacs selected as likely TeV emitters (Costamante and Ghisellini, 2002) that pass through the field of view of Milagro (Previous observations by TeV instruments are noted. 1ES 1959 + 650 has been detected by IACTs.)

Name	RA (J2000)	DEC (J2000)	z	I_0 U.L. 8 day	16 day	32 day	64 day	128 day	256 day
1ES 0033+595[a,b]	00 35 52.6	+59 50 05	0.086	22.2	15.4	11.8	7.9	5.5	3.1
1ES 0120+340[b]	01 23 08.5	+34 20 48	0.272	14.0	10.1	6.1	4.3	2.6	1.9
RGB 0136+391	01 36 32.4	+39 05 59	0.2[c]	14.0	9.0	6.9	3.7	2.8	1.9
RGB 0214+517[a,b]	02 14 17.9	+51 44 52	0.049	17.2	12.8	6.4	4.2	3.2	2.3
3C 66A[a,d,e]	02 22 39.6	+43 02 08	0.444	14.5	12.1	7.4	4.5	3.0	2.1
1ES 0229+200[a,b,e]	02 32 48.4	+20 17 16	0.139	16.6	11.0	6.8	4.8	3.4	2.5
1H 0323+022[a,f]	03 26 14.0	+02 25 15	0.147	47.1	38.5	26.8	18.7	8.5	5.2
1H 0414+009[e]	04 16 52.5	+01 05 24	0.287	59.7	33.5	28.3	17.4	11.8	6.1
1ES 0647+250[e]	06 50 46.5	+25 03 00	0.2[c]	15.1	9.3	6.3	3.6	2.5	1.7
1ES 0806+524[a,b]	08 09 49.1	+52 18 59	0.138	16.5	11.7	8.5	5.5	4.4	2.0
RGB 0812+026	08 12 01.9	+02 37 33	0.2[c]	45.5	29.9	23.2	14.7	10.9	5.4
OJ 287[d]	08 54 48.9	+20 06 31	0.306	14.6	11.7	7.2	5.7	3.1	2.3
1H 1013+498	10 15 04.1	+49 26 01	0.200	17.4	10.6	7.0	4.4	3.2	2.2
1ES 1028+511[a]	10 31 18.4	+50 53 36	0.361	16.4	11.4	7.5	4.8	2.4	1.4
RGB 1117+202[b]	11 17 06.2	+20 14 07	0.139	15.9	10.1	8.8	5.6	3.0	1.8
MRK 180[a]	11 36 26.4	+70 09 27	0.045	56.4	25.5	18.3	11.2	7.9	4.1
RGB 1136+676	11 36 30.1	+67 37 04	0.135	38.7	24.5	19.2	10.2	7.2	4.1
ON 325[a,d]	12 17 52.1	+30 07 01	0.237	12.9	9.4	6.7	4.2	2.7	2.2
1H 1219+301[a]	12 21 21.9	+30 10 37	0.182	16.1	10.8	7.7	4.9	3.4	2.5
RGB 1417+257	14 17 56.7	+25 43 26	0.237	18.2	10.3	6.4	4.2	3.2	2.1
1ES 1440+122	14 42 48.2	+12 00 40	0.162	21.7	15.0	8.7	5.3	3.5	2.6
1ES 1553+113[b]	15 55 43.0	+11 11 24	0.360	24.9	13.0	10.0	7.0	5.0	1.9
RGB 1725+118[a]	17 25 04.3	+11 52 15	0.018	25.5	14.0	11.0	7.6	5.5	3.5
I Zw 187[a,d]	17 27 18.6	+50 13 10	0.055	19.0	8.4	5.3	3.2	1.9	1.2
1ES 1741+196[a]	17 43 57.8	+19 35 09	0.084	21.2	11.0	8.2	6.0	3.0	2.2
1ES 1959+650[a,g]	19 59 59.9	+65 08 55	0.047	32.3	21.8	17.6	7.7	4.0	2.5
BL Lacertae[a,d,e]	22 02 43.3	+42 16 40	0.069	12.9	9.8	5.8	5.1	2.7	1.8

Note: The 95% c.l. upper limits on the flux amplitude are given for $dN/dE = I_0(E/\text{TeV})^{-\alpha}$ where I_0 is in $10^{-11}\text{cm}^{-2}\text{s}^{-1}\text{TeV}^{-1}$ and $\alpha = 2.5$. The limits given represent the largest excess found in six multi-day time windows applied to data taken between December 15, 2000, and September 8, 2003.

[a]1995–2000 (Horan et al., 2004).

[b]Oct. 2001–July 2002 (de la Calle Pérez et al., 2003).

[c]Unknown redshift set to be 0.2

[d]1992–1994 (Kerrick et al., 1995).

[e]1997–1998 (Aharonian et al., 2000).

[f]Sept. 1996 (Chadwick et al., 1999).

[g]Detected 1999 (Nishiyama et al., 1999), flaring detected 2001 (Holder et al., 2003).

locations and relative emitted power determined by the 5 GHz radio flux. Some additional improvements are made in Costamante and Ghisellini (2002) to better represent low power BL Lacs.

The SSC model fits assume a single emission zone and homogeneous jet. A finite time for the electron injection into the jet allows cooling to steepen the electron energy spectrum and, therefore, the resulting inverse-Compton photon spectrum at high energies. This model predicts fluxes that are lower than the Fossati parameterization predictions and that fall below the sensitivity of the TeV observations made to date. The results of both of the SED fits are used to provide integral flux predictions above 40 GeV, 300 GeV, and 1 TeV.

4. Summary of Searches for Predicted TeV Candidates

The sample in Costamante and Ghisellini (2002) includes objects that have been included in several AGN searches by TeV instruments. Table I notes the time periods and references for other observations of these BL Lacs. Many already have TeV limits, but six of the sample have not been observed by IACTs to date. Only eight of the BL Lacs have TeV observations overlapping in time with those presented in this paper.

The searches for TeV emission from BL Lac objects by IACTs have typically involved few HBLs and infrequent observations. The CANGAROO collaboration has reported upper limits on four HBLs in the Southern hemisphere (Roberts et al., 1998, 1999). The Durham group observed three different HBLs in the Southern hemisphere (Chadwick et al., 1999), one of which is near the equator and is included as part of the sample considered in this work. The HEGRA IACT array has published observations of eight BL Lacs, five of which are included in this sample, over a two-year period with exposures ranging from 1–15 h (Aharonian et al., 2000).

The most extensive searches have been conducted using the Whipple gamma-ray telescope. An early search included a few HBLs as part of a diverse blazar sample (Kerrick et al., 1995), but recent campaigns have focused on HBLs. No detections are reported for the selected BL Lacs with the exception of 1ES 1959+650. Whipple and Milagro are located at similar latitudes and have a large overlap in observed sources within this sample. The temporal characteristics of the observations, however, are different. The Whipple results for eight of the HBLs examined in this work are presented in de la Calle Pérez et al. (2003). The length of the exposure for each object ranged from several to twenty hours for observations made between October, 2001, and July, 2002, overlapping with the Milagro observations. Fifteen BL Lacs from the sample examined here are also part of a longer series of observations presented in Horan et al. (2004) which extend from 1995 to 2000 and have no temporal overlap with the search presented in this paper.

5. Description of Search

The data set used for this analysis begins on December 15, 2000, and ends on September 8, 2003 (MJD 51893–52889). The data were analyzed using the standard two-hour direct integration background estimation described in Atkins et al. (2003). The standard cuts on the number of photomultiplier tubes used to reconstruct direction ($n\text{Fit} > 20$) and to reject background events ($C > 2.5$) are applied. Details of the background rejection are in Atkins et al. (2003). The combination of all cuts retains 5.8% of the 1.58×10^9 events in the data set. If the data available for a background estimation map includes less than 2900 s (0.8 h) of exposure, the map is excluded from further analysis. This short map cut removed 44.2 h of the analyzed maps (0.2% of the total exposure). The resulting total exposure is 906.20 days within a period of 996 days for a 91% duty cycle. The Crab Nebula is detected in this data set at Gaussian significance of 6σ. The BL Lac Mrk 421 is observed at 4.1σ in the full data set and at higher significance for observations matched to flaring episodes.

The data are searched for emission over period from 8 days to the full length of the data set, 2.8 years. To maximize signal sensitivity the time integration of the searches increases by a factor of two. To insure that a time window encompasses flaring activity, the time windows for an integration length overlap by 50%. A search of six integration lengths and the full data set found no significant emission from any of the BL Lacs. In EGRET data, similar galaxies have been combined to produce a stacked limit. This is not practical for Milagro observations of BL Lacs due to the large effect of redshift on the spectrum at TeV energies.

6. Results of Search for TeV Candidate BL Lacs

Absolute 95% c.l. upper limits on the flux amplitude are set for each BL Lac and time scale (Table I) using the largest excess event rate observed. The flux amplitude is defined as I_0 where the assumed photon spectrum is a power law of the form $dN/dE = I_0(E/\text{TeV})^{-2.5}$. The limits from the full data set are also compared with predicted flux values from Costamante and Ghisellini (2002). The comparison is made by approximating the predicted spectral fits as a power law above 100 GeV. The approximate power-law index used is listed in Table II with the Milagro upper limits and the flux predictions. The integral fluxes presented in Costamante and Ghisellini (2002) have been converted to a differential flux amplitude using the same power-law approximation.

The predicted fluxes do not include the effects of absorption of photons by the EBL. Some of the difference between the limits and predictions may be explained by this effect. To account for the amount of flux that may be lost to attenuation in the upper limit, the assumed spectrum is modified with an additional factor, $e^{-\tau(E,z)}$. The optical depth τ for a photon of energy E from a redshift z is calculated using the baseline model from de Jager and Stecker (2002).

TABLE II

Comparison of differential flux 95% c.l. upper limits from 906 days of exposure in Milagro with predicted integral fluxes from Costamante and Ghisellini (2002) converted to a differential form

Object	$\alpha_{\rm Fos}/\alpha_{\rm SSC}$	I_0 U.L.	I_0 U.L. IR	Predicted I_0
1ES 0033+595[a,b]	2.16/2.50	4.69/8.82	81.2/79.9	6.03/0.649
1ES 0120+340	2.25/–	5.11/–	249/–	0.81/0.790
RGB 0136+391	2.25/4.28	2.49/2.22	68.3/4.18	1.62/0.104
RGB 0214+517[a,b]	2.14/3.01	3.51/9.84	20.4/22.2	17.63/0.137
3C 66A	3.19/–	9.75/–	148/–	0.24/–
1ES 0229+200	2.23/4.62	7.54/6.86	167/10.0	2.79/0.174
1H 0323+022	2.25/–	11.0/–	743/–	2.42/0.014
1H 0414+009	2.43/–	16.9/–	3660/–	0.62/0.133
1ES 0647+250	2.29/–	2.73/–	77.2/–	1.67/0.504
1ES 0806+524	2.31/–	4.46/–	84.3/–	3.82/–
RGB 0812+026	2.28/–	7.77/–	1010/–	1.66/0.074
OJ 287	3.19/–	10.7/–	107/–	0.73/–
1H 1013+498	2.47/–	5.34/–	111/–	0.32/0.336
1ES 1028+511	2.62/–	3.99/–	204/–	1.05/–
RGB 1117+202	2.15/–	3.91/–	104/–	3.48/0.157
Mrk 180[a,b]	2.19/–	5.56/–	54.2/–	24.91/0.050
RGB 1136+676	2.19/–	7.19/–	485/–	2.70/0.183
ON 325	2.72/–	9.34/–	123/–	0.37/–
1H 1219+301	2.21/–	7.17/–	194/–	1.96/0.336
RGB 1417+257	2.26/–	8.23/–	354/–	1.09/0.455
1ES 1440+122	2.10/2.82	3.53/11.8	234/134	2.35/0.198
1ES 1553+113	2.91/–	12.5/–	415/–	0.42/0.777
RGB 1725+118[a,b]	2.10/3.25	7.18/32.9	18.7/45.4	39.03/0.025
I Zw 187[a,b]	2.15/–	1.59/–	9.99/–	15.39/0.145
1ES 1741+196[a,b]	2.17/3.80	6.47/15.2	73.3/25.9	10.61/0.319
1ES 1959+650[a,b,c]	2.17/–	2.89/–	25.2/30.1	21.99/0.051
BL Lacertae[a,b]	2.69/–	6.66/–	22.8/24.7	7.87/0.173

Note: The assumed spectrum is $dN/dE = I_0(E/\text{TeV})^{-\alpha}$, where I_0 is in 10^{-12} cm^{-2}s^{-1}TeV^{-1}. The flux limits are given for two spectral indexes determined for the two fits of the SED. The first alpha, $\alpha_{\rm Fos}$ is the estimated power-law index using the modified Fossati parameterization. The second, $\alpha_{\rm SSC}$, represents the SSC model fit. The upper limits are also given with IR attenuation included using $dN/dE = I_0(E/\text{TeV})^{-\alpha}e^{\tau(E,z)}$ where τ is calculated using the baseline model from de Jager and Stecker (2002).

[a]Predicted flux constrained by Milagro limit.

[b]Predicted flux constrained by IACT TeV limit (Costamante and Ghisellini, 2002; de la Calle Pérez et al., 2003; Horan et al., 2004).

[c]TeV detection by IACTs (Holder et al., 2003).

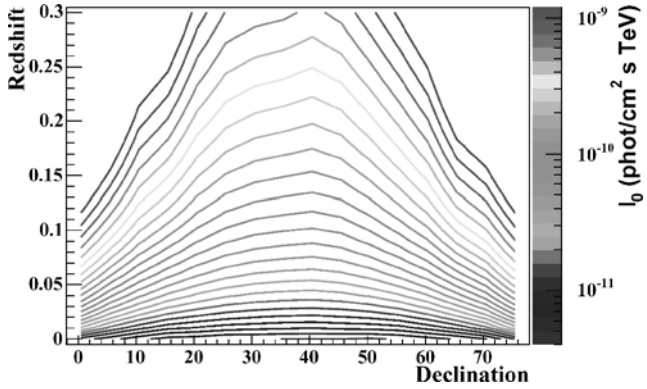


Figure 1. Sensitivity contours for constraint (not detection) in declination and redshift for a 3σ excess in Milagro for 906 days of exposure. The corresponding flux amplitude, I_0, is calculated for spectral index, $\alpha = 2$, where $dN/dE = I_0(E/\text{TeV})^{-\alpha}$.

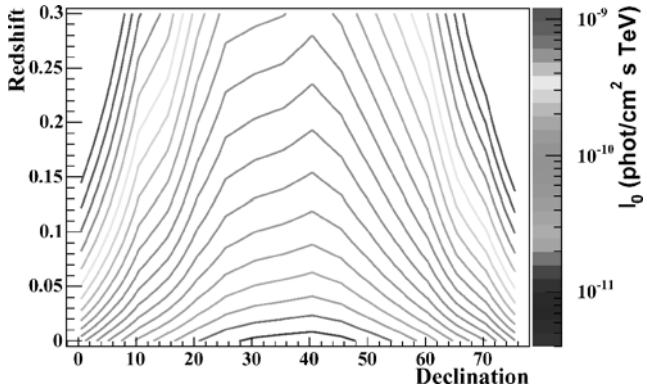


Figure 2. Same as Figure 1 with $\alpha = 3$.

Figures 1 and 2 indicate the flux level that can be constrained by Milagro upper limits. The flux amplitude necessary for a 3σ signal in Milagro in 906 days of exposure depends on source declination and redshift. The contours demonstrate the decrease in sensitivity for declinations further from overhead and for increased redshift. A comparison of the figures using $\alpha = 2$ and $\alpha = 3$ shows that although Milagro has more sensitivity to a flatter spectrum for sources at low redshift, at higher redshifts a steeper spectrum requires a smaller I_0 to achieve the same significance. The SSC model predictions fall below 5×10^{-12} cm^{-2}s^{-1}TeV^{-1} and cannot be constrained by these observations. Some of the modified Fossati parameterization flux predictions are above the constraint sensitivity for nearby sources at favorable declinations. The modified Fossati predictions are constrained for all eight BL Lacs with $z < 0.1$ (Table II) assuming no attenuation. The limits are additionally set assuming attenuation of the spectrum. For six of the constrained BL Lacs, the difference between the flux limit and the predicted flux can be explained by attenuation.

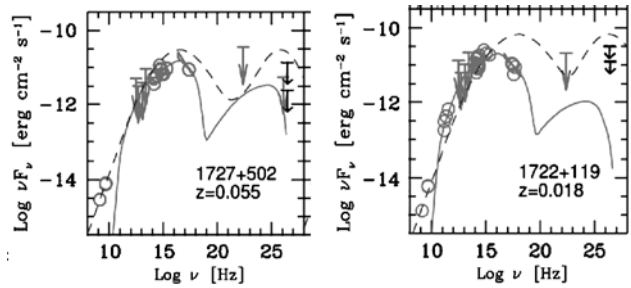


Figure 3. SED fits for I Zw 187 and RGB 1725+118 from Costamante and Ghisellini (2002) with Milagro upper limits in black. The solid red line represents a SSC emission model. The dashed blue line represents a parametrization based on Fossati et al. (1998). The Milagro upper limits are calculated for 906 days of exposure using a power law approximation to the Fossati SED fit. The higher limit assumes a spectrum including the effects of attenuation on the IR background. The IR model assumed is the baseline model from de Jager and Stecker (2002).

The predictions for I Zw 187 and RGB 1725+118, however, remain constrained when an attenuated spectrum is assumed in the flux calculation. The SED data and predictions from Costamante and Ghisellini (2002) for these BL Lacs are shown in Figure 3 with the Milagro upper limits for an attenuated and unattenuated spectrum.

7. Conclusion

Milagro provides a unique opportunity for observing the northern sky at TeV energies on a daily basis. The resulting time coverage allows a comprehensive search for transient emission throughout the field-of-view. The transient search technique is applied to a set of X-ray selected BL Lacs objects to set limits on both the quiescent and flaring emission levels during 2.8 years of observations. In some cases the limits are the first available at TeV energies. Although the limits do not constrain flux predictions using a single-zone SSC model, several do constrain predictions made using a parameterization based on the blazar sequence. In two cases, the difference is not explained by the amount of attenuation expected from interactions with IR photons. The variable nature of BL Lacs requires continued TeV observations for flaring activity and the sample observed here remains of interest. The limited scope of previous searches in terms of sample size and time coverage make the observations in Milagro a unique study of the time-averaged behavior of these sources over a variety of durations.

References

Aharonian, F.A., Akhperjanian, A.G., Barrio, J.A. et al.: 2000, *A&A* **353**, 847.
Atkins, R., Benbow, W., Berley, D. et al.: 2003, *ApJ* **595**, 803.

Chadwick, P.M., Lyons, K., McComb, T.J.L., Orford, K.J., Osborne, J.L., Rayner, S.M., Shaw, S.E. and Turver, K.E.: 1999, *ApJ* **521**, 547.
Costamante, L. and Ghisellini, G.: 2002, *A&A* **384**, 56.
de Jager, O.C. and Stecker, F.W.: 2002, *ApJ* **566**, 738.
de la Calle Pérez, I., Bond, I.H., Boyle, P.J. et al.: 2003, *ApJ* **599**, 909.
Fossati, G., Maraschi, L., Celotti, A., Comastri, A. and Ghisellini, G.: 1998, *MNRAS* **299**, 433.
Holder, J., Bond, I.H., Boyle, P.J. et al.: 2003, *ApJ Lett.* **583**, L9.
Horan, D., Badran, H.M., Bond, I.H. et al.: 2002, *ApJ* **571**, 753.
Horan, D., Badran, H.M., Bond, I.H.: 2004, *ApJ* **603**, 51.
Horan, D. and Weekes, T.C.: 2004, *New Astron. Rev.* **48**, 527.
Kerrick, A.D., Akerlof, C.W., Biller, S. et al.: 1995, *ApJ* **452**, 588.
Krawczynski, H., Hughes, S.B., Horan, D. et al.: 2004, *ApJ* **601**, 151.
Nishiyama, T., Chamoto, N., Chikawa, M. et al.: 1999, in: *Proceedings of the 26th ICRC, Salt Lake City*, Vol. 3, p. 370.
Padovani, P. and Giommi, P.: 1995, *ApJ* **444**, 567.
Primack, J.R., Bullock, J.S., Somerville, R.S. and MacMinn, D.: 1999, *Astroparticle Phys.* **11**, 93.
Roberts, M.D., Dazeley, S.A., Edwards, P.G. et al.: 1998, *A&A* **337**, 25.
Roberts, M.D., McGee, P., Dazeley, S.A. et al.: 1999, *A&A* **343**, 691.
Vassiliev, V.V.: 2000, *Astroparticle Phys.* **12**, 217.

BEAMING EFFECTS IN GRBs AND ORPHAN AFTERGLOWS

Y.F. HUANG,[1] T. LU[2] and K.S. CHENG[3]

[1]*Department of Astronomy, Nanjing University, Nanjing 210093, China; E-mail: hyf@nju.edu.cn*
[2]*Purple Mountain Observatory, CAS, Nanjing 210008, China*
[3]*Department of Physics, The University of Hong Kong, Hong Kong, China*

(Received 1 June 2004; accepted 26 July 2004)

Abstract. The overall dynamical evolution and radiation mechanism of γ-ray burst (GRB) jets are briefly introduced. Various interesting topics concerning beaming in GRBs are discussed, including jet structures, orphan afterglows and cylindrical jets. The possible connection between GRBs and neutron stars is also addressed.

Keywords: γ-ray bursts

1. Introduction

The discovery of γ-ray burst (GRB) afterglows in 1997, triggered by the famous Italian–Dutch BeppoSAX satellite, definitely shows that most, if not all, long GRBs are of cosmological origin. The so-called "fireball model" is strongly favored theoretically. In this standard model, the GRB fireball is assumed to be isotropic. However, as early as 1997, Rhoads (1997) had already suggested that GRB outflows may be highly collimated. In the beaming case, as the ultra-relativistic jet decelerates, it will expand laterally at approximately co-moving sound speed. Naturally, photons are emitted into larger and larger solid angle. As the result, an obvious break should be observed in the multi-band afterglow light curves. The break time is determined by $\gamma \sim 1/\theta$, where γ is the bulk Lorentz factor of the jet and θ is its half opening angle.

Observationally, the jet hypothesis gains some support soon in 1997. The γ-ray energy release of GRB 971214, if isotropic, is as large as $\sim 0.17\ M_{\odot}c^2$, well beyond the energy scope of a stellar object. Similar difficulty also exists in many other examples, such as GRBs 980703 ($\sim 0.06\ M_{\odot}c^2$), 990123 ($\sim 1.9\ M_{\odot}c^2$), 990510 ($\sim 0.16\ M_{\odot}c^2$), 991208 ($\sim 0.07\ M_{\odot}c^2$), 991216 ($\sim 0.38\ M_{\odot}c^2$), 000131 ($\sim 0.6\ M_{\odot}c^2$), 000926 ($\sim 0.15\ M_{\odot}c^2$), 010222 ($\sim 0.3\ M_{\odot}c^2$), and 020813 ($\sim 0.55\ M_{\odot}c^2$). In all these cases, emission should be highly collimated, so that the true energy release can be reduced to $\sim 10^{50}$–10^{51} ergs, within the energy output of a stellar object.

Also, it is very interesting that light curve breaks do have been observed in a few afterglows, for example, in GRBs 990123, 990510, 991216, 000301C, 000926, 010222, 011121, 020124, 020813, 030226, and 030329. Such breaks have been



Astrophysics and Space Science **297:** 53–61, 2005.
© Springer 2005

widely regarded as being due to jet effect. In a few other cases (GRBs 980326, 980519, 990705, 991208, 000911, 001007, 020405), although no breaks were observed, the light curves are still abnormal since the afterglows decay quite steeply ($\sim t^{-2}$). Such rapid fading of optical afterglows has also been argued as evidence for collimation (Huang et al., 2000b).

Beaming is an interesting topic in the field of GRBs. There are many researches concerning it, and many interesting results have been revealed. For example, Frail et al. (2001) suggested that the intrinsic energy releases of GRBs, after correction for the beaming angle, are strikingly clustered around 5×10^{50} ergs. Recently, it is also discovered that a GRB jet should be highly structured, but not homogeneous.

In this paper, we mainly discuss beaming effects in GRB afterglows. The dynamics and radiation mechanism will be described in Section 2. Structures of jets are then introduced in Section 3. The possible existence of cylindrical jets is addressed in Section 4. Section 5 is about orphan afterglows, and Section 6 investigates the possibility that the launch of a GRB jet may be associated with the kick of a high-speed neutron star. The final section is a brief discussion.

2. Dynamics and Radiation

After producing the main burst *via* internal shocks at a radius about 10^{13} cm, the GRB ejecta continues to expand ultra-relativistically in the circum-burst medium. The external shock occurs when the swept-up medium mass, m, exceeds $M_{\rm ej}/\eta$, where $M_{\rm ej}$ is the the initial mass of the ejecta and η the initial value of the Lorentz factor γ. Afterglows are produced by the shock-accelerated electrons. Denoting the radius of the external shock as R, the observer's time as t, the medium number density as n, the overall evolution of a GRB jet can be conveniently described as (Huang et al., 1999, 2000a,b,c),

$$\frac{dR}{dt} = \beta c\gamma(\gamma + \sqrt{\gamma^2 - 1}), \tag{1}$$

$$\frac{dm}{dR} = 2\pi R^2(1 - \cos\theta)nm_{\rm p}, \tag{2}$$

$$\frac{d\theta}{dt} = \frac{c_{\rm s}(\gamma + \sqrt{\gamma^2 - 1})}{R}, \tag{3}$$

$$\frac{d\gamma}{dm} = -\frac{\gamma^2 - 1}{M_{\rm ej} + \epsilon m + 2(1 - \epsilon)\gamma m}, \tag{4}$$

where $\beta = \sqrt{\gamma^2 - 1}/\gamma$, and ϵ is the radiative efficiency. $c_{\rm s}$ is the co-moving sound speed, which can be further expressed as,

$$c_{\rm s}^2 = \hat{\gamma}(\hat{\gamma} - 1)(\gamma - 1)\frac{1}{1 + \hat{\gamma}(\gamma - 1)}c^2, \tag{5}$$

where $\hat{\gamma} \approx (4\gamma + 1)/(3\gamma)$ is the adiabatic index.

This dynamical model has the advantage that it applies in both the ultra-relativistic and the non-relativistic phases, and that it describes the lateral expansion in an accurate way.

Synchrotron radiation is the main emission mechanism. To make our calculation appropriate even in the deep Newtonian phase (Huang and Cheng, 2003), we assume that the shock-accelerated electrons distribute according to their kinetic energy as (Huang and Cheng, 2003),

$$\frac{dN'_{\rm e}}{d\gamma_{\rm e}} \propto (\gamma_{\rm e}-1)^{-p}, \quad (\gamma_{\rm e,min} \leq \gamma_{\rm e} \leq \gamma_{\rm e,max}), \tag{6}$$

where $\gamma_{\rm e}$ is the thermal Lorentz factor of electrons. Assuming that there is an equipartition between the proton energy density, the magnetic energy density, and the electron energy density as well, it will then be relatively easy to calculate the afterglows by considering synchrotron radiation. Note that the equal-time-surface effect should be taken into account in calculations. Examples of such calculations have been given in Huang and Cheng (2003).

3. Jet Structure

The simplest jet model involves a homogeneous conical outflow. Recently, it was realized by more and more authors that GRB jets may have complicate structures. Basically, there are three kinds of structured jets: two-component jets (Berger et al., 2003), Gaussian jets (where the energy per unit solid angle depends as a Gaussian function on the angular distance from the axis), and power-law jets (where the energy density profile is a power-law function) (Mészáros et al., 1998; Dai and Gou, 2001; Zhang and Mészáros, 2002). Generally, the structured jet models have the potential of explaining normal GRBs, X-ray rich GRBs, and X-ray flashes in a uniform picture (Huang et al., 2004; Zhang et al., 2004).

Although the profile functions of Gaussian jets and power-law jets seem quite simple, their afterglows are in fact not easy to calculate, especially when the lateral expansion and the equal-time-surface effect are considered. The two-component jet model is relatively simple in these aspects. A two-component jet has two components: a narrow but ultra-relativistic outflow (with Lorentz factor typical of normal GRB fireballs, i.e. $\gamma \geq 100$–1000), and a wide but mildly relativistic ejecta (with $1 \ll \gamma \ll 100$). These two components are usually assumed to be coaxial. At first glance, the two-component jet model seems to be quite coarse, but interestingly enough, it gains some support from numerical simulations of the collapse of massive stars (Zhang et al., 2003). Additionally, Berger et al. (2003) found that the model can give a perfect explanation to the multiband observations of the famous GRB 030329. In their explanation, the gamma-ray and early afterglow emission

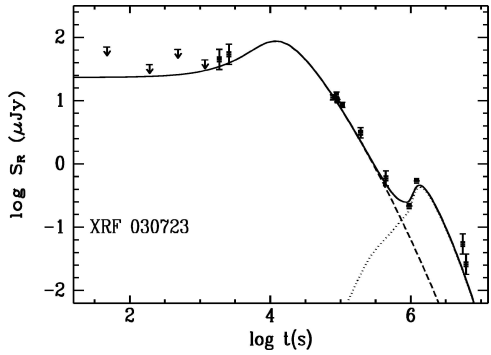


Figure 1. Fit to the optical afterglow of XRF 030723 by Huang et al. (2004), using the two-component jet model. The dashed line corresponds to emission from the wide component, and the dotted line is for the narrow component. The solid line illustrates the total light curve. The observer is assumed to be off-axis.

of GRB 030329 come from the narrow component, while the radio and optical afterglows beyond 1.5 days are produced by the wide component.

In a recent study, Huang et al. (2004) further proposed that the optical afterglow light curve of X-ray Flash (XRF) 030723 can also be well fit by the simple two-component model. To re-produce the re-brightening of the afterglow of XRF 030723, Huang et al. (2004) assumed that the observer is off-axis, and that the intrinsic energy of the wide component is less than that of the narrow component. Figure 1 illustrates the result of their fitting. Anyway, it should be noted that the re-brightening in this event can also be explained by an underlying supernova (Fynbo et al., 2004; Tominaga et al., 2004).

4. Cylindrical Jets

Usually GRB jets are assumed to be conical outflows. However, Cheng et al. (2001) have suggested that the relativistic outflows in GRBs might also be cylindrical. They have studied afterglows of cylindrical jet in detail. If a cylindrical jet does not expand laterally, it will remain in the ultra-relativistic phase for a very long period (typically longer than 10^9 s). The afterglow usually decays like $S_\nu \propto t^{-p/2}$, where p is the power-law index of the electron distribution. On the other hand, if the cylindrical jet expands laterally, it will enter the Newtonian phase quickly. In this case, the afterglow light curve evolves from $S_\nu \propto t^{-p}$ to $S_\nu \propto t^{-(15p-21)/10}$. As the example, Figure 2 illustrates the optical afterglow light curves of some cylindrical jets.

Huang et al. (2002b) specially pointed out that for a cylindrical jet without lateral expansion, the afterglow light curve will become $S_\nu \propto t^{-1} - t^{-1.3}$ if taking $p = 2.0$–2.6. Observationally, the decay of optical afterglows from many GRBs, such as GRBs 970508, 971214, 980329 and 980703, is in this range. In the most popular explanation, these GRBs are thought to be produced by isotropic fireballs.

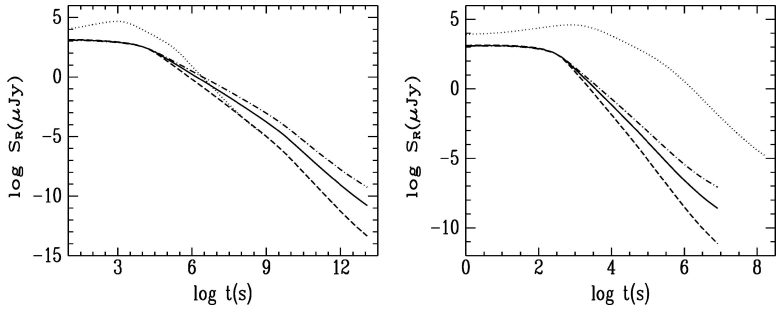


Figure 2. R-band afterglows from cylindrical jets without (left panel) and with (right panel) lateral expansion (Cheng et al., 2001). The dashed, solid and dash-dotted lines in each panel correspond to $p = 3$, 2.5 and 2.2, respectively. The dotted lines correspond to conical jets with $p = 2.5$.

However, we should not omit the possibility that these events may in fact be due to cylindrical jets, as suggested by Huang et al. (2002b). Figure 3 shows that the cylindrical jet model can fit the afterglows of these events perfectly.

The concept of cylindrical jets has gained support observationally in fields other than GRBs. For example, it has long been found that jets in many radio galaxies are cylindrical, i.e. they maintain constant cross sections on large scales. Jets in many Herbig–Haro (HH) objects are also cylindrical (e.g., Ray et al., 1996). In fact, observations have indicated clearly that HH jets are initially poorly focused, but are then asymptotically collimated into cylinders (Ray et al., 1996).

Theoretically, it is striking that cylindrical jets can be naturally produced in black hole-accretion disk systems (Shu et al., 1995; Krasnopolsky et al., 2003; Vlahakis and Königl, 2003a,b; Fendt and Ouyed, 2004). The collimation is mainly due to magnetic forces. It is well known that the poloidal component of a dipolar magnetic field decays as $B_P \propto r^{-3}$, where r is the distance from the central object. It is also known that the motion of matter along poloidal magnetic field lines will unavoidably

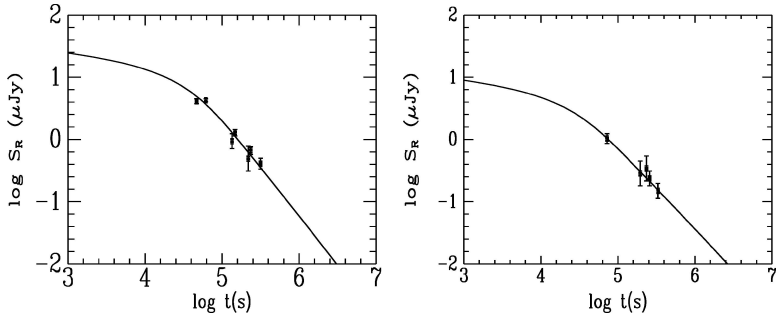


Figure 3. Fitting to the R-band afterglow light curves of GRB 971214 (left panel) and GRB 980329 (right panel) by using the cylindrical jet model (Huang et al., 2002b).

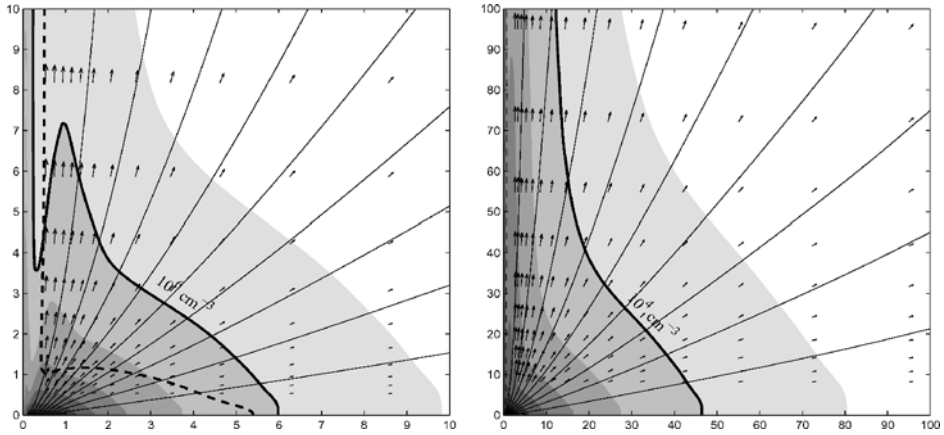


Figure 4. Numerical results from the calculation of MHD jets launched by a stellar accretion disk (Krasnopolsky et al., 2003). Shown are streamlines (light solid lines) and isodensity contours (heavy solid lines and shades). The arrows are for poloidal velocity vectors, with length proportional to the speed. In the Left panel, the jet is plot on 10 AU scale, and in the right panel the jet is plot on 100 AU scale. It is clearly seen from the isodensity contours that the jet has a cylindrical shape.

induce a strong toroidal field component, which decays as $B_{\rm T} \propto r^{-1}$ (Fendt and Ouyed, 2004). So, a magnetohydrodynamic (MHD) jet is asymptotically dominated by the toroidal magnetic field. This toroidal field exerts an inward force on the MHD jet through "hoop stress", which provides the collimation. Numerous numerical results have shown that MHD jets are conical initially, during the acceleration phase, but their half opening angles are turning smaller and smaller, until finally the outflows become cylindrical. Figure 4 shows examplar numerical results by Krasnopolsky et al. (2003). Of course, in the cases of GRBs, which are thought to occur in star forming regions, strong gradients in density might also play a role in collimating the jets.

5. Orphan Afterglows

If GRBs are really due to beamed ejecta, then the high-energy burst can be observed only when the observer is on-axis. However, in the off-axis case, since the afterglow emission is less beamed, it is still possible that the ejecta may be detected in optical and radio bands. These afterglows are called orphan afterglows, since they are not associated with any known GRBs. Rhoads (1997) has pointed out that the ratio of orphan afterglows with respect to GRBs can potentially give a measure of the beaming angle of GRB jets.

However, Huang et al. (2002a) argued that the detection of orphan afterglows does not necessarily mean that GRBs are jetted. They argued that in the isotropic fireball model, there should exist many failed GRBs, i.e., fireballs with initial

Lorentz factor $1 \ll \eta \ll 100$–1000. These fireballs cannot produce GRBs successfully. Huang et al. called them failed GRBs (FGRBs), although they sometimes are also called dirty fireballs (Dermer et al., 1999). It is obvious that FGRBs can also produce orphan afterglows. Huang et al. (2002a) thus suggest that when an orphan afterglow is observed, it should be monitored carefully for a relative long period so that its origin can be clarified. It can be used to estimate the beaming angle of GRBs only when we know for sure that it really comes from a jetted but off-axis GRB.

6. GRB Jets and Neutron Star Kicks

Since the discovery of afterglows in 1997, great progresses have been achieved in the field of GRBs. However, the energy mechanism of GRBs is still largely uncertain. Studies of beaming effects can potentially help to reveal this final enigma. A good example is the possibility that the launch of a GRB jet might be related to the kick of a neutron star. This idea was proposed as early as in 1998 (Cen 1998), and has been discussed by a few authors (Dar and Plaga, 1999; Huang et al., 2003).

In a recent study, Huang et al. (2003) further suggested that the neutron star should be of high speed, with proper motion larger than $\sim$1000 km/s. In this framework, when a new-born neutron star is kicked, a high-speed outflow should be launched into the opposite direction, whose energy can typically be $\sim 10^{52}$ ergs. The outflow may be composed of neutrinos and anti-neutrinos initially. However, annihilation of neutrinos and anti-neutrinos can deposit a small portion ($\sim 10^{-3}$–10^{-2}) of its energy into an $e^{\pm}$ firecone. The isotropic equivalent energy of this firecone is 10^{50}–10^{54} ergs, depending on the energy deposition efficiency and the half opening angle. It thus can give birth to a beamed GRB successfully.

This model, according to Huang et al.'s estimation, naturally meets many of the requirements of GRB engines. For example, the deposited energy is enough for normal GRBs; the collimation is naturally guaranteed; the ultra-relativistic motion is reasonably produced; the observed connection between GRBs and supernovae is well explained; the duration of GRBs is consistent with the timescale of a typical kick process; the event rate is satisfactory, i.e. consistent with the observed GRB rate of $\sim$1–3 per day; the model naturally produces the rapid variability in GRB light curves. Finally, it also explains the standard energy reservoir hypothesis found by Frail et al. (2001).

7. Discussion and Conclusions

In this article, we introduce various beaming effects in GRBs. A convenient way to calculate afterglows of beamed GRBs is introduced. Structures of GRB jets are described, with the major attention being paid on the two-component model. We

also discussed the possible existence of cylindrical jet in GRBs. The method of using orphan afterglow surveys to measure the beaming of GRB jets is discussed in some detail. It is shown that failed GRBs may play a role in the process, and thus make the problem much more difficult. We also addressed the possible connection between GRB jets and neutron star kicks. We believe it is an interesting idea that the launch of a GRB jet may be associated with the kick of a high-speed neutron star.

Collimation is important in GRBs, since it provides important clues on the progenitors. Collimation can also be identified *via* effects other than those mentioned above. For example, optical afterglows from a jet can be significantly polarized, in principle up to tens of percents (Gruzinov, 1999; Mitra, 2000). In fact, polarization has already been observed in a few afterglows on the level of a few percents (Bersier et al., 2003). These observations strongly indicate that GRBs are collimated. However, such observations still cannot be directly used to measure the beaming angle. Radio afterglows in the very late phase can be used to estimate the intrinsic kinetic energy of GRB remnant, and thus may provide information of beaming indirectly but independently.

Acknowledgements

We thank the referee for useful comments and suggestions. This research was supported by the Special Funds for Major State Basic Research Projects, the Foundation for the Author of National Excellent Doctoral Dissertation of P.R. China (Project No. 200125), Projects 10003001, 10233010 and 10221001 supported by NSFC, and an RGC grant of Hong Kong SAR.

References

Berger, E., Kulkarni, S.R., Pooley, G. et al.: 2003, *Nature* **426**, 154.
Bersier, D., McLeod, B., Garvanich, P.M. et al.: 2003, *ApJ* **583**, L63.
Cen, R.: 1998, *ApJ* **507**, L131.
Cheng, K.S., Huang, Y.F. and Lu, T.: 2001, *MNRAS* **325**, 599.
Dai, Z.G. and Gou, L.J.: 2001, *ApJ* **552**, 72.
Dar, A. and Plaga, R.: 1999, *A&A* **349**, 259.
Dermer, C.D., Chiang, J. and Böttcher, M.: 1999, *ApJ* **513**, 656.
Fendt, C. and Ouyed, R.: 2004, *ApJ* **608**, 378.
Frail, D.A., Kulkarni, S.R., Sari, R. et al.: 2001, *ApJ* **562**, L55.
Fynbo, J.P.U., Sollerman, J., Hjorth, J. et al.: 2004, *ApJ* **609**, 962.
Gruzinov, A.: 1999, *ApJ* **525**, L29.
Huang, Y.F. and Cheng, K.S.: 2003, *MNRAS* **341**, 263.
Huang, Y.F., Dai, Z.G. and Lu, T.: 1999, *MNRAS* **309**, 513.
Huang, Y.F., Gou, L.J., Dai, Z.G. and Lu, T.: 2000a, *ApJ* **543**, 90.
Huang, Y.F., Dai, Z.G. and Lu, T.: 2000b, *A&A* **355**, L43.
Huang, Y.F., Dai, Z.G. and Lu, T.: 2000c, *MNRAS* **316**, 943.

Huang, Y.F., Dai, Z.G. and Lu, T.: 2002a, *MNRAS* **332**, 735.
Huang, Y.F., Tan, C.Y., Dai, Z.G. and Lu, T.: 2002b, *Chin. Astron. Astrophys.* **26**, 414.
Huang, Y.F., Dai, Z.G., Lu, T., Cheng, K.S. and Wu, X.F.: 2003, *ApJ* **594**, 919.
Huang, Y.F., Wu, X.F., Dai, Z.G., Ma, H.T. and Lu, T.: 2004, *ApJ* **605**, 300.
Krasnopolsky, R., Li, Z.Y. and Blandford, R.D.: 2003, *ApJ* **595**, 631.
Mészáros, P., Rees, M.J. and Wijers, R.A.M.J.: 1998, *ApJ* **499**, 301.
Mitra, A.: 2000, *A&A* **359**, 413.
Ray, T.P., Mundt, R., Dyson, J.E., Falle, S.A.E.G. and Raga, A.C.: 1996, *ApJ* **468**, L103.
Rhoads, J.: 1997, *ApJ* **487**, L1.
Shu, F.H., Najita, J., Ostriker, E.C. and Shang, H.: 1995, *ApJ* **455**, L155.
Tominaga, N., Deng, J., Mazzali, P.A., Maeda, K., Nomoto, K., Pian, E., Hjorth, J. and Fynbo, J.P.U.: 2004, *ApJ* **612**, L105.
Vlahakis, N. and Königl, A.: 2003a, *ApJ* **596**, 1080.
Vlahakis, N. and Königl, A.: 2003b, *ApJ* **596**, 1104.
Zhang, B. and Mészáros, P.: 2002, *ApJ* **571**, 876.
Zhang, B., Dai, X., Lloyd-Ronning, N.M. and Meszaros, P.: 2004, *ApJ* **601**, L119.
Zhang, W., Woosley, S.E. and MacFadyen, A.I.: 2003, *ApJ* **586**, 356.

PULSAR SLOT GAPS AND UNIDENTIFIED EGRET SOURCES

ALICE HARDING and ALEXANDER MUSLIMOV

NASA Goddard Space Flight Center, Greenbelt, MD, USA; E-mail: harding@twinkie.gsfc.nasa.gov

(Received 30 June 2004; accepted 19 August 2004)

Abstract. A new picture of pulsar high-energy emission is proposed that is different from both the traditional polar cap and outer gap models, but combines elements of each. The slot gap model is based on electron acceleration along the edge of the open field region from the neutron star surface to near the light cylinder and thus could form a physical basis for the two-pole caustic model of Dyks and Rudak (2003). Along the last open field line, the pair formation front rises to very high altitude forming a slot gap, where the accelerating electric field is unscreened by pairs. The resulting radiation features both hollow cones from the lower-altitude pair cascades, seen at small viewing angles, as well as caustic emission on the trailing-edge field lines at high altitude, seen from both poles at large viewing angle. The combination of the small solid angle of slot gap emission ($\ll 1$ sr) with a high probability of viewing the emission predicts that more gamma-ray pulsars could be detected at larger distances. In this picture, many of the positional coincidences of radio pulsars with unidentified EGRET sources become plausible as real associations, as the flux predicted by the slot gap model for many of the pulsars would provide the observed EGRET source flux. The expected probability of seeing radio-quiet gamma-ray pulsars in this model will also be discussed.

Keywords: neutron stars, pulsars, acceleration, gamma-rays

1. Introduction

The number of rotation-powered pulsars with detected emission at X-ray and γ-ray energies has been steadily growing (Thompson, 2001; Becker and Aschenbach, 2002). Although the theory of pulsar acceleration and high-energy emission has been studied for over 30 years, the origin of the pulsed non-thermal emission is a question that remains unsettled. The observations to date have not been able to clearly distinguish between an emission site at the magnetic poles (Daugherty and Harding, 1996) and emission in the outer magnetosphere (Cheng et al., 1986; Hirotani and Shibata, 2001). In the case of polar cap (PC) models, while the energetics and pair-cascade spectrum have had success in reproducing the observations, the predicted beam size of radiation emitted near the neutron star (NS) surface is too small to produce the wide pulse profiles that are observed (Thompson, 2001). However, Arons (1983) first noted the possibility of a high-altitude acceleration region or "slot gap" along the last open field line where the electric field is lower. The slot gap forms because the pair formation front, above which the accelerating field is screened, occurs at increasingly higher altitude as the magnetic colatitude



Astrophysics and Space Science **297:** 63–70, 2005.
© Springer 2005

approaches the edge of the open field region (Arons and Scharleman, 1979 [AS79]). We have re-examined the slot-gap model (Muslimov and Harding, 2003 [MH03]) with the inclusion of two new features: (1) the acceleration due to inertial-frame dragging (Muslimov and Tsygan, 1992) and (2) the additional decrease in the electric field near the boundary at the edge of the polar cap due to the narrowness of the slot gap. These two effects combine to enable acceleration to altitudes approaching the light cylinder in the slot gap at all azimuthal angles around the polar cap. These features result in the production of a larger high-energy emission beam with small solid angle, both favorable for producing high fluxes for γ-ray pulsars.

2. Formation of the Slot Gap

In the space-charge limited flow acceleration model, electrons are freely emitted from the neutron star surface near the magnetic poles and accelerated in steady-state. When the electrons achieve a sufficient Lorentz factor they radiate curvature (CR) and inverse Compton (ICS) photons that can produce electron-positron pairs in the strong magnetic field. Some of the positrons turn around and accelerate downward toward the neutron star, while the electrons accelerate upward. This pair polarization screens the electric field above a pair formation front (PFF). These models assume a boundary condition that the accelerating electric field and potential are zero at the last open field line. Near the boundary, the electric field is lower and a larger distance is required for the electrons to accelerate to the Lorentz factor needed to radiate photons energetic enough to produce pairs. The PFF thus occurs at higher and higher altitudes as the boundary is approached and curves upward, approaching infinity and becoming asymptotically parallel to the last open field line. If the electric field is effectively screened above the PFF, then a narrow slot surrounded by two conducting walls is formed (see Figure 1). Within this slot gap, the electric field is further screened by the presence of the second conducting boundary and acceleration occurs at a reduced rate. Pair production and pair cascades therefore do not take place near the neutron star surface in the slot gap, as do the pair cascades along field lines closer to the magnetic pole (core), but occur at much higher altitudes.

There are several important differences between the revised slot-gap model of MH03 and the original slot-gap model of AS79. The inclusion of general relativistic frame dragging enables particle acceleration on both "favorably" curved (curving toward the rotation axis) and "unfavorable" curved (curving away from the rotation axis) field lines and also at all inclination angles. MH03 also consider the radiation from pair cascades occurring along the interior edge of the slot gap. The cascade radiation emission beam from the slot gap is thus a full hollow cone centered on the magnetic axis. A narrower emission beam from field lines interior to the slot gap will form a core component of pairs and high-energy emission.

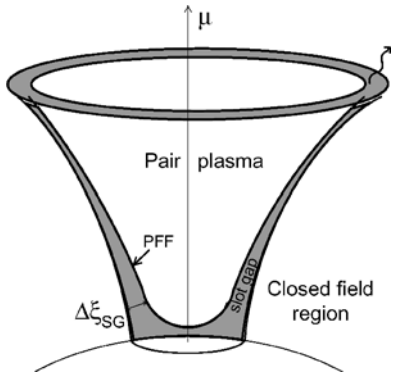


Figure 1. Schematic illustration of polar cap geometry, showing the outer boundary of the open field line region (where $E_\parallel = 0$) and the curved shape of the pair formation front (PFF) which asymptotically approaches the boundary at high altitude. The slot gap exists between the pair plasma, which results from the pair cascades above the PFF and the outer boundary. A narrow beam of high-energy emission originates from the low-altitude cascade on field lines interior to the slot gap. A broader, hollow-cone beam originates from the high-altitude cascade above the interior edge of the slot gap. $\Delta\xi_{SG}$ is the slot gap thickness (see text) and $\theta_{0,SG}$ is the colatitude at the center of the slot gap.

Since the potential in the slot gap is unscreened, electrons on field lines which thread the slot gap will continue accelerating to very high altitudes. Muslimov and Harding (2004, [MH04]) have derived the potential and accelerating electric field at high altitude in the extended slot gap by considering the effect of deviation of streamlines from the magnetic field lines of a static dipole. In the absence of this effect, the difference between the actual charge density along field lines and the corotation (or Goldreich-Julian) charge density, which grows with altitude above the polar caps, would become comparable to the Goldreich-Julian charge density itself, a situation which cannot be supported since it would disrupt the steady-state charge flow within the magnetic flux tube. However, long before this would occur, the drift of electrons in the slot gap across the magnetic field will largely damp the growth of the charge deficit and the large electric field, which would be induced perpendicular to the magnetic field. The residual parallel electric field is small and constant, but still large enough at all altitudes up to nearly the light cylinder to maintain a flux of electrons with Lorentz factors exceeding 10^7 in the slot gap.

MH04 matched the high-altitude slot gap solution for the parallel electric field to the solution found at lower altitudes (MH03). The result, for most inclination angles, is a continuously accelerating field from the neutron star surface to near the light cylinder along the last open field lines. The derived properties of the extended slot gap closely match the geometrical properties required for the two-pole caustic model of Dyks and Rudak (2003). Such a model can reproduce the double-peaked profiles seen in many γ-ray pulsars like the Crab, Vela and Geminga. MH04 demonstrated through numerical simulation of slot gap acceleration and radiation,

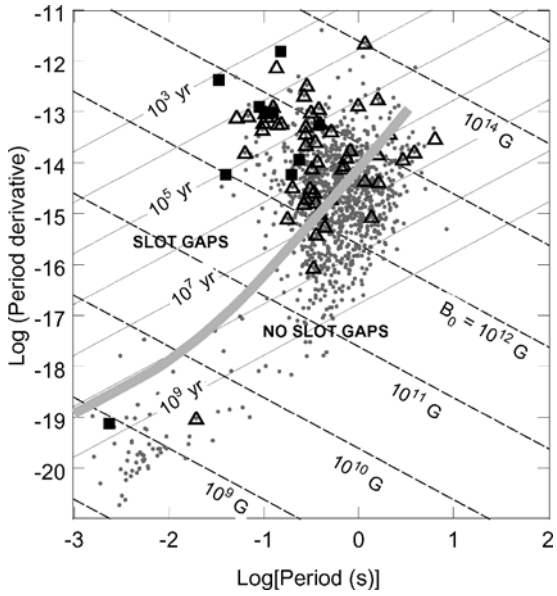


Figure 2. Radio pulsars from the ATNF catalog plotted on the P-$\dot{P}$ diagram. The gray dots are radio pulsars, solid squares are EGRET pulsars, and open triangles are radio pulsars in EGRET sources error circles. The gray line is the curvature radiation pair death line.

that the extended slot gap radiation will produce the caustic peaks and pulse profiles similar to those of the two-pole caustic model.

The existence of a slot gap requires a dense enough pair plasma on interior field lines to fully screen the parallel electric field, so that the inside walls of the gap have vanishing electric field. Harding and Muslimov (2002, [HM02]) found that pairs produced by CR are always able to fully screen the $E_{\parallel}$ whereas pairs from ICS were only able to screen locally, if at all. Therefore we can conclude that only those pulsars, which can produce CR pairs, will have slot gaps. Figure 2 reproduces the death line for CR pairs in P-$\dot{P}$ space from HM02, showing the region of pulsar parameter space required for slot gap formation. Generally, the younger pulsars, with ages less than 10^7 years and with higher magnetic fields fall into this region, although one or two ms pulsars may also have slot gaps.

3. Slot Gap Energetics

The electrodynamics of the slot gap is primarily dependent on a single parameter, the slot gap width, $\Delta\xi_{\rm SG}$. The ratio of the electric field in the slot gap to the electric field in the core region of the PC is $E_{\rm SG}/E_{\rm core} \propto \Delta\xi_{\rm SG}^2/4$ and the luminosity of particles accelerated in the slot gap is $L_{\rm prim} \propto \Delta\xi_{\rm SG}^3 L_{\rm sd}$ where $L_{\rm sd}$ is the spin-down luminosity of the pulsar (for full details see Muslimov and Harding, 2003). One

can estimate the width of the slot gap as the magnetic colatitude where the variation in height of the curvature radiation PFF becomes comparable to a fraction λ of the stellar radius R, or

$$\Delta\xi_{SG} \approx \begin{cases} 0.2\ P_{0.1}(\lambda B_{12})^{-4/7} I_{45}^{-3/7}. & B_{12} \lesssim 4.4 \\ 0.1\ P_{0.1}\left(\lambda B_{12}^{3/4}\right)^{-4/7} I_{45}^{-3/7} & B_{12} \gtrsim 4.4 \end{cases} \tag{1}$$

Where $I_{45} = I/10^{45}$ g·cm^2, I is the neutron star moment of inertia, $P_{0.1} = P/0.1$ s and $B_{12} = B_0/10^{12}$ G are the neutron star rotation period and surface magnetic field. Here, $\Delta\xi_{SG}$ is in units of the polar cap half-angle, $\theta_0 = \sin^{-1}(2\pi R/Pc)^{1/2}$. The emission solid angle of radiation from the slot gap can be estimated by integrating over the thin annulus defined by the slot gap width (Eq. (1)).

$$\Omega_{\rm SG} \approx \frac{9}{2}\pi\theta_0^2\eta\Delta\xi_{SG} \quad \text{ster}, \tag{2}$$

where $\eta \equiv r/R$ is the dimensionless radius of emission. Electrons accelerating in the slot gap will radiate curvature-radiation γ-rays, becoming radiation-reaction limited at Lorentz factors

$$\gamma \approx 3 \cdot 10^7 \left[\kappa_{0.15} B_{12} \frac{R_6^3}{P_{0.1}} \frac{\eta}{\eta_{\rm lc}} \nu_{\rm SG} |\cos\chi|\right]^{1/4}, \tag{3}$$

where $\kappa_{0.15} = \kappa/0.15 \approx I_{45}/R_6^3$, $\nu_{\rm SG} = 0.25\Delta\xi_{SG}^2$, $R_6 = R/10^6$ cm is the neutron star radius, χ is the pulsar inclination angle and $\eta_{\rm lc}$ is the dimensionless light cylinder radius. Based on the luminosity of the primary electrons and the above solid angle estimate, we may derive the quantity,

$$\begin{aligned} L_{\rm SG}(\Omega_\gamma) &= \frac{\varepsilon_\gamma L_{\rm prim}}{\Omega_{\rm SG}} \\ &= 3\times10^{34}\varepsilon_\gamma L_{\rm sd,35}^{3/7} P_{0.1}^{5/7} R_6^{17/7} \eta^{-1} \lambda^{-8/7} \mathbf{I}_{45}^{-6/7} \kappa_{0.15} \cos^2\chi \ \ \text{erg s}^{-1}\ \text{ster}^{-1} \end{aligned} \tag{4}$$

where $L_{\rm prim}$ is the luminosity in primary electrons accelerated in the slot gap, ε_γ is the radiation efficiency and $L_{\rm sd,35} \equiv L_{\rm sd}/10^{35}$ ergs^{-1} is the spin-down luminosity. The above expression for $L_{\rm SG}(\Omega_\gamma)$ is equivalent to the observed quantity $\Phi_\gamma\ d^2$, where Φ_γ is the high-energy bolometric flux observed at the Earth, and d is the distance to the pulsar. Figure 3 shows the observed (solid circles with error bars) and theoretical (upside-down triangles) values of $\Phi_\gamma d^2$ as a function of spin-down luminosity, $L_{\rm sd}$ for the 10 known γ-ray pulsars. The theoretical values are calculated for the parameters $\varepsilon_\gamma = 0.3$ and $\lambda = 0.1$ (see Eq. (4)). Note that parameter ε_γ can range from 0.2 to 0.5 in cascade simulations, and $\eta = 3$. In Figure 3 the dashed line represents the limit, where the spin-down luminosity is radiated into the unit solid

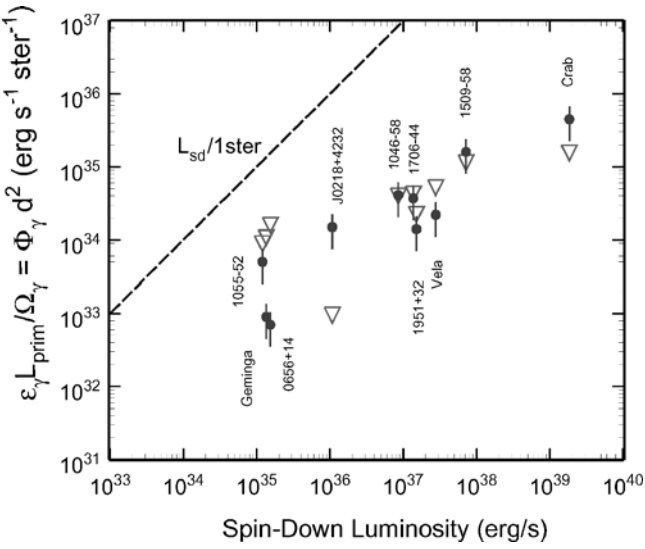


Figure 3. Observed flux above 1 keV, Φ_γ, times distance squared (from Thompson, 2001) (solid circles) and theoretical values of specific high-energy luminosity from the slot gap, $\varepsilon_\gamma\, L_{\rm prim}/\,\Omega_\gamma$ from Eq. (4) (upside-down triangles) vs. spin-down luminosity for known γ-ray pulsars. An efficiency of $\varepsilon_\gamma = 0.3$ was assumed. Also $\lambda = 0.1$, $\eta_\gamma = 3$ and the stellar parameters $R_6 = 1.6$ and $I_{45} = 4$ were used.

angle, i.e. where $\Phi_\gamma d^2 = L_{\rm sd}/1$ ster. One can see that there is good agreement for most high-energy pulsars except several of the pulsars, Geminga and PSR B0656 + 14, having low $L_{\rm sd}$, and for J0218 + 4232, which is a millisecond pulsar. These pulsars are near or below the curvature radiation pair death line (see Figure 2 and HM02), and therefore have either very wide slot gaps or no slot gaps at all. All other high-energy pulsars depicted in Figure 3 are well above the curvature radiation death lines and are expected to have slot gaps.

4. Slot Gap Emission and EGRET Unidentified Sources

There are presently 53 radio pulsars in the error circles of 28 EGRET unidentified sources (Kramer et al., 2003; Grenier, 2004). Nearly all of these pulsars have been discovered by surveys such as the Parkes Multibeam (Manchester et al., 2001) and by deep pointed searched by Arecibo and GBT radio telescopes (Camilo, 2004) after the end of EGRET operation. The pulsars coincident with EGRET sources are plotted in P-$\dot{P}$ space in Figure 2. Most of them are young ($\tau \lesssim 10^7$ years), high-field pulsars above the CR pair death line and many are expected to have slot gaps. There are unfortunately too few photons in any of the sources to do credible pulsation searches of the EGRET archival data, so such searches must await AGILE or GLAST. Many of the coincident EGRET sources contain multiple radio pulsars

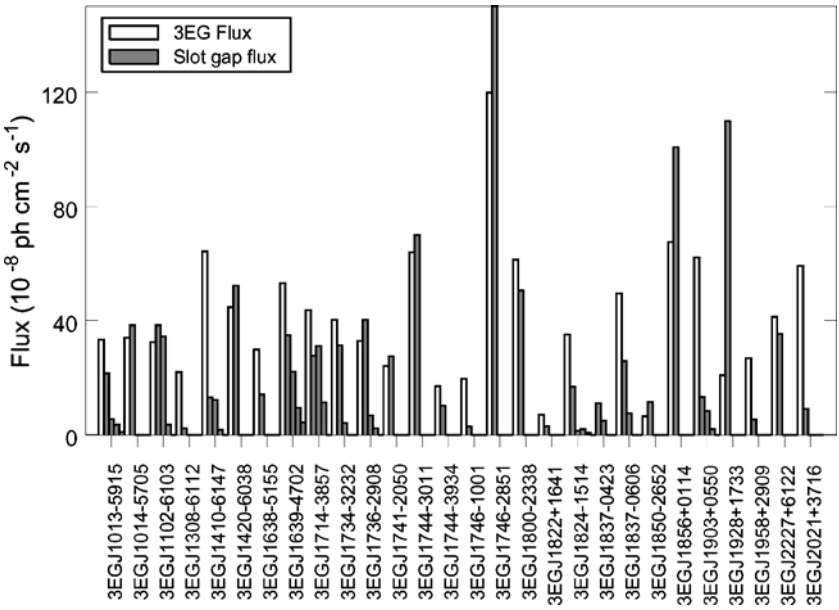


Figure 4. Comparison of fluxes of EGRET sources (white bars) and of associated radio pulsars (gray bars) as predicted by the slot gap model (Eq. (4) and Muslimov and Harding, 2003).

within the error circles. These are shown in Figure 4 with their observed average fluxes from the 3rd EGRET catalog (Hartman, 1999).

We have computed the γ-ray fluxes predicted by the slot gap model (Eq. (4)) for the EGRET source-coincident radio pulsars and the results are plotted in Figure 4. The fluxes of the pulsars, $L_{\rm SG}(\Omega_\gamma)/d^2$, where d is the distance, are shown as dark bars alongside the coincident EGRET source fluxes shown as light bars. In about 18–22 out of the 28 sources, the predicted slot gap flux from either an individual pulsar or several pulsars combined could account for the EGRET source flux. Thus more than two thirds of these associations are physically plausible, making the pulsars viable counterparts for the EGRET sources. In contrast, the predicted fluxes from the standard polar cap model (e.g. HM02), assuming a solid angle of 1 sr., would be comparable to the EGRET source fluxes in only about five of the cases.

5. Conclusions

In the slot gap model, pulsar high-energy emission comes from high altitudes, between 2 and 3 stellar radii above the neutron star surface to nearly the light cylinder. Two resulting characteristics of radiation from the slot gap: small solid angle and a wide emission beam, combine to provide a significantly larger flux for γ-ray pulsars than in the standard polar cap model. The small solid angle allows the

radiation from γ-ray pulsars to be seen by any given detector at larger distances, and many of the spatially coincident pulsars are at large distances, as determined from their dispersion measure. Thus, a larger number of the recently detected radio pulsars that are in or near EGRET source error circles become plausible candidates for the γ-ray sources. It is possible that half of the non-variable unidentified EGRET sources in the galactic plane are radio loud γ-ray pulsars. A population synthesis study of radio-loud and radio-quiet pulsars in the galaxy (Gonthier et al., 2004a,b) have found that in the slot gap model one expects that many more radio-loud than radio-quiet pulsars are counterparts to EGRET sources. This result is due to the fact that the radio emission occurs along the same open field lines as the γ-ray emission, in contrast to outer gap models where the radio emission is assumed to originate from open field lines on the opposite pole of the neutron star from the high-energy emission. The ratio of radio-loud to radio-quiet γ-ray pulsars detected by EGRET, and eventually by GLAST, will be a good discriminator between emission models.

References

Arons, J.: 1983, *ApJ* **302**, 301.

Arons, J. and Scharleman, E.T.: 1979, *ApJ* **231**, 854.

Becker, W. and Aschenbach, B.: 2002, in: *Neutron Stars, Pulsars, and Supernova Remnants*, Max-Plank-Institut für extraterrestrische Physik, Garching bei München, p. 64.

Camilo, F.: 2004, in: F. Camilo and B.M. Gaensler (eds.), *Young Neutron Stars and Their Environments*, IAU Symposium No. 218, Astronomical Society of the Pacific, San Francisco, CA, p. 97.

Cheng, K.S., Ho, C. and Ruderman, M.A.: 1986, *ApJ* **300**, 500.

Daugherty, J.K. and Harding, A.K.: 1996, *ApJ* **458**, 278.

Dyks, J. and Rudak, B.: 2003, *ApJ* **598**, 1201.

Grenier, I.A.: 2004, in: *The Multiwavelength Approach to Unidentified Gamma-Ray Sources*, Hong Kong.

Gonthier, P.L., Van Guilder, R. and Harding, A.K.: 2004, *ApJ* **604**, 775.

Gonthier, P.L., Harding, A.K., Grenier, I.A. and Perrot, C.: 2004, in: *The Multiwavelength Approach to Unidentified Gamma-Ray Sources*, Hong Kong.

Harding, A.K. and Muslimov, A.G.: 2002, *ApJ* **568**, 862.

Hartman, R.C., Bertsch, D.L., Bloom, S.D. et al.: 1999, *ApJS* **123**, 79.

Hirotani, K. and Shibata, S.: 2001, *MNRAS* **325**, 1228.

Kramer, M., Bell, J.F., Manchester, R.N. et al.: 2003, *MNRAS* **342**, 1299.

Manchester, R.N. et al.: 2001, *MNRAS* **328**, 17.

Muslimov, A.G. and Tsygan, A.I.: 1992, *MNRAS* **255**, 61.

Muslimov, A.G. and Harding, A.K.: 2003, *ApJ* **588**, 430.

Muslimov, A.G. and Harding, A.K.: 2004, *ApJ* **606**, 1143.

Thompson, D.J.: 2001, in: A.F. Aharonian and H.J. Völk (eds.), *Proceedings of the High Energy Gamma-Ray Astronomy*, American Institute of Physics (AIP), Vol. 558, AIP, Melville, New York.

RADIO-LOUD AND RADIO-QUIET GAMMA-RAY PULSARS FROM THE GALAXY AND THE GOULD BELT

P.L. GONTHIER[1], R. VAN GUILDER[2], A.K. HARDING[3], I.A. GRENIER[4] and C.A. PERROT[5]

[1]*Hope College, Department of Physics and Engineering, Holland, MI 49424, USA; E-mail: gonthier@hope.edu*
[2]*University of Colorado at Denver; E-mail: rvanguilder@usa.net*
[3]*NASA Goddard Space Flight Center; E-mail: harding@twinkie.gsfc.nasa.gov*
[4]*Université Paris VII & Service d'Astrophysique, CEA, Saclay; E-mail: isabelle.grenier@cea.fr*
[5]*Stanford Linear Accelerator Center; E-mail: cperrot@stanford.edu*

(Received 1 July 2004; accepted 31 August 2004)

Abstract. We present results of a population synthesis study of radio-loud and radio-quiet γ-ray pulsars from the Galactic plane and the Gould Belt. The simulation includes the Parkes multibeam pulsar survey, realistic beam geometries for radio and γ-ray emission from neutron stars and the new electron density model of Cordes and Lazio. Normalizing to the number of radio pulsars observed by a set of nine radio surveys, the simulation suggests a neutron star birth rate of 1.4 neutron stars per century in the Galactic plane. In addition, the simulation predicts 19 radio-loud and 7 radio-quiet γ-ray pulsars from the plane that EGRET should have observed as point sources. Assuming that during the last 5 Myr the Gould Belt produced 100 neutron stars, only 10 of these would be observed as radio pulsars with three radio-loud and four radio-quiet γ-ray pulsars observed by EGRET. These results are in general agreement with the recent number of about 25 EGRET error boxes that contain Parkes radio pulsars. Since the Gould Belt pulsars are relatively close by, the selection of EGRET radio-quiet γ-ray pulsars strongly favors large impact angles, β, in the viewing geometry where the off-beam emission from curvature radiation provides the γ-ray flux. Therefore, the simulated EGRET radio-quiet γ-ray pulsars, being young and nearby, most closely reflect the current shape of the Gould Belt suggesting that such sources may significantly contribute to the EGRET unidentified γ-ray sources correlated with the Gould Belt.

Keywords: pulsars, pulsar populations, γ-ray sources, Gould Belt, unidentified γ-ray sources

1. Introduction

While it continues to be a major challenge to identify the 150 EGRET unidentified γ-ray sources (Hartman et al., 1999 and the chapter by Grenier), the multi-wavelength approaches (Mukherjee and Halpern, 2001) have succeeded in identifying a few of these objects. Pulsars are believed to be an important class of the EGRET unidentified γ-ray sources. The largest group of EGRET sources appears to be AGNs (see chapter by Grenier). A group of 45 ± 6 unidentified sources (Grenier, 2000) have been spatially correlated to the location of the Gould Belt, which is a nearby structure of OB stars having produced about 100 supernova



Astrophysics and Space Science **297:** 71–80, 2005.
© Springer 2005

explosions during the past 5 Myr (Perrot and Grenier, 2003 and see the chapter by Grenier). However, such a large number suggests that nearly half of the anticipated 100 neutron stars from the Gould Belt are detectable by EGRET as point sources. We anticipate that the Gamma-ray Large Area Space Telescope (GLAST) will be able to determine whether many of these unidentified sources are radio-quiet γ-ray pulsars. GLAST will have the sensitivity and the ability to perform blind period searches required to identify nearby radio-quiet γ-ray pulsars.

Since the EGRET error boxes are quite large (1 degree), and it has not been possible to identify many of these sources, a statistical analysis of pulsar characteristics from a population synthesis study can provide important information on the likelihood that many of these unidentified sources are radio-quiet γ-ray pulsars. Such simulations also provide predictions for upcoming γ-ray telescopes like AGILE and GLAST. The ratio of radio-loud to radio-quiet γ-ray pulsars is an important parameter that will help in the discrimination of pulsar models. The polar cap model (Daugherty and Harding, 1996; Rudak and Dyks, 1999) predicts that the radio and γ-ray emission results from common field lines that are tied to the magnetic polar cap, the size of which is defined by the last open field line. As a result, the polar cap model predicts strong correlations between radio and γ-ray pulse profiles. Since the beams significantly overlap, the polar cap model predicts a large number of radio-loud γ-ray pulsars. However, the weaker off-beam γ-ray emission allows for some number of radio-quiet γ-ray pulsars. On the other hand, the outer gap model (Romani et al., 1995; Cheng et al., 2000) predicts that the region where γ-ray emission takes place is many stellar radii from the surface near the light cylinder along the null charge surface. The γ-ray emission from these regions tends to be anticorrelated to the radio emission, therefore, the outer gap model predicts a greater number of radio-quiet γ-ray pulsars. While the detections of GLAST may lead to a much larger number of unidentified γ-ray sources, it will detect a statistically significant number of radio-quiet and radio-loud γ-ray pulsars that may help resolve the location of the emission region in the pulsar magnetosphere.

2. Simulation – Assumptions

Our simulations are based on previous studies by Gonthier et al. (2002, 2004) with the addition of the contribution from the Gould Belt. Our current results represent an improvement over our previous study by Harding et al. (2004) that assumed for pulsars from the Gould Belt a simple geometry for the γ-ray beam and no consideration for radio emission. We have now included the geometry of the core and cone radio beams as well as the slot gap geometry as discussed more fully in Gonthier et al. (2004). For neutron stars born in the Galactic plane, we select a constant birth rate back time to 1 Gyr, while for the Gould Belt the oldest neutron stars are 5 Myr. The Gould Belt is assumed to be 26.4 Myr (Perrot and Grenier, 2003) with a recent supernova rate of the 2–5 times the local rate. The age of a

neutron star is randomly selected back to 5 Myr, and the shape of the Gould Belt at that time is determined by the evolution model of Perrot and Grenier (2003). The location of the neutron star is chosen uniformly over the disk of the Gould Belt. We then evolve the neutron stars in the Galactic potential to the present time. We find that in order to reproduce the distribution of the pulsars in the $\dot{P} - P$ diagram shown below in Figure 1a, we have to assume that the magnetic field decays with a

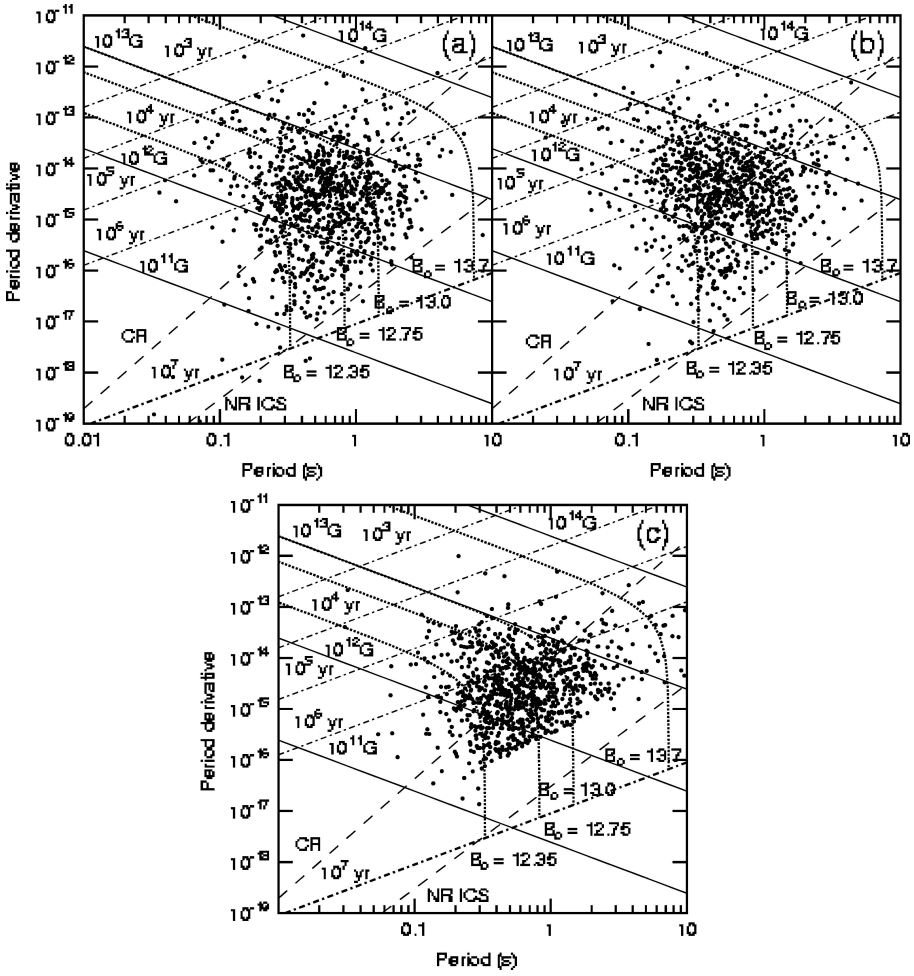


Figure 1. The distribution of 978 radio pulsars detected (1a) by a select group of surveys, same number of pulsars simulated from the plane (1b) and the same number simulated from the Gould Belt (1c) assuming magnetic field decay constant of 2.8 Myr. The solid lines represent the traditional no field decay lines of constant dipole magnetic field of 10^{11} to 10^{14} G. The dotted curves represent the paths of four 10^7-year-old pulsars with the indicated initial magnetic fields (Log), the dot-dashed lines show the lines of constant age assuming an initial period of zero seconds, and the dashed lines indicated the curvature radiation (CR) and nonresonant inverse Compton scattering (NRICS) death lines to the right of which pairs are no longer produced by these mechanisms.

constant of 2.8 Myr. For the radio beam geometry and luminosity, we have assumed the model of Arzoumanian et al. (2002) as well as their supernova kick velocity distribution. The geometry of the γ-ray beam is theoretically motivated by the work of Muslimov and Harding (2003) who describe the γ-ray emission from the slot gap. Alice Harding in the previous talk has described the slot gap emission model (Harding and Muslimov, 2004). The initial period of the pulsars is assumed to be a flat distribution from 0 to 150 ms with an initial magnetic field described by two Gaussians. We have included all-sky threshold maps for EGRET and AGILE and a more recent estimate for GLAST thresholds (Grenier, private communication) than was used in Gonthier et al. (2004).

3. Results

We normalize the number of neutron stars that are simulated in the plane in our select group of nine radio surveys (including the Parkes multibeam pulsar survey) to the number of pulsars (978) that have actually been detected by these surveys. We have included the information associated with each of these radio surveys that is required to obtain the flux threshold for each survey (see Gonthier et al., 2004). With this normalization, we are able to predict the neutron star birth rate in the plane. The normalization for the Gould Belt is based on simulating 100 neutron stars in the Gould Belt during the past 5 Myr. We are then able to predict the number of radio-quiet and radio-loud γ-ray pulsars from the plane and from the Gould Belt seen by various instruments. We show in Figure 1 the distribution of 978 detected radio pulsars (Figure 1a) by the select group of surveys, the same number of simulated radio pulsars from the plane (Figure 1b) and from the Gould Belt (Figure 1c). While we do not expect 978 pulsars from the Gould Belt, we show this number to see the overall distribution. The simulation predicts only a total of 10 radio pulsars from the Gould Belt. The Gould Belt pulsars occupy a similar place as the plane pulsars in the diagram except that they have an age limitation of 5 Myr. The small number of pulsars beyond the line is a result of the fact that the line represents the age of the pulsar with an initial period of zero seconds; while in the simulation we have assumed a flat distribution in period from 0 to 150 ms.

In order to predict an adequate birth rate and a distance distribution matching the observed distribution of radio pulsars, we had to reduce the radio luminosity of Arzoumanian et al. (2002) by a factor of 60 (see Gonthier et al., 2004). While it may be possible to tailor the radio luminosity model with a complicated dependence on the period and period derivative to account for the overall distribution, field decay leads quite naturally to the funnel-shaped distribution of the detected pulsars seen in the diagram.

In Figure 2, we compare the indicated characteristics between detected pulsars (shaded histograms) and simulated pulsars (open histograms). To improve

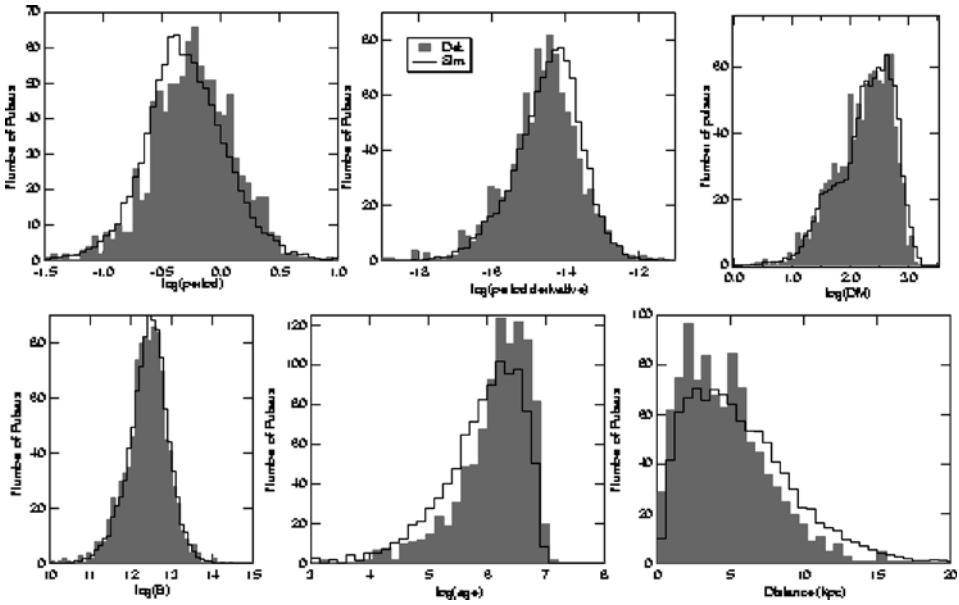


Figure 2. Distributions of various pulsar characteristics indicated as detected pulsars (shaded histograms) and simulated pulsars (open histograms) from the Galactic plane.

the statistics and smoothness of the simulated histograms, we run the simulation until the number of simulated pulsars detected by the radio surveys is equal to ten times the number of detected pulsars and then renormalize accordingly. As seen in the comparisons, the model simulation over predicts the number of pulsars with short periods, large period derivatives, and large distances. However, overall the agreement of the simulation of pulsars from the Galactic plane is fairly good.

In Figure 3, we present the distribution of pulsars in the $\dot{P} - P$ diagram of the known γ-ray pulsars detected by EGRET (a) and of those simulated for EGRET (b), AGILE (c) and GLAST (d), in which radio-loud γ-ray pulsars are shown as dots and the radio-quiet γ-ray pulsars are indicated by crosses. Young pulsars have higher γ-ray luminosities, which decrease as they approach the curvature pair death line where curvature radiation is no longer able to produce electron-positron pairs. Pulsars below the curvature pair death line are still able to produce pairs via nonresonant inverse Compton scattering of the thermal soft X-ray emission from the stellar surface. However, below the nonresonant inverse Compton scattering line, pulsars no longer produce pairs and become radio-quiet.

In Table I, we present the simulated γ-ray pulsar statistics for radio-quiet and radio-loud γ-ray pulsars as detected by various instruments as well as the ones that EGRET detected. The numbers to the left are those from the Galactic plane

TABLE I
Simulated γ-ray pulsar statistics

	Number of γ-ray pulsars (plane + Belt)		Ratio RL/RQ	
Source	Radio-loud	Radio-quiet	Plane	Gould Belt
Detected by EGRET	$6 + 1$	$0 + 1$		1
Simulated EGRET	$19 + 3$	$7 + 4$	2.3	0.8
Simulated AGILE	$37 + 5$	$13 + 4$	2.4	1.3
Simulated GLAST	$218 + 5$	$120 + 7$	1.8	0.7

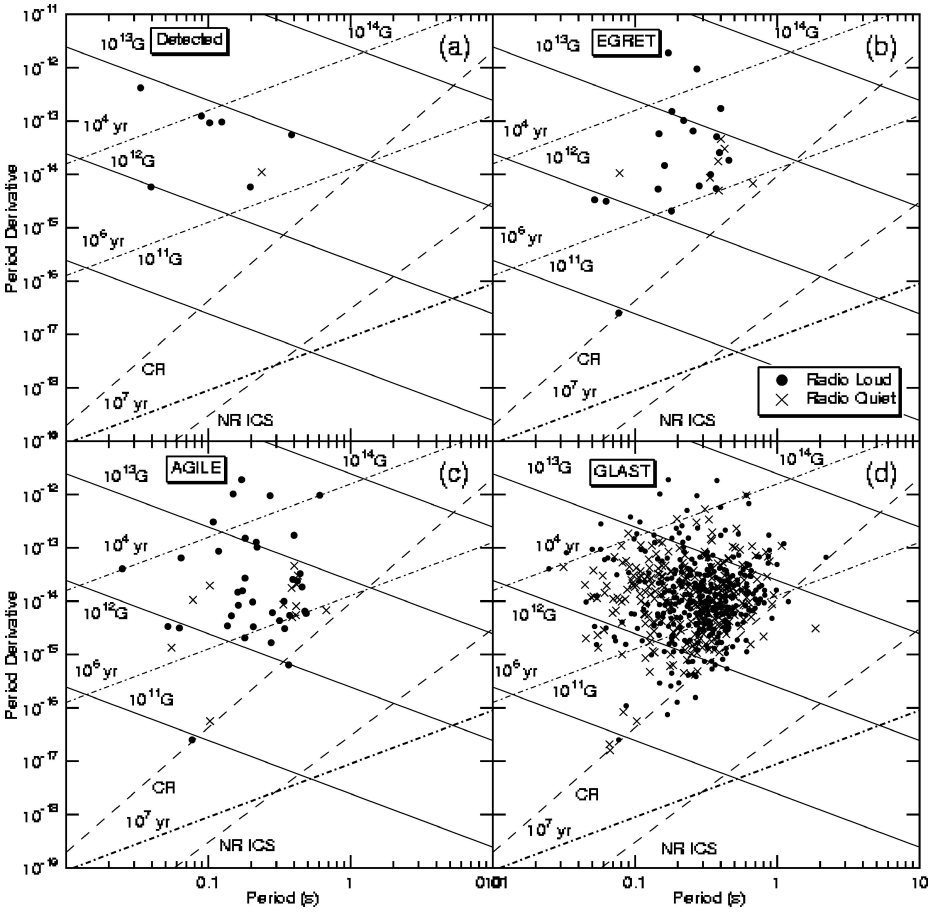


Figure 3. Distributions of radio-quiet (crosses) and radio-loud (dots) γ-ray pulsars (a) detected by EGRET, and simulated for (b) EGRET, (c) AGILE, and (d) GLAST, assuming a field decay constant of 2.8 Myr. Dashed lines represent the death lines for curvature radiation (CR) and for nonresonant inverse Compton scattering (NTICS). Dot-dashed lines represent the indicated pulsar age, assuming field decay, and solid lines represent the traditional magnetic surface field strength, assuming a constant dipole spin-down field.

and those added on the right represent the contribution from the Gould Belt. The last column represents the ratio of radio-loud to radio-quiet γ-ray pulsars. Our simulation predicts that EGRET should have detected 23 radio-loud and 12 radio-quiet γ-ray pulsars, AGILE should detect 42 radio-loud and 18 radio-quiet γ-ray pulsars, while GLAST, with increased sensitivity, should detect 224 radio-loud and 128 radio-quiet γ-ray pulsars from both the plane and the Gould Belt. For pulsars from the plane, the ratio of radio-loud to radio-quiet γ-ray pulsars goes down with GLAST, as GLAST begins to see pulsars that are further away than current radio telescopes can detect, thereby, seeing more γ-ray pulsars that escape radio detection.

Currently there are about 53 detected radio pulsars within about 28 of EGRET error boxes with about four pulsars detected using deep searches. So there are between 18 and 25 reasonably gamma-ray-bright radio pulsars (see chapter by Harding) within EGRET error boxes and eight previously detected γ-ray pulsars giving a total of about 32 radio-loud γ-ray point sources that EGRET has detected. Our simulation predicts a total of 22 radio-loud γ-ray pulsars with a contribution of three from the Gould Belt. In addition, our simulation indicates that there should be about 11 Geminga-like radio-quiet γ-ray pulsars with four of these being contributed by the Gould Belt. A total number of only seven γ-ray pulsars from the Gould Belt is significantly smaller than the 45 EGRET unidentified sources that have been previously correlated with the Gould Belt.

In order to explore the correlation of the Galactic position of γ-ray pulsars with the current location of the Gould Belt, we show in the Aitoff projections radio-quiet (crosses) and radio-loud (dots) γ-ray pulsars simulated for EGRET (a) and GLAST (b) in Figure 4. It is clear that there is a correlation especially for radio-quiet γ-ray pulsars simulated from the Gould Belt. We understand that there is a difficulty in detecting nearby radio pulsars as radio astronomers look for a dispersion signal above the local red noise that may identify it as a pulsar (Roberts, private conversation). However, we have not included such a filter into our simulation. As a result, we may be over estimating the number of nearby radio pulsars, and, therefore, due to the normalization of the pulsars from the plane, underestimating the number of γ-ray pulsars.

In Figure 5, we compare the distributions of the (a) impact angle, β, which is the angle between the line of sight, ζ, and the inclination angle, α, of the magnetic axis, and the distributions of the (b) age of the pulsars for radio pulsars from the Belt (shaded histograms), radio-loud (thin histograms) and radio-quiet (thick histograms) γ-ray pulsars simulated from the Gould Belt. The radio and radio-loud γ pulsars have smaller impact angles than radio-quiet γ-ray pulsars. However, γ-ray pulsars, either radio-quiet or radio-loud, must be younger in order to have sufficient γ-ray flux to be detected. Radio-quiet γ-ray pulsars have much larger impact angles than radio-loud γ-ray pulsars.

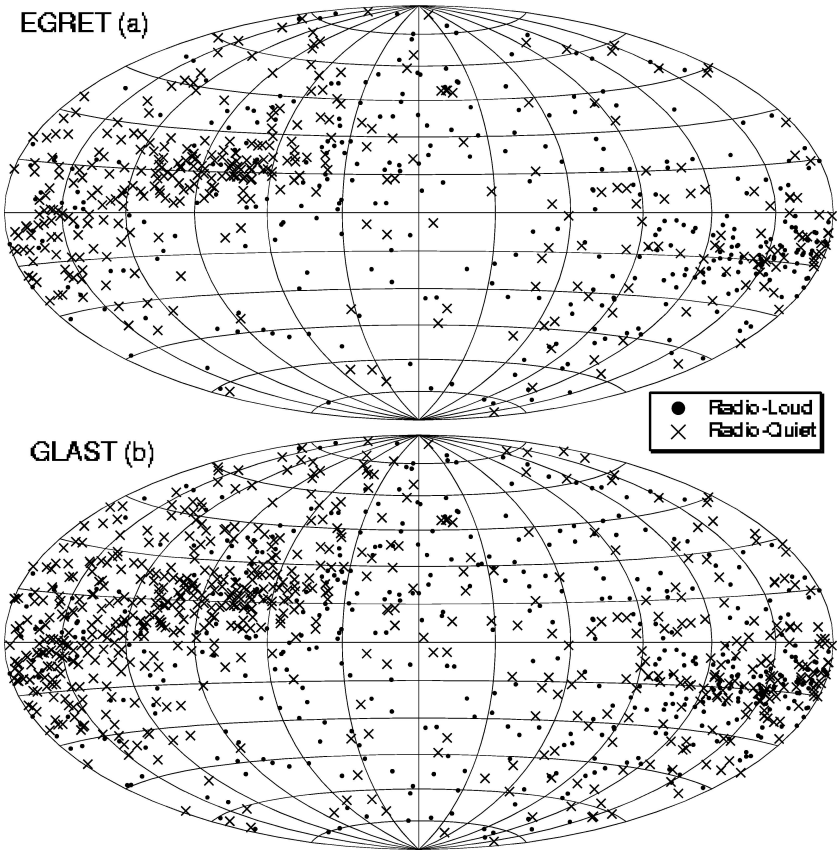


Figure 4. Aitoff plots of radio-quiet (crosses) and radio-loud (dots) γ-ray pulsars simulated for EGRET (a) and GLAST (b). An exaggerated number of pulsars contributed by the Gould Belt showing the correlation of Galactic position and the location of the Gould Belt.

A central assumption that is built into the radio geometry and luminosity model of Arzoumanian et al. (2002) is that the ratio of the core to cone peak fluxes varies as the reciprocal of the period, so that short period pulsars are core dominated and due to their small emission region (small solid angle) are harder to observe. On the other hand, the off beam curvature radiation of the γ-ray emission is much broader. Since the young neutron stars of the Gould Belt are fairly close, they are more probable to be detected in the γ rays than in radio due to the larger γ-ray solid angle. Therefore, radio-quiet γ-ray pulsars from the Gould Belt will have large impact angles (β) so that the viewer will miss the radio beam, but detect the off-beam γ-ray emission. Radio-loud γ-ray pulsars have smaller impact angles in order to see the radio core beam and the on-beam γ-ray emission. This viewing geometry has a larger radio and γ-ray luminosity. As a result, radio-loud γ-ray pulsars be older and have larger distances than radio-quiet γ-ray pulsars.

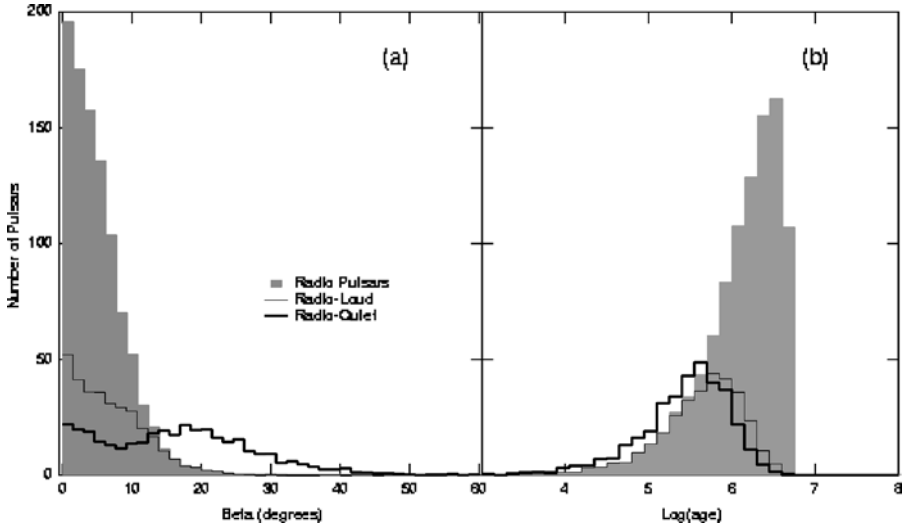


Figure 5. Distribution of (a) impact angles, β, which is the angle between the viewing angle, ζ, and the angle of inclination, α, and (b) the distribution of the age of the pulsars. We present in the figure the distributions of radio pulsars (shaded histograms), radio-loud (thin histograms) and radio-quiet (thick histograms) pulsars simulated from the Gould Belt for an arbitrary sample of neutron stars.

4. Conclusions

We present the results of a population synthesis study of radio and γ-ray pulsars from both the Galactic plane and the Gould Belt. The details of the simulation of pulsars from the plane are presented in Gonthier et al. (2004). There is a general consensus that many of the EGRET unidentified γ-ray sources are pulsars some of which must come from the Galactic plane and some from the Gould Belt. A significant number of EGRET error boxes have been found to contain one or more radio pulsars. We present some preliminary results in which neutron stars from the plane and the Gould Belt are treated consistently within the same set of assumptions. Consistent with the polar cap model, we find that the number of radio-loud γ-ray pulsars dominate over the radio-quiet γ-ray pulsars that have been simulated for EGRET but more especially for GLAST. This is in stark contrast to the outer gap model in which radio-quiet γ-ray pulsars dominate over radio-loud ones as indicated in the studies of Romani et al. (1995), Cheng et al. (2000) and the chapter by Cheng. Such model simulations indicate that GLAST may have the ability to then distinguish between these models, settling a long-standing debate over the location of the region within the neutron star magnetosphere where electrons are accelerated.

Our simulation indicates that the Gould Belt contributes 25% of the total number (9 out of 35) of simulated γ-ray pulsars that EGRET should have detected as point sources. Our simulations find that the positions of γ-ray pulsars from the Gould Belt does indeed map to the present location of the Gould Belt in a similar fashion as the positions of γ-ray pulsars from the plane map to the Galactic plane. This result

is expected as γ-ray pulsars must be young to be γ-ray bright, and, therefore, must not have moved very far from their birth location. However, nine γ-ray pulsars simulated from the Gould Belt is significantly smaller than the 45 EGRET unidentified sources that have been correlated to the Gould Belt. It may be that perhaps some of these are from the Galactic plane. Our simulation predicts a neutron star birth rate of 1.4 per century, which is somewhat lower than the findings of Tammann et al. (1994) who estimate a total supernova rate of $2.5^{+0.8}_{-0.4}$ per century with 85% arising from massive stars. Increasing the predicted supernova rate would require reducing the radio luminosity which is in the right direction as this would increase the number of γ-ray pulsars.

However, there are other larger uncertainties that must be settled. These include further understanding the ratio of the radio core to cone flux in radio pulsars as well as the inclusion the caustic γ-ray component (Dyks and Rudak, 2003; Muslimov and Harding, 2004). While the results of the simulation do depend on all the assumptions, there is a clear indication that polar cap and outer gap models predict significantly different ratios of radio-loud to radio-quiet γ-ray pulsars for EGRET but more so for GLAST.

Acknowledgements

We greatly appreciate the generous support from Research Corporation (CC5813), from the National Science Foundation (REU) and (AST-0307365) and from NASA – Astrophysics Theory Program.

References

Arzoumanian, Z., Chernoff, D.F. and Cordes, J.M.: 2002, *ApJ* **568**, 289.
Cheng, K.S., Ruderman, M. and Zhang, L.: 2000, *ApJ* **537**, 964.
Daugherty, J.K. and Harding, A.K.: 1996, *ApJ* **458**, 278.
Dyks, J. and Rudak, B.: 2003, *ApJ* **598**, 1201.
Gonthier, P.L. et al.: 2002, *ApJ* **565**, 482.
Gonthier, P.L., VanGuilder, R. and Harding, A.K.: 2004, *ApJ* **604**, 775.
Grenier, I.A.: 2000, *A&A* **364**, L93.
Harding, A.K., Gonthier, P.L., Grenier, I.A. and Perrot, C.A.: 2004, *Adv. Space Res.* **33**, 571.
Harding, A.K. and Muslimov, A.G., this conference.
Hartman, R.C. et al.: 1999, *ApJSS* **123**, 79.
Mukherjee, R. and Halpern, J.: 2001, in: A. Carraminaña, O. Reimer, D.J. Thompson (eds.), *The Nature of Unidentified Galactic High-Energy Gamma-Ray Sources* Vol. 267, Kluwer Academic Publishers, Dordrecht, p. 35.
Muslimov, A.G. and Harding, A.K.: 2003, *ApJ* **588**, 430.
Muslimov, A.G. and Harding, A.K.: 2004, *ApJ* **606**, 1143.
Perrot, C.A. and Grenier, I.A.: 2003, *A&A* **404**, 519.
Romani, R.W. et al.: 1995, *ApJ* **438**, 314.
Rudak, B. and Dyks, J.: 1999, *MNRAS* **303**, 477.
Tammann, G.A. et al.: 1994, *ApJSS* **92**, 487.

GAMMA-RAY EMISSION FROM PULSAR OUTER MAGNETOSPHERES

KOUICHI HIROTANI

Max-Planck-Institut fuer Kernphysik, Heidelberg, Germany; E-mail: hirotani@mpi-hd.mpg.de

(Received 25 June 2004; accepted 21 July 2004)

Abstract. We investigate a stationary pair production cascade in the outer magnetosphere of an isolated, spinning neutron star. The charge depletion due to global flows of charged particles, causes a large electric field along the magnetic field lines. Migratory electrons and/or positrons are accelerated by this field to radiate gamma-rays via curvature and inverse-Compton processes. Some of such gamma-rays collide with the X-rays to materialize as pairs in the gap. The replenished charges partially screen the electric field, which is self-consistently solved together with the energy distribution of particles and gamma-rays at each point along the field lines. By solving the set of Maxwell and Boltzmann equations, we demonstrate that an external injection of charged particles at nearly Goldreich-Julian rate does not quench the gap but shifts its position and that the particle energy distribution cannot be described by a power-law. The injected particles are accelerated in the gap and escape from it with large Lorentz factors. We show that such escaping particles migrating outside of the gap contribute significantly to the gamma-ray luminosity for young pulsars and that the soft gamma-ray spectrum between 100 MeV and 3 GeV observed for the Vela pulsar can be explained by this component. We also discuss that the luminosity of the gamma-rays emitted by the escaping particles is naturally proportional to the square root of the spin-down luminosity.

Keywords: gamma-rays: observations, gamma-rays: theory, magnetic fields, methods: numerical, pulsars: individual (Vela pulsar)

1. Introduction

Recent years have seen a renewal of interest in the theory of particle acceleration in pulsar magnetospheres, after the launch of the *Compton Gamma-ray Observatory* (CGRO). The Energetic Gamma Ray Experiment Telescope (EGRET) on board the CGRO has detected pulsed signals from at least seven rotation-powered pulsars (e.g., for the Vela pulsar, Kanbach et al., 1994; Fierro et al., 1998). Since interpreting γ-rays should be less ambiguous compared with reprocessed, non-thermal X-rays, the γ-ray pulsations observed from these objects are particularly important as a direct signature of basic non-thermal processes in pulsar magnetospheres, and potentially should help to discriminate among different emission models.

Attempts to model the pulsed γ-ray emissions have concentrated on two scenarios: Polar cap models with emission altitudes of $\sim 10^4$ cm to several neutron star radii over a pulsar polar cap surface (Harding et al., 1978; Daugherty and Harding,



Astrophysics and Space Science **297:** 81–91, 2005.
© Springer 2005

1982, 1996; Dermer and Sturner, 1994; Sturner et al., 1995; also see Scharlemann et al., 1978 for the slot gap model), and outer gap models with acceleration occurring in the open field zone located near the light cylinder (Cheng et al., 1986a,b, hereafter CHRa,b; Chiang and Romani, 1992, 1994; Romani and Yadigaroglu, 1995; Romani, 1996; see also Dyks et al., 2003, 2004 for two-pole caustic model). Both models predict that electrons and positrons are accelerated in a charge depletion region, a potential gap, by the electric field along the magnetic field lines to radiate high-energy γ-rays via the curvature process. However, there is an important difference between these two models: An polar-gap accelerator releases very little angular momenta, while an outer-gap one could radiate them efficiently. In addition, three-dimensional outer-gap models commonly explain double-peak light curves with strong bridges observed for the γ-ray pulsars. The purpose of the present paper is, therefore, to explore further into the analysis of the outer-gap models.

If a magnetized neutron star is rotating with angular velocity Ω, a static observer measures the rotationally induced charge density (Goldreich and Julian, 1969; Mestel, 1971)

$$\rho_{\rm GJ} \equiv -\frac{1}{4\pi c}\nabla\,[(\boldsymbol{\Omega}\times\boldsymbol{r})\times\boldsymbol{B}] = -\frac{\boldsymbol{\Omega}\cdot\boldsymbol{B}}{2\pi c}[1+O(\boldsymbol{\Omega}\times\boldsymbol{r}/c)^2], \tag{1}$$

where $\boldsymbol{\Omega}$ satisfies $|\boldsymbol{\Omega}| = \Omega$ and directs the rotation axis, $\boldsymbol{B}$ is the magnetic field at position $\boldsymbol{r}$ from the stellar center, c the speed of light. For a Newtonian dipole magnetic field, the null surface, where $\boldsymbol{\Omega}\cdot\boldsymbol{B}$ and hence $\rho_{\rm GJ}$ vanishes, is located on a constant colatitude in the outer magnetosphere on the poloidal plane.

If the real charge density, $\rho_{\rm e}$, deviates from $\rho_{\rm GJ}$ in any region, an electric field is exerted along $\boldsymbol{B}$. If the potential drop is sufficient, migratory electrons and/or positrons will be accelerated to radiate γ-rays via curvature and/or inverse-Compton (IC) processes.

In the CHR picture, the mainstream of the outer-gap model, the gap is hypothesized to be geometrically thin in the transfield direction on the poloidal plane in the sense $D_\perp \ll W$, where $D_\perp$ represents the typical *transfield* thickness of the gap, while W does the width *along* the magnetic field lines. In this limit, the acceleration electric field is partially screened by the zero-potential walls separated with a small distance $D_\perp$; as a result, the gap, which is assumed to be vacuum, extends from the null surface to (the vicinity of) the light cylinder, of which distance from the rotation axis is given by the so-called 'light cylinder radius', $\varpi_{\rm LC} \equiv c/\Omega$.

It should be noted that the null surface (where $\boldsymbol{\Omega}\cdot\boldsymbol{B}$ vanishes) is not a special place for the gap electrodynamics in the sense that the plasmas are not completely charge-separated in general and that the particles freely pass through this surface. Therefore, the gap inner boundary is located near to the null surface, not because a particle injection is impossible across this surface (as previously discussed), but because the gap is vacuum and transversely thin.

Then what happens in the CHR picture if the gap becomes no longer vacuum? To consider this problem rigorously, we have to examine the Poisson equation for the electrostatic potential. In fact, as have been demonstrated in Hirotani et al. (2003, Paper X), the original vacuum solution obtained in the pioneering work by CHR cannot be applied to a non-vacuum CHR picture. We are, therefore, motivated by the need to solve self-consistently the Poisson equation together with the Boltzmann equations for particles and γ-rays. Although the ultimate goal is to solve three-dimensional issues, a good place to start is to examine one-dimensional problems. In this context, Hirotani and Shibata (1999a,b,c; hereafter Papers I, II, III) and Hirotani (2000b, Paper VI) first solved the Boltzmann equations together with the Maxwell equations one-dimensionally along the field lines, extending the idea originally developed for black-hole magnetospheres by Beskin et al. (1992). Subsequently, Hirotani (2000a, Paper IV; 2001, Paper V) considered a 'gap closure condition' to constrain the gap width and estimated the γ-ray fluxes for individual pulsars.

There is one important finding in this new picture: The gap position shifts if there is a particle injection across either of the boundaries (Hirotani and Shibata, 2001, 2002a,b; hereafter Papers VII, VIII, IX). For example, when the injection rate across the outer (or inner) boundary becomes comparable to the typical Goldreich-Julian value, the gap is located close to the neutron star surface (or to the light cylinder). In other words, an outer gap is not quenched even when the injection rate of a completely charge-separated plasma across the boundaries approaches the typical Goldreich-Julian value.

In the next section, we formulate the basic equations. We then apply the theory to the Vela pulsar in §3 and we demonstrate that a soft power-law spectrum is generally formed in 100 MeV–3 GeV energies as a result of the superposition of the curvature spectra emitted by particles migrating at different positions. In the final section, we discuss the evolution of the γ-ray luminosity versus spin-down one.

2. A Self-Consistent Accelerator Model

2.1. One-dimensional poisson equation

For simplicity, we assume that a gap is transversely thick in the sense $D_\perp > W$ (or at least $D_\perp \sim W$). In this case, we can one-dimensionalize the Poisson equation as follows:

$$-\frac{\partial^2 \Psi}{\partial s^2} = -\frac{\Psi}{D_\perp^2} + 4\pi\left[\rho_{\rm e}(s) + \frac{\boldsymbol{\Omega}\cdot\boldsymbol{B}(s)}{2\pi c}\right], \tag{2}$$

where

$$\rho_{\rm e}(s) = e\int_1^\infty d\Gamma\,[N_+(s,\Gamma) - N_-(s,\Gamma)]\,. \tag{3}$$

The particle distribution functions N_+ and N_- obey the Boltzmann equations that will be described just below; Γ denotes the particle Lorentz factor.

2.2. Boltzmann equations for electrons and positrons

Imposing a stationary condition $\partial_t + \Omega\partial_\phi = 0$, and neglecting the pitch-angle dependence of the particle distribution functions, and approximating the collision term associated with the curvature process as an external force acting on a particle, we obtain the following Boltzmann equations for particles (Appendix A in Paper X)

$$B_{\rm p}\frac{\partial}{\partial s}\left(\frac{N_\pm}{B_{\rm p}}\right) \pm \left[eE_\parallel - \frac{P_{\rm CV}(s,\Gamma)}{c}\right]\frac{\partial N_\pm}{\partial\Gamma} = \pm S_\pm(s,\Gamma), \tag{4}$$

where the radiation-reaction force is given by $P_{\rm CV}/c = (2e^2\Gamma^4)/(3\rho_{\rm c}^2(s))$; $\rho_{\rm c}$ is the curvature radius of the magnetic field line. The collision terms are given by

$$\begin{aligned} S_\pm(s,\Gamma) = &-\int_{E_\gamma<\Gamma}\eta_{\rm IC}^\gamma(E_\gamma,\Gamma,\mu_\pm)N_\pm(s,\Gamma)\,dE_\gamma + \int_{\Gamma_i>\Gamma}\eta_{\rm IC}^{\rm e}(\Gamma_i,\Gamma,\mu_\pm)N_\pm d\Gamma_i \\ &+\int\left(\frac{\partial\eta_{\rm p}^+}{\partial\Gamma}G_+ + \frac{\partial\eta_{\rm p}^-}{\partial\Gamma}G_-\right)dE_\gamma, \end{aligned} \tag{5}$$

where G_+ and G_- denote the distribution functions of γ-rays propagating outwardly and inwardly, respectively. We suppose that the positrons (or electrons) collide with the soft photons at the same angle as the outwardly (or inwardly) propagating γ-rays. Then, the same collision angle $\cos^{-1}\mu_+$ (or $\cos^{-1}\mu_-$) is used for both IC scatterings and pair production. The collisions tend to be head-on (or tail-on) for inwardly (or outwardly) propagating γ-rays, as the gap approaches the star. The pair-production redistribution function is given by

$$\frac{\partial\eta_{\rm p}^\pm}{\partial\Gamma} \equiv \frac{\partial\eta_{\rm p}}{\partial\Gamma}(E_\gamma,\Gamma,\mu_\pm) = (1-\mu_\pm)\int_{E_{\rm th}}^\infty dE_{\rm s}\frac{dF_{\rm s}}{dE_{\rm s}}\frac{d\sigma_{\rm p}}{d\Gamma}, \tag{6}$$

where the pair-production threshold energy is defined by $E_{\rm th} \equiv [2/(1-\mu)][(m_{\rm e}c^2)^2/E_\gamma]$. The differential cross section $d\sigma_{\rm p}/d\Gamma$ is given in numerous textbooks in quantum electrodynamics.

The IC redistribution function $\eta_{\rm IC}^\gamma(E_\gamma,\Gamma,\mu)$ represents the probability that a particle with Lorentz factor Γ upscatters photons into energies between E_γ and $E_\gamma + dE_\gamma$ per unit time when the collision angle is $\cos^{-1}\mu$. On the other hand, $\eta_{\rm IC}^{\rm e}(\Gamma_i,\Gamma,\mu)$ describes the probability that a particle changes Lorentz factor from Γ_i to Γ in a scattering. Thus, energy conservation gives $\eta_{\rm IC}^{\rm e}(\Gamma_i,\Gamma_f,\mu) = \eta_{\rm IC}^\gamma[m_{\rm e}c^2(\Gamma_i - \Gamma_f),\Gamma_i,\mu]$. In general, $\eta_{\rm IC}^\gamma$ is defined by the soft photon flux $dF_{\rm s}/d\epsilon_{\rm s}$

and the Klein-Nishina cross section $\sigma_{\rm KN}$ as follows:

$$\eta_{\rm IC}^{\gamma}(E_\gamma, \Gamma, \mu_\pm) = (1 - \beta\mu_\pm) \int_0^\infty dE_{\rm s} \frac{dF_{\rm s}}{dE_{\rm s}} \int_{-1}^{1} d\Omega_\gamma^* \frac{d\sigma_{\rm KN}^*}{dE_\gamma{}^* d\Omega_\gamma^*} \frac{dE_\gamma{}^*}{dE_\gamma} \tag{7}$$

where $\beta \equiv \sqrt{1 - 1/\Gamma^2}$ is virtually unity, Ω_γ the solid angle of upscattered photon, the asterisk denotes the quantities in the electron (or positron) rest frame. The soft photon flux per unit photon energy $E_{\rm s}$ [$s^{-1}{\rm cm}^{-2}{\rm ergs}^{-1}$] is written as $dF_{\rm s}/dE_{\rm s}$. To obtain $\eta_{\rm IC}^{\gamma}$'s for individual pulsars, we substitute the observed X-ray spectrum $dF_{\rm s}/dE_{\rm s}$ and execute integration over $E_{\rm s}$ and Ω_γ^*. For further details of $\eta_{\rm IC}^{\gamma}$, see Appendix B in Paper X.

2.3. GAMMA-RAY BOLTZMANN EQUATIONS

In general, the γ-ray distribution function $G_\pm$ at momentum $\boldsymbol{k}$ obey the following Boltzmann equations

$$\frac{\partial G_\pm}{\partial t} + c\frac{\boldsymbol{k}}{|\boldsymbol{k}|} \cdot \nabla G_\pm(t, \boldsymbol{x}, \boldsymbol{k}) = S_\gamma(t, \boldsymbol{x}, \boldsymbol{k}), \tag{8}$$

where S_γ represents the collision terms. Imposing a stationary condition $\partial_t + \Omega\partial_\phi = 0$, we obtain

$$\pm c|\cos\Phi_\gamma| B_{\rm p} \frac{\partial}{\partial s}\left(\frac{G_\pm}{B_{\rm p}}\right) = -\int d\Gamma \frac{\partial \eta_{\rm p}}{\partial \Gamma} \cdot G_\pm(s, E_\gamma) + \int_1^\infty d\Gamma \left[\eta_{\rm IC}^{\gamma}(E_\gamma, \Gamma, \mu_\pm) + \eta_{\rm c}(E_\gamma, \Gamma)\right] N_\pm(s, \Gamma). \tag{9}$$

We integrate both sides of Eq. (9) over E_γ in appropriate energy bins to reduce them into ordinary differential equations.

2.4. BOUNDARY CONDITIONS

We consider the boundary conditions to solve the set of Maxwell and Boltzmann equations. Diving the γ-ray energies into m bins, and diving the Lorentz factors into n bins, we impose the following boundary conditions at the *inner* (starward) boundary ($s = s^{\rm in}$)

$$E_\parallel(s^{\rm in}) = 0, \quad \psi(s^{\rm in}) = 0, \tag{10}$$

$$\int_{b_i}^{b_{i+1}} G_+(s^{\rm in}, E_\gamma)\, dE_\gamma = 0 \quad \text{for } i = 1, 2, \ldots, m \tag{11}$$

$$N_+(s^{\rm in}, \Gamma_j) = \frac{\Omega B_{\rm p}(s^{\rm in})}{2\pi ce} y(\Gamma_j) \quad \text{for } j = 1, 2, \ldots, n, \tag{12}$$

where y is an appropriate function satisfying $\int_1^\infty y(\Gamma)d\Gamma = j^{\rm in}$. Moreover, current conservation law gives

$$\int_1^\infty N_-(s^{\rm in}, \Gamma)d\Gamma = \frac{\Omega B_{\rm p}(s^{\rm in})}{2\pi ce}(j_{\rm tot} - j^{\rm in}). \tag{13}$$

At the *outer* boundary ($s = s^{\rm out}$), we impose

$$E_\parallel(s^{\rm out}) = 0, \tag{14}$$

$$\int_{b_i}^{b_{i+1}} G_-(s^{\rm out}, E_\gamma)\, dE_\gamma = 0 \quad \text{for } i = 1, 2, \ldots, m \tag{15}$$

$$N_-(s^{\rm out}, \Gamma_j) = \frac{\Omega B_{\rm p}(s^{\rm out})}{2\pi ce} y(\Gamma_j) \quad \text{for } j = 1, 2, \ldots, n. \tag{16}$$

The current density created in the gap per unit flux tube can be expressed as $j_{\rm gap} = j_{\rm tot} - j^{\rm in} - j^{\rm out}$. We adopt $j_{\rm gap}$, $j^{\rm in}$, and $j^{\rm out}$ as the free parameters.

We have totally $2m + 2n + 4$ boundary conditions (10)–(16) for $2m + 2n + 2$ unknown functions $\int_{b_i}^{b_{i+1}} G_\pm(s, E_\gamma)dE_\gamma$, $N_\pm(s, \Gamma_j)$, $\Psi(s)$, and $E_\parallel(s)$. Therefore, two extra boundary conditions must be compensated by making the positions of the boundaries $s^{\rm in}$ and $s^{\rm out}$ be free. The two free boundaries appear because $E_\parallel = 0$ is imposed at *both* the boundaries and because $j_{\rm gap}$ is externally imposed. In other words, the gap boundaries ($s^{\rm in}$ and $s^{\rm out}$) shift, if $j^{\rm in}$ and/or $j^{\rm out}$ varies. That is, the gap position, as well as its width W, can be self-consistently solved from the set of Maxwell and Boltzmann equations.

3. Application to the Vela Pulsar

In this section, we apply the method described above to the Vela pulsar. For this aim, we first specify the X-ray field, $dF_{\rm s}/d\epsilon_{\rm s}$. ¿From Chandra observations in 0.25–8.0 keV, the spectrum of this pulsar is turned out to consist of two distinct component: A soft, thermal component and a hard, power-law component. Since the magnetospheric, power-law X-rays will be beamed away from the accelerator, we consider only the former component as the X-ray field illuminating the outer gap. This X-ray component can be modeled as a magnetic hydrogen atmosphere spectrum with effective temperature $kT = 0.68$ MK (Pavlov et al., 2001). We evaluate the IR photon field, which is needed to compute the IC scattering rate, from the Rayleigh-Jeans tail of the surface thermal emission.

Based on high-resolution Ca II and Na I absorption-line spectra toward 68 OB stars in the direction of the Vela supernova remnant, Cha et al. (1999) determined the distance to be 250 ± 30 pc. We assume that the solid angle of the emitted γ-rays is 1 ster throughout this paper.

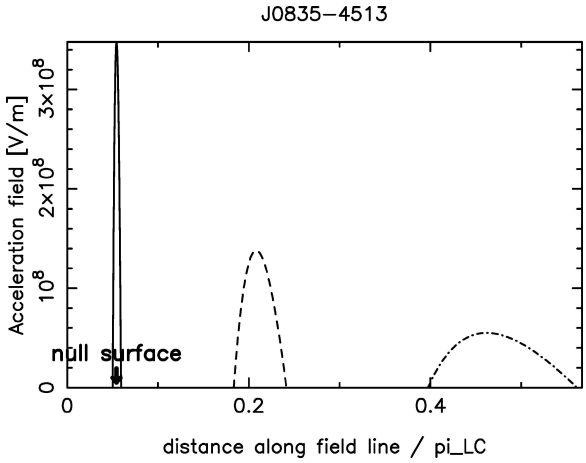


Figure 1. Spatial distribution of $E_\parallel(s)$ for $j^{\rm in} = 0$ (solid), 0.25 (dashed), and 0.5 (dash-dotted), for the Vela pulsar when $\alpha_{\rm i} = 75^\circ$ and $j_{\rm gap} = 4.6 \times 10^{-5}$ and $j^{\rm out} = 0$. The abscissa designates $s/\varpi_{\rm LC}$, the distance along the last-open field line normalized by the light cylinder radius.

3.0.1. *Acceleration Field and Characteristics*

Let us now consider the spatial distribution of $E_\parallel$. For this pulsar, a small created current density $j_{\rm gap} = 4.6 \times 10^{-5}$ gives the best-fit spectrum (see §3.0.3 for details). To compare the effects of particle injection, we present the $E_\parallel$ distribution for the three cases of $j^{\rm in} = 0$ (solid), 0.25 (dashed), and 0.50 (dash-dotted) in Figure 1. The magnetic inclination is chosen to be $\alpha_{\rm i} = 75^\circ$. We adopt $j^{\rm out} = 0$ throughout this paper, unless its value is explicitly specified.

As the solid line shows, the gap is located around the null surface when there is no particle injection across either of the boundaries. Moreover, $E_\parallel$ varies quadratically, because the Goldreich-Julian charge density deviates from zero linearly near to the null surface. As the dashed and dash-dotted lines indicate, the gap shifts outwards as $j^{\rm in}$ increases. When $j^{\rm in} = 0.5$ for instance, the gap is located on the half way between the null surface and the light cylinder. The gap width increases as it shifts outwards, because the γ-γ pair-production mean-free path increases due to decreased X-ray density.

3.0.2. *Particle Energy Distribution*

We present the energy distribution of positrons at several representative points along the field line in Figure 2. At the inner boundary ($s = 0.184\ \varpi_{\rm LC}$), particles are injected with Lorentz factors typically less than 4×10^6 as indicated by the solid line. Particles migrate along the characteristics in the phase space and gradually form a 'shock' as the dashed line (at $s = 0.205\varpi_{\rm LC}$) indicates, and attains maximum Lorentz factor at $s = 0.228\varpi_{\rm LC}$ as the dash-dotted line indicates. Then they begin to be decelerated gradually and escape from the gap with large Lorentz factors $\sim 2.8 \times 10^7$ (dotted line) at the outer boundary, $s = s^{\rm out} = 0.241\varpi_{\rm LC}$.

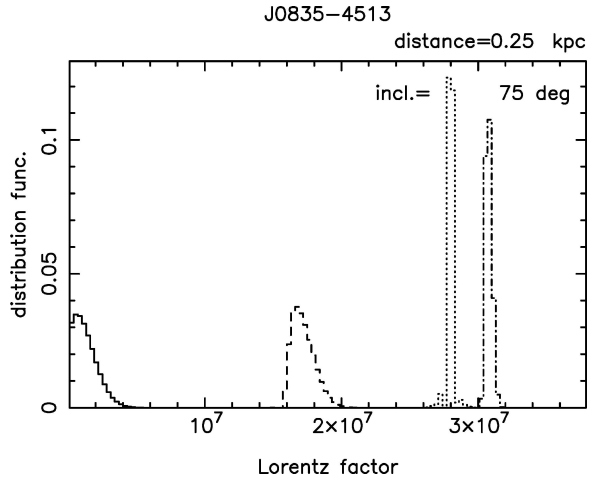


Figure 2. Particle energy distribution at several points along the magnetic field lines for $\alpha_{\rm i} = 75^\circ$ and $j^{\rm in} = 0.25$. Initial spectrum (solid line) evolves to dashed, dash-dotted, and dotted lines, as positrons propagate outwards.

The particles emit γ-rays not only inside of the gap but also outside of it, being decelerated by the curvature radiation-reaction force. The length scale of the deceleration is given by

$$l_{\rm curv} = c \cdot \frac{\Gamma m_{\rm e} c^2}{\frac{2e^2}{3c^3}\Gamma^4\left(\frac{c^2}{\rho_{\rm c}}\right)^2} = 0.4\varpi_{\rm LC}{\Omega_2}^{-1}\left(\frac{\Gamma}{10^7}\right)^{-3}\left(\frac{\rho_{\rm c}}{\varpi_{\rm LC}/2}\right)^2 \tag{17}$$

Since the typical Lorentz factor is a few times of 10^7, $l_{\rm curv}$ is typically much less than $\varpi_{\rm LC}$. Therefore, the escaping particles lose most of their energies well inside of the light cylinder.

3.0.3. *Formation of Power-Law Gamma-Ray Spectrum*

So far, we have seen that the outwardly propagating particles are not saturated at the equilibrium value and that such particles escape from the gap with sufficient Lorentz factors suffering subsequent cooling via curvature process. It seems, therefore, reasonable to suppose that a significant fraction of the γ-ray luminosity is emitted from such escaping particles.

We present in Figure 3 the γ-ray spectrum emitted from outwardly propagating particles (i.e., positrons) for $\alpha_{\rm i} = 75^\circ$ and $j^{\rm in} = 0.25$ (see also Takata et al., 2004). The dashed line represents the γ-ray flux emitted within the gap, while the solid one includes that emitted outside of the gap by the escaping particles. Therefore, the difference between the solid and the dashed lines indicates the γ-ray flux emitted by the particles migrating outside of the gap. For comparison, we plot

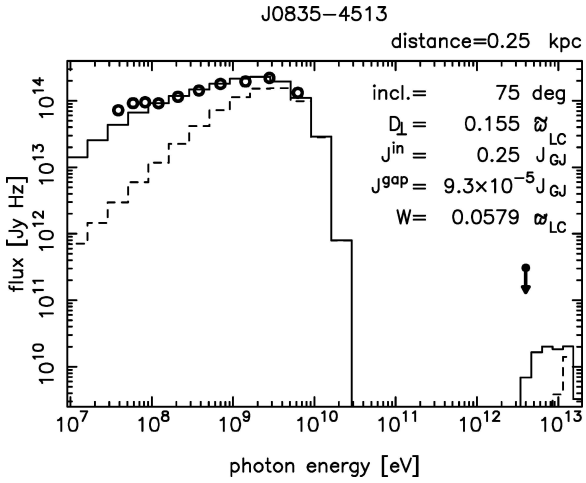


Figure 3. Computed γ-ray spectrum for the Vela pulsar for the same case as in Figure 2. The dashed line depicts the flux emitted within the gap, while the solid one includes that emitted outside it.

the phase-averaged EGRET spectrum, which is approximated by a power law with a photon index -1.7 (Kanbach et al., 1994) by open circles.

It follows from the figure that the γ-ray spectrum in 100 MeV–3 GeV energies can be explained by the curvature radiation emitted by the escaping particles. We adjusted the transfield thickness as $D_\perp = 0.16\varpi_{\rm LC} = 2.8W$ so that the observed flux may be explained. The luminosity of the γ-rays emitted outside of the gap contribute 48% of the total luminosity 5.08×10^{33}ergs s^{-1} between 100 MeV and 20 GeV.

4. Discussion

It should be noted that the emission from the escaping particles attain typically 40% of the total γ-ray luminosity for young pulsars. Thus, it is worth mentioning its relationship with the spin-down luminosity, $L_{\rm spin} = -I\Omega\dot{\Omega} \propto \Omega^{n+1}$, where the braking index n is related to the spin-down rate as $\dot{\Omega} = -k\Omega^n$. If the spin down is due to the magnetic dipole radiation, we obtain $n = 3$.

The outwardly propagating particles escape from the gap with spatial number density $N^{\rm out} = (j^{\rm in} + j_{\rm gap})(\Omega B)/(2\pi ce)$, Therefore, the energy carried by the escaping particles per unit time is given by $L_{\rm esc} = D_\perp^2 cN^{\rm out}\Gamma_{\rm esc}m_{\rm e}c^2$, where $\Gamma_{\rm esc}(\sim 10^{7.5})$ refers to the Lorentz factor of escaping particles. Let us assume that the position of the gap with respect to the light cylinder radius, $r^{\rm out}/\varpi_{\rm LC}$, does not change as the pulsar evolves; this situation can be realized if $j^{\rm in} - j^{\rm out}$ is unchanged. Evaluating B at $r = 0.5\varpi_{\rm LC}$, we obtain

$$L_{\rm esc} = \frac{4\Gamma_{\rm esc}m_{\rm e}c}{\pi e}\mu_{\rm m}\Omega^2\left(\frac{D_\perp}{\varpi_{\rm LC}}\right)^2 \propto {L_{\rm spin}}^{0.5}, \tag{18}$$

where $n = 3$ is assumed in the right-most proportionality. Note that Eq. (18) merely reflects the fact that the particles are unsaturated.

Let us compare this result with what would be expected in the CHR picture. Since the gap is extended significantly along the field lines in the CHR picture, particles are saturated at the equilibrium Lorentz factor to lose most of their energies within the gap, rather than after escaping from it. We can therefore estimate the γ-ray luminosity as (Paper X)

$$L_{\rm gap} = (D_\perp D_\phi W) \cdot N^{\rm out} = \frac{\mu_{\rm m}^2 \Omega^4}{4\pi c^3} \frac{D_\perp^3 D_\phi W}{\varpi_{\rm LC}^5} \left(\frac{\rho_{\rm c}}{0.5\varpi_{\rm LC}} \right)^{-1} \propto L_{\rm spin}, \tag{19}$$

where D_ϕ refers to the azimuthal thickness of the gap. As a pulsar ages, its declined surface emission results in a large pair-production mean free path, and hence W. As a result, particles tend to be saturated at the equilibrium value. On these grounds, we can predict that the γ-ray luminosity tends to be proportional to $L_{\rm spin}$ with age, deviating from $L_{\rm spin}^{0.5}$ dependence for young pulsars.

References

Beskin, V.S., Istomin, Ya.N. and Par'ev, V.I.: 1992, *Sov. Astron.* **36**(6), 642.
Cha, A.N., Sembach, K.R. and Danks, A.C.: 1999, *ApJ* **515**, L25.
Cheng, K.S., Ho, C. and Ruderman, M.: 1986a, *ApJ* **300**, 500.
Cheng, K.S., Ho, C. and Ruderman, M.: 1986b, *ApJ* **300**, 522.
Chiang, J. and Romani, R.W.: 1992, *ApJ* **400**, 629.
Chiang, J. and Romani, R.W.: 1994, *ApJ* **436**, 754.
Daugherty, J.K. and Harding, A.K.: 1982, *ApJ* **252**, 337.
Daugherty, J.K. and Harding, A.K.: 1996, *ApJ* **458**, 278.
Dermer, C.D. and Sturner, S.J.: 1994, *ApJ* **420**, L75.
Dyks, J. and Rudak, B.: 2003, *ApJ* **598**, 1201.
Dyks, J., Harding, A.K. and Rudak, B.: 2004, *ApJ* **606**, 1125.
Fierro, J.M., Michelson, P.F., Nolan, P.L. and Thompson, D.J.: 1998, *ApJ* **494**, 734.
Goldreich, P. and Julian, W.H.: 1969, *ApJ* **157**, 869.
Harding, A.K., Tademaru, E. and Esposito, L.S.: 1978, *ApJ* **225**, 226.
Hirotani, K.: 2000a, *MNRAS* **317**, 225 (Paper IV).
Hirotani, K.: 2000b, *PASJ* **52**, 645 (Paper VI).
Hirotani, K.: 2001, *ApJ* **549**, 495 (Paper V).
Hirotani, K. and Shibata, S.: 1999a, *MNRAS* **308**, 54 (Paper I).
Hirotani, K. and Shibata, S.: 1999b, *MNRAS* **308**, 67 (Paper II).
Hirotani, K. and Shibata, S.: 1999c, *PASJ* **51**, 683 (Paper III).
Hirotani, K. and Shibata, S.: 2001a, *MNRAS* **325**, 1228 (Paper VII).
Hirotani, K. and Shibata, S.: 2001b, *ApJ* **558**, 216 (Paper VIII).
Hirotani, K. and Shibata, S.: 2002, *ApJ* **564**, 369 (Paper IX).
Hirotani, K., Harding, A.K. and Shibata, S.: 2003, *ApJ* **591**, 334 (Paper X).
Kanbach, G., Arzoumanian, Z., Bertsch, D.L., Brazier, K.T.S., Chiang, J., Fichtel, C.E., Fierro, J.M., Hartman, R.C. et al.: 1994, *A&A* **289**, 855.
Mestel, L.: 1971, *Nat. Phys. Sci.* **233**, 149.

Pavlov, G.G., Zavlin, V.E., Sanwal, D., Burwitz, V. and Garmire, G.P.: 2001, *ApJ* **522**, L129.
Romani, R.W.: 1996, *ApJ* **470**, 469.
Romani, R.W. and Yadigaroglu, I.A.: 1995, *ApJ* **438**, 314.
Scharlemann, E.T., Arons, J. and Fawley, W.T.: 1978, *ApJ* **222**, 297.
Sturner, S.J., Dermer, C.D. and Michel, F.C.: 1995, *ApJ* **445**, 736.
Takata, J., Shibata, S. and Hirotani, K.: 2004, *MNRAS* **348**, 241.

PULSAR WIND NEBULAE IN EGRET ERROR BOXES

MALLORY S.E. ROBERTS[1], CRYSTAL L. BROGAN[2], BRYAN M. GAENSLER[2], JASON W.T. HESSELS[2], C.-Y. NG[3] and ROGER W. ROMANI[3]

[1]*McGill University/Eureka Scientific; E-mail: roberts@physics.mcgill.ca*
[2]*Institute for Astronomy, Harvard-Smithsonian CfA, McGill University*
[3]*Stanford University*

(Received 2 July 2004; accepted 7 September 2004)

Abstract. A remarkable number of pulsar wind nebulae (PWN) are coincident with *EGRET* γ-ray sources. X-ray and radio imaging studies of unidentified *EGRET* sources have resulted in the discovery of at least six new pulsar wind nebulae (PWN). Stationary PWN (SPWN) appear to be associated with steady *EGRET* sources with hard spectra, typical for γ-ray pulsars. Their toroidal morphologies can help determine the geometry of the pulsar which is useful for constraining models of pulsed γ-ray emission. Rapidly moving PWN (RPWN) with more cometary morphologies seem to be associated with variable *EGRET* sources in regions where the ambient medium is dense compared to what is typical for the ISM.

Keywords: PWN, EGRET, PSR J2021+3651, GeV J1809−2327, RABBIT, gamma-ray

1. Coincidence of PWN with EGRET Sources

A pulsar wind nebula (PWN) is a X-ray, radio, and/or Hα nebula caused by a relativistic particle wind from an energetic pulsar (see Kaspi et al., 2004; Gaensler, 2004 for recent reviews). Of the ∼50 known PWN, a large fraction are coincident with *EGRET* sources. If we consider only the ∼30 sources with significant emission above 1 GeV (listed in the catalog of Lamb and Macomb, 1997) which are probably associated with our galaxy, nearly half the error ellipses contain a known PWN, and several of the others have not yet been searched carefully for X-ray nebulae. In Table I, we list all the known PWN coincident with *EGRET* sources (for references to these sources, see http://www.physics.mcgill.ca/∼pulsar/pwncat.html). We also list the morphological type (S or R, see the table) if it can be determined, the pulsar spin-down energy $\dot{E}$ if pulsations have been detected, and the variability index V_{12} of the *EGRET* source as defined and determined by Nolan et al. (2003). $10^{-V_{12}}$ is the integrated likelihood that the variability measure $\tau \equiv \sigma_F/\langle F\rangle \leq 0.12$, or the >100 MeV flux is consistent with being constant. In other words, $V_{12} > 1$ indicates a >90% confidence level that the γ-ray source is variable. No value indicates there is no evidence for variability.

At least six of these PWN were discovered through X-ray searches of the *EGRET* error box, indicating that whatever the physical association, γ-ray sources in the

© Springer 2005

TABLE I
Pulsar wind nebulae coincident with *EGRET* sources

Name	3EG name	GeV name	Type	log $\dot{E}$	V_{12}
CTA 1	3EG J0010+7309	GeV J0008+7304	?	–	0.40
Crab	3EG J0534+2200	GeV J0534+2159	S	38.7	–
Geminga	3EG J0633+1751	GeV J0634+1746	R	34.5	0.16
Vela	3EG J0834−4511	GeV J0835−4512	S	36.8	0.61
MSH 11-62	3EG J1102−6103	–	R	–	–
PSR J1016−5857	3EG J1013−5915	–	?	36.4	0.18
PSR B1046−58	3EG J1048−5840	GeV J1047−5840	?	36.3	–
PSR J1420−6048	3EG J1420−6038	GeV J1417−6100	?	37.0	1.59
Rabbit	3EG J1420−6038	GeV J1417−6100	R	–	1.59
PSR B1706−44	3EG J1710−4439	GeV J1709−4430	S	36.5	–
G359.89−0.08	3EG J1746−2851	GeV J1746−2854	R	–	2.35
G7.4−2.0	3EG J1809−2328	GeV J1809−2327	R	–	3.93
G18.5−0.4	3EG J1826−1302	GeV J1825−1310	R	–	3.22
PSR B1853+01	3EG J1856+0114	GeV J1856+0115	R	35.6	1.57
3C 396	3EG J1903+0550	–	?	–	0.42
CTB 87	3EG J2016+3657	–	?	–	0.63
PSR J2021+3651	3EG J2021+3716	GeV J2020+3658	S	36.5	0.71
PSR J2229+6114	3EG J2227+6122	GeV J2227+6101	S	37.4	0.21

galactic plane can serve as guides to the location of energetic pulsars that otherwise might be difficult to find.

2. Pulsar Geometry from Stationary Pulsar Wind Nebulae

The environment of a young pulsar is the expanding ejecta of its progenitor star. This allows for fast expansion of the young PWN relative to the kick velocity imparted to the pulsar. Therefore, the motion of the pulsar does not greatly affect the structure of the PWN. The underlying symmetries of the pulsar's spinning magnetic field are then reflected in the structure of the X-ray emitting PWN. We refer to these as stationary PWN (SPWN). SPWN tend to have some sort of equatorial toroidal structure and polar jets. The apparent ellipticity and brightness variations of these toroidal structures can be used to infer the orientation of the pulsar's spin axis relative to the observer. In addition, the magnetic inclination angle may relate to the thickness of the torus in the case of single or concentric torii such as the Crab, or the separation between two parallel torii such as is apparently the case for the Vela PWN. For details in the methodology used to model observed SPWN torii, see Ng and Romani (2004).

This geometrical information is crucial for interpreting γ-ray pulse profiles and hence understanding the particle acceleration mechanisms in pulsar magnetospheres. It is therefore important to infer the geometry of many torii around γ-ray emitting pulsars. Unfortunately, in only a handful of cases is the PWN structure clear enough for unambiguous interpretation of the geometry, even with the high resolution of the Chandra X-ray observatory. Only three of the known γ-ray pulsars (Crab, Vela, and PSR B1706−44) have torii amenable to fitting. It is therefore important to expand the number of potential γ-ray emitting pulsars with torii. X-ray imaging of unidentified *EGRET* source error boxes has resulted in the detection of two energetic young pulsars with well-structured nebulae: PSR J2229+6114 (Halpern et al., 2001) and PSR J2021+3651 (Hessels et al., 2004).

The methodology used to discover PSR J2021+3651 is illustrative of how to discover and measure usable torii. The γ-ray source is in the crowded Cygnus region, which contains two highly significant GeV catalog sources, which are not listed in the third *EGRET* catalog. A refitting of the region using only photons above 1 GeV but including all known *EGRET* sources was performed in order to obtain the best position (see Figure 1). A low resolution, wide field, hard X-ray observation was made using the *ASCA* GIS detectors, discovering an apparent point source at the $\sim 1'$ resolution of *ASCA* (Roberts et al., 2001). This allowed the $3'$ beam of the Arecibo telescope to perform a very deep search of the source to discover

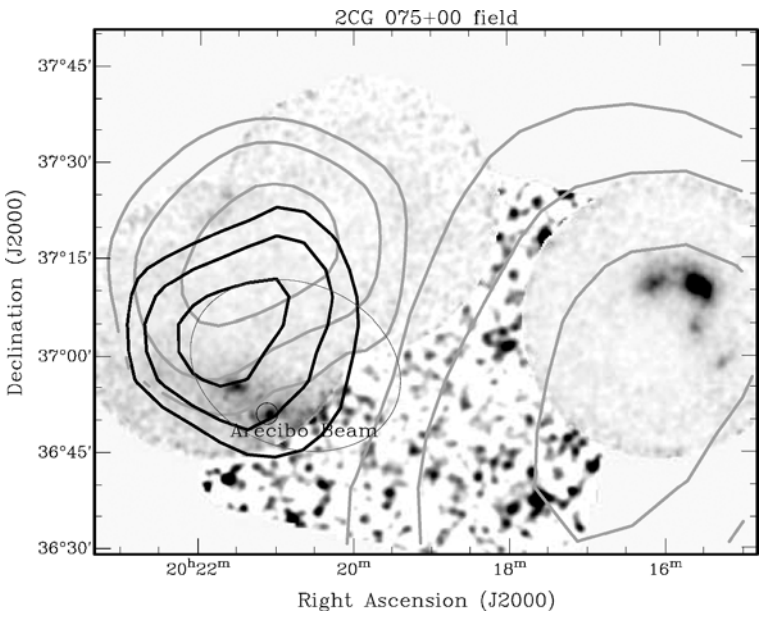


Figure 1. X-ray image of the region of the COS B source 2CG 075+00 containing two third EGRET catalog sources (light green contours), one GeV catalog source (ellipse) and the refit GeV contours. The Arecibo beam pointing is shown, which was used to discover PSR J2021+3651.

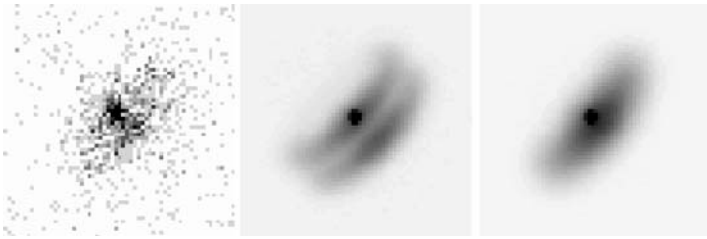


Figure 2. Chandra image of PSR J2021+3651 with best fit double and single torus models (Hessels et al., 2004).

the ∼0.1 mJy pulsar with spin properties virtually identical to PSR B1706−44 (Roberts et al., 2002). A 20 ks Chandra *ACIS* image of the X-ray source revealed a compact nebula with a morphology highly suggestive of a double torus with polar jets. However, the scarcity of counts in the image leaves some ambiguity as to whether or not it is a single or double torus, and whether the jets are real (Figure 2).

If the double torus interpretation is made, then the separation of the two torii can be assumed to be an indication of the magnetic inclination angle. This can be sanity checked by looking at the intrinsic radio pulse width, which may indicate whether the pulse is predominantly a core or conal component, and by measuring the radio polarization sweep and fitting it to a Radhakrishnan and Cooke (1969) model.

Unfortunately, the earlier five sources are the only known pulsars associated with *EGRET* sources whose nebulae are large enough and bright enough to be useful for fitting. However, there are several more PWN with toroidal morphologies which either do not yet have detected pulsations or are not yet associated with a γ-ray source. Even with *GLAST*, it is likely that only ∼10 γ-ray pulsars will be found whose geometry can be well constrained by their nebulae with Chandra imaging. We can only hope that will be enough to determine the location in the magnetosphere where γ-rays are emitted.

3. Rapidly Moving Pulsar Wind Nebulae Associated with Variable *EGRET* Sources

The SPWN discussed earlier tend to be associated with hard spectrum ($\Gamma \lesssim 2$), steady ($V_{12} < 1$) *EGRET* sources. Such sources tend to be nearly 100% pulsed in 100–10,000 MeV γ-rays, and be the youngest and most energetic pulsars. After a few thousand years, the reverse shock of the supernova blast wave reaches the PWN, after which the environment is no longer the freely expanding ejecta causing the PWN expansion to slow dramatically and become subsonic. If the pulsar has a significant space velocity, it will start to catch up to the forward edge of the PWN,

drastically affecting the morphology as ram-pressure becomes more important. If the space velocity exceeds the local sound speed, then the PWN will be confined in the forward direction by a bow-shock. These cometary shaped nebulae we refer to as rapidly moving or ram-pressure-confined PWN (RPWN). In X-rays, they generally have a narrow outflow trailing the pulsar, with the pulsar itself typically having a spin-down energy such that $\log \dot{E} \sim 35.5$–36.5 erg/s, somewhat less than the typical SPWN. This is expected, given their on average greater age.

Perhaps the best example of a RPWN is the Mouse nebula near the galactic center. The X-ray nebula of the Mouse is significantly brighter than other RPWN, and consequently shows significantly more structure (Figure 3). A "tongue" of brighter emission is surrounded by a fainter halo, which is contained within the bright radio "head" of the Mouse. A fainter radio body extends back from the head, which eventually narrows into an extremely long tail (Gaensler et al., 2003). Hydrodynamic models suggest the tongue is associated with the wind termination shock. However, much of the structure, especially downstream of the head, is currently not understood. The generally short Chandra observations of other RPWN contain very few counts, and only the structure corresponding to the Mouse's "tongue" is clearly delineated.

Remarkably, several RPWN have been discovered in the error boxes of *EGRET* sources which are apparently variable. The source with the highest V_{12} value in the galactic plane without a potential Blazar identification is GeV J1809−2327. An

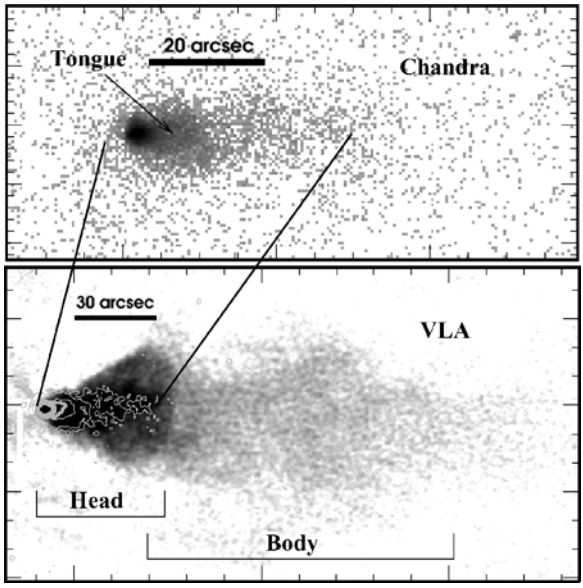


Figure 3. Chandra X-ray and VLA radio images of the Mouse nebula showing the various structures (Gaensler et al., 2003).

X-ray nebulae was discovered in its error box with *ASCA* (Roberts et al., 2001), which subsequent Chandra and VLA imaging showed to be a RPWN (Braje et al., 2002). An XMM-Newton EPIC-PN observation, which was unfortunately taken in small window mode, suggests a fainter X-ray halo surrounding the X-ray trail seen in the short Chandra exposure, strongly reminiscent of the Mouse (Figure 4). The X-ray emission seen in the EPIC-PN image is coincident with the front edge of the radio PWN, itself reminiscent of the head of the Mouse, with the suggestion of a fainter, extended body to the northwest. The radio and X-ray emission seems to extend back towards a possible X-ray SNR, G7.4−1.4, discovered by *ROSAT*. Wide-field 90 cm imaging is underway to determine if there is a corresponding radio SNR. The PWN appears to be embedded in the Lynds 227 dark Nebula, and CO imaging suggests a physical connection between the PWN and the molecular cloud (Oka et al., 1999).

The region near galactic longitude $l = 18^\circ$ contains several *EGRET* sources, one or more of which are probably associated with the well-known unidentified 1–30 MeV Comptel source (see Collmar et al., these proceedings). Wide-field radio imaging (Brogan et al., manuscript in preparation) of the region shows several SNR and the Sharpless 53 cluster of HII regions. One of the *EGRET* sources, GeV J1825−1310, has the second highest V_{12} value of galactic plane sources. *ASCA* imaging of this source followed by a short Chandra image again revealed a faint RPWN in a stellar cluster (Romani et al., manuscript in preparation). There is some hint of a larger radio nebula in the 90 cm image.

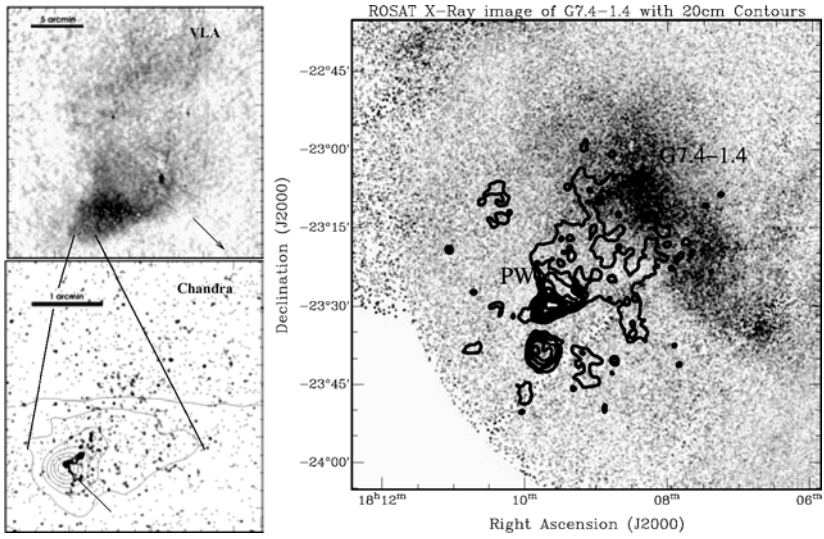


Figure 4. *Left*: VLA and Chandra images of the PWN in GeV J1809−2327. The contours on the Chandra image are from the EPIC-PN, which are cut off due to the small window used. *Right*: *ROSAT* image of the SNR G7.4−1.4, with contours from the VLA image of the PWN.

Two other sources with $V_{12} > 1.3$ (95% confidence of variability) contain apparent RPWN. One is the PWN around PSR B1853+01 in the X-ray composite SNR W44 (Petre et al., 2002). The other is the source containing the Kookaburra radio complex, the wings of which contain the PWN around PSR J1420−6048 and the Rabbit PWN (Roberts et al., 1999). Chandra and XMM-Newton imaging of the Rabbit nebula (Ng et al., manuscript in preparation; Roberts et al., manuscript in preparation) show the X-ray emission going from a point source in the front paw back towards the body and the southern wing of the Kookaburra. This strongly suggests the Rabbit is the head of a RPWN, with the wing being the fainter body. In addition to these sources, there is a probable RPWN, G369.89−0.08 (Lu et al., 2003), within the error box of the variable source near the galactic center. The Mouse is very near the galactic center source, and could also be contributing to the emission.

Overall, around half of the galactic plane sources with good evidence of variability and no candidate Blazar counterpart seem to contain RPWN. All of them also seem to be in regions containing molecular clouds or other evidence of relatively high densities in the ambient medium. This suggests the γ-ray emission may be associated with the pulsar passing through local density enhancements.

4. Conclusions

There is an intimate relationship between the generation of PWN and of γ-ray emission. This is not surprising since both indicate particles being accelerated to very high energies in the pulsar magnetosphere. Because of this, γ-ray sources in the galaxy tend to pick out PWN that otherwise might be hard to find in the crowded galactic plane. SPWN with clear toroidal morphologies are key to determining pulsar geometries, but require deep Chandra imaging. No other X-ray telescope now operating or currently planned has the necessary resolution. RPWN appear to be associated with variable *EGRET* sources, which $AGILE$ and $GLAST$ should easily confirm. However, there is no real theory developed yet as to how they might be generating γ-ray emission, and much deeper Chandra X-ray imaging is required to determine their true structure.

References

Braje, T.M., Romani, R.W., Roberts, M.S.E. and Kawai, N.: 2002, *ApJ* **565**, L91–L95.

Gaensler, B.M.: 2004, Shocks and wind bubbles around energetic pulsars, in: IAU Symposium, 151 pp.

Gaensler, B.M., van der Swaluw, E., Camilo, F., Kaspi, V.M., Baganoff, F.K., Yusef-Zadeh, F. and Manchester, R.N.: 2003, *ArXiv Astrophys.*, e-prints.

Halpern, J.P., Camilo, F., Gotthelf, E.V., Helfand, D.J., Kramer, M., Lyne, A.G., Leighly, K.M. and Eracleous, M.: 2001, *ApJ* **552**, L125–L128.

Hessels, J.W.T., Roberts, M.S.E., Ransom, S.M., Kaspi, V.M., Romani, R.W., Ng, C., Freire, P.C.C. and Gaensler, B.M.: 2004, *ApJ* **612**, 389–397.
Kaspi, V.M., Roberts, M.S.E. and Harding, A.K.: 2004, *ArXiv Astrophys.*, e-prints.
Lamb, R.C. and Macomb, D.J.: 1997, *ApJ* **488**, 872–880.
Lu, F.J., Wang, Q.D. and Lang, C.C.: 2003, *AJ* **126**, 319–326.
Ng, C.-Y. and Romani, R.W.: 2004, *ApJ* **601**, 479–484.
Nolan, P.L., Tompkins, W.F., Grenier, I.A. and Michelson, P.F.: 2003, *ApJ* **597**, 615–627.
Oka, T., Kawai, N., Naito, T., Horiuchi, T., Namiki, M., Saito, Y., Romani, R.W. and Kifune, T.: 1999, *ApJ* **526**, 764–771.
Petre, R., Kuntz, K.D. and Shelton, R.L.: 2002, *ApJ* **579**, 404–410.
Radhakrishnan, V. and Cooke, D.J.: 1969, *Astrophys. Lett.* **3**, 225–229.
Roberts, M.S.E., Hessels, J.W.T., Ransom, S.M., Kaspi, V.M., Freire, P.C.C., Crawford, F. and Lorimer, D.R.: 2002, *ApJ* **577**, L19–L22.
Roberts, M.S.E., Romani, R.W., Johnston, S. and Green, A.J.: 1999, *ApJ* **515**, 712–720.
Roberts, M.S.E., Romani, R.W. and Kawai, N.: 2001, *ApJS* **133**, 451–465.

PULSAR RADIO AND GAMMA-RAY EMISSION

R.N. MANCHESTER

Australia Telescope National Facility, CSIRO, Epping NSW, Australia;
E-mail: dick.manchester@csiro.au

(Received 10 August 2004; accepted 12 August 2004)

Abstract. A total of eight gamma-ray sources are identified with pulsars and these include some of the strongest gamma-ray sources in the sky. About 20 of the unidentified gamma-ray sources are very likely to be associated with currently known pulsars and there is little doubt that many of the others, at least those at low Galactic latitudes, will ultimately be identified with pulsars. How many of these and future gamma-ray detections will be detectable at radio wavelengths depends on the details of the radio and gamma-ray beaming. There is good evidence that the radio beams in young and millisecond pulsars are very wide, implying that most gamma-ray pulsars will be detectable in the radio band.

Keywords: pulsars:general, gamma rays:observations

1. Introduction

Pulsars are important sources of gamma rays. It has been known since the 1970s that the Crab and Vela pulsars emit pulsed emission in the gamma-ray band. These two sources are among the strongest gamma-ray sources detected in all-sky surveys, for example, that done by the EGRET telescope on the *Compton Gamma Ray Observatory* (CGRO). The most comprehensive current catalogue of gamma-ray sources is the Third EGRET (3EG) Catalog, which contains 271 sources (Hartman et al., 1999). Currently, there are eight gamma-ray sources which are identified with pulsars. All but one of these were detected using EGRET in the energy band $E > 100$ MeV; the exception (PSR B1509−58) was detected by the COMPTEL and OSSE instruments on CGRO in the energy band 100 keV–1 MeV. Likewise, all but one of these pulsars are young and highly energetic, with large spin-down luminosities. The exception is a millisecond pulsar, PSR 0218+4232, recently detected by folding all available EGRET data at the radio pulsar period.

About 170 EGRET sources from the 3EG catalogue are as yet unidentified and a significant fraction of these are at low Galactic latitudes. The fact that the strongest EGRET sources are pulsars suggests that many of the unidentified sources are also pulsars. Searches of the EGRET error boxes for radio pulsars have identified several likely candidates. Many young pulsars have also been found in large-scale radio searches, especially those made with the Parkes multibeam receiver, and it is probable that many of these are EGRET sources.



Astrophysics and Space Science **297:** 101–108, 2005.
© Springer 2005

The sky coverage of the radio and gamma-ray beams is currently a major uncertainty in studies of radio pulsar—gamma-ray source associations. Most current models assume that the radio beam is much narrower than the gamma-ray beam and hence that many gamma-ray sources will not be detected at radio wavelengths. With the exception of the Geminga pulsar, the detection of pulsed emission from gamma-ray sources has depended on an ephemeris derived from radio observations. Future missions such as GLAST will likewise depend on radio observations for verifying associations with pulsars. Clearly, the beaming issue will be an important factor in these studies.

2. Known Radio Pulsar Associations

A total of eight gamma-ray sources are identified with pulsars (See Thompson, 1996; Kuiper et al., 2000). Table I lists these sources and gives the pulsar period (in ms), the $\log_{10}$ of the characteristic age ($\tau_c = P/(2\dot{P})$ in yr), the EGRET (3EG) gamma-ray (>100 MeV) flux F in units of 10^{-8} photons cm^{-2} s^{-1} averaged over the four cycles of the mission (P1234) and the $\log_{10}$ of the pulsar spin-down luminosity divided by the square of the estimated distance ($\dot{E}d^{-2}$, where $\dot{E} = -I\Omega\dot{\Omega}$, I is the neutron-star moment of inertia, $\Omega = 2\pi/P$ and d is the pulsar distance, in units of erg s^{-1} kpc^{-2}). All of these pulsars except PSR J0218+4232 are young and highly energetic. For all pulsars known in the EGRET era (1991–1995), the top four pulsars in Table I (in which the ordering is by observed gamma-ray flux) are also the top four pulsars ordered by $\dot{E}d^{-2}$, effectively the flux of the spin-down luminosity at the Earth. Furthermore, PSR B1509−58 and PSR B1951+32 are fifth and seventh respectively in the $\dot{E}d^{-2}$ list. PSR B1055−52 is much lower, in about 30th position, despite its relatively high gamma-ray flux. The detection of PSR J0218+4232 at EGRET energies (Kuiper et al., 2000) is at a relatively low significance level, although the phase alignment of the pulse components with the

TABLE I

Gamma-ray sources identified with pulsars

3EG	PSR	P	$\log(\tau_c)$	$F_{>100\,\mathrm{MeV}}$	$\log(\dot{E}d^{-2})$
J0834−4511	B0833−45	89.3	4.1	834	37.9
J0633+1751	J0633+1746	237.1	5.5	353	36.1
J0534+2200	B0531+21	33.1	3.1	226	38.1
J1710−4439	B1706−44	102.4	4.2	112	36.0
J1058−5234	B1055−52	197.1	5.7	33	34.1
J0222+4253	J0218+4232	2.3	8.7	19	33.8
–	B1951 +32	39.5	5.0	16	35.8
–	B1509 −58	150.6	3.2	–	36.0

radio pulses makes the case stronger. This is so far the only millisecond pulsar detected at gamma-ray wavelengths.

3. The EGRET Unidentified Sources

In the 3EG catalogue, four of the six strongest sources, measured by the P1234 flux, are known to be pulsars. Of these four, three are radio pulsars, PSR B0833−45 (Vela), PSR B0531+21 (Crab), PSR B1706-44, and one, PSR J0633+1746 (Geminga), emits detectable pulsed radiation only at high energies. A total of 52 EGRET sources are close to the Galactic plane ($|b| < 4^\circ$). Most of the low-latitude sources are unidentified and about 80% of these have the hard spectra and low variability associated with the known pulsars (Harding et al., 2004). These observations strongly suggest that many of the unidentified sources, especially those at low latitudes, are likely to be powered by young pulsars.

This idea is strongly supported by Figure 1 which shows an excess of about 20 pulsars within EGRET error boxes compared to a randomized sample formed by shifting the real pulsar sample by $\pm 4^\circ$ in Galactic longitude. The lower parts of this figure show that the real sample has a much lower characteristic age and much higher value of $\dot{E}d^{-2}$ compared to the randomized sample, convincingly demonstrating that there are about 20 real associations amongst the presently known pulsar sample. Most of these likely associations come from the Parkes multibeam pulsar survey. Unfortunately, because of the period instabilities inherent in young pulsars, it is not possible to reliably extrapolate the pulsar periods back to the EGRET era (1991–1995) and so these associations cannot be confirmed at present.

These results have inspired a number of searches for the pulsars associated with unidentified gamma-ray sources. The main problem with such searches is the relatively poor spatial resolution of the EGRET instrument, leading to error boxes typically a degree or more across. Two main approaches have had success in finding likely counterparts. In the first, the source is localized, generally by identifying a probable X-ray counterpart, and then a deep radio search for a pulsar is made at that position. In several such searches, a high $\dot{E}d^{-2}$ pulsar has been discovered. Since such pulsars are relatively rare, there is a high probability that the gamma-ray source is powered by this pulsar. Good examples of this type of search are provided by the discovery of PSR J2229+6114 within the error box for 3EG J2227+6122 (Halpern et al., 2001) and of PSR J2021+3651 within the error box for 3EG 2021+3716 (Roberts et al., 2002).

In the former case, an X-ray source was identified in ASCA data as a probable counterpart to the gamma-ray source. A deep search at the position of the X-ray source using the Lovell Telescope at Jodrell Bank Observatory revealed a pulsar with a spin period of 51.6 ms and characteristic age of just 10 kyr. This pulsar has a very high spin-down luminosity $\dot{E} = 2.2 \times 10^{37}$ erg s^{-1} and is almost

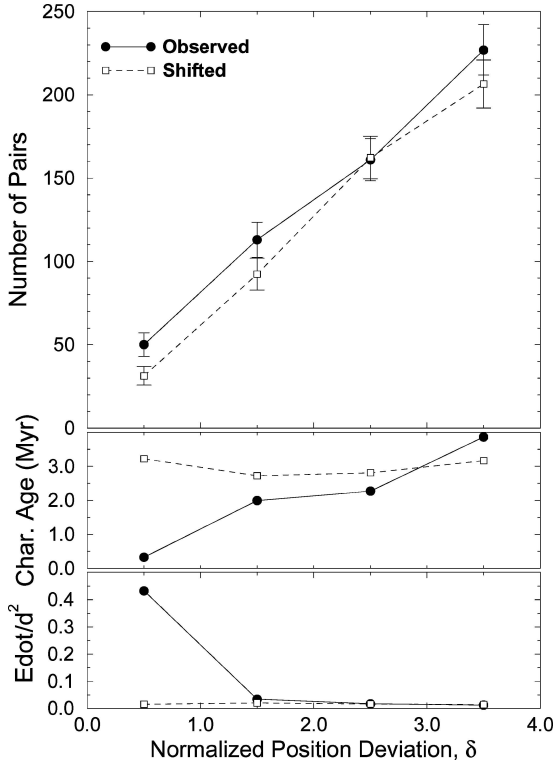


Figure 1. Number of pulsars as a function of radial distance from an EGRET source position, normalized in units of the EGRET error circle radius. The full line is for the pulsar sample and the dashed line is the average number of alignments for the pulsar sample shifted by $\pm 4^\circ$ in Galactic longitude. The mean characteristic age of the included pulsars is shown in the middle plot and the mean value of $\dot{E}d^{-2}$ is given in the lower plot. (Kramer et al., 2003).

certainly the source of the gamma-ray emission. In the second case, the positional uncertainty of the gamma-ray source was first reduced by selecting only EGRET photons with energy $>$ 1 Gev (Figure 2). An ASCA X-ray image showed two X-ray sources within the improved error box, one of which was identified with a Wolf–Rayet binary system. A deep search at the other X-ray position using the Arecibo radio telescope uncovered a weak radio pulsar with a period of 104 ms and characteristic age of 17 kyr, again almost certainly the source of the gamma-ray emission.

Large-scale radio searches such as the Parkes multibeam pulsar survey (Manchester et al., 2001) also find high $\dot{E}d^{-2}$ pulsars and, as described above, many of these are within EGRET error boxes. Three such possible associations for pulsars discovered in this survey are discussed by D'Amico et al. (2001) (J1420−6048, J1837−0604) and Camilo et al. (2001) (J1016−5857). Table II lists pulsars from the ATNF Pulsar Catalogue[1] lying within unidentified EGRET error boxes

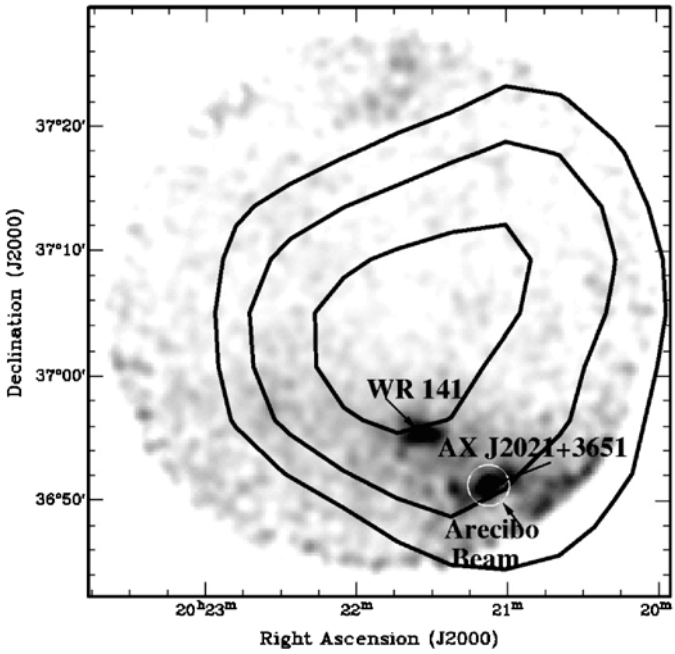


Figure 2. Region around the gamma-ray source 3EG 2021+3716. The greyscale is the ASCA 2–10 keV image and the contours are the 68%, 95% and 99% confidence regions derived from the > 1 GeV EGRET data. WR 141 is an unrelated Wolf-Rayet binary system. The circle shows the size of the Arecibo beam used to detect the young and energetic pulsar PSR J2021+3651 which is almost certainly the source of the gamma-ray photons (Roberts et al., 2002).

($\Delta\theta < 1.2 \times \theta_{95}$) for which the estimated gamma-ray luminosity L_γ is less than $\dot{E}$. For one EGRET source there are two associated pulsars; it is interesting that these are the two known young pulsars in the Magellanic Clouds. With a couple of exceptions, all the estimated gamma-ray efficiencies ($L_\gamma/\dot{E}$) are small, suggesting that most of these associations are real.

In a survey that is in some sense intermediate between the directed searches and the wide-area surveys, Roberts et al. (2004) surveyed the error boxes for 56 unidentified EGRET sources having $|b| > 5^\circ$ using the Parkes multibeam system. These mid-latitude sources may be either older 'normal' pulsars (Cheng et al., 2004) or millisecond pulsars similar to PSR J0218+4232; millisecond pulsars have typical ages > 1 Gyr and hence form a halo population in the Galaxy. This survey covered a total of about 140 square degrees and had a sensitivity comparable to that of the Parkes Multibeam Pulsar Survey (better for millisecond pulsars). Thirteen pulsars were detected, six of which were new discoveries (although one was independently discovered in the Parkes Multibeam Pulsar Survey). Two of these are binary millisecond pulsars (both in the same EGRET error box) and a third is a 172-ms pulsar in a 4.6-h binary orbit. This latter source (PSR J1744−3922) is not energetic enough

TABLE II
High $\dot{E}$ pulsars associated with unidentified EGRET sources

PSR	3EG	P (ms)	Dist. (kpc)	$\log(\dot{E})$	$\log(\dot{E}d^{-2})$	Efficiency
J0537−6910	J0533−6916	16.1	49.4	38.68	35.30	0.003
J0540−6919	J0533−6916	50.4	49.4	38.17	34.78	0.011
J1016−5857[a]	J1013−5915	107.4	8.0	36.41	34.61	0.041
J1015−5719[a]	J1014−5705	139.9	5.1	35.92	34.51	0.099
J1048−5832	J1048−5840	123.7	2.7	36.30	35.43	0.011
J1105−6107	J1102−6103	63.2	5.0	36.39	35.00	0.016
J1413−6141[a]	J1410−6147	285.6	10.1	35.75	33.74	0.584
J1420−6048[a]	J1420−6038	68.2	5.6	37.02	35.52	0.011
J1637−4642[a]	J1639−4702	154.0	5.1	35.81	34.39	0.107
J1715−3903[a]	J1714−3857	278.5	4.1	34.84	33.61	0.534
J1826−1334	J1826−1302	101.5	3.9	36.45	35.26	0.018
J1837−0604[a]	J1837−0606	96.3	6.4	36.30	34.69	0.050
J1856+0113	J1856+0114	267.4	3.3	35.63	34.60	0.085
J2021+3651[b]	J2021+3716	103.7	12.4	36.53	34.34	0.134
J2229+6114	J2227+6122	51.6	7.2	37.35	35.63	0.004

[a]Discovered in the Parkes Multibeam Pulsar Survey.
[b]Included for completeness although $\Delta\theta \sim 1.4 \times \theta_{95}$.

to power the gamma-ray source (Faulkner et al., 2004). The spin-down luminosity of the other pulsars is not yet known.

4. Radio and Gamma-Ray Pulse Beaming

There are two main models for the gamma-ray emission from pulsars: polar-cap models and outer-gap models. In the polar-cap models (e.g. Harding and Muslimov, 1998) the gamma-ray emission originates relatively close to the neutron star on open field lines (those which penetrate the light cylinder) and has an annular emission beam concentric with the radio beam and directed along the dipole magnetic axis. The beam radius is less than or comparable to that of the radio beam, that is, about $6^\circ P^{-1/2}$ (Biggs, 1990). Observed gamma-ray pulse profiles are typically wide double profiles with separation of the pulse components of 0.3 to 0.5 of the pulse period. If the intrinsic conal beamwidth is small, then the magnetic axis must be nearly aligned with the rotation axis to produce the wide observed pulse widths. However, we know from *Chandra* X-ray images that, at least for the Crab and Vela pulsars, the rotation axes are *not* close to the line of sight; fits to the pulsar wind torii give inclination angles of about 60° (Ng and Romani, 2004). This is a severe problem for the polar-cap models.

In outer-gap models (e.g. Romani and Yadigaroglu, 1995; Cheng and Zhang, 1998) the gamma-rays are generated by ultra-relativistic charged particles in the

so-called 'outer gap', where $\Omega.B = 0$, producing very wide gamma-ray beams from each pole. In existing models, the radio emission is assumed to come from a polar-cap region near the neutron star and hence has a narrow beam. One would therefore expect that most pulsars with a sufficient gamma-ray luminosity would be detected at gamma-ray energies, but that relatively few of these would be radio pulsars. However, as discussed in Section 3, three of the four brightest (steady) gamma-ray sources in the sky are radio pulsars and there are good arguments which suggest that about half of the low-latitude unidentified EGRET sources are known radio pulsars. Therefore, the radio and gamma-ray beams from a typical gamma-ray pulsar must cover comparable solid angles on the sky as the star rotates.

This dilemma would be avoided if the radio emission from young pulsars and millisecond pulsars is emitted from near the outer gap and also has a very wide beam. Then, at least for the outer-gap models, the radio and gamma-ray beams would be of similar form and most gamma-ray pulsars would also have detectable radio pulsed emission. In fact, there is good independent evidence for this proposition.

There is a class of very young pulsars which is characterized by a very high degree of linear polarization; this group includes the Vela pulsar and PSR B1706−44, both gamma-ray emitters. These pulsars generally have a rather flat variation of position angle across the pulse, suggesting an impact parameter (angle between the magnetic axis and line of sight) which is larger than the pulse width in many cases. It also includes several pulsars with so-called 'interpulse' emission, that is two main pulse components separated by about 50% of the pulse period, for example PSR B1259−63 and PSR B1055−52, also a gamma-ray pulsar. The mean pulse profile in these pulsars has a very wide 'double' form, suggesting that both pulse components originate from field lines associated with a single magnetic pole (Manchester, 1996). Most millisecond pulsars also have wide profiles and in some cases these also have a 'wide double' form, again suggesting that the radio beam is very wide and emitted from field lines associated with a single magnetic pole.

It is well known that the Crab pulsar occasionally emits 'giant' pulses at radio wavelengths, that is, pulses which are many times stronger than the average pulse (e.g., Gower and Argyle, 1972). These pulses are aligned in pulse phase with the main pulse and interpulse peaks, which are also aligned with the peaks of the high-energy emission. There can be no doubt that these radio giant pulses and the associated radio pulse components are emitted from a region very close to the region where the high-energy pulses are emitted. We argued above that this was most likely to be associated with the outer-gap region, high in the pulsar magnetosphere. Giant radio pulses have also been observed from two millisecond pulsars, PSR B1937+21 and PSR B1821−24 and these two pulsars have also been detected at hard X-ray energies (Takahashi et al., 2001; Saito et al., 1997).

These results suggest that radio and gamma-ray emission in young and millisecond pulsars both originate from the outer regions of the pulsar magnetosphere, possibly associated with the outer gap. If this is the case, most gamma-ray pulsars will also be radio pulsars. This conclusion has important implications for the identification

of gamma-ray sources with pulsars, both for currently known unidentified sources and those detected in future gamma-ray missions such as AGILE and GLAST.

Note

1. http://www.atnf.csiro.au/research/pulsar/psrcat

References

Biggs, J.D.: 1990, *MNRAS* **245**, 514.

Camilo, F., Bell, J.F., Manchester, R.N., Lyne, A.G., Possenti, A., Kramer, M., Kaspi, V.M., Stairs, I.H., D'Amico, N., Hobbs, G., Gotthelf, E.V. and Gaensler, B.M.: 2001, *ApJ* **557**, L51.

Cheng, K.S. and Zhang, L.: 1998, *ApJ* **498**, 327.

Cheng, K.S., Zhang, L., Leung, P. and Jiang, Z.J.: 2004, *ApJ* **608**, 418.

D'Amico, N., Kaspi, V.M., Manchester, R.N., Camilo, F., Lyne, A.G., Possenti, A., Stairs, I.H., Kramer, M., Crawford, F., Bell, J. and McKay, N.P.F.: 2001, *ApJ* **552**, L45.

Faulkner, A.J., Stairs, I.H., Kramer, M., Lyne, A.G., Hobbs, G., Possenti, A., Loriner, D.R., Manchester, R.N., McLaughlin, M.A., D'Amico, N., Camilo, F. and Burgay, M.: 2004, *MNRAS* **355**, 147.

Gower, J.F.R. and Argyle, E.: 1972, *ApJ* **171**, L23.

Halpern, J.P., Camilo, F., Gotthelf, E.V., Helfand, D.J., Kramer, M., Lyne, A.G., Leighly, K.M. and Eracleous, M.: 2001, *ApJ* **552**, L125.

Harding, A.K., Gonthier, P.L., Grenier, I.A. and Perrot, C.A.: 2004, *Adv. Space Res.* **33**, 571.

Harding, A.K. and Muslimov, A.G.: 1998, *ApJ* **500**, 862.

Hartman, R.C., Bertsch, D.L., Bloom, S.D., Chen, A.W., Deines-Jones, P., Esposito, J.A., Fichtel, C.E., Friedlander, D.P., Hunter, S.D., McDonald, L.M., Sreekumar, P., Thompson, D.J., Jones, B.B., Lin, Y.C., Michelson, P.F., Nolan, P.L., Tompkins, W.F., Kanbach, G., Mayer-Hasselwander, H.A., Mücke, A., Pohl, M., Reimer, O., Kniffen, D.A., Schneid, E.J., von Montigny, C., Mukherjee, R. and Dingus, B.L.: 1999, *ApJS* **123**, 79.

Kuiper, L., Hermsen, W., Verbunt, F., Lyne, A.G., Stairs, I.H., Thompson, D.J. and Cusumano, G.: 2000, in: M. Kramer, N. Wex and R. Wielebinski (eds.), Pulsar Astronomy – 2000 and Beyond, IAU Colloquium 177, Astronomical Society of the Pacific, San Francisco, p. 355.

Manchester, R.N.: 1996, in: S. Johnston, M.A. Walker and M. Bailes (eds.), Pulsars: Problems and Progress, IAU Colloquium 160, Astronomical Society of the Pacific, San Francisco, p. 193.

Manchester, R.N., Lyne, A.G., Camilo, F., Bell, J.F., Kaspi, V.M., D'Amico, N., McKay, N.P.F., Crawford, F., Stairs, I.H., Possenti, A., Morris, D.J. and Sheppard, D.C.: 2001, *MNRAS* **328**, 17.

Ng, C.-Y. and Romani, R.W.: 2004, *ApJ* **601**, 479.

Roberts, M., Ransom, S., Hessels, J., Livingstone, M., Tam, C., Kaspi, V. and Crawford, F.: 2004, in: F. Camilo and B.M. Gaensler (eds.), Young Neutron Stars and Their Environments, IAU Symposium 218, Astronomical Society of the Pacific, San Francisco, p. 415.

Roberts, M.S.E., Hessels, J.W.T., Ransom, S.M., Kaspi, V.M., Freire, P.C.C., Crawford, F. and Lorimer, D.R.: 2002, *ApJ* **577**, L19.

Romani, R.W. and Yadigaroglu, I.-A.: 1995, *ApJ* **438**, 314.

Saito, Y., Kawai, N., Kamae, T., Shibata, S. and Dotani, T.: 1997, *ApJ* **477**, 37.

Takahashi, M., Shibata, S., Torii, K., Saito, Y., Kawai, N., Hirayama, M., Dotani, T., Gunji, S., Sakurai, H., Stairs, I.H. and Manchester, R.N.: 2001, *ApJ* **554**, 316.

Thompson, D.J.: 1996, in: S. Johnston, M.A. Walker, and M. Bailes (eds.), Pulsars: Problems and Progress, IAU Colloquium 160, Astronomical Society of the Pacific, San Francisco, p. 307.

UNIDENTIFIED γ-RAY SOURCES OFF THE GALACTIC PLANE AS LOW-MASS MICROQUASARS?

I.A. GRENIER[1], M.M. KAUFMAN BERNADÓ[2,*], and G.E. ROMERO[2,†]

[1]*Université Paris VII & Service d'Astrophysique, CEA Saclay, Gif/Yvette, France; E-mail: isabelle.grenier@cea.fr*

[2]*Instituto Argentino de Radioastronomía, C.C. 5, Villa Elisa, Argentina*

(Received 11 August 2004; accepted 12 August 2004)

Abstract. A subset of the unidentified EGRET γ-ray sources with no active galactic nucleus or other conspicuous counterpart appears to be concentrated at medium latitudes. Their long-term variability and their spatial distribution indicate that they are distinct from the more persistent sources associated with the nearby Gould Belt. They exhibit a large scale height of 1.3 ± 0.6 kpc above the Galactic plane. Potential counterparts for these sources include microquasars accreting from a low-mass star and spewing a continuous jet. Detailed calculations have been performed of the jet inverse Compton emission in the radiation fields from the star, the accretion disc, and a hot corona. Different jet Lorentz factors, powers, and aspect angles have been explored. The up-scattered emission from the corona predominates below 100 MeV whereas the disc and stellar contributions are preponderant at higher energies for moderate ($\sim 15^\circ$) and small ($\sim 1^\circ$) aspect angles, respectively. Yet, unlike in the high-mass, brighter versions of these systems, the external Compton emission largely fails to produce the luminosities required for 5 to 10 kpc distant EGRET sources. Synchrotron-self-Compton emission appears as a promising alternative.

Keywords: X-rays, binaries, gamma rays, observations, theory, gamma-ray sources, unidentified, microquasars

1. Variable γ-Ray Sources in the Galactic Disc

The EGRET telescope has detected 263 γ-ray sources above 100 MeV (Hartman et al., 1999), half of which have been firmly or plausibly associated with flat radio spectrum AGN and a handful of nearby radiogalaxies (Sowards-Emmerd et al., 2003, 2004; Mattox et al., 2001). Six are identified with pulsars. The other 126 sources remain unidentified because of their poor localization, typically within a degree, or their faintness at lower energies.

Thirty three bright sources along the Galactic plane are associated with star-forming regions that harbour many likely γ-ray emitters, steady ones such as pulsars and supernova remnants, and more variable ones such as pulsar wind nebulae, massive star binaries, and accreting X-ray binaries (Romero et al., 1999; Grenier,

*Fellow of CONICET.
†Member of CONICET.

Astrophysics and Space Science **297:** 109–118, 2005.
© Springer 2005

2004). Nolan et al. (2003) found a group of 17 sources, concentrated in the inner Galaxy, that exhibit variability on timescales of weeks to months, hence ruling out a supernova remnant or a young pulsar origin. This group is brighter than the other low-latitude sources (Bosch-Ramon et al., 2004). Their luminosity ranges from 0.8 to 20×10^{34} $(D/\ 5\ \mathrm{kpc})^2$ erg s^{-1} sr^{-1} above 100 MeV. They may be associated with variable pulsar wind nebulae or with lower-energy versions of the colliding winds from a pulsar and a massive star, as recently observed at TeV energies by HESS in PSR B1259-63 (Kirk et al., 1999).

Kaufman et al. (2002) have alternatively suggested that they are microquasars with persistent jets and high-mass stellar companions. The long-term variability may be caused by the precession of the accretion disc, henceforth of the jet, that is induced by the gravitational torque of the star, or by variations in the accretion rate along an eccentric orbit, or by instabilities and inhomogeneities in the stellar wind. Synchro-self-Compton (SSC) radiation in the expanding radio blobs ejected during sporadic flares shine too briefly to account for EGRET sources (Atoyan and Aharonian, 1999). Three microquasars with high-mass companions indeed coincide with EGRET sources: LS5039 in 3EG J1824−1514, LSI+61 303 in 3EG J0241+6103, and AX J1639.0−4642 in 3EG J1639−4702 (see Ribó et al, these proceedings). The former and the latter do not exhibit variability in the EGRET data (Nolan et al., 2003). The jet from LSI+61 303 is known to precess and the observed γ-ray flux is variable, though it does not correlate with the radio flares (Kniffen et al., 1997; see, however, Massi, 2004). Energetic electrons or pairs in the jet can spawn γ-rays by up-scattering photons from the bright UV star, the soft X-ray accretion disc, a hard X-ray corona, or their own synchrotron radiation. External inverse Compton (EC) emission from a cylindrical jet (Romero et al., 2004), as well as SSC emission or EC emission from an expanding jet (Bosch-Ramon et al., 2004), can both reproduce the observed luminosities. SSC emission predominates for large jet magnetic fields, typically >100 G. EC emission yields a large variety of γ-ray spectra, depending on the relative contributions of the different radiation fields and on the jet/accretion power ratio. The latter should typically exceed 10^{-4} to power an EGRET source.

2. Variable γ-Ray Sources off the Galactic Plane

The 93 unidentified sources detected away from the Galactic plane are displayed in Figure 1. Their concentration at $3^\circ < |b| < 30^\circ$ and in the inner half steradian clearly indicates (at a 7σ confidence level) that 70 to 100% of them have a Galactic origin, depending on the choice of Galactic scale height. Their temporal and spatial characteristics reveal a heterogeneous sample. A subset of steadier sources, marked as circles in Figure 1, has been associated with the nearby Gould Belt (Gehrels et al., 2000; Grenier, 2000). The others are clearly more variable. Figure 2 shows their variability index distribution which closely follows that of the variable firm

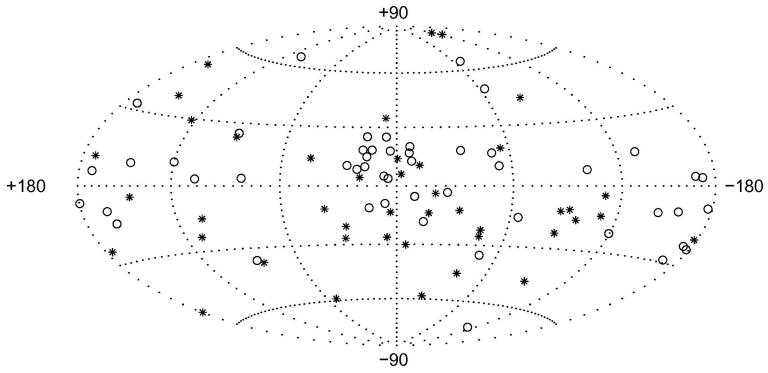


Figure 1. All-sky plot, in Galactic coordinates, of the unidentified EGRET sources at latitudes $|b| > 3^\circ$. The steadier sources associated with the Gould Belt and the variable sources are marked as circles and stars, respectively.

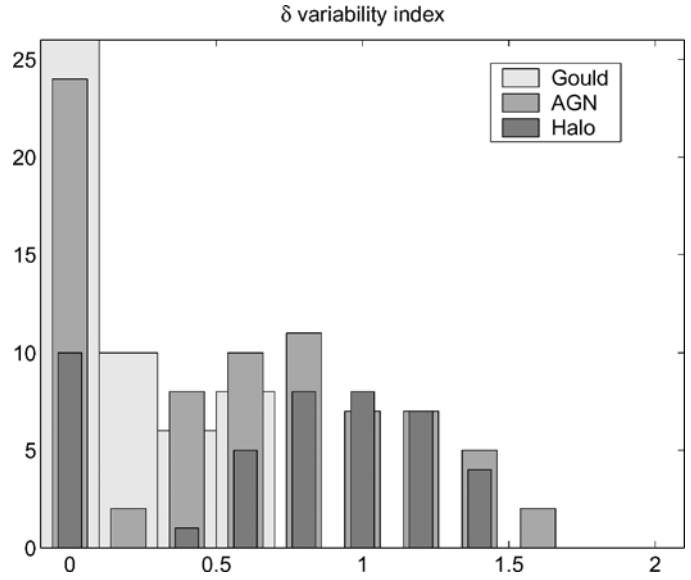


Figure 2. Distributions of the δ variability indices from Nolan et al. (2003) for the firm AGN, Gould Belt, and halo sources at latitudes $|b| > 3^\circ$.

AGN sources (Nolan et al., 2003). The two distributions are consistent under the Kolmogorov (K) test or the T test developed by Eadie et al. (1977), and both are significantly at variance with the Belt source distribution (5σ and 4σ). The average $\overline{\delta}$ indices of the three sets are 0.79 ± 0.08, 0.66 ± 0.06, and 0.42 ± 0.06 for the variable, AGN, and Belt sources, respectively. The spectral index distributions of the three sets are quite consistent according to the K and T tests, so the slightly softer average index of 2.43 ± 0.05 for the variable sources, compared with 2.23 ± 0.02

for the Belt and AGN sources, is not significant. Taking into account the detection biases (Grenier, 2000), the spatial distribution of the variable sources implies an origin in a thick Galactic disk with a scale height of 1.3 ± 0.6 kpc. A fit to the whole, persistent and variable, source sample with various combinations of Galactic distributions nearly equally shares the sources between the Gould Belt and a large scale height component, with a 3.4σ and a 4.2σ improvement over the single distribution fits. At typical distances of 5 to 10 kpc, the luminosities of the variable sources range from 2 to 30×10^{34} erg s^{-1} sr^{-1} above 100 MeV. They exhibit large luminosity L_γ / L_X ratios of a few hundred.

The compact objects likely to power sources high above the plane include ms pulsars and microquasars with a low-mass star companion, both having migrated away from the Galactic plane or escaped from globular clusters. None of the γ-ray sources coincides with a globular cluster. Pulsed γ-rays have been detected from the ms pulsar PSR J0218+4232, in phase with the radio and X-ray peaks (Kuiper et al., 2002). This object shares many traits with the halo sources: a distance of 5.7 kpc and an altitude of 1.6 kpc, a luminosity of 1.6×10^{34} erg s^{-1} sr^{-1} and a spectral index of 2.6 above 100 MeV. PSR J0218+4232 does not belong to a globular cluster either. Yet, no long-term variability is expected from theory (Zhang and Cheng, 2003). In the next section, we explore whether low-mass microquasars can produce the halo sources despite their intrinsic faintness and softness compared with the young high-mass systems. Their stellar and disc intensities are reduced by 4–6 and 1 order of magnitude, respectively, and their thermal emissions peak a decade or two lower in energy.

3. Emission from Low-Mass Microquasars

Microquasars are found up to very high Galactic latitude and height above the plane (Mirabel et al., 2001). For instance, XTE J1118+480, at $b = 62^\circ$ and a distance of 1.8 ± 0.6 kpc, lies at 1.6 ± 0.5 kpc above the plane (McClintock et al., 2001a). The central object accretes matter through a disc from a low-mass star via Roche lobe overflow. McClintock et al. (2001a) and Wagner et al. (2001) constrained the companion spectral type to be between K5 V and M1 V. A large mass function, $f(M) \approx 6\,M\odot$, strongly suggests that the compact object is a black hole in a fairly compact binary system with a short orbital period of 4.1 h (Wagner et al., 2001). The disc may be precessing under the stellar tidal influence (Torres et al., 2002). The rapid and correlated UV-optical-X-ray variability in the low-hard state is interpreted as a signature of the strong coupling between a hot corona and a jet emitting synchrotron radiation up to, at least, the UV band (Hynes et al., 2003; Chaty et al., 2003; Malzac et al., 2004). So, pairs in the jet can reach 10 GeV in a modest magnetic field of 10 G. Whether the synchrotron emission extends to hard X rays is quite possible since the data require the jet to dominate the energy budget and drive the variability, so jet pairs could reach hundreds of GeV. The outflow has remained steady through

TABLE I
Parameter set used in the model

Black hole mass	$M_{\rm bh} = 6.5$ M$\odot$
Mass accretion rate	$\dot{M} = 3 \times 10^{-8}$ M$\odot$ year^{-1}
K-M star bolometric luminosity	$L_{\rm KM} = 4 \times 10^{32}$ erg s^{-1}
F star bolometric luminosity	$L_{\rm F} = 1.5 \times 10^{34}$ erg s^{-1}
Star temperature	$kT_{\rm KM} = 1$ eV and $kT_{\rm F} = 1.8$ eV
Star orbital radius	$D_* = 1.7 \times 10^{11}$ cm
Jet/accretion power ratio	$q_{\rm jet} = P_{\rm jet}/\dot{M}c^2 = 10^{-3}$ to 10^{-2}
Corona luminosity	$L_{\rm cor} = 7.8 \times 10^{34}$ erg s^{-1}
Corona outer radius	$R_{\rm cor} = 10^8$ cm
Corona photon index ($dN_X/dE \propto E_X^{-\alpha}$)	$\alpha_{\rm cor} = 1.8$
Corona cut-off energy	$E_{\rm cor} = 150$ keV
Disc luminosity	$L_{\rm disc} = 8.6 \times 10^{35}$ erg s^{-1}
Disc temperature	$kT_{\rm disc} = 24$ eV
Initial jet radius	$R_{\rm jet} = 1.9 \times 10^7$ cm
Jet bulk Lorentz factor	$\Gamma_{\rm jet} = 3$ to 10
Jet viewing angle	$\Phi = 1^\circ$ to 30°
Jet electron index ($dN_e/dE \propto E_e^{-p}$)	$p = 2$ to 3
Maximum electron energy	$E_{e\,\rm max} = 5$ GeV to 5 TeV
Minimum electron energy	$E_{e\,\rm min} = 1$ to 5 MeV

the outburst evolution (Chaty et al., 2003). The coronal emission extends to $\sim$150 keV (McClintock et al., 2001b). The optical to hard X-ray data can be modelled by the Comptonisation in a hot corona or in the inner accretion flow of the soft photons emitted by the outer cold disc with an inner radius of $\sim 55 R_{\rm Schw}$ and a temperature of $\sim$ 24 eV (Esin et al., 2001; McClintock et al., 2001b; Malzac et al., 2001).

XTE J1118+480 therefore serves as a good example for a low-mass microquasar and we adopt its characteristics as input to our model (see Table I). The spectral energy distributions (SED) of the thermal stellar, disc and coronal components, taken from the afore mentioned publications, are displayed in Figure 3a. The case of an F star companion is also considered in Figure 3b. We calculate the EC emission from the three radiation fields assuming a population of $e^+ - e^-$ pairs in a persistent, cylindrical jet, with a power-law E_e^{-p} distribution in number density per unit energy between $E_{e\,\rm min}$ and $E_{e\,\rm max}$. The jet is assumed to be parallel to the disc axis, at an angle Φ to the line of sight. It moves with a bulk Lorentz factor $\Gamma_{\rm jet}$ and carries a total power $P_{\rm jet} = q_{\rm jet}\dot{M}c^2$. The coronal emission is assumed to fill a sphere inscribed in the inner disc radius. The particles are isotropically distributed in the jet frame and see the transformed energy densities from the external seed photons. The cross-section for both the Thompson and Klein-Nishina regimes is used. The Compton losses in the different regions modify the injected electron spectrum,

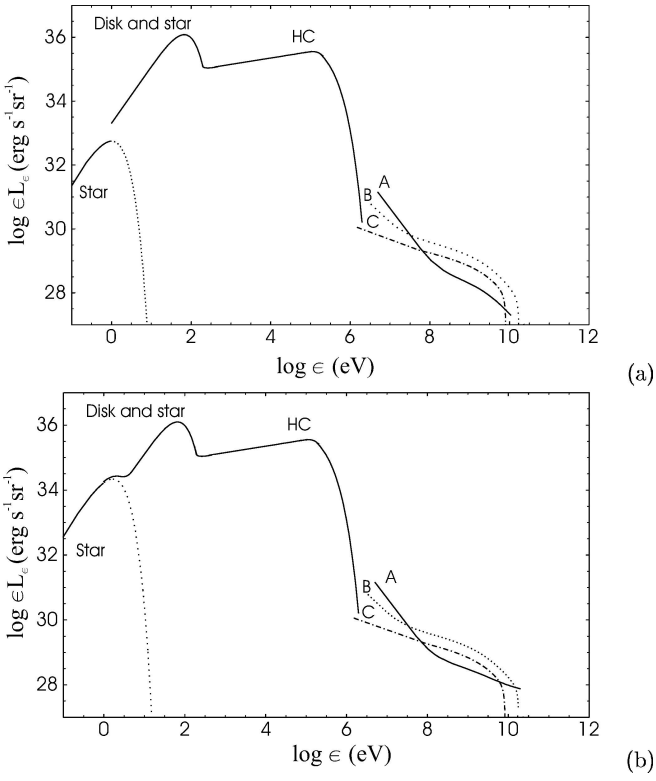


Figure 3. Spectral energy distribution of the EC emission from the jet of a microquasar with a K-M star (a) or an F star (b) companion, seen at angles of 5° (A), 15° (B), and 30° (C) from its axis, for $\Gamma_{\rm jet} = 3$, $q_{\rm jet} = 1\%$, and an $E^{-2.3}$ pair spectrum between 1 MeV and 5 GeV.

introducing a break in the power-law from an index p to $p + 1$ at the energy at which the cooling time equals the escape time. This is effective in the disc radiation field. Another important ingredient is the absorption from two-photon pair creation in the ambient radiation (Romero et al., 2002). It turns out to be quite effective near the disc while the coronal and stellar fields are optically thin to the γ rays. Back to the observer's frame, and to observed energies shifted by the Doppler factor $D = \Gamma_{\rm jet}^{-1}(1 - \beta_{\rm jet}\cos\Phi)^{-1}$, the stellar and coronal contributions to the SED ϵL_ϵ are amplified by D^{2+p} and the disc one by $D^{2+p}(1 - \cos\Phi)^{(1+p)/2}$ because of the anisotropic seed field (Dermer et al., 1992; Dermer and Schlickeiser, 2002). The former amplification factor peaks along the jet axis and the latter near $\Phi = 15^\circ$ for $\Gamma_{\rm jet} \sim 3$ and $p = 2$ to 3. The jet synchrotron emission is only amplified by $D^{(3+p)/2}$.

This scenario differs from that of Georganopoulos et al. (2002) who have imposed a much lower energy cutoff to the electrons so that the hard X-ray emission result from their EC interactions with the stellar and disc photons rather than from a hot inner accretion flow or from a hot coronal plasma energized by magnetic flares above the disc.

Figure 3 shows the SED obtained per steradian in the laboratory frame, adding the contributions from the three external photon fields. The coronal component (in the Klein-Nishina regime) is preponderant in the COMPTEL 3–30 MeV band whereas the disc component (in the Thomson regime) takes over above 100 MeV. This is why the maximum γ-ray luminosity is reached for Φ close to 15°, reflecting the angle dependance of the disc amplification factor. The disc component is rather weak because of the local absorption. It has a photon spectral index of 2.5 between 0.1 and 1 GeV. The stellar component is small at all viewing angles, so the star spectral type has little impact on the γ-ray flux. These results show that, even though the spectral index in the EGRET band matches that of the unidentified sources, the maximum predicted luminosity, $L_{\max} \sim 4 \times 10^{29} (E/100\,\mathrm{MeV})^{-0.5}$ erg s^{-1} sr^{-1}, is 5 orders of magnitude too faint to account for the halo source flux at distances of 5 to 10 kpc.

The relative contributions of the three EC components change in the case of an extreme microblazar where the bulk Lorentz factor $\Gamma_{\rm jet}$ reaches 10, electron energies extend to 5 TeV, and where the jet axis is close to the line of sight ($\Phi = 1°$). The generation of such a highly relativistic outflow, with $\Gamma_{\rm jet} \geq 10$, has been recently observed from Circinus X-1, a neutron star with a stellar-mass companion (Fender et al., 2004). Particle energies as high as 10 TeV have been inferred in the jets of the stellar-mass microquasar XTE J1550–564, 0.1 pc away from the black hole, even though the jet is seen decelerating in the interstellar medium (Corbel et al., 2002). High-mass extreme microblazars are unlikely counterparts to the low-latitude EGRET sources because of their extreme brightness. Bosch-Ramon et al. (2004) predict a luminosity of 3×10^{37} erg s^{-1} sr^{-1} at 1 GeV, well in excess of any EGRET source. Such an event would appear as bright as Vela at 5 kpc. Figure 4 shows the result for a low-mass system. The soft EC emission from the corona

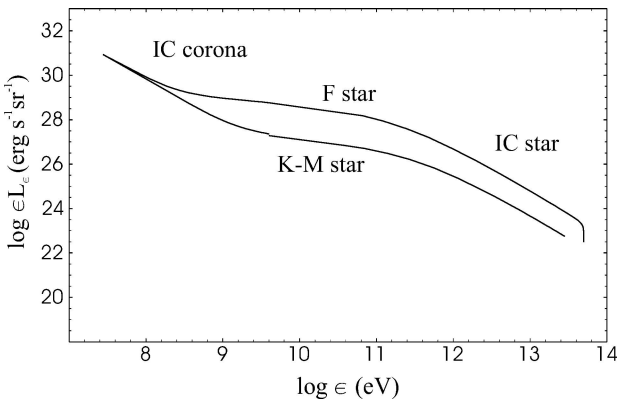


Figure 4. Spectral energy distribution of the EC emission from the jet of an extreme microblazar with an F or K-M star companion, seen at 1° from its axis, for $\Gamma_{\rm jet} = 10$, $q_{\rm jet} = 1\%$, and an $E^{-2.3}$ pair spectrum between 5 MeV and 5 TeV.

predominates up to several hundred MeV for an F star and to several GeV for a K-M star, beyond which the harder, $E^{-2.3}$, stellar component takes over. The disc EC emission is negligible because of the lesser amplification at small aspect angle. The 35 times larger energy density that the jet encounters around an F star compared with the K-M one results in a modest luminosity increase by a factor <5 in the EGRET band. Anyhow, the very low luminosities, as well as the very soft spectra, with photon indices ranging from 3 to 4, however, cannot account for the EGRET source characteristics. Nor would these systems be detected above 100 GeV by the new-generation Cerenkov telescopes since the predicted luminosity falls orders of magnitude below their sensitivity at a few kpc distance.

These objects can remain quiescent for years or decades before brightening by as much as 10^7 in X rays in a week. One should, however, keep in mind that the adopted keV luminosity of $\sim 10^{35}$ erg s^{-1} sr^{-1} corresponds to such a flaring state, i.e., to a bright X-ray source with a νF_ν flux of $2.6 \times 10^{-4}\,(D/5\,\mathrm{kpc})^{-2}$ MeV cm^{-2} s^{-1}. The GeV emission being mainly due to the disc or corona (depending on the more or less extreme conditions in the jet), the predicted luminosity should be considered as an upper limit for comparison with the unidentified sources. Therefore, EC emission in low-mass microquasars largely fails to explain the variable EGRET sources at large scale heights.

In contrast with high-mass systems where the external radiation energy density largely surpasses the magnetic one, SSC emission is likely to dominate even for a modest field strength of $\sim$ 10 G in the jet for which the magnetic energy density compares with that of a K-M star. Applying the model developed by Bosch-Ramon et al. (2004) to a cylindrical jet, one gets luminosities in excess of the necessary EGRET ones (see Figure 5). The synchrotron part of the spectrum is 100–1000 times fainter than the near-IR to UV synchrotron emission recorded from XTE

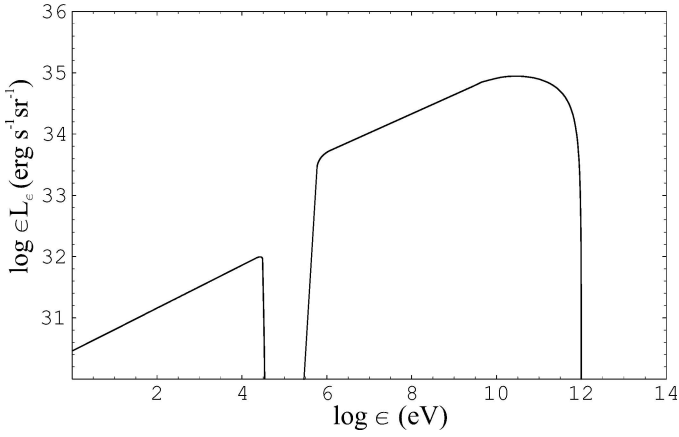


Figure 5. Spectral energy distribution of the synchrotron and SSC emission from the jet of an extreme microblazar, with a 10 G magnetic field, seen at 1° from its axis, for $\Gamma_{\rm jet} = 10$, $q_{\rm jet} = 0.1\%$, and an $E^{-2.3}$ pair spectrum between 5 MeV and 50 GeV.

J1118+480 during the outburst, the adopted electron index in Figure 5 being softer than that of XTE J1118+480 to avoid too hard spectra at high energy. The latter softens beyond 10 GeV because of Klein-Nishina effects. One should keep in mind, however, that $\gamma\gamma$ absorption against the disc photons is not included although it efficiently limits the emerging γ-ray flux. Adiabatic losses in an expanding jet would also modify the result although not severely. Nevertheless, SSC emission in a low-mass microquasar appears as an interesting possibility to be investigated in greater detail, bearing in mind that modelling the high-energy radiation from these fascinating objects is severely limited by the highly uncertain choice of the jet bulk motion and magnetic field.

Acknowledgements

We thank Valenti Bosch-Ramon and J.M. Paredes for valuable discussions on leptonic models of MQs and details of some calculations. This work has been supported in part by an ECOS-Sud cooperation agreement between France and Argentina. GER also thanks additional support from Fundación Antorchas and ANPCyT.

References

Atoyan, A.M. and Aharonian, F.A.: 1999, *MNRAS* **302**, 253.
Bosch-Ramon, V., Romero, G.E. and Paredes, J.M.: 2004, *A&A*, submitted, astro-ph/0405017.
Chaty, S., Haswell, C.A., Malzac, J., Hynes, R.I., Shrader, C.R. and Cui, W.: 2003, *MNRAS* **346**, 689.
Corbel, S., Fender, R.P., Tzioumis, A.K., Tomsick, J.A., Orosz, J.A., Miller, J.M., Wijnands, R. and Kaaret, P.: 2002, *Science* **298**, 196.
Dermer, C.D., Schlickeiser, R. and Mastichiadis, A.: 1992, *A&A* **256**, L27.
Dermer, C.D. and Schlickeiser, R.: 2002, *ApJ* **575**, 667.
Esin, A.A., McClintock, J.E., Drake, J.J., Garcia, M.R., Haswell, C.A., Hynes, R.I. and Muno, M.P.: 2001, *ApJ* **555**, 483.
Eadie, W.T., et al.: 1977, *Statistical Methods in Experimental Physics,* North-Holland Publ., p. 279.
Fender, R., et al.: 2004, *Nature* **427**, 222.
Gehrels, N., Macomb, D.J., Bertsch, D.L., Thompson, D.J. and Hartman R.C.: 2000, *Nature* **404**, 363.
Georganopoulos, M., Aharonian, F.A. and Kirk, J.G.: 2002, *A&A* **388**, L25.
Grenier, I.A.: 2000, *A&A* **364**, L93.
Grenier, I.A.: 2004, in: K. S. Cheng and G.E. Romero (eds.), *Cosmic Gamma-Ray Sources*, Kluwer Academic Publishers, in press.
Hartman, R.C., Bertsch, D.L., Bloom, S.D., et al.: 1999, *ApJ* **123**, 79.
Hynes, R.I., et al.: 2003, *MNRAS* **345**, 292.
Kaufman Bernardó, M.M., et al.: 2002, *A&A* **385**, L10.
Kirk, J.G., Ball, L. and Skjaeraasen, O.: 1999, *Astroparticle Phys.* **10**, 31.
Kniffen, D.A., et al.: 1997, *ApJ* **486**, 126.
Kuiper, L., et al.: 2002, *ApJ* **577**, 917.
Malzac, J., Merloni, A. and Fabian, A.C.: 2004, *MNRAS* **351**, 253.
Massi, M.: 2004, *A&A* **422**, 267.
Mattox, J.R., Hartman, R.C. and Reimer, O.: 2001, *ApJS* **135**, 155.
McClintock, J.E., et al.: 2001, *ApJ* **551**, L147.

McClintock, J.E., et al.: 2001, *ApJ* **555**, 477.
Mirabel, I.F., et al.: 2001, *Nature* **413**, 139.
Nolan, P., et al.: 2003, *ApJ* **597**, 615.
Paredes, J.M., Marti, J., Ribo, M. and Massi, M., 2000, *Science* **288**, 2340.
Romero, G.E., Benaglia, P. and Torres, D.F.: 1999, *A&A* **348**, 868.
Romero, G.E., Kaufman Bernardó, M.M. and Mirabel, I.F.: 2002, *A&A* **393**, L61.
Romero, G.E., Grenier, I.A., Kaufman Bernardó, M.M., Mirabel, I.F. and Torres, D.F.: 2004, *Proceedings of the Vth INTEGRAL Workshop, Munich 2004,* ESA SP-552, in press. astro-ph/0402285.
Sowards-Emmerd, D., Romani, R.W. and Michelson, P.: 2003, *ApJ* **590**, 109.
Sowards-Emmerd, D., Romani, R.W., Michelson, P.F. and Ulvestad, J.S.: 2004, *ApJ* **609**, 564.
Torres, M.A.P., et al.: 2002, *ApJ* **569**, 423.
Wagner, R.M., et al.: 2001, *ApJ* **556**, 42.
Zhang, L. and Cheng, K.S.: 2003, *A&A* **398**, 639.

ON THE NATURE OF THE VARIABLE GAMMA-RAY SOURCES AT LOW GALACTIC LATITUDES

VALENTÍ BOSCH-RAMON[1], GUSTAVO E. ROMERO[2] and JOSEP M. PAREDES[1]
[1]*Universitat de Barcelona, Spain; E-mail: vbosch@am.ub.es*
[2]*Instituto Argentino de Radioastronomía, FCAGLP, Universidad Nacional de La Plata, Spain*

(Received 2 June 2004; accepted 5 August 2004)

Abstract. Population studies of EGRET gamma-ray sources indicate that there is a distinctive population of bright sources at low galactic latitudes. The sources have a distribution consistent with that of young galactic objects, with a concentration toward the inner spiral arms. There is a subgroup that displays strong variability with timescales from days to months. Following an earlier suggestion by Kaufman Bernadó et al. (2002), we explore the possibility that these sources could be high-mass microquasars. Detailed models for the gamma-ray emission that include inverse Compton interactions of electrons in the relativistic jets and photons from all local fields (stellar UV photons, synchrotron photons, soft X-ray photons from the accretion disk, and hard X-ray photons from a corona) are presented. We conclude that microquasars are excellent candidates for the parent population of the subgroup of variable low-latitude EGRET sources.

Keywords: microquasars, X-ray binaries, jets, gamma-rays

1. Introduction

Population studies of EGRET gamma-ray sources indicate that there is a distinctive population of bright sources at low galactic latitudes (Gehrels et al., 2000; Grenier, 2001, in press; Romero, 2001). They are well correlated with star forming regions and HII regions, which is indicative of an association with young stellar objects (Romero et al., 1999; Romero, 2001). Log N–log S studies suggest that they are more abundant toward the inner spiral arms (Gehrels et al., 2000; Bhattacharya et al., 2003). These are bright sources (isotropic luminosities in the range 10^{34-36} erg s^{-1}), with an average photon spectral index $\langle\Gamma\rangle = 2.18$ (Gehrels et al., 2000), where $F(E) \propto E^{-\Gamma}$. These sources, whose number is $\sim 45 \pm 9$, form the Gamma-Ray Population I (GRP I, Romero et al., in press). Among GRP I sources there is a subgroup that displays significant variability on timescales of weeks to months (Torres et al., 2001; Nolan et al., 2003). Recently, Kaufman Bernadó et al. (2002) and Romero et al. (in press) have suggested that this subgroup of GRP I sources might be high-mass microquasars (i.e. microquasars formed by a compact object and an early-type stellar companion), where the gamma-ray emission arises from interactions between relativistic particles in the jet and external photon fields, most notably the stellar UV emission.



Astrophysics and Space Science **297:** 119–129, 2005.
© Springer 2005

In the present paper we explore in more detail this hypothesis, presenting more realistic models for the gamma-ray emission. In particular, we will include effects of the interaction of the microquasar jet with the X-ray fields produced by the accretion disk and the hot corona that is thought to surround the compact object. We will also include synchrotron self-Compton emission, Klein-Nishina effects, and the back-reaction of the different losses in the particle spectrum of the jet. We will calculate, for some representative sets of the parameters that characterize high-mass microquasars, the spectral energy distribution (SED) from radio wavelengths up to GeV gamma-rays.

2. GRP I Sources

GRP I sources concentrate along the galactic plane and present a good spatial correlation with young stellar objects (Romero et al., 1999). The variability analysis of these sources by Torres et al. (2001) clearly shows evidence for the existence of a subgroup with variable emission on timescales from weeks to months. This is corroborated by the recent results presented by Nolan et al. (2003), which are based on a maximum likelihood re-analysis of the EGRET data. These authors identify 17 variable sources within 6° from the galactic plane. These sources are clumped within 55° of the galactic center.

A $\log N$–$\log S$ analysis for all GRP I sources yields a distribution that is consistent with a power-law with index $\langle\beta\rangle = 3.1 \pm 0.4$ (Bhattacharya et al., 2003). This is far steeper than what is expected for a population uniformly distributed along the galactic disk. For instance, for pulsars detected at 400 MHz the slope results $\langle\beta\rangle \sim 1.05$ (Bhattacharya et al., 2003). The unidentified gamma-ray sources, on the contrary, seem to be concentrated mainly in the inner spiral arms. In order to find possible further evidence for different populations among GRP I sources, we have implemented a $\log N$–$\log S$ analysis of both variable and non-variable low-latitude sources.

First we have considered the 17 variable sources listed by Nolan et al. (2003). In order to take into account systematic effects introduced by different exposure and background resulting in non-uniform detectability, we have adopted the procedure described by Reimer (2001). The obtained $\log N$–$\log S$ plot is shown in Figure 1. The normalized distribution can be fitted by a power-law $N(S) \propto S^{-\beta}$, with $\langle\beta\rangle = 1.66 \pm 0.31$, significantly flatter than for the entire sample. If we now consider those sources classified as non-variable or dubious cases, we get the $\log N$–$\log S$ plot shown in Figure 2. In this case the distribution can be fitted by a power-law with index $\langle\beta\rangle = 2.92 \pm 0.36$. Quoted errors for β are 1 sigma errors.

The average spectral index is also different for both samples: in the case of the variable sources we have $\langle\Gamma\rangle = 2.04 \pm 0.1$, whereas for the remaining sources is $\langle\Gamma\rangle = 2.16 \pm 0.2$. However, the averaged errors are still large, due to the low number of sources, and do not allow yet to distinguish both populations properly.

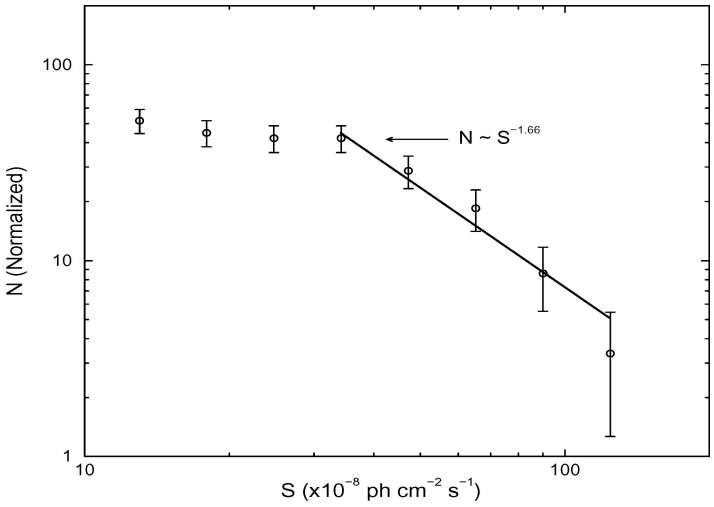


Figure 1. Log N–log S plot for variable gamma-ray sources within $|b| < 6^\circ$.

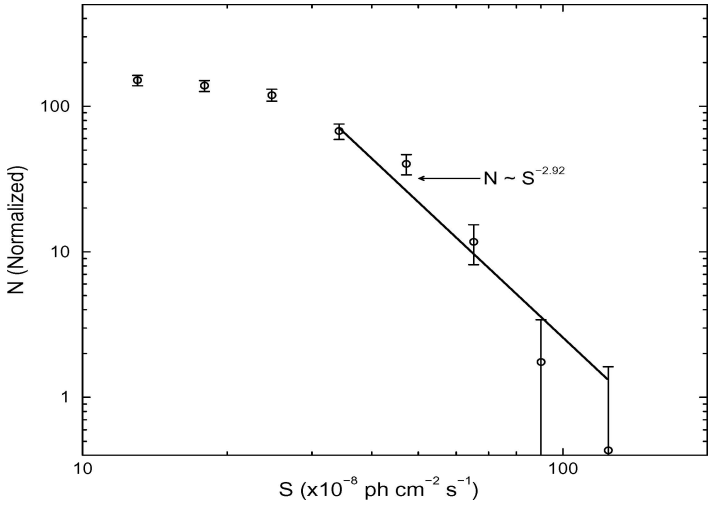


Figure 2. Log N–log S plot for non-variable gamma-ray sources within $|b| < 6^\circ$.

In any case, log N–log S analysis suggest that there are two different groups of sources, one formed by steady sources concentrated toward the inner spiral arms, and a second group with variable sources and a wider distribution along the galactic plane, although not as wide as that of radio pulsars (Bhattacharya et al., 2003).

High-mass microquasars appear to be good candidates for compact and variable sources in the galactic plane. Since they can have very large proper motions (e.g. Ribó et al., 2002), their distribution along the plane should be broader than that presented by supernova remnants and molecular clouds, which can be traced by star-forming regions and OB associations. Their spread, however, is limited by the

lifespan of the companion massive star, and hence it is not as extended as that of radio pulsars. In the next section we will discuss the potential of microquasars as gamma-ray sources.

3. Gamma-Ray Emission from Microquasars

In the present paper we will consider a relativistic inhomogeneous jet flow moving along the z-axis (assumed to be perpendicular to the disk) with a bulk Lorentz factor $\Gamma_{\rm jet}$. We shall allow the jet to expand laterally, in such a way that the radius R at a distance z from the compact object will be given by $R(z) = \xi z^{\varepsilon}$, with $\varepsilon \leq 1$ and $z_0 \leq z \leq z_{\rm max}$. ξ is related to the opening angle of the jet. For $\epsilon = 1$ we have a conical jet. The electron energy distribution ($N(z, \gamma_{\rm e})$, a power-law of index p), the maximum electron Lorentz factor ($\gamma_{\rm emax}(z)$) and the magnetic field ($B(z)$) will be parametrized like in Ghisellini et al. (1985).

The synchrotron radiation density within the jet can be estimated using the local approximation to the synchrotron radiation field (e.g. Ghisellini et al., 1985). We have used the formulae presented in Pacholczyk (1970), adapted to an expanding jet. The total radiation field to which the leptons are exposed in the jet will have also contribution from external sources. These contributions can be modeled as two black body components, one peaked at UV energies (the companion star field) and other at energies $kT \sim 1$ keV (the inner accretion disk field), plus a power-law with an exponential cutoff at $kT \sim 150$ keV (the corona). With the exception of the disk, these contributions are assumed to be isotropic (Romero et al., 2002; Georganopoulos et al., 2002).

Once $N(z, \gamma_{\rm e})$ and the total energy density in seed photons ($U_{\rm tot}(\epsilon_0, z)$) have been determined, the inverse Compton (IC) interaction between them can be studied calculating the IC spectral energy distribution per energy unit. The cross section ($\sigma(x, \epsilon_0, \gamma_{\rm e})$) for both the Thomson and the Klein-Nishina regimes has been taken from Blumenthal and Gould (1970). The spectral energy distribution for the optically thin case in the jet's reference frame is:

$$\epsilon L_\epsilon = \epsilon \int_{z_{\rm min}}^{z_{\rm max}} \int_{\epsilon_{0\rm min}(z)}^{\epsilon_{0\rm max}(z)} \int_{\gamma_{\rm emin}(z)}^{\gamma_{\rm emax}(z)} \Sigma(z) U_{\rm tot}(\epsilon_0, z) \times N(\gamma_{\rm e}, z) \frac{d\sigma(x, \epsilon_0, \gamma_{\rm e})}{d\epsilon} \frac{\epsilon}{\epsilon_0} d\gamma\, d\epsilon_0\, dz, \quad (1)$$

where ϵ_0 and ϵ are the energies of the incoming and the outgoing photons, respectively. The parameter x is actually a function which depends on both of the former quantities and on the electron Lorentz factor. $\Sigma(z)$ is the surface of a perpendicular jet slice located at z. Notice that the external fields contributing to $U_{\rm tot}(\epsilon_0, z)$ should be transformed to the co-moving frame. Detailed expressions for such transformations are given by Dermer and Schlickeiser (2002).

In the observer's reference frame we have:

$$\epsilon' L'_{\epsilon'} = D^{2+p} \epsilon' L_{\epsilon'}. \tag{2}$$

The integration is performed in the co-moving system and then the result is transformed to the observer's frame, hence the factor D^{2+p}, which is the Doppler boosting for a continuous jet. The energy of the scattered photons in the jet's reference frame (ϵ) is boosted to $\epsilon' = D\epsilon$. The Doppler factor D for the approaching jet is given by

$$D = \frac{1}{\Gamma_{\rm jet}(1 - \beta \cos\theta)}, \tag{3}$$

where β is the velocity of the jet in speed of light units and θ is the angle between the jet and the line of sight.

In the case of the IC interactions with disk photons, a factor $(1 - \cos\theta)^{(p+1)/2}$ must be introduced in Eq. (1) in order to take into account the fact that the photons come from behind the jet (Dermer et al., 1992).

In order to make any calculation of the IC emission of a given microquasar, we have to specify first the jet power. In this work we shall adopt the disk/jet coupling hypothesis formulated by Falcke and Biermann (1995, 1999), i.e. the jet power is proportional to the accretion rate:

$$L_{\rm jet} = q L_{\rm ac}. \tag{4}$$

where $L_{\rm ac} = \dot{M} c^2$ is the accretion power onto the compact object and q is a number <1. For a leptonic jet, as in our case, $q \ll 1$. The jet power determines the energy content of the electron energy distribution for a leptonic jet (see, e.g. Georganopoulos et al., 2002).

Although the model outlined above concerns primarily to the high energy emission range since it focuses on the IC radiation from the inner jet, the synchrotron formulae can be used to make predictions also at radio wavelengths. With this aim, we have developed an outer jet model appropriate for regions farther from the compact object. This outer jet model will fulfill most of the conditions of the former one, but it will require a different geometry because of the expected lower energy loss rate of the particles.

For further details about our model, see Bosch-Ramon et al. (in press).

4. Specific Models

In order to explore a plethora of situations, we have adopted a set of assumptions, which are summarized in Tables I. In Table II we list those parameters that were

TABLE I
Main fixed parameters in the models

Parameter (symbol)	Value
Black hole mass ($M_{\rm bh}$)	$10\,M_\odot$
Gravitational radius ($R_{\rm g}$)	1.48×10^6 cm
Accretion luminosity ($L_{\rm ac}$)	$10^{-8}\ M_\odot {\rm c}^2$ year^{-1}
Stellar radius (R_*)	$15\ R_\odot$
Stellar bolometric luminosity (L_*)	5×10^{38} erg s^{-1}
Distance from jet's apex to the compact object (z_0)	$50\ R_{\rm g}$
Initial jet radius (R_0)	$0.1 z_0$
Orbital radius ($R_{\rm orb}$)	$45\ R_\odot$
Peak energy of the disk ($kT_{\rm disk}$)	1 keV
Peak energy of the corona ($kT_{\rm cor}$)	150 keV
Peak energy of the star ($kT_{\rm star}$)	10 eV
Expansion coefficient of the inner jet (ε)	1
Electron power-law index (p)	2
Photon index for the corona ($\Gamma_{\rm cor}$)	1.6

TABLE II
Changing parameters in the different cases considered in the text

Parameter (symbol)	Value mild/extreme/realistic
Corona luminosity ($L_{\rm cor}$)	10^{35}, 10^{35}, 3×10^{32} erg s^{-1}
Total disk luminosity ($L_{\rm disk}$)	10^{37}, 10^{37}, 5×10^{32} erg s^{-1}
Inner jet magnetic field ($B(z_0)$)	10, 10, 200 G
Maximum electron Lorentz factor ($\gamma_{\rm emax}(z_0)$)	10^4, 10^6, 10^4
Bulk Lorentz factor of the jet ($\Gamma_{\rm jet}$)	2.5, 10, 1.1
Viewing angle to jet's axis θ	10°, 1°, 10°
Disk/jet coupling constant (q)	10^{-4}, 10^{-4}, 10^{-3}

allowed to change along with the values adopted for three representative cases: a 'mild' microquasar, a microblazar, and a system similar to LS 5039 and LS I $+61$ 303[1] .

In Figure 3, we show the whole SED of the 'mild' case. We plot here the spectra for all contributions to the emission, i.e. the outer jet, the seed photon sources, and the IC components (for outer jet parameters, see Table III). In Figure 4 we show a more extreme case, for a source with a high bulk Lorentz factor $\Gamma_{\rm jet} = 10$, a high-energy cutoff for electrons of $\gamma_{\rm emax}(z_0) = 10^6$, and a small viewing angle $\theta = 1^\circ$ (see Table II). Finally, we plot a SED similar (realistic case in Tables II and III) to the one presented by two microquasars that are considered as the

TABLE III
Outer jet parameters (different cases considered in the text)

Parameter (symbol)	Value mild/extreme/realistic
Expansion coefficient of the outer jet (ε)	0.2, 0.3, 0.2
Initial point of the outer jet (z_0)	500 R_g, 5000 R_g, 500 R_g
Initial radius of the outer jet (R_0)	50 R_g, 500 R_g, 50 R_g
(Computed) maximum length of the jet (few GHz)	$\sim 10^{16}$, $\sim 10^{17}$, $\sim 10^{15}$ cm
Maximum electron Lorentz factor of the outer jet (γ_{emax})	10^3, 10^4, 10^3
Outer jet magnetic field ($B(z_0)$)	1, 0.1, 20 G
Electron power-law index (p)	2

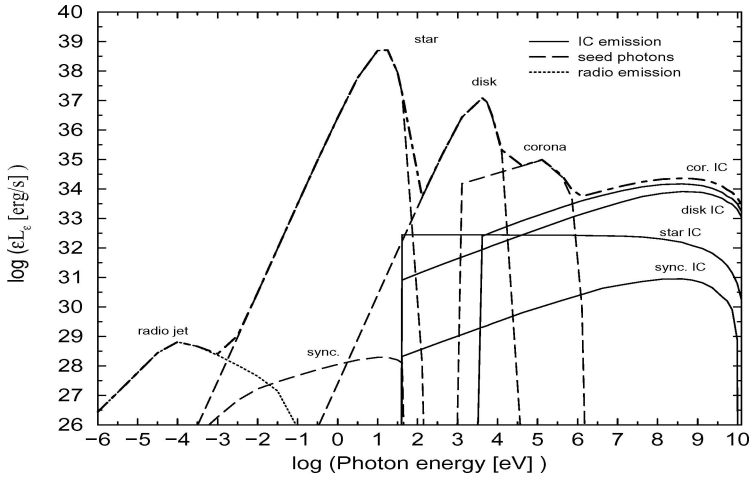


Figure 3. Complete SED for a model with $q = 10^{-4}$, B=10 G, $L_{disk} = 10^{37}$ erg s^{-1}, $L_{cor} = 10^{35}$ erg s^{-1}, $\gamma_{emax}(z_0) = 10^4$, $\Gamma_{jet} = 2.5$, and a viewing angle of 10°. The synchrotron seed photons come from the inner jet.

best candidates to counterparts of unidentified EGRET sources, LS 5039 and LSI +61°303 (3EG 1824+1514, Paredes et al., 2000, and 3EG 0241 + 6103, Kniffen et al., 1997, respectively; see Figure 5); the selected set of parameter is consistent with those adopted in Bosch-Ramon and Paredes (2004a, in press).

5. Discussion

In a previous work (Bosch-Ramon et al., in press), it was shown that for several models with disk/jet coupling constant $q = 10^{-3}$ we can get the expected luminosities in the observer's frame inferred for GRP I sources with the right photon index at energies $\sim$1 GeV, i.e. $\Gamma \sim 2$. When the magnetic field is strong enough

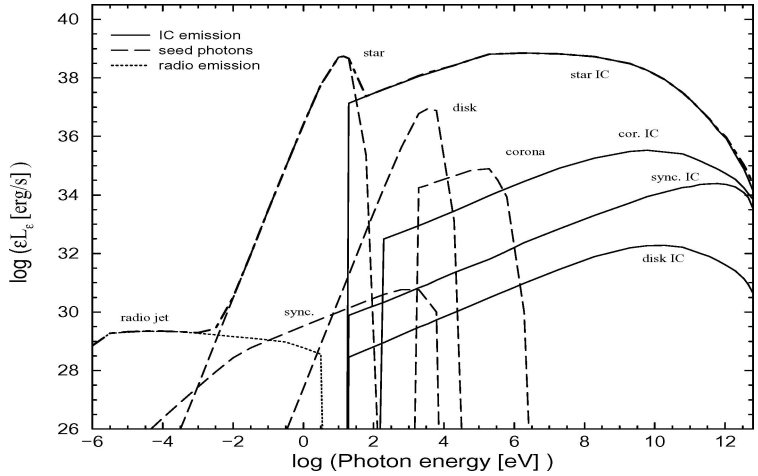


Figure 4. SED for a model with $q = 10^{-4}$, $B = 10$ G, $L_{\rm disk} = 10^{37}$ erg s^{-1}, $L_{\rm cor} = 10^{35}$ erg s^{-1}, $\gamma_{\rm emax}(z_0) = 10^6$, $\Gamma_{\rm jet} = 10$, and a viewing angle of 1°. The synchrotron seed photons come from the inner jet.

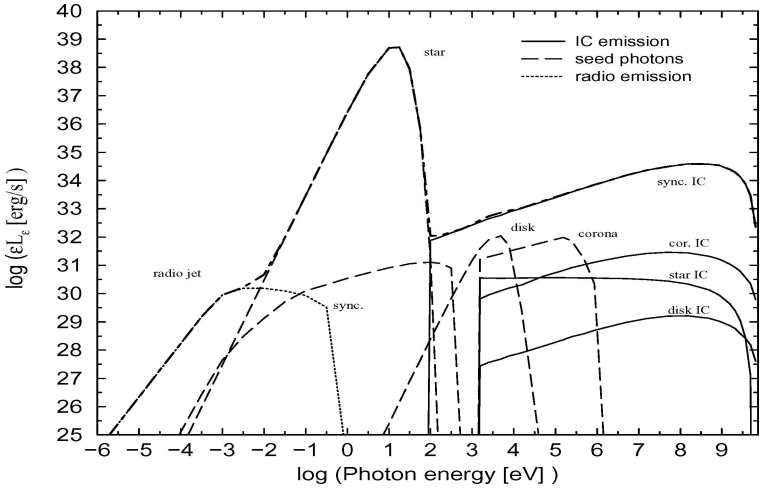


Figure 5. SED for a model with $q = 10^{-3}$, $B = 200$ G, $L_{\rm cor}$ and $L_{\rm disk} = 3 \times 10^{32}$ erg s^{-1}, $\gamma_{\rm emax}(z_0) = 10^4$, $\Gamma_{\rm jet} = 1.1$, and a viewing angle of 10°. The synchrotron seed photons come from the inner jet.

($B(z_0) \sim 100$ G), SSC emission alone can account for luminosities $\sim 10^{35}$ erg s^{-1} at 1 GeV. Models with bulk Lorentz factors $\Gamma_{\rm jet} = 1.5$ and 5 do not produce dramatically different results for a jet with a viewing angle of $\sim 10^\circ$ except for the case of the scattered stellar photons. In case of lower magnetic fields, the IC scattering upon external fields clearly dominates. It is interesting to notice that even models with light jets ($q = 10^{-5}$) can produce significant gamma-ray sources ($\sim 10^{34}$ erg s^{-1} at 100 MeV) when a strong corona is present. In these models, the spectrum tends to

be a bit harder than in the case of stellar photons, with our current set of assumptions (value of $\Gamma_{\rm cor}$, etc.).

In the present study of concrete cases, we compare Figures 3–5. From these figures, it is possible to see the differences between 'mild' microquasars, with $\Gamma_{\rm jet} = 2.5$, a viewing angle of $\theta = 10^\circ$ and $q = 10^{-4}$, and more 'extreme' cases with $\Gamma_{\rm jet} = 10$ and $\theta = 1^\circ$. Since we have assumed in both cases a magnetic field of $B(z_0) = 10$ G, external IC scattering always dominates over SSC. In the 'mild' microquasar the emission at MeV–GeV energies is mainly due to upscattering of coronal photons whereas, in the extreme case, the IC emission in the stellar field exceeds by far the other contributions. For the case similar to LS 5039/LSI $+61^\circ 303$, we have taken the magnetic field to be high enough to be the main contribution at high energies to reproduce the observed features of the spectra; mainly, higher luminosities at gamma-rays than at X-rays and no strong disk/corona hints at X-rays. In the three cases the radio counterpart is rather weak, with a $L_{\rm radio}/L_\gamma \ll 1$. The hard X-ray counterpart, on the contrary, can be important, even beyond the cutoff for the corona (at $\sim$150 keV). Hence, INTEGRAL observations can be useful to unmask candidates that are obscured at optical wavelength (see Combi et al., 2004, for a recent study in this direction).

An interesting feature of the extreme case is that the gamma-ray emission with a hard spectrum $\Gamma \sim 2$ extends up to $\sim$100 GeV. Above 10^{11} eV the spectrum becomes softer due to the Klein-Nishina effect. This type of sources should be detectable with modern Imaging Cherenkov Telescopes like HESS and MAGIC. Even systems with low-mass companions and weak coronas might be detectable since the SSC component has luminosities of $\sim 10^{35}$ erg s^{-1}. The soft spectrum can be used to differentiate this leptonic model from other hadronic alternatives which predict a harder spectrum at very high energies (e.g. Romero et al., 2003).

6. Conclusions

We have shown that the variable gamma-ray sources found on the galactic plane have some common features that make reasonable to consider them as a distinctive group of GRP I sources. We have suggested that these sources might be microquasars with high-mass stellar companions and we have elaborated some detailed models to explain the gamma-ray production in this type of objects. In particular, we have considered inhomogeneous jet models where gamma-rays are the result of inverse Compton interactions of leptons in the inner jet with locally produced synchrotron photons as well as external photon fields. We have calculated the emission resulting from the upscattering of disk, coronal, and stellar photons, incorporating a full Klein-Nishina calculation and the effect of losses in the particle spectrum. We have shown that different spectral energy distributions at high energies can be obtained from different and reasonable combinations of the physical parameters such as magnetic field, jet power, coronal and disk luminosities, etc. The model

can compute with a reasonable set of parameters a realistic SED, reproducing the ones associated to known microquasars. It seems to be clear that the microquasar phenomenon can be naturally extended up to the highest energies and that we can expect these objects to manifest themselves as a distinctive group of gamma-ray sources that might be detectable with satellite-borne instruments like those to be carried by AGILE and GLAST and even by ground-based Cherenkov telescopes like HESS and MAGIC.

Microquasars are not, of course, the only kind of galactic object that might display variable gamma-ray emission. Other alternatives include early-type binaries (Benaglia and Romero, 2003), accreting neutron stars (Romero et al., 2001), pulsar wind nebulae (Roberts et al., 2002) and exotic objects (Punsly et al., 2000). However, microquasars are perhaps the most attractive candidates to explain a significant fraction of the variable GRP I sources because of the well-established presence of relativistic jets in these objects, along with several external photon fields.

Acknowledgements

J.M.P. and V.B.-R. acknowledge partial support by DGI of the Ministerio de Ciencia y Tecnología (Spain) under grant AYA-2001-3092, as well as additional support from the European Regional Development Fund (ERDF/FEDER). During this work, V.B.-R. has been supported by the DGI of the Ministerio de Ciencia y Tecnología (Spain) under the fellowship FP-2001-2699. G.E.R. is supported by Fundación Antorchas and the Argentine Agencies CONICET and ANPCyT. This research has benefited from a cooperation agreement supported by Fundación Antorchas. We thank an anonymous referee by for constructive comments on manuscript.

Note

1. LS 5039 and LSI $+61^{\circ}303$ present significant differences though, regarding gamma-rays, they are pretty similar. Also, at lower energies, both systems can be treated in a similar way at this stage.

References

Benaglia, P. and Romero, G.E.: 2003, *A&A* **399**, 1121.
Bhattacharya, D., Akyüz, A., Miyagi, T., Samimi, J. and Zych, A.: 2003, *A&A* **404**, 163.
Blumenthal, G.R. and Gould, R.J.: 1970, *Rev. Mod. Phys.* **42**, 237.
Bosch-Ramon, V. and Paredes, J.M.: 2004a, *A&A* **417**, 1075.
Bosch-Ramon, V. and Paredes, J.M.: 2004b, *A&A* **425**, 1069.
Bosch-Ramon, V., Romero, G.E. and Paredes, J.M.: 2005, *A&A* **429**, 267.
Combi, J.A., Ribó, M., Mirabel, I.F. and Sugizaki, M.: 2004, *A&A* **422**, 1031.
Dermer, C.D., Schlickeiser, R. and Mastichiadis, A.: 1992, *A&A* **256**, L27.
Dermer, C.D. and Schlickeiser, R.: 2002, *ApJ* **575**, 667.

Falcke, H. and Biermann, P.L.: 1995, *A&A* **293**, 665.
Falcke, H. and Biermann, P.L.: 1999, *A&A* **342**, 49.
Gehrels, N., Macomb, D.J., Bertsch, D.L., Thompson, D.J. and Hartman, R.C.: 2000, *Nature* **404**, 363.
Georganopoulos, M., Aharonian, F.A. and Kirk, J.G.: 2002, *A&A* **388**, L25.
Ghisellini, G., Maraschi, L. and Treves, A.: 1985, *A&A* **146**, 204.
Grenier, I.A.: 2001, in: A. Carraminana, O. Reimer and D. Thompson (eds.), *The Nature of Unindentified Galactic High-Energy Gamma-Ray Sources*, Kluwer Academic Publishers, Dordrecht, p. 51.
Grenier, I.A.: 2004, in: *Cosmic Gamma-Ray Sources*, K.S. Cheng and G.E. Romero (eds.), Kluwer Academic Publishers, Dordrecht, p. 47.
Kaufman Bernadó, M.M., Romero, G.E. and Mirabel, I.F.: 2002, *A&A* **385**, L10.
Kniffen, D.A., Alberts, W.C.K., Bertsch, D.L. et al.: 1997, *ApJ* **486**, 126.
Nolan, P.L., Tompkins, W.F., Grenier, I.A. and Michelson, P.F.: 2003, *ApJ* **597**, 615.
Pacholczyk, A.G.: 1970, *Radio Astrophysics*, Freeman, San Francisco, CA.
Paredes, J.M., Martí, J., Ribó, M. and Massi, M.: 2000, *Science* **288**, 2340.
Punsly, B., Romero, G.E., Torres, D.F. and Combi, J.A.: 2000, *A&A* **364**, 552.
Reimer, O.: 2001, in: A. Carramiñana, O. Reimer and D. Thompson (eds.), *The Nature of Unindentified Galactic High-Energy Gamma-Ray Sources*, Kluwer Academic Publishers, Dordrecht, p. 17.
Ribó, M., Paredes, J.M., Romero, G.E., Benaglia, P., Marti, J., Fors, O., Garcia-Sanchez, J.: 2002, *A&A* **384**, 954.
Roberts, M.S.E., Gaensler, B.M. and Romani, R.W.: 2002, in: Patrick O. Slane and Bryan M. Gaensler (eds.), *Neutron Stars in Supernova Remnants*, ASP Conference Series, Vol. 271, ASP, San Francisco, 2002, p. 213.
Romero, G.E., Benaglia, P. and Torres, D.F.: 1999, *A&A* **348**, 868.
Romero, G.E.: 2001, in: A. Carramiñana, O. Reimer and D. Thompson (eds.), *The Nature of Unindentified Galactic High-Energy Gamma-Ray Sources*, Kluwer Academic Publishers, Dordrecht, p. 65.
Romero, G.E., Kaufman Bernadó, M.M., Combi, J.A. and Torres, D.F.: 2001, *A&A* **376**, 599.
Romero, G.E., Kaufman Bernadó, M.M. and Mirabel, I.F. 2002, *A&A* **393**, L61.
Romero, G.E., Torres, D.F., Kaufman Bernadó, M.M. and Mirabel, I.F.: 2003, *A&A* **410**, L1.
Romero, G.E., Grenier, I.A., Kaufman Bernadó, M.M. and Mirabel, I.F. and Torres, D.F.: in press, ESA-SP, [astro-ph/0402285].
Torres, D.F., Romero, G.E., Combi, J.A., Benaglia, P., Andernach, H. and Punsly, B.: 2001, *A&A* **370**, 468.

SPECTRAL PROPERTIES OF BLACK HOLES IN GAMMA RAYS

SANDIP KUMAR CHAKRABARTI

S.N. Bose National Centre for Basic Sciences, JD Block, Salt Lake, Kolkata, India; Centre for Space Physics, Chalantika, Garia Station Road, Kolkata, India; E-mail: chakraba@bose.res.in

(Received 26 August 2004; accepted 6 September 2004)

Abstract. Black holes are the most compact objects in the universe. Therefore, matter accreting onto them is likely to radiate photons of energy comparable to very high gravitational potential energy. We discuss the nature of the emitted radiation in X-rays and gamma-rays from black hole candidates. We present theoretical solutions, which comprise both Keplerian and sub-Keplerian components and suggest that shocks in accretion and outflows may play a major role in producing these spectra.

Keywords: black hole physics, shocks, hydrodynamics, spectral properties: γ-rays, X-rays

1. Introduction

It is well known that the black holes themselves do not emit any radiation, but the matter, which accretes on to them, does. There are three distinct ways one could study the spectral properties: the first is through direct observation of the radiation. Here, one has to use separate instruments, either ground based (IR, optical, UV, very high energy gamma rays) or space based (optical, X-rays, gamma-rays). The goal would be to find if there are fast variabilities or spectral signatures of high velocity (which may point to massive compact objects at the core or some spectral signatures especially predicted for black holes). A second method which is really the other extreme, is to solve equations which govern the motion of matter around a black hole and produce the most likely solutions which explain both the steady and non-steady behaviour of the radiation. A third way is intermediate between the other two approaches: here, one assimilates the gist of the theoretical results and gives models and fits the observational results with these models using several free parameters. (The reverse may also be appropriate sometimes: theoreticians may get clues from 'models' to select the best solution out of many possible ones.) Very often, this third approach requires separate models for separate objects.

In the present paper, I will present the theoretical reasoning behind the most accurate solution of the black hole accretion of today in order to assist the observers to more fruitfully plan their observations and perhaps to provide hints to the model builders so that they may fine tune their present models accordingly. Historically, in the present subject, tentative models came first (such as disks with corona, see, e.g., Galeev et al., 1979) and as the theoreticians sharpened their tools



Astrophysics and Space Science **297:** 131–142, 2005.
© Springer 2005

through viscous transonic solutions with heating, cooling, steady and oscillating shocks (Chakrabarti, 1990, 1996a), both theoretically and through numerical simulations, new models started emerging (a good example being Something or the Other Dominated Accretion Flow [SODAF] models; dynamical corona models, etc.) which converge to the outcome similar to these transonic theoretical solutions. Consequently, these models do not throw any new insights into the problem.

Because correct theoretical works incorporates proper boundary conditions (such as entering through the black hole with velocity of light, or hitting the hard surface of a neutron star with zero radial velocity) the solutions got to be correct beyond doubt. However, in certain situations (such as inclusion of all the components of the magnetic field self-consistently) it may not be possible to obtain solutions in the first place. In such cases 'patch-up' works are done (such as putting toroidal field or radial field on the top of hydrodynamics solutions) which are often satisfactory.

2. The Advective Disk Paradigm

A cartoon diagram of the flow geometry, which comes out of extensive analytical and numerical works (see, e.g., Chakrabarti, 1990, 1993, 1996a,b) is shown in Figure 1. The Keplerian disk, because of its low energy, resides at the equatorial plane, while matter with lower angular momentum flows above and below it (Chakrabarti, 1994; Chakrabarti and Titarchuk, 1995 [CT95]; Ebisawa et al., 1996; Chakrabarti et al., 1996a,b; Chakrabarti, 1997 [C97]). The wind is predominantly produced from the CENBOL area or the CENtrifugal barrier supported BOundary Layer of the black hole, which is the post-shock region. A transient shock may be present just outside the inner sonic point. The inner edge of the Keplerian disk is terminated at the transition radius as dictated by the viscosity of the flow. The wind

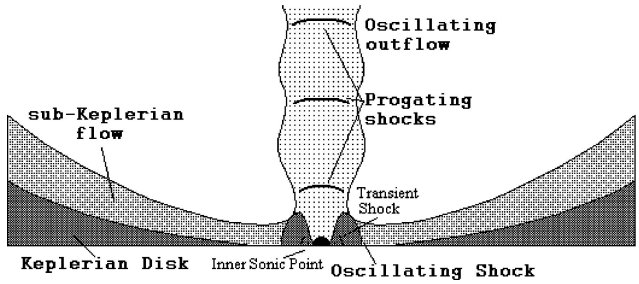


Figure 1. Cartoon diagram of the Two Component Advective Flow (TCAF) solution highlighting different components. The centrifugal pressure dominated boundary layer or CENBOL is the post-shock region of the combined Keplerian and sub-Keplerian flow. There could be transient shocks close to the inner sonic point. Propagating shocks are expected to form once in each cycle of shock oscillation.

may be variable because of shock-oscillation and every supersonic puff of wind is expected to produce a propagating shock in the jet. It is to be noted that all the components in this diagram could be variable (see, Chakrabarti and Nandi, 2000). Not surprisingly, this paradigm, created almost a decade ago, is now vindicated by most of the observations. Indeed, the cartoon diagrams (see, e.g., Esin et al., 1998; Zdziarski and Gerlinski, in press; Nowak, 2002; Fender et al., 1999; Fender, this volume) are slowly, but surely, converging to those predicted by our exact approach. Whereas our exact approach identifies the reason of the movement of the inner edge of the disk with viscosity and accretion rate, other models merely take these as facts and proceed fitting with observations assuming such behaviours *a priori*.

The advective paradigm, which requires two component advective flows (TCAF) has been tested for a varied range of observational facts. It is the only solution, which explains QPOs and their variations quite naturally as manifestations of the shock oscillations (Chakrabarti et al., 2004 and references therein). Hence it is worthy to look at the high-energy predictions within this paradigm in order to find an interpretation of recent gamma-ray observations.

3. Spectral Properties at Soft and Hard X-Rays

Detailed properties of the spectrum coming out of TCAF solution have been discussed in CT95 and C97. The soft radiation coming from the Keplerian disk is intercepted by the sub-Keplerian hot flows in the CENBOL region and is re-radiated as the hard radiation. Depending on the relative importance of the Keplerian disk rate $\dot{M}_{\rm d}$ in comparison to the sub-Keplerian halo rate $\dot{M}_{\rm h}$, the electrons in the sub-Keplerian disk may or may not be cooled down. If not, then the system is in the hard state and if yes, the system is in the soft state. The hard state is thus dominated by a power-law hard photon component produced by inverse Comptonization of the soft photons. In the soft state, the electrons in CENBOL cooled down and collapses, but due to the inner boundary condition of supersonicity, the matter accelerates rapidly and up-scatters photons to its energy ($\sim m_e c^2$). Thus, power-law photons can also be seen due to this, so-called, bulk motion Comptonization (BMC) (CT95). Occasionally, as we shall show below, photons of much higher energies are seen. But that does not imply that the BMC is not taking place. BMC only asserts what should be the *minimum* intensity of power-law photons in soft-states as dictated purely by gravitational pull of the black hole. Of course, in presence of other physical processes (such as synchrotron radiation, see, below), very high-energy photons should be expected. It is to be noted that CT95 solution already incorporates all the iterations of re-processing between the Keplerian and sub-Keplerian components. Therefore, it is no longer necessary to include a 'Compton reflection' component that is usually assumed by some model builders.

Being almost freely falling, the sub-Keplerian flow would bring forth faster changes to spectral indices than the Keplerian flow, which moves in viscous

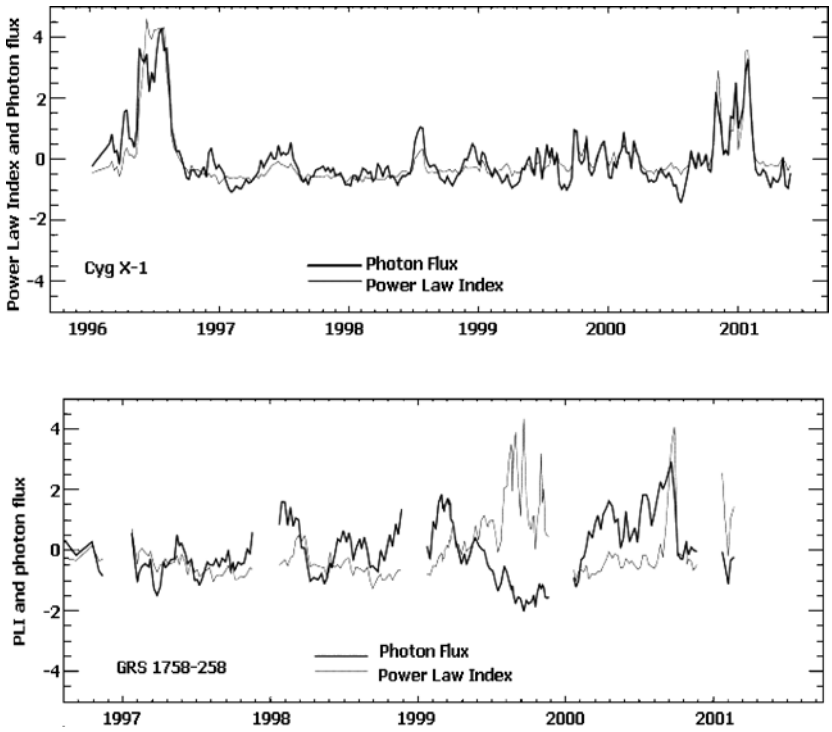


Figure 2. ASM light curves for a wind accretor (Cyg X-1) and a low-mass binary system (GRS1758-258) from RXTE data (Smith et al., 2002) showing distinctly different behaviour due to the absence and presence of a dominant Keplerian disk in these objects. Photon flux is in the units of photons/cm^2/s.

time-scale. Figure 2 shows the variation of photon flux and power-law index of Cyg X-1 (upper panel) and for GRS 1758–258 (lower panel) for more than four years as seen by RXTE. This distinctly different behaviour of a preferentially wind accretor (Cyg X-1) and the Roche-lobe accretor (GRS 1758–258) could be interpreted very clearly when two independent components as predicted by TCAF solution are used (Smith et al., 2002). For instance, if there is a reduction in the accretion rate at the outer edge, the sub-Keplerian component at the inner edge will be reduced in free fall time $t_{\rm ff} \sim r^{3/2}$. Until this information propagates through the Keplerian disk with viscous time scale, the source would behave like a soft state, but then, after the viscous time, the spectrum will harden as the soft photons go down. In Cyg X-1, Cyg X-3, etc., which are known to be wind accretors, the Keplerian disk is very small and the power-law index basically correlates with the photon flux. In 1E 1740.7-2942, GRS 1758–258, and GX 339-4, which are in low-mass X-ray binary systems, the Keplerian disk is big and the delay of tens of days are common (Smith et al., 2002). Another very important point made in C97 was that a single component ADAF (Esin et al., 1998) model is incapable of producing state transition unless the inner edge is moved back and forth unphysically. These problems

are avoided when TCAF solution is chosen. The complete spectral variation of the type seen in Cyg X-1 and other binaries are presented in C97.

Having thus established that the behaviour of a large population of galactic black hole candidates can be understood only with TCAF solution, attempts were made to explain fast variabilities. In case the shock oscillates back and forth (Molteni et al., 1996; Molteni et al., 1996; Ryu et al., 2004; Chakrabarti et al., 2004), the hard X-ray emission is likely to be modulated at the shock oscillation frequency. With the increasing of the Keplerian rate, i.e., cooling of the CENBOL, the shock moves in due to fall of pressure and the frequency of QPO rises. This behaviour is also well known. According to the TCAF solution, different length scales of the flow are responsible for different QPO frequency range or the break frequency. For instance, the oscillation at the transition radius is responsible for 0.1–0.3 Hz QPO, the oscillation of the shock is responsible for 1–15 Hz QPO, the oscillation of the inner transient shock is responsible for the 60–450 Hz QPO and the cooling time scale of the sonic sphere of the jet is responsible for the 0.01–0.03 Hz QPO. The jets and outflows are also found to be coming out from the CENBOL region (Chakrabarti, 1999) and the outflow rates were computed exactly (Chakrabarti, 1999; Das and Chakrabarti, 1999) as a function of the inflow rate. These outflows are found to change the spectral slope of the outgoing radiation indirectly since they modify the particle density at CENBOL. Since the presence of CENBOL is a function of the spectral state, this paradigm naturally explains the relation between the outflow rate and the size of the Comptonizing region. These behaviours have now been verified by observers and model builders (e.g., Fender et al., 2000 and references therein).

When the magnetic field is included, the synchrotron photons must be included into the solution as they play a major role in cooling the sub-Keplerian flow. As the sub-Keplerian rate is increased, the density of soft photons goes up, but it needs not be sufficient to cool the electrons as the number of electrons themselves also goes up. Furthermore, the shocks in the flow can accelerate electrons to a high energy which in turn may be able to produce photons at very high energy γ-ray. In the next section, we shall discuss the spectral properties of black hole candidates in high energies.

4. Spectral Properties of Galactic Black Holes in γ-Rays

The TCAF solution usually has a single static, oscillating or a propagating shock. However, numerical simulations suggest the presence of a transient shock just before the flow passes through the inner sonic point (Samanta et al., in press). Thus, there are possibilities to produce power-law high-energy emissions by the power-law electrons generated by repeated passages through these shocks. Details are presented in Mandal and Chakrabarti (in press) and some of the highlights are presented in Mandal and Chakrabarti (this volume). It is entirely possible that

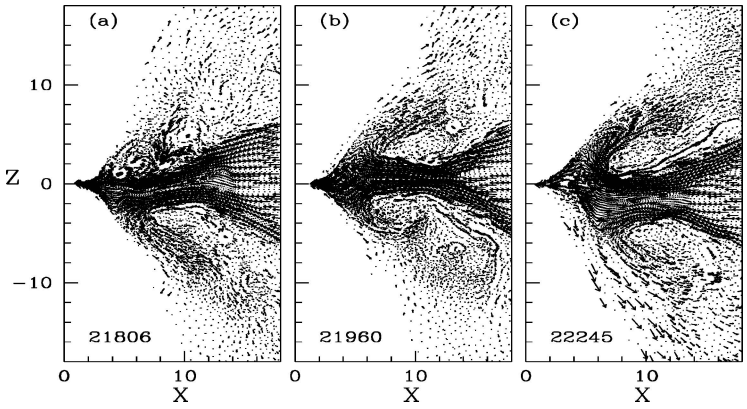


Figure 3. Oscillating accretion shocks, which are responsible for QPOs are also responsible for variable outflows which steepen into shocks in the jets (Chakrabarti et al., 2004).

the bulk of the high-energy gamma-rays could be contributed by emissions from shocked regions of the outflow and jet. The physics of the shock formation in jets is not yet understood properly. Numerical simulations indicate periodic flaring of matter emerging as outflows as the shock oscillates back and forth (Chakrabarti et al., 2004). Figure 3 shows the oscillation of the inner region of the advective flow. Arrows indicate puffs of matter getting out in the alternating sides during oscillation. Such oscillations of the accretion shocks are not only responsible for the QPOs; they may also be responsible for injecting non-linear perturbations in the outflows. These shocks may steepen up as they propagate away from the central body (see, Figure 1) and cause acceleration of particles and synchrotron radiation. This is to be investigated in future. It is possible that other triggering mechanisms, such as reconnection of magnetic fields near the base of the jet suddenly releases energy in the outflows producing shocks as well.

Figures 4a–4b show generic nature of the spectra of galactic black hole candidates in both high and low states for two sets of black holes: Set A includes GROJ1719–24, GROJ0422+32 and CYGNUS X-1 while Set B includes GRO1655–40 and GRS 1915+105. The high energy regions are adapted from the results from McConnell et al. (2002), Ling and Wheaton (2004, in press), Case et al. (in press), etc. Here 'high' and 'low' states mean the soft and hard states using the nomenclature as in Chakrabarti and Titarchuk (1995) (see also, Tanaka and Lewin, 1995) where the high power is observed in soft ($\sim$1 keV) and hard ($\sim$40–100) keV energies, respectively. These states can also be defined using the energy spectral index $F_E \sim E^{-\alpha}$ in the 2–20 keV range: $\alpha > 1$ for soft state and $\alpha < 1$ for hard state. CT95 model has been discussed in the previous section.

In the gamma-ray regime, the nomenclature is not unique yet. Ling and Wheaton (in press) like to call the above-mentioned 'canonical' high and low states as the 'low γ intensity state' and 'high γ intensity state', respectively. When seen in

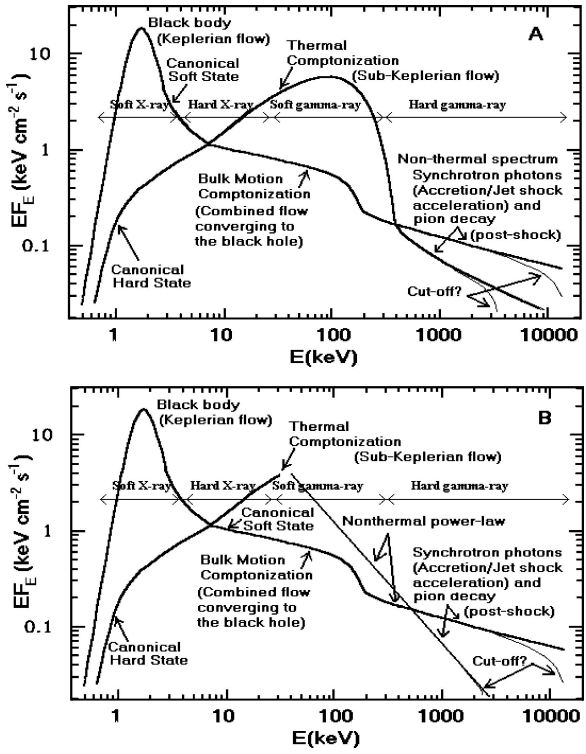


Figure 4. Soft and hard state transitions of two classes of black holes which supposedly differ in the very high gamma-ray region for the high (soft) gamma intensity state. In A, it consists of thermal Comptonization till 200–300 keV and power-law after that. In B, it consists of non-thermal power-law.

high-energy gamma rays $\gtrsim$400 keV, the high state also corresponds to the high (hard) γ-ray state and similarly for hard states. The difference in these two sets (marked A and B) in Figures 4a–4b lies in the very high energy gamma-ray region: while in Set A, the so-called 'high γ-ray intensity state' has a thermal spectrum below 200–300 keV and a weaker and softer power-law tail for higher energies, in Set B, the same state is manifested as simply a continuous non-thermal power-law with or without a break (Case et al., in press).

Examples of the observations in the two sets are presented in Figure 5 (from Ling and Wheaton, in press) and in Figure 6 (from Case et al., in press). The latter figures show the nature of changes, which are taking place in the power law in the high (soft) gamma-intensity state during a hard X-ray flare. The spectrum steepens at the peak of the flare. Case et al. (in press) find that while Cyg X-1, GRO J0422+32, GRO J1719–24 belong to Set A (Figure 4a), GRO 1655–40 and GRS 1915+105 belong to the Set B (Figure 4b). It is interesting to note that while both candidates in Set B are considered to be LMXRBs, the candidates in Set A are mixed: only Cyg X-1 is HMXRB while others are LMXRBs. Thus, this difference in the spectra

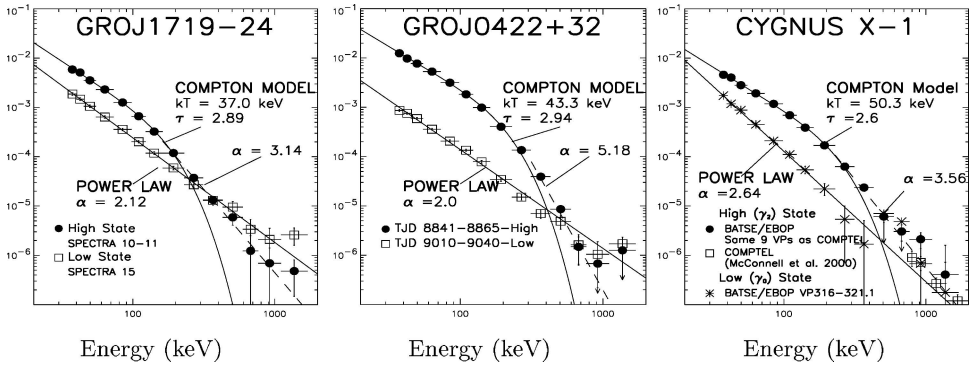


Figure 5. Photon fluxes (in photons/cm^2/s/keV) of three black hole candidates, which show thermal Comptonization and a non-thermal power component in canonical hard states (from Ling and Wheaton, in press).

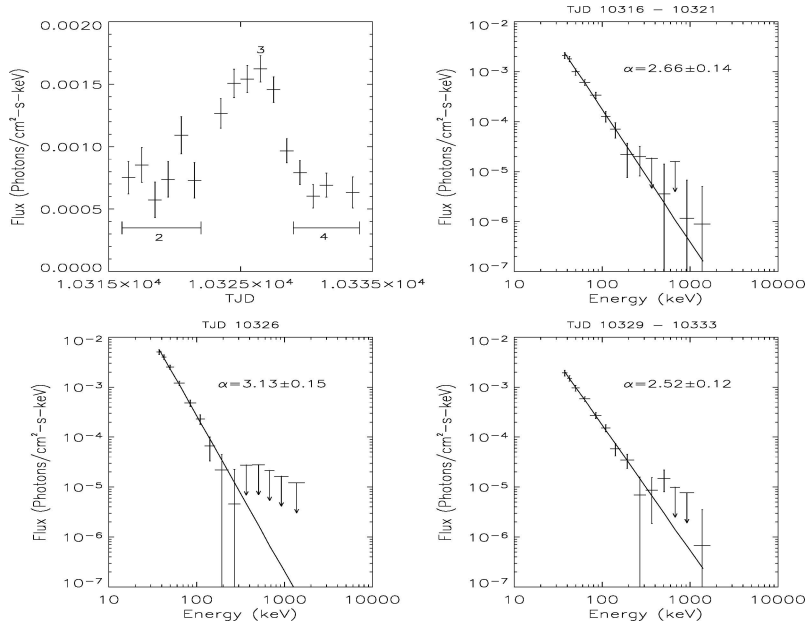


Figure 6. Example of non-thermal power-law in the very high-energy gamma-ray region in the canonical hard state of GRO J1655–40 (from Case et al., in press). Here, a flare is analyzed. The second, third and the fourth panels refer to the spectra of the marked regions of the photon flux shown in Panel 1. At the peak of the flare, the spectrum is steeper.

is puzzling. It is also important that for all the candidates in Set A, the time lag in hard X-ray with respect to the softer X-ray is around 0.1–1 s (van der Hooft et al., 1999), which point to an extended region of hard X-ray emission region. It is possible that these two properties of Set A candidates are related. The

explanation may not thus lie in the difference in the primary composition of the accretion flow, which is known to be predominantly of low angular momentum for HMXRBs and Keplerian for LMXRBs but to a common cause, namely, the shock formation.

Physically, it is clear that the accretion shocks and the shocks in jets and outflows could be responsible for the production of very high-energy gamma rays. One of the advantages of the TCAF solution is that the accretion shocks, jets and shocks in jets are built into the solution. Thus, one could imagine having shock acceleration of electrons in the accretion and the power-law electrons producing power-law photons most naturally without having to guess about the origin of the shocks. As we mentioned, shocks in jets could be produced due to perturbations of the CENBOL (e.g., oscillation of shocks) or sudden deposition of energy at the base of the jet through reconnection of magnetic fields. Usual photopion production in the jets and gamma-ray production in pion decay cannot be ruled out also.

As a general comment, we might add that in the canonical soft states, the highest energy gamma ray is also the most intense (see Figures 4a–4b). One could ask the following questions.

1. If the highest energy γ-rays are coming from the jets, and at the same time, if the Keplerian rate is so high that the object is in the canonical soft state, then, can the jets or outflows be very strong as well?
2. If the jet and outflows are produced in harder states as the analytical work (Chakrabarti, 1999) and some observations tend to show, then why the highest energy gamma rays are not seen in canonical hard states as well?
   To understand this, one has to perhaps go back to the basics: Analytically it is easy to show that the *ratio R* of the outflow rate ($\dot{M}_{\rm out}$) to the inflow rate ($\dot{M}_{\rm in}$) is very low in the soft state, and low in the hard state (see, Chakrabarti, 1999), but it is the highest when the strength of the shock is intermediate. In other words, if the inflow rate is high, as in a canonical soft state, the outflow rate could also be high, though it needs not be relativistic.

In the case of HMXRBs, such as Cyg X-1, the accretion is dominated by low-angular momentum winds and it needs not to produce any strong accretion shocks or jets as the centrifugal barrier needs not to be strong enough even in the hard state. Indeed, broad QPOs at very low frequency ($\sim$0.04 Hz) have been observed so far (Paul et al., 1998) which indicates a shock at around 10^3–$10^4 r_{\rm g}$. The jets are also found to be very slow, continuous (Fender et al., 2000). So, it may be easy to understand why in canonical hard states, the very high-energy gamma-ray is weaker. In order to understand its behaviour in soft states, it may be pertinent to invoke the most relevant solution of this problem presented by Chakrabarti and Molteni (1995). Here, it was shown that the shock in an inviscid flow tends to recede outward in presence of viscosity parameter higher than a critical value (Figure 7a). The post-shock subsonic region acquires a Keplerian distribution and the inner part essentially becomes a Keplerian disk (Figure 7b). (In fact, this is how a Keplerian

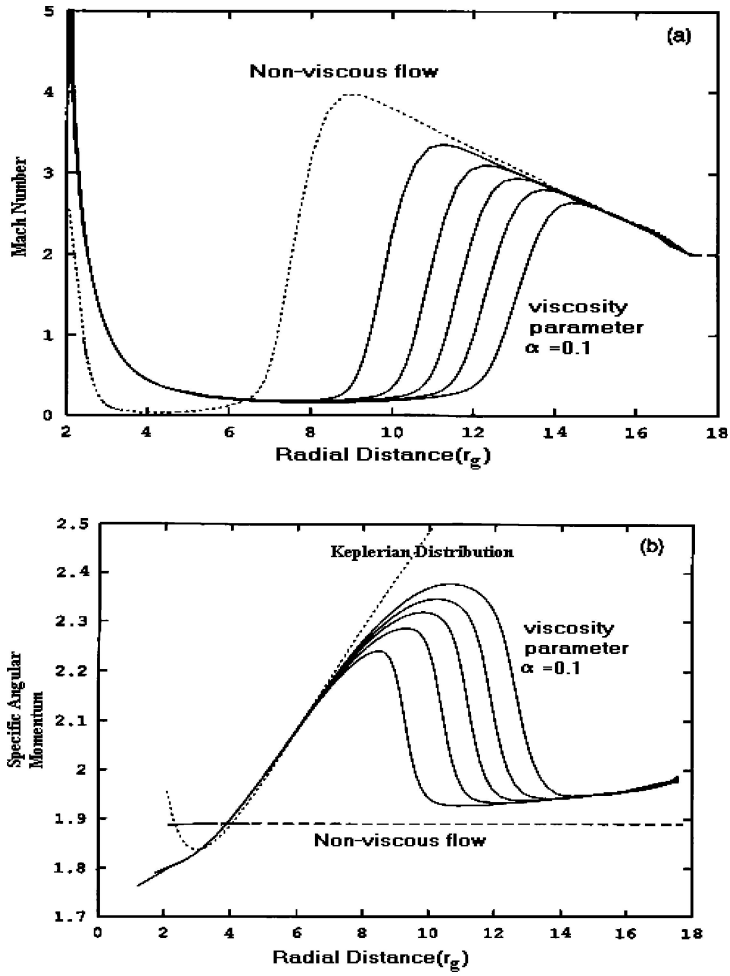


Figure 7. Example of propagating shock solution in presence of larger viscosity (Chakrabarti and Molteni, 1995). Variation of (a) Mach number and (b) specific angular momentum as a function of the radial distance. Solutions for inviscid flow are also placed for comparison.

disk forms in the first place.) It is possible that the temporary presence of a large viscosity is the reason for Cyg X-1 to go to a soft-state. The sub-Keplerian region at $r \sim 10^3$–$10^4 r_g$ could become the Comptonizing region (Figure 8). It is not unlikely that some jets could come out from the interface of the Keplerian and sub-Keplerian flow taking away excess angular momentum. Could the shocks in this outer jet or at the propagating interface be responsible for the gamma-rays, as well as the time lag of 0.1–1 s as observed? In GRO 1655–40 and GRS 1915+105, jets are present and they also show various class transitions because of slow variation of accretion rates and because of interaction of jets with Comptonized photons. These cause blobby

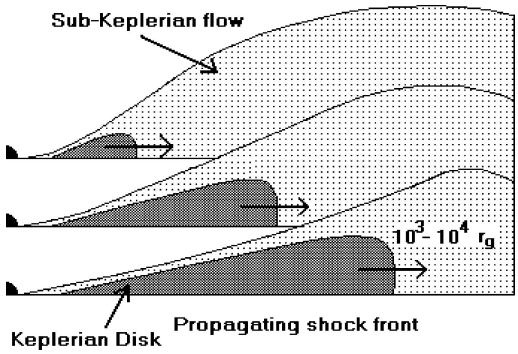


Figure 8. Possible cause of soft state in Cyg X-1 and similar black hole candidates based on Chakrabarti and Molteni (1995) solution. In this case the inner part becomes Keplerian while outer region remains sub-Keplerian.

nature of the jets and perhaps stronger ultra-relativistic shocks in jets which, in turn, produce shock acceleration of particles eventually producing power-law γ-rays as reported by Case et al. (in press).

So far, we mostly discussed the solutions and interpretations in the case of galactic black holes. Fortunately, the nature of solutions does not change with the black hole mass and most of the considerations discussed above remain valid for supermassive black holes. The major difference would be in timing properties as all the time intervals will scale with the central mass. Since in this case, we do not expect any 'binary companion' to supply matter, the matter is likely to be from the winds of nearby stars or from disruption of the stars. Thus, the formation of steady, oscillating or propagating shocks will be even more relevant.

Acknowledgements

The author acknowledges the organizers for the invitation. This work was made possible in part through a grant (Grant No. SP/S2/K-15/2001) from Department of Science and Technology (DST).

References

Case, G.L. et al.: in press, *Chin. J. Astron. Astrophys.*

Chakrabarti, S.K.: 1990, *Theory of Transonic Astrophysical Flows*, World Scientific.

Chakrabarti, S.K.: 1993, in: J. Franco et al. (eds.), *Numerical Simulations in Astrophysics*, Cambridge University Press, UK, Mexico City, Mexico.

Chakrabarti, S.K.: 1994, in: H. Böhringer et al. (eds.), *Proceedings of 17th Texas Symposium*, Munich, Germany, New York Academy of Sciences, New York.

Chakrabarti, S.K. and Molteni, D.: 1995, *MNRAS* **272**, 80.

Chakrabarti, S.K.: 1996a, *ApJ* **464**, 664.
Chakrabarti, S.K.: 1996b, *Phys. Rep.* **266**, 229.
Chakrabarti, S.K.: 1997, *ApJ* **484**, 313.
Chakrabarti, S.K.: 1999, *A&A* **351**, 185.
Chakrabarti, S.K., Acharyya, K. and Molteni, D.: 2004, *A&A* **421**, 1.
Chakrabarti, S.K. and Nandi, A.: 2000, *Ind. J. Phys.* **75**(B), 1.
Chakrabarti, S.K. and Titarchuk, L.G.: 1995, *ApJ* **455**, 623.
Das, T.K. and Chakrabarti, S.K.: 1999, *Classical Quant. Gravity* **16**(19), 3879.
Esin, A.A., McClintock, J.E. and Narayan, R.: 1998, *ApJ* **505**, 854.
Fender, R. et al.: 1999, *ApJ* **519**, L165.
Fender, R.P., Pooley, G.G., Durouchoux, P., Tilanus, R.P.J. and Brocksopp, C.: 2000, *MNRAS* **312**, 853.
Galeev, A.A., Rosner, R. and Vaiana, G.S.: 1979, *ApJ* **229**, 318.
Ling, J.C. and Wheaton, W.A.: 2003, *ApJ* **584**, 399.
Ling, J.C. and Wheaton, W.A.: in press, *Chin. J. Astron. Astrophys.*
Mandal, S. and Chakrabarti, S.K.: in press, *A&A*.
McConnell, M.L. et al.: 2002, *ApJ* **572**, 984.
Molteni, D., Sponholz, H. and Chakrabarti, S.K.: 1996, *ApJ* **457**, 805.
Molteni, D., Ryu, D. and Chakrabarti, S.K.: 1996, *ApJ* **470**, 460.
Nowak, M.: 2002, in: P. Durouchoux et al. (eds.), *New Views on Microquasars*, Corsica, Centre for Space Physics, Kolkata, India.
Paul, B., Agrawal, P.C. and Rao, A.R.: 1998, *J. Astrophys. Astron.* **19**, 55.
Ryu, D., Chakrabarti, S.K. and Molteni, D.: 2004, *ApJ* **474**, 378.
Samanta, M.M., Ryu, D. and Chakrabarti, S.K.: in press.
Smith, D.M., Heindl, W.A. and Swank, J.H.: 2002, *ApJ* **569**, 362.
van der Hooft, F. et al.: 1999, *ApJ* **519**, 332.
Zdziarski, A.A. and Gierlinski, M.: 2004, *Prog. Theor. Phys.* **155**, 99.

TOWARDS A POPULATION OF HMXB/NS MICROQUASARS AS COUNTERPARTS OF LOW-LATITUDE UNIDENTIFIED EGRET SOURCES

M. RIBÓ,[1] J.A. COMBI[2,3] and I.F. MIRABEL[1,4]

[1]*Service d'Astrophysique, CEA Saclay, Gif-sur-Yvette, France;*
E-mail: mribo@discovery.saclay.cea.fr
[2]*Departamento de Física (EPS), Universidad de Jaén, Jaén, Spain*
[3]*Instituto Argentino de Radioastronomía (IAR), Villa Elisa, Argentina*
[4]*Instituto de Astronomía y Física (IAFE), Buenos Aires, Argentina*

(Received 1 July 2004; accepted 3 August 2004)

Abstract. The discovery of the microquasar LS 5039 well within the 95% confidence contour of the Unidentified EGRET Source (UES) 3EG J1824−1514 was a major step towards the possible association between microquasars (MQs) and UESs. The recent discovery of precessing relativistic radio jets in LS I +61 303, a source associated for long time with 2CG 135+01 and with the UES 3EG J0241+6103, has given further support to this idea. Finally, the very recently proposed association between the microquasar candidate AX J1639.0−4642 and the UES 3EG J1639−4702 points towards a population of High Mass X-ray Binary (HMXB)/Neutron Star (NS) microquasars as counterparts of low-latitude unidentified EGRET sources.

Keywords: γ-ray sources, X-ray binaries, microquasars

1. Introduction

The third EGRET catalog (Hartman et al., 1999) contains 271 point sources detected at energies above 100 MeV. The majority of these sources, ∼168 or ∼62%, still remain unidentified. Among them, there are 72 sources located at low galactic latitudes, having $|b|<10^{\circ}$, which represents around 45% of the UES population. Therefore, several of these objects are presumably of galactic nature. Similar properties between some of these UESs, indicate that there are at least three different groups of galactic populations (Romero et al., 2004; Grenier, 2004). The group of young stellar objects and star-forming regions (Romero, 2001), those sources forming a halo around the galactic center and a group of sources correlated with the Gould Belt (Grenier, 2000).

Based both on multiwavelength observations and theory, microquasars (see Mirabel and Rodríguez, 1999 for a review) with massive companions have been proposed as possible counterparts of the first group of galactic UESs by several authors (Paredes et al., 2000; Kaufman Bernadó et al., 2002; Romero et al., 2004; Bosch-Ramon et al., 2005). In Sections 2 and 3 of this paper we will briefly review



Astrophysics and Space Science **297:** 143–154, 2005.
© Springer 2005

the properties of the two well-known microquasars LS 5039 and LS I +61 303, typically associated with the first group of UESs, while in Section 4 we will present the possible association between the microquasar candidate AX J1639.0−4642 and the UES 3EG J1639−4702. Finally, in Section 5 we will compare the available data of these three sources from radio to gamma-rays, and we will discuss on similarities pointing towards a population of HMXB with NS microquasars as counterparts of low-latitude UESs.

2. LS 5039

The high mass X-ray binary system LS 5039 (Paredes et al., 2000) is one of the ∼15 confirmed galactic microquasars (Ribó, 2004). LS 5039 is a bright $V \sim 11.2$ star with an ON6.5V((f)) spectral type (McSwain et al., 2004). The binary system has a short orbital period of $P = 4.4267 \pm 0.0005$ d, a high eccentricity of $e = 0.48 \pm 0.06$, and a low mass function $f(m) = 0.0017 \pm 0.0005\ M_{\odot}$, suggesting the presence of a NS as the compact object in the system (McSwain et al., 2004).

Observations conducted with the EVN and MERLIN (see Figure 1) confirmed the persistent nature of this MQ, and revealed the presence of an asymmetric two-sided jet reaching up to 1000 AU on the longest jet arm (Paredes et al., 2002). These observations also suggest a bending of the jets with increasing distance from the core and/or precession.

The possibility that LS 5039 is a γ-ray emitter was suggested by Paredes et al. (2000), who proposed the association of the system with the UES 3EG J1824−1514 (Hartman et al., 1999). We show in Figure 2 the location map of the γ-ray source together with the NVSS and bright/faint ROSAT sources. The only simultaneous X-ray/radio source within the statistical contours of 3EG J1824−1514

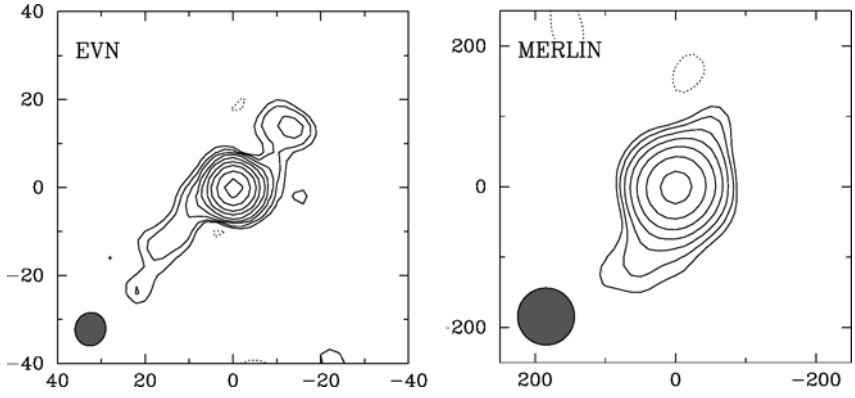


Figure 1. Left: EVN self-calibrated image of LS 5039 at 5 GHz obtained on 2000 March 1. Axes units are in mas. The synthesized beam is plotted in the lower left corner. Right: Same as left but obtained with MERLIN. From Paredes et al. (2002).

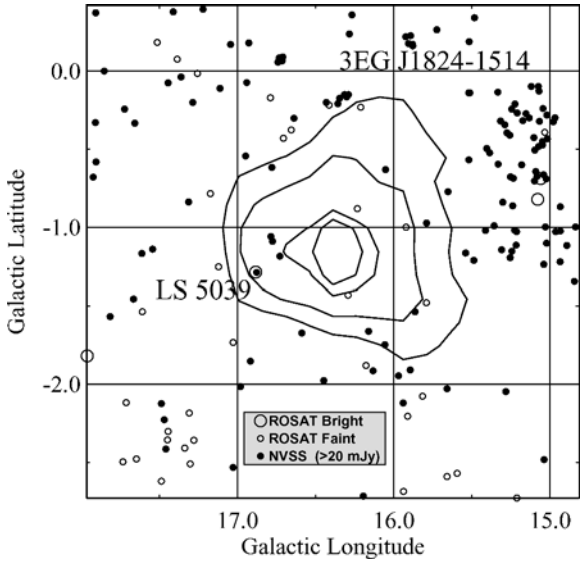


Figure 2. Location map of 3EG J1824−1514. The contours represent, from inside to outside, the 50%, 68%, 95%, and 99% statistical probability that a γ-ray source lies within the given contour. The only source with X-ray and radio emission (filled circle inside an open big circle, $l = 16.88^\circ$ and $b = -1.29^\circ$), and well inside the 95% contour, is LS 5039 (Ribó, 2002).

is the microquasar LS 5039. We note that this binary system is present in the BATSE Earth occultation catalog of low-energy gamma-ray sources (Harmon et al., 2004), with a positive detection of a few mCrab up to ∼100 keV. The source is not present in cumulative observations conducted with the INTEGRAL satellite (Bird et al., 2004), although it is expected to be detected when adding a few more months of data. We also point out that there is an unidentified COMPTEL source with a position compatible with LS 5039 (Collmar, 2004).

Astrometric studies carried out by Ribó et al. (2002), show that it is a runaway system with a systemic velocity of ∼150 km s^{-1} that moves away from the Galactic plane with a velocity of ∼100 km s^{-1}. This result, combined with the possible lifetime of the donor star, indicates that it could reach a not-so-low galactic latitude of $b = -12^\circ$ still behaving as a microquasar.

Bosch-Ramon and Paredes (2004a) have recently developed a detailed numerical model to test whether this system can actually produce the emission detected by EGRET through inverse Compton (IC) scattering. Their numerical approach considers a population of relativistic electrons entrained in a cylindrical inhomogeneous jet, which interact with both the radiation and the magnetic fields. The computed spectrum is able to reproduce the observed spectral characteristics at very high (GeV) energies.

3. LS I +61 303

The Be/X-ray binary system LS I +61 303 is a well-studied object since it presents radio and X-ray variability linked to its ∼26.5 d orbital period (Gregory, 2002; Paredes et al., 1997). The donor star in this system is a rapidly rotating B0V star with variable mass loss (Hutchings and Crampton, 1981). Some properties of this system can be explained assuming that the unseen companion is a non-accreting young pulsar with a relativistic wind strongly interacting with the wind of the Be star (Maraschi and Treves, 1981). On the contrary, other properties of LS I +61 303 fit better a model where the companion is accreting even with two episodes of super-critical accretion along the orbit (Martí and Paredes, 1995).

This X-ray binary system has been associated for long time with the gamma-ray source 2CG 135+01/3EG J0241+6103 (see Figure 3), which displays variability on timescales of days (Tavani et al., 1996, 1998; Wallace et al., 2000). During the last years, Massi et al. (2001, 2004) have revealed its MQ nature through the discovery of a radio jet (see Figure 4) extending 200 AU at both sides of a central core, that appears to experience a fast precession, which could explain the short-term gamma-ray variability of 3EG J0241+6103 (as proposed by Kaufman Bernadó et al., 2002) and the puzzling VLBI structures found in previous observations. This result points to the occurrence of accretion/ejection processes in this system, ruling out, in principle, the non-accreting young pulsar scenario.

Massi (2004) has recently studied the data acquired within the pointed EGRET observations of 3EG J0241+6103 and claimed the detection of a periodicity of $P = 27.4 \pm 7.2$ d, consistent with the orbital period of the binary system. If this is confirmed, the identification of LS I +61 303 as the counterpart of 3EG J0241+6103

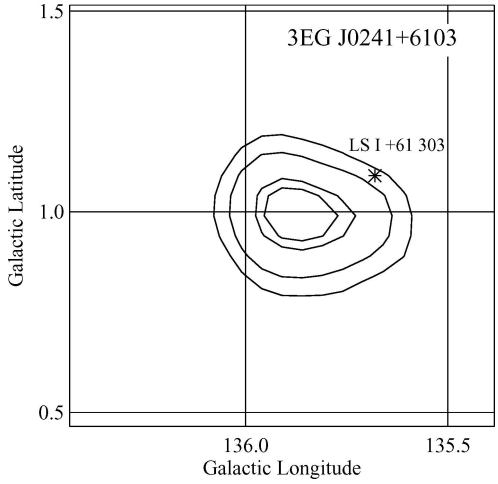


Figure 3. Location map of 3EG J0241+6103. The position of LS I +61 303 is marked with an asterisk. Adapted from Hartman et al. (1999).

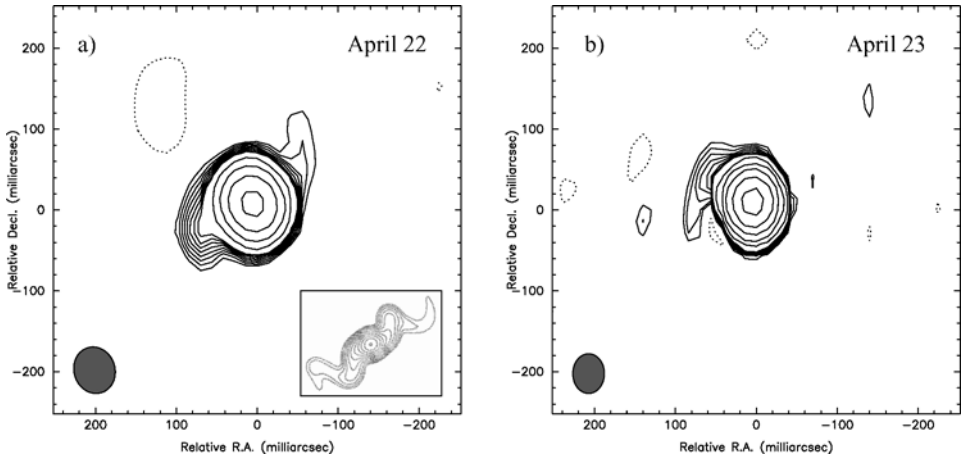


Figure 4. a) MERLIN self-calibrated image of LS I +61 303 at 5 GHz and using natural weights, obtained on 2001 April 22. The synthesized beam is plotted in the lower left corner. The S-shaped morphology strongly recalls the precessing jet of SS 433, whose simulated radio emission (Figure 6b in Hjellming and Johnston, 1988, rotated here for comparison purposes) is given in the small box. b) Same as before but for the April 23 run and using uniform weights for better displaying. From Massi et al. (2004).

would be unambiguous. In any case, an important point is that all the available data are compatible with an increase of γ-ray emission around periastron, that can be tested with Cherenkov telescopes and future satellites.

This binary system is also present in the BATSE Earth occultation catalog of low-energy gamma-ray sources (Harmon et al., 2004), with a positive detection of a few mCrab up to $\sim$100 keV, although the detection is not as significant as in the case of LS 5039. LS I +61 303 is not present in cumulative observations conducted with the INTEGRAL satellite (Bird et al., 2004), although it is expected to be detected when adding a few more months of data, like in the case of LS 5039. We note that there is a COMPTEL source containing LS I +61 303 and the quasar QSO 0241+622 (van Dijk et al., 1996).

A numerical model to explain the EGRET emission of LS I +61 303 has also been developed by Bosch-Ramon and Paredes (2004b).

4. AX J1639.0−4642

Aimed at discovering new MQs, Combi et al. (2004) have recently carried out a multiwavelength study of the unidentified X-ray source AX J1639.0−4642. This object was discovered by the Advanced Satellite for Cosmology and Astrophysics (ASCA) observatory at the 0.7–10 keV energy range, and presented as a possible HMXB (Sugizaki et al., 2001). Its measured flux was $F_{\mathrm{X(0.7-10\ keV)}} = 19.2 \times 10^{-12}$ erg cm^{-2} s^{-1}, and it showed variable X-ray emission, with a confidence ≥ 99 %. Its

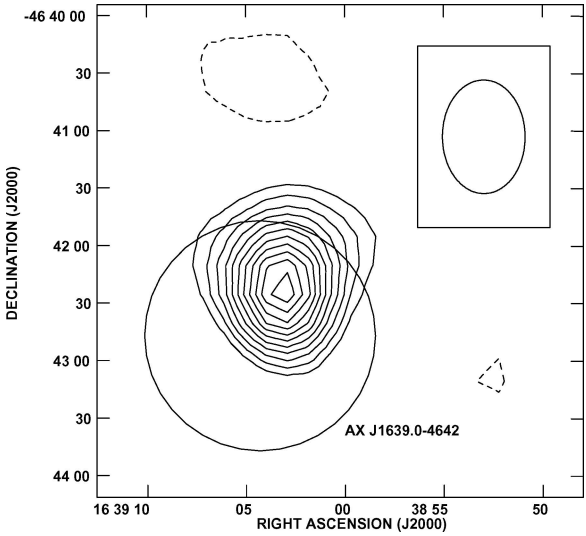


Figure 5. Contour image of the MGPS data obtained with MOST at 843 MHz on 1992 April 16. The radio source MOST J1639.0−4642 is well within the 90% uncertainty error circle of the X-ray source AX J1639.0−4642. The ellipse in the top right corner is the convolving beam. From Combi et al. (2004).

spectrum was fitted with a power law with a very hard photon index $\Gamma = -0.01^{+0.66}_{-0.60}$ and a poorly constrained hydrogen column density of $N_{\rm H} = 12.82^{+8.58}_{-6.88} \times 10^{22}\,{\rm cm}^{-2}$. Combi et al. (2004) re-analyzed these data and found evidences for variability on timescales of hours.

In searching for radio sources in the field of AX J1639.0−4642, Combi et al. (2004) found that the Molonglo Galactic Plane Survey (MGPS) at 843 MHz (Green et al., 1999) revealed a point-like radio source (see Figure 5), dubbed MOST J1639.0−4642, well within the error box of the X-ray source, with a flux density of 136 ± 18 mJy. At near infrared (NIR) wavelengths Combi et al. (2004) inspected the 2 Micron All Sky Survey (2MASS, Cutri et al., 2003), and found 10 sources in the 3σ error circle in position of MOST J1639.0−4642, some of them visible in the K_s-band image shown in Figure 6. At the far infrared part of the spectrum, from 12 to 100 microns, they found that the source IRAS 16353−4636 lies inside the error box of the X-ray source. This source overlaps the southern part of the 3σ position error circle of MOST J1639.0−4642, and its location uncertainty ellipse contains several 2MASS sources, as can be seen in Figure 6. The X-ray source AX J1639.0−4642 has been recently re-discovered at higher energies with the IBIS telescope onboard the INTEGRAL satellite, dubbed IGR J16393−4643 (Malizia et al., 2004; Bird et al., 2004). This source shows an average flux of $F_{\rm X(20-100\ keV)} \simeq 5 \times 10^{-11}$ erg cm^{-2} s^{-1}, and presents a factor of 2–3 flux variability on timescales of months.

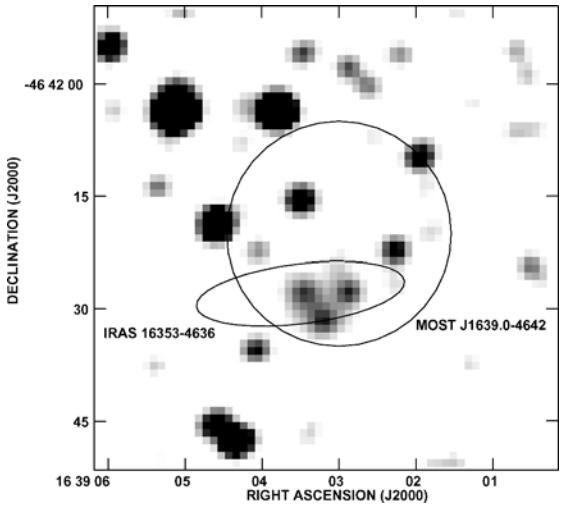


Figure 6. 2MASS K_s-band image of the environment of the radio source MOST J1639.0−4642, whose 3σ position error circle is shown, together with the 2σ position error ellipse of the far infrared source IRAS 16353−4636. Several NIR sources from the 2MASS catalog are possible counterparts of both sources. From Combi et al. (2004).

Although there is no spectroscopic/photometric information of a NIR/optical counterpart to derive a distance to the source, assuming that it is located in the Scutum-Crux or in the Norma spiral arms, a range of distances between 3 and 13 kpc is obtained.

Combi et al. (2004) pointed out that AX J1639.0−4642 lies inside the 95% location contour of the UES 3EG J1639−4702 (Hartman et al., 1999) as can be seen in Figure 7. Its γ-ray flux is $(53.2 \pm 8.7) \times 10^{-8}$ photon cm^{-2} s^{-1}, presents a steep γ-ray spectral index of $\Gamma = 2.5 \pm 0.18$ and has a variability index of $I = 1.95$. Although Torres et al. (2001a) found three radio pulsars inside the 95% confidence contour of the γ-ray source, its possible variability and steep photon index do not seem to agree, in principle, with a pulsar origin. Similarly, these properties would rule out an association with the three SNRs found within the 95% confidence contour (Torres et al., 2003). Moreover, no identified blazar has been found within the γ-ray contours. Therefore, Combi et al. (2004) suggested that the microquasar candidate AX J1639.0−4642/MOST J1639.0−4642 (=IGR J16393−4643) is the counterpart of 3EG J1639−4702. Observations with ATCA are in progress to unveil the nature of this source.

5. HMXB/NS Microquasars as Counterparts of Low-Latitude Unidentified EGRET Sources

As discussed above, the possibility of MQs being γ-ray emitters was suggested by Paredes et al. (2000), who proposed the association between the HMXB LS 5039

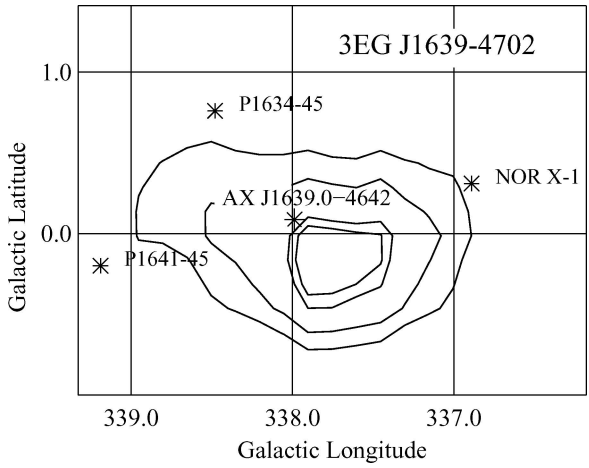


Figure 7. Location map of 3EG J1639−4702. The position of the X-ray source AX J1639.0−4642, well within the 95% probability contour, is marked with an asterisk. Other sources appearing outside the 99% probability contour are also indicated. From Combi et al. (2004).

and the UES 3EG J1824−1514. In their scenario (Paredes et al., 2000, 2002) the γ-rays are produced by IC upscattering of stellar ultraviolet (UV) photons by the non-thermal relativistic electron population that later on will produce the detected radio emission. Recently, more detailed models considering precession (Kaufman Bernadó et al., 2002), hadronic jets in windy microquasars (Romero et al., 2003) and all possible photon fields (Bosch-Ramon et al., 2005) have been proposed to explain the high-energy gamma-ray emission from HMXB microquasars.

On the other hand, as already stated, the X-ray binary system LS I +61 303 has been associated with the UES 3EG J0241+6103, and Massi et al. (2001, 2004) have revealed its MQ nature. If the MQ nature of AX J1639.0−4642 is confirmed, it could be the third MQ source related to a UES.

We quote the basic properties of these three γ-ray sources in Table I, and the properties of the proposed X-ray counterparts in Table II. There are three observational facts that should be noted. The first one is that LS 5039 and LS I +61 303, and probably AX J1639.0−4642, have massive optical companions, which provide an intense stellar UV photon field. On the other hand, the compact object appears to be compatible with a neutron star in the cases of LS 5039 (McSwain et al., 2004) and LS I +61 303 (Hutchings and Crampton, 1981; Casares et al., 2005; but see Massi, 2004). Finally, it is interesting to point out that the luminosities obtained in each spectral domain are very similar in all three sources, specially for the shorter distances to AX J1639.0−4642, giving support to the idea that all of them have similar emission processes.

Moreover, it should be noted that LS 5039 and LS I +61 303 are the only microquasars having both a high-mass donor and (possibly) a NS as the compact

TABLE I

Properties of the three γ-ray sources discussed in the text

γ-Ray source	Γ_γ [a]	I [b]	$L_{\gamma(>100\ \mathrm{MeV})}$ [c] (erg s^{-1})	d (kpc)
3EG J1824−1514	2.19±0.18	3.00	3.6×10^{35}	2.9 [d]
3EG J0241+6103	2.21±0.07	1.31	3.1×10^{35}	2.0 [e]
3EG J1639−4702	2.50±0.18	1.95	$(3–50)\times10^{35}$	3–13 ?

Note. The luminosity interval for AX J1639.0−4642 reflects the range of assumed possible distances.
[a]Hartman et al. (1999). [b]Torres et al. (2001b).
[c]Computed using the photon fluxes and indices from Hartman et al. (1999).
[d]Ribó et al. (2002).
[e]Frail and Hjellming (1991).

TABLE II

Proposed X-ray/optical/radio counterparts of the three γ-ray sources of Table I

X-Ray source	$L_{\mathrm{X(0.7-10\ keV)}}$ (erg s^{-1})	$L_{\mathrm{radio(0.1-100\ GHz)}}$ (erg s^{-1})	Spectral type	P_{orb} (days)	d (kpc)
LS 5039	$(0.5–5)\times10^{34}$ [a]	$\sim1.0\times10^{31}$ [b]	ON6.5V((f)) [c]	4.4 [c]	2.9 [d]
LS I +61 303	$(1–6)\times10^{34}$ [e]	$(1–17)\times10^{31}$ [f]	B0Ve [g]	26.5 [h]	2.0 [i]
AX J1639.0−4642	$(2–40)\times10^{34}$	$(0.8–16)\times10^{31}$ [j]	?	?	3–13 ?

Note. In the cases of the microquasars LS 5039 and LS I +61 303 the luminosity intervals correspond to intrinsic variability of the sources at the corresponding distances, while in the case of AX J1639.0−4642 they reflect the range of assumed possible distances.
[a]Reig et al. (2003).
[b]Martí et al. (1998), Ribó et al. (1999).
[c]McSwain et al. (2004).
[d]Ribó et al. (2002).
[e]Paredes et al. (1997).
[f]Computed from the values quoted in Strickman et al. (1998).
[g]Hutchings and Crampton (1981).
[h]Gregory (2002).
[i]Frail and Hjellming (1991).
[j]Computed assuming $\alpha = -1$.

object, and that there are no other microquasars (containing low-mass donors and/or black holes) located within the probability contours of unidentified EGRET sources. Therefore, a strong statement can be made: HMXB/NS microquasars appear as good counterparts of low-latitude unidentified EGRET sources.

This statement is followed by some natural questions. 1) May LS 5039 and LS I +61 303 still contain black holes (BHs)? Although formally possible, this

is unlikely, because regarding the properties of their X-ray emission they should be in the so-called low/hard state (Fender and Maccarone, 2004), but they do not follow the empirical correlation between X-ray and radio flux found by Gallo et al. (2003), in the sense that they are clearly too radio loud. 2) Why no HMXB microquasars with BHs (e.g., Cygnus X-1) are present in the third EGRET catalog? A possibility is that black hole state changes may play a role, preventing the detection of gamma-ray emission when the jet is not present during the high/soft state (but this state is very rare in the case of Cygnus X-1 and in fact, as discussed by Romero et al. (2002), a low high-energy cutoff of a few hundreds in the Lorentz factor of the electrons is compatible with the data). 3) Why no Low Mass X-ray Binary (LMXB) microquasars are present in the third EGRET catalog? One possibility is that the optical companions do not provide the necessary intense UV radiation fields needed for an effective IC process to produce high-energy gamma-rays. This possibility is strongly model dependent, and not valid if Self Synchrotron Compton losses are dominant. The other possibility is that LMXBs are in general terms transient objects, that maybe were not active during the EGRET viewing periods, while HMXBs tend to be persistent systems. 4) Of course, BH and LMXB microquasars could still emit high-energy gamma-rays and not be present in the third EGRET catalog because of the relatively poor sensitivity threshold of the instrument.

In conclusion, persistent HMXBs containing NSs not experiencing state changes are good candidates for the counterparts of the still unidentified high-energy gamma-ray sources at low-galactic latitudes (approximately up to $|b| < 10^{\circ}$, as discussed for LS 5039), and we consider that these objects may define a population among UESs. Observations with the future missions AGILE and GLAST will confirm or reject both the proposed associations between these microquasars and the corresponding high-energy gamma-ray sources, and the hypothesis discussed above.

Acknowledgements

We thank Sylvain Chaty, Paula Benaglia, Gustavo E. Romero, Josep M. Paredes, Josep Martí, Valentí Bosch-Ramon and Rob Fender for useful discussions, and an anonymous referee for useful comments that helped to improve the paper. M.R. acknowledges support by a Marie Curie Fellowship of the European Community programme Improving Human Potential under contract number HPMF-CT-2002-02053. M.R. also acknowledges partial support by DGI of the Ministerio de Ciencia y Tecnología (Spain) under grant AYA2001-3092, as well as partial support by the European Regional Development Fund (ERDF/FEDER). J.A.C. is a researcher of the programme *Ramón y Cajal* funded by the Spanish Ministery of Science and Technology and the University of Jaén. J.A.C. was supported by CONICET (under grant PEI 6384/03).

References

Bird, A.J., Barlow, E.J., Bassani, L. et al.: 2004, *ApJ* **607**, L33.

Bosch-Ramon, V. and Paredes, J.M.: 2004a, *A&A* **417**, 1075.

Bosch-Ramon, V. and Paredes, J.M.: 2004b, *A&A* **425**, 1069.

Bosch-Ramon, V., Romero, G.E. and Paredes, J.M.: 2005, *A&A* **429**, 267.

Casares, J., Ribas, I., Paredes, J.M., Martí, J. and Allende Prieto, C.: 2005, *MNRAS*, submitted.

Combi, J.A., Ribó, M., Mirabel, I.F. and Sugizaki, M.: 2004, *A&A* **422**, 1031.

Cutri, R.M., Skrutskie, M.F. and van Dyk, S.: 2003, VizieR Online Data Catalog, II/246.

Fender, R.P. and Maccarone, T.: 2004, in: K.S. Cheng and G.E. Romero (eds.), Cosmic Gamma-Ray Sources, Kluwer Academic, Dordrecht, The Netherlands, *Ap&SS Library* **304**, 205.

Frail, D.A. and Hjellming, R.M.: 1991, *AJ* **101**, 2126.

Gallo, E., Fender, R.P. and Pooley, G.G.: 2003, *MNRAS* **344**, 60.

Green, A.J., Cram, L.E., Large, M.I. and Ye, T.: 1999, *ApJS* **122**, 207.

Gregory, P.C.: 2002, *ApJ* **575**, 427.

Grenier, I.A.: 2000, *A&A* **364**, L93.

Grenier, I.A.: 2004, in: K.S. Cheng and G.E. Romero (eds.), Cosmic Gamma-Ray Sources, Kluwer Academic, Dordrecht, The Netherlands, in press.

Harmon, B.A., Wilson, C.A., Fishman, G.J. et al.: 2004, *ApJS* **154**, 585.

Hartman, R.C., Bertsch, D.L., Bloom, S.D. et al.: 1999, *ApJS* **123**, 79.

Hjellming, R.M. and Johnston, K.J.: 1988, *ApJ* **328**, 600.

Hutchings, J.B. and Crampton, D.: 1981, *PASP* **93**, 486.

Kaufman Bernadó, M.M., Romero, G.E. and Mirabel, I.F.: 2002, *A&A* **385**, L10.

Malizia, A., Bassani, L., Di Cocco, G. et al.: 2004, *ATel* 227.

Maraschi, L. and Treves, A.: 1981, *MNRAS* **194**, 1P.

Martí, J. and Paredes, J.M.: 1995, *A&A* **298**, 151.

Martí, J., Paredes, J.M. and Ribó, M.: 1998, *A&A* **338**, L71.

Massi, M.: 2004, *A&A* **422**, 267.

Massi, M., Ribó, M., Paredes, J.M. et al.: 2004, *A&A* **414**, L1.

Massi, M., Ribó, M., Paredes, J.M., Peracaula, M. and Estalella, R.: 2001, *A&A* **376**, 217.

McSwain, M.V., Gies, D.R., Huang, W., Wiita, P.J., Wingert, D.W. and Kaper, L.: 2004, *ApJ* **600**, 927.

Mirabel, I.F. and Rodríguez, L.F.: 1999, *ARA&A* **37**, 409.

Paredes, J.M., Martí, J., Peracaula, M. and Ribó, M.: 1997, *A&A* **320**, L25.

Paredes, J.M., Martí, J., Ribó, M. and Massi, M.: 2000, *Science* **288**, 2340.

Paredes, J.M., Ribó, M., Ros, E., Martí, J. and Massi, M.: 2002, *A&A* **393**, L99.

Reig, P., Ribó, M., Paredes, J.M. and Martí, J.: 2003, *A&A* **405**, 285.

Ribó, M.: 2002, PhD Thesis, Universitat de Barcelona.

Ribó, M.: 2004, in: J.D. Romney and M.J. Reid (eds.), Future Directions in High Resolution Astronomy: A Celebration of the 10th Anniversary of the VLBA, ASP Conference Series [astro-ph/0402134].

Ribó, M., Paredes, J.M., Romero, G.E. et al.: 2002, *A&A* **384**, 954.

Ribó, M., Reig, P., Martí, J., Paredes, J.M. et al.: 1999, *A&A* **347**, 518.

Romero, G.E.: 2001, in: A. Carramiñana, O. Reimer and D.J. Thompson (eds.), Proceedings of The Nature of Unidentified Galactic High-energy Gamma-ray Sources, Vol. 267, ASSL Series, Kluwer Academic, p. 65.

Romero, G.E., Grenier, I.A., Kaufman Bernadó, M., Mirabel, I.F. and Torres, D.F.: 2004, in: Proceedings of the Fifth INTEGRAL Workshop *The Integral Universe*, ESA SP-552, 703.

Romero, G.E., Kaufman Bernadó, M.M. and Mirabel, I.F.: 2002, *A&A* **393**, L61.

Romero, G.E., Torres, D.F, Kaufman Bernadó, M.M. and Mirabel, I.F.: 2003, *A&A* **410**, L1.

Strickman, M.S., Tavani, M., Coe, M.J. et al.: 1998, *ApJ* **497**, 419.
Sugizaki, M., Mitsuda, K., Kaneda, H. et al.: 2001, *ApJS* **134**, 77.
Tavani, M., Hermsen, W., van Dijk, R. et al.: 1996, *A&AS* **120**, 243.
Tavani, M., Kniffen, D., Mattox, J.R., Paredes, J.M. and Foster, R.S.: 1998, *ApJ* **497**, L81.
Torres, D.F., Butt, Y.M. and Camilo, F.: 2001a, *ApJ* **560**, L155.
Torres, D.F., Romero, G.E., Combi, J.A. et al.: 2001b, *A&A* **370**, 468.
Torres, D.F., Romero, G.E., Dame, T.M., Combi, J.A. and Butt, Y.M.: 2003, *Phys. Rep.* **382**, 303.
van Dijk, R., Bennett, K., Bloemen, H. et al.: 1996, *A&A* **315**, 485.
Wallace, P.M., Griffis, N.J., Bertsch, D.L. et al.: 2000, *ApJ* **540**, 184.
Zhang, S., Collmar, W. and Schönfelder, V.: 2005, *Ap&SS* **297**, 283.

THE LARGE-SCALE, DECELERATING X-RAY JETS FROM THE MICROQUASAR XTE J1550−564: EVIDENCE FOR EXTERNAL SHOCKS CAUSED BY THE JET-ISM INTERACTION?

X.Y. WANG[1], Z.G. DAI[1] and T. LU[2]

[1]*Department of Astronomy, Nanjing University, Nanjing, China; e-mail: xywang@nju.edu.cn; xywang@bohr.physics.hku.hk*

[2]*Purple Mountain Observatory, Chinese Academy of Sciences, Nanjing, China*

(Received 4 June 2004; accepted 6 July 2004)

Abstract. Large-scale, decelerating, relativistic X-ray jets from microquasar XTE J1550−564 has been recently discovered with *Chandra* by Corbel et al. (2002). We find that the dynamical evolution of the approaching jet at the late time is consistent with the well-known Sedov evolutionary phase $R \propto t^{2/5}$. A trans-relativistic external shock dynamic model by analogy with the evolution of gamma-ray burst remnants, is shown to be able to fit the proper-motion data of the approaching jet reasonably well. The inferred interstellar medium density around the source is well below the canonical value $n_{\rm ISM} \sim 1\,{\rm cm}^{-3}$. The rapidly fading X-ray emission can be interpreted as synchrotron radiation from the non-thermal electrons in the adiabatically expanding ejecta. These electrons were accelerated by the reverse shock (moving back into the ejecta) which becomes important when the inertia of the swept external matter leads to an appreciable slowing down of the original ejecta.

Keywords: stars: individual (XTE J1550-564), gamma rays: bursts, ISM: jets and outflows, radiation mechanisms: non-thermal

1. Introduction

X-ray binaries with relativistic jets resemble, on a much smaller scale, many of the phenomena seen in quasars and are therefore called microquasars (Mirabel and Radríguez, 1999; Fender, 2004). The motions of the apparently superluminal radio jets from microquasars GRS 1915+105 (Mirabel and Rodríguez, 1994; Fender et al., 1999) and GRO J1655-40 (Tingay et al., 1995; Hijellming and Rupen, 1995) are consistent with being purely ballistic, up to a projected separation of 0.08 pc from the compact object on a maximum time scale of 4 months after the ejection for GRS 1915+105. With the help of *Chandra* Observatory, Corbel et al. (2002) recently discovered large-scale (with projected separation more than a half pc from the compact object), relativistically moving and decelerating radio and X-ray emitting jets from the microquasar XTE J1550–564. It is the first time that an X-ray jet proper-motion measurements spanning several years are obtained for accretion-powered Galactic sources. Hence, XTE J1550–564 provides a good opportunity to study the dynamical evolution of relativistic jets.

Astrophysics and Space Science **297:** 155–166, 2005.
© Springer 2005

Here we propose that the dynamical evolution and radiation of the large-scale X-ray jets from XTE J1550–564 can be understood as the interaction between the jet and the surrounding interstellar medium (ISM), quite similar to the external shock model for afterglows of gamma-ray bursts (GRBs) (Rees and Mészáros, 1992; Mészáros and Rees, 1997). The main differences lie in the initial Lorentz factor and the kinetic energy of the jets. The microquasar jets are inferred to be at least mildly relativistic with initial Lorentz factor $\Gamma_0 \sim 2$–5 (Mirabel and Radriguez, 1999), in contrast to the ultra-relativistic jets ($\Gamma_0 > 100$) in GRBs. When the relativistic ejecta from the microquasar is significantly decelerated by the ISM, a relativistic *forward* shock expands into the ISM and a *reverse* shock moves into and heats the original ejecta. The shocked ambient and ejecta materials are in pressure balance and separated by a contact discontinuity. The forward shock continuously heats fresh ISM and accelerates electrons, while the reverse shock operates only once and after that the shocked gas in the ejecta expands and cools adiabatically. As more and more ISM matter are swept-up, the ejecta and the shocked ISM – we shall call them 'jet' – should be decelerated more and more and finally transit to the non-relativistic motion phase. We find that this dynamic model can fit well the observed proper-motion evolution of the large scale eastern X-ray jet from XTE J1550–564.

First, we give a brief review of the observations of the large scale jets from XTE J1550–564 in Section 2. We present the dynamic model fit in Section 3 and interpret the radiation in Section 4. Finally, we give conclusions and discussions.

2. Observations of the Large-Scale Jets from XTE J1550–564

After the discovery of the X-ray transient XTE J1550–564 by the All-Sky Monitor on aborad the *Rossi X-ray Timing Explorer* on 7 September 1998 (Smith, 1998), an extremely strong X-ray flare was observed on 20 September 1998 (Sobczak et al., 2000; Homan et al., 2001), and radio jets with apparent superluminal velocities (the initial proper motion was greater than 57 mas day^{-1}) was observed beginning 24 September 1998 (Hannikainen et al., 2001). During the 2002 X-ray outburst, radio observations were made with the *Australia Telescope Compact Array (ATCA)*. The detection of the large-scale radio jet ~22 arcsec to the west of XTE J1550–564 led to a re-analysis of the archival *Chandra* data and discovery of an X-ray jet to the east of XTE J1550–564 (Corbel et al., 2002; Tomsick et al., 2003). It is thought that both jets are connected with the 20 September 1998 ejection event, based on the detection of superluminal jets following an extremely large X-ray flare and the absence of any other X-ray flare of similar magnitude in continual X-ray monitoring from 1996 to 2002.

According to the archival *Chandra* data, the field of view of XTE J1550–564 was imaged by *Chandra* on 9 June, 21 August, and 11 September 2000. These observations present for the first time the proper-motion measurement for an X-ray

TABLE I

Angular separations and the absorbed X-ray flux of the eastern and western jets

Date	Time after X-ray flare (days)	Angular Separation (arcsec)		Flux (10^{-14} erg cm^{-2}s^{-1})	
		eastern jet	western jet	eastern jet	western jet
June 9 2000	628	21.3 ± 0.5		20 ± 6	<1.1
Aug. 21 2000	700	22.7 ± 0.5		6.1 ± 1.3	<1.1
Sept. 11 2000	720	23.4 ± 0.5		8.2 ± 1.5	<1.1
Mar. 11 2002	1265	29.0 ± 0.5	~ 23	1.1 ± 0.3	19 ± 1.0
			$\sim 23+$		
June 19 2002	1335		0.52 ± 0.13	$<0.3 \pm 0.2$	16 ± 1.0

References – Corbel et al., 2002; Kaaret et al., 2003; Tomsick et al., 2003.

jet from microquasars, which show direct evidence for gradual deceleration. Radio observations with ATCA show a decaying and moving radio source consistent with the position of the eastern X-ray jet. Remarkably, the overall radio flux detected on 1 June 2002 for the eastern jet is consistent with an extrapolation of the X-ray spectrum with a single power law of spectral index of $\alpha \simeq -0.6$ ($F_\nu \propto \nu^\alpha$) (Tomsick et al., 2003), which provides evidence for a synchrotron X-ray emission mechanism. The broadband spectral energy distribution of the western jet around 11 March 2002, which is consistent with a single power law of spectral index of -0.660 ± 0.005, strengthened the synchrotron radiation origin of the X-ray emission (Corbel et al., 2002). The field of view of XTE J1550–564 was further observed by *Chandra* on 11 March 2002. We summarize the observations for both the eastern and western jets in Table I.

For the western jet, Kaaret et al. (2003) also examined the archival *Chandra* data on XTE J1550–564 at June, August and September 2000, but found no evidence for X-ray emission in any of the archival observations with an upper bound on the absorbed flux of 1.1×10^{-14} erg cm^{-2}s^{-1}. The facts that no X-ray emission detected from the western jet during 2000 and that the eastern source apparently moves faster than the western one are consistent with the interpretation in which the eastern jet is the approaching one and the western jet is the receding one. The brightening of the western jet at the late time argues against symmetric jet propagation and may reflect the non-uniformity in the ISM.

3. The Dynamic Model

As we only know the proper motion measurements and the light curve of the eastern jet, we focus on modelling the dynamical evolution and radiation of this jet. We consider a beamed outflow with kinetic energy E_0 and Lorentz factor Γ_0 ejected from the microquasar XTE J1550–564 expands conically with a half opening angle

θ_j into the ambient medium with a constant number density n. The interaction between the relativistic ejecta and the surrounding medium is analogous to GRB external shock, but with quite different E_0 and Γ_0. The supersonic motion of the ejecta should drive a blast wave propagating into the ISM. We shall assume that the radiation loss of the shock wave is a negligible fraction of the total energy, so the dynamic is adiabatic throughout. From the view of the energy conservation, the dynamic equation can be simplified as

$$(\Gamma - 1)M_0c^2 + \left(\Gamma_{\rm sh}^2 - 1\right)m_{\rm sw}c^2 = E_0, \tag{1}$$

where Γ and $\Gamma_{\rm sh}$ are the Lorentz factors of the jet material and the shock front respectively, $m_{\rm sw} = (4/3)\pi R^3 m_{\rm p} n(\theta_j^2/4)$ is the mass of the swept-up ISM (where R is the shock radius, $m_{\rm p}$ is the mass of the proton) and M_0 is the mass of the original ejecta. The first term on the left of the equation is the kinetic energy of the ejecta and the second term is the internal energy of the shock.

The kinematic equation of the approaching jet is

$$\frac{dR}{dt} = \frac{\beta(\Gamma)c}{1 - \beta(\Gamma)\cos\theta}, \tag{2}$$

where $v = \beta c$ is the bulk velocity of the jet with $\beta(\Gamma) = (1 - \Gamma^{-2})^{1/2}$, t is the observer time and θ is the jet inclination angle to the line of sight.

Given the initial condition at $t = 0$, which is chosen to be $R_0 = 10^7$ cm and $\Gamma_0 = 3$, the two equations can be solved and we can get the relation between the proper motion μ ($\mu = R\sin\theta/d = R\ \sin\theta/5.3$ kpc) and time t.

We find that the following combination of the parameters fits the observed proper-motion data reasonably well: $\theta = 50^\circ$, $\theta_j = 1.5^\circ$, $E_0 = 3.6 \times 10^{44}$ erg and $n = 1.5 \times 10^{-4}\,{\rm cm}^{-3}$. The model fit is plotted in Figure 1 as the solid line. The late time behavior approaches the well-known Sedov solution $R \propto t^{2/5}$ (see the dashed line in Figure 1). This is expected since the second term on the left of Eq. (1) becomes dominant at the late time, so $\beta^2 R^3 =$ constant. In addition, $\frac{dR}{dt} \simeq \beta c$ when $\beta\cos\theta \ll 1$. The earlier phase can be regarded as the transition regime from the mildly relativistic motion to the non-relativistic motion. By comparison, we also plot the $R \propto t^{0.5}$ and $R \propto t^{0.3}$ cases in Figure 2, which show clear deviations from the data. The inferred value of the ISM density is surprisingly low. Such low densities with $n \leq 10^{-3}\,{\rm cm}^{-3}$ have been inferred around another two microquasars GRS 1915+105 and GRO J1655−40 by Heinz (2002) from the fact that jets move with constant velocities up to distance $\geq$0.04 pc. As argued by Heinz (2002), this implies that either the sources are located in regions occupied by the hot ISM phase or previous activities of the jets have created evacuated bubbles around the sources.

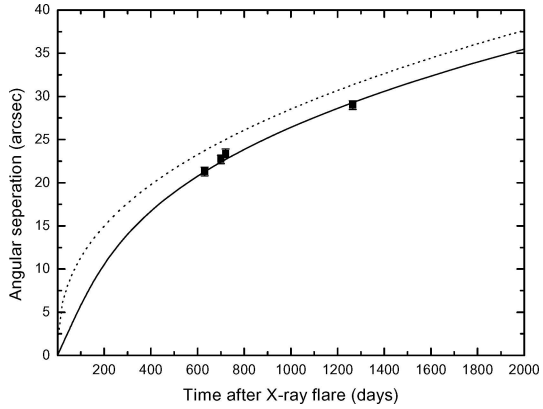


Figure 1. Model fit to the position of the eastern X-ray jet verse time. Observation data are taken from Tomsick et al. (2003) and Kaaret et al. (2003). The solid line is the fit in terms of the trans-relativistic external shock model. We also plot the function $R \propto t^{2/5}$ (dotted line) for comparison.

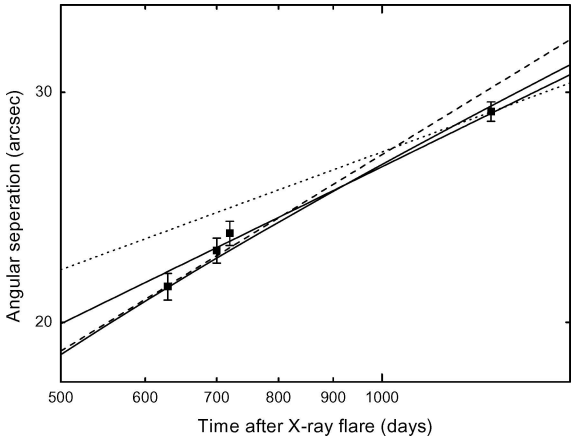


Figure 2. Comparison of the model fits for the position of the eastern X-ray jet verse time. The thick solid line is the tran-relativistic external shock model developed in this paper. The (blue) thin solid line, (green) dotted line and (red) dashed line represent $R \propto t^{0.4}$, $R \propto t^{0.3}$, $R \propto t^{0.5}$, respectively. It shows that the dynamical evolution of the eastern jet is consistent with the Sedov evolutionary phase $R \propto t^{0.4}$ at the late time.

4. The Radiation Model

4.1. The forward shock emission

First, we try to fit the X-ray emission of the eastern jet using the forward shock model, the mechanism believed to be responsible for GRB afterglows. In the standard picture of GRBs, an afterglow is generally believed to be produced by the

synchrotron radiation or inverse Compton emission of the shock-accelerated electrons in an ultra-relativistic shock wave expanding into the ambient medium. As more and more ambient matter is swept up, the shock gradually decelerates while the emission from such a shock fades down. The microquasar jet is similar to the GRB remnant at the time that its Lorentz factor has decreased to $\Gamma \sim 1$–3, usually months to years after the burst. So, we expect that similar emission processes should also occur in the case of the microquasar decelerating jet.

If the distribution of the shock-accelerated electrons takes a power-law form with the number density given by $n(\gamma_e)d\gamma_e = K\gamma_e^{-p}d\gamma_e$ for $\gamma_m < \gamma_e < \gamma_M$, the volume emissivity at the frequency ν' in the comoving frame of the shocked gas is (Rybicki and Lightman, 1979)

$$j_{\nu'} = \frac{\sqrt{3}q^3}{2m_e c^2}\left(\frac{4\pi m_e c\nu'}{3q}\right)^{\frac{1-p}{2}} B_\perp^{\frac{p+1}{2}} K F_1(\nu', \nu'_m, \nu'_M), \tag{3}$$

where q and m_e are respectively the charge and mass of the electron, $B_\perp$ is the strength of the component of magnetic field perpendicular to the electron velocity, ν'_m and ν'_M are the characteristic frequencies for electrons with γ_m and γ_M, respectively, and

$$F_1(\nu', \nu'_m, \nu'_M) = \int_{\nu'/\nu'_M}^{\nu'/\nu'_m} F(x)x^{(p-3)/2}\,dx \tag{4}$$

with $F(x) = x\int_x^{+\infty} K_{5/3}(t)dt$ ($K_{5/3}(t)$ is the Bessel function). The physical quantities in the pre-shock and post-shock ISM are connected by the jump conditions:

$$n' = \frac{\hat{\gamma}\Gamma + 1}{\hat{\gamma} - 1}n, \quad e' = \frac{\hat{\gamma}\Gamma + 1}{\hat{\gamma} - 1}(\Gamma - 1)nm_p c^2, \tag{5}$$

$$\Gamma_{sh}^2 = \frac{(\Gamma + 1)[\hat{\gamma}(\Gamma - 1) + 1]^2}{\hat{\gamma}(2 - \hat{\gamma})(\Gamma - 1) + 2}, \tag{6}$$

where e' and n' are the energy and the number densities of the shocked gas in its comoving frame and $\hat{\gamma}$ is the adiabatic index, which equals 4/3 for ultra-relativistic shocks and 5/3 for sub-relativistic shocks. A simple interpolation between these two limits $\hat{\gamma} = (4\Gamma + 1)/3\Gamma$ gives a valid approximation for trans-relativistic shocks (Dai et al., 1999).

Assuming that shocked electrons and the magnetic field acquire constant fractions (ϵ_e and ϵ_B) of the total shock energy, we get

$$\gamma_{\rm m} = \epsilon_{\rm e}\frac{p-2}{p-1}\frac{m_{\rm p}}{m_{\rm e}}(\Gamma-1), \quad B_{\perp} = \sqrt{8\pi\epsilon_{\rm B}e'} \tag{7}$$

and

$$K = (p-1)\,n'\gamma_{\rm m}^{p-1} \tag{8}$$

for $p > 2$. It is reasonable to believe that $\nu'_{\rm M}$ is well above the X-ray band throughout the observations, because the forward shock continuously heats fresh ISM and accelerates electrons. The observer frequency ν relates to the frequency ν' in the comoving frame by $\nu = D\nu'$, where $D = 1/\Gamma(1-\beta\cos\theta)$ is the Doppler factor. The observed flux density at ν and the X-ray flux in the band 0.3–8 keV are respectively given by

$$F_\nu = \frac{\theta_j^2}{4}\left(\frac{R}{d}\right)^2 \Delta R D^3 j_{\nu'}; \quad F(0.3\text{–}8\ {\rm keV}) = \int_{\nu_1}^{\nu_2} F_\nu d\nu, \tag{9}$$

where ΔR is the width of the shock region and is assumed to be $\Delta R = R/10$ in the calculation. The model fit to the light curve of the eastern jet is presented in Figure 3. Clearly, the model light curve decays too slowly to fit the observed data. This is expected from the following analytic study. For $\nu'_{\rm m} \ll \nu' \ll \nu'_{\rm M}$, $F_\nu \propto D^3 B_\perp^{(p+1)/2} K R^3 \propto D^3 B_\perp^{(p+1)/2} n' \gamma_{\rm m}^{p-1} R^3$. When $\beta \ll 1$, $\beta \propto t^{-3/5}$, $R \propto t^{2/5}$, $B \propto \beta$, $\gamma_{\rm m} \propto \beta^2$ and $n' = 4n =$ constant. So, we get $F_\nu \propto t^{-(15p-21)/10} \propto t^{-1.2}$ for

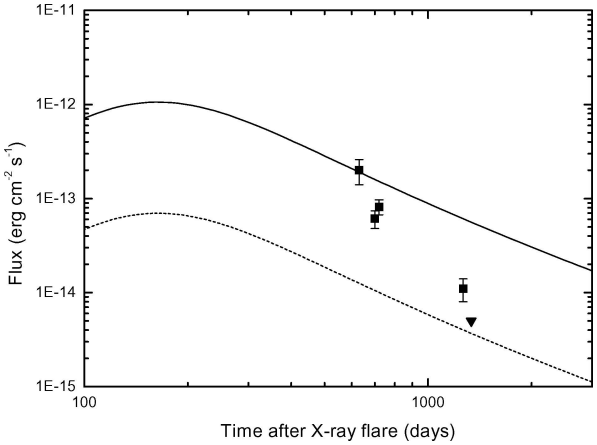


Figure 3. Model and observed X-ray light curves of the eastern jet. Detections and upper limits for the non-detections, taken from Tomsick et al. (2003) and Kaaret et al. (2003), are indicated by the filled squares and arrows respectively. The solid line and dotted line represent X-ray emission from the shocked ISM (forward shock) with different electron ($\epsilon_{\rm e}$) and magnetic field ($\epsilon_{\rm B}$) equipartition factors used. The solid and dotted lines are corresponding to $\epsilon_{\rm e} = 0.1$, $\epsilon_{\rm B} = 0.004$ and $\epsilon_{\rm e} = 0.1$, $\epsilon_{\rm B} = 10^{-4}$, respectively. This figure shows that the forward shock emission decays too slowly to fit the observations.

$p = 2.2$. We also consider the case in which the jet spreads laterally with the sound velocity as discussed in GRBs (Rhoads, 1999), but find that it makes little difference.

4.2. The reverse shock emission

Another probable emitting region for X-rays is the adiabatically expanding ejecta itself. A reverse shock wave that moves back through the original ejecta becomes important when the swept-up matter mass equals $1/\Gamma_0$ of the ejecta mass. The reverse shock accelerates electrons in the ejecta and may amplify the original magnetic field to be close to equipartition. The emission from the non-thermal ($N(\gamma_e) \propto \gamma_e^{-p}$) relativistic electrons in the adiabatically expanding ejecta with radius R is described by the van der Laan (1966) model, where the flux density is given by $F_\nu \propto R^{-2p}\nu^{(1-p)/2}$ in the optically-thin regime. So, when $\beta \ll 1$, $F_\nu \propto t^{-4p/5} \propto t^{-1.76}$ for $p = 2.2$. This decay is still too slow to fit the observed light curve of the X-ray jet for which the power-law fit gives a decay index of -3.7 ± 0.7 (Kaaret et al., 2003). However, different from the continuous forward shock, the reverse shock operates only once, so the electrons, including those with the maximum energy in the ejecta, all cool adiabatically. So it is likely that, at some time, the characteristic frequency of the electrons with the maximum energy $\gamma_M m_e c^2$ may fall close to the X-ray band and the X-ray flux would decay quite rapidly since then.

The physical quantities in the adiabatically expanding ejecta with radius R relate with their initial value at t_0 by (van der Laan, 1966)

$$\gamma_m = \gamma_m(t_0)\frac{R_0}{R}, \quad \gamma_M = \gamma_M(t_0)\frac{R_0}{R}; \tag{10}$$

$$K = K(t_0)\left(\frac{R}{R_0}\right)^{-(2+p)}, \quad B_\perp = B_\perp(t_0)\left(\frac{R}{R_0}\right)^{-2} \tag{11}$$

if the synchrotron emission cooling is negligible, where R_0 is the radius of the ejecta at time t_0 and $\gamma_M(t_0) = E_M^0/m_e c^2$. These relations are derived from the assumption that total number of the electrons is conserved and that the magnetic field is frozen to the plasma fluid.

From the dynamic model in Section 3, we get $t_0 = 121$ days and $R_0 = 0.71 \times 10^{18}$ cm for the eastern X-ray jet from XTE J1550–564. Given the initial condition for $K(t_0)$, $B_\perp(t_0)$, $\gamma_m(t_0)$ and $\gamma_M(t_0)$, we can obtain the model light curves of the emissions from the expanding ejecta using Eqs. (3), (4), (9) and $R(t)$. In the calculation, we have assumed $\gamma_m(t_0) = E_{M,cool}/m_e c^2 = 6\pi m_e c/(\sigma_T B_\perp(t_0)^2 t_0')$. We find that the following combination of the initial values can fit the flux data well (see Figure 4): $B_\perp(t_0) = 0.5$ mG and $K(t_0) = 0.8$ cm^{-3} and $\gamma_m(t_0) = 100$.[1] For these values, $\gamma_M(t_0) = 3.55 \times 10^8$.

Noting that $K = \epsilon_e(p-2)e'\gamma_m^{p-2}$ and $B_\perp = \sqrt{8\pi\epsilon_B e'}$, the above value for $K(t_0)$ and $B_\perp(t_0)$ imply that the equipartition parameters for energies in electrons

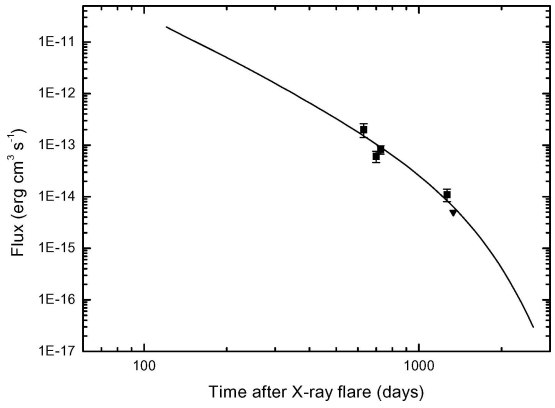


Figure 4. Model fit to the X-ray light curve using the synchrotron radiation from the adiabatically expanding ejecta heated by the reverse shock.

and magnetic field in the reverse shock are $\epsilon_e = 0.6$ and $\epsilon_B = 0.44 \times 10^{-2}$, respectively, if the internal energy density in the reverse shock is equal to that in the forward shock region at time t_0. Surprisingly, these equipartition values are close to the typical values inferred for GRB afterglows (Granot et al., 1999, Wijers and Galama, 1999; Wang et al., 2000).

We further calculate the model spectrum for the eastern jet on 1 June 2000 using the above parameter values and plot the fit of the observed data in Figure 5. Clearly the model fits quite well the energy spectrum on 1 June 2000, 621 days after the ejection of the eastern jet from XTE J1550–564. At this time, the characteristic frequency of the electrons with γ_M is just near the X-ray band, so the X-ray spectrum doesn't become steeper. The model predicts that there should be significant

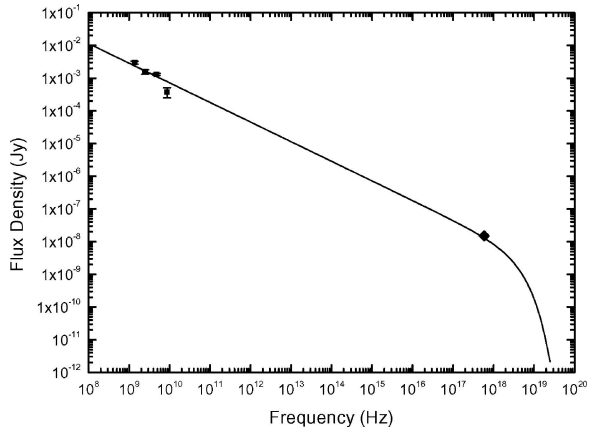


Figure 5. Model fit to the broadband spectrum of the eastern jet on 1 June 2000 using the synchrotron radiation from the adiabatically expanding ejecta heated by the reverse shock.

steepness of X-ray spectrum at March 2002, but the relatively few counts do not give a reliable spectral index (Kaaret et al., 2003).

We have shown that the emission from the shocked ejecta provides a viable mechanism for the rapidly decaying X-ray flux from the eastern jet of XTE J1550–564. To guarantee the dominance of the emission from the shocked ejecta over that from the forward shock region during the period of the observations, the forward shock emission should be below the upper limit of the observation made on June 19 2002. Figure 3 tells us that the forward shock emission for $\epsilon_{\rm e} = 0.1$ and $\epsilon_{\rm B} = 10^{-4}$ is inferred to be below the limit. Because $F_\nu \propto \gamma_{\rm m}^{p-1} B^{(p+1)/2} \propto \epsilon_{\rm e}^{p-1} \epsilon_{\rm B}^{(p+1)/4}$, the magnetic field and electron energy fractions in the forward shock region must satisfy (see Figure 3)

$$\left(\frac{\epsilon_{\rm e}}{0.1}\right)^{p-1} \left(\frac{\epsilon_{\rm B}}{10^{-4}}\right)^{(p+1)/4} \leq 1. \tag{12}$$

The high value for $\epsilon_{\rm B}$ in the reverse shock region relative to that in the forward shock region can be accounted for if the ejecta has already been magnetized before the further shock compression. This is reasonable as the ejecta from microquasars are suggested to originate from the inner accretion disks (Mirabel and Rodríguez, 1999). A pair-rich outflow from the microquasar probably account for the comparatively large value of $\epsilon_{\rm e}$ in the reverse shock. Future observations of large-scale jets from microquasars may provide better understanding of the shock physics and physical condition in relativistic jets.

5. Discussions and Summary

The western (receding) jet from XTE J1550–564 was detected in radio and X-rays in 2002 while archival *Chandra* data on this source from June, August and September 2000 only give upper limits. The non-detection in 2000 is consistent with the deduction that the western source is the receding jet. Unlike the smoothly decaying eastern jet, the western jet brightens at the late time. The brightening might be caused by the inhomogeneities in the ISM (Kaaret et al., 2003) or internal shocks produced by a faster jet overtaking a slower one (Kaiser et al., 2000), and need further careful study. The western jet moved by 0.52 ± 0.13 arcsec between 11 March and 19 June 2002 with a mean apparent speed significantly less than the average apparent speed from 1998 to early 2002. Interestingly, we find that the decay of the X-ray flux of the western jet between March and June 2002 is also consistent with that predicted by the reverse shock emission $F_\nu \propto t^{-4/5p} \propto t^{-1.86}$ for $p = 2.32$ of the western jet.

Besides the relativistically moving, decelerating jets from XTE J1550–564, large-scale X-ray jets and radio lobes up to ∼40 arcmin size have been observed from SS433 (Brinkmann et al., 1996; Dubner et al., 1998). The radiation is suggested

to come from the termination shock which results from the interaction of the mass outflow with the nebula W50. Recently, reheating of baryonic material in X-ray jets of SS433 is inferred to take place within $\sim 10^{17}$ cm from the core, based on the observed iron emission lines (Migliari, Fender and Méndez, 2002). We think that external shock is a possible mechanism for such reheating.

In summary, we developed a model for the dynamical evolution and radiation of the large-scale X-ray jets from the microquasar XTE J1550–564 analogous to the external shock model for GRB afterglows. In this model, the observed jet emission is due to interaction between the jets and external ISM. Future continuous, follow-up multi-wavelength observations of new ejection events from microqusasrs up to the significant deceleration phase should provide more valuable insights into the nature and physical condition (e.g. shock and particle acceleration physics) of relativistic jets. Owing to the proximity of the Galactic X-ray binaries, further studies on them also offer an exciting way for a better understanding of relativistic jets seen elsewhere in the Universe.

Acknowledgements

This work was supported by the Special Funds for Major State Basic Research Projects, the National 973 Project, the National Natural Science Foundation of China under grants 10403002, 10233010 and 10221001.

Note

1. The model result is very insensitive to the value of $\gamma_{\rm m}(t_0)$

References

Blandford, R.D. and Mckee, C.F.: 1976, *Phys. Fluids* **19**, 1130.
Brinkmann, W., Aschenbach, B. and Kawai, N.: 1996, *A & A* **312**, 306.
Corbel, S., Fender, R., Tzioumis, A.K. et al.: 2002, *Science* **298**, 196.
Dai, Z.G., Huang, Y.F. and Lu, T.: 1999, *ApJ* **520**, 634.
Dubner, G.M., Holdaway, M., Goss, W.M. and Mirabel, I.F.: 1998, *AJ* **116**, 1842.
Fender, R., Carrington, S.T., McKay, D.J. et al.: 1999, *MNRAS* **304**, 865.
Fender, R.: 2004, in: W.H.G. Lewin and M. van der Klis (eds.), 'Compact Stellar X-Ray Sources', Cambridge University Press.
Granot, J., Piran, T. and Sari, R.: 1999, *ApJ* **527**, 236.
Hannikainen, D., Campbell-Wilson, D., Hunstead, R. et al.: 2001, *ApSS* **276**, 45.
Heinz, S.: 2002, *A&A* **388**, L40.
Hijellming, R.M. and Rupen, M.P.: 1995, *Nature* **375**, 464.
Homan, J., Wynands, R., van der Klis, M. et al.: 2001, *ApJS* **132**, 377.
Kaaret, P., Corbel, S., Tomsick, J.A., et al.: 2003, *ApJ* **582**, 945.
Kaiser, C.R., Sunyaev, R. and Spruit, H.C.: 2000, *A&A* **356**, 975.

Mészáros, P. and Rees, M.J.: 1997, *ApJ* **476**, 232.
Migliari, S., Fender, R. and Méndez, M.: 2002, *Science* **297**, 1673.
Mirabel, I.F. and Rodríguez, L.F.: 1994, *Nature* **371**, 46.
Mirabel, I.F. and Rodríguez, L.F.: 1999, *ARA&A* **37**, 409.
Rees, M.J. and Mészáros, P.: 1992, *MNRAS* **258**, P41.
Rhoads, J.E.: 1999, *ApJ* **525**, 737.
Rybicki, G.B. and Lightman, A.P.: 1979, Radiative Process in Astrophysics, New York, Wiley.
Sari, R. and Piran, T.: 1999, *ApJ* **517**, L109.
Smith, D.A.: 1998, IAU Circ. No 7008.
Sobczak, G.J., et al.: 2000, *ApJ* **544**, 993.
Tingay, S.J.: 1995, *Nature* **374**, 141.
Tomsick, J.A., Corbel, S., Fender, R., et al.: 2003, *ApJ* **582**, 933.
van der Laan, H.: 1966, *Nature* **211**, 1131.
Wang, X.Y., Dai, Z.G. and Lu, T.: 2000, *MNRAS* **319**, 1159.
Wijers, R.A.M.J. and Galama, T.J.: 1999, *ApJ* **523**, 177.

GAMMA-RAY EMISSION FROM Be/X-RAY BINARIES

M. ORELLANA[1,2] and G.E. ROMERO[1,2,3]

[1]*Instituto Argentino de Radioastronomía, C.C. 5, 1894 Villa Elisa, Argentina*
[2]*Facultad de Ciencias Astronómicas y Geofísicas, UNLP, Paseo del Bosque, 1900 La Plata, Argentina*
[3]*Member of CONICET; E-mail: romero@irma.iar.unlp.edu.ar*

(Received 4 June 2004; accepted 14 July 2004)

Abstract. Be/X-ray binaries are systems formed by a massive Be star and a magnetized neutron star, usually in an eccentric orbit. The Be star has strong equatorial winds occasionally forming a circumstellar disk. When the neutron star intersects the disk the accretion rate dramatically increases and a transient accretion disk can be formed around the compact object. This disk can last longer than a single orbit in the case of major outbursts. If the disk rotates faster than the neutron star, the Cheng-Ruderman mechanism can produce a current of relativistic protons that would impact onto the disk surface, producing gamma-rays from neutral pion decays and initiating electromagnetic cascades inside the disk. In this paper we present calculations of the evolution of the disk parameters during both major and minor X-ray events, and we discuss the generation of gamma-ray emission at different energies within a variety of models that include both screened and unscreened disks.

Keywords: X-ray binaries, neutron stars, gamma-rays

1. Introduction

A significant number of variable gamma-ray sources of likely galactic origin has been found by satellite-borne experiments such as COMPTEL and EGRET (e.g. Torres et al., 2001; Zhang, et al. 2002; Nolan et al., 2003). These sources vary their flux on timescales from weeks to months, similar to the timescales exhibited by X-ray transients at lower energies. The fact that some Be/X-ray binaries with major X-ray outbursts are located within the positional error boxes of unidentified and variable gamma-ray sources (e.g. Zhang et al., 2002; Romero et al., 2001, 2004) posits the problem of whether such systems are capable of generating non-thermal high-energy emission. In this paper we discuss how MeV, GeV and even TeV gamma-rays might be produced by accreting neutron stars in some Be/X-ray binaries and what is the expected time evolution of the high-energy radiation.

2. Be/X-Ray Binaries

Be/X-ray binaries are the most abundant type of massive X-ray binary systems in the Galaxy, with an inferred population in the range 10^3–10^4. These systems are



Astrophysics and Space Science **297:** 167–178, 2005.
© Springer 2005

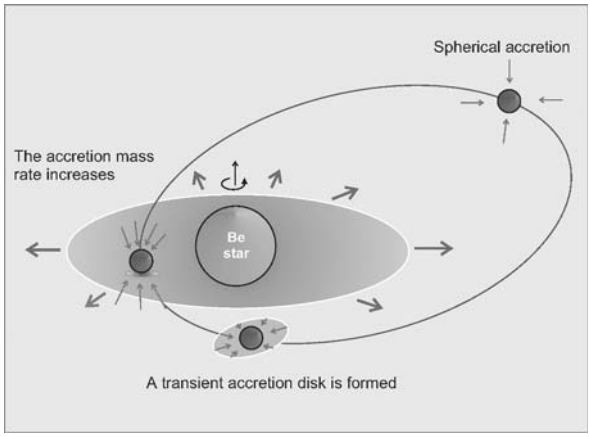


Figure 1. Sketch of a Be/X-ray binary system.

formed by a rapidly rotating Be star and a neutron star, which is usually observed in an eccentric orbit. In some cases, known as Transient X-Ray Sources (TXRS), significant long-term X-ray variability is observed. These sources can vary from 1 to 3 orders of magnitude going from a quiescent phase to a major outburst, over timescales that can go from days to a few years. Sometimes, a major outburst is followed by a series of smaller bursts. Perhaps the most extensively studied source of this class is A0535 + 26 (e.g. Giovanelli and Sabau Graziati, 1992), although a few tens are known.

The general situation in a TXRS is depicted in Figure 1. The Be star loses mass in the form of a thick equatorial disk with a low expansion velocity and a low-density, fast polar wind. Far from the Be star, the neutron star accretes in the Bondi-Hoyle regime. Usually, X-ray flares occur once per orbit when the accretion rate increases dramatically close to the periastron passage. Occasionally, the equatorial disk of the primary can extend beyond the orbit of the compact star, which can then penetrate the disk leading to a major outburst. A transient accretion disk can be formed around the neutron star in such systems. The disk can survive during more than a single orbit in the case of a major outburst or it can last only for a fraction of the orbit in the case of minor outbursts. Evidence for the existence of such transient disks has been found through the detection of quasi-periodic oscillations (QPOs) in the power spectra of the hard X-ray flux of some objects (e.g. Finger et al., 1996a).

When the equatorial disk of the Be star retracts a major outburst may be followed by a series of minor ones in the same object, as observed, for instance, in the system 2S 1417-64 (Finger et al., 1996b).

3. The Magnetosphere of Accreting Neutron Stars

Once formed, the accretion disk can penetrate the magnetosphere of the rotating neutron star (Gosh and Lamb, 1979). This penetration creates a broad transition

region between the unperturbed disk flow and the co-rotating magnetospheric flow. In this transition zone, at the inner radius R_0 the angular velocity is still Keplerian. Between R_0 and the co-rotation radius $R_{\rm co}$ there is a thin boundary layer where the angular velocity departs from the Keplerian value. At $R_{\rm co}$ the disk is disrupted by the magnetic pressure and the matter is channeled by the magnetic field lines to the neutron star polar cap, where it impacts producing hard X-ray emission.

Cheng and Ruderman (1989, 1991) have studied the magnetosphere of accreting neutron stars when the disk rotates faster than the star, showing that three definite regions are formed: 1. A region coupled to the star by the magnetic field lines that do not penetrate the disk, 2. An equatorial region linked to the disk by the field attached to it, and 3. A gap entirely empty of plasma separating both regions. In this gap $\mathbf{E} \cdot \mathbf{B} \neq 0$ and a strong potential drop ΔV is established (see Figure 3 in Romero et al., 2001 for a sketch of the situation). For typical parameters in Be/X-ray binaries, $\Delta V \sim 10^{13-14}$ V (Romero et al., 2001). Protons entering into the gap from the stellar co-rotating region will be accelerated to multi-TeV energies and directed to the accretion disk by the field lines, where they will impact producing $\pi^{\pm}$ and π^0 in pp interactions with the disk material. These pions will decay inside the disk producing electron-positron pairs, high-energy (TeV) photons, and neutrinos. The neutrinos will escape from the system (see Anchordoqui, et al., 2003 for estimates of the neutrino flux), but the pairs and the gamma-rays initiate electromagnetic cascades that will degrade the energy of the gamma-ray photons to form a standard cascade spectrum with a cut-off at MeV-GeV energies. The leptons in the disk will lose energy by inverse Compton (IC) interactions with the thermal X-ray photons, by synchrotron radiation in the field that penetrates the disk, and by relativistic Bremsstrahlung in the ions of the accreting gas. The details of the cascade development will be determined by the relative ratios of the cooling times among all these processes and the opacities for the produced photons in the specific cases.

4. Gamma-Ray Production in the Accretion Disk

Protons entering into the gap from the stellar co-rotating region are accelerated up to energies $E_p \sim e\,V_{\rm max}$, where the potential drop $V_{\rm max}$ is given by Cheng and Ruderman (1991):

$$V_{\rm max} \sim 4 \times 10^{14} \beta^{-5/2} \left(\frac{M_*}{M_\odot}\right)^{1/7} R_6^{-4/7} L_{37}^{5/7} B_{12}^{-3/7} \ \ {\rm V}. \tag{1}$$

Here, $M_* \sim 1.4\,M_\odot$ is the mass of the neutron star, R_6 is its radius in units of 10^6 cm, B_{12} is the magnetic field in units of 10^{12} G, and L_{37} is the X-ray luminosity in units of 10^{37} erg s^{-1}. The parameter $\beta \equiv 2r_0/r_{\rm A} \sim 1$ is twice the ratio of the inner accretion disk radius to the Alfvén radius (Gosh and Lamb, 1979). The Alfvén radius

for spherical accretion can be determined by the condition that the unscreened magnetic energy density of the stellar field, $B^2/8\pi$, becomes comparable to the kinetic energy density of the accreting matter, $\rho v^2/2$, i.e. $B(r_A)^2/8\,\pi = \rho(r_A)\ v(r_A)^2/2$, which yields $r_A = \mu^{4/7}\,\dot{M}^{-2/7}\,(2\,G\,M_*)^{-1/7}$, with μ being the dipolar magnetic moment and $\dot{M}$ the accretion rate.

The ultra-relativistic proton flux will be directed to the accretion disk by the field lines. The maximum current that can flow through the gap can be determined from the requirement that the azimuthal magnetic field induced by the current does not exceed that of the initial field **B**: $J_{\max} \sim B_* R_*^3 r_0^{-2}$ (Cheng and Ruderman, 1989).

The number of protons that impact on the disk per unit of time is huge: $N_p = J_{\max}/e \sim \mathcal{O}\ (10^{33})\ \mathrm{s}^{-1}$ and the total power injected in the disk results: $\dot{E}_{\mathrm{inj}} \sim J_{\max} V_{\max} \sim \mathcal{O}\ (10^{36})$ erg s^{-1}.

Since all protons arrive to the disk surface with basically the same energy, we can estimate the proton flux as:

$$J_p(E) \sim \frac{\delta(E - E_p)}{2\pi} \frac{J_{\max}}{\pi e R_0^2} \quad \frac{\text{protons}}{\text{s cm}^2\ \text{sr}}. \tag{2}$$

These protons will have a probability of penetrating up to a distance L in the disk given by $P(L) = 1 - e^{-L/\lambda_{pp}}$, with $\lambda_{pp} = (\sigma_{pp} n_p^{\mathrm{disk}})^{-1}$. At the relevant energies $\sigma_{pp} \sim 4 \times 10^{-26}$ cm^2. Once the protons interact, neutral and charged pions are produced. The decay of the charged pions leads to neutrino production in the disk (Cheng et al., 1990; Anchordoqui et al., 2003) and the injection of new $e^{\pm}$-pairs. The gamma-ray emissivity from the neutral pions is:

$$q_\gamma(E_\gamma) = 2 \int_{E_\pi^{\min}}^{\infty} \frac{q_\pi(E_\pi)}{\sqrt{E_\pi^2 - m_\pi^2 c^4}}\, dE_\pi, \tag{3}$$

where $E_\pi^{\min}(E_\gamma) = E_\gamma + \frac{m_\pi^2 c^4}{4E_\gamma}$, and

$$\begin{aligned} q_\pi(E_\pi) &= \int \delta(E_\pi - f_\pi(E - m_p c^2))\sigma_{pp}(E) J_p(E)\, dE \\ &= \frac{1}{f_\pi}\sigma_{pp}\left(m_p c^2 + \frac{E_\pi}{f_\pi}\right) J_p\left(m_p c^2 + \frac{E_\pi}{f_\pi}\right). \end{aligned} \tag{4}$$

Here f_π is the fraction of the kinetic energy of the proton that goes into the neutral pion (and then to gamma-rays). Then, using expression (2) we obtain:

$$q_\gamma(E_\gamma) \simeq \frac{J_{\max}}{e\,\pi} \frac{\sigma_{pp}(E_p)}{f_\pi\, E_p} \delta(E_\gamma - f_\pi E_p)\, \frac{\text{ph}}{\text{atom eV s sr}}. \tag{5}$$

The intensity of the gamma-ray emission generated in the disk through π^0-decays results:

$$I_\gamma^o(E_\gamma) = \int_0^{2h} q_\gamma(E_\gamma) {E_\gamma}^2 n_p \, e^{-z/\lambda_{pp}} \, dz. \tag{6}$$

The energy released per unit of time in the disk by these photons is

$$L^{\pi^0}(E_\gamma) = 2 \, f_\pi \, \dot{E}_{\rm inj}\left(1 - e^{-2h/\lambda_{pp}}\right), \tag{7}$$

and the gamma-ray luminosity emerging from the other side of the disk is:

$$L_{\rm esc}^{\pi^0}(E_\gamma) = L^{\pi^0}(E_\gamma) e^{-2h\sigma_{\gamma p} n_p}. \tag{8}$$

Here, $\sigma_{\gamma p} \sim 10^{-26}$ cm^2. The gamma-rays that are absorbed can initiate electromagnetic cascades inside the disk.

5. Time-Dependent Estimates

In order to calculate the evolution of all relevant parameters during both a major and a normal outburst, we have adopted the X-ray light curves observed for the Be/X-ray transient 2S 1417-624 (Finger et al., 1996b), with a normalization[1] such that at the peak of the major outburst, which is coincident with the periastron passage, the luminosity is $L_{37} = 1$. The light curves are shown in Figure 2.

In Figures 3–6 we show the evolution of different parameters that characterizes the system and the high energy emission for the cases of an unscreened disk ($\eta = 1$) and a partially screened disk ($\eta = 0.2$). The relation of the screening factor η and

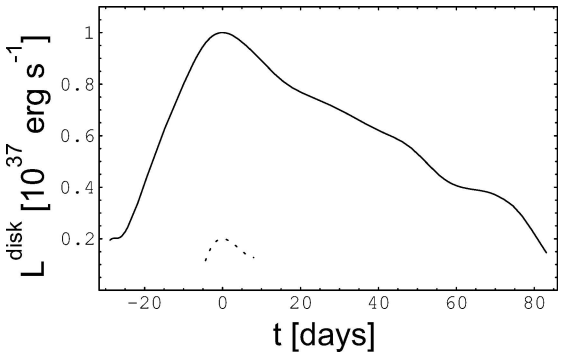


Figure 2. Time evolution of the X-ray luminosity of the disk for a major ($L_{37}^{\rm peak} = 1$) and a normal outburst ($L_{37}^{\rm peak} = 0.2$, dashed curve). $t = 0$ corresponds to the periastron passage.

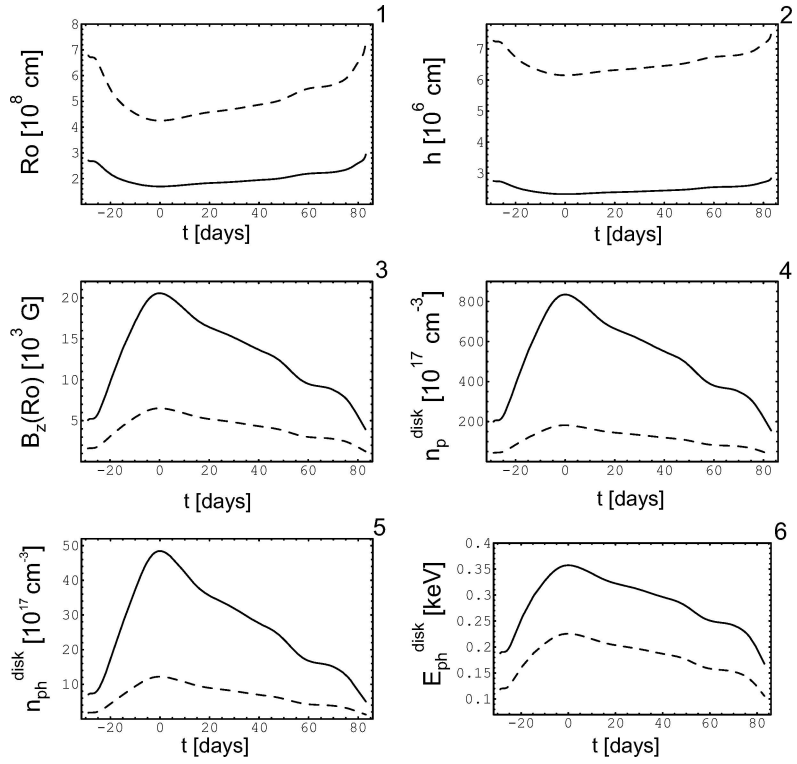


Figure 3. Time-evolution of disk parameters during a major outburst for models with $\eta = 1$ (dashed curve) and $\eta = 0.2$ (solid curve). $t = 0$ corresponds to the periastron passage. 1. Inner radius of the accretion disk (R_0). 2. Half-height of the accretion disk at R_0. 3. Magnetic field inside the disk at R_0. 4. Particle density of the disk at R_0. 5. Photon density in the disk at R_0. 6. Average energy of the disk photons at R_0.

the inner radius of the accretion disk is given by Wang (1996):

$$R_0 = 1.35\gamma_0^{2/7}\eta^{4/7}r_{\rm A}, \tag{9}$$

where $\gamma_0 = -B_{\phi_0}/B_{z_0} \sim 1$ is the magnetic pitch angle.

In the figures we show, for each case, the evolution of the inner radius of the accretion disk, the half-height of the disk, the z-component of the magnetic field, the particle density inside the disk, the photon density, the average energy of the photons, the energy of the first-generation gamma-rays inside the disk, the injected energy into the disk in the form of relativistic particles, the opacity of the disk to proton propagation, the gamma-ray luminosity produced inside the disk as a consequence of the π^0-decays, the opacity of the disk to these high-energy gamma-rays, and the luminosity of the gamma-rays that finally emerge from the other side of the disk. All values are given at R_0.

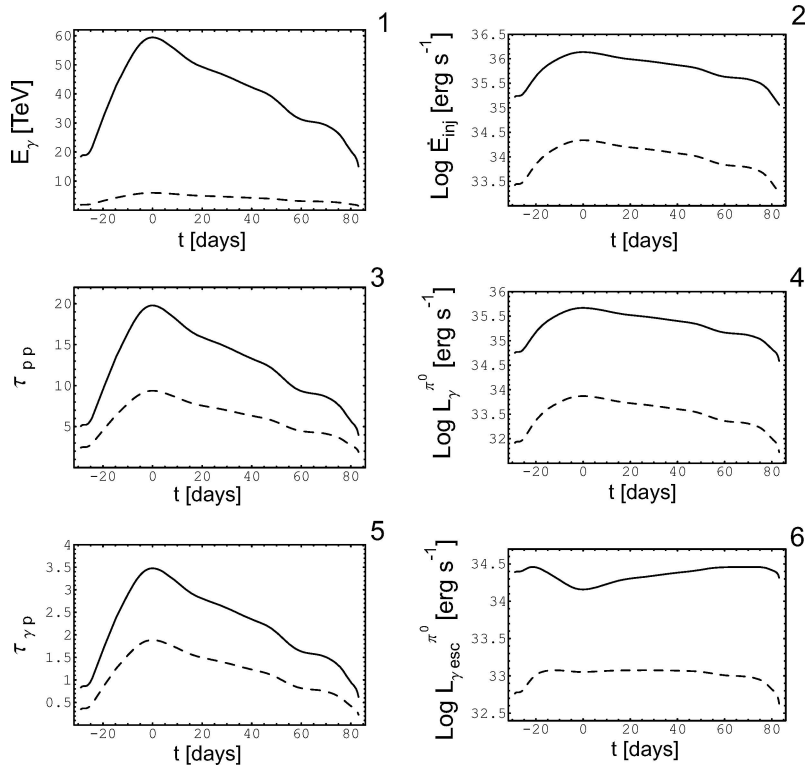


Figure 4. Time-evolution of different parameters related to the high-energy emission during a major outburst for models with $\eta = 1$ (dashed curve) and $\eta = 0.2$ (solid curve). $t = 0$ corresponds to the periastron passage. 1. Energy of the first-generation photons from π^0-decays. 2. Power injected into the disk in the form of relativistic protons. 3. Opacity to proton propagation in the disk. 4. Gamma-ray power from π^0-decays produced inside the disk. 5. Opacity to TeV gamma-ray propagation in the disk. 6. High-energy gamma-ray luminosity that emerges from the other side of the disk.

As we have already mentioned, those gamma-rays that are absorbed in the disk can initiate an electromagnetic cascade if the secondary pairs are energetic enough as to generate a second generation of gamma-rays. In Figure 7 we show the evolution of the different ratios of cooling times for secondary pairs in the disk. During major outbursts in models with $\eta = 0.2$ three generations of pairs are created. The first generation cools mainly by synchrotron radiation, whereas in the other generations the cooling is dominated by relativistic Bremsstrahlung. The GeV gamma-rays produced by the last generation of pairs escape from the disk but not necessarily from the system. Inverse Compton losses, which were not dominant inside the disk, are now responsible for further cascades in the photosphere (see next section). In models of major outbursts with $\eta = 1$ only two generations of pairs are produced close to the periastron, and just one when the disk is far from it. These pairs cool by synchrotron radiation mainly, although Bremsstrahlung takes over far in the

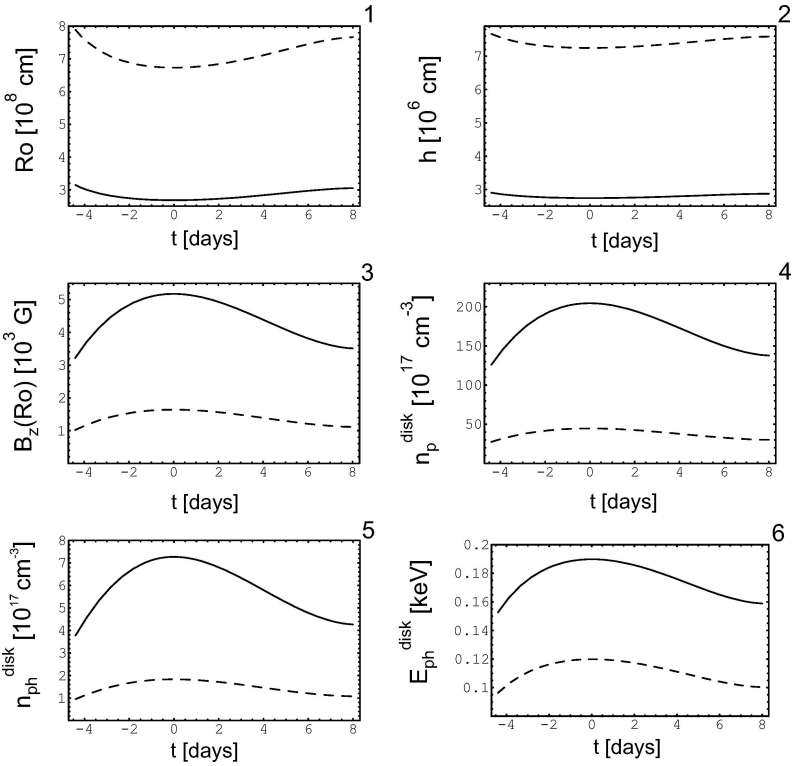


Figure 5. Same as Figure 3, but for a normal outburst.

extremes of the light curve. During minor outbursts cascades cannot be sustained: TeV gamma-rays from π-decays and MeV-GeV photons from synchrotron and Bremsstrahlung cooling of pairs originated in the $\pi^{\pm}$-decays are directly injected through the disk into the photosphere.

6. Absorption in the Photosphere

The optical depth for a photon with energy E_γ in the photosphere of the accreting neutron star is

$$\tau(R_o,\ E_\gamma) = \int_{E_{\min}(E_\gamma)}^{\infty} \int_{R_o}^{\infty} n_{\rm ph}(E_{\rm X}, r)\sigma_{e^-e^+}(E_{\rm X}, E_\gamma) dr\, dE_{\rm X}, \tag{10}$$

where $E_{\rm X}$ is the energy of the ambient thermal X-ray photons, $n_{\rm ph}(E_{\rm X}, r)$ is their density, and $\sigma_{e^-e^+}(E_{\rm X}, E_\gamma)$ is the photon-photon pair creation cross section given by:

$$\sigma_{e^+e^-}(E_{\rm X},\ E_\gamma) = \frac{\pi r_0^2}{2}(1-\xi^2)\left[2\xi(\xi^2-2) + (3-\xi^4)\ln\left(\frac{1+\xi}{1-\xi}\right)\right], \tag{11}$$

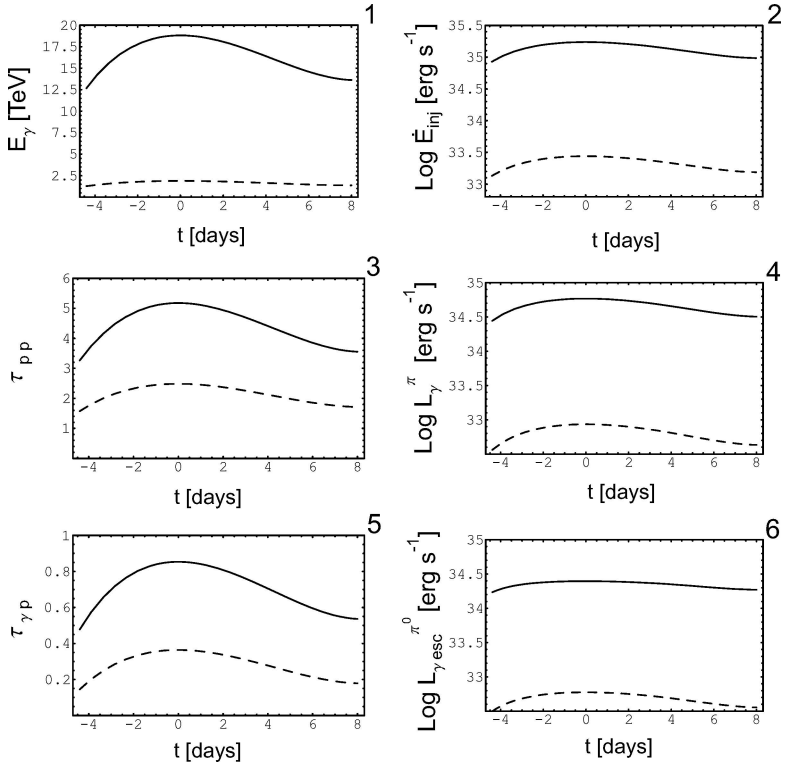


Figure 6. Same as Figure 4, but for a normal outburst.

where r_0 is the classical radius of the electron and

$$\xi = \left[1 - \frac{(m_e c^2)^2}{E_{\rm X} E_\gamma}\right]^{1/2}. \tag{12}$$

In Eq. (10), $E_{\rm min}$ is the threshold energy for pair creation in the X-ray field. This field can be considered as formed by two components, one from the disk and the other from the neutron star: $n_{\rm ph} = n_{\rm ph,1} + n_{\rm ph,2}$. Here,

$$n_{\rm ph,1}(E_{\rm X}, r) = \left(\frac{\pi B(E_{\rm X})}{hc\, E_{\rm X}}\right)\frac{R_o^2}{r^2}, \tag{13}$$

with

$$B(E_X) = \frac{2E_{\rm X}^3}{(hc)^2\left(e^{E_{\rm X}/kT_{\rm disk}} - 1\right)} \tag{14}$$

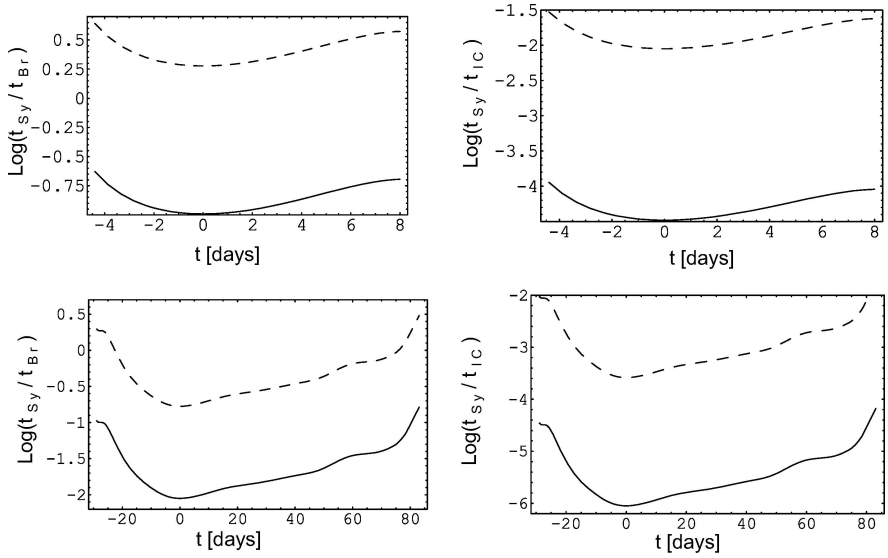


Figure 7. Evolution of the different ratios of cooling times for secondary pairs in an average electromagnetic cascade developed in the accretion disk of a system with screening factor $\eta = 0.2$ (dashed) and $\eta = 1$ (solid) during normal (upper panels) and major (lower panels) outbursts.

and $T_{\rm disk} = E_{\rm ph,disk}/k$, is the disk contribution. The emission from the heated polar caps of the star can be approximated by a Bremsstrahlung spectrum:

$$n_{\rm ph,2}(E_{\rm X}, r) = \frac{L_o}{4\pi c\, r^2\, E_{\rm X}^2\, e^{E_{\rm X}/kT}} \text{ for } E_{\rm X} \geq 2 \text{ keV}, \tag{15}$$

where L_o is the total luminosity in hard X-rays and $kT \sim 100$ keV.

In Figure 8 we show the opacity to gamma-ray propagation at the periastron passage as a function of the gamma-ray energy for major and normal outbursts in both models with $\eta = 0.2$ and $\eta = 1$. We see that gamma-rays with energies between ~ 1 GeV and ~ 1 TeV energies are absorbed. These gamma-rays initiate

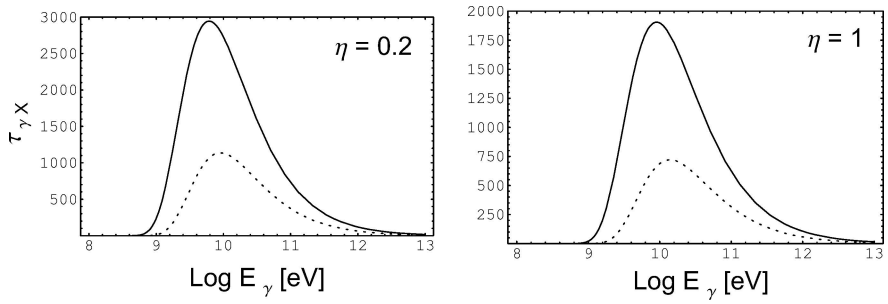


Figure 8. Opacity to gamma-ray propagation in the photosphere at the periastron passage for both major (solid) and normal (dashed) outbursts and disks with $\eta = 0.2$ (left) and $\eta = 1$ (right).

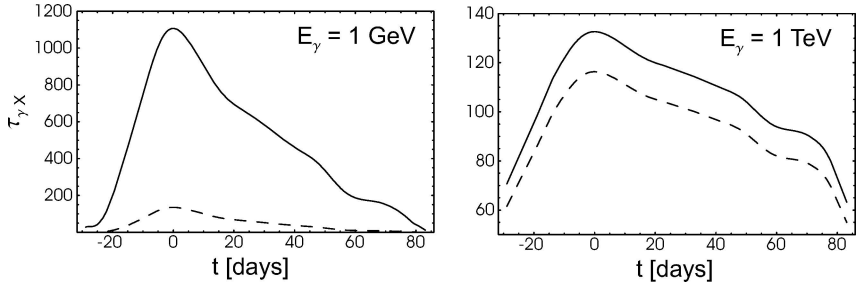


Figure 9. Time evolution of the opacity to gamma-ray propagation in the photosphere for a major outburst in disks with $\eta = 0.2$ (solid curve) and $\eta = 1$ (dashed curve) at two different energies.

inverse Compton cascades that degrade their energy. The final spectrum will be soft with an index of ~ 2.5 and a high-energy cutoff around $\sim 2m_e^2c^4/\langle E_{\rm X}\rangle \approx 250(\langle E_{\rm X}\rangle /1\ {\rm keV})^{-1}$ MeV (Aharonian et al., 1985; Aharonian and Plyasheshnikov, 2003). In Figure 9 we show the time evolution of the opacity at 1 GeV and 1 TeV for different models during a major outburst. Photons with energies above 10 TeV and below 500 MeV always can escape from the photosphere.

7. Discussion

The variability pattern of a given source at gamma rays will depend on both the physical parameters that characterize the particular system and the energy band of the observations. For instance, almost all GeV sources will be strongly absorbed in their X-ray photosphere during major outbursts. In some normal outbursts, however, a flaring GeV event might be observable. At TeV energies the gamma rays are partially absorbed in the disks, especially during major outbursts (a fact already noticed by Cheng et al., 1991). The TeV flux can be detectable for sources in the inner spiral arms of the Galaxy, once again, mainly during normal outbursts. During major flaring X-ray events, the TeV gamma rays can be variable or not, depending on the particular combination of parameters. At MeV energies the sources should be detectable for a wide range of parameters, for both normal and major bursts. A correlation between the X-ray and the MeV gamma-ray flux should be observed in these systems, whereas an anti-correlation should be the case in GeV sources, due to the different absorptions.

Future detection of Be/X-ray binaries by GLAST and Cherenkov telescopes might be favored by the observation of the candidates during normal X-ray outbursts.

Acknowledgements

We have benefited from illuminating discussions with Felix Aharonian, Luis Anchordoqui, K.S. Cheng, and Diego Torres. This work has been supported by

Fundación Antorchas, ANPCyT (PICT 03-13291), and CONICET. GER thanks the SECyT (Argentina) for a Houssay Prize.

Note

1. The distance to this source is not well-established

References

Aharonian, F.A.: 1985, *Ap&SS* **115**, 201.
Aharonian, F.A. and Plyasheshnikov, A.V.: 2003, *Astrop. Phys.* **19**, 525.
Anchordoqui, L.A.: 2003, *ApJ* **589**, 481.
Cheng, K.S.: 1991, *ApJ* **379**, 290.
Cheng, K.S., Cheung, T. and Lau, M.M.: 1990, *J. Phys. G* **6**, 1115.
Cheng, K.S. and Ruderman, M.: 1989, *ApJ* **337**, L77.
Cheng, K.S. and Ruderman, M.: 1991, *ApJ* **373**, 187.
Finger, M.H.: 1996a, *ApJ* **459**, 288.
Finger, M.H.: 1996b, *A&AS* **120**, 209.
Giovannellli, F. and Sabau Graziati, L.: 1992, *Sp. Sci. Rev.* **59**, 1.
Gosh, P. and Lamb, F.K.: 1979, *ApJ* **234**, 296.
Nolan, P.L.: 2003, *ApJ* **597**, 615.
Romero, G.E.: 2001, *A&A* **376**, 599.
Romero, G.E.: 2002, *A&A* **393**, L61.
Romero, G.E.: 2004, *ESA-SP*, in press.
Torres, D.F.: 2001, *A&A* **370**, 478.
Wang, Y.M.: 1996, *ApJ* **465**, L111.
Zhang, S.: 2002, *A&A* **396**, 923.

LOW-MASS QUARK STARS

RENXIN XU

School of Physics, Peking University, Beijing 100871, China; E-mail: r.x.xu@pku.edu.cn

(Received 21 June 2004; accepted 3 August 2004)

Abstract. More and more observational hints of quark stars are proposed these years though pulsars are considered conventionally to be normal neutron stars. The existence of *low-mass* quark stars is a direct consequence of the possibility that pulsar-like stars are actually quark stars, because of the ability that quark matter can confine itself by color interaction. After a brief introduction to the study of quark stars, the various astrophysical implications of low-mass quark stars are investigated. It is addressed that some of the transient unidentified γ-ray sources are probably merging quark stars. The observability of low-mass quark stars is discussed.

Keywords: dense matter, pulsars, neutron stars, elementary particles

1. Introduction to Quark Stars

It challenges still physicists to understand comprehensively the color interaction though we have a general fundamental framework for this strong force: the quantum chromodynamics (QCD). Two well known properties of QCD (asymptotic freedom in $\sim$0.1 fm scales and color confinement in $\sim$1 fm scales) conduce towards two remarkable states in the QCD phase-diagram: the hadron gas and the quark matter (or QGP, quark-gluon plasma). It is a clear goal for part of laboratory physicists to find quark matter in order to research into the problem of the elemental color interaction, whereas to detect astrophysical quark matter may be a shortcut, since astrophysics offers an alternative channel for us to explore the fundamental laws in the nature.

Pulsars, soon after the discovery in 1967, were identified to be *normal* neutron stars (dominantly of neutron fluid) proposed by Landau in 1932. However, since quarks are more fundamental than neutrons, it is possible that quarks enclosed in hadrons could be unconfined in compact stars with much high densities (and probably high temperatures) according to the asymptotic freedom. Stars composed of quark matter are called quark stars. Unfortunately, one is *not* able to determine whether neutron or quark stars remain during supernova explosion or other astrophysical processes via calculations of QCD because of its highly nonlinear nature. In case of this mathematical difficulty of QCD to find a certain answer for "what's the nature of pulsar-like stars?", *how* and *what* can the astrophysical observations *teach* us?



Astrophysics and Space Science **297:** 179–190, 2005.
© Springer 2005

One kind of quark stars on which astrophysicists focus highly are those with strangeness, so called strange (quark) stars (Xu, 2003a, 2004), the existence of which depends on the Bodmer-Witten's conjecture (Bodmer, 1971; Witten, 1984): strange quark matter is absolutely stable among color interaction systems. Though one can *not* prove or disprove this conjecture by first principles, there are actually several observational hints of strange stars (with *bare* quark surfaces), including drifting subpulses of radio pulsars and super-Eddington bursts of soft γ-ray repeaters ($\Rightarrow$ strong binding of both negatively and positively charged particles above pulsar surfaces), non-atomic thermal X-ray spectra, the discrepancy between free precession and glitch of radio pulsars (Zhou et al., 2004), and pulsar γ-ray profiles (Qiao et al., 2004).

2. The Motivations of Studying Quark Stars with Low Masses

Besides the argument that one can *not* simply rule out the possibility of the existence of low-mass quark stars, we have at least two more reasons for us to study quark stars with low masses.

1. *To identify a quark star in reality*. As is addressed in Section 1, it is very essential to identify a quark star in the new century. Stellar mass and radius are observable parameters, however, they are not distinguishable now for neutron and quark stars with almost the maximum mass (Lattimer and Prakash, 2004). Nevertheless, the term of "*low-mass*" may do us a favor to find crucial evidence for quark stars, since the radii of bare strange stars can be very small, while normal neutron stars (or crusted strange stars) cannot. A neutron star with mass $\sim 0.2 M_\odot$ has a radius of >15 km, whereas a quark star with mass $0.2 M_\odot$ is only $< \sim 5$ km. It is consequently possible that one can distinguish neutron and quark stars by direct measurements of the radii of low-mass pulsar-like stars by future X-ray satellites.

Also the very distinguishable mass-radius ($M - R$) relations of neutron and quark stars are helpful. The general relativistic effects of both low-mass neutron and quark stars are negligible due to small values of M/R. One is then able to study the structure of low-mass neutron stars by the Lane-Emden equation (Shapiro and Teukolsky, 1983) with $n = 2/3$ (corresponding to the state of non-relativistic neutron gas), which results in neutron star mass

$$M_{\rm NS} = 3.73\ R_6^{-3}\ M_\odot, \tag{1}$$

where the state equation is approximated by perfect neutron gas, $P = 5.52 \times 10^9 \rho^{5/3}$ dyne/cm^2, $R = 10^6 R_6$ cm. In case of very low masses ($M < 0.1 M_\odot$) in Eq. (1), the neutron gas approximation may not be applicable, since the mass and radius of such a star could be controlled by its crust that is not considered in deriving Eq. (1). Realistic neutron star modelling shows that the minimum mass of a stable neutron star is $\sim 0.1 M_\odot$, with radius $R \sim 160$ km (Shapiro and Teukolsky,

1983). However, for low-mass bare quark stars, due to the color self-confinement of quark matter,[1] the density is roughly homogeneous, and the mass would thus be,

$$M_{\rm QS} = \frac{4}{3}\pi R^3(4\bar{B}) = 0.9\, R_6^3\, \bar{B}_{60}\, M_\odot, \tag{2}$$

where the bag constant $\bar{B} = 60\bar{B}_{60}$ MeV fm^{-3}. In this sense, identifying a pulsar-like star with mass $<0.1M_\odot$ is evident for quark stars. Additionally, this striking difference between $M_{\rm NS} \propto R^{-3}$ and $M_{\rm QS} \propto R^3$ is certainly helpful for us to identify low-mass quark stars.

It is worth noting that, the identification of a low-mass quark star, with mass $<\sim 0.1M_\odot$, may also tell us whether the star has a *bare* quark surface, since the radius of a bare quark star is much smaller than that of a crusted one in this low-mass limit (Xu, 2003b).

2. *To probe the magnetic fields of isolated pulsars*. The conventional method to estimate the polar magnetic fields of isolated radio pulsars *has to* be modified if no certain reason forces us to rule out the possibility that low-mass bare strange stars could be born in the Universe. The energy conservation for an orthogonal star (i.e., the inclination angle between magnetic and rotational axes is $\alpha = 90^{\rm o}$) with a magnetic dipole moment μ, a moment of inertia I, and angular velocity Ω gives

$$\dot{\Omega} = -\frac{2}{3Ic^3}\mu^2\Omega^3. \tag{3}$$

This rule keeps quantitatively for any α, as long as the braking torques due to magnetodipole radiation and the unipolar generator are combined (Xu and Qiao, 2001). For a star with polar magnetic field B and radius R, the magnetic moment

$$\mu = \frac{1}{2}BR^3, \tag{4}$$

if the fields are in pure dipole magnetic configuration or if the star is an uniformly magnetized sphere. One comes then to the conventional way to derive magnetic field from P and $\dot{P}$ ($P = 2\pi/\Omega$ is the spin period),

$$B = 6.4 \times 10^{19}\sqrt{P\dot{P}}\ \ {\rm G}, \tag{5}$$

if "*typical*" values $I = 10^{45}$ g $\cdot$ cm^2 and $R = 10^6$ cm are assumed. Note: the field is only half the value in Eq. (5) if one simply suggests $\mu = BR^3$.

However, neutron star's I and R change significantly for different equations of state, or for different masses even for a certain equation of state (Lattimer and Prakash, 2004). This means that the "typical" values may actually be not typical. The inconsistency becomes more serious if pulsar-like stars are in fact quark stars since such a "star" could be as small as a few hundreds of baryons (strangelets).

3. Astrophysics of Low-Mass Quark Stars

Magnetic field plays a key role in pulsar life, but there is still no consensus on its physical origin although some ideas relevant (e.g., the flux conservation during collapse, the dynamo action) appeared in the literature. As pulsars could be solid quark stars (Xu, 2003c), we may propose an alternative mechanism for the generation of strong magnetic fields: the spontaneously broken ferromagnetism in quark matter when the temperature is lower than the Curie critical one, $T < T_{\rm curie}$. One of the advantages of ferromagnetic origin could be the unchangeable nature of magnetic fields since there is no convincing observation that fields decay in isolated pulsar-like stars. The magnetic domain structure may be destroyed by the turbulent motion in a fluid quark star, but this worry does not exist if pulsars are solid quark stars.

We may define $\mu_{\rm m}$ as the magnetic momentum per unit mass for ferromagnetism-saturated stars. The value of $\mu_{\rm m}$ could certainly depend on the properties of solid quark matter born in different astrophysical processes.

3.1. Rotation-powered low-mass quark stars

Assuming a mass-radius function of Eq. (2) for low-mass quark stars in rotation-powered phases, one can derive (Xu, 2005)

$$P\dot{P} = \frac{320\pi^3\mu_{\rm m}^2}{9c^3}\bar{B}R. \tag{6}$$

A pulsar may evolve along with constant $P\dot{P}$ if its $\mu_{\rm m}$, $\bar{B}$, M, and R are almost not changed during the life. With reasonable bag constant $\bar{B}$ and seven masses detected in pair neutron stars (and thus seven radii by Eq. (2)), we can obtain $\mu_{\rm m}$ for different pulsars. It is found that the values of $\mu_{\rm m}$ are grouped into two classes: high $\mu_{\rm m}\sim 10^{-4}$ G·cm^3·g^{-1} for normal pulsars but low $\mu_{\rm m} \sim 10^{-6}$ G·cm^3·g^{-1} for millisecond pulsars.

We can draw constant-$P\dot{P}$ lines in the $P - \dot{P}$ diagram, with averaged $\mu_{\rm m}$ for normal and millisecond pulsars, respectively (Xu, 2005). For normal pulsars with three different masses ($2M_\odot$, $1.5M_\odot$, and $1M_\odot$), they evolve passing through almost the middle region of normal pulsars. It is thus suggestive that the distribution of scattered points of normal pulsars could be the result of the variation of $\mu_{\rm m}$, rather than that of pulsar mass. Actually, if the mass is fixed to be $1.5M_\odot$, most of the normal pulsars are between $\mu_{\rm m} = 5 \times 10^{-3}$ and 5×10^{-5} G · cm^3·g^{-1}. However, for millisecond pulsars (e.g., for the case of $\mu_{\rm m} = 10^{-6}$ G · cm^3·g^{-1}), the line with mass $\sim 1M_\odot$ of constant $P\dot{P}$ does *not* pass through the center of the millisecond pulsar points. It is unlikely that the variance of $\mu_{\rm m}$ is responsible for this unless the $\mu_{\rm m}$ values of those millisecond pulsars are not representative. A natural proposal is that some of the millisecond pulsars could be low-mass quark stars, with mass

$\ll M_\odot$. The reason that the observed masses of millisecond pulsars in pair neutron stars are $\sim 1.4 M_\odot$ could be due to the selection effect in astronomy: low-mass quark stars produced in binary may be ejected from the system owing to the strong kick at birth, while only high-mass quark stars can survive.

What can the quark star mass be as low as? This is still a question to be solved by future observations. Possibly the low-limit could be $10^{-1\sim-3} M_\odot$. A quark star with much lower mass than $\sim 10^{-3} M_\odot$ should be called as a strange (quark) planet, rather than a strange (quark) star.

A nucleon has a magnetic momentum of $\sim \mu_{\rm N} = 5 \times 10^{-24}$ erg/G, and the corresponding value $\mu_{\rm m} \sim \mu_{\rm N}/m_{\rm p} \sim 3$ G·cm^3·g^{-1}, which is much larger than that observed in pulsars. This hints that the quark clusters in solid quark stars may have a magnetic momentum per baryon to be $\sim 10^{-(4\sim6)}$ orders weaker than that of nucleons.

The potential drop in the open-field-line region is essential for pulsar magnetospheric activity. In case of approximately constant $\mu_{\rm m}$, the potential drop between the center and the edge of a polar cap can be expressed as (Xu, 2005),

$$\phi = \frac{64\pi^3}{3c^2} \bar{B} \mu_{\rm m} R^3 P^{-2}. \tag{7}$$

Pair production mechanisms are essential for pulsar radio emission. A pulsar is called to be "death" if the pair production condition cannot be satisfied. Although a real deathline depends upon the dynamics of detail pair and photon production, the deathline can also be conventionally taken as a line of constant potential drop ϕ. Anyway, it is very necessary and worthwhile to investigate the pulsar death in the $P - \dot{P}$ diagram, with the inclusion of this "low-mass" ingredient for the case of pulsars being quark stars, by calculating the magnetospheric dynamics and simulating the spindown behaviors of both normal and millisecond pulsars.

3.2. ACCRETION-DOMINATED SPINDOWN

The physical process of accretion onto rotating pulsar-like stars with strong magnetic fields is very complex but is essential to know the astrophysical appearance of the stars (e.g., the variation of X-ray flux, the evolutional tracks, etc.), which is still not understood very well. Nevertheless, it is possible and useful to describe the physical process of accretion semi-quantitatively.

For an accretion scenario in which the effect of kinematic energy of accreted matter at infinite distance is negligible (such as the case of supernova fall-back accretion), three typical radii are involved. The radius of light cylinder of a spinning star with period P is

$$r_{\rm l} = \frac{cP}{2\pi} = 4.8 \times 10^9 P \text{ cm}. \tag{8}$$

If all of the accretion material is beyond the cylinder, the star and the accretion matter could evolve independently. The magnetospheric radius, defined by equating the kinematic energy density of free-fall particles with the magnetic one $B^2/(8\pi)$, is (Xu, 2005)

$$r_{\rm m} = \left(\frac{32^3\pi^3}{27G}\right)^{1/7} \bar{B}^{3/7}\mu_{\rm m}^{4/7}R^{9/7}\dot{M}^{-2/7} = 4.9\times10^7\bar{B}_{60}^{3/7}\mu_{\rm m}^{4/7}R^{9/7}\dot{M}^{-2/7}, \quad (9)$$

if a star is homogenously magnetized per unit mass (i.e., with constant $\mu_{\rm m}$). Due to the strong magnetic fields around a spinning star, matter is forced to co-rotate, and both gravitational and centrifugal forces work. At the so-called corotating radius $r_{\rm c}$, these two forces are balanced,

$$r_{\rm c} = \left(\frac{GM}{4\pi^2}\right)^{1/3} P^{2/3} = 1.2\times10^{-3}M^{1/3}P^{2/3}. \quad (10)$$

Due to the centrifugal inhibition, since the radius of matter nearest to the star could be $r_{\rm m}$, massive accretion onto stellar surface is impossible when $r_{\rm m} > r_{\rm c}$. This is the so-called *supersonic* propeller spindown phase. A star spins down to the equilibrium period $P_{\rm eq}$, defined by $r_{\rm m} = r_{\rm c}$. In the low-mass limit, with the assumption of constant $\mu_{\rm m}$, one has

$$P_{\rm eq} = 15G^{-5/7}\bar{B}^{1/7}\mu_{\rm m}^{6/7}R^{3/7}\dot{M}^{-3/7}. \quad (11)$$

However, accretion with rate $\dot{M}$ onto the stellar surface is not possible, although the centrifugal barrier is not effective when $P > P_{\rm eq}$, until the star spins down to a so-called break period (Ikhsanov, 2003),

$$P_{\rm br} = 60\mu_{30}^{16/21}\dot{M}_{15}^{-5/7}M_1^{-4/21}\ {\rm s} = 36\bar{B}_{60}^{-4/21}B_{12}^{16/21}\dot{M}_{15}^{-5/7}R_6^{12/7}\ {\rm s} = 0.49\bar{B}_{60}^{12/21}\mu_{m-6}^{16/21}\dot{M}_{15}^{-5/7}R_6^{12/7}\ {\rm s}, \quad (12)$$

in the low-mass limit, where the convention $Q = 10^n Q_n$ has been adopted. Pulsars with periods between $P_{\rm eq}$ and $P_{\rm br}$ do still spin down. This phase is called as *subsonic* propeller. Only a negligible amount of accretion matter can penetrate into the magnetosphere (onto the stellar surface) during both the supersonic and subsonic propeller phases (Ikhsanov, 2003), and the expected accretion luminosity is thus very low. It is obviously that pulsars with $P \sim P_{\rm br}$ may spin randomly: to spins up if $P > P_{\rm br}$, but spin down when $P < P_{\rm br}$.

3.3. OTHERS

The implications of low-mass quark stars are more than that presented in Section 3.1. and Section 3.2. We then select some of the issues interested, and try efforts to give general ideas for them.

1. *The birth of low-mass quark stars*. Millisecond pulsars could be of low-mass, but the origin of them is still an open debate even now. Millisecond pulsars are conventionally regarded as recycled ones in low-mass X-ray binaries, the magnetic fields of which decay (by, e.g., enhanced Ohmic dissipation, diamagnetic screening effect, etc.) during accretion process. Recently, five accretion-driven millisecond pulsars have been discovered since 1998, which are important to test the idea. However, besides the old problems (e.g., birthrate, millisecond pulsars with planets, etc.), new puzzling issues are raised in this argument (Rappaport et al., 2004).

The puzzles may disappear if low-mass quark stars, which are rapidly spinning, result directly from accretion-induced collapse (AIC) of white dwarfs, but could be covered by normal matter in their later accretion phases (while the core collapses might produce only normal pulsars with mass $\sim M_\odot$ and radius $\sim 10^6$ cm). The possibility of forming a quark star with $\sim M_\odot$ by AIC might not be ruled out. The newborn low-mass quark stars could rotate very fast, even to be super-Keplerian, and would spin down if the accretion rates are not high enough. Unless the mass is smaller than $(0.1\text{–}0.3)M_\odot$, the thickness of crust could be negligible, and the maximum X-ray luminosity at the break period [$\dot{M} = 2.3\times 10^{16} P_{\rm br-3}^{-7/5} \bar{B}_{60}^{12/15} \mu_{\rm m-6}^{16/15} R_5^{12/5}$ g/s from Eq. (12)] is approximately,

$$L_{\rm x} = \frac{GM\dot{M}}{R} \sim 2.8\times 10^{34} P_{\rm br-3}^{-7/5} \bar{B}_{60}^{9/5} \mu_{\rm m-6}^{16/15} R_5^{22/5} \ \ {\rm erg/s}. \tag{13}$$

A quark star with low mass may explain the low time-averaged accretion luminosity in bursting millisecond X-ray pulsars since $L_{\rm x} \propto R^{4.4}$, if it is assumed that bursting X-ray pulsars are in a critical stage of $P \sim P_{\rm br}$. It is worth noting that, in this stage, the real accretion-luminosity could be much lower than $L_{\rm x}$ presented in Eq. (13) because only part of the accretion matter with rate $\dot{M}$ could bombard directly the stellar surfaces. Alternatively, it is recently suggested (Popov, 2004) that low-mass compact objects can form by fragmentation of rapidly rotating protoneutron stars, and that such objects should have large kick velocities. But, fragmentation might hardly be possible for quark stars due to the color-confinement.

It is generally suggested that, during a iron-core collapse supernova, the gravitation-released energy $\mathcal{E}_{\rm g}\sim 10^{53}$ erg is almost in the form of neutrinos, $\sim 10^{-2}$ of which is transformed into the kinetic energy of the outgoing shock and $\sim 10^{-4}$ of which contributes to the photon radiation. However, this ideal is not so successful in modern supernova simulations, since the neutrino luminosity could not be large enough for a successful explosion even in the models with the inclusion of convection below the neutrinosphere (2D-calculations). We note that the bare

quark surfaces may be *essential* for successful explosions of both types of iron-core collapse and AIC. The reason is that, because of the color binding, the photon luminosity of a quark surface is not limited by the Eddington limit. It is possible that the prompt reverse shock could be revived by photons, rather than neutrinos. A hot quark surface, with temperature $T > 10^{11}$ K, of a newborn bare quark star will radiate photons at a rate of

$$\dot{E}_{\rm p} > 4\pi R^2 \sigma T^4 \sim 7 \times 10^{50} R_5^2 T_{11}^4 \ \ {\rm erg/s}, \tag{14}$$

while the Thomson-scattering-induced Eddington luminosity is only

$$L_{\rm Edd} = \frac{64\pi^2 c G m_{\rm p}}{3\sigma_{\rm T}} \bar{B} R^3 \sim 10^{35} \bar{B}_{60} R_5^3 \ \ {\rm erg/s}. \tag{15}$$

This means that the photon emissivity may play an important role in both types of supernova explosions (i.e., for the birth of solar-mass as well as low-mass quark stars).

2. *How fast could a low-mass quark star spin?* The fastest rotating millisecond pulsar is PSR 1937+21 ($P = 1.558 \times 10^{-3}$ s, $\dot{P} = 1.051 \times 10^{-19}$ s/s). In order to explain its polarization behavior of radio pulses and the integrated profile (pulse widths of main-pulse and inter-pulse, and the separation between them), this pulsar is supposed to have mass $<0.2 M_\odot$ and radius <1 km (Xu et al., 2001). Additionally, a low-mass quark star may actually favor a high spin frequency Ω during its birth. The Kepler frequency of such stars could be approximately a constant,

$$\Omega_{\rm k} = \sqrt{\frac{GM}{R^3}} = 1.1 \times 10^4 \bar{B}_{60}^{1/2} \ \ {\rm s}^{-1}. \tag{16}$$

The initial rotation periods of strange stars are limited by the gravitational radiation due to r-mode instability (Madsen, 1998). The critical Ω satisfies the equation

$$\frac{1}{\tau_{\rm gw}} + \frac{1}{\tau_{\rm sv}} + \frac{1}{\tau_{\rm bv}} = 0, \tag{17}$$

where the growth timescale for the instability (the negative sign indicates that the model is unstable) is estimated to be,

$$\tau_{\rm gw} = -3.85 \times 10^{81} \Omega^{-6} M^{-1} R^{-4}, \tag{18}$$

and $\tau_{\rm sv}$ and $\tau_{\rm bv}$ are the dissipation timescales due to shear and bulk viscosities, respectively,

$$\begin{cases} \tau_{\rm sv} = 1.85 \times 10^{-9} \alpha_{\rm s}^{5/3} M^{-5/9} R^{11/3} T^{5/3}, \\ \tau_{\rm bv} = 5.75 \times 10^{-2} m_{100}^{-4} \Omega^2 R^2 T^{-2}, \end{cases} \tag{19}$$

and α_s the coupling constant of strong interaction, T the temperature, m_{100} the strange quark mass in 100 MeV.

It is found (Xu, 2005) that low-mass bare strange stars can rotate very fast, even faster than the Kepler frequency (Note: The surface matter is not broken at super-Kepler frequency, due to the self-bounding of quark matter). However, though it needs advanced technique of data collection and analysis to detect sub-millisecond radio pulsar, we have not found one yet. This negative result could be due to: (1) The dynamical processes do not result in a sub-millisecond rotator; (2) No magnetospheric activity exists for very low-mass strange stars whose $\dot{P}$'s are small, since the potential drop is not high enough for pair-production (see Eq. (7) of Section 3.1). In the later case, a nearby sub-millisecond radio pulsar could be found by X-ray observations since a hotspot, powered by rotation and/or accretion, may form on the stellar surface.

3. *What happens when two quark-matter objects collide?* Quark matter with mass $\ll M_\odot$ could be ejected by a massive quark star ($\sim M_\odot$) during its birth, and such low-mass matter may explain a few astrophysical phenomena (Xu and Wu, 2003): the planets around pulsars could be quark matter with mass $\sim 10^{23-28}$ g, while very low mass strange quark matter (called as strangelets) with baryon numbers of $\sim 10^9$ may be the nature of ultra-high energy cosmic rays beyond the GZK cutoff. The bursts of soft γ-ray repeaters could be due to either the starquake-induced magnetic reconnection or the collision between a strange planet and solar-mass bare strange star. The collision chance would be not low if both objects form during a same supernova. Some of the transient unidentified EGRET sources (Wallace et al., 2000) may represent such collision events, the gravitational energy release of which is

$$E_g \sim \frac{G M_a M_b}{\left(R_a^3 + R_b^3\right)^{1/3}} = 2 \times 10^{23} \bar{B}_{60}^2 \frac{R_a^3 R_b^3}{\left(R_a^3 + R_b^3\right)^{1/3}}, \tag{20}$$

where "a" and "b" denotes two objects of strange quark matter. The released energy could be $\sim 10^{45}$ erg if $R_a \sim 10^5$ cm and $R_b \sim 10^4$ cm. This strong (color) interaction may result in photon emission by various hadron process (e.g., hadron annihilation), with energy $> \sim 100$ MeV (the EGRET telescope covers an energy range from 30 MeV to over 20 GeV), and could be another way to produce strangelets.

Merging quark stars, rather than neutron stars (Eichler et al., 1989), may result in cosmic γ-ray bursts observed (GRBs), which could help to eliminate the baryon load problem. The released energy is $\sim 10^{53}$ ergs during the collision of two quark stars with $\sim 10^6$ cm. The residual body should be expected to rapidly rotate, and such a high spin frequency may result in a beaming pattern of emission. A fire ball with low-baryon contamination in this color interaction even may favor the emission of photons and neutrinos with high energy.

4. Conclusions and Discussions

General properties of both rotation- and accretion-powered low-mass quark stars, as well as other issues relevant, are presented. It is suggested that normal pulsars with $\sim M_\odot$ masses are produced after core-collapse supernova explosions, whereas millisecond pulsars with $\sim(0.1\text{–}1)M_\odot$ (and even lower) masses could be the remains of accretion-induced collapses (AIC) of massive white dwarfs. These different channels to form pulsars may result in two types of ferromagnetic fields: weaker for AIC ($\mu_{\rm m} \sim 10^{-6}$ G·cm^3·g^{-1}) while stronger for core-collapse ($\mu_{\rm m} \sim 10^{-4}$ G $\cdot$ cm^3 $\cdot$ g^{-1}). A newborn low-mass strange star could rotate very fast, even with a super-Kepler frequency. It is proposed that some of the transient unidentified EGRET sources may result from the collisions of two low-mass quark stars.

In fact, some potential candidates for low-mass quark stars were addressed (Xu, 2005). One is the radio-quiet central compact object, 1E 1207.4–5209, which could be a low-mass bare strange star with polar surface magnetic field $\sim 6 \times 10^{10}$ G and likely a few kilometers in radius, and be now at a critical point of subsonic propeller phase, $P \sim P_{\rm br}$, in order to understand its timing behavior. Another one is the dim thermal object, RX J1856.5–3754, the radius of which is $R > 0.1$ km if its soft UV-optical component radiates from a spherically quasi-static atmosphere around.

Can we confirm the small radius of a low-mass quark star by a direct observation of future advanced space telescope? This work might be done by the next generation Constellation X-ray telescope (to be launched in 2009–2010), which covers an energy band of (0.25–100) keV. The radii, R, of neutron stars are generally greater than 10 km (R of $0.1M_\odot$ mass neutron stars is $\sim$160 km). If pulsars are neutron stars, their surfaces should be imaged by the Constellation-X with much high space resolution, as long as the separation between the four satellites is greater than $\sim \lambda d/R \sim 3\lambda_{-8} d_{100\rm pc}/R_6$ km (Note: the wavelength of X-ray photon with 10 keV is $\lambda \sim 10^{-8}$ cm, the distance to a neutron star is $d = d_{100\rm pc} \times 100$pc). However, if these objects are quark stars with low masses, Constellation-X may not be able to resolve their surfaces.

Can a core-collapse supernova also produce a low-mass quark star? This possibility could not be ruled out in principle. Likely astrophysical hints could be that the thermal X-ray emission and rotation power of such a star should be lower than expected previously. Additionally, the cooling history of a low-mass quark star should be significantly different from that of solar-mass ones.

It is sincerely proposed to search low-mass quark stars, especially with masses of $\sim(10^{-1}\text{–}10^{-3})M_\odot$, by re-processing the timing data of radio pulsars. Some of the companion masses of pulsar/white-dwarf binaries are *estimated* to be a few $0.1M_\odot$. Are all these companions real white dwarfs (or part of them to be just low-mass quark stars)? Only part of the companions (a few 10%s) of pulsar/white-dwarf systems have been optically detected. A further study on this issue is then surely necessary. Additionally, it is very necessary and essential to probe quark stars through various observations of millisecond-pulsar's environments (planets,

accretion disks), in order to distinguish these two scenarios on millisecond-pulsar's nature: to be (A) recycled or (B) supernova-originated. In case (A), planets and residual accretion disks could be around such pulsars, but possible mid- or far-infrared emission is still not been detected, although the formation of pulsar planets is still a matter of debate. In case (B), however, observations relevant could be well understood, since a pulsar (with possibly low mass) and its planet(s) may be born together during a supernova (Xu and Wu, 2003), and no infrared emission can be detected if no significant supernova-fall-back disk exists. If the first scenario is right, infrared radiations from both the disks and the planets could be detectable by the Spitzer Space Telescope and by the present SCUBA-1 or future -2 detectors of JCMT 15-m ground telescope. But if the later is true, the sub-mm emission from pulsar circumambience should be much weak, even not detectable. Surely, these are exciting and interesting subjects to be proposed when these advanced telescopes operate.

Acknowledgements

This work is supported by National Nature Sciences Foundation of China (10273001) and the Special Funds for Major State Basic Research Projects of China (G2000077602).

Note

1. Quark stars with masses lower than the maximum mass is bound dominantly by color confinement, whereas other Fermi stars (e.g., neutron stars and white dwarfs) are gravitation-tied bodies.

References

Bodmer, A.R.: 1971, *Phys. Rev.* **D4**(6), 1601.
Eichler, D., Livio, M., Piran, T. and Schramm, D.N.: 1989, *Nature* **340**, 126.
Ikhsanov, N.R.: 2003, *Astron. Astrophys.* **399**, 1147.
Lattimer, J.M. and Prakash, M.: 2004, *Sci.* **304**, 536.
Madsen, J.: 1998, *Phys. Rev. Lett.* **81**, 3311.
Popov, S.B.: *Preprint* (astro-ph/0403710).
Qiao, G.J., Lee, K.J., Wang, H.G., Xu, R.X. and Han, J.L.: 2004, *Astrophys. J.* **606**, L49.
Rappaport, S.A., Fregeau, J.M. and Spruit, H.: 2004, *Astrophys. J.* **606**, 436–443, (astro-ph/0310224).
Shapiro, S.L. and Teukolsky, S.A.: 1983, Black Holes, White Dwarfs, and Neutron Stars: The Physics of Compact Objects, Wiley, New York.
Wallace, P. M.: 2000, *Astrophys. J.* **540**, 184.
Witten, E.: 1984, *Phys. Rev.* **D30**(2), 272.
Xu, R.: 2005, in: F. Camilo and B.M. Gaensler (eds.), Proceedings of IAU Symposium No. 218, Young neutron stars and their environments, p. 299, (astro-ph/0310050).
Xu, R.X.: 2003a, in: X.D. Li, Z.R. Wang and V. Trimble (eds.), Proceedings of IAU Symposium No. 214, High Energy Processes, Phenomena in Astrophysics, p. 191, (astro-ph/0211348).

Xu, R.X.: 2003b, *Chin. J. Astron. Astrophys.* **3**(2), 33.
Xu, R.X.: 2004, *Astrophys. J.* **596**, L59.
Xu, R.X.: *Preprint* (astro-ph/0402659).
Xu, R.X. and Qiao, Q.J.: 2001, *Astrophys. J.* **561**, L85.
Xu, R.X. and Wu, F.: 2003, *Chin. Phys. Lett.* **20**(6), 806.
Xu, R.X., Xu, X.B. and Wu, X.J.: 2001, *Chin. Phys. Lett.* **18**(6), 837.
Zhou, A.Z., Xu, R.X., Wu, X.J. and Wang, N.: *Astroparticle Phys.*, in press.

THE SPIRAL ARM CONNECTION OF EGRET UNIDENTIFIED SOURCES

TORAFUMI MIYAGI, DIPEN BHATTACHARYA and ALLEN D. ZYCH

Institute of Geophysics and Planetary Physics, University of California, Riverside, CA 92551, USA; E-mail: miyagi1969@yahoo.com

(Received 2 July 2004; accepted 5 August 2004)

Abstract. Based on a LogN-LogS relation we have shown that the EGRET unidentified source (UnidS) distribution closely follows the Galactic spiral arm structure. This seems to satisfy the hypothesis that the EGRET UnidS arise due to energetic interactions with molecular clouds that reside on the spiral arms. Furthermore, the luminosity distribution of the unidentified sources features a double Gaussian distribution. We suggest that a combined distribution of OB associations, SNR and superbubbles interacting with molecular clouds within the spiral arms are the most likely counterparts of the unidentified sources.

Keywords: molecular clouds, gamma rays: observations, interstellar medium

1. Introduction

In a previous work we have used LogN-LogS graphs of the Galactic plane EGRET unidentified sources (UnidS) detected above 100 MeV to understand their inherent geometrical distribution (Bhattacharya et al., 2003). 26 stable (or non-variable) UnidS within $|b| < 5^\circ$ from the EGRET Third Catalog (Hartman et al., 1999) were used. If these sources are associated with a population which is uniformly distributed in a thin Galactic disk, we would expect a $N \sim S^{-1}$ relation from the LogN-LogS curve. In Figure 1 the LogN-LogS relation for the UnidS (open circles) is shown. The relation takes into account the detectability of EGRET sources due to exposure and background gamma-ray emission. The EGRET UnidS with GeV emission are also shown (filled triangles). The bright UnidS with flux values greater than 3.4×10^{-7} photons cm^{-2} s^{-1} have a power law slope β_1 of approximately -3.

Young radio pulsars are suggested to be one of the potential counterparts of many EGRET UnidS (Mukherjee et al., 1995; Yadigaroglu and Romani, 1997; Zhang, Zhang and Cheng, 2000; Harding and Zhang, 2001; Halpern et al., 2001). The LogN-LogS curves of the radio pulsars (a possible candidate population for EGRET UnidS), both young and old, can be fit with power laws that have indices close to -1.0. This would seem to indicate that the pulsar population is uniformly distributed in the Galactic thin disk. We also find that there is no clear difference in the distribution of pulsars throughout the Galaxy and the distribution of pulsars only within the EGRET detection range. On the other hand, the steep LogN-LogS graph

Astrophysics and Space Science **297:** 191–199, 2005.
© Springer 2005

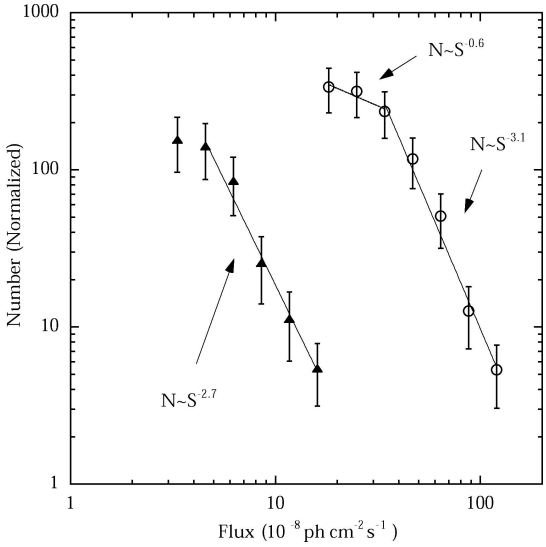


Figure 1. LogN-LogS of EGRET unidentified >100 MeV and GeV sources with normalization.

for the EGRET UnidS is not indicative of a uniform disk population (e.g., pulsar). This steep index can be understood in a model where sources are not uniformly distributed. In this context it is important to study the spatial distribution of spiral arm sources in order to see whether they can simulate such a distribution.

2. Molecular Clouds

To explore the above idea we studied the distribution of molecular clouds in the Carina-Sagittarius and Perseus arms. The infrared LogN-LogS curves of the compact molecular clouds (CMC) in the first and fourth Galactic quadrants have slopes ranging from 1.65–2.25 (Little and Richards, 1989). If molecular clouds are associated with EGRET UnidS, we can derive a phenomenological LogN-LogS curve based on the molecular cloud masses.

In Figure 2, a face-on map of molecular clouds in spiral arms is presented. The solid lines show the directions toward the stable Galactic plane EGRET UnidS. The distance scale is in kpc and the Sun is located at the coordinate origin. The Galactic center is marked with a cross. The "four arm" Galactic structure by Taylor and Cordes (1993) is also shown where Perseus arm is the 4th spiral from the bottom and Carina-Sagittarius arm is the 3rd spiral. The cloud data are taken from the Sagittarius arm (Dame et al., 1986), Carina arm (Grabelsky et al., 1988) and Perseus arm (Leisawitz, 1990). The maximum EGRET detectable range (using a maximum standard luminosity of 7×10^{35} erg s^{-1}) is the range within the dotted area.

We combined two catalog data sets to produce a complete LogN-LogS curve of the Carina-Sagittarius arm molecular clouds. The simulated gamma-ray source

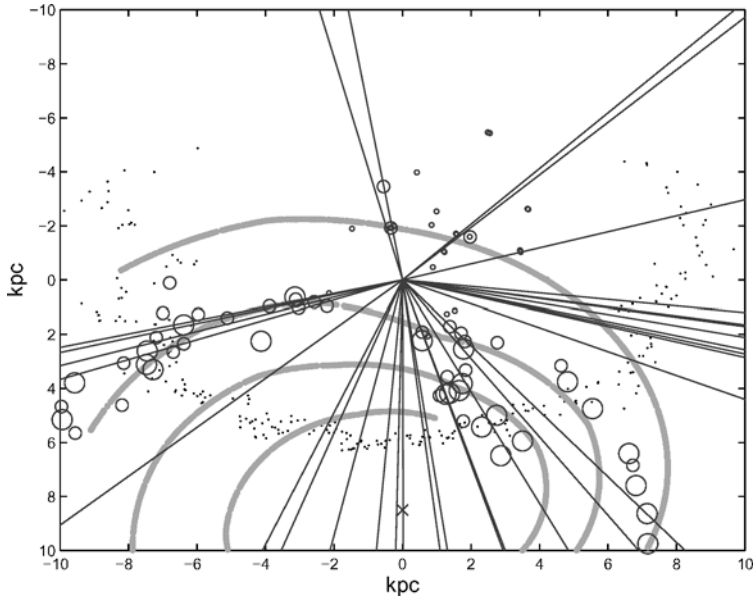


Figure 2. Face-on map of molecular clouds in spiral arms. Large circle: molecular clouds with Mass $>10^5 M_\odot$ Medium circle: molecular clouds with $10^4 M_\odot <$ Mass $<10^5 M_\odot$ Small circle: molecular clouds with 10^3 $M_\odot$ < Mass $<10^4 M_\odot$

number is normalized by the cloud mass in units of 10^5 $M_\odot$. We assumed a standard gamma-ray luminosity of 2.1×10^{35} erg s^{-1} for each source; this luminosity is chosen so that the break of the EGRET UnidS LogN-LogS curve occurs at about $F = 3.4\times10^{-7}$ photons cm^{-2} s^{-1}. This luminosity is also within the range given by Kanbach et al. (1996) for EGRET Galactic plane sources. The combined LogN-LogS relation can be fitted with a β_1 of 2.8 ± 0.3. The result is close to the LogN-LogS relation of the EGRET UnidS (slope $= -3.1\pm0.4$). The steep slope is indicative of the molecular cloud concentration in the spiral arm. Furthermore, for clouds that are located in the Perseus arm, which is outside the solar circle, the LogN-LogS curve has a slope value of $\beta_1 = 2.14 \pm 0.09$. The β_1 is flatter than 3, however the break point coincides with 3.4×10^{-7} photons cm^{-2} s^{-1} as well. These results imply that large molecular clouds in interactions with Galactic cosmic rays and/or embedded cosmic-ray sources must be considered one of the potential counterparts of EGRET UnidS. An interesting case of molecular clouds as sites of particle acceleration and independent sources of gamma rays has been made by Dogiel et al. (2004).

3. Supernova Remnants

Many investigators have pointed out the spatial coincidence of supernova remnants (SNR) with unidentified EGRET sources (Sturner and Dermer, 1995; Esposito et al.,

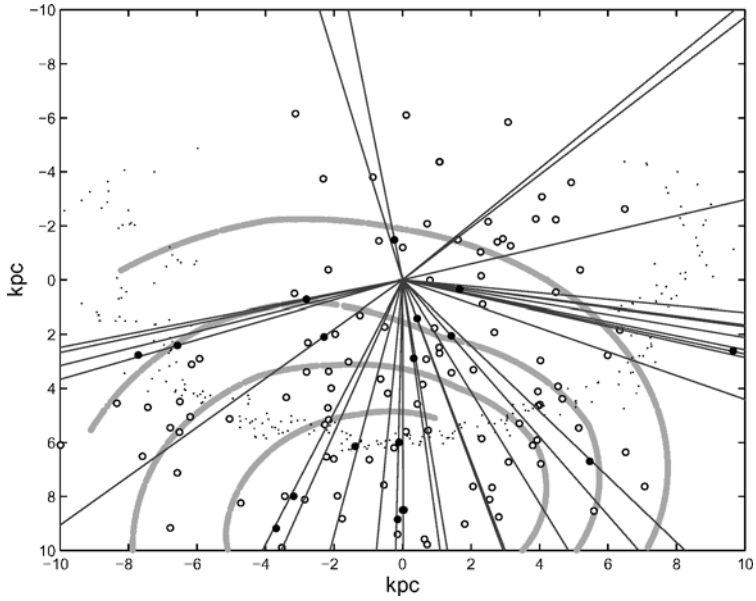


Figure 3. Positional coincidences with SNRs.

1996; Romero et al., 1999). In Figure 3, we plot the SNRs in the solar neighborhood. The SNR distances are taken from Miyagi (2003) and references therein. The filled circles designate SNRs which coincide with stable EGRET UnidS whereas the open circles are the ones that are not coincident. The small dots designate the maximum EGRET detectable range. As seen in Figure 3, within the EGRET detectability range most of SNR-UnidS coincidences lie on or near the major spiral arms, which might underscore the role of high ambient interstellar density in gamma-ray production. We suggest there are a total of seven SNRs within the EGRET detectable range. These are $\gamma-$Cygni, IC 443, MSH 10-53, G312.4-0.4, W28, G16.8-1.1, and W44. Three more SNRs are located close to the edge of the EGRET detectable range and seven SNRs are outside of the EGRET detectable range. These conclusions are compatible with the in-depth study of the SNR-UnidS connection carried out by Torres et al. (2003).

Using all the radio SNRs within the EGRET detectable range (a total of 70 SNR were considered) we constructed a SNR LogN-LogS curve based on radio fluxes. The SNR radio flux values at 1 GHz are taken from Green's Catalog (2000). The plot shows a clear break at $\sim$100 mJy, with β_2 of $0.60 \pm .08$ and β_1 of $1.7 \pm .6$. The SNR β_1 is not as steep as UnidS's 3.1, which may indicate that the spatial distribution of the SNRs does not perfectly follow the EGRET UnidS distribution. However, the SNR LogN-LogS slope is subjected to selection effects in radio ranges and may change with future SNR detections.

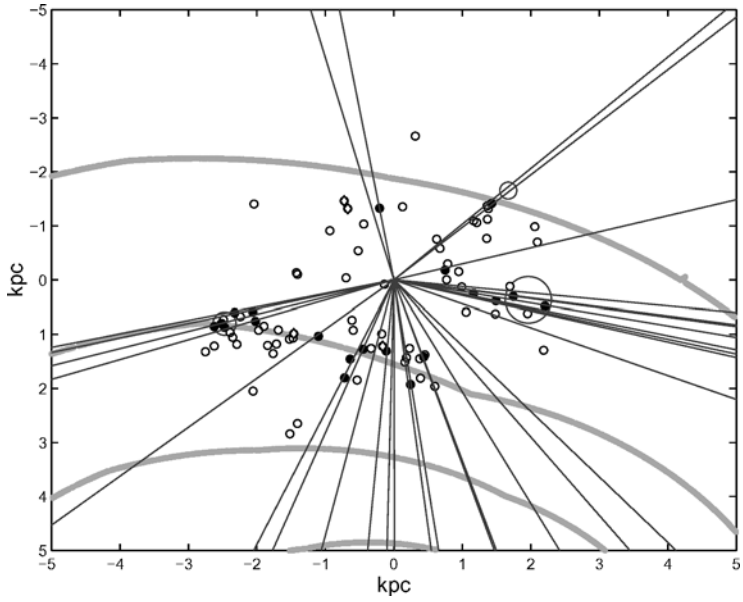


Figure 4. Positional coincidences with OBAs and Superbubbles (large circles).

4. OBA and Superbubbles

Many OB stellar associations are also found to be spatially coincident with EGRET UnidS (Kaaret and Cottam 1996; Romero et al., 1999). In Figure 4 we show the OB association positions with respect to the direction of the EGRET UnidS (small circles, filled or open). Many of the UnidS-OBA positional coincidences occur deep inside the spiral arms. For example, OBA Cas 6 ($l = 134.66^\circ$, $b = 0.93^\circ$), a possible counterpart for 3EG J0229+6151, is located within the Perseus Arm (arm 4). There are also several positional coincidences in the Carina-Sagittarius Arm (arm 3). Even though it is not shown in the figure, several coincidences are found in the Orion arm (local arm) that extends from the Cygnus region to the Orion region. The Cyg OB 1, 2, 8, and 9 associations are located in this local arm.

Some stable EGRET UnidS along the Galactic plane form clustered regions at specific directions. The most obvious clusters are within the star forming regions, W4 ($l \sim 135^\circ$), Cygnus ($l \sim 79^\circ$), and Carina ($l \sim 285^\circ$) with clustering radii of roughly 1.5°, 5°, and 4° respectively. These regions contain superbubbles – large HI shells created by multiple SNR shocks or stellar winds. The spatially coincident superbubbles are also shown in Figure 4 with large circles. The role of these superbubbles in gamma-ray generation is yet to be clearly identified.

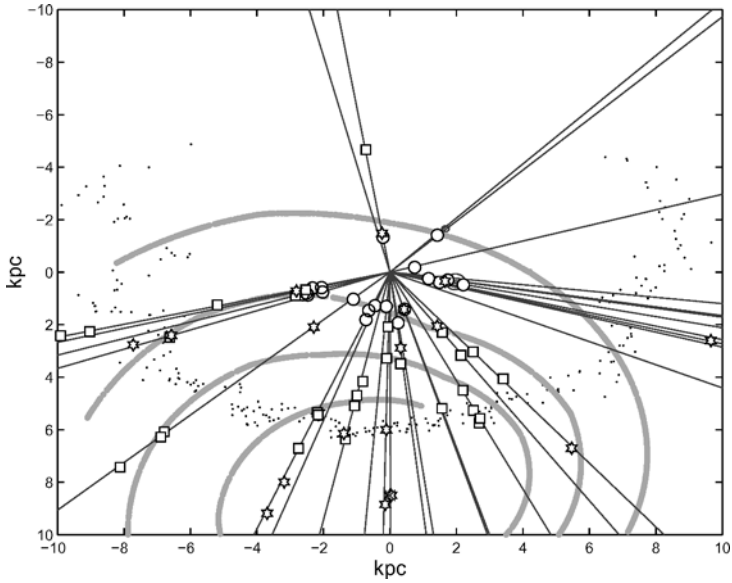


Figure 5. Positional coincidences with pulsars, SNRs and OBAs.

5. LogN-LogS Simulation

Figure 5 is the face-on map of OBAs (small circles), SNRs (pointed stars), and pulsars (squares) which have positional coincidences with the EGRET UnidS. The majority of positional coincidences occur on or near the spiral arms. Positional coincidences with OBAs, SNRs, and superbubbles are relatively close to the Sun. However within 3 kpc from the Sun, the pulsar coincidences are few.

The combined luminosity distribution of OBAs, SNRs, and superbubbles shows a double Gaussian distribution (Figure 6). The lower luminosity population in Figure 6 has a mean of $L_{\rm low} = 7.6 \times 10^{34}$ erg s^{-1}, $\sigma_{\rm low} = 2.8 \times 10^{34}$ erg s^{-1} with an amplitude of 12. The higher luminosity population has a mean of $L_{\rm high} = 1.7 \times 10^{35}$ erg s^{-1}, $\sigma_{\rm high} = 8.0 \times 10^{34}$ erg s^{-1} with an amplitude of 4.9. The luminosities are calculated assuming the UnidS source counterparts are actually coincident with identified objects. The possible mean luminosity of detectable EGRET UnidS is $L_{\rm det} = 1.1 \times 10^{35}$ erg s^{-1}.

The double Gaussian distribution shows that EGRET UnidS could be from more than one population. Molecular clouds, whose spatial distribution traces spiral structures, through interaction with OB stellar winds, superbubbles or SNR shocks could give rise to gamma rays. Based on the double Gaussian luminosity distribution, we have simulated a LogN-LogS curve for sources situated within the Galactic spirals. We considered selection effects and generated the actual low luminosities with a mean of $L_1 = 6.38 \times 10^{34}$ erg s^{-1} with $\sigma_1/L_1 = 0.47$ ($\sigma_{L_1} = 3.02 \times 10^{34}$ erg s^{-1}. We also generated high luminosities with a mean of $L_2 = 1.06 \times 10^{35}$ erg s^{-1} with

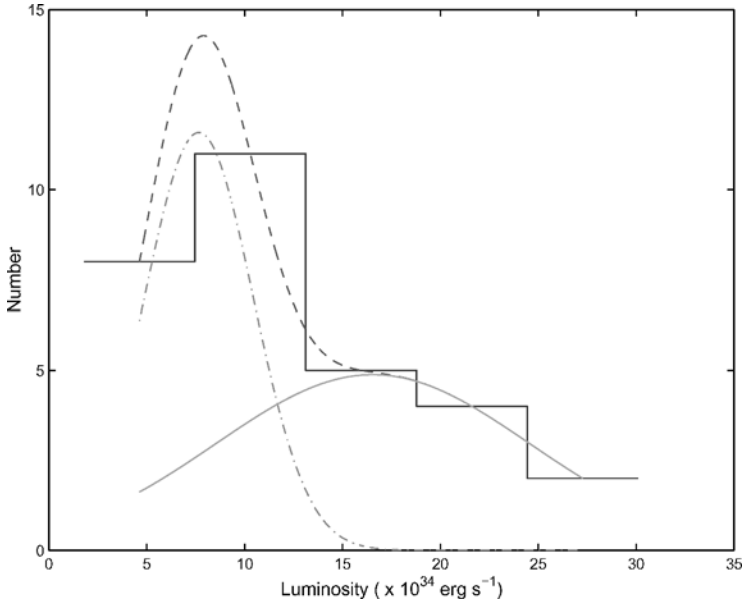


Figure 6. Double Gaussian distribution for EGRET UnidS source candidates.

$\sigma_2/L_2 = 0.95$ ($\sigma_2 = 1.00 \times 10^{35}$ erg s^{-1}). The low to high luminosity source number ratio was 53/47. A total of 10^6 sources were generated using the spiral model. The spatial deviation σ_{SP} was 100 pc.

The detectability parameter, D, which is a function of the source flux, instrument exposure and the Galactic diffuse gamma ray background, is used to judge if the sources are "detectable" or "not detectable". The parameter D corresponds to the EGRET source significance $\sqrt{TS}$ (TS = test statistic) obtained by a likelihood analysis (Mattox et al., 1996). The EGRET Group has chosen the sources which lie close to the Galactic plane as detected that have $\sqrt{TS} \geq 5$. Hence, we count only those sources with $D \geq 5$ in our simulation. For cases where the exposure and the background are not considered, sources with flux values greater than 1.0×10^{-7} photons cm^{-2} s^{-1} are considered detected.

In Figure 7, we show the LogN-LogS curve where the EGRET exposure and diffuse background have been taken into account. The figure show a steep plot with a break point occurring at $\sim 3.5 \times 10^{-7}$ ph cm^{-2} s^{-1}. The β_1 is 2.88 ± 0.08 which is within the error of EGRET UnidS source β_1 of 3.1 ± 0.4. These results imply that more than one population type is responsible for the EGRET UnidS. (For comparison, we simulated a LogN-LogS plot where the sources are assumed to be uniformly distributed on the disk. This yielded a β_1 of 1.22). The LogN-LogS index and break point of the combined distribution of OB associations, and SNR/superbubbles that are concentrated on the spiral arms closely match the LogN-LogS index and the break point of EGRET UnidS. This multi-population distribution, within a distance

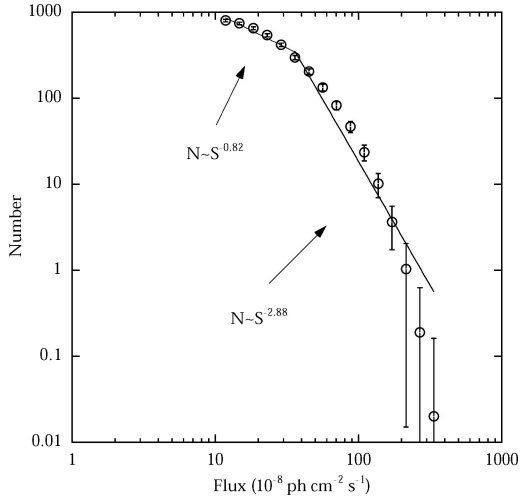


Figure 7. Simulated LogN-LogS plot of EGRET UnidS.

of 3 kpc, may be the counterparts of most EGRET UnidS. Furthermore, a narrow spatial deviation σ_{SP} of 100 pc is indicative of very young sources.

Finally, in Figure 8 we show the predicted detection ranges for the GLAST detector assuming some specific standard luminosity numbers. We assumed the

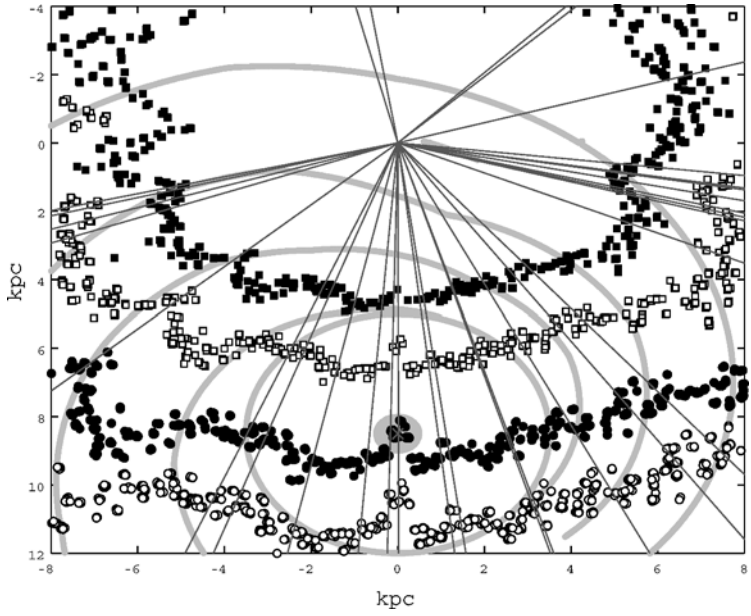


Figure 8. GLAST detection ranges. Assumed standard luminosities (in ergs s^{-1}) are filled square 2.9×10^{34}, open square 5.8×10^{34}, filled circle 1.16×10^{35}, open circle 1.74×10^{35}.

GLAST sensitivity to be at least a factor of 15 better than the EGRET sensitivity. Compare the detection ranges with the EGRET range in Figure 2 where a maximum standard luminosity of 7×10^{35} ergs s^{-1} was adopted. The GLAST sky will include sources near the Galactic center and within the 3 kpc molecular ring which will modify the LogN-LogS plot of the expected sources. A preliminary analysis suggests the slope of the curve will flatten and will be in the range of 2.2–2.6.

References

Bhattacharya, D., Akyuz, A. and Miyagi, T.: 2003, *A&A* **404**, 163.
Dame, T.M., Elmegreen, B.G. and Cohen, R.S.: 1986, *ApJ* **305**, 892.
Dogiel, V.A., Gurevich, A.V. and Istomin, Ya.N.: 2004, in: Cosmic Ray Acceleration Inside Molecular Clouds, this proceeding.
Esposito, J.A., Hunter, S.D. and Kanbach, G.: 1996, *ApJ* **461**, 820.
Grabelsky, D.A., Cohen, R.S. and Bronfman, L.: 1988, *ApJ* **331**, 181.
Green, D.A.: 2000, A Catalog of Galactic Supernova Remnants, Mullard radio Astronomy Observatory, Cambridge, UK.
Halpern, J.P.: 2001, *ApJ* **552**, L125.
Harding, A.K. and Zhang, B.: 2001, *ApJ* **548**, L37.
Hartman, R.C., Bertsch, D.L. and Bloom, S.D.: 1999, *ApJS* **123**, 79.
Kaaret, P. and Cottam, J.: 1996, *ApJ* **462**, L35.
Leisawitz, D.: 1990, *ApJ* **359**, 319.
Little, L.T. and Richards, P.J.: 1989, *MNRAS* **240**, 397.
Mattox, J.R.: 1996, *ApJ* **461**, 396.
Miyagi, T.: 2003, PhD Thesis, University of California, Riverside.
Mukherjee, R.: 1995, *ApJ* **441**, L61.
Romero, G.E., Benaglia, P. and Torres, D.F.: 1999, *A&A* **348**, 868.
Sturner, S.J. and Dermer, C.D.: 1995, *A&A* **293**, L17.
Taylor, J.H. and Cordes, J.M.: 1993, *ApJ* **411**, 674.
Torres, D.F.: 2003, *Phys. Rep.* **382**, 303.
Yadigaroglu, I.A. and Romani, R.W.: 1997, *ApJ* **476**, 347.
Zhang, L., Zhang, Y.J. and Cheng, K.S.: 2000, *A&A* **357**, 957.

COSMIC RAY ACCELERATION INSIDE MOLECULAR CLOUDS

V.A. DOGIEL, A.V. GUREVICH, YA.N. ISTOMIN and K.P. ZYBIN

P.N. Lebedev Physical Institute, Leninskii pr. 53, Moscow, Russia;
E-mail: dogiel@lpi.ru

(Received 28 June 2004; accepted 21 July 2004)

Abstract. Acceleration of charged particles by neutral gas turbulence in giant molecular clouds is considered. The gamma-ray emission from these clouds is estimated. It is shown that molecular clouds can be the counterparts of some of unidentified sources.

Keywords: unidentified gamma-ray sources, giant molecular clouds, CR acceleration

1. Introduction

One of the most interesting results of the studies carried out by the satellite COS-B (Bignami and Hermsen, 1983) and then by the observatory COMPTON (Hartman et al., 1999) was the discovery of unidentified gamma-ray sources whose origin is not yet ultimately clear. Many models have been proposed to explain emission of these sources. Among them are pulsars (Zhang et al., 2000), Wolf-Rayet and of stars, supernova remnants (Romero et al., 1999) and others. Analysis of LogN-LogS relation shows that at least a part of EGRET unidentified sources are most likely to be associated with molecular clouds (Miyagi et al., 2004). An excess of gamma-ray emission can be provided in this case by nearby external sources of cosmic rays such as OB associations, superbubbles or supernova remnants (see e.g. Aharonian, 2001). However, Dogiel et al. (1987) have shown that charged particles can be accelerated directly in clouds without any external source. At first glance giant molecular clouds hardly seem to be regions of particle acceleration. Indeed, these clouds are the most massive objects in the Galaxy with mass up to 10^{5-6} $M_\odot$ and dimension up to 300 pc. The neutral gas density in clouds is $n_H \sim 10^{2-3}$ cm^{-3} and their temperature is equal to 10–50 K. The magnetic field strength B is estimated to be of the order of 5×10^{-5} G (see e.g. Bourke et al., 2001). The degree of ionization is very low, $n_i/n_H \sim 10^{-5}$. It is difficult to imagine these cold dense clouds to be regions of particle acceleration. However, the gravitational energy of clouds is extremely high ($\sim 10^{51-52}$ erg s^{-1}). When a cloud collapses under the influence of the gravitational forces, a part of the gravitational energy should be transformed into the energy of turbulent motions.

Indeed, from observations it follows that the gas of clouds is strongly turbulent. The speed of turbulent motions reaches about 10 km s^{-1}. The turbulence

© Springer 2005

has a power-law Kolmogorov-like spectrum in a very broad range of scales from supersonic (Larson, 1981) to subsonic (Myers, 1983) region:

$$v(L) = 1.1\, L^{\alpha}(\mathrm{pc})\ \mathrm{km\ s^{-1}} \text{ where } \alpha \simeq 0.3 - 0.5 \tag{1}$$

where v is the velocity of turbulent motions and L is its scale ($0.01 < L < 300$ pc).

If at least a part of the turbulent energy were transformed into the energy of accelerated particles, then molecular clouds could be effective "accelerators". However, in such a cold and dense medium fast particles would rather seem to lose than to gain energy. But the situation changes radically in the presence of magnetic fields. A magnetic field promotes necessary energy conversion. Below we consider how the energy of a neutral turbulent gas can be converted into the energy of accelerated particles.

2. Spectrum of Hydrodynamic and MHD Turbulence

Before discussing the spectrum of magnetic fluctuations in a weakly ionized medium we recall the main characteristics of hydrodynamic and magnetohydrodynamic (MHD) turbulent fluctuations.

In the model proposed by Kolmogorov (1941) the energy of turbulent motions injected on large scales ($\sim L_0$) cascades to smaller scales by means of kinetic energy conserving interactions in the inertial range of scales ($L_0 > L > L_{\min}$) which is independent of large-scaling forcing processes and small scaling dissipative processes. Therefore, under steady state conditions the energy cascade rate of hydrodynamic turbulence ε in the inertial range is constant. On a given scale L with velocity $v(L)$, the rate of change of kinetic energy per mass unit is $v^2(L)$ divided by the characteristic timescale

$$\tau(L) \sim \frac{L}{v(L)} \text{ i.e. } \varepsilon \sim \frac{v^2(L)}{\tau(L)}. \tag{2}$$

The condition of constant energy rate in the inertial range gives the Kolmogorov velocity spectrum

$$v(L) \sim \varepsilon^{1/3} L^{1/3} \tag{3}$$

In terms of wave numbers k this gives the well-known energy spectrum of Kolmogorov turbulence

$$E(k) \propto \frac{u_k^2}{k} \propto k^{-5/3} \tag{4}$$

Then the characteristic time for eddies of size L is $\tau(L) \sim \varepsilon^{-1/3} L^{2/3}$. An extrapolation of the Kolmogorov spectrum to the dissipative scales gives the minimum scale of the inertial scale range $L_{\min} \sim (\nu^3/\varepsilon)^{1/4}$, where ν is the fluid viscosity.

The physics of MHD turbulence is more complex than that of fluid turbulence. In the MHD turbulence one should take into account nonlinear energy exchanges among the velocity-velocity, magnetic-velocity, and magnetic-magnetic modes as can be seen from the MHD equations

$$\left(\frac{\partial \mathbf{u}}{\partial t} + (\mathbf{u}\cdot\nabla)\mathbf{u}\right) = \frac{1}{\rho}\left[\nabla P_{\rm th} + \frac{(\nabla\times\mathbf{B})\times\mathbf{B}}{4\pi}\right] + \nu\nabla^2\mathbf{u} + \frac{2\nu}{3}\nabla\nabla\cdot\mathbf{u}\,,$$
$$\frac{\partial \mathbf{B}}{\partial t} = \nabla\times(\mathbf{u}\times\mathbf{B}) + \eta\nabla^2\mathbf{B}, \quad \frac{\partial\rho}{\partial t} + \nabla\cdot(\rho\mathbf{u}) = 0, \quad \nabla\mathbf{B} = 0\,. \tag{5}$$

It was shown by Kraichnan and Nagarajan (1967) that at the initial linear stage, when magnetic fluctuations are small, growth of the magnetic field increases mainly on the scales near $L_{\min}$. Later on back-reaction of the magnetic field on the velocity field leads to a nonlinear evolution of the system and to saturation mechanisms. In the stationary state an equipartition between velocity and magnetic fluctuations is expected. Numerical calculations show that in this case Kolmogorov like MHD turbulence is established when $E(k) \propto k^{-5/3}$ (see e.g. Goldreich and Sridhar, 1995; Verma, 1999) for both velocity and magnetic fluctuations. Hence, the energy of magnetic fluctuation is concentrated near large scales ($L \sim L_0$). The spectrum of magnetic fluctuations is

$$B^2(L) \propto L^{2/3} \tag{6}$$

Let us now return to the turbulence in molecular clouds where the gas ionization degree is very low.

3. Spectrum of Magnetic Turbulence in Weakly Ionized Gas

We denote the velocity of the ionized component of the gas as u. The spectrum of velocity fluctuations of the neutral gas is fixed and described by Eq. (1). Then the system of equations for fluctuations of the ionized component and magnetic fields derived for cloud parameters is (Dogiel et al., 1987)

$$\left(\frac{\partial \mathbf{u}}{\partial t} + (\mathbf{u}\cdot\nabla)\mathbf{u}\right) = \frac{1}{\rho_{\rm i}}\left[-\nabla P_{\rm i} + \frac{(\nabla\times\mathbf{B})\times\mathbf{B}}{4\pi}\right]$$
$$+ \nu_{\rm i}\nabla^2\mathbf{u} + \frac{2\nu_{\rm i}}{3}\nabla\nabla\cdot\mathbf{u} - \mu_{\rm in}(\mathbf{u}-\mathbf{v})\,,$$
$$\frac{\partial \mathbf{B}}{\partial t} = \nabla\times(\mathbf{u}\times\mathbf{B}), \quad \frac{\partial\rho}{\partial t} + \nabla\cdot(\rho\mathbf{u}) = 0, \quad \nabla\cdot\mathbf{B} = 0\,, \tag{7}$$

where $\rho_{\rm i}$, $\nu_{\rm i}$ etc. are characteristics of the ionized fraction of the gas and $\mu_{\rm ei}$ is the frequency of collision between ionized ions and neutral hydrogen. One can see a considerable difference between systems of Eq. (6) and (7). For the latter case we have a given external force in the form of friction between ionized and neutral components of the gas. Though the system of equations is nonlinear as before we can neglect back reactions of the ionized fraction and magnetic fluctuations. These components are in a sense "test particles" for the neutral gas turbulence. This circumstance allows the system (7) to be solved analytically.

The eigenfrequency of (7) is imaginary,

$$\omega(L) \sim i\frac{V_{\rm A}^2}{\mu_{\rm in}L^2}. \tag{8}$$

The magnetic fluctuations are excited when the friction is substantial, i.e. $V(L)/(\mu_{\rm in}L) \ll 1$. Then expansion in the parameter $\omega/\mu_{\rm in} \ll 1$ simplifies system (7):

$$\begin{aligned} \mathbf{u} &= \mathbf{v} - \frac{1}{4\pi\rho_{\rm i}\mu_{\rm in}}\mathbf{B}\times(\nabla\times\mathbf{B}) \\ \frac{\partial\mathbf{B}}{\partial t} &= \nabla\times(\mathbf{v}\times\mathbf{B}) - \nabla\times\left(\frac{1}{4\pi\rho_{\rm i}\mu_{\rm in}}\mathbf{B}\times(\nabla\times\mathbf{B})\times\mathbf{B}\right) \end{aligned} \tag{9}$$

For the Fourier transformation of velocity and magnetic fluctuations we have

$$\mathbf{v}(\mathbf{k},t) = \frac{1}{(2\pi)^3}\int \exp(-i(\mathbf{kr}))\mathbf{v}(\mathbf{r},\mathbf{t})d\mathbf{r} \tag{10}$$

A paired correlator of isotropic turbulence of a neutral gas has the form

$$\langle v_i(\mathbf{k},t)v_j(\mathbf{k}',t')\rangle = P(k,|t-t'|)\left(\delta_{ik} - \frac{k_ik_j}{k^2}\right)\delta(\mathbf{k}+\mathbf{k}') \tag{11}$$

We assume the simplest delta-correlated spectrum of this turbulence

$$P(k,|t-t'|) = P(k)\tau_{\rm c}\delta(t-t'), \tag{12}$$

where $\tau_{\rm c} = L_0/v_0$ is the correlation time of the neutral turbulence. Then for the correlator of magnetic fluctuations

$$\langle B_i(\mathbf{k},t)B_j(\mathbf{k}',t')\rangle = Q(k,t)\left(\delta_{ik} - \frac{k_ik_j}{k^2}\right)\delta(\mathbf{k}+\mathbf{k}') \tag{13}$$

we obtain the equation

$$\frac{1}{\tau_c}\frac{\partial Q(k,t)}{\partial t} = -\frac{2}{3}Q(k,t)\int P(q,t)d\mathbf{q} + k^2\int P(q)Q(p) \times\left[1-\frac{(\mathbf{kp})(\mathbf{kq})(\mathbf{pq})}{k^2p^2q^2}\right] - \frac{1}{3\pi\rho_i\mu_{in}\tau_c}k^2Q(k)\int Q(q)d\mathbf{q}\,, \quad (14)$$

where $\mathbf{p} = \mathbf{k} - \mathbf{q}$. The first term in the rhs describes the diffusion of the magnetic field due to stochastic motions with the coefficient $D_m \sim \langle v^2\rangle\tau_c$, the second term describes the magnetic line turning which are frozen in the turbulence. The last term, which exists only in the case of a partially ionized gas, provides an instability saturation. Therefore the stationary spectra of the excited magnetic fields for the case of ordinary MHD and a weakly ionized gas are determined by different nonlinear terms (processes). In our case the maximum magnetic field energy is concentrated near $L \sim L_{min}$, where $B^2_{max} \sim 4\pi\rho_i\mu_{in}v(L_{min})L_{min} \sim 10^{-6}-10^{-5}$ G for parameters of molecular clouds that corresponds with Zeeman measurements of magnetic field strength in molecular clouds (Crutcher, 1999) though some measurements give even higher values of B for dense cloud cores where the gas density is $>10^5$ cm^{-3}.

The magnetic field lines are strongly tangled on scales $L_{min} \ll L_0$ (spaghetti-like structure). If the characteristic scale of vortex containing the main energy of neutral gas motions equals $L_0 \simeq 10^{19}$ cm then the correlation length of magnetic fluctuations is $L_{min} \simeq 10^{13}$ cm. The spectrum of magnetic fluctuations in the case of low ionized medium is $B^2(L) \simeq B^2_{max}(L_{min}/L)^3$ which is completely different from the Kolmogorov spectrum (6).

We should emphasize that the magnetic field is not in equipartition with turbulent motions in this case. Their energy is much higher than the energy of the ionized component but smaller than the energy of the neutral gas turbulence:

$$\rho_i v_0^2 \ll \frac{B^2_{max}}{8\pi} \ll \rho_n v_0^2 \quad (15)$$

which is not surprising because the magnetic fluctuations are amplified by the neutral gas turbulent motions.

4. Kinetic Equation for Magnetized and Non-Magnetized Particles in a Random Magnetic Field

The kinetic equation describing particle propagation in these stochastic magnetic fields was derived by Dogiel et al. (1987). An analysis was performed separately for magnetized $r_L(\gamma) \ll L_{min}$ and non-magnetized $r_L(\gamma) \gg L_{min}$ particles. Here $r_L(\gamma)$ is the Larmor radius of a particle with gamma-factor γ. We start from the

Boltzmann equation for a particle distribution function f

$$\frac{\partial f}{\partial t} + \frac{d\mathbf{r}}{dt}\frac{\partial f}{\partial \mathbf{r}} + \frac{d\gamma}{dt}\frac{\partial f}{\partial \gamma} = 0. \tag{16}$$

For magnetized particles we have

$$\frac{d\mathbf{r}}{dt} = c\theta\mathbf{h}, \quad \frac{d\gamma}{dt} = \gamma\mathbf{v}(\mathbf{h}\nabla\mathbf{h}) - R. \tag{17}$$

Here $\mathbf{h} = \mathbf{B}/|\mathbf{B}|$, $\theta = \pm 1$ denotes particle propagation in both directions along magnetic field lines, and R describes the energy loss by a particle.

If we represent the distribution function as a sum of its average part F and its fluctuations δf, $f = F + \delta f$, then we obtain a diffusion-like equation for the function F

$$\frac{\partial F}{\partial t} = \nabla\Delta_{\mathrm{x}}\nabla F + \frac{\partial}{\partial\gamma}\left[\gamma\Delta_{\gamma}\frac{\partial}{\partial\gamma}(\gamma F) + kRF\right] \tag{18}$$

with the diffusion coefficient in the coordinate space in the form

$$\Delta_{\mathrm{x}} = c^2\int_{-\infty}^{t}\int_{-\infty}^{\infty}\langle\mathbf{h}(\mathbf{r},t)G(\mathbf{r},t \mid \mathbf{r}',t')\mathbf{h}(\mathbf{r}',t')d\mathbf{r}dt \tag{19}$$

determined by the structure of magnetic field line and therefore independent of particle energy. The diffusion in the energy space

$$\Delta_{\gamma} = \int_{-\infty}^{t}\int_{-\infty}^{\infty}\langle v_i v_j' G(\mathbf{r},t \mid \mathbf{r}',t')\nabla_{\nu}\nabla_{\mu}' h_{\nu}h_{\mu}' d\mathbf{r}dt \tag{20}$$

due to random electrical fields $\tilde{\mathbf{E}} = -1/c[\tilde{\mathbf{v}}\tilde{\mathbf{B}}]$. Here the brackets denote the averaging procedure and the Green function G is calculated from the equation

$$\frac{\partial G}{\partial t} + c\theta\nabla(\mathbf{h}G) = \delta(t-t')\delta(\mathbf{r}-\mathbf{r}') \tag{21}$$

To describe the motions of non-magnetized particles, one should use the equation

$$\frac{\partial f}{\partial t} + \boldsymbol{v}\nabla\frac{\partial f}{\partial \mathbf{r}} + e\tilde{\mathbf{E}}\frac{\partial f}{\partial \mathbf{p}} = 0. \tag{22}$$

Repeating the averaging procedure we obtain

$$\frac{\partial F}{\partial t} = \left(\frac{p^2}{mc}\right)D_{\mathrm{x}}\frac{1}{r^2}\frac{\partial}{\partial r}r^2\frac{\partial F}{\partial r} + \frac{1}{p^2}\frac{\partial}{\partial p}p^2 D_{\mathrm{p}}\frac{\partial F}{\partial p} \tag{23}$$

with the coefficients equal to

$$D_{\rm x} = \frac{m^2c^4}{6\nu_0}, \quad D_{\rm p} = \frac{2}{3}\frac{e^2}{c^2}\int_0^\infty \langle v^2\rangle_{\tau,\nu\tau}\langle B^2\rangle_{\tau,\nu\tau}d\tau. \tag{24}$$

due to scattering on magnetic fluctuations. Here the frequency of particle collisions with magnetic fluctuations is

$$\begin{aligned} \nu_0 &= e^2\int_0^\infty \langle B^2\rangle_{\tau,\nu\tau} \quad \text{and} \\ \langle B^2\rangle_{\tau,\nu\tau} &= \int_{-\infty}^{\infty} |B(k,\omega)|^2 \exp[i(\omega - \mathbf{k}\boldsymbol{v})\tau]\, d\omega d\mathbf{k}. \end{aligned} \tag{25}$$

From the analysis of these equations it follows that the spatial diffusion coefficient is constant for magnetized particles and increases as $\propto p^2$ for non-magnetized particles. On the other hand, the momentum diffusion coefficient is proportional to p^2 for magnetized particles and is constant in the "non-magnetized" energy range, i.e. only magnetized particles are accelerated by this mechanism. When the particles become non-magnetized, they quickly escape from the clouds.

Numerical estimates show that for a cloud with size $L_0 \sim 10^{19}$ cm the spatial diffusion coefficient is of the order of $\Delta_{\rm x} \sim 10^{23-24}$ cm^2 s^{-1}, i.e., is approximately four–five orders of magnitude smaller than the diffusion coefficient in the interstellar medium (Berezinskii et al., 1990). The characteristic time of stochastic particle acceleration is about $1/\Delta_\gamma \sim 10^{11}$ s. These estimations show that acceleration can be very effective in the clouds. The maximum energy of relativistic particles can be estimated from the condition $r_{\rm L}(\gamma_{\max}) \sim L_{\min}$ which gives

$$\gamma_{\max} \sim \frac{eB_{\max}L_{\min}}{mc^2}. \tag{26}$$

For a cloud with $L_0 = 10^{19}$ cm the maximum energy of accelerated protons is about 30 GeV.

5. Spectra of Accelerated Electrons and Protons in Clouds

Different factors can inject particles into the clouds for their further acceleration: sources near or inside the clouds, charged particles of the ionized component of the gas, cosmic rays penetrating from outside, and secondary particles generated in clouds. We shall briefly analyze the last two.

We shall seek a solution for the spectrum of charged particles inside a cloud of a radius R whose spectrum far from the cloud $F_\infty(\gamma)$ is known. Particle propagation outside the cloud is supposed to be described as diffusion with coefficient Δ_0. If

we introduce the function $w = \gamma F$ and the energy variable $\xi = \ln\gamma/\sqrt{\Delta_\gamma}$, the solution for the magnetized particles is

$$w(\xi, r) = \int_{-\infty}^{\infty} \frac{q\mu(s)}{q - [1 - sR\coth(sR)]} \frac{R}{r} \frac{\sinh(sr)}{\sinh(sR)} \exp(i\xi s)\, ds. \tag{27}$$

Here $q = \Delta_0/\Delta_x$ and $\mu(s)$ is the coefficient of Fourier transformation of the function

$$\mu_\infty(\xi) = \int_{-\infty}^{\infty} \mu(s) \exp(i\xi s)\, ds. \tag{28}$$

For the most favorable conditions the spectrum of magnetized particles inside clouds is

$$F_{\rm mg}(\gamma) = \frac{C_0}{\gamma} \exp\left[k\left(\frac{\alpha_{\rm i}}{\Delta_\gamma \gamma} - \frac{\alpha_{\rm br}}{\Delta_\gamma}\ln\gamma - \frac{\alpha_{\rm B}\gamma}{\Delta_\gamma}\right)\right], \tag{29}$$

where $\alpha_{\rm i}$, $\alpha_{\rm br}$, and $\alpha_{\rm B}$ are coefficients for ionization, bremsstrahlung, and magnetobremsstrahlung losses.

The solution for non-magnetized particles inside clouds is described as

$$F_{\rm nmg}(\gamma) = C_1 \gamma^{3/2} K_{1/4}\left(\frac{\sqrt{\beta}}{2}\gamma\right), \tag{30}$$

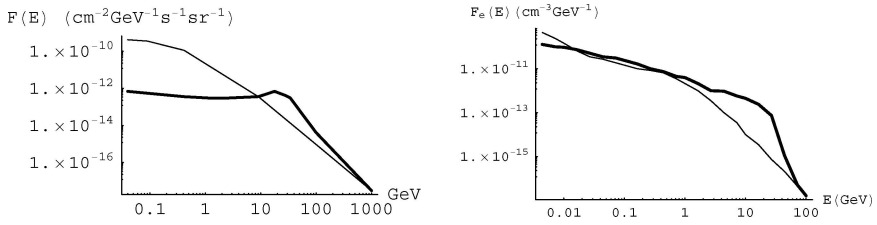
where $K_{1/4}$ is a modified Bessel function and

$$\beta = \frac{\pi^2 D_{\rm x}(mc^2)}{R^2 D_{\rm p}}. \tag{31}$$

This solution describes an exponential cut-off of the spectrum in the energy range of non-magnetized particles which turns into the intercloud spectrum F_∞ because non-magnetized particles freely penetrate and escape from the clouds.

For parameters: $L_0 = 10^{19}$ cm, $n_{\rm H} = 10^3$ cm^3, $B = 10^{-5}$ G, $\Delta_{\rm x} = 10^{24}$ cm^2 s^{-1}, and $\Delta_{\rm p} = 10^{-11}$ s^{-1} the spectrum of cosmic ray protons in the intercloud medium and its transformation due to acceleration and ionization loss inside clouds is shown in Figure 1. We see excess of protons in a rather narrow GeV range inside clouds. We note that the energy range of this excess depends strongly on parameters of the clouds.

High-energy electrons inside clouds are mainly secondary because of knock-on and $\pi^{\pm}$-decay processes. Their spectrum inside clouds is given in Figure 1b which also shows an excess above the interstellar spectrum in a very broad energy range.



a. Proton spectra b. Electron spectra

Figure 1. Spectra of protons (a) and electrons (b) in clouds (thick lines) and in the intercloud medium (thin lines).

6. Gamma-Ray and Radio Emission from Molecular Clouds

With these spectra of cosmic rays inside the clouds we can calculate a flux of gamma-ray emission from there. The results of calculations are shown in Figure 2 where the ratio of emissivity in the clouds $q_{\rm cl}(E)$ to that in the interstellar medium of the Galaxy $q_{\rm G}$ taken from Berezinskii et al. (1990) is shown by the solid curve. Molecular clouds can be observed as "sources" if their emissivity is higher than $q_{\rm G}(E)$, i.e., if $g_{\rm cl}/q_{\rm G} > 1$. We see that molecular clouds can be observed as sources of gamma-ray emission in a rather narrow energy range: from tens of GeV to several MeV. In the GeV energy range the excess is produced by high-energy protons and in the MeV region this excess is due to bremsstrahlung radiation of electrons.

The maximum energy of accelerated protons as a function of cloud size L_0 is $E_{\rm max} = 30(L_0/10^{19}\ {\rm cm})^{0.87}$ GeV, which means that the maximum energy of accelerated protons may extend to the TeV range for very large clouds.

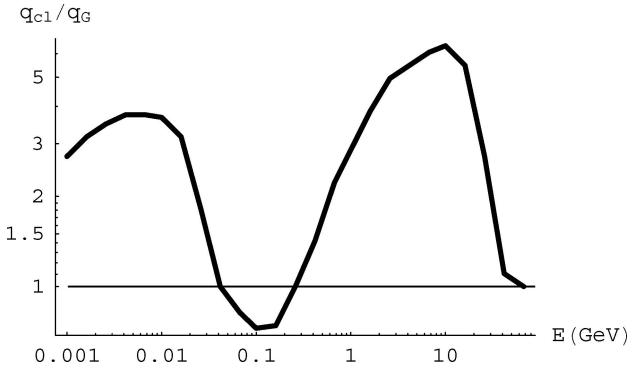


Figure 2. Ratio of the gamma-ray emissivity of molecular cloud ($L_0 = 10^{19}$ cm) to the gamma-ray emissivity in the interstellar medium, $q_{\rm cl}/q_{\rm G}$, as a function of the energy of gamma-ray photons.

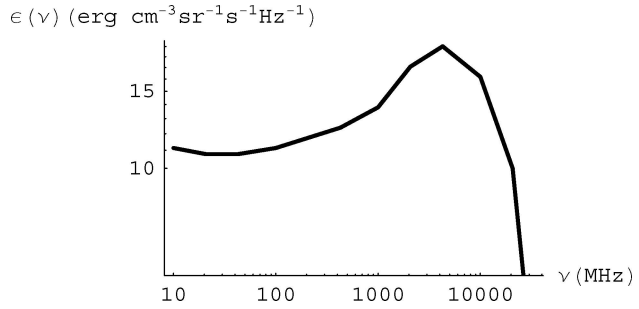


Figure 3. Spectrum of synchrotron radio emission for a cloud with size $L_0 = 10^{19}$ cm and magnetic field strength $B = 10^{-5}$ G.

The gamma-ray flux which for a cloud with $L_0 = 10^{19}$ cm is estimated to be $F_\gamma \sim 10^{35}$ erg s^{-1} for the energy of about several hundred MeV increases as

$$F_\gamma = 10^{35} \left(\frac{L_0}{10^{19} \text{ cm}} \right)^{1.25} \text{ erg s}^{-1}, \tag{32}$$

but for all that the peak of emission shifts to higher energies.

Therefore these clouds can be observed as gamma-ray sources with a variety of spectral characteristics.

The secondary electrons generate a specific synchrotron radio emission from clouds. Calculations of the radio flux for $L_0 = 10^{19}$ cm are shown in Figure 3. The spectrum is flat and is similar to the spectrum of thermal radio emission, but these high-energy electrons do not produce radio-lines in the spectrum.

7. Conclusion

It may be concluded from our model of particle acceleration in molecular clouds that molecular clouds, at least some of them, are counterparts of the unidentified sources. This acceleration provides a variety of gamma-ray sources with different energy ranges of emission, different spectral indices, different luminosity etc. The maximum energy of accelerated electrons is of the order several tens of GeV for a cloud with size of $\sim 10^{19}$ cm, but it can be much larger for very extended clouds with strong magnetic fields.

It is difficult now to give a reliable conclusion of whether this process is effective enough but fortunately the future GLAST experiment will be able to provide necessary information about gamma-ray emission from Galactic molecular clouds.

We can mention several observational results in favor of this model, which can easily be explained in the framework of our model:

– An excess of gamma-ray emission above 1 GeV observed in the direction of local molecular clouds (Digel et al., 2001). If so, the observed excess for $E > 1$ GeV of the diffuse gamma ray flux from the Disk (Hunter et al., 1997) can also be provided by emission of molecular clouds;
– There is also an excess of gamma-ray emission from the disk for energies below 30 MeV which cannot be explained in the frameworks of standard models (Strong et al., 2000). As we see from Figure 2, secondary electrons generate an excess of gamma-ray emission in this very region;
– Molecular clouds also generate a flux of secondary particles which can escape into the interstellar medium. A prediction of the model was that there should be an excess of positrons in GeV energy range in the spectrum of these particles. An excess was observed actually and as it was shown by Coutu et al. (1999) and Du Vernois et al. (2001) the data can be explained with the highest level of confidence if this excess is produced by molecular clouds.

References

Aharonian, F.A.: 2001, *SSRv* **99**, 187.
Berezinskii, V.S., Bulanov, S.V., Dogiel, V.A., Ginzburg, V.L. and Ptuskin, V.S.: 1990, in: V.L. Ginzburg (ed.), Astrophysics of Cosmic Rays, North Holland, Amsterdam.
Bignami, G.F. and Hermsen, W.: 1983, *ARAA* **21**, 67.
Bourke, T.L., Myers, P.C., Robinson, G. and Hyland, A.R.: 2001, *ApJ* **554**, 916.
Coutu, S., Barwick, S.W., Beatty, J.J., et al.: 1999, *Astroparticle Phys.* **11**, 429.
Crutcher, R.M.: 1999, *ApJ* **520**, 706.
Digel, S.W., Grenier, I.A., Hunter, S.D., Dame, T.M. and Thaddeus, P.: 2001, *ApJ* **555**, 12.
Dogiel, V.A., Gurevich, A.V., Istomin, Ya.N. and Zybin, K.P.: 1987, *MNRAS* **228**, 843.
Dogiel, V.A. and Sharov, G.S.: 1990, *A&A* **229**, 259.
DuVernois, M.A., Barwick, S.W., Beatty, J.J., et al.: 2001, *ApJ* **559**, 296.
Goldreich, P. and Sridnar, S.: 1995, *ApJ* **438**, 763.
Hartman, R.C., Bertsch, D.L., Bloom, S.D., et al.: 1999, *ApJS* **123**, 79.
Hunter, S.D., Bertsch, D.L., Catelli, J.R., et al.: 1997, *ApJ* **481**, 205.
Kolmogorov, A.N.: 1941, *Dokl. Akad. Nauk SSSR* **30**, 9.
Kraichnan, R.H. and Nagarajan, S.: 1967, *Phys. Fluids* **10**, 859.
Larson, R.B.: 1981, *MNRAS* **194**, 809.
Miyajgi, T., Bhattachrya, D. and Zych, A.E.: 2004, EGRET unidentified sources – the Spiral Arm Connection. *These Proceedings*.
Myers, P.C.: 1983, *ApJ* **270**, 105.
Romero, G.E., Benaglia, P. and Torres, D.F.: 1999, *A&A* **348**, 868.
Strong, A.W., Moskalenko, I.V. and Reimer, O.: 2000, *ApJ* **537**, 763.
Verma, M.K.: 1999, *Phys. Plasmas* **6**, 1455.
Zhang, L., Zhang, Y.L. and Cheng, K.S.: 2000, *A&A* **357**, 957.

METHANOL MASERS AS PRECURSORS OF GAMMA-RAY SOURCES

M. HOLLERAN and O.C. DE JAGER

Unit for Space Physics, School of Physics, North-West University, Potchefstroom Campus, Potchefstroom, South Africa; E-mail: fskmh@puk.ac.za

(Received 1 July 2004; accepted 27 August 2004)

Abstract. Methanol masers are known to be associated with regions of massive star formation. By studying the distribution of these masers with respect to unidentified EGRET sources, one may be able to identify regions of enhanced star formation leading to either supernova remnants and/or pulsars. In this study, we test for positional coincidences between class II methanol masers and EGRET sources and determine the statistical significance of these coincidences.

Keywords: methanol maser, massive star formation, supernova remnants, unidentified EGRET sources

1. Introduction

Masers in star formation regions (SFRs) most commonly arise from transitions of the molecules of methanol, hydroxyl and water (Caswell, 2002). While hydroxyl and water masers are often associated with UCHII regions, methanol masers are exclusively associated with a very young stage of massive star formation (MSF). The brightest class II methanol maser arises from the 5_1 to 6_0 A^+ transition of methanol, corresponding to a frequency 6.7 GHz (Sobolev et al., 1997). Since their discovery in 1991 by Menten, the list of 6.7 GHz methanol masers has accumulated from the contributions of various authors to a current total of 556 sources, as found in the general catalogue of Pestalozzi (2004).

Methanol masers occur in SFRs located inside molecular clouds. Figure 1 shows molecular clouds tracing the spiral arms of M51. Since it is known that molecular clouds are distributed in a similar manner in our Galaxy, the figure should give the reader an idea where methanol masers are located. These clouds contain baryonic material that provides a target for cosmic-rays, and hence we should expect to find unidentified EGRET sources (UnidS) in close proximity to them.

It is also known that dense molecular clouds may interact with a supernova shell emanating from a supernova remnant (SNR) (Combi et al., 1998) during the Sedov phase (Aharonian et al., 1994), when the shock front begins to decelerate. It has been suggested, at least in the case of the SNR W44, that relativistic brehmsstrahlung and inverse Compton scattering of electrons from the associated pulsar B1853+01 in molecular gas to the east of the cloud may account for the gamma-ray flux from this



Astrophysics and Space Science **297:** 213–221, 2005.
© Springer 2005

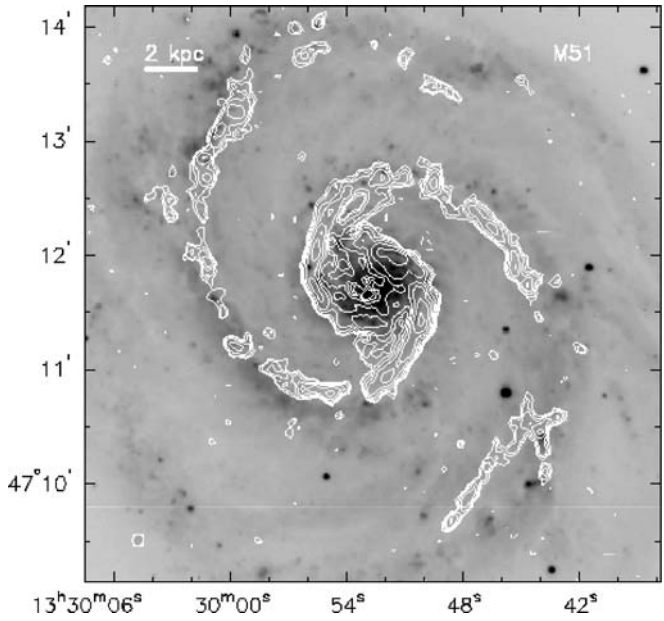


Figure 1. CO data from the BIMA survey for M51 overlaid on the spiral structure of M51 itself. (Blitz and Williams, 1999).

source (de Jager and Mastichiadis, 1997). It is possible that particles accelerated in the supersonic wind of massive stars can interact with UV photons in the stellar radiation field (Benaglia and Romero, 2003). Walker et al. (2003) argue that cold, dense clouds may be connected with the cosmological problem of dark matter, and that an unexplained gamma-ray flux from these objects may be a signature of dark matter. The authors also comment that the low mass ($10^{-4} M_{\odot}$) of isolated clouds makes them undetectable by EGRET due to a low photon flux above 100 MeV. A small number of methanol masers, and therefore massive stars, may very well be associated with isolated, low mass clouds (Holleran, 2002).

Previous studies of Sturner and Dermer (1995) and Yadigaroglu and Romani (1997) have investigated the association between SNRs and OB associations. Supernovae are generally regarded as potential triggers for the collapse of "hot cores" in molecular clouds, leading inexorably to star formation. The idea of star formation providing the stimulation for further star formation was first conceived in the notion of sequential star formation of Elmegreen and Lada (1977). (See Figure 2 for a graphical representation of sequential star formation.)

Yadigaroglu and Romani sought tracers of recent MSF using catalogues of OB associations, SNRs, young pulsars, HII regions and young open clusters to find counterparts for EGRET sources. In the present study we have set our sights on an earlier evolutionary stage of MSF to find if this association extends further back in time to stellar nurseries themselves.

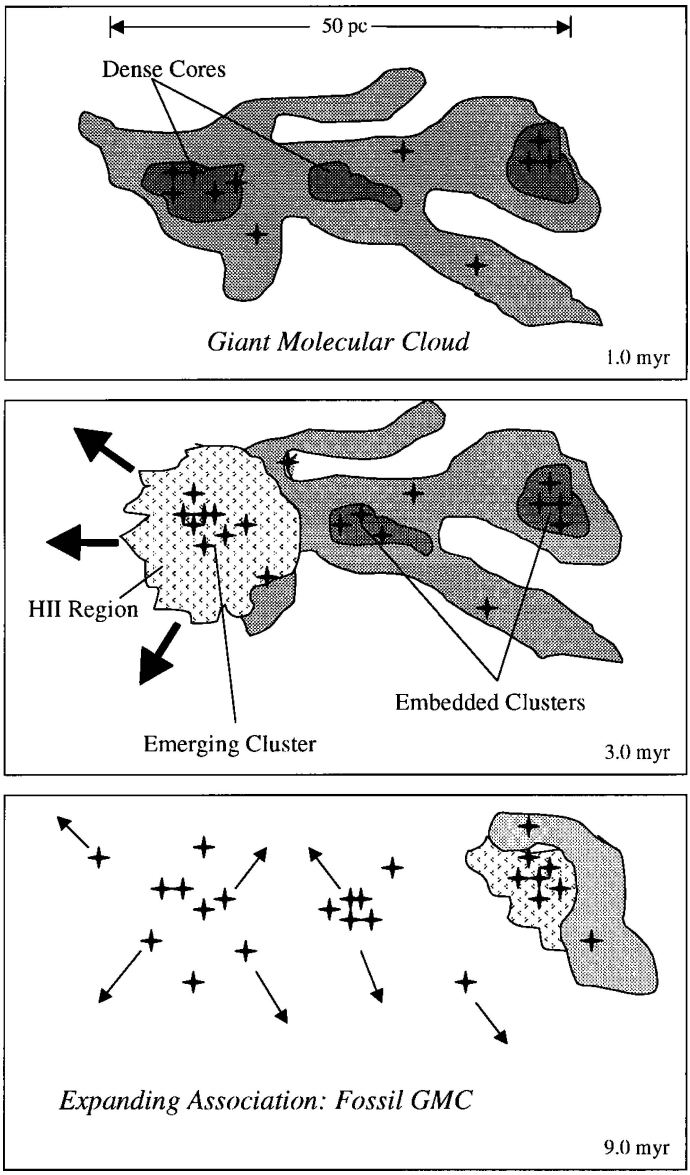


Figure 2. A representation of sequential star formation (Lada, 1999). The reader should imagine a scenario involving several of these environments evolving simultaneously.

Sturner and Dermer assigned a probability to the possible associations between UnidS and neighbouring SNRs. They concluded that the probability that this association was due to a chance alignment is $\leq 1/2200$. They then went further to examine possible mechanisms for gamma-ray production, but this subject

is not within the scope of this paper, and is covered by other authors in the proceedings.

In a study similar to this one, which involved 81 UnidS in the Galactic plane, a positional coincidence was found with 6 WR stars, 4 Of stars, 22 SNRs and 26 OB associations (Romero et al., 1999). The authors found a strong statistical correlation of $\sim 6\sigma$ for SNRs and $\sim 4\sigma$ for OB associations. A less compelling statistical significance of $\sim 3\sigma$ was found for WR and Of stars. In terms of pure chance associations for the 1° bin the values obtained were 8.3×10^{-3} for WR stars, 1.5×10^{-2} for Of stars, 1.2×10^{-5} for OB associations and 1.6×10^{-8} for SNRs. The authors also remarked on finding even lower chance probabilities for OB associations (9.8×10^{-6}) and SNRs (5.4×10^{-10}) in the 2° bin. A comparison with our results will be made in the results section of this paper.

Against the background of the large fraction of EGRET sources that are UnidS, with 90% of the sources at $|b| \leq 10^\circ$ awaiting identification, we find that a compelling positional coincidence appears to exist between some methanol masers and UnidS in the Galactic plane.

2. Catalogue Details

This study makes use of the GeV point source catalogue of Lamb and Macomb (1997), as well as new sources from Lamb and Macomb (1999), the 3rd EGRET catalogue of 100 MeV sources (Hartman et al., 1999), and the list of pulsars with EGRET counterparts that Kramer et al. (2003) obtained from the Parkes Multibeam Survey. From the GeV p.s. catalogue we have pruned away quasars and pulsars, and anything outside the Galactic plane ($|b| \leq 10^\circ$). In the case of the EGRET catalogue we have removed all sources outside the Galactic plane, as well as pulsars. We then compiled a list of pulsars with EGRET counterparts using the above-mentioned list in Kramer et al.

3. Statistical Study Method

The nature of this study was more of a "nearest-neighbour" search than a correlation or association test, although it was expected that some indication of a positional coincidence may be the result. The basic idea was to search for the nearest-neighbour (smallest angular separation) of each of the 28 GeV point sources against the 556 source methanol maser catalogue, the list of 10960 OB stars and the list of 107265 A–F type stars from the Hipparcos catalogue respectively. The null hypothesis (H_0) is simply that if the distribution of the angular separations (θ) for the methanol masers is the same as that for Hipparcos A–F type stars, then no positional coincidence exists between GeV point sources and methanol masers. If, however, the distributions were found to differ, then the test hypothesis (H_A) would be correct,

i.e. that a fraction of the unidentified GeV point sources would be positionally coincident with methanol masers.

As an alternate test hypotheses, the same test was done for 59 EGRET 100 MeV sources in the Galactic plane, as well as for 30 pulsar counterparts to EGRET sources. The probability for a chance alignment was then calculated for the 1° bin for the methanol masers. We also calculated the probability of a chance alignment had we used the Hipparcos OB stars for H_0 instead.

One advantage of using Hipparcos A–F type stars is that they yield an unbiased H_0. Sturner and Dermer assumed that nearest neighbours are randomly distributed about the EGRET sources, which neglects the spiral structure of the Galaxy.

A disadvantage of using the Hipparcos catalogue is that although it is the best available catalogue, it does not list all the main-sequence stars in our Galaxy. With astrometry on the 1 milliarcsecond (mas) level in the final Hipparcos catalogue, and an astrometric standard error of 0.7–0.9 mas (Perryman et al., 1997), it was an improvement over ground-based parallax measurements.[1] Hipparcos was not capable of resolving parallax angles out to the distances of several kpc that we typically find SNRs at. Furthermore, the 118218 catalogued stars form a very small sample of the Galactic population. Even the Tycho catalogue, which contains a far larger number of stars, albeit with a lower astrometric precision of 20–30 mas, does not come close to a complete list of stars in our Galaxy. The simple reality is that no catalogue does, and until GAIA completes its Galactic consensus after the planned launch in June 2010, creative approaches will have to be undertaken to circumvent this problem.

Some comments on the steps taken to provide accurate probability density functions (PDFs) are warranted at this point:

1. The lists of OB and A–F type stars extracted from the Hipparcos catalogue are more populated than the list of methanol masers, hence if one does not correct for bias due to the higher spatial densities, oversampling will be the result.
2. Bootstrapping (random sampling with replacement) of the data is necessary to smooth out fluctuations in the distribution plot and simultaneously push down the error margins so that they converge to their true value.

4. Results and Discussion

The distribution plots of the smallest angular separations can be seen in Figures 3–5. The distributions of the methanol masers and those of the Hipparcos OB stars are clearly different from the distributions of our null hypothesis, the Hipparcos A–F stars.

For $\sim$50% of the point sources of GeV emission we have a probability of 3×10^{-11} for the 1° methanol maser bin being due to a chance positional alignment. For $\sim$30% of the EGRET 100 MeV sources in the Galactic plane it is 6×10^{-12} for the 1° bin. The statistical significance of the positional coincidences

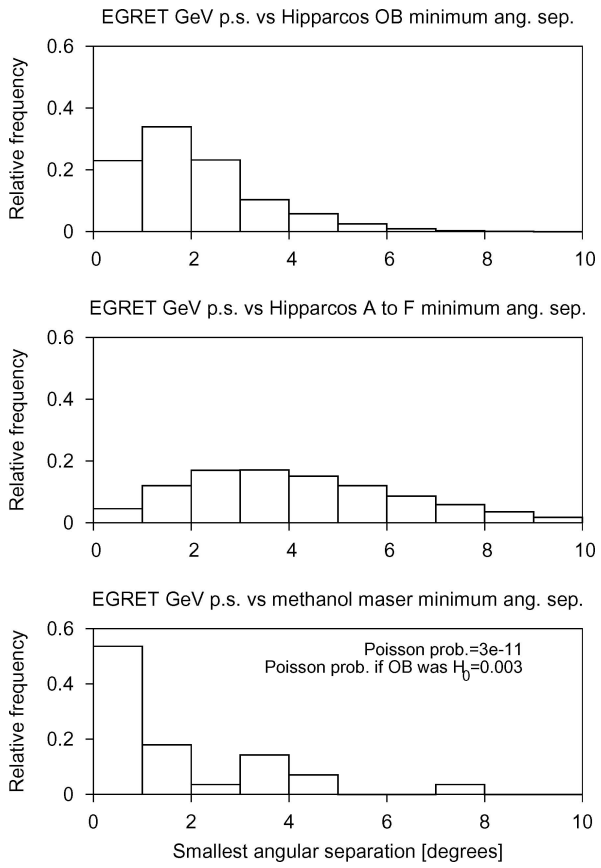


Figure 3. Distributions of smallest angular separations for GeV point sources.

of methanol masers and EGRET sources in the Galactic plane is even higher than what Romero et al. obtained for SNRs. This may point to interactions between supernova shocks and molecular gas in SFRs. It could also be that the processes related to MSF contribute to the observed gamma-ray flux from the relevant sources.

One interesting result is that the correlation of positional coincidences is higher for methanol masers than for OB stars. This is an unexpected result, and perhaps this suggests that regions of MSF render a contribution to the gamma-ray flux that is not negligible. It may also simply be that the interaction of supernova shocks with molecular gas is enhanced in these regions.

For the list of EGRET pulsar counterparts, we obtained a chance alignment probability of 8×10^{-6} for the 1° bin, which contains $\sim$40% of the 30 pulsars. Perhaps the scenario suggested by de Jager and Mastichiadis for W44 is not that uncommon.

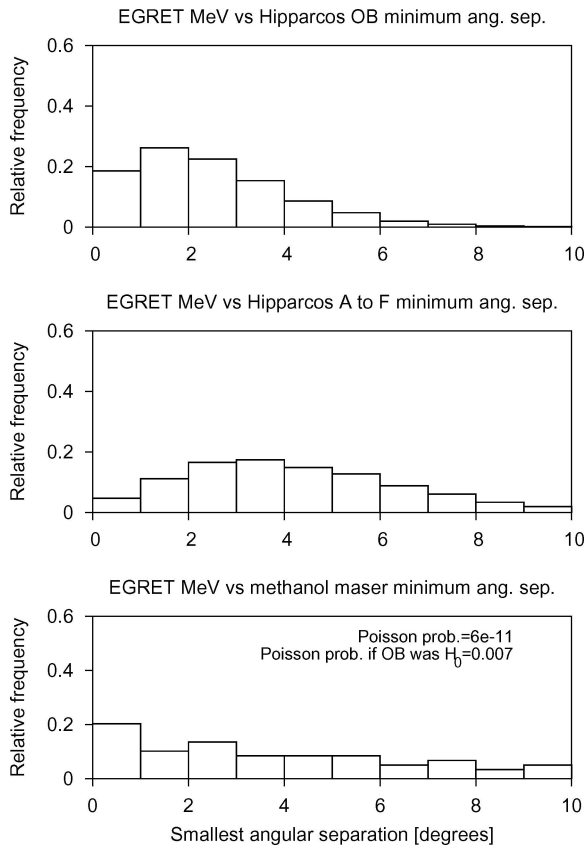


Figure 4. Distributions of smallest angular separations for EGRET 100 MeV point sources.

For the Hipparcos OB type stars we see a result similar to what Romero et al. obtained in the 2° bin. This may be due to some systematic effect of the EGRET data.

Furthermore, we obtained a mean angular separation of 2.5° for EGRET 100 MeV sources in the Galactic plane versus Hipparcos OB type stars, which is somewhat higher than the 1.3° we calculated from the offsets of Yadigaroglu and Romani (1997). This discrepancy is probably due to the fact that OB associations were used in that study, whereas the individual positions of OB stars were used in this analysis.

The distribution plots and the very small chance alignment probabilities point to a compelling positional coincidence for a fraction of EGRET sources in the Galactic plane and class II methanol masers. We have also shown that this positional coincidence exists for ∼40% of the EGRET pulsar counterparts. Since the ages of pulsars are known from their spin-down power, and the crossing-time for supernova shocks can be calculated, it would be useful to have a diagnostic tool to more

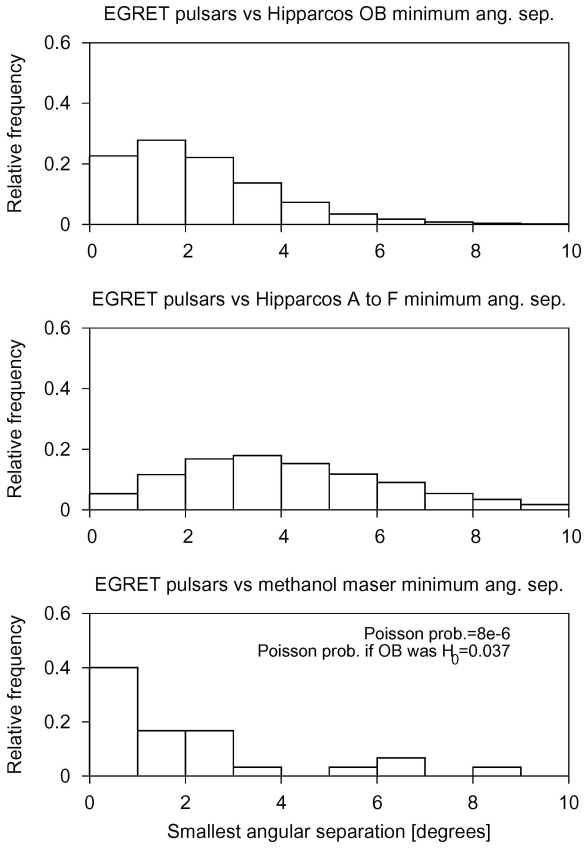


Figure 5. Distributions of smallest angular separations for EGRET pulsar counterparts.

accurately pinpoint when an association with a UnidS occurs and not just where. This could be done using the timescales for class 0 and class 1 spectral energy distributions (SEDs) from star formation theory.

Acknowledgements

We would like to thank the referee for a number of helpful suggestions. This research is funded by the National Research Foundation in South Africa and the Unit for Space Physics at North-West University, Potchefstroom campus, South Africa.

Note

1. The recent unresolved controversy over the distance determination to the Pleides cluster notwithstanding.

References

Aharonian, F.A., O'C. Drury, L. and Völk, H.J.: 1994, *A&A* **285**, 645.
Benaglia, P. and Romero, G.E.: 2003, *A&A* **399**, 1121.
Blitz, L. and Williams, J.P.: 1999, in: C.J. Lada and N.D. Kylafis (eds.), *The Origin of Stars and Planetary Systems*.
Caswell, J.L.: 2002, in: V. Migenes and M.J. Reid (eds.), *Cosmic Masers: From Protostars to Black-holes*, Vol. 1, pp. 1.
Combi, J.A., Romero, G.E. and Benaglia, P.: 1998, *A&A* **333**, L91.
de Jager, O.C. and Mastichiadis, A.: 1997, *ApJ* **482**, 874.
Elmegreen, B.G. and Lada, C.J.: 1977, *ApJ* **214**, 725.
Hartman et al.: 1999, *ApJS* **123**, 79.
Holleran, M.: 2002, MSc Thesis, Potchefstroom University.
Kramer et al.: 2003, *MNRAS* **342**, 1299.
Lada, C.J.: 1999, in: C.J. Lada and N.D. Kylafis (eds.), *The Origin of Stars and Planetary Systems*.
Lamb, R.C. and Macomb, D.J.: 1997, *ApJ* **488**, 872.
Lamb, R.C. and Macomb, D.J.: 1999, *Exploring the Universe Above 1GeV, Utah ICRC Proceedings*, **4**(2.4.21).
Perryman, M.A.C. et al.: 1997, *A&A* **323**, L49.
Pestalozzi, M.R.: 2004, PhD Thesis, Chalmers University of Technology.
Romero, G.E., Benaglia, P. and Torres, D.F.: 1999, *A&A* **348**, 868.
Sobolev, A.M., Cragg, D.M. and Godfrey, P.D.: 1997, *A&A* **324**, 211.
Sturner, S.J. and Dermer, C.D.: 1995, *A&A* **293L**, L17.
Walker, M., Mori, M. and Ohishi, M.: 2003, *ApJ* **589**(2), 810.
Yadigaroglu, I.-A. and Romani, R.W.: 1997, *ApJ* **476**, 347.

IDENTIFYING VARIABLE γ-RAY SOURCES THROUGH RADIO OBSERVATIONS

JOSEP M. PAREDES,[1] J. MARTÍ,[2] D.F. TORRES,[3] G.E. ROMERO,[4] J.A. COMBI,[2] V. BOSCH-RAMON[1] and J. GARCÍA-SÁNCHEZ[1]

[1]*Departament d'Astronomia i Meteorologia, Facultat de Física, Universitat de Barcelona, Av. Diagonal 647, 08028 Barcelona, Spain; E-mail: jmparedes@ub.edu*
[2]*Universidad de Jaén*
[3]*Lawrence Livermore National Laboratory*
[4]*Instituto Argentino de Radioastronomía, FCAGLP, Universidad Nacional de la Plata*

(Received 3 June 2004; accepted 6 July 2004)

Abstract. We present preliminary results of a campaign undertaken with different radio interferometers to observe a sample of the most variable unidentified EGRET sources. We expect to detect which of the possible counterparts of the γ-ray sources (any of the radio emitters in the field) varies in time with similar timescales as the γ-ray variation. If the γ-rays are produced in a jet-like source, as we have modelled theoretically, synchrotron emission is also expected at radio wavelengths. Such radio emission should appear variable in time and correlated with the γ-ray variability.

Keywords: γ-ray sources, radio sources, microquasars, microblazars

JEL codes: D24, L60, 047

1. Introduction

The Third EGRET Catalog (Hartman et al., 1999) lists 271 point sources. About two thirds of them have no conclusive counterparts at lower frequencies. Even worse, 40 of them do not show any positional coincidence (within the 95% EGRET contour) with possible γ-ray emitting objects known in our galaxy (Romero et al., 1999; Torres et al., 2001). In order to understand the origin of all these unidentified detections, their variability status is of fundamental importance. Classic known models for γ-ray sources in our galaxy would produce non-variable sources during the timescale of observations. This is the case of pulsars (Thompson, 2001), supernova remnants in interaction with molecular clouds (Torres et al., 2003) and microquasar jets in interaction with high-density interstellar medium (Bosch-Ramon et al., 2004a). Alternatively, if some of the sources are produced by compact objects, such as isolated magnetized black holes (Punsly et al., 2000) or microquasars (Paredes et al., 2000), high levels of flux variability can be expected.

According to recent theoretical models, the observed variable γ-ray emission could be associated with galactic compact objects such as X-ray binary systems and



Astrophysics and Space Science **297:** 223–233, 2005.
© Springer 2005

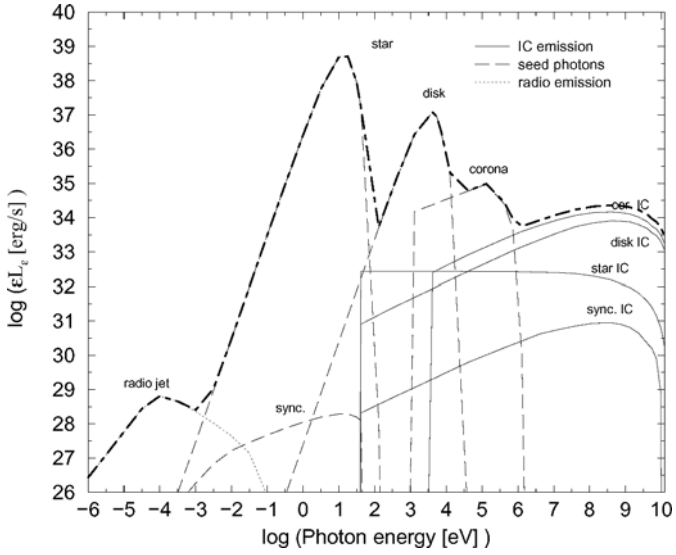


Figure 1. Spectral energy distribution of a typical microquasar emitting up to EGRET energies (Bosch-Ramon et al., 2004b).

isolated black holes. A model considers the so-called microquasar and microblazar X-ray binaries, in which the optical/UV photons from an optical star are inverse Compton up-scattered by relativistic electrons in the jets emanating from the accretion disc of a black hole/neutron star companion. Variability is then naturally induced by the precession of the jets, eccentricity of the orbit and/or variable accretion rates. Moreover, it should be also detectable at radio wavelengths where synchrotron radio photons are produced by the same relativistic electrons. A semi-analytical model (see Figure 1) of this and other processes in a microquasar scenario is currently being developed by us, with the purpose of understanding the spectral energy distribution of EGRET sources across the whole electromagnetic spectrum (Bosch-Ramon et al., 2004b). The non-thermal spectral energy distribution has two peaks, one from the synchrotron jet emission, at radio-IR energies, and other from comptonization of seed photons (stellar, coronal, disc and/or synchrotron photons), at MeV–GeV energies. The amplitude of the radio variation would be somewhere between 10%, as observed in the microquasar LS5039/3EG J1824–1514 (Ribó, 2002; Ribó et al., 2004), and one order of magnitude, as predicted in some microblazar models (Romero et al., 2002; Kaufman-Bernadó et al., 2002). The timescales could range between the orbital and the precession periods typical of X-ray binaries (from days to a few months).

Another possibility for a variable galactic γ-ray source is that of an isolated black hole. It has been suggested that such objects could radiate γ-rays due to spherical accretion from the interstellar medium (Dermer, 1997) or thanks to a charged magnetosphere (Punsly, 1998; Punsly et al., 2000). Finally, yet another possibility

is the γ-ray emission produced in the disc of a binary system formed by a pulsar and a massive star. The pulsar accelerates charged particles in its magnetosphere, which ultimately collide against the accretion disc formed by the matter from the companion star. This collision yields hadronic (pp) interactions, and variability naturally results as a consequence of the formation and loss of the accretion disc along the binary orbit. A situation like this was explored in the case of A0535+26 by Romero et al. (2001), and was found able to explain the observations for 3EG 0542+2610. In this case, however, the γ-ray emission is mainly hadronic, and we do not expect intense radio counterparts. All the previous models could produce variability indices in agreement with those determined by Torres et al. (2001).

Identifying the most variable sources – and particularly those which simultaneously show steep spectral indices at γ-rays – is bound to yield very interesting discoveries. In this work, we report preliminary results of a search for variable radio counterparts of γ-ray variable EGRET sources using different radio interferometers.

2. Selected Sources to be Studied

From the original set of unidentified EGRET sources at $|b| \leq 10^\circ$, a large fraction $\sim$50% (40 sources) remains without any known possible galactic counterpart (Romero et al., 1999). Since it is most unlikely that all these sources are extragalactic, they must encompass a population of variable galactic γ-ray sources yet to be discovered.

To quantify the variability status of these sources, we use the I index, which establishes how variable a source is with respect to the pulsar population. The reader is referred to Torres et al. (2001a,b) for details and comparisons with other variability estimators proposed in the literature. Sources with $I > 2.5$ are already 3σ away from the statistical variability of pulsars, and we can be confident that its variability status might be indicative of its ultimate nature. Selected EGRET sources that, not being in positional coincidence with any known plausible galactic counterpart, are most likely variable are listed in Table I. There, we give their 3EG name, their galactic coordinates, the error in their position, in degrees (assumed to be the 95% confidence contours given by the 3EG catalog), their gamma spectral index, Γ (such that the photon distribution is given by $N(E) \propto E^{-\Gamma}$), their EGRET flux and the index of variability I. In a first step, we included only those with smaller EGRET position error and/or without hour angle limitation for the interferometer to be used. Their range of variability index is 2.61–5.33, which can be considered as very significant. The typical size of the EGRET 95% confidence contours is $\sim 0.6^\circ$. It is also worth noticing that the mean value of the EGRET spectral indices is quite steep, steeper than the steepest pulsar spectrum known.

The sample in Table I was initially investigated for possible radio counterparts (although no information on source variability could be gathered at this stage). We

TABLE I

Unidentified 3EG sources without known possible galactic counterparts and visible from WSRT

γ-Source (3EG J)	l (°)	b (°)	$\Delta\theta$	Γ	$\langle F_\gamma \rangle \times 10^{-8}$ photons/(cm^2 s)	I
1735–1500	10.73	9.22	0.77	3.24 ± 0.47	19.0	8.86
1746–1001	16.34	9.64	0.76	2.55 ± 0.18	29.7	3.19
1810–1032	18.81	4.23	0.39	2.29 ± 0.16	31.5	2.61
1812–1316	16.70	2.39	0.39	2.29 ± 0.11	43.0	2.60
1828+0142	31.90	5.78	0.55	2.76 ± 0.39	30.8	5.33
1834–2803	5.92	−8.97	0.52	2.62 ± 0.20	17.9	2.83
1904–1124	24.22	−8.12	0.50	2.60 ± 0.21	22.5	2.91
1928+1733	52.91	0.07	0.75	2.23 ± 0.32	38.6	3.99
2035+4441	83.17	2.50	0.54	2.08 ± 0.26	39.1	3.35

constructed radio maps at the 20 cm wavelength using data from the NRAO VLA Sky Survey[1] (NVSS; Condon et al., 1998) for each of these EGRET detections and classified the radio sources within each EGRET confidence contours. There are between 7 and 30 possible radio counterparts (mostly uncatalogued) in each case that need to be monitored in order to establish which of them – if any – is varying in time.

The γ-ray variability of all our targets clearly points out to a compact object as the origin of the high-energy emission. 3EG J1828+0142 has a previously known possible extragalactic counterpart although outside the 95% EGRET confidence contour. It is an active galactic nucleus referred to as J1826+0149 by Sowards-Emmerd et al. (2003), who report it to be a flat spectrum radio quasar. Halpern et al. (2003) also found this association plausible. However, an alternative galactic model also exists for this source (Punsly et al., 2000; Butt et al., 2002; Combi et al., 2001; Bosch-Ramon et al., 2004c). In another case, 3EG J1735−1500, a radiogalaxy within the location error box has been proposed as a counterpart, although alternative candidates exist as well (Combi et al., 2003; Bosch-Ramon et al., 2004c).

3. Radio Observations

In order to identify the origin of our selected γ-ray sources, we have undertaken a programme of radio observations using different interferometers. Most of our data has been obtained with the Westerbork Synthesis Radio Telescope (WSRT) at the 21 cm wavelength. In addition, the very large array (VLA) of the NRAO was also used for an initial test of our identification strategy. With this approach, we expect to detect which of the possible counterparts of the γ-ray sources (any of the radio emitters in the field) varies in time with similar timescales to that

of the γ-ray variation. If the γ-ray emission is produced in a jet-like source, for instance, synchrotron emission leading to radio detections, will also show a time dependence. Flux densities of at least $\sim$1 mJy are expected by analogy with radio emitting X-ray binaries. The current status of our identification project is described in the following sections.

3.1. WSRT MULTI-EPOCH OBSERVATIONS

The WSRT observations were conducted so far for two of the targets in Table I, namely 3EG J1928+1733 and 3EG J2035+441. We observed them on 15 June 2003 (WSRT1) and 20 September (WSRT2), thus with a time separation of 3 months. In both cases, we observed at the 21 cm wavelength, with a 20 MHz bandwidth, a correlator setup of 64 channels, 4 polarizations and 8 bands. The array of antennas was always in the same configuration in order to facilitate variability studies, with 72 m of separation between the dishes of the two movable pairs of antennae. Calibrator sources were observed 1 h before and after each observing run, following the standard procedures at the WSRT.

The first observing epoch was devoted to obtain a 21 cm mosaicked full track of 12 h duration for each EGRET field with the idea of using it as a template for future variability studies. The different pointings, seven per EGRET field, were arranged with a hexagonal packing covering a field of $\sim 2^\circ$ squared. In most cases, this should be enough to fully cover the 95% confidence contour of the EGRET position. The pointings were corrected for the primary beam response before being combined into a mosaic. This process increases significantly the noise in the map far from the central pointing positions. The sky positions covered by more than one pointing were weighted with the inverse square of the rms noise before averaging and combining them. The resulting mosaic has a typical rms noise of $\sim$0.2 mJy beam^{-1} over most of its solid angle. A circular restoring beam of $45''$ was used in order to make easier the comparison with NVSS images.

During the second observing epoch, the two EGRET fields were mosaicked during a single 12 h track with the same instrumental setup of the first epoch. Sensitivity with the mosaicked snapshots was, of course, lower but well enough to control the variability of already known NVSS sources, as well as to look for new fainter radio variables in the field (up to $\sim$1 mJy level). Subtraction maps between the two epochs, in the image plane were found to be a suitable tool to look for possible variables in the field.

3.2. VLA OBSERVATIONS

A Director Discretionary Time (DDT) observation was also conducted at the VLA as a test of our identification strategy for this project. The target was 3EG J1812–1316, whose field we mosaicked with four pointings only during a single observing epoch (10 February 2003). The VLA data were taken at the 20 cm wavelength in D

configuration with the idea of comparing them directly with the NVSS images. The corresponding results are discussed below together with those from the WSRT.

4. Results

Examples of our WSRT mosaics are presented in Figures 2 and 3. Both correspond to our first observing epoch and have been computed using uniform weight. Many radio sources are detected in each WSRT mosaic ($\sim$100) up to a brightness limit of 0.5 mJy.

The comparison of our two WSRT epochs revealed initially no strongly flaring sources, at least in timescales of months. In Tables II and III, we list the WSRT positions and flux densities of the possible radio variables detected (six in each field) as measured with the IMFIT task of the AIPS package. Some of the variable candidates reported here, with $\leq$10% amplitude, are barely above the uncertainty in absolute flux calibration and further observations are required to confirm them. In spite of this, the comparison of our WSRT maps with the NVSS has actually revealed remarkable cases of apparent radio transient, or flaring. At least one radio

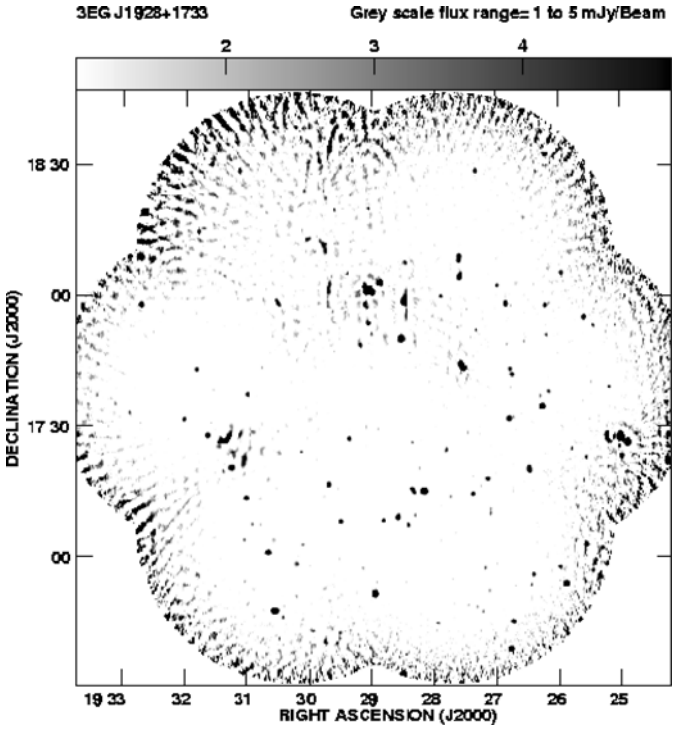


Figure 2. WSRT mosaic of the 3EG J1928+1733 field at 21 cm taken on 15 June 2003, the first of our two WSRT observing epochs. A circular restoring beam of 45″ has been used for easy comparison with the NVSS.

TABLE II
Possible variable radio sources in the 3EG J1928+1733 field

RA (2000) (h min s)	DEC (2000) (° ′ ″)	NVSS (mJy)	WSRT1 (mJy)	WSRT2 (mJy)
19 27 35.56 ± 0.03	+18 04 38.2 ± 0.6	38.1 ± 2.1	30.8 ±0.8	25.6 ±1.1
19 28 09.95 ± 0.01	+17 15 17.4 ± 0.1	55.0 ± 1.7	62.8 ± 0.6	61.0 ± 0.8
19 30 31.40 ± 0.07[a]	+17 58 14.4 ± 0.7	5.2 ± 0.6	14.6 ± 0.6	22.8 ± 1.0
19 31 00.91 ± 0.03*	+17 13 30.7 ± 0.5	2.5 ± 0.5	13.3 ± 0.5	14.3 ± 0.8
19 32 00.90 ± 0.05*	+17 31 44.4 ± 0.8	<1.2	7.3 ± 0.5	7.0 ± 0.8
19 30 59.85 ± 0.04*	+17 37 32.7 ± 0.6	<1.2	9.0 ± 0.5	7.2 ± 0.7

The most reliable variables are marked with (*).
[a]Extended object. Apparent variability possibly affected by strong primary beam correction.

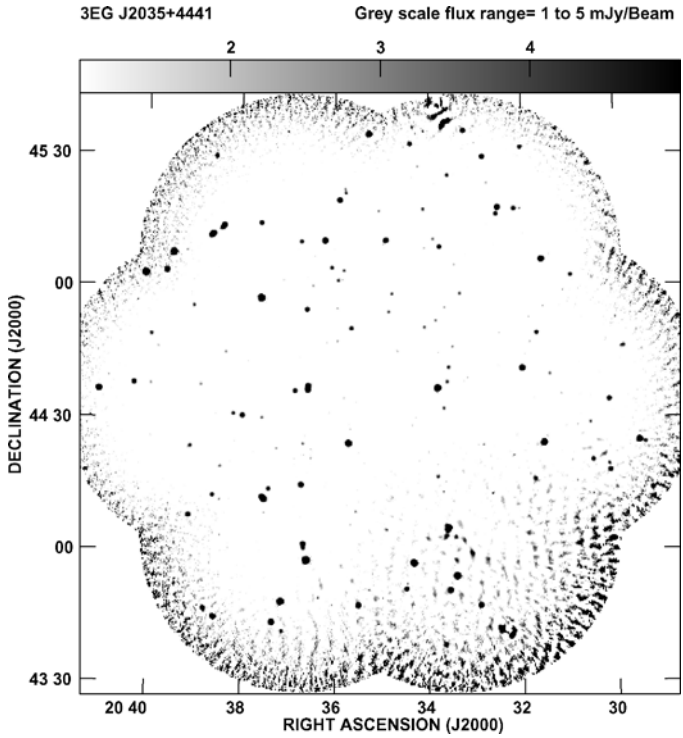


Figure 3. WSRT mosaic of the 3EG J2035+4441 field at 21 cm taken also on 15 June 2003. Nearly 100 radio sources are detected in this image, but only a few of them display possible evidence of variability. A circular restoring beam of 45″ has been used as well.

transient source, in timescales of years, is present among our variable candidates in both EGRET fields. These interesting objects are marked with an asterisk in Tables II and III, where the corresponding NVSS flux density at the 20 cm wavelength is also included (upper limits are 3σ). In addition, we illustrate them as well in Figures 4

TABLE III
Possible variable radio sources in the 3EG J2035+4441 field

RA (2000) (h min s)	DEC (2000) (° ′ ″)	NVSS (mJy)	WSRT1 (mJy)	WSRT2 (mJy)
20 37 31.42 ± 0.01	+44 11 35.8 ± 0.1	91.6 ± 3.3	92.5 ± 0.4	87.5 ± 0.7
20 36 34.34 ± 0.01[a]	+44 36 53.6 ± 0.2	80.6 ± 3.0	87.3 ± 0.7	79.1 ± 0.7
20 36 04.26 ± 0.05*	+45 03 52.8 ± 0.5	<1.4	7.2 ± 0.3	7.9 ± 0.5
20 39 55.62 ± 0.12	+44 37 38.9 ± 1.2	<1.4	2.3 ± 0.3	2.0 ± 0.4
20 30 57.85 ± 0.03	+45 02 14.1 ± 0.3	7.1 ± 0.6	8.3 ± 0.3	9.0 ± 0.5
20 37 02.85 ± 0.25	+44 57 29.3 ± 3.2	<1.4	<0.6	2.2 ± 0.5

The most reliable variables are marked with (*).
[a]Double source. Position of brighter component given.

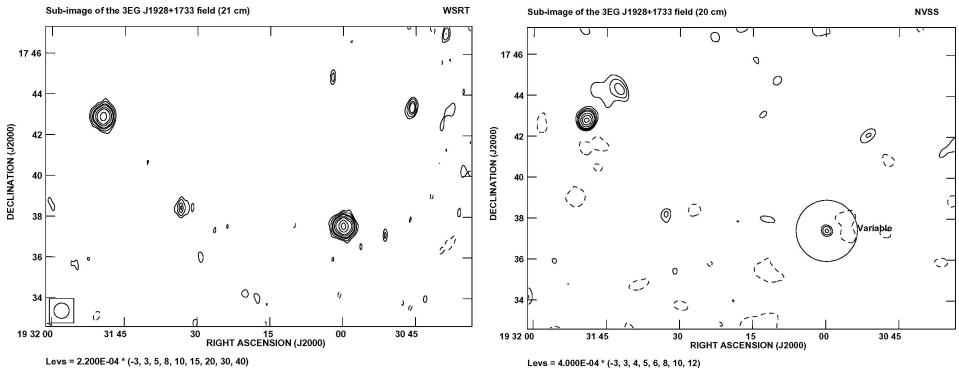


Figure 4. Example of a clearly compact variable radio source discovered when comparing our 3EG J1928+1733 mosaic (left panel) with the NVSS (right panel). The proposed variable source, indicated with a circle, appeared significantly fainter a few years before our WSRT observations.

and 5. The small wavelength difference between the WSRT and the NVSS is not likely to affect the reality of the proposed radio transient sources for physically plausible spectral indices.

The comparison with the NVSS has been also very useful to identify radio variable candidates in our single epoch VLA observations of 3EG J1812–1316, again in timescales of years. The results are presented in Table IV together with the NVSS data. Two of the sources in the field, also marked with an asterisk, appear as reliable variable radio sources. It is important to mention here that our VLA data was obtained in the same D configuration of the array as the NVSS, hence comparison is straightforward.

Multiwavelength follow-up observations (X-ray, infrared, optical, and eventually VLBI) of these so-detected confident candidates can ultimately yield to the discovery of new microquasars or other γ-ray–emitting galactic compact objects. We have initially inspected both the Digitized Sky Survey (DSS) and other databases

TABLE IV
Possible variable radio sources in the 3EG J1812–1316 field

RA (2000) (h min s)	DEC (2000) (° ′ ″)	NVSS (mJy)	VLA/DDT (mJy)
18 13 52.65 ± 0.13*	−13 30 11.8 ± 3.5	6.4 ± 0.5	10.4 ± 1.7
18 14 32.83 ± 0.06	−13 30 37.4 ± 1.8	13.7 ± 1.1	18.9 ± 1.6
18 14 26.88 ± 0.06*	−13 20 18.6 ± 1.8	12.0 ± 0.6	23.2 ± 1.8

The most reliable variables are marked with (*).

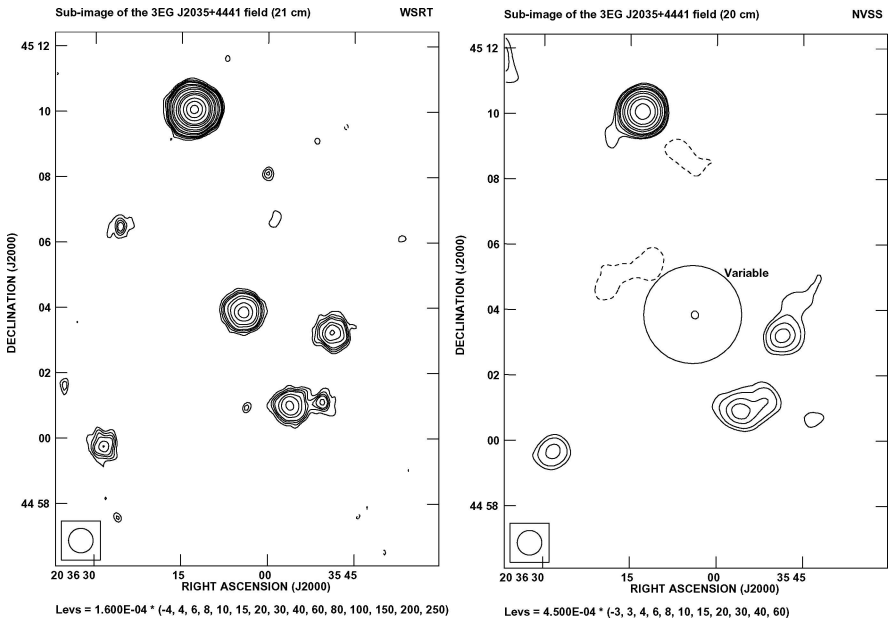


Figure 5. Example of a clearly variable and compact radio source discovered inside de 95% confidence contour of the unidentified EGRET source 3EG J2035+4441. The left panel is a zoomed region of a WSRT mosaic of the field as obtained by us on 15 June 2003 at 21 cm. The right panel is the same region of the sky as it appeared in the NVSS in 1995. The proposed variable source, indicated with a circle, was practically undetectable some years ago.

(e.g. 2MASS) looking for possible counterparts of our discovered radio variables. The strong absorption in the galactic plane at optical wavelengths makes the search for an optical counterpart very difficult. In the infrared, the 2MASS has evidence of a few sources having $K \sim 15$ that could be consistent with some of our $\pm 1''$ radio positions. However, a confirmation with deep K-band images is strongly necessary specially in cases where the 2MASS revealed no clear infrared source and a proposal for this goal has been recently submitted to the Calar Alto 3.5 m telescope in Spain. To determine the nature of the candidates, either galactic or extragalactic, infrared spectroscopy studies on the near infrared counterparts will be performed.

Similarly, the most interesting radio variable candidates have been proposed for Chandra observations in the X-ray band.

Acknowledgements

The Westerbork Synthesis Radio Telescope is operated by the ASTRON (The Netherlands Foundation for Research in Astronomy) with support from The Netherlands Foundation for Scientific Research NWO. J.M.P., V.B.-R. and J.M. acknowledge partial support by DGI of the Ministerio de Ciencia y Tecnología (Spain) under grant AYA-2001-3092, as well as additional support from the European Regional Development Fund (ERDF/FEDER). During this work, V.B.-R. has been supported by the DGI of the Ministerio de Ciencia y Tecnología (Spain) under the fellowship FP-2001-2699. J.M. is also supported by the Plan Andaluz de Investigación (Spain) under project FQM322. The work of D.F.T. was performed under the auspices of the US DOE (NNSA), by UC's LLNL under contract no. W-7405-Eng-48. G.E.R. is supported by Fundación Antorchas and the Argentine Agencies CONICET and ANPCyT. This research has benefited from a cooperation agreement supported by Fundación Antorchas.

Note

1. The National Radio Astronomy Observatory is a facility of the National Science Foundation operated under cooperative agreement by Associated Universities, Inc.

References

Bosch-Ramon, V., Aharonian, F.A. and Paredes, J.M.: 2004a, *A&A*, [astro-ph/0411508], in press.
Bosch-Ramon, V., Romero, G.E. and Paredes, J.M.: 2004b, *A&A* **429**, 267.
Bosch-Ramon, V., Paredes, J.M., Romero, G.E. and Torres, D.F.: 2004c, in: Proceedings of the Fifth Microquasar Workshop, Beijing.
Butt, Y., Torres, D.F., Romero, G.E. et al.: 2002, in: Ph. Durouchoux, Y. Fuchs and J. Rodríguez (eds.), *Proceedings of the 4th Microquasar Workshop, Cargese*, France, May 2002 [astro-ph/0206132].
Combi, J.A., Romero, G.E., Paredes, J.M., Torres, D.F. and Ribó, M.: 2003, *ApJ* **588**, 731.
Combi, J.A., Romero, G.E., Torres, D.F. and Punsly, B.: 2001, *ESA* Special Publications, **459**, 235.
Condon, J.J., Cotton, W.D., Greisen, E.W. et al.: 1998, *AJ* **115**, 1693.
Dermer, C.D.: 1997, in: *Proceedings of the Fourth Compton Symposium*, AIP, New York, p. 1275.
Halpern, J.P., Eracleous, M. and Mattox, J.R.: 2003, *ApJ* **125**, 572.
Hartman, R.C., Bertsch, D.L., Bloom, S.D. et al.: 1999, *ApJS* **123**, 79.
Kaufman-Bernadó, M.M., Romero, G.E. and Mirabel, I.F.: 2002, *A&A* **385**, L10.
Mattox, J.R., Hartman, R.C. and Reimer, O.: 2001, *ApJS* **135**, 155.
Paredes, J.M., Martí, J., Ribó, M. and Massi, M.: 2000, *Science* **288**, 2340.
Punsly, B.: 1998, *ApJ* **498**, 440.
Punsly, B., Romero, G.E., Torres, D.F. and Combi, J.A.: 2000, *A&A* **364**, 552.

Ribó, M.: 2002, PhD Thesis, Universitat de Barcelona.
Ribó, M., García-Sánchez, J., Paredes, J.M. and Martí, J.: 2004, *A&A*, manuscript in preparation.
Romero, G.E., Benaglia, P. and Torres, D.F., 1999, *A&A* **348**, 868.
Romero, G.E., Kaufman-Bernadó, M.M., Combi, J. and Torres, D.F.: 2001, *A&A* **376**, 599.
Romero, G.E., Kaufman-Bernadó, M.M. and Mirabel, I.F.: 2002, *A&A* **393**, L61.
Sowards-Emmerd, D., Romani, R.W. and Michelson, P.F.: 2003, *ApJ* **590**, 109.
Thompson, D.J.: 2001, in: F.A. Aharonian and H. J. Völk (eds.), AIP, vol. 558, p. 103.
Torres, D.F., Romero, G.E., Combi, J.A. et al.: 2001a, *A&A* **370**, 468.
Torres, D.F., Pessah, M.E. and Romero, G.E.: 2001b, *Astron. Nach.* **322**, 223.
Torres, D.F., Romero, G.E., Dame, T.M., Combi, J.A. and Butt, Y.M.: 2003, *Phys. Rep.* **382**(6), 303.

REVEALING THE NATURE OF THE OBSCURED HIGH MASS X-RAY BINARY IGR J16318-4848*

SYLVAIN CHATY and PHILIPPE FILLIATRE

Université Paris 7 Denis-Diderot, 2 Place Jussieu, Paris Cedex 05, & Service d'Astrophysique, CEA-Saclay, France; E-mail: chaty@cea.fr

(Received 4 June 2004; accepted 6 September 2004)

Abstract. The X-ray source IGR J16318-4848 was the first source discovered by INTEGRAL on January 29, 2003. The high energy spectrum exhibits such a high column density that the source is undetectable in X-rays below 2 keV. On February 23–25, 2003 we triggered a Target of Opportunity (ToO) Program using the EMMI and SOFI instruments on the New Technology Telescope of the European Southern Observatory (La Silla) to get optical and near-infrared (NIR) observations. We discovered the optical counterpart, and confirmed the already proposed candidate in the NIR. NIR spectroscopy revealed a large amount of emission lines, including forbidden iron lines and P-Cygni profiles, showing a strong similarity with CI Cam, another strongly absorbed source. Together with the spectral energy distribution (SED), these data point to a high luminosity, high temperature source, with an intrinsic absorption greater than the interstellar absorption, but two orders of magnitude below the X-ray absorption. All these observations show that IGR J16318-4848 is a high mass X-ray binary (HMXB) at a distance between 0.9 and 6.2 kpc, the mass donor being an early-type star, probably a sgB[e] star, surrounded by a dense and absorbing circumstellar material. This would make the second HMXB with a sgB[e] star as the mass donor after CI Cam.

Other sources, discovered by INTEGRAL near IGR J16318-4848 in the direction of the Norma arm, present the same characteristics, at least in X-rays. Such sources may represent a different evolutionary state of X-ray binaries previously undetected with the lower energy space telescopes; if it is so, a new class of strongly absorbed X-ray binaries is being unveiled by INTEGRAL. Out of the 15 sources present in this region, only one might be associated with an unidentified EGRET source: IGR J16393-4643. Therefore these obscured INTEGRAL sources do not seem to be powerful high energy ($E > 100$ MeV) emitters.

Keywords: stars: circumstellar matter, emission-line, Be–X-rays: binaries, IGR J16318-4848

1. Introduction

1.1. Discovery of IGR J16318–4848

IGR J16318-4848 was the first new source discovered by the INTEGRAL IBIS/ISGRI imager (Ubertini et al., 2003; Lebrun et al., 2003). The source was detected on January 29, 2003 in the energy band 15–40 keV with a mean 20–50 keV

*Based on observations collected at the European Southern Observatory, Chile (proposal ESO N° 70.D-0340).

Astrophysics and Space Science **297:** 235–244, 2005.
© Springer 2005

flux of 6×10^{11} erg cm^{-2} s^{-1}, 0.5° south from the galactic equator (Courvoisier et al., 2003). The source was thereafter regularly observed for two months. No X-ray counterpart could be found in the ROSAT All Sky Survey (Voges et al., 1999). The source was observed by XMM-Newton on February 10, 2003, which detected a single X-ray source within the INTEGRAL error box using the EPIC PN and MOS cameras (Strüder et al., 2001; Turner et al., 2001), giving the most precise position to date: $\alpha = 16^{\rm h}31^{\rm m}48\overset{\rm s}{.}6$, $\delta = -48°49'00''$ with a $4''$ error box (Schartel et al., 2003). X-ray spectroscopy revealed a very high absorption column density: $N_{\rm H} > 10^{24}$ cm^{-2} (Matt and Guainazzi, 2003; Walter et al., 2003, 2004), which renders the source invisible below 2 keV. This amount of absorption is unusual in Galactic sources. This could explain the non detection by ROSAT, although the source was discovered at a similar flux level in archival ASCA observations in 1994 (Murakami et al., 2003) on both GIS and SIS instruments (between 0.4 and 10 keV). Relatively bright and highly absorbed sources like IGR J16318-4848 could have escaped detection in past X-ray surveys and could still contribute significantly to the Galactic hard X-ray background in the 10–200 keV band. Based on the broad high-energy spectral and variability characteristics, Walter et al. (2004) suggest that IGR J16318-4848 is an X-ray binary, the low temperature and presence of cutoff at low energy suggesting that the compact object is a neutron star.

The high column density prompted counterpart research in near-infrared (NIR): within the EPIC error box, a possible counterpart was proposed by Foschini et al. (2003) using the Two Micron All Sky Survey (2MASS) with the following magnitudes: $J = 10.2$, $H = 8.6$, $K_{\rm s} = 7.6$ with an uncertainty of ± 0.3 mag. On the other hand, no radio emission at the position of the source was detected with a 1σ upper limit of 0.1 mJy both at 4.8 and 8.6 GHz (Walter et al., 2003).

1.2. Our observations

In the course of a Target of Opportunity (ToO) program at the European Southern Observatory (ESO) dedicated to look for counterparts of high energy sources newly discovered by satellites including INTEGRAL (PI S. Chaty), we carried out on February 23–25, 2003 photometric observations in the optical and NIR, and spectroscopic observations in the NIR with EMMI and SOFI instruments on ESO/NTT. The goals were to search for likely counterparts within the EPIC error box, to get informations about the environment and the nature of the source, especially about the mass donor.

In the following, we describe briefly in Section 2 our observations, report our main results on astrometry, photometry, spectral energy distribution, absorption and temperature estimates of the most likely candidate. We also summarize our results on spectral lines, distance to the source, and conclude on its nature and the nature of its components. In Section 3 we discuss the possibility of IGR J16318-4848 being the prototype of a new class of obscured binary sources, and look for associations

between these obscured INTEGRAL sources and unidentified gamma-ray sources. The reader should consult Filliatre and Chaty (2004) for more details.

2. Observations and Results

The source IGR J16318-4848 was the first source discovered by INTEGRAL. In the course of a ToO program using the NTT telescope, we performed photometric and spectroscopic observations less than one month after its discovery in the optical and NIR domains. We list here the main results:

- We discovered the optical counterpart and confirmed an already proposed NIR candidate (see Walter et al., 2003), by performing an independent astrometry for this candidate, giving the following position for the candidate: $\alpha = 16^{\rm h}31^{\rm m}48\overset{\rm s}{.}3$, $\delta = -48^{\circ}49'01''$. The optical/NIR images are shown in Figures 1 and 2.
- We obtained photometric measurements for the R, I and J bands, and got flux upper limits for B and V, flux lower limits for H and $K_{\rm s}$: $Bb > 25.4 \pm 1$, $V > 21.1 \pm 0.1$, $R = 17.72 \pm 0.12$,$I = 16.05 \pm 0.54$, $J = 10.33 \pm 0.14$, $H < 10.35 \pm 0.15$ and $K_{\rm s} < 9.13 \pm 0.10$.
- By fitting the optical/NIR magnitudes of IGR J16318-4848 and other stars in the field of view, we derived the absorption towards the candidate along the line of sight: $A_{\rm v} \sim 17.4$ magnitudes, greater than interstellar (11.8 mag, see Figure 3) but two orders of magnitude lower than in X-rays.
- With the continua of our GBF (Grism Blue Filter) and GRF (Grism Red Filter) spectra, our photometric measurements and with X-ray, radio (Walter et al.,

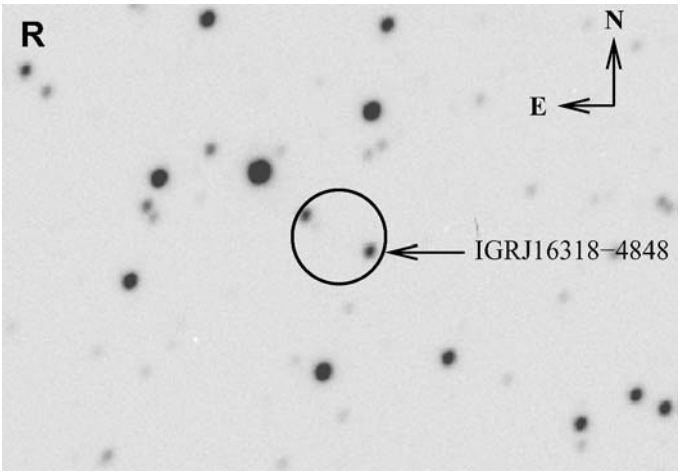


Figure 1. EMMI *R* band image of the field of view of IGR J16318-4848. We overplot the XMM error box of 4″. North is up, east is left. The scale is given by the error box. The most likely candidate is at the south-west border of the circle as indicated by the arrow.

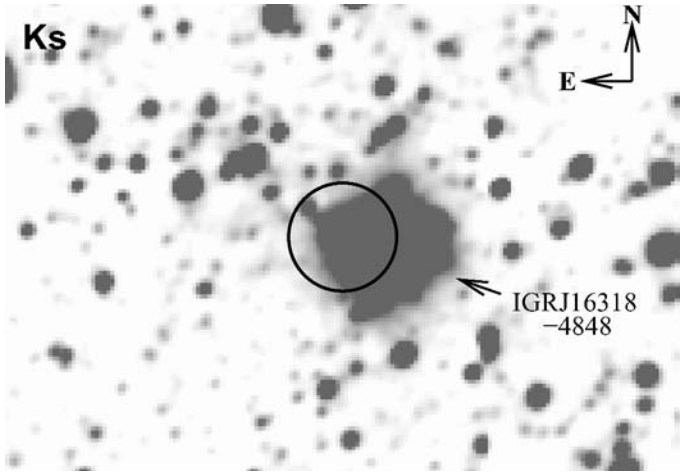


Figure 2. K_s band image of the same field than in Figure 1.

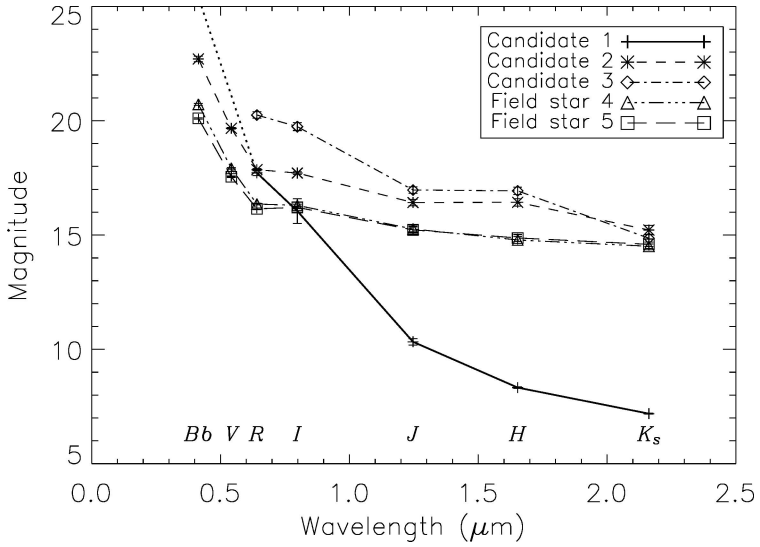


Figure 3. Magnitudes of IGR J16318-4848 (called here candidate 1) and field stars versus the wavelengths. This plot shows the unusual colours of the candidate, mostly due to the fact that the absorption along the line of sight is much stronger towards the candidate ($A_v \sim 17.4$ magnitudes) than towards the other stars of the field of view ($A_v \sim 11.8$ magnitudes).

2003) and archival 2MASS[1] and IRAS[2] data, we constructed a SED, shown in Figure 4, covering 10 decades in wavelength.

– By fitting the SED with an absorbed black body, we derived that the companion star must be a high luminosity ($\log(L/L_\star) > 4$), high temperature (above 10 000 K) star.

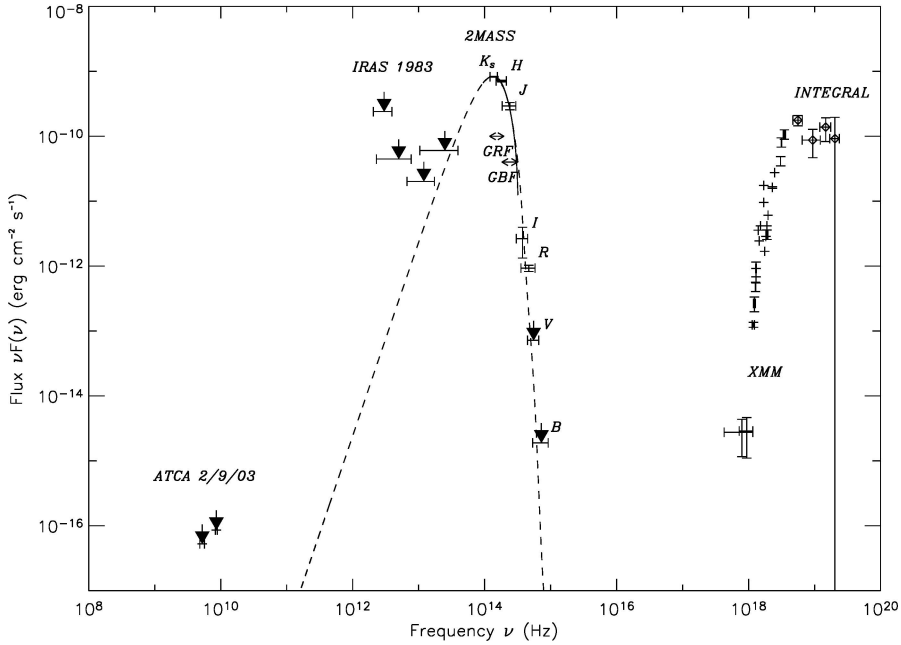


Figure 4. Observed SED of IGR J16318-4848 in $(\nu,\ \nu F(\nu))$ units, including the results of our photometry, our rescaled continuum GBF and GRF spectra, and literature data. The B and V data are upper limits only. The dashed curve corresponds to an absorbed black body, representing well the data. The results of INTEGRAL, XMM, IRAS and ATCA are also shown.

- According to the correlation between X-ray and radio emission in low/hard state black hole binaries proposed in Gallo et al. (2003), and given the XMM flux and absorption in the 2–10 keV band (Matt and Guainazzi, 2003), a radio flux of 43 ± 30 mJy is expected, more than one order of magnitude above the upper limit given by ATCA (Walter et al., 2004). This is a hint that the compact object is a neutron star instead of a black hole.
- The 0.95–2.52 μm NIR spectra, shown in Figures 5–7, are highly unusual, very rich in emission lines (we identified 72 emission lines), including forbidden iron lines and P-Cygni profiles. The lines in the spectrum show no cosmological redshift, confirming that the object is galactic.
- Eighty percent of these lines have been detected in CI Cam, suggesting a similar nature.
- These spectra favor the existence of a highly complex, stratified and dense circumstellar environment, with stellar wind or envelope.
- Study of the spectral lines, of the SED and of the color-magnitude HR diagram (CMD) suggest a sgB[e] star so the system would be a HMXB, probably hosting a neutron star, like CI Cam (Clark et al., 1999). This HMXB hosting a sgB[e] star is the most likely hypothesis; it would then be the second case after CI Cam.

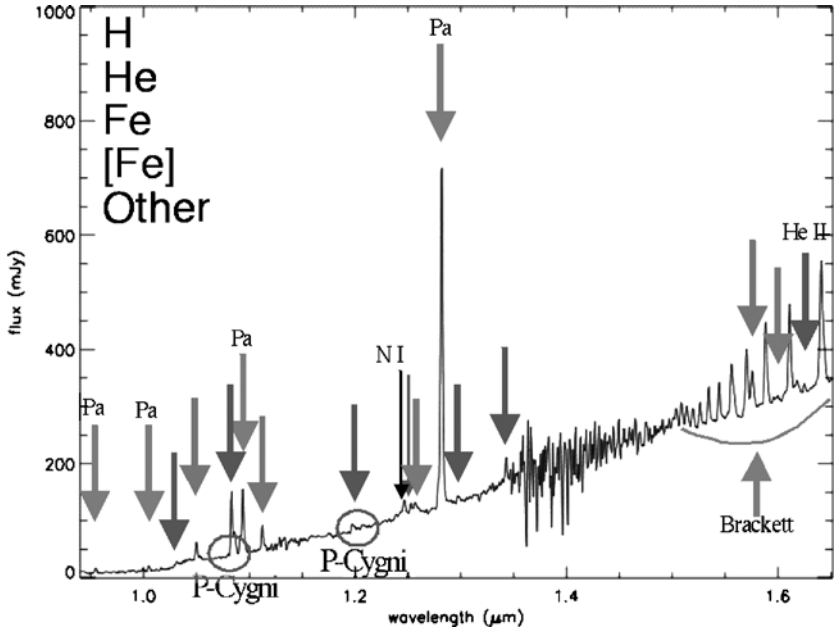


Figure 5. NIR GBF spectrum (0.95–1.65 μm).

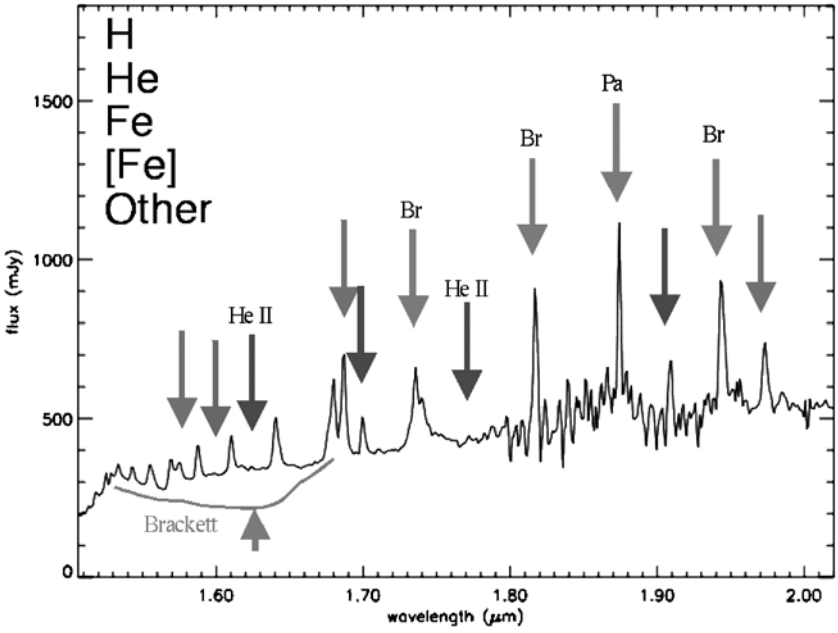


Figure 6. NIR GRF spectrum (1.5–2.05 μm).

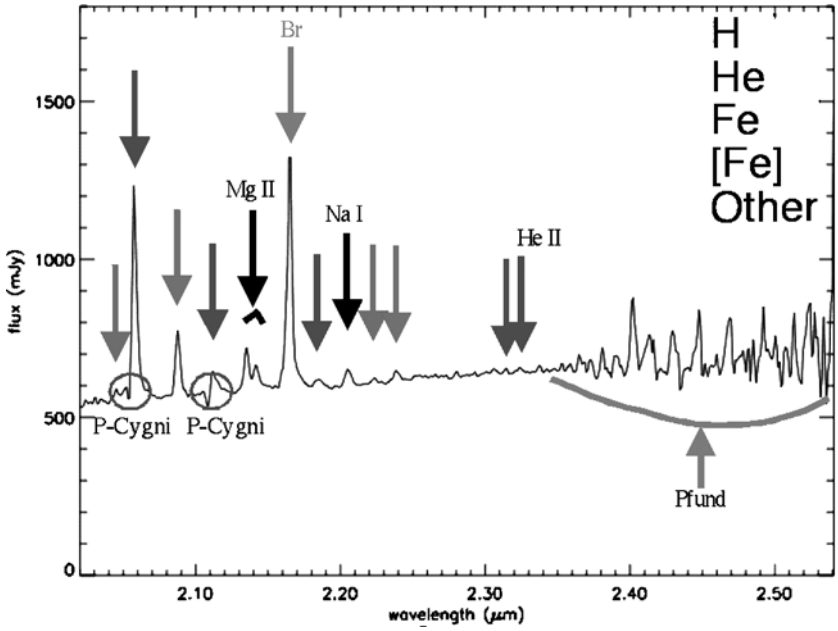


Figure 7. NIR spectrum (2.0–2.55 μm).

– The type of the companion star is consistent with the position on the CMD, computed for various absorption values and distances (see Figure 8).
– The distance of the source, estimated from the SED radius/distance fit of the companion star, assuming a sgB[e] star, is constrained between 0.9 and 6.2 kpc.

Complementary observations are needed in order to confirm our results, among them we propose the following.

– High resolution NIR spectroscopy, if possible extended to optical, in order to:
  - extend the SED in the optical to directly see a NIR excess;
  - check if the similarity with CI Cam observed in the NIR is still valid in the optical; however this will be difficult because of the absorption; and
  - improve our results concerning P-Cygni profiles, and line broadening.
– Long term follow-up spectroscopy and photometry, in order to:
  - seek for line variability;
  - seek for a periodic behavior to infer the orbital elements.
– simultaneous multi-wavelength observations, in order to better understand the nature and geometry of the system.

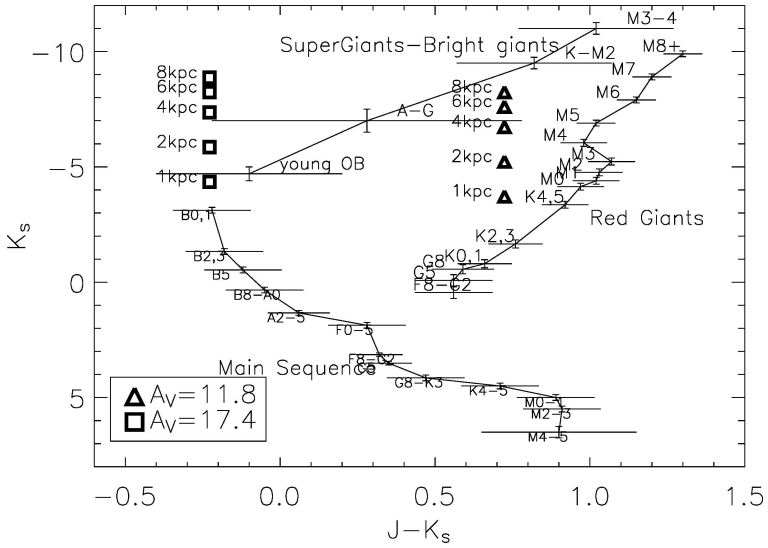


Figure 8. Position on the colour-magnitude HR diagram computed from template stars of Ruelas-Mayorga (1991), for distances from 1 to 8 kpc, and for two absorption values: $A_v = 17.4$ and $A_v = 11.8$. The low absorption value is compatible with a distant red supergiant, or a close red giant. The high absorption case is compatible with an early-type supergiant, an OB or a B, provided that the distance is not greater than 4 kpc.

3. Discussion

3.1. Are we facing a new class of obscured binaries?

This source shows many unusual features, the first being its strong intrinsic absorption. Interestingly, among the ten sources that INTEGRAL has discovered near this source, in the line of sight of the Norma arm of our Galaxy, this feature is common (at least in the X-rays), to the three sources discussed by Revnivtsev (2003): IGR J16318-4848, IGR J16320-4751 and IGR J16358-4726, although the N_H column density is lower by an order of magnitude in the two latter systems (Rodríguez et al., 2003; Patel et al., 2004; see also Walter et al., 2004). A clear identification for the optical/NIR counterpart has been done only for IGR J16318-4848, and the type of the mass donor, as inferred from our study, has been considered up to now as very rare. There is therefore the possibility that INTEGRAL, with the discovery of IGR J16318-4848, has unveiled a new class of obscured high energy binaries.

3.2. Is there a link with unidentified gamma-ray sources?

If these sources really constitute a new class, it is interesting to see if they could be candidates for unidentified gamma-ray sources. We therefore looked for possible

associations between these obscured INTEGRAL sources and EGRET sources by cross-correlating these catalogues. We found that out of the fifteen INTEGRAL sources present in or near the Norma arm region, only IGR J16393-4643 is well inside the circle containing the same solid angle as the 95% confidence contour of the unidentified EGRET source 3EG J1639-4702 (for this possible association see Combi et al., 2004). IGR J16393-4643 is indeed at 0.332° of the EGRET source 3EG J1639-4702 (error box radius 0.560°). IGR J16318-4848 is located at 2.157° of the closest EGRET source 3EG J1639-4702 (error box radius 0.560°). Therefore these obscured INTEGRAL sources do not seem to be powerful high-energy ($E > 100$ MeV) emitters, and this might be due to the presence of matter surrounding the compact object, as evidenced by the high level of absorption.

It is also interesting to point out that if we extrapolate the INTEGRAL spectrum to higher energies, the source would have been nearly at the limit of sensitivity with EGRET, but then would be easily detected by AGILE and GLAST, respectively one and two orders of magnitude more sensitive than EGRET. However, we have to be extremely cautious by doing this, since the INTEGRAL spectrum of IGR J16318-4848 is very crude at energies higher than 50 keV, and most of all because we do not know the shape of its spectrum at energies higher than 100 keV.

To conclude, IGR J16318-4848 seems to be the prototype of a new class of obscured high energy binaries, which will deserve much attention in the future, since they might help us to understand the evolution of high-energy binary systems.

Acknowledgements

SC is thankful to the ESO panel who understood the utility of multi-wavelength ToO programmes to reveal the nature of high-energy sources, and to the ESO staff (especially Malvina Billeres), who conducted the observations. SC is also grateful to the anonymous referee for a careful reading of the manuscript, and for his/her suggestion of adding a discussion on the link between these obscured sources and unidentified gamma-ray sources.

Notes

1. http://irsa.ipac.caltech.edu.
2. http://irsa.ipac.caltech.edu/IRASdocs/iras.html.

References

Clark, J.S., Steele, I.A., Fender, R.P. and Coe, M.J.: 1999, *A&A* **348**, 888.

Combi, J.A., Ribó, M., Mirabel, I.F. and Sugizaki, M.: 2004, *A&A* **422**, 1031.

Courvoisier, T.J.-L., Walter, R., Rodríguez, J., Bouchet, L. and Lutovinov, A.A.: 2003, *IAU Circ.* 8063.

Filliatre, P. and Chaty, S.: 2004, *ApJ* **616**, 469.
Foschini, L., Rodríguez, J. and Walter, R.: 2003, *IAU Circ*. 8076.
Gallo, E., Fender, R.P. and Pooley, G.G.: 2003, *MNRAS* **344**, 60.
Lebrun, F., Leray, J.P. and Lavocat, P. et al. 2003, *A&A* **411**, L141.
Matt, G. and Guainazzi, M.: 2003, *MNRAS* **341**, L13.
Murakami, H., Dotani, T. and Wijnands, R.: 2003, *IAU Circ*. 8070.
Patel, S.K. et al.: 2004, *ApJ* **602**, L45.
Revnivtsev, M.G.: 2003, *Astron. Lett.* **29**, 644.
Rodríguez, J., Tomsick, J.A., Foschini, L., Walter, R., Goldwurm, A., Corbel, S. and Kaaret, P.: 2003, *A&A* **407**, 41L.
Ruelas-Mayorga, R.A.: 1991, *RevMexAA* **22**, 27.
Schartel, N., Ehle, M., and Breitfellner, M. et al.: 2003, *IAU Circ*., 8072.
Strüder, L., Briel, U., and Dennerl, K. et al.: 2001, *A&A* **365**, L18.
Turner, M.J.L., Abbey, A., and Arnaud, M. et al.: 2001, *A&A* **365**, L27.
Ubertini, P., Lebrun, F., and Di Cocco, G. et al.: 2003, *A&A* **411**, L131.
Voges, W. et al.: 1999, *A&A* **349**, 389.
Walter, R., Rodríguez, J., Foschini, L., de Plaa, J., Corbel, S., Courvoisier, T.J.-L., den Hartog, P.R., Lebrun, F., Parmar, A.N., Tomsick, J.A., and Ubertini, P.: 2003, *A&A* **411**, L427.
Walter, R., Courvoisier, T.J.-L., Foschini, L., Lebrun, F., Lund, N., Parmar, A.N., Rodríguez, J., Tomsick, J.A. and Ubertini, P.: 2004, The 5th INTEGRAL Workshop, The Integral Universe, February 16–20, 2004, in press.

STATUS AND FIRST RESULTS OF THE MAGIC TELESCOPE

JUAN CORTINA (for the MAGIC collaboration)
Institut de Fisica d'Altes Energies, Universitat Autònoma de Barcelona, Bellaterra 08190, Spain;
E-mail: cortina@ifae.es

(Received 4 June 2004; accepted 1 September 2004)

Abstract. The 17 m Major Atmospheric Gamma Imaging Cherenkov (MAGIC) telescope for gamma-ray astronomy between 30 and 300 GeV started operations in its final configuration in October 2003 and is currently well into its calibration phase. Here I report on its present status and its first gamma-ray source detections.

Keywords: very-high-energy gamma-ray, Cherenkov telescope, MAGIC

1. Introduction

The Major Atmospheric Gamma Imaging Cherenkov (MAGIC) Telescope was designed in 1998 (Barrio et al., 1998) with the main goal of being the Imaging Atmospheric Cherenkov Telescope (IACT) with the lowest possible gamma-energy threshold. It was based on the experience acquired with the first generation of Cherenkov telescopes and intended to incorporate a large number of technological improvements.

There was a clear-case motivation to head for the low-energy threshold: there was a well-populated sky-map of sources detected by EGRET (but more than half of them still unidentified due to poor angular resolution) around 10 GeV in contrast to the handful of sources observed by the existing IACTs above 300 GeV. The main idea was to cover the unexplored energy gap with an IACT. These detectors provide much larger effective areas (around 4×10^4 m^2) than satellite detectors, better angular resolution (ranging from 0.2° close to the threshold down to 0.1° at higher energies), acceptable energy resolution (going down from 30% at the threshold energy to less than 20% above 100 GeV) and a well-tested capability to separate gamma-rays from other backgrounds.

From the purely experimental point of view, covering that gap with IACTs could allow:

– to study the mechanisms which cut-off the spectrum of several of the EGRET sources precisely in this energy gap and to explain why they were not detected by the first generation of IACTs above 300 GeV;
– to study all the EGRET sources with a much higher flux sensitivity and angular resolution and hence, identify the EGRET unidentified sources;

© Springer 2005

– to eventually discover a plethora of new sources (Barrio et al., 1998), since for most of known sources the energy spectrum follows a soft index power-law and therefore they should exhibit a much higher flux at lower energies.

Several innovative technical solutions started being worked out as early as in (Lorenz et al., 1995) and, since then the R&D has not stopped. During this time, several options were discussed such as the convenience of a single very large IACT incorporating the latest technological developments or a solution based on an array of somewhat smaller conventional telescopes. A cost-and-physics comparison led to the conclusion that a single very large diameter IACT would be cheaper and would allow us to cope better with the prime goal of reducing the threshold as much as possible. We were nevertheless aware that the single large telescope choice had some drawbacks: a less efficient background rejection, a somewhat worse sensitivity at higher energies and a somewhat poorer angular and energy resolution than a system of telescopes.

Nevertheless, we deem that these drawbacks are offset by the exploratory character of our telescope. From an instrumental point of view, this is a telescope whose main intention is to bring the Imagining Cherenkov Technique below 100 GeV and from the astrophysical point of view it intends to go as deep as possible into the unexplored gap and get as close in energy as possible to the range explored by EGRET.

2. Description and Status of the Telescope

MAGIC is a large and light-weight Cherenkov telescope, which incorporates a large number of technical innovations. It is located at the Roque de los Muchachos Observatory (ORM) at 2200 m a.s.l. (28.8° north, 17.9° west) on the Canary island of La Palma.

2.1. THE FRAME AND THE DRIVE SYSTEM

The 17 m diameter $f/D = 1$ telescope frame is made of light-weight carbon fiber tubes (the frame itself weighs $<$20 ton, while the whole structure plus the undercarriage amounts to about 60 ton). The construction of the foundation for the MAGIC telescope started in September 2001 and just a few months later the whole telescope structure was completed (December 2001). In fact, the assembly of the whole frame took only 1 month because of a construction based on the so-called tube and knot system of the company MERO.

The telescope drive system of the alt-az mount was installed during 2002. The azimuth axis is equipped with two 11 kW motors, while the elevation axis has a single motor of the same power. The position of the telescope is measured in the mechanical telescope frame by three absolute 14-bit shaft encoders. With this

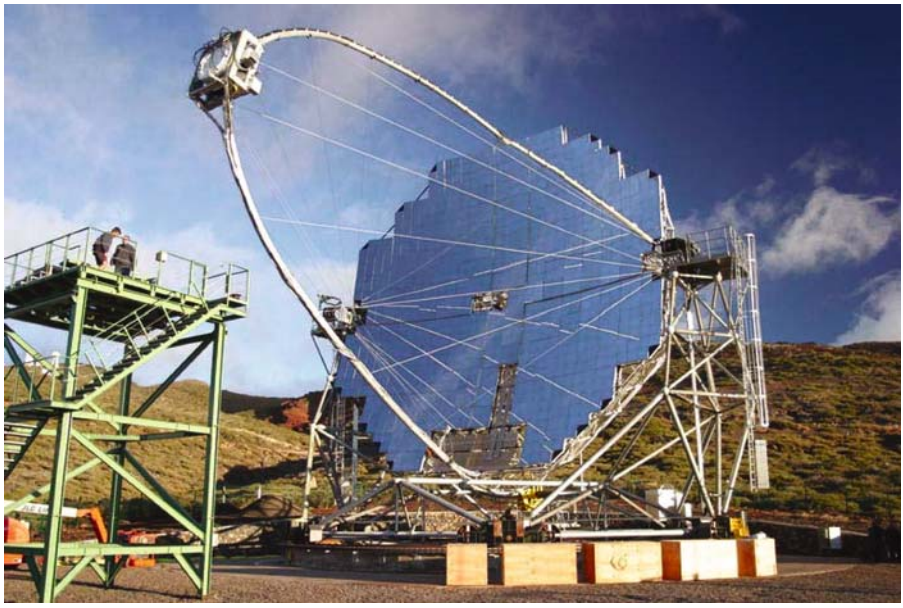


Figure 1. View of the MAGIC telescope just before its inauguration in October 2003. Its 17 m diameter reflector makes it the largest Imaging Cherenkov Telescope in the world. The main mirror is composed of 940, 1 m^2 mirror panels that are fully steerable using an active mirror control system.

configuration it is possible to measure the telescope position with an accuracy of about 0.02°. The maximum repositioning time of the telescope is 22 s, well below the 30-s target required for gamma-ray burst follow-up. By using a CCD camera mounted on the reflector frame, we have established that the telescope tracks to better than 0.01°.

2.2. THE REFLECTOR

The overall reflector shape is parabolic to minimize the time spread of the Cherenkov light flashes in the camera plane. The preservation of the time structure of the Cherenkov pulses is important to increase the signal-to-noise ratio with respect to the night-sky background light (NSB). The dish is tessellated by 956, 0.5 m × 0.5 m mirrors covering a total surface of 234 m^2. Each mirror is a sandwich of aluminium honeycomb on which a 5-mm plate of an alloy of Al, Mg and Si is glued. The aluminium plate is diamond milled to achieve a spherical reflecting surface with the radius of curvature that is more adequate for its position in the paraboloid. A thin quartz layer protects the mirror surface from aging. The reflectivity of the mirrors is around 90%. The alignment of the mirrors in the telescope surface has been done using an artificial light source at a distance of 960 m. The overall spot has a FWHM of roughly half a pixel size (<0.05°).

2.3. THE ACTIVE MIRROR CONTROL

A large diameter telescope has strong requirements on the stiffness of the reflector frame. When directing the telescope to different elevation angles the reflector's surface deviates from its ideal shape under gravitational load. Two solutions are possible to counteract the deformations: (a) either to construct a very heavy and stiff frame or (b) allow for small deformations by constructing a light-weight structure and correct its mirror profile. We have chosen the second option for the MAGIC telescope and equipped the reflector with an "Active Mirror Control" system. Each of the four mirror facets is mounted on a single panel. Two of the three mounting points of the panel are equipped with actuators, which can be used to adjust its position on the frame. The main elements of each actuator are a two-phase stepping motor (full step 1.8°, holding torque 50 N cm) and a ball-spindle (pitch 2 mm, maximum range 37 mm). In the center of the panel (a), laser module is pointed towards the common focus of the four mirrors. The panels are aligned using the artificial light source, the positions of all the laser spots are recorded and can be used as a reference to re-align them for each elevation angle. The AMC has undergone extensive tests during the winter 2003/2004 and it is presently close to its nominal performance. The light spot of bright stars focused at infinity fit within one pixel (RMS of the point spread function less than 0.1°) for practically all elevation angles (elevation angle greater than $\sim$30°).

2.4. THE CAMERA

The MAGIC camera has 1.5 m diameter, 450 kg weight and 3–4° FOV. The inner hexagonal area is composed by 397 0.1° FOV hemispherical photomultipliers of 1 in. diameter (Electron Tubes 9116A (Ostankov et al., 2000)) surrounded by 180 0.2° FOV PMTs of 1.5 in. diameter (ET 9116B, see Figure 2a). The time response FWHM is below 1 ns. The photocathode quantum efficiency is enhanced up to 30% and extended to the UV by a special coating of the surface using wavelength shifter (Paneque et al., 2000) (see Figure 2b). Each PMT is connected to an ultra-fast low noise transimpedance pre-amplifier, the six-dynode high-voltage system is stabilized with an active load. Dedicated light collectors have been designed to let the photon double-cross the PMT photocathode for large acceptance angles. The anode current and HV are read out for each pixel and digitized by a 12-bit ADC. The temperature and humidity of the camera are controlled by a water–based cooling system. The camera was completed in summer 2002 after extensive testing and characterization; it was installed on the site in November 2002 and commissioned in March 2003. First starlight using the dc current readout was recorded on 8 March 2003. During 2003–2004, the camera has been demonstrated to meet its specifications.



Figure 2. On the left a view of the telescope camera with its 577 PMTs. The inner section of the camera is made up of 397 0.1° field-of-view pixels, surrounded by four rings of 0.2° pixels. The second picture shows two Electron Tubes PMTs. The "frosted" PMT on the right has been been coated with a wavelength shifter lacquer that increases the quantum efficiency by 30% (coating all the PMTs is roughly equivalent to increasing the mirror area from 240 to 300 m^2).

2.5. THE READOUT SYSTEM

The PMT signals are amplified at the camera and transmitted over 162 m long optical fibers using Vertical Cavity Emitting Laser Drivers (VCSELs, 850 nm wavelength). Transmission over optical links drastically reduces the weight and size of the cables and protects the Cherenkov signal from ambient electromagnetic noise in the line. In the receiver boards in the electronics room, the signal is amplified and split. One branch goes to a software adjustable threshold discriminator that generates a digital signal for the trigger system. The signal in the second branch is stretched to 6 ns FWHM and again split into a high-gain line, where it is further amplified by a factor $\sim$10, while the low-gain line is just delayed by 50 ns. If the signal is above a preset threshold, both lines are combined using a GaAs analog switch and digitized by the same FADC channel.

The 8-bit, 300 MHz Flash ADCs continuously digitize the analog signals and store the digital data into a 32 kB long ring buffer. If a trigger signal arrives within less than 100 μs the position of the signal in the ring buffer for each pixel is determined and for each pixel 15 high-gain plus 15 low-gain samples are written to a 512 kB long FIFO buffer at a maximum rate of 80 MB/s. The readout of the ring buffer results in a dead time $\sim$20 μs. This corresponds to about 2% dead time at the design trigger rate of 1 kHz. The time and trigger information for each event are recorded by dedicated digital modules, which are read out along with the FADC analog modules. The readout is controlled by an FPGA (Xilinx) chip on a PCI (MicroEnable) card. The data are saved to a RAID0 disk system at a rate up to 20 MB/s which results in up to 800 GB raw data per night.

2.6. THE TRIGGER

MAGIC is equipped with a two-level trigger system with programmable logic (Bastieri et al., 2001). The first level (L1T) applies tight time coincidence and simple next neighbour logic. The trigger is active in 19 hexagonal overlapping regions of 36 pixels each, to cover 325 of the inner pixels of the camera. The second level (L2T) can be used to perform a rough analysis and apply topological constraints on the event images. Using, for instance, a fast evaluation of the size of the Cherenkov image, it is possible to reduce significantly the effect of the NSB, thus, allowing a reduction of the discrimination level and the gamma-ray threshold. The individual pixel rates of the channels included in the trigger are monitored using 100 MHz scalers.

The first- and second-level trigger systems were installed and commissioned during the winter of 2003, as well as the whole computing system for the telescope control and DAQ.

2.7. THE CALIBRATION SYSTEM

The calibration system consists of a light pulser and a continuous light source (both situated in the center of the mirror dish), a darkened, single photoelectron counting PMT ("blind pixel"), located in the camera plane and a calibrated PIN-diode 1.5 m above the light pulser. The pulsed light is emitted by very fast (3–4 ns FWHM) and powerful (10^8–10^{10} photons/sr) light emitting diodes in three different wavelengths (370 nm, 460 nm and 520 nm) and different intensities (up to 2000–3000 photoelectrons per pixel and pulse). It is therefore possible to calibrate the whole readout chain in wavelength and linearity. The continuous light source consists of LEDs simulating the NSB at La Palma with different intensities. The light pulser and continuous light source were commissioned during the winter 2003/2004, while the blind pixel and PIN diode are currently in their commissioning phase.

3. First Data

3.1. PERFORMANCE

During the winter we have reached the expected performance of most of the systems in the telescope. We are presently working on the evaluation of the global performance of the instrument.

Muons generate very-well-defined rings in the camera that are used to calibrate the telescope and to derive the point spread function of the reflector.

The point spread function can also be derived by means of the distribution of pixel anode currents of bright stars. In addition, the distribution of currents allows

us to monitor the intensity of the NSB in the field of view. NSB generates about one photoelectron RMS per 3.3 ns FADC sample in the inner PMT pixels. We also make use of anode currents to estimate the pointing error of the telescope and to crosscheck the absolute position of the source.

The telescope trigger rate has been found to vary smoothly with the discriminator threshold level as expected if it is dominated by cosmic rays and not by night-sky background noise. This happens for all multiplicities of the trigger (3, 4 and 5 next-neighbours pixels). Most of our data have been recorded with a threshold level around four photoelectrons (phe) and four next-neighbour pixel trigger multiplicity.

The arrival time of the Cherenkov pulses to the different pixels in the camera can be determined with a precision better than 1 ns. This allows the characterization of the time profile of the shower and gives another handle to estimate the direction of the incident γ-ray.

The dead time of the system has been calculated from the time difference of consecutive events and is well within the specifications of the readout system (less than 0.1%).

3.2. DATA SAMPLE AND ANALYSIS

It is worth noting that the telescope is still in its commissioning phase. All the results presented here are preliminary, since the configuration and performance of the telescope are not the nominal ones yet and the analysis software is still in its development phase.

In the period October 2003–May 2004, we have mainly concentrated on low zenith angle ($<40^\circ$) observations of standard TeV candles like Crab Nebula, Mrk 421, Mrk 501, 1ES 1426 and 1ES 1959. A roughly equivalent amount of OFF source data have been recorded under the same conditions of the ON data for background substraction.

We have selected only very short data samples for which the weather conditions were excellent on the basis of the trigger rates and star extinction measurements, all the telescope hardware systems were performing nominally and the data have been already preprocessed and calibrated.

The calibration of the telescope has been performed mainly using the so-called F-Factor method: the number of photoelectrons produced by the light pulser in a pixel are estimated using the width of the charge distribution recorded by the FADCs. Images are cleaned using two levels (tail and boundary cuts).

We have applied a standard Hillas analysis based on dynamic "SUPERCUTS" (for a review of the Hillas analysis see for example Fegan (1997)). Cuts on the so-called Hillas parameters WIDTH, LENGTH and DIST (that describe the shape and position of the shower image) are applied to the data in order to reject the background of cosmic rays that exhibit slightly different image shapes. Further discrimination is obtained using the orientation of the shower image: the ALPHA parameter is defined as the angle between the shower axis and the line that joins the

source position and the shower centroid. Gamma-rays have small ALPHAs, since they point to the source, while cosmic rays are distributed isotropically.

The gamma-hadron discrimination cuts are optimized on a small sample of the data and then applied to the whole sample. The cuts are dynamical, that is, they scale with the size of the shower. Any pointing error of the telescope has been corrected using reference stars in the anode currents and the "false source method" where the standard Hillas analysis is performed in a grid of positions in the camera field of view.

A lower cut on the shower size of 2000 photons has been applied. This cut selects only high-energy showers for which a standard analysis based on the Hillas parameters is straightforward. However, this increases substantially the analysis threshold with respect to the trigger threshold.

3.2.1. *Crab Nebula*

The Crab Nebula is a steady emitter at GeV and TeV energies. The γ-ray emission is produced by Inverse Compton (IC) scattering of a population of electrons that are accelerated in the plerion around the central pulsar. The spectrum of this source has been measured in the GeV range by EGRET and at energies above 300 GeV by a number of Cherenkov telescopes. The expected level of emission between 30 and 300 GeV makes it an excellent calibration candle for MAGIC. The spectrum in this energy range is interesting by itself, since it allows the IC emission parameters (magnetic field and/or size of the emission region) to be further constrained.

The Crab Nebula was observed during the winter months for about 20 h under very different weather and instrumental conditions. We have selected a sample of Crab Nebula data of 60 min lifetime at low zenith angle. Figure 3 displays the distribution of the ALPHA Hillas parameter for the ON and the corresponding

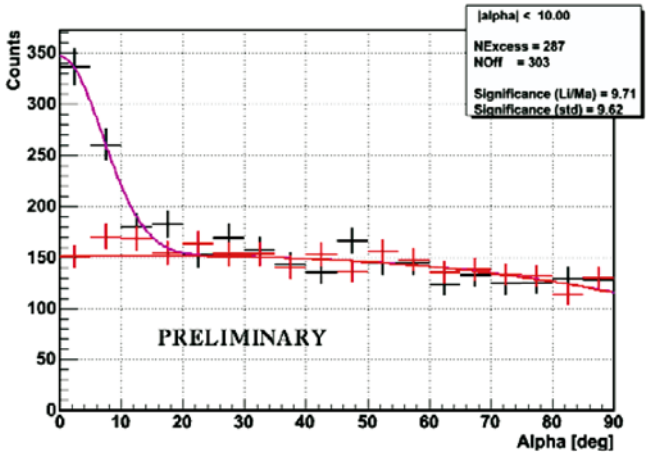


Figure 3. First detection of the Crab Nebula using the MAGIC telescope.

OFF data. An excess is clearly visible at low ALPHAs. We detect 290 gamma candidate events over an expected background of 300 events. This corresponds to a significance of $\sim 10\sigma$.

3.2.2. *Mrk 421*

Mrk 421 is one of the so-called TeV BL Lacs that have been detected above 100 GeV. It undergoes the fastest flares that have been observed at these energies, with flux doubling times as short as 20 min. The very-high-energy emission is attributed to IC scattering of electrons that are accelerated in the base of the jet. The IC peak of the spectral energy distribution is probably around $\sim$100 GeV. During 2004, the source has undergone an episode of intense flaring in X-rays. Since the correlation between the X-ray and the high-energy emission is well established, this source was also an excellent candidate for MAGIC.

The 2004 observation campaign started in January 2004 and finished in May 2004. A simple online analysis running on site has shown clear evidence for signals during most of the campaign. MAGIC also joined a multiwavelength campaign with VERITAS and RXTE on 9 May. The data are still not available for full analysis, but again showed a significant signal in the online analysis.

Here we present the results of a small sample of 96 min in optimal conditions in the night of 14/15 March 2004. Figure 4 (left) shows the pointing angle "alpha" distribution for these data and the corresponding OFF source data. A total of 1307 excess events are observed over an expected background of 565 events. The significance of the detection is around 27σ. It is worth mentioning that there was a visible excess in the alpha distribution even before any cuts.

The false method plot in the right of Figure 4 confirms the detection and the position of the excess coincides with the source position after pointing corrections. It must be noted that this plot provides only a rather poor estimate of the angular

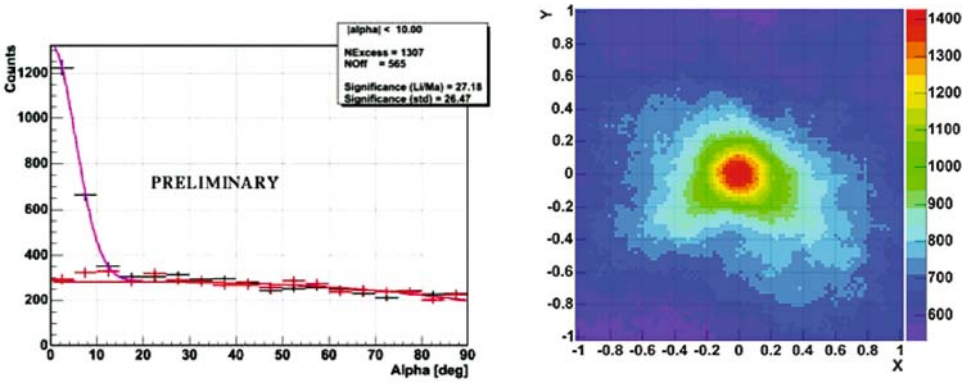


Figure 4. Left: Alpha plot for the selected sample of Mrk 421 data (2004/03/15). Right: Result of the false source analysis of the Mrk 421 data sample.

resolution of the telescope that is normally calculated using more sophisticated methods.

3.2.3. *Further Progress*
An estimate of the energy threshold of the telescope during this observation of the source's γ-ray flux is under way. We are working to improve the significance and the excess of the detection by reducing the analysis threshold energy and by applying optimized cuts on other parameters, and using the Cherenkov pulse time profile. These data will be complemented soon with the analysis for the full sample that has been recorded during January–May 2004.

4. Future Instrumental Developments

MAGIC, as it stands now, has always been thought as the first of a series of instruments aimed at reducing the energy threshold and increasing the sensitivity in the GeV energy range.

The second instrument in this series is already under construction and will have a reflector of the same size as MAGIC's, but will incorporate a number of new techniques that will improve its performance (Mirzoyan et al., 2003). Among them is a faster digitizing system (with >2 GHz sampling rate) in its latest stage of development. We are also working on several light detectors with increased efficiency (HPDs and arrays of Geiger mode SiPM) that may be incorporated in the camera of the second telescope or even in the original MAGIC telescope. The frame for the second telescope is already under construction and will be delivered to La Palma in 2005.

The third instrument is ECO-1000 (Merck et al., 2003; Baixeras et al., 2004), a Cherenkov telescope with 1000 m^2 reflector surface (roughly four times larger than MAGIC). ECO-1000 intends to take the Cherenkov Telescope technique to its extreme and reduce the threshold down to 5 GeV with a sensitivity of $\sim 3 \times 10^{-10}$ $cm^{-2}\,s^{-1}$. This is an energy range where it fully overlaps detectors on board satellites like GLAST. Due to its large collection area and high flux sensitivity, ECO-1000 is the ideal instrument to complement GLAST's huge field of view in the study of transient sources.

5. Conclusions

MAGIC, a very large, new-generation IACT designed specifically for the exploration of the 10–300 GeV gamma energy gap is in its final commissioning phase and is expected to enter regular operation after the summer.

So far, all the new technical components are working with their nominal performance and are now undergoing extensive checks. The telescope has

already detected two very-high-energy sources, Crab and Mrk 421, with high significance.

We can conclude that MAGIC is well on its way and entering the discovery phase. In the months following this workshop, it is hoped that full potential of MAGIC, which has been designed to have the lowest energy threshold of any imaging Cherenkov telescope, will be demonstrated.

Acknowledgements

We would like to thank the IAC for excellent working conditions. The support of the Italian INFN, German BMBF and Spanish CICYT is gratefully acknowledged.

References

Baixeras, C., et al.: 2004, Design studies for a European Gamma-ray Observatory, Preprint astro-ph/0403180.

Barrio, J.A., et al.: 1998, The MAGIC Telescope Design report, MPI Institute Report MPI-PhE/98-5, March 1998.

Bastieri, D., et al.: 2001, *Nuclear Instrum. Methods A* **461**, 521.

Fegan, D.J.: 1997, *J. Phys. G* **23**, 1013.

Lorenz, E., et al.: 1995, in: M. Cresti (eds.), The MAGIC Telescope Project Based on a 17 m Diameter Parabolic Solar Concentrator, Proceedings of the Workshop: Towards a Major Atmospheric Cherenkov Detector IV, Padova, Italy, p. 277.

Merck, M., et al.: 2003, in: Extending The Cherenkov Technique Down To An Energy Threshold of A Few GeV: The Ultimate Instrument For Ground-Based Gamma-Ray Astronomy, Proceedings of the International Cosmic Ray Conference, Tokyo.

Mirzoyan, R., et al.: 2003, in: Technical Innovations for the MAGIC Project, Proceedings of the International Cosmic Ray Conference, Tokyo.

Ostankov, A., et al.: 2000, *Nuclear Instrum. Meth. A* **442**, 117.

Paneque, D., et al.: 2000, *Nuclear Instrum. Meth. A*, in press.

THE NEUTRINO TELESCOPE ANTARES

JUAN JOSÉ HERNÁNDEZ-REY (for the ANTARES collaboration)
IFIC – Instituto de Física Corpuscular, CSIC-Universitat de València, apdo. 22085, E46071 Valencia, Spain; E-mail: juan.j.hernandez@ific.uv.es

(Received 7 June 2004; accepted 22 July 2004)

Abstract. Whilst the number of observed astrophysical sources of γ-rays is now moderately high, only three astrophysical objects have been studied with neutrinos, namely the Sun, a supernova (SN1987A) and the Earth (its atmosphere). However, astro-neutrinos may give a new boost to astrophysics, similar to the impressive progress provided during the last decades by γ-rays. The ANTARES collaboration aims to build a large neutrino telescope under the Mediterranean Sea at a depth of 2500 m. To reach this goal, a remarkable effort of R&D has been performed in recent years that has culminated in the deployment, connection and operation of two prototype strings. The final detector will be composed of 12 strings and will be ready by 2007.

Keywords: neutrino telescope, high-energy astrophysics

1. The Link Between γ- and ν Astrophysics

There are only a few elementary particles at our disposal as cosmic messengers. The electromagnetic radiation has traditionally provided most of the astrophysical information and the advent of new detection techniques covering increasingly wider ranges of electromagnetic wavelengths has historically lead to the discovery of new phenomena or to a deeper understanding of already known astrophysical sources. A few decades ago, γ-ray astrophysics "opened a new window to the Universe", a most fruitful one for that matter. But in addition to photons, other messengers such as cosmic rays or neutrinos are available for the investigation of the Universe and deserve our attention.

The information obtained from the different cosmic messengers is to a certain extent complementary, in such a way that the limitations of one type of messenger or wavelength is overcome by another. This is particularly the case in the high-energy regime, where cosmic rays, γ-rays and neutrinos have widely different features. Protons and nuclei bring information of the most energetic astrophysical phenomena, but their trajectories are bent by magnetic fields, so that even in the presence of weak fields any directional information is lost, unless they come from short distances and have extremely high energies, according to the expression: $\theta(\text{rad}) \sim L(\text{kpc}) \cdot Z \cdot B(\mu\text{G})/E(\text{EeV})$, where θ, L, Z, B and E are the bending angle, the distance travelled, the electric charge, the magnetic field and the energy

Astrophysics and Space Science **297:** 257–267, 2005.
© Springer 2005

of the particle or nucleus in the units shown. Neutrons do not undergo deflection, but since they quickly decay, they can hardly travel the distance that separates the Earth from the centre of the Galaxy even with energies above a few EeV. Furthermore, at very high energies, cosmic rays interact with the cosmic microwave background, so that the distance they can travel before being absorbed is limited and depends on their energy (the so-called GKZ limit). In the TeV region, their mean free path is around a few tens of Mpcs (the Virgo cluster is at about 20 Mpcs) and at energies of the order of hundreds of TeV they can hardly reach the Earth travelling from the Galactic centre. Being electrically neutral, γ-rays do not suffer the deflection due to the magnetic fields. Nevertheless, at high energies, they interact with the low-energy photon soup present in the Universe (the infrared and cosmic microwave backgrounds), so that at a few TeV they travel on average a few tens of Mpcs, whilst in the $\sim$100 TeV region, they can hardly travel 10 kpcs without being absorbed. Neutrinos, as γ-rays, are electrically neutral and stable. Moreover, due to their low probability of interaction they can come from very distant or very dense objects without being absorbed. A 50 TeV neutrino has an interaction length of the order of the Earth's diameter. Since neutrinos are part of the final debris of elementary particles in a number of processes, they are a very convenient tool to investigate high-energy, long-distance phenomena. The advantage of having a low interaction cross section is at the same time a drawback from the experimental point of view: the detection of even the highest fluxes of neutrinos requires huge detectors.

Neutrino astrophysics does exist, but its realm reduces at present to the observation of three astrophysical objects: the Sun, a supernova (SN1987A) and the Earth (or more precisely, its atmosphere) and to the energy region spanning from a few MeV to a few tens of MeV. No matter how modest this may seem, the discoveries surrounding this neutrino observations have had a very important impact.

Several projects have been launched to detect cosmic neutrinos in wider energy ranges. The first generation of high-energy ($E > 10$ GeV) neutrino telescopes, namely AMANDA and BAIKAL have already provided some interesting limits to diffuse and point-like neutrino fluxes. A second wave of projects, such as ANTARES, NEMO and NESTOR are now under construction. New initiatives to build yet bigger detectors exist, such as IceCube and KM3. IceCube, in particular, is approved and its 80 strings will be completely deployed by 2010. In addition, new ideas based on the detection of neutrinos through radiowaves or sound have been proposed and progress is being made in that front too.

Candidates for neutrino sources are in general also γ-ray sources, since most of the mechanisms that produce neutrinos also produce high-energy photons and cosmic rays. Indeed, rather stringent limits on the diffuse neutrino flux are based on this connection (see Section 5). Moreover, the possibility that the more energetic γ-rays are not produced through inverse Compton scattering, but in the decay of neutral pions produced in hadronic collisions could be clarified by the detection of neutrinos. Candidates for such processes are at present scarce and contested (Enomoto et al., 2002; Reimer and Pohl, 2002). It is natural to think that the

understanding of astronomical objects such as active galactic nuclei or gamma-ray bursts outside the Galaxy and supernova remnants, micro-quasars or pulsars in the Galaxy will greatly improve if an unambiguous neutrino signal, no matter how faint, is detected.

2. The ANTARES Neutrino Telescope

The European collaboration ANTARES is currently building a neutrino detector under the Mediterranean Sea (Aslanides et al., 1999). Muonic neutrinos will be detected through the muons they produce when interacting with the matter that surrounds the detector. Even though this type of neutrino is the main detection goal, electronic neutrinos will be detected too by the secondary electromagnetic showers they produce. Muons – and charged particles in general – will be detected through the Cherenkov light they emit when traversing the sea water. To this end, an array of photomultipliers (PMTs) will be distributed in a large volume of water. The ANTARES detector (see Figure 1) will consist of 12 strings (also called lines), with 25 storeys each. Each storey contains a triplet of three optical modules (OMs). An OM (Amram et al., 2002) consists in a pressure-resistant glass sphere housing

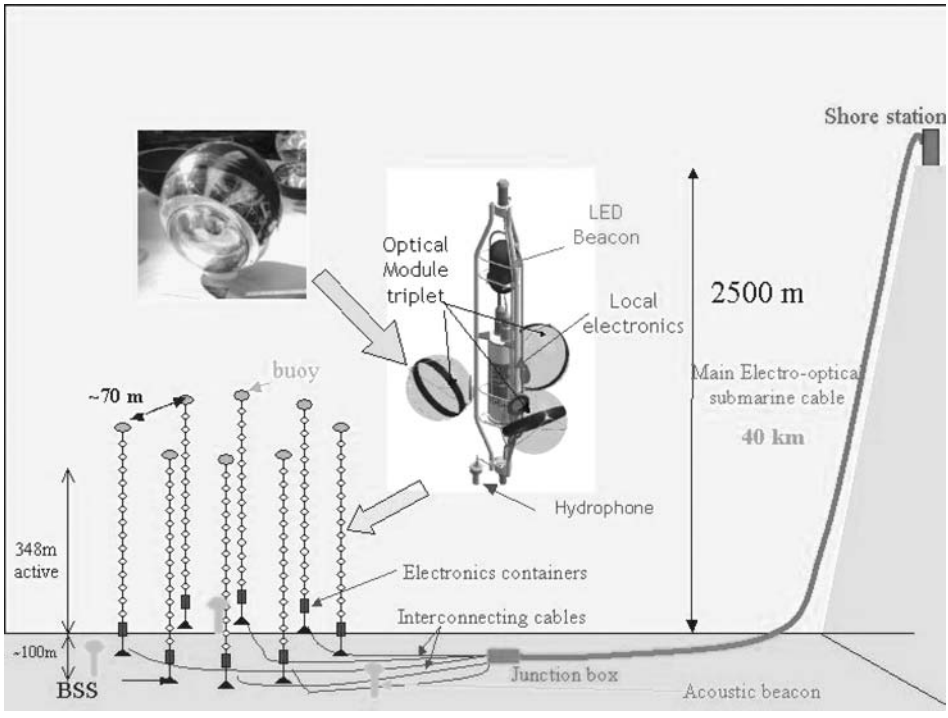


Figure 1. Scheme of the ANTARES detector. Inserted is a sketch of one of the 25 storeys that each string will hold. The total number of strings is 12 plus a special instrumentation line.

a 10 in. PMT, its base and a LED for calibration purposes. The three OMs of a storey are angularly separated by 120° in the horizontal plane and the axis of their PMTs are looking 45° below the horizontal. A storey also holds a titanium container housing the front-end readout electronics of the PMT, an ethernet board for data acquisition, electronic boards for triggering and for clock distribution and a tiltmeter compass to measure the angles of the storey. Some storeys also include a hydrophone for acoustic positioning and a LED optical beacon for timing calibration (Hernández-Rey, 2003a).

The distance between storeys of a string is 14.5 m, the first storey being located 100 m above the sea bed, so that the total height of each string is more than 450 m. The strings are anchored to the sea bed and held taut by means of a buoy at their top. At the bottom of each string there is a container housing the general electronics of the string, acoustic emitters for positioning and in some strings laser beacons for timing calibration. In addition to the 12 standard strings, the detector will also include a special instrumentation line that will support devices to monitor the main environmental parameters, such as the speed of the water currents, the sound velocity and optical properties of water, e.g. the absorption length, and will also act as a dedicated host for studies in other fields, such as marine biology, seismology and oceanography. The strings lay on the sea floor, separated from each other by ∼65 m on average and filling an octagonal surface.

The detector is located at a depth of 2500 m in the Mediterranean Sea (42°48′N,6°10′E), in front of Toulon in the south of France. This location provides a 3.5 π sr coverage of the sky and allows in particular the survey of the Galactic centre for 67% of the time.

The detector is controlled from the shore station situated at La-Seyne-sur-Mer, a village close to Toulon. A standard telecommunication electro-optical cable, 40 km in length, links the detector to the shore. The cable that contains 48 optical fibres provides a two-way communication tool to issue commands to and retrieve data from the detector, and delivers the necessary electric power for its proper operation. The cable is linked in the sea bed of the ANTARES site to the junction box, the distributing device to which the strings are connected by several cables a few hundred meter long.

The shore station is currently operative, the electro-optical cable has been deployed and was connected to the junction box and is working steadily for almost 1.5 years. Furthermore, two prototype strings were deployed, operated and recovered (see next section). The full detector is expected to be ready by 2007.

3. Progress and Status of the Project

The ANTARES collaboration had a first phase of R&D in which several studies were performed and prototypes built and deployed. During this phase, several versions of different autonomous strings were used in about 50 deployments. These strings,

which sent the data to the surface by means of sonar devices or recorded them until their recovery, were used to measure in different sites several quantities, such as the optical properties of the surrounding water (Aguilar et al., 2004), the bio-fouling on optical surfaces and their subsequent loss of transparency (Amram et al., 2003) and the optical backgrounds due the decay of the radioactive salts present in sea water and to bioluminescence (Amram et al., 2000). These studies lead to the selection of the present site, which was further investigated in terms of the geological characteristics of its ground (Amram et al., 2003) and inspected by means of a submarine in order to know in detail its orography and to spot all the objects present in the area.

From November 1999 to June 2000 a "demonstrator line" was deployed and operated in order to prove the feasibility of the project and to test several of its systems. The capability to deploy properly a long structure in the intended place was proven with this line. The designed acoustic positioning system was shown to locate the OMs with a precision of 5 cm with respect to several points in the sea floor. Several thousand atmospheric muons were recorded and reconstructed.

The final electro-optical cable linking the shore and the ANTARES site was deployed in October 2001. Meanwhile, a small version of a detector string was built. This so-called Pre-production Sector Line (PSL) was composed of the anchor, five storeys and the buoy. It represents one fifth ("a sector") of a full final line and constitutes its minimal functional unit concerning power distribution and data transmission. The line had 15 OMs in total, but it also contained all the types of components of a full line, such as the hydrophones of the acoustic positioning system, the tiltmeters/compasses and a LED optical beacon. The PSL was finally assembled and tested in the laboratory during the Summer and Autumn of 2002.

A second line, called Mini-Instrumentation Line (MIL) was assembled and tested in November 2002. This line had two storeys, 100 m apart, which contained devices to measure environmental parameters, namely, a current profiler, a sound velocimeter, a conductivity and temperature probe and a light transmissiometer. The MIL also contained devices for acoustic positioning and inter-string timing calibration (a laser beacon and an LED optical beacon).

Starting from December 2003 and ending in March 2003, a series of major marine operations ended in the full installation of these two lines. This included the deployment of the Junction Box and its connection to the previously deployed electro-optical cable and the deployment of the PSL and MIL and their connection to the Junction Box by the manned submarine *Nautile*. Both lines were then recovered in May and July 2003. All these marine operations have factually proven the mastering of the deployment techniques.

With this setup, around 130 GB of data were recorded at the shore station in about 100 days of running, so that the front-end acquisition, the digital transfer, the slow control and the power distribution, among other systems, were thoroughly checked. Counting rates, line shape and several other control parameters (temperatures, power consumption, etc.) were recorded and monitored. Two main problems

appeared during operation: the failure of an optical fibre inside the cables of the lines, which prevented the transmission of the clock signal, and a water leak in an electronic container of the MIL. The first problem was due to the pressure-induced collapse of the plastic tube protecting the optical fibres and will be avoided in the future by enclosing them in steel tubes. The second problem was due to a bad manufacturer's specification in the tolerance of the hole's dimension of a specific type of connector. This will be avoided in the future using other type of connectors with larger security margins.

The absence of a clock signal prevented us from having the timing of the OM signals synchronized at the nanosecond level, as it is needed to reconstruct muon tracks. Nevertheless, counting rates of the OMs were recorded during the whole data-taking period. The left plot in Figure 2 shows the median values of the rates in kHz recorded during periods of 15 min as a function of the date of data taking for the three OMs of one of the storeys of the PSL. The right plot in Figure 2 shows the burst fraction of the same OMs as a function of data-taking date. The burst fraction is defined as the fraction of time (during the same 15-min periods) that the rate is 20% higher than the median rate. In our previous measurements with stand-alone strings (Amram et al., 2000), the results showed that in addition to a continuous baseline of 60 kHz due to ^{40}K decays slowly modulated possibly by bioluminescence coming from bacteria, there were sudden bursts of several hundreds kHz lasting from seconds to minutes (possibly by bioluminescence coming from larger animals). These new data confirm these measurements, but show a larger variability. Correlations between the burst fraction and the baseline rate or the water currents are also observed. This optical background is 50–70% of the time below 100 kHz, a rate acceptable for data taking.

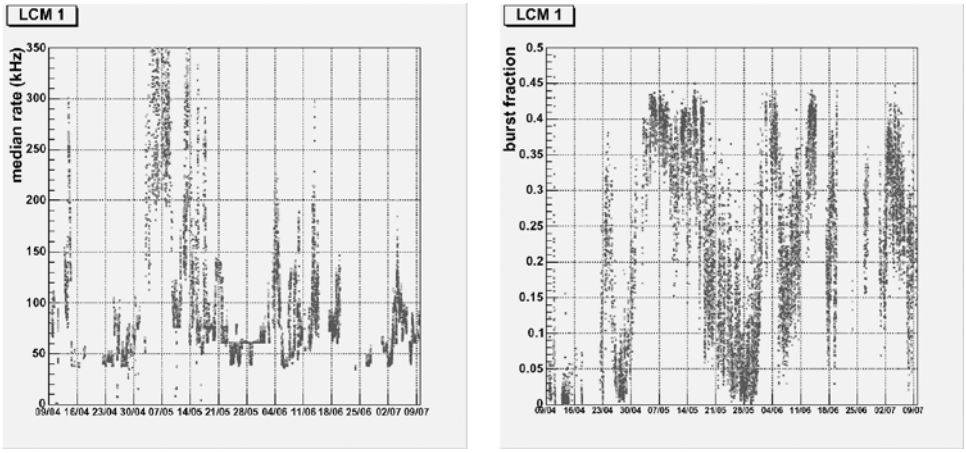


Figure 2. Median rate in kHz (left) and burst fraction in percentage (right) as a function of the data-taking date. See text for explanations.

4. Expected Performances

The expected performances of the full 12-string detector have been estimated by computer simulation (Hernández-Rey, 2003b). The capabilities of the telescope can be characterized by several magnitudes. The muon effective area gives the ratio of the number of well-reconstructed ("selected") muon events to the incoming muon flux. In Figure 3, the effective area for muons as a function of the parent neutrino energy is shown for an isotropic neutrino signal. Selection criteria have been applied in order to keep only well-reconstructed tracks and to reject the atmospheric muon background (for other specific analyses, such as the search for point-like transient sources at known positions in the sky the criteria to be applied can be less stringent than those applied here). The upper curve (asterisks) represents all the events after reconstruction and selection. As can be seen, the effective area increases with energy and is somewhat lower than 0.1 km^2 for the highest energies. An indication of the angular resolution of the selected events is given by the lower curves in the same plot (triangles and stars), which correspond to those selected events that have an angle between the simulated and the reconstructed muon track smaller than 1 and 0.3°, respectively.

The angular resolution of the telescope is better seen in Figure 4, where the median of the distribution of the angular difference in space between the reconstructed

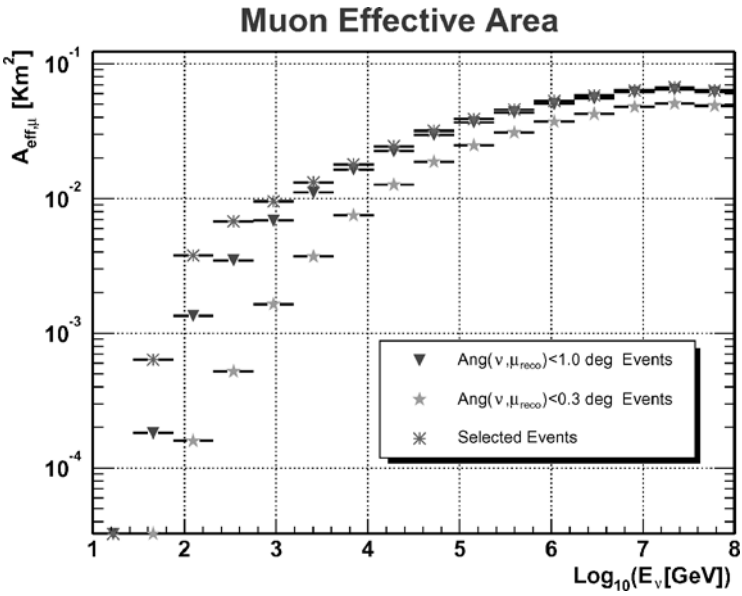


Figure 3. Effective area for muons as a function of the parent neutrino energy. Asterisks (upper curve) show the effective area for all the well-reconstructed ("selected") events, while triangles and stars (lower curves) show the effective area for those selected events for which the difference between the true and the reconstructed muon angle is smaller than 1 and 0.3°, respectively.

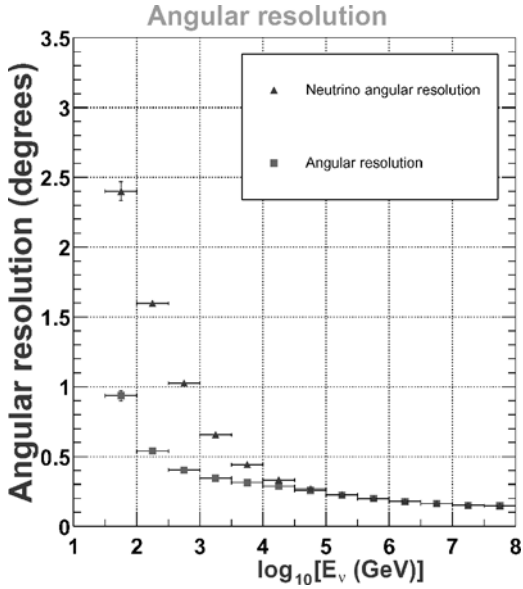


Figure 4. Angular resolution as a function of neutrino energy. The resolution is defined as the median of the distribution of the angle in space between the reconstructed muon and (a) the parent neutrino (triangles) or (b) the produced muon (squares).

muon track and (a) the original parent neutrino (triangles) or (b) the true muon track (squares) is shown as a function of the neutrino energy. The angle between the parent neutrino and the offspring muon dominates up to around 10 TeV. Above that energy, the instrumental resolution – which depends, in particular, on the effect of the scattering of light in water and on the overall timing resolution of the detector – is the limiting factor. A resolution of 0.15° can be reached. Note that a good angular resolution helps to reject the background in the case of point-like sources and is therefore of utmost importance in those studies where the source position is relevant. Due to the dependence of the resolution on the neutrino energy, the final resolution for a given source depends on its energy spectrum. The hardest the spectrum, the better the resolution. For an E^{-2} spectrum, the neutrino angular resolution is 0.3°.

The energy of the crossing muon can be estimated from the amount of light deposited in the PMTs. Several estimators based on different techniques have been developed (Romeyer et al., 2003) to this end. Since the energy released from the muons at high energies has large fluctuations, a convenient magnitude is the logarithmic energy resolution, $log_{10}(\frac{\sigma_E}{E})$. Monte Carlo studies show that this resolution is between 0.2 and 0.3 for muons with energy above 1 TeV.

For muon energies below ∼200 GeV, the energy of the muon can be measured from its range in the water. This can be used to make neutrino oscillation studies in the 10–100 GeV muon energy range.

5. Sensitivity and Predictions

There is a general consensus within the astro-neutrino community that the minimum scale of a neutrino telescope to gather the appropriate event statistics in a reasonable amount of time is of the order of the kilometre cube. This is based on two facts. From the theoretical point of view, the link between the extra-galactic sources of cosmic rays, gamma-rays and neutrinos leads to severe limits on the neutrino diffuse flux expressed in the Waxman–Bahcall upper limit (W&B), $E^2\Phi < 4.5 \times 10^{-8}$ GeV cm^{-2} s^{-1} sr^{-1} (Waxman and Bahcall, 1998; Bahcall and Waxman, 2001). This limit can be challenged – in more or less contrived scenarios –, assuming that some of the required hypotheses do not hold (Mannheim et al., 2000; Kalashev et al., 2002). It nevertheless marks a limit for a list of first class candidate sources. Note that if oscillations with the present measured parameters are taken into account, the proportion of neutrino species observed from these sources changes from $\nu_e : \nu_\mu : \nu_\tau = 1 : 2 :< 10^5$ to $\nu_e : \nu_\mu : \nu_\tau = 1 : 1 : 1$, so that predictions for muonic neutrinos are approximately a factor two smaller than given earlier. The second recent reason to aim at kilometre cube volumes is that the AMANDA-II experiment has already set an upper limit on diffuse fluxes of $E^2\Phi < 8.6 \times 10^{-7}$ GeV cm^{-2} s^{-1} sr^{-1} in the energy range 50TeV $< E <$ 5PeV, assuming $\nu_e : \nu_\mu : \nu_\tau = 1 : 1 : 1$ and an E^{-2} spectrum (Ribordy, 2004).

For ANTARES, estimates by Monte Carlo simulation indicate that after 1 year of data taking and assuming an E^{-2} spectrum the experiment will be able to set an upper limit for diffuse fluxes of $E^2\Phi < 7.8 \times 10^{-8}$ GeV cm^{-2} s^{-1} sr^{-1}, that will improve after 3 years of data taking to $E^2\Phi < 3.9 \times 10^{-8}$ GeV cm^{-2} s^{-1} sr^{-1}, just below the W&B limit (see left plot in Figure 5). Nevertheless, this estimate does

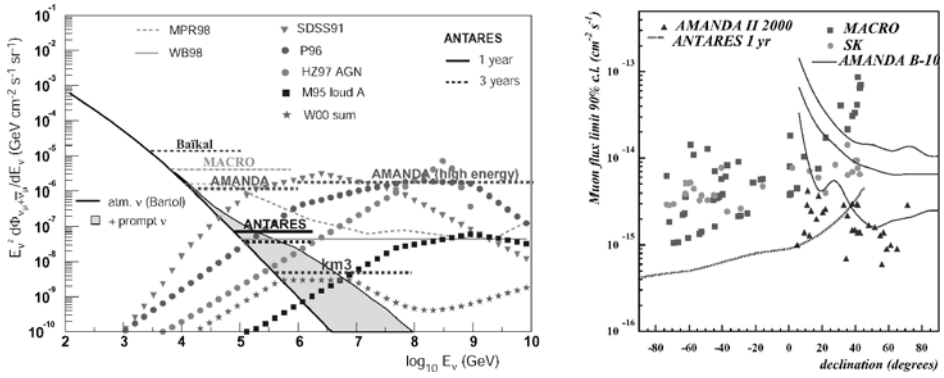


Figure 5. Left plot: Diffuse flux scaled to an E^{-2} spectrum as a function of the energy of the neutrino. The upper limits that can be set by ANTARES after 1 year (solid line) and 3 years (dashed line) of data taking are indicated together with the expected atmospheric flux and some theoretical predictions are shown. Right plot: Sensitivity to point-like sources as a function of declination for different experiments expressed in terms of the 90% C.L. upper limit that they can set in case of a negative signal. See text for explanations and references.

not take into account oscillations, which will worsen the limit by about a factor 2 if only muons are detected. However, in this case, the detection of electromagnetic cascades can improve the limit by an amount not yet estimated. Although more detailed background studies are underway to confirm these numbers, they give an idea of the sensitivity of ANTARES to the diffuse flux, very close to beating the W&B limit.

The right plot in Figure 5 shows the 90% confidence level upper limit for muon fluxes (in cm^{-2} s^{-1}) from point-like sources as a function of the declination of the source for different experiments. The triangles are the upper limit set by the AMANDA-II experiment for northern declinations (Ahrens et al., 2004). Previous results of AMANDA-B-10 can be found in (Ahrens et al., 2003). The limits that ANTARES will set after 1 year of data taking will clearly improve those of SuperKamiokande and MACRO in the southern hemisphere and are comparable to those of AMANDA-II in the region of the sky where they overlap.

6. Conclusions and Outlook

The ANTARES collaboration has deployed and operated two prototype strings in the Mediterranean Sea at a depth of 2500 m. The production and installation phase of this neutrino telescope has started. The full 12-string detector is expected to be in place in 2007. By then, this telescope will be able to explore the Southern hemisphere in the search for extra-terrestrial neutrinos with a sensitivity much better than any other experiment before. Meanwhile, new steps will be taken in a still larger scientific collaboration to design a kilometre cube detector in the Mediterranean Sea.

Acknowledgements

Financial support for the ANTARES project is provided by the following funding agencies: Commisariat à l'Energie Atomique, Centre Nationale de la Recherche Scientifique, European Commission (FEDER fund), Département du Var, Région P.A.C.A. et city of La Seyne-sur-Mer, France; Ministerio de Educación y Ciencia, Spain (FPA2003-00531); Istituto Nazionale de Fisica Nucleare, Italy; the Russian Foundation for Basic Research, Russia; the Foundation for Fundamental Research on Matter, FOM, and the National Scientific Research Organization, NWO, The Netherlands.

References

Aguilar, J.A. et al.: 2004, *Astropart. Phys.*, accepted for publication (see also astro-ph/0412126).
Ahrens, J. et al.: 2003, *Astrophys. J.* **583**, 1040.
Ahrens, J. et al.: 2004, *Phys. Rev. Lett.*, 92:071102-1-5.
Amram, P. et al.: 2000, *Astropart. Phys.* **13**, 127.

Amram, P. et al.: 2002, *Nuclear Instrum. Meth.* **A484**, 369.
Amram, P. et al.: 2003, *Astropart. Phys.* **19**, 253.
Aslanides, E. et al.: 1999, *astro-ph/9907432*.
Bahcall, J. and Waxman, E.: 2001, *Phys. Rev.* D64:023002-1-8.
Enomoto, R. et al.: 2002, *Nature* **416**, 823.
Hernández-Rey, J.J.: 2003a, *Proceedings of the 28th International Conference on Cosmic Rays*, vol. 3, pp. 1537.
Hernández-Rey, J.J.: 2003b, *Nuclear Phys. B (Proc. Suppl.)* **114**, 211.
Kalashev, O.E. et al.: 2002, *Phys. Rev.* D66:063004-1-11.
Mannheim, K., Protheroe, R.J. and Rachen, J.P.: 2000, *Phys. Rev.* D63:023003-1-16.
Reimer, O. and Pohl, M.: 2002, *Astronom. Astrophys.* **390**, L43.
Romeyer, A., Bruijn, R. and de Zornoza, J.D.: 2003, *Proceedings of the 28th International Conference on Cosmic Rays*, vol. 3, pp. 1329–1332.
Ribordy, M.: 2004, *hep-ex/0405035* and references therein.
Waxman, E. and Bahcall, J.: 1998, *Phys. Rev.* D59:023002-1-8.

IDENTIFICATION OF SHOCKS IN THE SPECTRA FROM BLACK HOLES

SAMIR MANDAL[1] and SANDIP KUMAR CHAKRABARTI[1,2]

[1]*Centre for Space Physics, Chalantika, Garia Station Road, Kolkata, India;*
E-mail: space_phys@vsnl.com; chakraba@bose.res.in
[2]*S.N. Bose National Centre for Basic Sciences, JD Block, Salt Lake, Kolkata, India*

(Received 27 August 2004; accepted 6 September 2004)

Abstract. We study the spectral properties of a low angular momentum flow as a function of the shock strength, compression ratio, accretion rate and flow geometry. In the absence of a satisfactory description of magnetic fields inside the advective disk, we consider the presence of only stochastic fields and use the ratio of the field energy density to the gravitational energy density as a parameter. We not only include 'conventional' synchrotron emission and Comptonization by Maxwell-Boltzmann electrons in the gas, but we also compute these effects due to power-law electrons. For strong shocks, a bump is produced due to the post-shock flow. Power-law spectral components due to the thermal and non-thermal electrons appear after this bump.

Keywords: black hole physics, shocks, hydrodynamics, spectral properties: γ-rays, X-rays

1. Introduction

In Chakrabarti and Titarchuk (1995, hereafter CT95), a two-component advective flow (TCAF) solution was introduced (see, Chakrabarti, this volume). The sub-Keplerian flow has a steady shock but depending on the flow parameters it could also be oscillating or propagating. The post-shock region is called CENtrifugal pressure supported BOundary Layer or CENBOL. Given that the accretion flow largely passes through this shock, it is likely that the hot electrons may be *accelerated* by the shock just as high energy cosmic rays are produced by the transient super-novae shocks (Bell, 1978a,b; Longair, 1981). We assume this process in computing the spectra and show that the presence of shocks makes their mark distinctly. Our solution also produces gamma-rays naturally since shocks are generally produced due to the centrifugal barrier (e.g., Chakrabarti, 1996). It is possible that occasionally an additional source of high energy photons, perhaps in the form of shocks in outflows and jets, is necessary to explain the complete spectra. Details of our model are presented in Mandal and Chakrabarti (2004).

2. Relevant Heating and Cooling Processes and the Solution Procedure

Protons loss energy through Coulomb interaction and inverse bremsstrahlung. Electrons are heated through this Coulomb coupling. Electrons are cooled by

© Springer 2005

bremsstrahlung, cyclo-synchrotron and Comptonization of the soft photons due to cyclo-synchrotron radiation. The Comptonization is computed by using this cooling term augmented by the enhancement factor. In the present situation, the flow passes through the shocks and thus the electrons will have a power-law distribution. Thus, both the thermal and the non-thermal electrons are present.

The geometry of the flow is chosen to be conical for simplicity and the flow surface makes an angle Θ with the z-axis. We assumed the form of infall velocity $v(x) = v_0 x^{-1/2}$. At the shock, $x = x_s$, the velocity is reduced by a factor R, the compression ratio, i.e., $v_+(x_s) = v_-(x_s)/R$. The number density also goes up by a factor R.

As for the initial conditions, we fix the outer boundary at a large distance (say, $10^6\, r_g$) and supply matter (both electrons and protons) with the same temperature (say, $T_p = T_e = 10^6$ K). By integrating energy equation, we obtained the temperature. The radiation emitted by the flow through bremsstrahlung and synchrotron radiation is inverse Comptonized by the hot electrons in the flow.

A shock of compression ratio R causes the formation of power-law electrons of slope (Bell, 1978a,b), $p = (R + 2)/(R - 1)$. This power-law electrons produce a power-law synchrotron emission with an index (Longair, 1981) $q = (1 - p)/2$. The power-law electrons have energy minimum at $\mathcal{E}_{\rm min}$ and energy maximum at $\mathcal{E}_{\rm max}$. $\mathcal{E}_{\rm max}$ is obtained self-consistently by conserving the number of power-law electrons and by computing the number of scatterings that the electrons undergo inside the disk before they escape and $\mathcal{E}_{\rm min}$ is obtained from the temperature of the injected electrons. This temperature is obtained self-consistently through our integration procedure.

In presence of magnetic field (used here as the ratio of the magnetic energy density to gravitational energy density), the pre-shock flow and the CENBOL would emit synchrotron radiation. We assume that the number of black body photons generated by the electrons obeying power-law distribution (assumed to be of constant fraction ζ of thermal electrons) below self-absorption frequency is the same fraction ζ of the total black body photons. We followed the procedures presented in CT95 and Titarchuk and Lyubarskij (1995) while computing the Comptonized spectrum due to scattering from thermal electrons and power-law electrons. However, unlike CT95 where a Keplerian disk was supplying soft photons, here the source is everywhere, i.e., distributed throughout. This has been taken into account. At the end, we add contributions from all the components to get the net photon emission from the flow.

In the next section, we present the spectral characteristics by varying parameters such as Θ, x_s, R, ζ and $\dot{m}$. We use a black hole of mass $10 M_\odot$.

3. Results and Interpretations

In Figure 1 we show our simplified flow geometry to capture the essential physics and show how the temperature of the electrons and protons differ as the flow moves

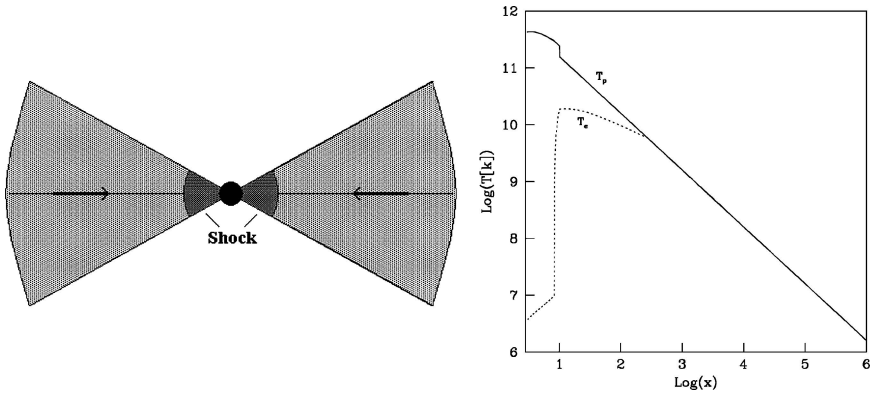


Figure 1. (Left) Wedge shaped flow model assumed in this paper which included a shock at the inner region. (Right) Variation of proton and electron temperatures (marked as T_p and T_e) as functions of dimensionless radial distance x for $\dot{m} = 0.00059$. Other parameters are $M = 10M_\odot$, $R = 3.9$, $\Theta = 77^\circ$, $\zeta = 0.7$ and $x_s = 10$. Closer to the black hole, the electrons cool more rapidly than the protons.

closer to the black hole. The deviation is more prominent in the post-shock region. Here, the radial distance x is measured in units of the Schwarzschild radius r_g.

In Figure 2, we show a typical spectrum obtained from our solution. The curve marked 1 is due to pre-shock flow and the curve marked 2 is due to the post-shock flow. The synchrotron self-absorption frequency at ν_a is marked. The bump due to post-shock flow is at frequency $\nu_{bump} \sim \nu_{inj}[1 + \frac{4}{3}\frac{R-1}{R}\frac{1}{x_s^{1/2}}]^{x_s^{1/2}}$, where, ν_{inj} is the frequency of the dominant photons from the pre-shock flow, R is the compression

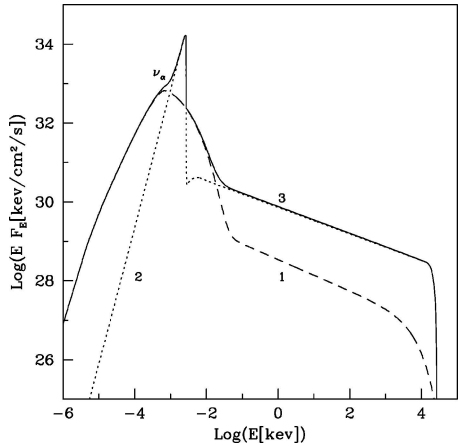


Figure 2. A typical complete spectrum from a sub-Keplerian accretion flow with all the contributions shown for the same parameters as in Figure 1b. The curve marked '1' is due to Comptonization of the synchrotron emission from the pre-shock region. The curve marked '2' is due to the Comptonized spectra from the post-shock (CENBOL) region. The curve marked '3' indicates the net radiation from the flow. ν_a represents synchrotron self-absorption frequency for the CENBOL.

ratio of the shock located at x_s. The power law is produced by the power-law electrons from the shock acceleration.

In Figure 3, we compare three cases with shock locations at $x_s = 10$, 40 and 80, respectively. The shock locations can vary with specific angular momentum in the flow which in turn is governed by the viscosity parameter (Chakrabarti, 1990, 1996).

With the rise in the accretion rate of the sub-Keplerian disk, the spectrum is likely to become harder. This can be seen more clearly in Figure 4, where we vary the

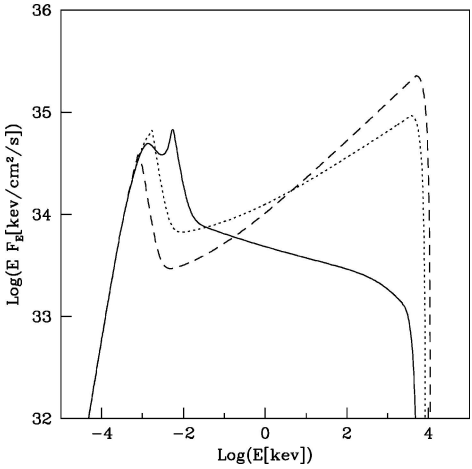


Figure 3. Variation of the total emitted spectrum when the shock location x_s is varied. The solid, dotted and dashed curves are drawn for $x_s = 10$, 40, 80, respectively. The spectrum becomes softer when x_s is reduced. Here, $\dot{m} = 0.1$ has been chosen.

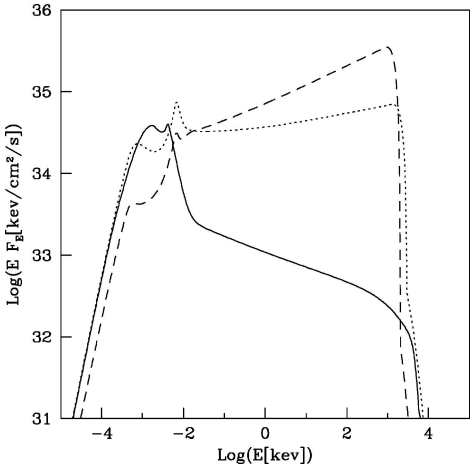


Figure 4. Variation of the spectra with the dimensionless accretion rate. Solid, dotted and dashed curved are for $\dot{m} = 0.05$, 0.5 and 1.5, respectively. The spectrum becomes harder when the accretion rate is increased.

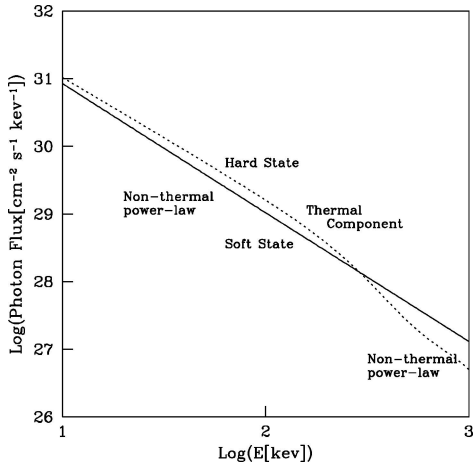


Figure 5. Example of a typical soft state and a hard state spectra of a galactic black hole candidate of mass $10M_{\odot}$. The parameters for the hard state are: $\dot{m} = 2.4$, $R = 4$, $x_{\rm s} = 250$, $\Theta = 80$, $\zeta = 0.24$. The parameters for the soft state are: $\dot{m} = 0.02$, $R = 4$, $x_{\rm s} = 100$, $\Theta = 80$, $\zeta = 0.3$.

accretion rate. A higher accretion rate is expected to increase the density of the flow and it becomes difficult to cool the matter by the soft photons of the synchrotron radiation. The Comptonized spectrum becomes harder. At lower accretion rate, it is easy to cool the flow and the spectrum becomes softer. The curves are drawn for: $\dot{m} = 0.05$ (solid), 0.5 (dotted) and 1.5 (dashed).

4. A Typical Soft/Hard Spectra in Gamma-Ray Region

Typical broad band soft state and hard state spectra are presented in Figure 4 of Chakrabarti (this volume). In Figure 5 of Chakrabarti (this volume) behavior at high energy has been shown for Cyg X-1, GROJ1719–24 and GROJ0422+32 (taken from Ling and Wheaton, 2004). In Figure 5 we present the photon flux in soft and hard states as obtained by our solution with shocks. No jet contribution was added. Not surprisingly, they look similar. However, a second kind of high γ intensity state was reported (see, Case et al., in press) in which non-thermal power-law has been observed from a few tens of keV to few MeVs (see, Figure 4 of Chakrabarti, this volume). It has been difficult to obtain such a behavior without invoking jets or other mechanisms.

Acknowledgement

SM acknowledges a RESPOND project from Indian Space Research Organization, which supports his research.

References

Bell, A.R.: 1978a, *MNRAS* **182**, 147.
Bell, A.R.: 1978b, *MNRAS* **182**, 443.
Case, G.L. et al.: in press, *Chin. J. Astron. Astrophys.*
Chakrabarti, S.K.: 1990, in: *Theory of Transonic Astrophysical Flows*, World Scientific, Singapore.
Chakrabarti, S.K.: 1996, *ApJ* **464**, 664.
Chakrabarti, S.K., Acharyya, K. and Molteni, D.: 2004, *A&A* **421**, 1.
Chakrabarti, S.K. and Manickam, S.G.: 2000, *ApJ* **531**, L41.
Chakrabarti, S.K. and Titarchuk, L.G.: 1995, *ApJ* **455**, 623.
Ling, J.C. and Wheaton, W.A.: in press, *Chin. J. Astron. Astrophys.*
Longair, M.S.: 1981, *High Energy Astrophysics*, Cambridge University Press, UK.
Mandal, S. and Chakrabarti, S.K.: *Signature of Accretion Shocks in Emitted Radiation from a Two Temperature Advective Flows Around Black Holes, A&A* (in press).
Titarchuk, L.G. and Lyubarskij, Y.: 1995, *ApJ* **450**, 876.

AN OVERVIEW OF THE VERITAS PROTOTYPE TELESCOPE AND CAMERA

PETER COGAN (for the VERITAS collaboration)*
University College Dublin, National University of Ireland; E-mail: peter@ferdia.ucd.ie

(Received 4 June 2004; accepted 10 August 2004)

Abstract. The Very Energetic Radiation Imaging Telescope Array System (VERITAS) is the next-generation ground-based gamma-ray observatory that is being built in southern Arizona by a collaboration of 10 institutions in Canada, Ireland, the UK and the USA. VERITAS is designed to operate in the range from 50 GeV to 50 TeV with optimal sensitivity near 200 GeV; it will effectively overlap with the next generation of space-based gamma-ray telescopes. The first phase of VERITAS, consisting of four telescopes of 12 m aperture, will be operational by the time of the GLAST launch in 2007. Eventually, the array will be expanded to include the full array of seven telescopes on a filled hexagonal grid of side 80 m. A prototype VERITAS telescope with a reduced number of mirrors and signal channels has been built. Its design and performance is described here. The prototype is scheduled to be upgraded to a full 499 pixel camera with 350 mirrors during the autumn of 2004.

Keywords: VERITAS, IACT, gamma-ray astronomy, AGN, supernova remnants

1. Introduction – Very-High-Energy γ-ray Astronomy

Very-High-Energy (VHE) γ-ray astronomy is the study of photons in the 50 GeV to 50 TeV energy range. Such photons are only produced by the most exotic objects in the universe with active galactic nuclei (AGN) and supernova remnants (SNR) among the source categories detected thus far. Given that VHE γ-rays are at the extreme end of the electromagnetic spectra of these objects, they provide excellent constraints on their emission models. The study of VHE γ-rays may also be used to help determine the source of cosmic rays, measure the density of the extragalactic background infrared (IR) radiation and measure the magnetic fields in the shells and nebulae of SNRs. The effective detection of VHE photons is impractical with space-based telescopes due to the low flux of photons and the small collection area of such telescopes. Instead, VHE γ-rays may be indirectly quantified by measuring the extensive air shower (EAS) produced when a γ-ray strikes the Earth's atmosphere.

*The VERITAS collaboration consists of universities and institutions from Ireland, UK, USA and Canada. See http://veritas.sao.arizona.edu/VERITAS_members.html for a full listing.



Astrophysics and Space Science **297:** 275–281, 2005.
© Springer 2005

2. The Imaging Atmospheric Cherenkov Technique

Upon interacting with the Earth's atmosphere, VHE γ-rays produce cascades of charged particles known as EASs. These may be detected indirectly at ground level by instruments capable of recording the Cherenkov radiation emitted by the relativistic shower constituents. Unfortunately, there exists an almost overwhelming background of EAS produced by charged cosmic rays and an extremely efficient background rejection method is required. The Imaging Atmospheric Cherenkov Technique (IACT) (Weekes and Turver, 1977) allows discrimination between cosmic-ray- and gamma-ray-initiated EAS by recording the images of the Cherenkov light emitted by the EAS as they develop in the atmosphere (Hillas, 1985). Off-line image analysis techniques are employed to exploit the subtle differences in the physics of the hadronic and electromagnetic EAS, resulting in the rejection of over 99.7% of the background. The imaging cameras are made from arrays of photo-multiplier tubes (PMTs) located in the focal planes of large optical reflectors.

3. VERITAS

The Whipple 10 m telescope was the first IACT telescope to be operated (Cawley, 1990). It detected its first VHE γ-ray source, the Crab Nebula, in 1989 (Weeks et al., 1989). Since that time, several other collaborations have built IACT telescopes and the catalogue of detected γ-ray sources has blossomed to nearly 20 objects (Horan and Weekes, 2004). The angular and energy resolution of the Imaging Atmospheric Cherenkov Technique can be improved by utilising an array of such telescopes. This approach will also lower the energy threshold, thus narrowing the energy gap between space- and ground-based telescopes. The operation of multiple IACT telescopes in stereo mode has been demonstrated by the HEGRA group (Konopelko, 1999).

VERITAS (Weekes et al., 1989) is a next-generation IACT telescope array currently being built in Arizona by the VERITAS collaboration. The first stage in building VERITAS was to construct a single prototype telescope (Wakely et al., 2003). This telescope was erected during the summer of 2003 at the basecamp of the Fred Lawerence Whipple Observatory in Arizona. The primary mission of the prototype telescope was to field test the new technologies being employed by VERITAS and to test system integration. The prototype telescope operated from September 2003 until April 2004.

4. The VERITAS Prototype

4.1. Telescope and optics

The VERITAS prototype telescope was built using a custom-designed, welded steel, space-frame optical support structure (OSS) mounted on a commercial positioner

(Gibbs et al., 2003). The telescope uses the Davies Cotton (Davies and Cotton, 1957) reflector design. This design comprises multiple identical small mirrors arranged such that they mimic a large single reflector. The most significant advantage of this design is that it removes the requirement to build a single large mirror – which would be problematic in terms of cost, weight and gravitational slumping. The Davies Cotton design is cheap, the mirrors are light and individually adjustable. If a single mirror is damaged, it can be easily replaced. The most significant disadvantage of the Davies Cotton design is that it is not isochronous. This means that a spread is introduced to the light pulse arrival time at the camera. The VERITAS telescope's focal length is 12 m, making it an $f/1$ system for a 12 m aperture. This is a significant improvement over the Whipple telescope, which is $f/0.7$ as it will reduce the effect of optical aberrations and is required in order to match the angular size of the PMTs (0.15°). It also reduces the light pulse arrival time spread to 4 ns.

The total mass of the OSS, mirrors, counterweights and camera is estimated to be 16,000 kg. RPM has provided a positioner, model PG-4003, to meet the requirements of the VERITAS telescope. The positioner has a design azimuth slew speed of 1°/s and a design elevation slew speed of 0.5°/s, although it was being exercised at more conservative speeds while its performance was evaluated.

Although the prototype employed a full-sized OSS, it only held 84 mirrors giving a surface area of 34 m^2. Each full VERITAS telescope will hold 350 mirrors giving a total mirror area of 140 m^2. The optical qualities of the VERITAS prototype mirrors were tested at the Whipple Observatory basecamp. They were found to exceed

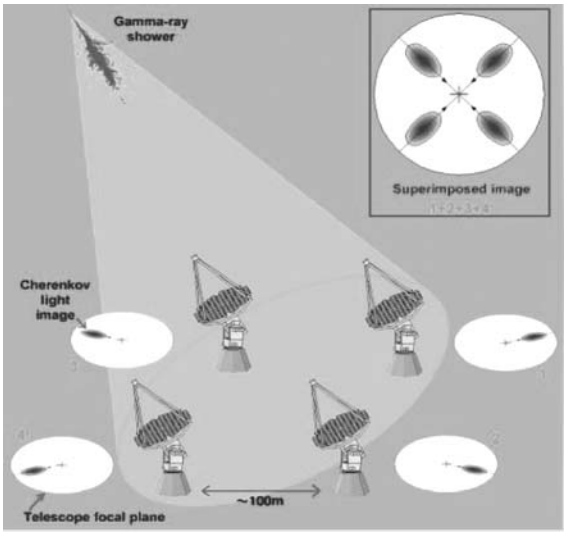


Figure 1. Several telescopes may lie in the light pool generated by an EAS. This is the key to stereoscopic imaging (Holder, University of Leeds).

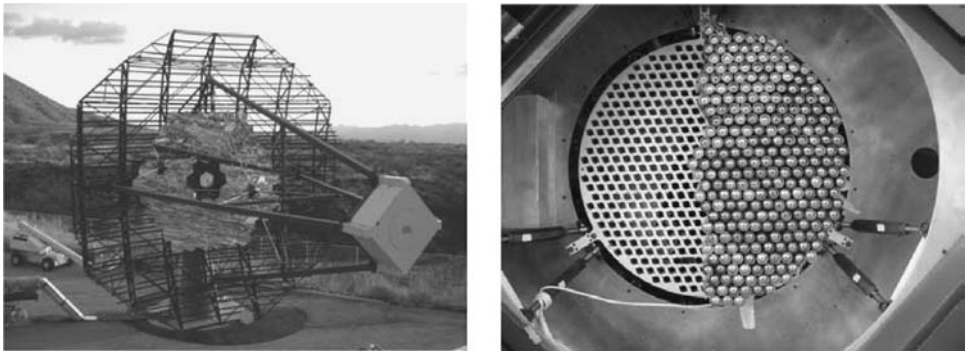


Figure 2. Left: The VERTIAS prototype. Right: The prototype camera.

design specifications in terms of reflectivity and curvature. Mirror alignment is achieved using a laser-based Mirror Alignment System. The Point Spread Function of the prototype telescope, which is a measure of the mirror alignment, was 0.05° which is within design specifications.

4.2. Camera

In order to detect the extremely faint and brief Cherenkov flash, a low noise, high-gain photon counting device with a fast (2.5 ns) risetime is required. Despite steady advances in the field of solid-state detectors, only PMTs currently meet these requirements. A VERITAS camera will comprise 499, $1\frac{1}{8}$ in. Photonis XP 2970 PMTs. The PMTs are supplemented with a high-bandwidth preamplifier integrated into the PMT base. A charge-injection system is also present in the camera for calibration and diagnostic purposes. This system injects pulsed charges into the preamplifier which simulates Cherenkov events. This can be used to test the electronics and data acquisition systems downstream of the PMTs in a controlled manner without activating the PMTs. Current monitoring systems in the camera provide a measurement of the brightness of the field of view in each pixel and may be used to check tracking. Each full VERITAS camera will also contain environmental sensors. The high voltage (HV) for the PMTs is provided by a multichannel modular commercial power supply (CAEN SY1527/A1932). The VERITAS prototype camera consisted of 255 Hamamatsu PMTs in a 'half-moon' configuration. Despite the reduced camera size, the VERITAS prototype performed excellently as a full IACT telescope.

5. Trigger and Calibration Systems

VERITAS utilises a flexible three-level trigger system which allows full-array, sub-array and individual telescope operation. Trigger level one consists of individually

programmable constant-fraction discriminators (CFDs) which determine whether an individual pixel has triggered. The level two trigger is a topological hardware trigger that can discriminate between compact Cherenkov events and random night-sky or afterpulse-induced events (Bradbury et al., 1999). Trigger levels one and two constitute the telescope-level trigger, while the level three system receives inputs from all the telescopes and generates array-level triggers, and event numbers, based on a geometry-adjusted multiplicity condition. The VERITAS prototype has operated with full implementations of the level one and level two triggers for 250 channels but with a simplified level three trigger as sophisticated multi-telescope triggering is not yet required.

Calibration systems installed on the VERITAS prototype telescope include a charge-injection system and a nitrogen/dye laser flasher. In addition, atmospheric monitoring stations, a mid-infra-red pyrometer system, and CCD sky quality monitoring cameras are under development.

6. Signal Digitisation and Data Acquisition

The signals from each of the PMTs are digitised by a custom-designed 500 MSPS flash-analogue-to-digital converter (FADC) system (Buckley et al., 2003). The prototype telescope has 25 FADC boards, containing 10 channels each, situated in two VME crates. A third VME crate contains GPS clocks and ancillary modules. Each FADC channel has a dynamic range of 11 bits and a memory depth of $\sim 8\ \mu$s. The

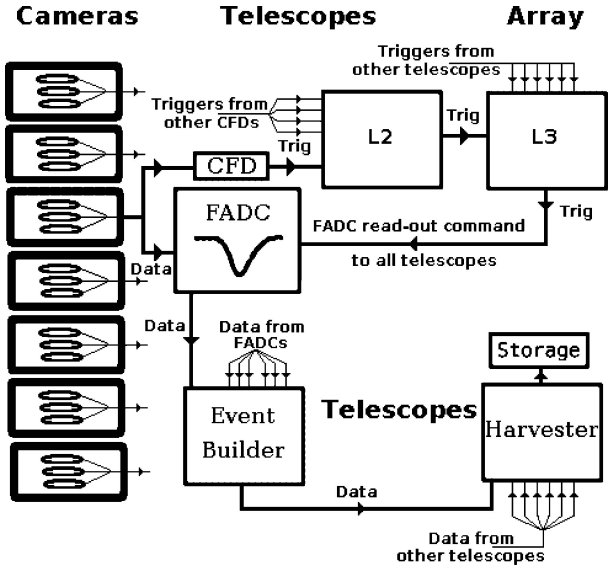


Figure 3. A rough map of the data/trigger chain for the VERITAS array. For the prototype there was only one camera/telescope; however, the array trigger section was present.

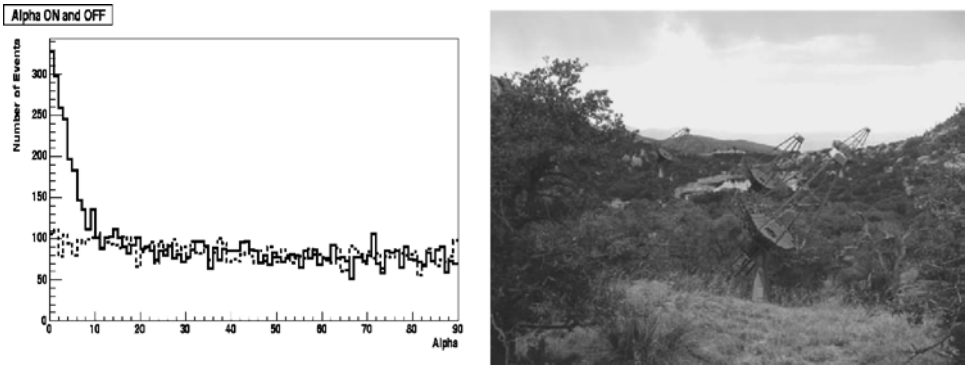


Figure 4. Left: An alpha plot indicating the detection of Mrk421 (Holder, University of Leeds). Right: An impression of the complete VERITAS-4 array at Horseshoe Canyon, Arizona.

FADCs have zero-suppression capabilities, so that channels whose signal do not exceed a programmable threshold do not appear in the data stream.

With the FADCs, VERITAS can sample the charge deposited in each pixel every 2 ns. This provides a pulse profile for each pixel for each event. In addition to improving the signal to noise ratio, eliminating the need for delay cables and reducing deadtime, the pulse profile may provide a new technique for discriminating against hadronic events using the time evolution of the EAS.

Readout of the FADCs is accomplished using VMIC Pentium crate computers running the Linux operating system. Each crate computer buffers multiple event fragments until an optimal depth has been reached, when they are then transferred via Scalable Coherent Interface to the telescope event-building system. The telescope event-building system consists of a dual-processor Xeon server running Linux and the data acquisition software is implemented in C++. Built telescope events are sent via ethernet to the harvester machine, where they are combined into array events and analysed, and stored locally on disk for redundancy. The DACQ software is controlled from the central array-control system via a CORBA interface.

This integrated data acquisition system has been thoroughly tested on the prototype telescope and found to perform reliably. During the prototype telescope evaluation stage 64 samples were read out for every channel with each event, resulting in a data size of $\sim$16.5 kB per event, at a rate of $\sim$30 Hz. The full VERITAS telescopes will operate with a considerably reduced event size due to zero-suppression and a reduced number of FADC samples per event.

7. Early Results

The VERITAS prototype operated from September 2003 until the end of April 2004. While much of this time was spent testing systems and system integration, a

significant amount of quality data was taken on the well-established TeV source, Markarian 421 (Mrk421). During this period, the nearby Whipple 10 m telescope observed this BL Lac in a flaring state, allowing a meaningful comparison in gamma-ray rate between the Whipple 10 m telescope and the VERITAS prototype. The prototype detected Mrk421 at 20.5σ over 19.2 h of observations. During the same period, the prototype telescope's average rate was 0.8 γ/min and the Whipple 10 m observatory's was 7 γ/min.

8. Schedule

During the summer of 2004, the prototype camera will be completely disassembled and the new Photonis pixels installed. The remainder of the 350 mirrors will be mounted. When these upgrades are completed the prototype will be redesignated telescope 1 and will operate at the basecamp of the Whipple Observatory for 2 years. In the interim, the VERITAS site at Horseshoe Canyon will be prepared and three telescopes identical to telescope 1 will be constructed. Upon their completion, telescope 1 will be moved to Horseshoe Canyon, completing the VERITAS-4 array. This is expected to occur before the summer of 2006.

References

Bradbury, S.M., et al.: 1999, Proceedings of the 26th ICRC, Salt Lake, G 4.3.21.
Buckley, J., et al.: 2003, Proceedings of the 28th ICRC, Tsukuba, Japan.
Cawley, M.F.: 1990, *Exp. Astron.* **1**, 173.
Davies, J. and Cotton, E.: 1957, *J. Solar Energy* **1**, 16.
Gibbs, K., et al.: 1985, Proceedings of the 28th ICRC, Tsukuba, Japan, vol. 3, p. 445.
Hillas, M.: 1985, Proceedings of the 19th ICRC, La Jolla, vol. 3, p. 445.
Horan, D. and Weekes, T.C.: 2004, *New Astron. Rev* **48**, 527.
Konopelko, A.: 1999, *Astropart. Phys.* **11**, 263.
Wakely, S.P.: Proceedings of the 28th ICRC, Tsukuba, Japan.
Weekes, T.C., et al.: 1989, *ApJ* **342**, 370.
Weekes, T.C., et al.: 2002, *Astropart. Phys.* **12**, 221.
Weekes, T.C. and Turver, K.E.: 1977, Proceedings of the 12th ESLAB Symposium, Frascati, p. 279.

COMPTEL CONSTRAINTS ON UNIDENTIFIED EGRET SOURCES

SHU ZHANG[1,2], WERNER COLLMAR[2] and VOLKER SCHÖNFELDER[2]

[1]*Laboratory of Particle Astrophysics, Institute of High Energy Physics, Beijing, China; E-mail: szhang@mail.ihep.ac.cn*

[2]*Max-Planck-Institut für Extraterrestrische Physik, Garching, Germany*

(Received 8 July 2004; accepted 28 July 2004)

Abstract. A major legacy of the EGRET experiment aboard the Compton Gamma-Ray Observatory (CGRO) is the detection of a large number of unidentified Gamma-ray sources. Out of the 271 EGRET sources are 170 not identified yet [Hartman et al. *ApJS* (123) (1999) 79]. To provide additional information on these unidentified EGRET sources, we derived simultaneous MeV fluxes or flux limits for each source by analyzing the contemporaneous COMPTEL data. Then we compare these MeV fluxes to the extrapolations of the published EGRET spectra. Our results can be grouped into 4 categories [Zhang et al. *A&A* (421) (2004) 983]: (1) non-constraining upper limits ($\sim$120 sources), (2) hints ($>$2 sigma) or detections with consistent MeV fluxes ($\sim$16 sources), (3) enhanced MeV emission (2 sources), and (4) constraining MeV flux limits, requiring a spectral break ($\sim$22 sources). In summary, for about 40 of the unidentified EGRET sources we can provide supplementary spectral information in the neighboring gamma-ray band, which – together with other source parameters – might provide clues to the underlying source nature.

Keywords: γ rays: unidentified γ-ray sources

1. Introduction

The spark-chamber telescope EGRET covered the γ-ray range from $\sim$ 30 MeV to $\sim$30 GeV. The instrument was mounted on the Compton Gamma-Ray Observatory (CGRO), whose mission lasted from April 1991 to June 2000. The instrument and its calibration are described in detail by Thompson et al. (1993) and Esposito et al. (1999). During its mission EGRET has detected 271 γ-ray sources (Hartman et al., 1999). One hundred seventy of them are unidentified and 27 are only tentatively identified. As possible counterparts, objects of various classes (e.g., AGN and pulsars) are supposed to be behind those unidentified EGRET sources.

The COMPTEL experiment aboard CGRO (0.75–30 MeV) covers the softer γ-ray band adjacent to the EGRET one. Since COMPTEL and EGRET were mounted parallel on CGRO and both had a large field of view (the COMPTEL one larger than the EGRET one), COMPTEL observed simultaneously the same sky region as EGRET. To exploit this coincident field of view, we have analyzed the contemporaneous COMPTEL data on all unidentified EGRET sources to supplement the EGRET results. In this paper, we report on the discovery of



Astrophysics and Space Science **297:** 283–290, 2005.
© Springer 2005

subgroups of the unidentified EGRET sources with further spectral informations provided from the MeV data.

2. Instrument, Data Analysis and CGRO Observations

The imaging Compton telescope COMPTEL consisted of two layers of detectors. In its primary mode – the double scatter mode – a γ-ray photon is first Compton scattered in one of the upper detector modules and then absorbed by a detector module of the lower layer. In this mode COMPTEL was sensitive to γ-radiation in the energy range 0.75–30 MeV with an energy-dependent energy and angular resolution of 5–8% (FWHM) and 1.7–4.4° (FWHM), respectively. Its field of view is circular and covers $\sim$1 steradian. Imaging in its large field of view is possible with a location accuracy of the order of 1–3°, depending on source flux. For details on the COMPTEL experiment see Schönfelder et al. (1993).

The COMPTEL data analysis is performed in the standard three-dimensional data space by applying the standard COMPTEL analysis procedures and standard data cuts. Skymaps and source parameters, like detection significances, fluxes, and flux errors, are obtained by the standard COMPTEL maximum-likelihood procedure (de Boer et al., 1992). An estimate for the instrumental background of COMPTEL is derived by using the standard filter technique in the COMPTEL data space (Bloemen et al., 1994). In the presented analyses we applied instrumental point spread functions assuming an E^{-2} power-law shape for the source spectra. The detection significance can be conservatively calculated by the ratio of flux to flux error. This approach is adopted in this paper for estimating the source detection significances. In fitting the fluxes of the relevant EGRET sources, nearby prominent COMPTEL sources and the celestial background components, galactic and extra-galactic diffuse γ-ray radiation, are accounted for by model fitting.

CGRO observations were organized in so-called 'Mission Phases' and 'Viewing Periods (VPs)'. A 'Mission Phase' covers typically 1 year of data and contains many VPs, which typically last for 1–2 weeks each. For each EGRET source of interest we analyzed the simultaneous COMPTEL data. To be able to combine simultaneous COMPTEL and EGRET results, we analyzed the MeV data for periods for which the EGRET spectral index was estimated (Hartman et al., 1999).

To compare our flux results to EGRET, we plot the EGRET spectra as best-fit power-law shapes with 1σ errors in shape for energies above 100 MeV. Systematic errors of 10% are included in these EGRET spectra. For comparison to the COMPTEL data, these spectra are extrapolated below 100 MeV into the COMPTEL band. The COMPTEL data are given as flux points for 4 standard COMPTEL bands (0.75–1, 1–3, 3–10, 10–30 MeV). For a detection significance $<2\sigma$ the source flux is presented by a 2σ upper limit, otherwise by a flux point. Additionally, when comparing with the EGRET spectral extrapolations, the COMPTEL error bars and

subsequently also the upper limits are enlarged by 20 percent to account for systematic errors.

3. Results

3.1. General results

We investigated unidentified or tentatively identified EGRET sources for which spectral indices are available in the third EGRET catalogue. By excluding five artifacts near the Vela pulsar and one artifact near Crab (Thompson et al., 2001), an ensemble of 173 sources was selected for our analyses. In some sky regions the unidentified EGRET sources are 'crowded'. For cases where they are closer than the COMPTEL location accuracy, no precise and unambiguous MeV flux could be attributed to individual sources. The fluxes of these sources are not fitted simultaneously and therefore their fluxes are given as upper limits.

In most cases, we derive only upper flux limits or marginal ($<4\sigma$) hints for MeV emission. We find significant MeV detections in four sky regions. Three of them are locations of already known unidentified MeV sources ($(l, b) = (358.5, 0.5), (311.5, -2.5), (18.5, -0.5)$). The fourth one, at $\sim(l, b) = (188.7, -4.4)$ and dubbed GRO J0550+19 in Bronsveld et al. (2002), is near the location of the Crab, which is by far the strongest MeV source. Detailed studies of these sky regions have been already done or are currently in progress. The results were or will be reported elsewhere (Strong et al., 2001; Zhang et al., 2002; Bronsveld et al., 2002; Collmar et al., 2005).

In general our results can be grouped into four categories. For the majority of sources COMPTEL cannot provide any constraints on the EGRET spectra (category 1). We detect evidence (detection significance $>2\sigma$) for about 16 sources whose MeV fluxes are consistent with the EGRET extrapolations, showing that the measured EGRET spectra extend into the MeV band (category 2). A third source category indicates for 2 sources a spectral upturn of the EGRET spectra at MeV energies, suggesting the presence of an additional spectral component. Finally we found 22 sources whose COMPTEL fluxes or upper flux limits are below the expected fluxes from the EGRET spectra, requiring a spectral turnover/break at MeV energies or above (category 4). See Figure 1 for representatives of each category.

3.2. Sources of category 2

This subgroup of sources has marginal detections at MeV energies and the MeV emission is consistent with the EGRET spectral extrapolation within error bars. As one example, the combined COMPTEL/EGRET spectrum for 3EG J0130–1758 is shown in Figure 1. The total number of sources in this subgroup is 16 and the parameters of individual sources are given in Table I. Six sources located within

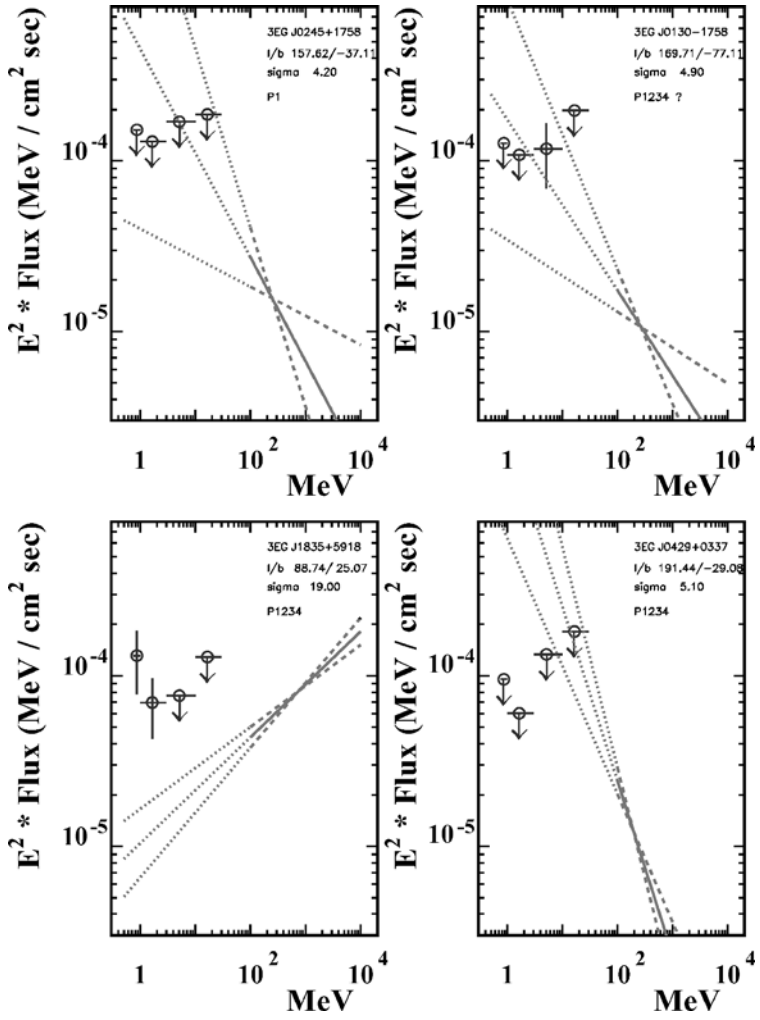


Figure 1. Combined COMPTEL/EGRET energy spectra of individual examples of the four COMPTEL categories of unidentified EGRET sources. The inserted text gives the EGRET third catalogue informations (Hartman et al., 1999) on the source (source name, sky location, EGRET detection significance, and detection period). The solid line represents the best-fit EGRET spectrum, the dashed lines its 1σ error in spectral index, and the dotted lines the spectral extrapolations below 100 MeV down to 0.75 MeV. The COMPTEL upper limits are 2σ and the error bars on the flux points are 1σ. 3EG J0245+1758, 3EG J0130–1758, 3EG J1835+5918 and 3EG J0429+0337 represent individual examples of the categories 1–4 (see text), respectively.

the sky regions of three strong unidentified COMPTEL sources (GRO J1410–64, $l = 18$, and GRO J1743–30). They are not considered and therefore not included in Table I. 3EG J0512–6150 and 3EG J2227+6122 might be the possible counterparts of the COMPTEL sources GRO J0516-609 and GRO J2227+61, respectively, since they are the only EGRET sources within the COMPTEL error locations. The two

TABLE I

Catalogue of the 16 unidentified EGRET sources which have MeV fluxes consistent with EGRET spectral extrapolations

						Flux (10^{-5} ph cm^{-2} s^{-1})			
Name 3EG J	l (deg)	b (deg)	α	VP	I	0.75–1	1–3	3–10	10–30
0130−1758	169.71	−77.11	2.5 ± 0.29	P1234	0.1	<4.2	<7.3	2.8 ± 1.1	<1.3
0500+2529	177.18	−10.28	2.52 ± 0.32	P1	2.2	<4.9	5.1 ± 2.3	<2.4	<0.7
0512−6150	271.25	−35.28	2.4 ± 0.26	P1234	2.3	<6.1	4.6 ± 1.7	<2.2	<0.5
0542+2610	182.02	−1.99	2.67 ± 0.22	P12	2.7	<8.0	5.3 ± 2.4	<2.2	<0.8
0556+0409	202.81	−10.29	2.45 ± 0.16	P1234	1.7	<3.4	<3.3	2.1 ± 0.7	<0.5
0917+4427	176.11	44.19	2.19 ± 0.14	P1234	1.6	<5.4	3.5 ± 1.6	<1.6	<0.9
1014−5705	282.8	−0.51	2.23 ± 0.2	P34	1.5	<5.1	<8.2	<2.3	1.2 ± 0.4
1133+0033	264.52	57.48	2.73 ± 0.63	P3	5.4	<6.1	<5.8	2.9 ± 1.3	0.9 ± 0.4
1316−5244	306.85	9.93	2.54 ± 0.18	P1234	2.2	3.9 ± 1.7	<5.4	2.2 ± 0.8	<0.6
1631−1018	5.55	24.94	2.2 ± 0.27	P1234	2.0	<3.9	4.0 ± 1.9	<2.0	<0.7
1659−6251	327.32	−12.42	2.54 ± 0.37	314+	2.6	<17.6	<16.9	<5.7	2.3 ± 1.1
1718−3313	353.2	2.56	2.59 ± 0.21	5.0	2.2	<13.9	11.9 ± 5.4	<4.7	<2.1
1824+3441	62.49	20.14	2.03 ± 0.5	20.0	2.7	<12.1	<12.3	8.5 ± 3.2	<3.0
2006−2321	18.82	−26.26	2.33 ± 0.36	P1	3.1	<5.3	<5.2	4.9 ± 1.3	<1.0
2227+6122	106.53	3.18	2.24 ± 0.14	P1234	3.5	<3.9	4.1 ± 1.9	<1.8	<0.7
2255−5012	338.75	−58.12	2.79 ± 0.53	404.0	1.6	<24.6	<21.1	<5.7	2.5 ± 1.0

The source parameters of the first five columns are taken from the third EGRET catalogue, column 6 is for variability analysis, and the last four columns give the COMPTEL fluxes/upper limits in the four standard energy bands. The abbreviations are the following:

Name: 3EG source name.

l/*b*: source coordinate of galactic longitude and latitude.

α: photon spectral index and its error.

VP: CGRO observation periods for which the spectral index is derived. P1 means phase 1, P12 the combination of P1 and P2, and so on. Observation 314+ is the combined VPs 314 and 315.

I: index defined by Torres et al. (2001) for measuring source variability with respect to γ-ray pulsars; derived by our variability analysis on the published EGRET fluxes.

Flux (10^{-5} ph cm^{-2} s^{-1}): COMPTEL fluxes and the flux unit in the four standard energy bands: 0.75–1, 1–3, 3–10 and 10–30 MeV. The upper limits are 2σ and the error bars are 1σ.

COMPTEL sources are weak on a level averaged over years (Phases 1-4). We would like to note that 3EG J1014–5705 can not be resolved from 3EG J1013–5915 and the same problem exists for 3EG J1718–3313, which is too close to 3EG J1734–3232. The marginal detections of all other 12 sources are unambiguous, i.e. not confused by a nearby EGRET or COMPTEL source. These 16 sources show a relatively homogeneous spatial distribution. Investigating their time variability by the so-called I-index (Zhang et al., 2000; Torres, et al., 2001), we find that five sources are variable (I-index > 2.5; no obvious spatial trend), and one source (3EG J0130–1758) is stable, which is located at high latitude. The spectral index averaged over the 16 sources is 2.38.

3.3. Sources of category 3

This category consists of two high-latitude sources, 3EG J1337+5029 and 3EG J1835+5918. Preliminary analyses indicate, that their MeV emission overshoots the EGRET spectral extrapolations (see 3EG J1835+5918 in Figure 1 as example). Such spectra resemble to the so-called "MeV" blazars, and probably indicate the existence of an additional spectral component at MeV energies. The I-index shows 3EG J1337+5029 to be variable and 3EG J1835+5918 to be dubious. However, both sources have rather hard energy spectra which are comparable to γ-ray pulsars. 3EG J1835+5918 is in fact too close to another EGRET unidentified source, 3EG J1850+5903, to be clearly resolved by COMPTEL. Therefore the derived source flux cannot be attributed unambiguously to 3EG J1835+5918. However, 3EG J1850+5903 was detected by EGRET only in VP 2.0 (duration 9 days) at a relatively low significance, and therefore is not likely to contribute much to the detected MeV emission averaged over Phases 1–4 ($\sim$4.5 years), including the location of 3EG J1850+5903. To provide final results on 3EG 1835+5918 an individual analysis of this source has still to be done.

3.4. Sources of category 4

Sources of category 4 show a spectral flattening at MeV energies (see 3EG J0429+0337 in Figure 1 as example). The parameters of all 22 members are listed in Table II. These sources tend to concentrate in the inner galactic region, which suggests a galactic origin for most of them. The averaged spectral index is 2.72 for the 22 sources. The I-index investigation suggests half of them to be variable and half dubious. For the details on the results and the discussions of these 22 sources see Zhang et al. (2004).

4. Discussion and Summary

By analyzing the COMPTEL data of unidentified and tentatively identified EGRET sources, and comparing these results to the EGRET spectra, we found about 40 sources, grouped into different categories, for which the simultaneous MeV spectra provide additional constraints. The most interesting case is category 4, consisting of 22 sources, which show a spectral turnover at MeV energies. At least two of them, but most likely the majority, have an emission maximum at energies between 1 and 100 MeV. Variability analyses showed that half of the sources are variable above 100 MeV. For the other half no significant time variability could be proven. Their spatial distribution tends to concentrate toward the inner galaxy region. Potential counterparts which have to fulfill these requirements, could be blazars at high-latitude, microquasars, XRBs, pulsars, SNRs, etc. The corresponding emission mechanisms producing the observed MeV spectral turnover might

TABLE II

Catalogue of the 22 unidentified EGRET sources which – by inclusion of the COMPTEL results – have to have a spectral break or their γ-ray luminosity maxima at MeV energies

Name 3EG J	l (deg)	b (deg)	α	*VP*	I	Flux (10^{-5} ph cm^{-2} s^{-1}) 0.75–1	1–3	3–10	10–30
0429+0337	191.44	−29.08	3.02 ± 0.27	P1234	1.6	<3.2	<4.0	<3.1	<1.2
0520+2556	179.65	−6.40	2.83 ± 0.24	P1234	1.1	4.8 ± 1.7	8.3 ± 1.6	<2.1	<0.5
0546+3948	170.75	5.74	2.85 ± 0.21	P1234	1.7	<2.9	<2.9	<1.4	<0.9
1300−4406	304.6	18.74	3.07 ± 0.40	P12	3.0	<5.0	<4.7	<2.2	<1.0
1424+3734	66.82	67.76	3.25 ± 0.46	P1	1.9	<6.4	8.5 ± 3.1	<5.6	<2.2
1500−3509	330.91	20.45	2.99 ± 0.37	P1234	1.5	<5.1	<3.3	<1.6	<1.0
1612−2618	349.40	17.90	2.71 ± 0.23	423.	4.1	<41.0	<19.1	<9.3	<4.2
1638−5515	334.05	−3.34	2.56 ± 0.21	P2	2.4	<15.6	<7.0	<6.7	2.8 ± 1.0
1639−4702	337.75	−0.15	2.50 ± 0.18	P1234	2.0	<3.1	<4.5	<3.0	<0.9
1709−0828	12.86	18.25	3.00 ± 0.35	P1234	2.7	<3.2	<3.2	<2.8	<0.6
1735−1500	10.73	9.22	3.24 ± 0.47	231.0	8.9	<29.0	<23.1	<11.8	<4.5
1741−2312	4.42	3.76	2.49 ± 0.14	P12	2.2	<11.9	<4.4	<3.0	<0.9
1800−0146	25.49	10.39	2.79 ± 0.22	P34	1.9	<8.1	<7.0	<2.2	<1.4
1823−1314	17.94	0.14	2.69 ± 0.19	P3	3.0	10.2 ± 2.9	5.6 ± 2.8	3.7 ± 1.2	2.7 ± 0.5
1825+2854	56.79	18.03	4.47 ± 1.15	9.2	2.5	<30.1	<13.9	<8.6	<2.2
1828+0142	31.90	5.78	2.76 ± 0.39	13.1	5.3	<16.4	<15.8	<11.3	<4.4
1837−0423	27.44	1.06	2.71 ± 0.44	423.0	8.4	<23.4	<18.5	<14.3	<3.0
1858−2137	14.21	−11.15	3.45 ± 0.38	P1234	2.8	<4.2	<5.0	1.6 ± 0.7	<0.6
1903+0550	39.52	−0.05	2.38 ± 0.17	P1234	2.3	<3.3	<3.4	<2.7	<0.7
1940−0121	37.41	−11.62	3.15 ± 0.39	330.+	4.0	<16.6	<10.9	<6.8	<1.8
2020−1545	28.09	−26.62	3.40 ± 0.55	P1	0.9	<5.2	<7.7	<2.6	<1.0
2034−3110	12.25	−34.64	3.43 ± 0.78	P1	5.7	<5.4	<5.4	<3.2	<1.7

Observation 330+ is the combined VPs 330 and 332. The columns have the same meanings as in Table I.

be: incomplete cooling or cut-off in the spectrum of the relativistic jet electron population (e.g. blazars, microquasars); absorption of high-energy photons by the strong magnetic field (e.g. pulsars) or by a dense soft photon environment (e.g. XRB). The category 2 is also interesting. It consists of 16 sources, showing MeV emission consistent with the extrapolation of the EGRET spectrum. Because generally no strong hard X-ray source is found within the corresponding EGRET error locations, these sources, in particular the ones with steep spectra, might have their maximum luminosities just below MeV energies. These results provide further clues in probing the origin of these sources. Detailed follow-up researches on individual sources by including these new and additional informations, might reveal the nature of some unidentified EGRET sources. Because the COMPTEL data are currently in a process of consistent reanalysis, further and improved MeV informations on some of these unidentified EGRET sources can be expected.

Acknowledgements

This research was supported by the German government through DLR grant 50 QV 9096 8, by NASA under contract NAS5-26645, and by the Netherlands Organization for Scientific Research NWO. S. Zhang was also subsidized by the Special Funds for Major State Basic Research Projects and by the National Natural Science Foundation of China under Grant 10373013.

References

Bloemen, H., Hermsen, W., Swanenburg, B.N. et al.: 1994, *ApJS* **92**, 419.

Bronsveld, C.P., Hermsen, W., Kuiper, L. and Schönfelder, V.: 2002, in: A. Goldwurm, D.N. Neumann, J.T.T. Vân (eds.), *Proceedings of the XXXVIIth Rencontres de Moriond in the Gamma-Ray Universe*, Thẽ Giòi Publishers, Vietnam, p. 113.

de Boer, H., Bennett, K., Bloemen, H. et al.: 1992, in: V. Di Gesù, L. Scarsi, R. Buccheri, et al. (eds.), *Data Analysis in Astronomy IV*, Plenum Press, New York, p. 241.

Collmar., W. et al.: 2005, *A&A*, in preparation.

Esposito, J.A., Bertsch, D.L., Chen, A.W. et al.: 1999, *ApJS* **123**, 203.

Hartman, R.C., Bertsch, D.L., Bloom, S.D. et al.: 1999, *ApJS* **123**, 79.

Schönfelder, V., Aarts, H., Bennett, K. et al.: 1993, *ApJS* **86**, 657.

Strong, A.W., Collmar, W., Bennett, K. et al.: 2001, in *Proceedings of the AIP Conference on Gamma-Ray Astrophysics 2001*, Vol. 587, p. 21.

Thompson, D.J., Bertsch, D.L., Fichtel, C.E. et al.: 1993, *ApJS* **86**, 629.

Thompson, D.J., Bertsch, D.L. and Hartman, R.C.: 2001, in *Proceedings of the AIP Conference on Gamma-Ray Astrophysics 2001*, Vol. 587, p. 668.

Torres, D.F., Romero, G.E., Combi, J.A. et al.: 2001, *A&A* **370**, 468.

Zhang, L., Zhang, Y.J. and Cheng, K.S.: 2000, *A&A* **357**, 957.

Zhang, S., Collmar, W. and Schönfelder, V.: 2002, *A&A* **396**, 923.

Zhang, S., Collmar, W., Hermsen, W. and Schönfelder, V.: 2004, *A&A* **421**, 983.

ON THE MULTIPLICITY OF THE O-STAR Cyg OB2 #8A AND ITS CONTRIBUTION TO THE γ-RAY SOURCE 3EG J2033+4118*

MICHAEL DE BECKER, GREGOR RAUW and JEAN-PIERRE SWINGS

Institut d'Astrophysique et de Géophysique, Université de Liège, 17, Allée du 6 Août, B5c, Sart Tilman, Belgium; E-mail: dbecker@astro.ulg.ac.be

(Received 4 June 2004; accepted 28 July 2004)

Abstract. We present the results of an intensive spectroscopic campaign in the optical waveband revealing that Cyg OB2 #8A is an O6+O5.5 binary system with a period of about 21.9 days. Cyg OB2 #8A is a bright X-ray source, as well as a non-thermal radio emitter. We discuss the binarity of this star in the framework of a campaign devoted to the study of non-thermal emitters, from the radio waveband to γ-rays. In this context, we attribute the non-thermal radio emission from this star to a population of relativistic electrons, accelerated by the shock of the wind-wind collision. These relativistic electrons could also be responsible for a putative γ-ray emission through inverse Compton scattering of photospheric UV photons, thus contributing to the yet unidentified EGRET source 3EG J2033+4118.

Keywords: binaries: spectroscopic, stars: individual: Cyg OB2 #8A, stars: early-type, radiation mechanisms: non-thermal

1. Introduction

Cyg OB2 #8A (BD $+40^{\circ}4227$, $m_{\rm V} = 9.06$) is one of the optically brightest O-stars in Cyg OB2. This star is classified as O5.5I(f) (Massey and Thompson, 1991), and is known to be a bright non-thermal and strongly variable radio emitter (Bieging et al., 1989). Up to now, Cyg OB2 #8A had never been shown to be a binary system.

However, in the context of the multiwavelength study of non-thermal radio emitters, the binarity is expected to play a crucial role. Indeed, as described in this communication, the most plausible scenario that could explain the non-thermal emission from hot stars relies on the existence of shocks able to accelerate electrons up to relativistic energies. Whether these shocks are intrinsic to the wind or due to a wind-wind collision in a binary system remains an open question. For this reason, we initiated an optical monitoring of non-thermal emitting massive stars. The result we report here is the discovery that Cyg OB2 #8A is a binary system. In this context, we discuss the expected emission of X and γ-rays from its interacting wind zone, and its contribution to the unidentified EGRET source 3EG J2033+4118 (Benaglia et al., 2001).

*Based partly on data Obtained at the Observatoire de Haute-Provence, France.



Astrophysics and Space Science **297:** 291–298, 2005.
© Springer 2005

This communication is organized as follows. Section 2 discusses the binarity of Cyg OB2 #8A and presents its first orbital solution. Section 3 deals with archive X-ray data in the context of a binary scenario. A discussion of non-thermal processes in the framework of massive stars is given in Section 4, and the conclusions appear in Section 5.

2. Cyg OB2 #8A as a Binary System

2.1. SPECTROSCOPIC ANALYSIS

We obtained a series of 35 spectra in the blue range (between about 4455 and 4900 Å) at the Observatoire de Haute-Provence (OHP, France) during four observing runs in September 2000, September 2001, September 2002 and October 2003. For details on the observations and the reduction procedure, see De Becker et al. (2004a).

Our spectra clearly indicate that Cyg OB2 #8A is a binary system consisting of an O6 primary and an O5.5 secondary revolving around each other in *21.908 days* (De Becker et al., 2004a). The intensities of the lines in the spectra of the two components roughly yield a visual brightness ratio of 2 between the primary and the secondary (see Figure 1). Since the spectral types of both components are similar, this suggests that their luminosity classes might be different.

Figure 1 shows some profiles of the HeI λ 4471 and HeII λ 4686 lines. We clearly see that the HeII line displays a strong variability. Some phases show P-Cygni

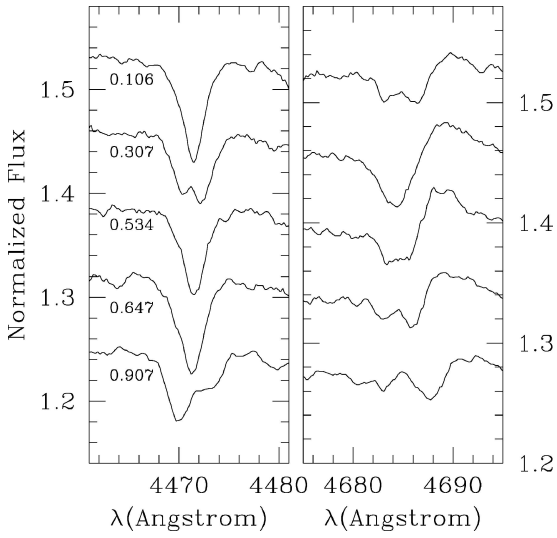


Figure 1. Profiles of the HeI λ 4471 (left) and HeII λ 4686 (right) lines displayed at five different phases specified in the left panel. (Preliminary results from De Becker and Rauw, 2005).

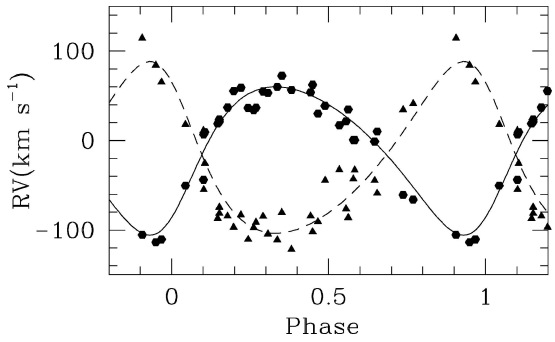


Figure 2. Radial velocity (RV) curve of Cyg OB2 #8A for an orbital period of 21.908 days. The hexagons (resp. triangles) stand for the primary (resp. secondary) RVs. The solid and dashed lines yield our best fit orbital solution respectively for the primary and the secondary (from De Becker et al., 2004a).

profiles ($\phi = 0.307$), but at other phases the profiles are much more complicated (e.g. $\phi = 0.907$). The observed variations are phase-locked and most probably reflect an interaction between the stellar winds of the two components (De Becker and Rauw, 2005).

2.2. Orbital solution

By simultaneously fitting two Gaussians to the HeI λ4471 line profiles, we determined the radial velocities of the two stars. We obtained the first orbital solution for this system using the method described by Sana et al. (2003). We assigned various weights to our data to take into account the different errors affecting our RV measurements. Due to the intensity ratio of the lines of the two components ($\sim$2), there was no ambiguity on the identification of the lines respectively of the primary and the secondary. Table I yields the main parameters of the system (De Becker et al., 2004a). However, we emphasize that the errors on the eccentricity and the period probably underestimate the actual error as a result of the rather heterogeneous phase coverage of our time series.

3. Archive X-ray Data

Cyg OB2 #8A archive data obtained with the *ROSAT* X-ray satellite were analyzed. For the pointings obtained with the PSPC (Position Sensitive Proportional Counter) instrument, we extracted spectra which were fitted with optically thin thermal plasma models (Mewe et al., 1987). After convolution with the HRI (High Resolution Imager) response matrix we estimated the equivalent HRI count rates. These results are quoted as filled triangles in Figure 3 that yields the archive X-ray

TABLE I
Orbital solution for Cyg OB2 #8A

	Primary	Secondary
P (days)	21.908 (fixed)	
e	0.24 ± 0.04	
$T_\circ$ (HJD–2 450 000)	1807.139 ± 0.894	
γ (km s^{-1})	-8.1 ± 3.3	-25.0 ± 3.6
K (km s^{-1})	82.8 ± 3.5	95.8 ± 4.0
$a \sin i$ ($R_\odot$)	34.8 ± 1.5	40.3 ± 1.7
$m \sin^3 i$ ($M_\odot$)	6.4 ± 0.6	5.5 ± 0.5

$T_\circ$ refers to the time of periastron passage. γ, K, and $a \sin i$ denote respectively the systemic velocity, the amplitude of the radial velocity curve, and the projected separation between the center of the star and the center of mass of the binary system.

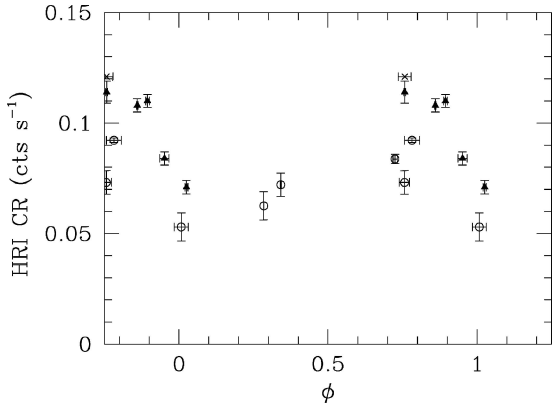


Figure 3. Equivalent *ROSAT*/HRI count rates folded with the ephemeris taken from Table I. Filled triangles, open circles and the cross stand respectively for *ROSAT*/PSPC, *ROSAT*/HRI and *ASCA*/SIS data.

count rates folded with the orbital parameters given in Table I. The six open circles correspond to observations performed with the HRI.

This star was also observed with the *ASCA* satellite. In that case, a complete spectral analysis of the SIS (Solid-state Imaging Spectrometer) data was performed (De Becker, 2001). The X-ray spectrum was successfully fitted with an absorbed two-temperature optically thin plasma model (Mewe et al., 1987), with temperatures of about 8×10^6 and 2×10^7 K respectively for the two components. The high temperature of the second component is suggestive of a plasma heated by a wind-wind interation within a binary system (Stevens et al., 1992). The cross in Figure 3 quotes the equivalent *ROSAT*/HRI count rate of this *ASCA* observation.

Archive *Einstein* data were also retrieved, but a first examination revealed important discrepancies, probably partly due to different locations of the source in the IPC (Imaging Proportional Counter) detector plane. For this reason, we did not include these data in our archive X-ray data investigation.

Although the X-ray light curve is too scarce to draw firm conclusions, Figure 3 clearly reveals that there are important variations in the X-ray flux of this system. We see that the PSPC and SIS data point to a high emission level at phases just before periastron. Then, the count rate apparently decreases. This trend is compatible with an interacting wind scenario, leading to a higher X-ray flux when the stars are closer. The fact that the maximum does not coincide with the minimum separation could possibly be explained by the fact that, at these phases, the winds have not reached their terminal velocities before they collide. Variable circumstellar absorption is also expected to play a role in the shape of this curve. However, these trends are less clear if we consider the HRI data. This X-ray lightcurve will be confronted to the results of several *XMM-Newton* pointings scheduled for the end of 2004.

4. Non-Thermal Emission from Massive Stars

4.1. General scenario

The non-thermal radio emission from massive stars raises some issues in the context of massive star physics. First, it reveals the existence of a mechanism that accelerates electrons up to relativistic energies. This acceleration could be achieved through the first order Fermi mechanism, believed to be responsible for, e.g., the production of cosmic particles (Bell, 1978a,b). Second, the identification of the non-thermal radio emission from several early-type stars as synchrotron emission by White (1985) implies that a magnetic field must be present in their winds.

Figure 4 summarizes the main aspects of the general scenario currently proposed to produce non-thermal emission in the context of massive stars. Box 1 schematically illustrates the physics of stellar winds, from the production of a stellar wind through the radiation pressure (Castor et al., 1975) to the formation of hydrodynamic shocks through intrinsic instabilities (Feldmeier et al., 1997) or wind-wind collision in a binary systems (Stevens et al., 1992). Box 2 illustrates the Fermi acceleration mechanism occurring within shocks, with the support of Alfvén waves generated by magnetohydrodynamic phenomena. The magnetic field of a massive star (box 3) is expected either to be produced through a classical dynamo mechanism inside the convective core, and to travel up to the surface with the support of meridional circulation (Charbonneau and MacGregor, 2001) and/or buoyancy (MacGregor and Cassinelli, 2003), or through a Tayler–Spruit type dynamo driven by the differential rotation in the non-turbulent radiative zone (Spruit, 2002). Finally, box 4 illustrates the non-thermal emission of radiation in the radio waveband, as well as in the

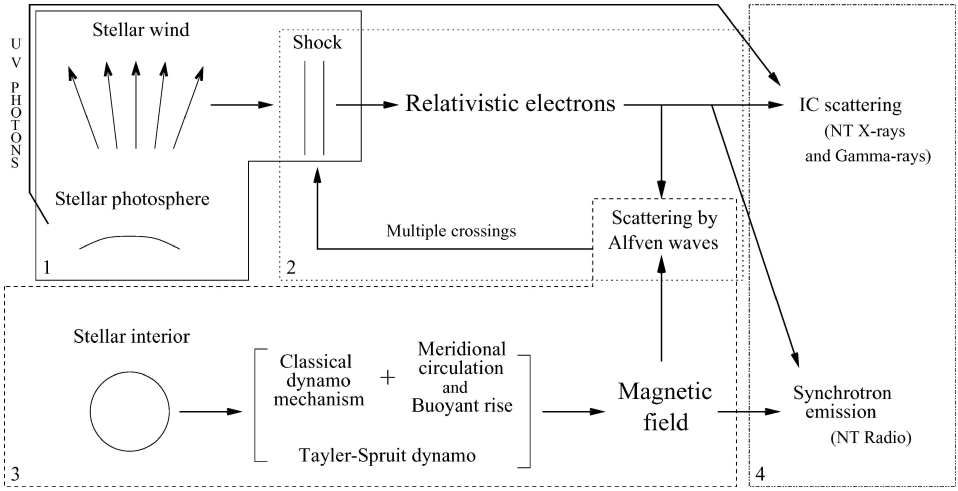


Figure 4. General scenario proposed for the production of the non-thermal emission of massive stars in the radio, X-ray and γ-ray wavebands.

X-ray and γ-ray domains (the latter two through inverse Compton (IC) scattering). The intersections between boxes illustrate the noticeable interconnections between these different fields of astrophysics.

4.2. Cyg OB2 #8A IN THE CONTEXT OF THIS SCENARIO

As Cyg OB2 #8A is now a confirmed binary, we can expect that the interaction zone between the two winds is responsible for the acceleration of the relativistic electrons that produce the radio synchrotron emission (Eichler and Usov, 1993). Therefore, the same region could be at the origin of a high energy counterpart of this non-thermal radio emission. Indeed, IC scattering of UV photospheric photons could produce X-rays and γ-rays (Chen and White, 1994). For a general discussion of non-thermal emission from early-type binaries, see Rauw (2004, this conference).

In the X-rays, the strong thermal emission due to the colliding winds prevents us from clearly detecting a (putative) non-thermal emission component, like in the case of the non-thermal radio emitter HD 168112 studied by De Becker et al. (2004). However, in the γ-ray domain, no thermal emission mechanism is expected and the detection of an object like Cyg OB2 #8A in this energy domain would provide unambiguous evidence for a high-energy counterpart to the non-thermal radio emission. For this reason, we obtained observing time with the European *INTEGRAL* satellite. With these observations, we intend to detect the counterpart of the EGRET source 3EG J2033+4118 (Benaglia et al., 2001) and to evaluate the contribution of Cyg OB2 #8A to this yet unidentified γ-ray source. Following

the study of Hartman et al. (1999), Cyg OB2 #8A lies within the 99% probability contour of this EGRET source.

We estimated the expected IC luminosity ($L_{\rm IC}$) following the same approach as Benaglia et al. (2001). For Cyg OB2 #8A, we adopted a radial dependence of the magnetic field (Eichler and Usov, 1993). The collision zone is indeed closer to the stars than in the case considered by Benaglia et al. (2001). Adopting typical radii for O6I and O5.5III stars (Howarth and Prinja, 1989), a surface magnetic field of 1 G, a bolometric luminosity of $10^{6.3}\,L_{\odot}$ and a synchrotron luminosity of 3.7×10^{28} erg s^{-1} (Bieging et al., 1989), we obtain an orbit averaged $L_{\rm IC}$ of ~ 2–3×10^{34} erg s^{-1} for a range of orbital inclinations of 30–45°. A surface magnetic field of ∼100 G would give a $L_{\rm IC}$ a factor 10^4 lower. For comparison, Benaglia et al. (2001) derived a value of about 8×10^{34} erg s^{-1} for Cyg OB2 #5. We also estimated the maximum energy that can be reached by the relativistic electrons under these conditions, using the relation given by Benaglia and Romero (2003). A lower limit of the maximum Lorentz factor should be about 10^4. This should lead to photons up to a few GeV. For a detailed discussion of the expected IC luminosity of Cyg OB2 #8A, see De Becker and Rauw (2005).

5. Prospects and Conclusions

We presented the results of an optical campaign revealing that the early-type star Cyg OB2 #8A is an O6+O5.5 binary system likely seen under a relatively low inclination angle, with a period of about 21.9 days and an eccentricity of 0.24. The binarity of this star is discussed in the context of the X-ray emission through archive data.

The binarity of this non-thermal radio emitter is of fundamental importance in the framework of our multiwavelength campaign devoted to the non-thermal emission from massive stars (Rauw et al., 2002; De Becker et al., 2004b). The acceleration of relativistic electrons responsible for non-thermal emission (radio, X-rays, γ-rays) is believed to occur within the interaction zone of the colliding winds of the binary system (Eichler and Usov, 1993). The IC scattering of UV photons of Cyg OB2 #8A is expected to account for 8–10% of the γ-ray luminosity of the unidentified EGRET source 3EG J2033+4118. Forthcoming observations with the *INTEGRAL* satellite should allow to unambiguously detect the lower energy γ-ray emission of the Cyg OB2 stars and then help to constrain the general scenario of non-thermal radiation from massive stars.

Acknowledgements

We are greatly indebted to the FNRS (Belgium) for multiple support including the rent of the OHP telescope in 2000 and 2002 through contract 1.5.051.00 "Crédit aux chercheurs". The travels to OHP were supported by the Ministère de l'Enseignement

Supérieur et de la Recherche de la Communauté Française. This research is also supported in part by contract PAI P5/36 (Belgian Federal Science Policy Office) and through the PRODEX XMM-OM and INTEGRAL Projects.

References

Bell, A.R.: 1978a, *MNRAS* **182**, 147.
Bell, A.R.: 1978b, *MNRAS* **182**, 443.
Benaglia, P., Romero, G.E., Stevens, I.R. and Torres, D.F.: 2001, *A&A* **366**, 605.
Benaglia, P. and Romero, G.E.: 2003, *A&A* **399**, 1121.
Bieging, J.H., Abbott, D.C. and Churchwell, E.: 1989, *ApJ* **340**, 518.
Castor, J.I., Abbott, D.C. and Klein, R.I.: 1975, *ApJ* **195**, 157.
Charbonneau, P. and MacGregor, K.B.: 2001, *ApJ* **559**, 1094.
Chen, W. and White, R.L.: 1994, *Ap&SS* **221**, 259.
De Becker, M.: 2001, Master Thesis, University of Liège.
De Becker, M. and Rauw, G.: 2004, *A&A* in preparation.
De Becker, M., Rauw, G. and Manfroid, J.: 2004a, *A&A* **424**, L39.
De Becker, M., Rauw, G., Blomme, R., et al.: 2004b, *A&A* **420**, 1061.
Eichler, D. and Usov, V.: 1993, *ApJ* **402**, 271.
Feldmeier, A., Puls, J. and Pauldrach, A.W.A.: 1997, *A&A* **322**, 878.
Hartman, R.C., Bertsch, D.L., Bloom, S.D. et al.: 1999, *ApJS* **123**, 79.
Howarth, I.D. and Prinja, R.K.: 1989, *ApJS* **69**, 527.
MacGregor, K.B. and Cassinelli, J.P.: 2003, *ApJ* **586**, 480.
Massey, P. and Thompson, A.B.: 1991, *AJ* **101**, 1408.
Mewe, R., Gronenschild, E.H.B.M. and van den Oord, G.H.J.: 1985, *A&AS* **62**, 197.
Rauw, G.: 2004, this conference.
Rauw, G., Blomme, R., Waldron, W.L., et al.: 2002, *A&A* **394**, 993.
Sana, H., Hensberge, H., Rauw, G. and Gosset, E.: 2003, *A&A* **405**, 1063.
Spruit, H.C.: 2002, *A&A* **381**, 923.
Stevens, I.R., Blondin, J.M. and Pollock, A.M.T.: 1992, *ApJ* **386**, 265.
White, R.L.: 1985, *ApJ* **289**, 698.

DO THE UNIDENTIFIED EGRET SOURCES TRACE ANNIHILATING DARK MATTER IN THE LOCAL GROUP?

J. FLIX[1], J.E. TAYLOR[2], M. MARTÍNEZ[1], F. PRADA[3], J. SILK[2] and J. CORTINA[1]

[1]*Institut de Física d'Altes Energies, Universitat Autònoma de Barcelona, Barcelona, Spain; E-mail: jflix@ifae.es*

[2]*Astrophysics, University of Oxford, Denys Wilkinson Building, Keble Road, Oxford, U.K.*

[3]*Instituto de Astrofísica de Andalucía (CSIC), Granada, Spain*

(Received 4 June 2004; accepted 13 September 2004)

Abstract. In a cold dark matter (CDM) framework of structure formation, the dark matter haloes around galaxies assemble through successive mergers with smaller haloes. This merging process is not completely efficient, and hundreds of surviving halo cores, or *subhaloes*, are expected to remain in orbit within the halo of a galaxy like the Milky Way. While the dozen visible satellites of the Milky Way may trace some of these subhaloes, the majority are currently undetected. A large number of high-velocity clouds (HVCs) of neutral hydrogen *are* observed around the Milky Way, and it is plausible that some of the HVCs may trace subhaloes undetected in the optical. Confirming the existence of concentrations of dark matter associated with even a few of the HVCs would represent a dramatic step forward in our attempts to understand the nature of dark matter. Supersymmetric (SUSY) extensions of the Standard Model of particle physics currently suggest neutralinos as a natural well-motivated candidate for the non-baryonic dark matter of the universe. If this is indeed the case, then it may be possible to detect dark matter indirectly as it annihilates into neutrinos, photons or positrons. In particular, the centres of subhaloes might show up as point sources in gamma-ray observations. In this work, we consider the possibility that some of the unidentified EGRET γ-ray sources trace annihilating neutralino dark matter in the dark substructure of the Local Group. We compare the observed positions and fluxes of both the unidentified EGRET sources and the HVCs with the positions and fluxes predicted by a model of halo substructure, to determine up to what extent any of these three populations could be associated.

Keywords: dark matter substructure, gamma rays: observations, HII clouds

1. Introduction

Determining the nature of the unidentified EGRET sources (Hartman et al., 1999) is an important unsolved problem in modern high-energy Astrophysics. These sources constitute a major part of all the discrete sources sample detected by EGRET. Despite continuing efforts, most of them have not yet been associated with sources at other wavelengths. Identification of EGRET sources is particularly difficult because of the large uncertainties in source positions and the lack of other observations at similar wavelengths.

While a few of the unidentified EGRET sources may simply be artifacts of the Galactic diffuse emission, it is normally thought that most are genuine detections,



Astrophysics and Space Science **297:** 299–308, 2005.
© Springer 2005

and that some fraction may even represent a completely new population of γ-ray emitters. As the sources are located predominantly at low to mid-Galactic latitudes, it seems likely they are mainly Galactic in origin, rather than being extragalactic objects like quasars (although this may account for some faction of them, e.g. Sowards-Emmerd et al., 2003). Thus most of the effort to identify the EGRET sources has focused on possible Galactic counterparts such as young pulsars (Hobbs et al., 2004), supernova remnants (Torres et al., 2003), isolated neutron stars (Goldoni and Mussol, 1996), molecular clouds (Benaglia et al., 2001), objects in Gould's Belt (Gehrels et al., 2000), microquasars (Paredes, 2002), or young stellar objects like Wolf-Rayet stars or OB associations (Romero et al., 1999).

On extragalactic scales, observational cosmology has recently converged on a 'concordance' model, which appears to satisfy all or most of the observational constraints simultaneously. In this 'ΛCDM' cosmology, the present-day energy density of the universe is dominated by 'dark energy', possibly in the form of a cosmological constant Λ, while the remaining matter content is constrained by nucleosynthesis and the microwave background to be predominantly non-baryonic cold dark matter (CDM) (Spergel et al., 2003). The nature of this dark matter is still unknown, and its identification is currently a top priority for theoretical and experimental Astrophysics.

Weakly interacting massive particles (WIMPs), non-relativistic relics from the early universe, have been proposed as one good candidate for non-baryonic dark matter. Although none of the particles in the Standard Model satisfy the requirements of being weakly interacting, massive and stable enough to be suitable relic particle, supersymmetric (SUSY) extensions of the Standard Model do provide a candidate that satisfies these requirements: the lightest SUSY particle (LSP), which ends up being one of the neutralinos (χ) in most of the SUSY-breaking scenarios. The neutralino is a majorana particle and can annihilate with itself in pairs, producing high-energy neutrinos, positrons, antiprotons and γ-rays (Bergstrom et al., 2001). Thus in principle it can be detected through high-energy observations.

In this paper, we will discuss about the possibility that γ-ray emission from χ self-annihilation, occurring in dark matter subhaloes in the halo of our Galaxy, may be responsible for some of the unidentified EGRET sources. We consider the spatial distribution and fluxes of these sources, and compare them with the predictions of a model of halo substructure. We will also compare the source positions with the high-velocity clouds (HVCs), a population of neutral hydrogen clouds that may also trace dark matter concentrations in the galactic halo.

2. Dark Matter Substructure in Galaxy Haloes

In CDM cosmologies, galaxies form within dense concentrations of dark matter, called 'haloes' by analogy with the stellar halo of the Milky Way. Dark matter haloes are assembled through a process of accretion and the hierarchical merging

of smaller subunits (cf. Taylor et al. (2003) and references therein). High-resolution numerical simulations of CDM structure formation have shown that this merging process is not completely efficient; they predict that hundreds of dense halo cores, or *subhaloes*, should remain in orbit around present-day galaxies (e.g. Klypin et al. (1999)). While some of these subhaloes may correspond to the few dozen satellites which surround the Milky Way Galaxy and our neighbour M31 (Mateo, 1998), the expected number of satellites exceeds the number observed by approximately an order of magnitude (Klypin et al., 1999; Moore et al., 1999).

The current census of dwarf satellites is probably still incomplete. The local dwarf galaxies are often faint, low-brightness objects, and thus very difficult to detect, as evidenced by several discoveries made only recently (e.g. the Canis Major dwarf, Martin et al., 2004). Nonetheless, it seems unlikely that most of the subhaloes predicted to orbit the Milky Way will ever be detectable by stellar emission alone.

2.1. SUBHALOES AS γ-RAY SOURCES

The specific properties of the dark matter particle may provide an alternate means of detecting local substructure. Neutralino annihilation can generate continuum γ-ray emission, via the process $\chi\chi \rightarrow q\bar{q}$. The subsequent decay of π^0-mesons created in the resulting quark jets produces a continuum of γ-rays. Given a neutralino density profile $\rho_{\rm dm}(r)$ (i.e. the dark matter density profile within a subhalo), the expected annihilation γ-ray flux above an energy E_0 arriving to Earth is given by:

$$\Phi_\gamma(E > E_0) = \frac{1}{4\pi}\frac{N_\gamma \langle\sigma v\rangle_{\rm ann}}{2m_\chi^2} \cdot J(\Psi) \tag{1}$$

$$J(\Psi) = \int_{\rm l.o.s} \rho_{\rm dm}^2(r)\, dl \tag{2}$$

where N_γ is the number of continuum gammas emitted per neutralino annihilation of m_χ mass above an energy E_0, and $\langle\sigma v\rangle_{\rm ann}$ the averaged product of annihilation cross-section and relative velocities. The first part of Eq. 1 can be evaluated for any given SUSY scenario, although the result varies by several orders of magnitude over the span of SUSY parameter space (Prada et al., 2004).

All the information about the dark matter distribution is contained in the $J(\Psi)$ term. Cosmological simulations indicate that dark matter haloes are approximately spherical, with a cuspy central density profile that scales as $\rho_{\rm dm}(r) \propto r^{-\alpha}$. The central slope of the density profile is thought to lie somewhere between $\alpha = 1$ (Navarro et al., 2004) (the 'NFW profile') and $\alpha = 1.5$ (Moore et al., 1998), although recent simulations generally find that central slopes are shallower than 1.5.

This profile should characterise both the main halo within which the Milky Way resides, and the subhalo cores that survive within it. The central cusp of the main halo may be affected by subsequent stages in galaxy formation, however, since baryons dominate the gravitational potential within the luminous part of bright

galaxies. In particular, processes like starbursts, galaxy mergers or bar formation could heat and disrupt the dark matter cusp in the centre of the Milky Way, M31 or the brighter members of the Local Group. Smaller subhaloes should be less strongly affected by baryonic processes, and thus they may preserve 'pristine' dark matter cores, where the annihilation rate is still relatively high. Thus we will focus on comparing EGRET sources with small subhaloes, and ignore γ-ray emission (or lack thereof) from the brightest members of the Local Group.

Using the semi-analytic model described in Taylor et al. (2003), we have generated a number of realisations of halo substructure for a galaxy like the Milky Way. For each subhalo surviving at the present day, we calculated the 'flux multiplier' $J(\Psi)$ and the relative flux, as measured by an observer 8.5 kpc from the centre of the galaxy. A cut on subhalo masses of $>5 \times 10^7 M_\odot$ was applied, as the models are incomplete below this mass limit.

In Figure 1 (left) we compare the predicted fluxes from the subhaloes in the each of our model systems with the fluxes measured for the unidentified EGRET sources. For each realisation, we have scaled the luminosity of the brightest subhalo to the luminosity of the brightest EGRET source. This gives an upper limit on the emissivity of the dark matter, for that particular model halo. By comparing the cumulative luminosity functions, we can also determine how many of the unidentified sources could be subhaloes, assuming this scaling and a luminosity function

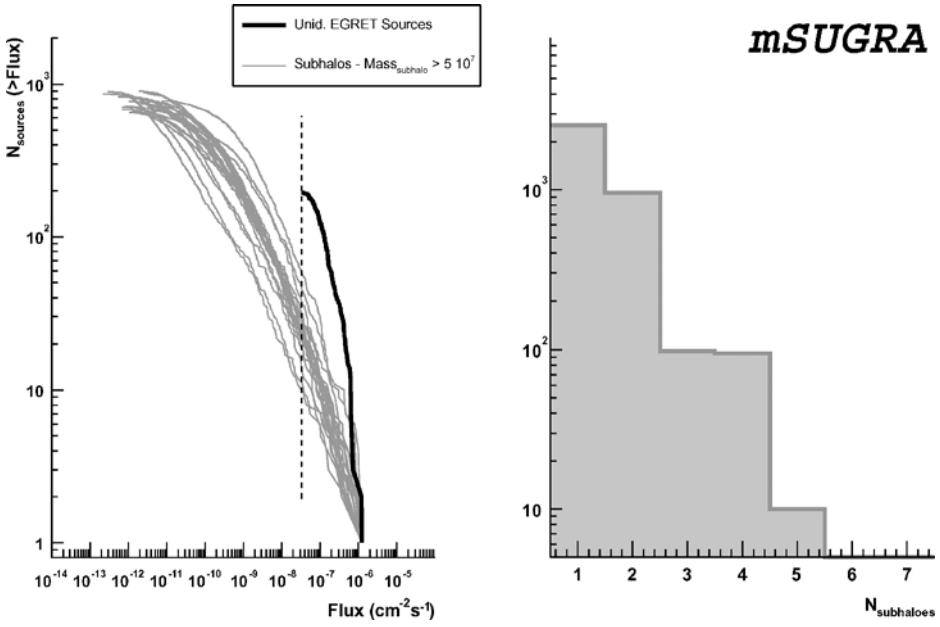


Figure 1. (left) Constrains to the maximum number of subhaloes compatible to unidentified EGRET sources. (right) Number distribution of all subhaloes with fluxes detectable by EGRET in a mSUGRA scenario.

like that of the model halo. This upper limit is between 10 and 58 of the EGRET sources, depending on the realisation, with a mean value of 26 ± 11. If we consider a neutralino of with $m_\chi = 100$ GeV, we can compute the number of gammas above the EGRET energy threshold with the *Darksusy* package (Gondolo et al., 2004). The $\langle \sigma v \rangle_{\rm ann}$ needed to achieve such fluxes are from 1×10^{-25} to 5×10^{-24} cm^3 s^{-1}. These values exceed by one or two orders of magnitude the allowed WMAP $\langle \sigma v \rangle_{\rm ann}$ in some SUSY scenarios. These numbers constrain an upper bound on the $\langle \sigma v \rangle_{\rm ann}$ for a 100 GeV neutralino.

As an example for a particular SUSY model, we consider to the set of mSUGRA scenarios discussed in Prada et al. (2004). The range of models satisfying the WMAP relic density limits correspond to χ masses between approximately 70 and 1400 GeV, while $\langle \sigma v \rangle_{\rm ann}$ lies in the range 1×10^{-29}–3×10^{-26}cm^3 s^{-1}. For these SUSY models, we compute the expected γ-ray flux above 100 GeV for all simulated subhaloes. Figure 1 (right) shows the number distribution of all subhaloes with fluxes detectable by EGRET in this mSUGRA scenario. The number of detectable subhaloes vary from 1 to 5. Most favourable models correspond to those neutralinos with $\langle \sigma v \rangle_{\rm ann}$ ranging between 3×10^{-26} and 10^{-27} cm^3 s^{-1} with masses from 100 to 400 GeV.

3. Comparison with a Different Population of Halo Objects

Given the small number of possible matches to between subhaloes and EGRET sources, it would be very useful to find another observable tracer of halo substructure. The HVCs are isolated concentrations of neutral hydrogen whose velocities distinguish them from the gas in the galactic disk (Blitz et al., 1999). The kinematics of these clouds suggest that they may orbit the Milky Way at large distances, or that they may even be distributed throughout the Local Group. While the Compact HVCs (CHVCs) seem the most promising tracers of dark substructure (Braun and Burton, 1999), even the less compact clouds show similarities to subhaloes in their distribution, once cuts in halo distance are applied (Putman and Moore, 2001). The detection of a tidal interaction between a non-compact HVC and the dwarf galaxy LGS 3 further supports this association (Robishaw et al., 2002). Thus we will compare the distribution of both types of clouds with that of our model subhaloes, and with the distribution of EGRET sources.

3.1. An all-sky catalogue of high velocity clouds

Two different catalogues of high velocity clouds are available for the two hemispheres, and they can be combined to form an all-sky catalogue of HVCs. The northern LDS survey (de Heij et al., 2002) covered the sky north of declination -30°, while southern HIPASS survey (Putman et al., 2002) covered the sky south declination $+2^\circ$. Both surveys are different in terms of sensitivity, angular

TABLE I
Observational properties for HIPASS and LDS HVCs surveys

	LDS survey	HIPASS survey
V_{LSR} coverage	-450 km s^{-1} to $+400$ km s^{-1}	-700 km s^{-1} to $+500$ km s^{-1}
V resolution	1.0 km s^{-1}	26.4 km s^{-1}
5σ T sensitivity	70 mK	1 mK
Angular resolution	$36'$	$15.5'$
Positional accuracy	$15'$	$10'$

resolution, velocity coverage and velocity resolution, but the same selection criteria was applied to both to identify isolated hydrogen clouds (de Heij et al., 2002). In Table I we list the main parameters of each catalogue. Approximate positional accuracies were estimated by comparing published values for known dwarf galaxies with the positions of the associated hydrogen clouds.

A total of 917 clouds were catalogued in the northern LDS survey, of which 777 are HVCs, 90 are CHVCs (isolated clouds in position and velocity), 37 were designated as CHVC: and 13 designated as CHVC? (clouds which were not unambiguously designated as CHVCs by the criteria described in Putman et al. (2002)). For the HIPASS southern survey, a total of 1997 clouds were detected, of which 41 are actually galaxies (GLXY), 1618 are HVCs, 179 are CHVCs and 159 are designated as: HVC as they could not be unambiguously classified as CHVCs because their elongation towards low level extended emissions. All the hydrogen clouds detected by either survey are shown in Figures 2 and 3.

3.2. Positional coincidences between HVCs and unidentified EGRET sources

Given the HVC positions from the HIPASS and LDS catalogues, we can test for positional coincidence between hydrogen clouds and γ-ray sources. More specifically, we can compare the positions of the maximum column density in neutral hydrogen for each cloud with the positions of the unidentified EGRET sources, on the supposition that both trace the dynamical centres of bound dark matter subhaloes. In order to determine the significance of positional coincidences, we define a relative distance between each hydrogen cloud and each of the unidentified EGRET sources as:

$$\delta^2 = \frac{|\vec{x}_{\text{egret}} - \vec{x}_{\text{cloud}}|^2}{\sigma^2_{\text{egret}} + \sigma^2_{\text{cloud}}} \tag{3}$$

where $\vec{x}_{\text{egret}}$ and $\vec{x}_{\text{cloud}}$ are the galactic longitude and latitude of the unidentified EGRET sources and the hydrogen clouds, expressed in degrees. We take as a characteristic uncertainty in the EGRET positions $\sigma_{\text{egret}} = \theta_{95}/2$, where θ_{95} is the

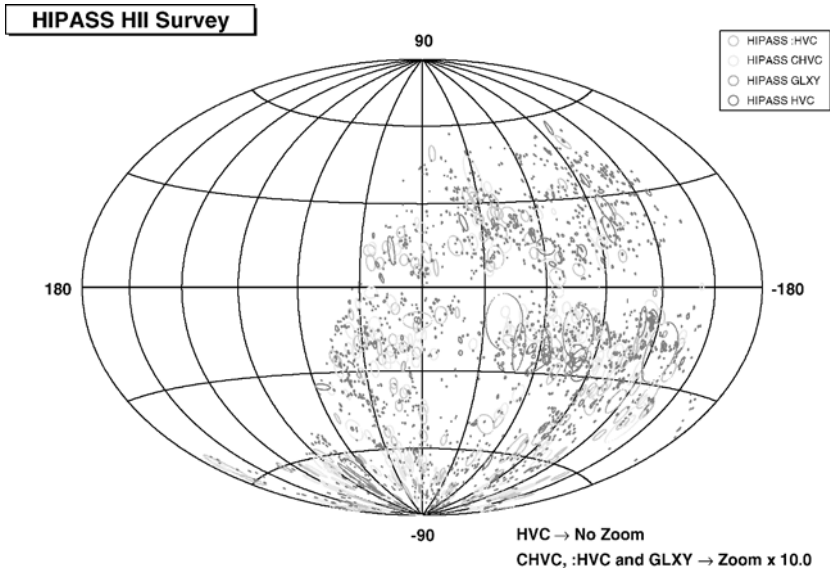


Figure 2. Hydrogen clouds included in HIPASS survey.

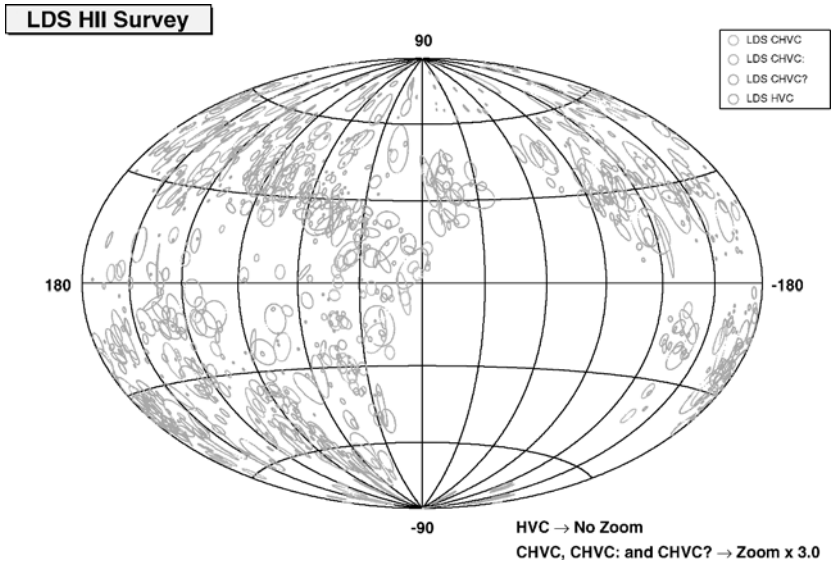


Figure 3. Hydrogen clouds included in LDS survey.

95% EGRET detection confidence contour. For σ_{cloud} we choose the positional accuracies of HIPASS and LDS surveys given above. As $\sigma_{\text{egret}} > \sigma_{\text{cloud}}$, δ values will be dominated by σ_{egret}.

A total of 10 HIPASS HVCs and 2 LDS HVCs have an unidentified EGRET source lying within $\delta \leq 1$ of their point of maximum emission. As the number

of unidentified EGRET sources in the field of view of HIPASS(LDS) surveys are quite similar, the different number of coincidences found for the two catalogues may be explained because the better sensitivity of HIPASS survey (HIPASS contains roughly double HI clouds than LDS) and worst LDS positional accuracies.

The γ-ray emission from neutralino annihilation should be steady on observationally accessible timescales. The variability of all sources in the 3rd EGRET catalogue has been evaluated, assuming a model of the flux distribution to characterise the flux variation, and using both positive flux detections and upper limits (Nolan et al., 2003). This method is quite successful at distinguishing between the known (variable) quasars and the known (non-variable) pulsars. As we are only interested in those steady γ-ray emitters, independent of how much variable they are, we make use of the V_{12} parameter, which indicates the confidence with which the hypothesis of variability can be rejected for a given source (100% = steady source). If we apply a cut at the 68% level to our $\delta \leq 1$ sample, 6 sources are rejected, resulting in 5 (1) remaining coincidences between HVCs to and unidentified EGRET sources for the HIPASS (LDS) surveys. These sources are shown in Figure 4 and listed in Table II.

To check for significance of these coincidences, we perform several simulations in which we distribute 10^4 fake EGRET sources isotropically and evaluate the probability of finding coincident HVCs and EGRET sources, after including the rejection factor from variability. The average number of random associations found were 1.0 ± 0.3 for LDS survey and 3.1 ± 0.5 for HIPASS survey, for the same

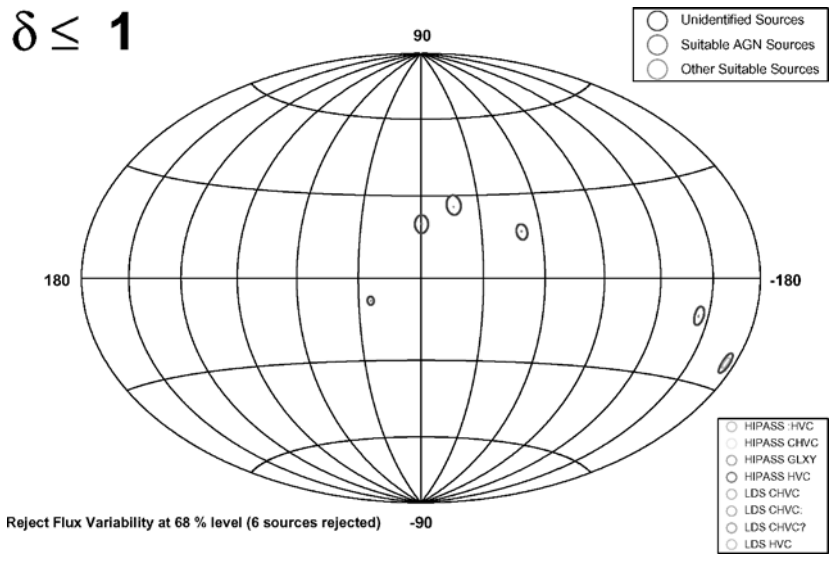


Figure 4. Unidentified EGRET sources whose positions coincide with HVCs at $\delta \leq 1$, after applying 68% flux variability rejection.

TABLE II
Unidentified EGRET sources and HVCs found to be spatially coincident

3rd EGRET name	HII name	σ
J0439+1105	HVC 186.2−22.8−206[a]	0.18
J0616-0720	HVC 215.8−11.2+162[b]	0.54
J1329-4602	HVC 310.0+16.5+182[b]	0.51
J1527-2358	HVC 343.1+25.9−144[b]	0.98
J1635-1751	HVC 359.6+19.7−149[b]	0.32
J1904-1124	HVC 024.1−08.2−238[b]	0.48

[a]LDS Survey, [b]HIPASS Survey.

coincidence cut criteria of $\delta \leq 1$. Thus the real result obtained for HIPASS clouds is only marginally (4σ) above the level expected from random coincidence.

4. Conclusions

If the dark matter particle is a supersymmetric neutralino, one of the most popular candidates currently under consideration, then local concentrations of dark matter may be detectable as γ-ray sources distributed throughout the halo of the Milky Way. In this paper, we have compared the luminosities of unidentified sources in the EGRET γ-ray catalogue with the luminosities of local dark matter substructure predicted by a semi-analytic model of neutralino annihilation in the halo of the Milky Way. We have also looked for spatial coincidences between EGRET sources and high-velocity neutral gas, which could be an observational tracer of local dark matter.

We find that most of the unidentified EGRET sources cannot be dark matter subhaloes. Whatever the emissivity of annihilating dark matter, the cumulative luminosity function for the two populations is sufficiently different that only $\sim 26 \pm 11$ of the EGRET sources could correspond to local substructure. Applying further cuts to sources on the basis of location or variability should place an even stronger constraint on the number of possible sources, and thus on the properties of dark matter.

We also find that most of the HVCs cannot correspond to EGRET sources either. While there are a few close positional coincidences between the two populations, the overall number is roughly that expected from random superposition. Thus there is no indication that the EGRET sources are associated with HVCs, whether or not the latter trace dark matter. This is interesting, because HVCs could also produce γ-rays through other, less exotic mechanisms, such as interactions with cosmic rays. Comparing HVCs with sources in lower energy catalogues might produce a stronger constraint on this mechanism, however, since the spectrum of γ-rays produced in this case is broader than that expected for χ annihilation.

References

Benaglia, P. et al.: 2001, *A&A* **366**, 605.
Bergstrom, L. et al.: 2001, *Phys. Rev. Lett.* **87**, 251301.
Blitz, L. et al.: 1999, *ApJ* **514**, 818.
Braun, R. and Burton, W.B.: 1999, *A&A* **341**, 437.
de Heij, V., Braun, R. and Burton, W.B.: 2002, *A&A* **391**, 159.
de Heij, V., Braun, R. and Burton, W.B.: 2002, *A&A* **392**, 417.
Gehrels, N. et al.: 2000, *Nature* **404**, 363.
Goldoni, P. and Musso, C.: 1996, *A&AS* **120**, 103.
Gondolo, P. et al.: 2004, *JCAP* **407**, 8.
Hartman, R.C. et al.: 1999, *ApJS* **123**, 79.
Hobbs, G. et al.: 2004, *MNRAS* **352**, 1439.
Klypin, A. et al.: 1999, *ApJ* **522**, 82.
Martin, N.F. et al.: 2004, *MNRAS* **348**, 12.
Mateo, M.L.: 1998, *Annu. Rev. A&A* **36**, 435.
Moore, B. et al.: 1998, *ApJL* **499**, L5.
Moore, B. et al.: 1999, *ApJL* **524**, L19.
Navarro, J.F. et al.: 2004, *ApJ* **490**, 493.
Nolan, P.L. et al.: 2003, *ApJ* **597**, 615.
Paredes, J.M.: 2002, *Mem. Soc. Astron. Ital.* **73**, 900.
Prada, F. et al.: 2004, *Phys. Rev. Lett.* **93**, 241301.
Putman, M. and Moore, B.: 2001, *ASP Conf. Proc.* **273**, 195.
Putman, M. et al.: 2002, *ApJ* **123**, 873.
Robishaw, T., Simon, J.D. and Blitz, L. 2002, *ApJ* **580**, 129.
Romero, G.E. et al.: 1999, *A&A* **348**, 868.
Sowards-Emmerd, D. et al.: 2003, *ApJ* **590**, 109.
Spergel, D.N. et al.: 2003, *ApJS* **148**, 175.
Taylor, J.E. et al.: 2003, in: *Proceedings of International Astronomical Union on Dark Matter in Galaxies*, Symposium No. 220, 22–25 July, 2003, Sydney, Australia.
Torres, D.F., Romero, G.E., Dame, T.M., Combi, J.A. and Butt, Y.M.: 2003, *Phys. Rep.* **382**, 303.

COHERENT SYNCHROTRON RADIATION OF GAMMA-RAY BURSTS

K.G. GAINULLIN and A.M. ZLOBIN
Russian Federal Nuclear Center – VNIIEF, Sarov 607190, Russia;
E-mail: gcamel@rol.ru, zlobin@vniief.ru

(Received 4 June 2004; accepted 19 August 2004)

Abstract. By now there is no doubt that the gamma-ray bursts (GRB) have a cosmological origin. This allows to regard GRB as the most powerful known energy sources, $\varepsilon \sim 10^{54}$ erg (with a total number of gamma quanta $N_\gamma \sim 10^{60}$). A plausible mechanism of coherent synchrotron radiation (CSR) of relativistic electrons driven by a local magnetic field is studied in this paper. We consider relativistic electrons arising in the Compton scattering of a GRB in directions close to that of the ray from the source to a ground-based observer. The synchrotron pulses from Compton electrons located at different points on the line between the GRB source and the observer arrive at the observation point simultaneously. This simultaneity ensures the coherence of the detected radiation. Both molecular clouds in the host galaxy of the GRB and our own Galaxy, as well as the Earth atmosphere are assumed to be scatterers of the GRB radiation. Signals of each scatterer reach the Earth surface, and can be detected at radio wavelengths. We estimate the characteristics of this radiation. The comparison of GRB data with the corresponding information on CSR pulses offers a way to determine some global characteristics of the medium between the Earth and the GRB source.

Keywords: coherent synchrotron radiation, gamma-ray burst, Compton electrons, molecular clouds

1. Introduction

Cosmic gamma ray bursts (GRB) were first recorded in the mid-1960s by instruments in satellites intended for nuclear test monitoring (Luchkov et al., 1996). The GRB spectrum ranges within 0.1–10 MeV, with the characteristic mean energy of W ∼1 MeV. The typical pulse duration is 10^{-2}–10^3 s, whereas there exist both short (less than 1 s) and long (more than 10 s) pulses. Near the Earth surface, the GRB flux peaks at about 10^{-3} erg/cm^2, and the frequency is $\nu \sim 10^3$ events per year, with the minimal recorded threshold being 10^{-7} erg/cm^2. The GRB distribution seems to be isotropic.

Nowadays, the cosmological nature of GRB is beyond question. GRB are therefore among the most powerful known gamma sources, with a radiated energy of $\sim 10^{54}$ erg and a number of gamma quanta of $N_\gamma \sim 10^{60}$ (Luchkov et al., 1996; Postnov, 1999). This paper presents a plausible mechanism for generation of coherent synchrotron radiation (CSR) of relativistic Compton electrons resulting from GRB scatterings along the line-of-sight. We believe that both molecular clouds of our own Galaxy and the host galaxies of the GRB, as well as Earth's atmosphere


Astrophysics and Space Science **297:** 309–318, 2005.
© Springer 2005

may be the scattering media. Local magnetic fields H_0 make recoiled Compton electrons to proceed along curved trajectories and hence they emit radiation. The very fact that pulses emitted by electrons at different points on the line between the source of CSR and the observer arrive at the observation point simultaneously may provide insight into the observed coherence of CSR. When the Earth atmosphere serves as the scattering medium, a pulse (in the radio interval) reaches the surface of the Earth, and can in principle be recorded. A simple linear radiation regime exists when GRB experiences scattering in molecular clouds of our Galaxy or in the Earth atmosphere. The emitted electromagnetic wave is weaker in comparison to local magnetic fields, and hence has little or no effect on the electron motion and its radiation. Using the available data on GRB, density of the scattering medium, and local magnetic fields, we find the CSR pulse as an integral of some known functions. The time-dependence of CSR pulses is assumed to be close to that of the GRB. We then estimate the CSR pulse magnitude taking into account some typical parameters of the Galaxy and Earth's atmosphere.

The nonlinear radiation regime becomes essential in the host galaxy's molecular clouds when the GRB flux is sufficiently intense. The emitted electromagnetic wave propagating toward the ground-based observer is then tangible to an extent that it exerts influence on the motion and radiation of Compton electrons (back-reaction effects). The electric field magnitude of the radiated electromagnetic wave is limited to the so-called saturation field E_{sat}, while the CSR pulse may be lengthened (as opposed to the linear regime). The upper CSR frequency peaks at about 10^9 Hz. Below we estimate the CSR pulse magnitude for typical parameters inherent to GRB and the host galaxy.

The analysis of GRB-versus-CSR pulses will enable determining some integral characteristics of the media between the Earth and GRB source, namely the total mass content, the local magnetic field, and the ratio of distances separating the Earth from the GRB source and the relevant scattering object.

2. Linear Radiation Regime

We begin with the following truncated problem: monoenergetic directed electrons are contained in a thin planar layer (to form the surface density j_0) which begins to move with the velocity $\vec{\beta}(t)$. Let $\beta_{||}$ be the component of the velocity normal to the layer (the suffix $||$ signifies the propagation in the direction parallel to the line connecting the source and the observer), and $\vec{\beta}_\perp$ the transversal component of the velocity (we adopt units in which the speed of light is 1). We assume that the local magnetic field H_0 is uniform and perpendicular to the line between the source and the observer. If variations in time of the transversal component of the velocity are correlated for all the electrons, then the layer radiates coherent electromagnetic waves. The problem of determining the radiated transversal components of electric and magnetic fields $\vec{E}_\perp$ and $\vec{H}_\perp$ has been solved by Bashurin and Gainullin

(1992):

$$\frac{\vec{E}_\perp(\tau)}{2\pi e j_0} = \frac{\vec{\beta}_\perp(t)}{1-\beta_{||}(t)} - \frac{\vec{\beta}_\perp(0)}{1-\beta_{||}(0)}, \quad |\vec{E}_\perp| = |\vec{H}_\perp|, \tag{1}$$

where e is the electronic charge. The relation between the lab time of the observer τ and time in the rest frame of the electron prior to its transverse motion t is (Landau and Lifshitz, 1975)

$$\frac{d\tau}{dt} = 1 - \vec{n}\cdot\vec{\beta} = 1 - \beta_{||}, \tag{2}$$

or, equivalently,

$$\tau(t) = \int_0^t [1 - \vec{n}\cdot\vec{\beta}(t')]dt'. \tag{3}$$

In the case under study, the Compton mechanism is responsible for scattering of the gamma quanta with energies 0.1–10 MeV, and the acceleration of resulting Compton electrons is due to their orbiting in the local magnetic filed. Let the z-axis be chosen for the GRB path (along the ray from the source to the observer), then the initial velocity of the Compton electron $\vec{\beta}_0$ is expressed in Cartesian and spherical coordinates:

$$\vec{\beta}_0 = (\beta_x, \beta_y, \beta_z) = \beta_0\,(\sin\theta\cos\varphi, \sin\theta\sin\varphi, \cos\theta). \tag{4}$$

The electron will spiral in the magnetic field $\vec{H}_0 = \vec{h}_0 H_0 = H_0(h_x, h_y, h_z)$ with the Larmor rotation rate $\Omega = (eH_0/mc)\sqrt{1-\beta_0^2}$,

$$\vec{\beta}(t) = \vec{\beta}_0\cos\Omega t + \vec{h}_0\beta_{||}(1-\cos\Omega t) + [\vec{\beta}_0\times\vec{h}_0]\sin\Omega t, \tag{5}$$

where m is the electronic mass, and $\vec{h}_0$ is a unit vector along the magnetic field. The scattering of gamma quanta with energy W brings into existence a flux of Compton electrons with known spectral and angular distributions, characterized by the axial symmetry around the direction of the initial gamma flux $\vec{n} = (0, 0, 1)$.

We should average expression (1) over the angle φ. However, we can conveniently evaluate the vector potential $\vec{A}$,

$$\begin{aligned}\frac{\vec{A}(\tau)}{2\pi e j_0} &= \int_0^\tau \frac{\vec{E}(\tau')}{2\pi e j_0}\,d\tau' = \int_0^\tau \left[\frac{\vec{\beta}(t')}{1-\beta_{||}(t')} - \frac{\vec{\beta}(0)}{1-\beta_{||}(0)}\right]d\tau' \\ &= \int_0^\tau \vec{\beta}(t')dt' - \frac{\vec{\beta}(0)\tau}{1-\beta_{||}(0)},\end{aligned} \tag{6}$$

rather than averaging $\mathbf{E}_\perp$ in (1); in doing so, the denominator (2) has been eliminated.

We thus obtain the averaged transversal components of the vector potential

$$\int \frac{A_x(\tau)\Omega}{2\pi e j_0} d\varphi = h_z h_x \beta_0 \cos\theta\,(\Omega t - \sin\Omega t) - h_y \beta_0 \cos\theta\,(1 - \cos\Omega t), \quad (7)$$

$$\int \frac{A_y(\tau)\Omega}{2\pi e j_0} d\varphi = h_z h_y \beta_0 \cos\theta\,(\Omega t - \sin\Omega t) - h_x \beta_0 \cos\theta\,(1 - \cos\Omega t). \quad (8)$$

We then multiply (8) by the imaginary unit i and subtract the result from (7), to recast the transversal components of the complex vector potential $A_\perp = A_x - i A_y$ as

$$\int \frac{A_\perp(\tau)\Omega}{2\pi e j_0} d\varphi = h_{||} h_\perp \beta_0 \cos\theta\,(\Omega t - \sin\Omega t) - h_\perp \beta_0 \cos\theta\,(1 - \cos\Omega t), \quad (9)$$

where $h_{||} = h_z$ and $h_\perp = h_x - i h_y$. Averaging the constraint (2) yields

$$\int (1 - \vec{n}\cdot\vec{\beta}) d\varphi = 1 - \beta_0 \cos\theta \left(h_{||}^2 + h_\perp^2 \cos\Omega t\right), \quad (10)$$

$$\Omega\tau = \Omega t - \beta_0 \cos\theta \left(h_{||}^2\, \Omega t + h_\perp^2 \sin\Omega t\right). \quad (11)$$

These relations can be readily used to evaluate the transversal electric field,

$$E_\perp = E_x - i E_y = \frac{dA_\perp}{d\tau} = 2\pi e\, j_0\, \beta_0\, h_\perp \cos\theta\, \frac{i \sin\Omega t + h_{||}(1 - \cos\Omega t)}{1 - \beta_0 \cos\theta \left(h_{||}^2 + h_\perp^2 \cos\Omega t\right)}. \quad (12)$$

The maximum of this expression, $|E_\perp^{\max}| = (2\pi e j_0 \beta_0 \cos\theta)/(\sqrt{1-\beta_0^2\cos^2\theta})$, is found at the instant t^* defined through the relation

$$\cos\Omega t^* = \frac{\beta_0 \cos\theta - h_{||}^2}{1 - h_{||}^2}.$$

If the scatterer of GRB is an extended object, the radiation of different thin layers is combined coherently along the line connecting the source and the observer, because it is just this line for which the sum of propagation lengths of GRB and CSR is constant. In the linear regime, we integrate contributions of all layers along this line within the interval R, taking into account the time dependence of GRB, $f(t)$, as well as its spectral and angular Compton distribution $G_2(W,\theta)$, throughout the polar angle θ and the GRB spectrum G_1(W),

$$E_\perp^\Sigma(\tau) = 2\pi e \int n_e(r) h_\perp(r) \frac{r}{R} \times \iiint f(\tau - \tau')\, G_1(W) G_2(W,\theta) \frac{\beta_\perp(r, W, \theta, \tau)}{1 - \beta_{||}(r, W, \theta, \tau)} \times \sin\theta\, d\theta\, dW\, dr\, d\tau'. \quad (13)$$

3. Evaluation of CSR Parameters for GRB Scattering in the Earth Atmosphere

Let a homogeneous GRB flux of density $j_0 \sim 10^3$ quanta/cm^2, extended over an area of size $\Delta_0 \sim 8000$ m, come to the Earth atmosphere, and experience a scattering. For gamma quanta with energy $W = 1$ MeV, the characteristic free path is $R_\gamma \sim 300\,\text{m}\,(\rho_\gamma \sim 40\,\text{g/cm}^2)$ at sea level. The maximum of the Compton electron density is at the height $Z_0 = \Delta_0 \ln(\Delta_0/R_\gamma) \sim 20$ km. For such electrons, their free run at this height is $R_\text{e} \exp(Z_0/\Delta_0) \sim 100$ m ($R_e \sim 3$ m) which is comparable with radius of their Larmor rotation in the geomagnetic field $H_0 = 0.5$ G with frequency $\Omega \sim 10^7$ s^{-1}. Since the characteristic duration of the GRB pulse $f(t)$ is much longer than the Compton electron lifetime $t_\text{e} \sim R_\text{e} \exp(Z_0/\Delta_0) \sim 30$ ns, the total contribution of all layers is evaluated, using (1), as:

$$E_\perp(\tau) \approx 2\pi e j_0 f(\tau) \int_0^{t_\text{e}} \frac{\beta_0 \sin \Omega t'}{1 - \beta_0 \cos \Omega t'} d\tau'(t') \sim 2\pi e j_0 f(\tau) \frac{\Omega}{2} \left(\frac{R_\text{e} \Delta_0}{R_\gamma c} \right)^2 . \tag{14}$$

Substituting numerical values for all the pertinent quantities and taking the maximum of the normalized GRB pulse to be $f^\text{max} \sim 0.1$ s^{-1} ($\int f(\tau')d\tau' = 1$), one can estimate the maximal CSR electric field $\sim 10^{-9}$ V/m at sea level. The correction for the deviation from the normal of the GRB impinging angle appears to be of little significance. The analysis of expression (14) shows that the CSR pulse carries information about the integral flux $j_0 f(t)$; detailed spectrum data have been smeared out by the energy transfer from GRB to CSR characterized by lower frequencies. One may conclude from the above estimates that, for such a small GRB flux density, the role of the radiation-induced air conductivity is negligible.

4. Evaluation of CSR Parameters for GRB Scattering in Galactic Molecular Clouds

In our Galaxy, there are approximately $N_m = 5000$ of the so-called atomic and molecular clouds whose masses add up to half the Galaxy mass. Their characteristic size is $L_m = (1 - 3) \times 10^{20}$ cm, with a particle density of $n = 10^3 - 10^4$ cm^{-3}, a mass thickness of ~ 1 g/cm^2, a temperature $T = 50$–100 K, and a magnetic field $H_0 > 10^{-5}$ G (sometimes up to 10^{-3} G). Since the typical region of variation from uniformity for H_0 is of size 3×10^{21} cm, it would be reasonable to consider the CSR formation for GRB passing through a single galactic molecular cloud toward the Earth. The incidence of such events can be roughly estimated as $(\pi L_\text{m}^2 N_\text{m} \upsilon)/(4\pi L_\text{G}^2) \sim 1 - 10$ year^{-1} , where $L_G = 10^{23}$ cm is the characteristic galactic scale, $\nu \sim 10^3$ year^{-1} is the GRB frequency, with a total energy flux $\geq 10^{-7}$ erg/cm^2.

Since the source of the GRB is cosmological, we assume its distance to the Earth as $R \sim 10^{28}$ cm, and the Compton electron flux in molecular clouds as $j_0 = (N_\gamma L_\mathrm{m})/(4\pi R^2 R_\gamma)$. With the additional supposition that Compton electrons are monoenergetic and directed, and the magnetic field is perpendicular to them, we may evaluate the CSR pulse, representing it as the convolution of the GRB pulse $f(t)$ (the kernel) with thin-layer CSR's (primary sources),

$$E_\perp(\tau) = 2\pi e j_0 \int_0^\tau f(\tau - \tau') \frac{\beta_0 \sin \Omega t(\tau')}{1 - \beta_0 \cos \Omega t(\tau')} \, d\tau'. \tag{15}$$

Since the distance from the cloud to the Earth is small as compared to R, the fall of $E_\perp$ with distance is small. Furthermore, the period of the Larmor rotation of Compton electrons, $\sim 10^{-2}$ s, is usually much less than the GRB characteristic duration, hence, taking $f(t)$ to be a smooth function, we approximate expression (15), as

$$E_\perp \sim 2\pi e j_0 \frac{\beta_0}{\Omega} \left\{ 1.5 f(\tau) - \frac{f'(0)}{\Omega} \left[\sin \Omega t(\tau) - 0.25 \cdot \beta_0 \sin 2\Omega t(\tau) \right] \right\}.$$

If we ignore the term involving $f'(0)$, we would be able to estimate the CSR electric field in the cloud and at the Earth to be $\sim 10^{-5}$ V/m for the maximal flux $j_0 \sim 10^2$ cm^{-2}. The corresponding CSR magnetic field turns out to be $\sim 10^{-9}$ G, which suggests that the response of Compton electrons to the radiated field (the back reaction) may be omitted. Therefore, the general expression for CSR from the GRB scattering in a single molecular cloud of the Galaxy is given by (13), with the time dependence being identical to $f(t)$.

To summarize, given the GRB spectrum $G_1(W)$ and time dependence $f(t)$, it is possible to evaluate the mass contents and magnetic field in a molecular cloud of our Galaxy, which is located on the line of the GRB propagation toward the Earth.

5. A Model of CSR Due to Intense GRB

So far we discussed the linear radiation regime, which may be motivated by the fact that the emitted fields are weak compared to the local magnetic fields H_0. A numerical criterion can be introduced through the dimensionless parameter (Gainullin, 1999)

$$\xi = 2\pi e \int \frac{n_\mathrm{e}(z)}{H_0} \, dz \tag{16}$$

which is the integral of the Compton electron density $n_e(z)$ along the GRB path (z-axis). If $\xi \ll 1$, the linear radiation regime is the case. If $\xi \gg 1$, we should take into consideration the influence of the radiated field on the motion of the Compton

electrons and the associated back-reaction effect. When a GRB is scattered in a molecular cloud of our Galaxy, $\xi \sim (2\pi e N_\gamma L_\mathrm{m})/(4\pi R^2 R_\gamma H_0) \approx 0.1$. On the other hand, if we are concerned with the scattering in a molecular cloud of the GRB's host galaxy, then $\xi \sim (2\pi e N_\gamma L_\mathrm{m})/(4\pi R_\mathrm{G}^2 R_\gamma H_0) \approx 10^8 \gg 1$, and the self-consistency condition should be imposed. To this aim, we go back to the truncated problem of a thin layer of electrons, but make it more sophisticated by extending the volume. We assume that a short and intense GRB generates monoenergetic directed Compton electrons which move under both the initial magnetic field $\mathbf{H}_0 = \mathrm{H}_0\,(h_x, h_y, h_z)$ and radiated transversal fields $\mathbf{E} = (E_x, E_y, 0)$ and $\mathbf{H} = (-E_y, E_x, 0)$, which depend on time and the distance from the source along the line of the GRB propagation, the z-axis. The equation of motion for an electron in vector notation is

$$(1 - \beta_z)\frac{\partial \vec{P}}{\partial \tau} = -e\vec{E} - e[\vec{\beta} \times \vec{H}] - e[\vec{\beta} \times \vec{H}_0]. \tag{17}$$

In the simple case that the magnetic field is perpendicular to the direction of the GRB propagation, $\mathbf{H}_0 = \mathrm{H}_0\,(0, 1, 0)$, and (17) becomes a one-dimensional equation containing the single transverse field E_x (Gainullin, 1999),

$$(1 - \beta_z)\frac{\partial P_x}{\partial \tau} = e\beta_z H_0 - e\,(1 - \beta_z)E_x. \tag{18}$$

It follows that if E_x is small in comparison with the so-called saturation field E_sat,

$$E_x < \frac{\beta_z}{1 - \beta_z} H_0 = E_\mathrm{sat}, \tag{19}$$

then the transversal momentum grows with time, and *viceversa*. In the former case, the electron loses energy for radiation, whereas in the latter case, it gains energy and lowers the field magnitude. We see that the radiated electric field oscillates near the saturation field E_sat, which limits the CSR amplitude in the nonlinear radiation regime. The equation for the emitted wave might be derived from (1), based on the assumption that the electron executes its motion along the z-axis,

$$\frac{\partial E_{x,y}}{\partial z} = 2\pi e\, n_\mathrm{e}(z)\, \frac{\beta_{x,y}(z, \tau)}{1 - \beta_z(z, \tau)}. \tag{20}$$

The nonlinear system of Eqs. (18) and (20) is solved analytically by Gainullin (1999) in a particular case of the field $\mathbf{H}_0 = \mathrm{H}_0\,(0, 1, 0)$ for the initial stage of the process when transverse displacements of the electron are small, and the longitudinal velocity is close to the initial one β_0,

$$E_x = \frac{\beta_0 H_0}{1 - \beta_0}[1 - J_0(2\sqrt{\xi \omega \tau / a})]. \tag{21}$$

Here, J_0 is the Bessel function of zero order, $\omega = eH_0/mc$, and $a = \sqrt{1-\beta_0}/\sqrt{1+\beta_0}$. It is clear from (21) that the electric field is represented by damped oscillations near $E_{\rm sat}$. The maximum $E_x^{\max}(\tau^*) = 1.4\,\beta_0 H_0/(1-\beta_0)$ is reached at the instant $\tau^* = 3.7\,a/\xi\omega$ (Gainullin, 1999). In this reference, it was found the corresponding solution for the electron velocity which shows that the transverse velocity is given by small oscillations around the z-axis, and the trajectory resembles "a snake." A plausible physical interpretation of this result is as follows: in the nonlinear regime of radiation, $\xi \gg 1$, the amplitude of radiated field is limited by $E_{\rm sat}$, and, according to (19), the transverse velocity of the electron does not change (that is, the electron does not radiate at all), as the radiated field approaches $E_{\rm sat}$. The wave which accompanies the electron may "approve" its energy loss for radiation only when the driving field is less than $E_{\rm sat}$. In this case, the CSR duration increases as compared to initial GRB pulse. The electron may loss a major portion of its energy W_e owing to the fact that $H_0 \ll E_{\rm sat}$. The CSR pulse duration might be roughly estimated from the equality of the total energy of all the electrons and the wave energy,

$$W_{\rm e}\int n_{\rm e}(z)\,dz \sim \frac{E_{\rm sat}^2}{4\pi}\,\tau_{1/2}, \quad \Longrightarrow \quad \tau_{1/2} \sim \frac{2\xi\, W_{\rm e}\, H_0}{e\, E_{\rm sat}^2}. \tag{22}$$

If the GRB duration is less than this amount, then the CSR pulse is taken to be short. For an extended discussion of the form of CSR in the nonlinear regime, taking into account a variation of $E_{\rm sat}$ along the length of the wave packet, and the spectral and anglular Compton distributions of scattered electrons, see Gainullin (1999).

If the duration of the GRB, specified by $f(t)$, exceeds that of (22), then the field equation (20) becomes a convolution equation,

$$\frac{\partial E_{x,y}}{\partial z} = 2\pi\, e\, n_{\rm e}(z)\int f(\tau-\tau')\frac{\beta_{x,y}(z,\tau')}{1-\beta_z(z,\tau')}d\tau'. \tag{23}$$

Combining solutions to (20) and (18) gives the spectral density

$$\hat{E}_\perp(\omega) = \hat{f}(\omega)\frac{e\,\xi\,\beta_0\,H_0^2}{a\,(1-\beta_0)\,\omega^2 m}. \tag{24}$$

The CSR amplitude due to an intense GRB and an arbitrarily directed magnetic field is

$$E_\perp = A\,H_0\,h_\perp\left[1 - e^{-ih_Z\omega\tau/a}J_0(2\sqrt{\xi\omega\tau/a}) - ih_z\int_0^{\omega\tau/a} e^{-ih_Z x}J_0(2\sqrt{\xi x})dx\right]. \tag{25}$$

It is seen from (25) that CSR amplitude is determined by the sole transversal component of magnetic field, while the angular velocity of the CSR polarization is dependent of only the longitudinal component of magnetic field.

6. Evaluation of CSR Parameters for GRB Scattering in the Host Galaxy

The analysis of the truncated problems suggests that, at the initial stage of the strong nonlinear regime, the rotation of Compton electrons in the initial magnetic field is suppressed, and the saturation field is close to its mean value,

$$E_{\text{sat}} \sim H_0 \left\langle \frac{\beta_z}{1-\beta_z} \right\rangle = AH_0.$$

In particular, for $W_\gamma = 1$ MeV the mean values of the parameters involved are

$$\langle a \rangle \approx 1, \qquad \langle A \rangle = \left\langle \frac{\beta_z}{1-\beta_z} \right\rangle \approx 10.$$

Hence, the field amplitude at the Earth E_{observ} is estimated

$$R\, E_{\text{observ}} \sim E_{\text{sat}}\, R_0.$$

Taking the distance between GRB and a molecular cloud to be $R_0 \sim L_{\text{G}}/3$, we find that the electric field at the Earth is $\sim 10^{-4}$ V/m. The CSR pulse duration emitted by the cloud is evaluated with the use of (22) and typical values of the quantities involved, to yield 10^4–10^5 s.

The evaluation of the signal amplification duration (for the leading edge) τ^* proves more involved. Indeed, one may find from (20) the rate of the field growth in the opening stage (using of the derivative), and this result, multiplied by the number of Compton electrons generated by that time, would give the saturation field,

$$2\pi e \left\langle \frac{\beta_z \sqrt{1-\beta_z^2}}{(1-\beta_z)^2} \right\rangle \frac{N_\gamma L_{\text{m}} \omega \tau^*}{4\pi R_\gamma R_0^2} \int_0^{\tau^*} f(\tau')\, d\tau' = E_{\text{sat}} = H_0 \left\langle \frac{\beta_z}{1-\beta_z} \right\rangle. \tag{26}$$

Using characteristic values for GRB and molecular clouds, one can obtain $\tau^* \sim 1$ ns.

Although the probability of a GRB signal passing through a molecular cloud of a host galaxy is comparable to that for our Galaxy, the respective CSR parameters differ drastically. We can find CSR using numerical methods in the belief that GRB and CSR parameters are unaffected by the inter-galactic medium (Ginzburg, 1967), and specifying the magnetic field and mass thickness of the medium under examination. The wide spectrum of a radio pulse evaluated in this fashion might serve as a test probing tool for cosmic space between GRB sources and the Earth.

7. Conclusion

We outlined a plausible mechanism of coherent synchrotron radiation due to the GRB scattering by Compton electrons located on the line between the GRB source

and the Earth. Molecular clouds of our Galaxy and in the host galaxies, as well as Earth's atmosphere, are regarded as the scattering objects. The incidence of a GRB with the total energy flux $\geq 10^{-7}$ erg/cm^2 might be roughly estimated as 1–10 year^{-1}. The simultaneity of arrival at the ground-based observation point of pulses radiated by Compton electrons located at different points of the path of the wave propagation may explain the coherence of the observed CSR. The linear radiation regime realizes in the case that a lower-power GRB comes to scatter in our Galaxy or the Earth atmosphere. With established data of GRB properties, scattering medium density, and local magnetic fields, the CSR pulse is found as the integral of some known functions. We take the time-dependence of CSR pulse close to that of GRB. Using typical parameters of the scattering medium gives the CSR pulse (at sea level) of order 10^{-5} V/m for GRB that experience scattering in a molecular cloud of our Galaxy, and $\sim 10^{-9}$ V/m for GRB that comes to scatter in the Earth atmosphere.

A nonlinear radiation regime is the case in the host galaxy if the GRB flux is sufficiently intense. The electromagnetic field of the wave propagating from the GRB source to the Earth is so strong that the motion and radiation of Compton electrons are affected by it (a back-reaction effect). The electric field in the radiated wave is limited to $E_{\rm sat}$, and the CSR pulse duration is within the interval of 10^4–10^5 s. The upper frequency CSR is of order 10^9 Hz. For typical parameters of GRB and the host galaxy, the CSR magnitude near the Earth surface is estimated to be 10^{-4} V/m.

We have seen that the analysis of GRB-versus-CSR pulses can be of help in determining integral characteristics of the medium between the Earth and GRB source: the total mass contents, the magnetic field, and the ratio between distances to the GRB source and the scattering object.

Acknowledgement

This work was supported partly by the ISTC under the Project # 729.

References

Bashurin, V.P. and Gainullin, K.G.: 1992, *Voprosy Atomnoi Nauki i Tekhniki*. Ser.: Teoreticheskaya i Prikladnaya Fizika, **3**, 33, (In Russian).

Gainullin, K.G.: 1999, *Voprosy Atomnoi Nauki i Tekhniki*. Ser.: Teoreticheskaya i Prikladnaya Fizika, **3**, 37, (In Russian).

Ginzburg, V.L.: 1967, Propagation of Electromagnetic Waves in Plasma, Nauka, Moscow, (In Russian).

Landau, L.D. and Lifshitz, E.M.: 1975, The Classical Theory of Fields, Pergamon, Oxford.

Luchkov, B.I., Mitrofanov, I.G. and Rozental, I.L.: 1996, *Uspekhi Fizicheskikh Nauk*, **166**, 743, (In Russian).

Postnov, K.A.: 1999, *Uspekhi Fizicheskikh Nauk*, **169**, 545, (In Russian).

CONSTRAINTS ON EXTRA-DIMENSIONS AND VARIABLE CONSTANTS FROM COSMOLOGICAL GAMMA-RAY BURSTS

T. HARKO and K.S. CHENG

Department of Physics, University of Hong Kong, Pok Fu Lam Road, Hong Kong;
E-mails: harko@hkucc.hku.hk, hrspksc@hkucc.hku.hk

(Received 14 June 2004; accepted 15 July 2005)

Abstract. The observation of the time delay between the soft emission and the high-energy radiation from cosmological gamma ray bursts can be used as an important observational test of multi-dimensional physical theories. The main source of the time delay is the variation of the electromagnetic coupling, due to dimensional reduction, which induces an energy dependence of the speed of light. For photons with energies around 1 TeV, the time delay could range from a few seconds in the case of Kaluza–Klein models to a few days for models with large extra-dimensions. Based on these results we suggest that the detection of the 18-GeV photon ∼4500 s after the keV/MeV burst in GRB 940217 provides a strong evidence for the existence of extra-dimensions. The time delay of photons, if observed by the next generation of high energy detectors, like, for example, the SWIFT and GLAST satellite based detectors, or the VERITAS ground-based TeV gamma-ray instrument, could differentiate between the different models with extra-dimensions.

Keywords: cosmology-extra-dimensions, gamma rays, bursts-radiation mechanisms, photon delay

1. Introduction

One of the most challenging issues of modern physics is the possible existence of the extra-dimensions of the space-time continuum. Multi-dimensional geometries are the natural framework for the modern string/M theories (Witten, 1996) or brane models (Horava and Witten, 1996). String models also provide a natural and self-consistent explanation for the possible variation of the fundamental constants (Forgacs and Horvath, 1979). Hence the problem of the extra-dimensions of the space-time continuum is closely related to the problem of the variations of the fundamental constants, like, for example the fine structure constant α or the speed of light c. Most of the multi-dimensional theories contain a built-in mechanism, which allows the variation of α and c. The speed of propagation of particles in vacuum is modified due to the supplementary effects induced by the extra-dimensions.

The confirmation that at least some gamma-ray bursts (GRBs) are indeed at cosmological distances raises the possibility that observations of these could provide interesting constraints on the fundamental laws of physics. The study of short-duration photon bursts, propagating over cosmological distances, is the most promising way to probe the effects related to the existence of extra-dimensions and quantum gravity



Astrophysics and Space Science **297:** 319–326, 2005.
© Springer 2005

effects. Data on GRBs may be used to set limits on variations in the velocity of light. This has been illustrated, by using BATSE and OSSE observations of the GRBs that have recently been identified optically, and for which precise redshifts are available, in Ellis et al. (2000).

It is the purpose of the present paper to consider the effects of the existence of the extra-dimensions on the propagation of high energy photons. Based on the expressions for the photon time delay we suggest that the detection of the 18-GeV photon ∼4500 s after the keV/MeV burst in GRB 940217 provides a strong evidence for the existence of a multi-dimensional Universe.

The present paper is organized as follows. In Section 2, we review the main physical mechanisms for TeV photon emission from GRB's. The time delay of photons in multi-dimensional cosmological models is considered in Section 3. We discuss and conclude our results in Section 4.

2. TeV Photons from Gamma-Ray Bursts

The mechanisms for TeV photon production in GRBs have been reviewed recently by Wang et al. (2004). One such mechanism is the electron inverse Compton emission in GRB shocks, with an energy spectrum that can be commonly described as $\nu F_\nu \propto \nu^{-p+1/2}$, with $2.05 < p < 2.9$. On the other hand, in the reverse shocks the TeV spectrum is given by $\nu F_\nu \propto \nu^{-p/2+1}$, where $2 < p < \sqrt{6}$.

Similar to the electrons, protons can also be accelerated up to ultra-high energies higher than 10^{20} eV (Wang et al., 2004), producing a spectrum characteristic of Fermi mechanism $dN_{\rm p}/dE_{\rm p} \propto E_{\rm p}^{-p}$, where $E_{\rm p}$ is the energy of the proton. These protons, accelerated in both internal and external shocks can produce gamma rays with energies of the order of TeV (Wang et al., 2004). The protons can be accelerated up to 10^{20}–10^{21} eV for $\Gamma_0 = 10^2$–10^3 and therefore the energy of the synchrotron photons can extend to the TeV band for $\epsilon_{\rm B} n \sim 1$, where $\epsilon_{\rm B}$ is the shock energy carried out by the magnetic field and n is the number density of the external medium. The energy spectrum from proton-synchrotron radiation is $\nu F_\nu \propto \nu^{(3-p)/2}$. If the spectrum of the accelerated protons is that of the standard shock theory, then $(3 - p)/2 \approx 0.5$ (Wang et al., 2004).

TeV gamma rays emitted from extra-galactic sources may collide with diffuse cosmic infrared background photons, leading to secondary e^+e^- electron-positron pairs. The pair production optical depth $\tau_{\gamma\gamma}$ depends on the spectral energy distribution and the intensity of the cosmic infrared background. Because of the high redshift of the cosmological GRB sources, $\tau_{\gamma\gamma}$ also depends on the evolution of the cosmic infrared background with the redshift.

For TeV γ-photons the pair production cross section is maximized when the soft photon energy $\epsilon_{\rm IR}$ is in the infrared range. For a 1 TeV gamma ray this corresponds to a soft photon wavelength near the K-band (∼2 μm). Thus, infrared photons with wavelengths around 2 μm will contribute most to the absorption of TeV gamma

rays. Absorption of γ-rays of energies below $\sim$15 GeV is negligible (Stecker et al., 1992).

To estimate the number of high-energy photons from a gamma-ray burst we assume that the source gives a continuous spectrum, from keV to TeV photons. The fluence (the energy per unit area) F_γ can be represented, as a function of the photon energy E_γ, in the general form $F_\gamma(E_\gamma) = C E_\gamma^{-\beta} \exp(-\tau_\gamma)$, where we assume that β is a (model dependent) constant. The proportionality constant can be obtained from the observational result that the observed fluence, for $E_\gamma \sim 100$ keV, is of the order of $F_\gamma \left(E_\gamma = 100 \text{ keV}\right) \sim 10^{-6}$–$10^{-4}$ erg cm^{-2}. Then the fluence can be represented as

$$F_\gamma(E_\gamma) = (10^{-6}\text{–}10^{-4}) 10^{-7\beta} \left(\frac{E_\gamma}{1 \text{ TeV}}\right)^{-\beta} e^{-\tau_\gamma} \text{ erg cm}^{-2}. \tag{1}$$

The photon number N_γ, which can be observed by a detector with collection area A_{col}, is given by

$$N_\gamma(E_\gamma) = 1.602 \times (10^{-6}\text{–}10^{-4}) \times 10^{-7\beta} \times \left(\frac{E_\gamma}{1\text{TeV}}\right)^{-\beta-1} \times e^{-\tau_\gamma} \times A_{\text{col}}. \tag{2}$$

By using Eq. (2) one could estimate the number of TeV photons that could be detected by using one of the next-generation of ground based TeV gamma ray instruments, the VERITAS system. It consists of a seven, 12-m aperture telescopes, with six telescopes located at the corners of a hexagon of side 80 m (Weekes, 2004a). For TeV photons the photon collection area for this system can be as large as 5×10^8 cm^2. For the VERITAS ground-based array the variation of A_{col} is represented, as a function of the photon energy E_γ, in Figure 1.

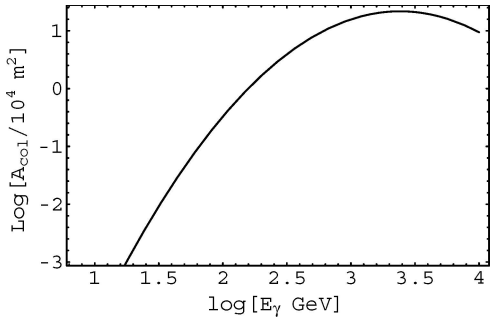


Figure 1. Variation, as a function of the photon energy E_γ, of the photon collection area A_{col} for the VERITAS ground-based TeV gamma-ray instrument.

The number of high energy TeV photons is represented, for three different gamma ray emission models and for two optical depth models (corresponding to the lower and upper limit of the infrared extra-galactic background, respectively), in Figures 2 and 3.

Hence, as one can see from Figures 2 and 3, the large collection area, which for the VERITAS-4 array is of the order of 2.2×10^5 m^2 for 10 TeV photons (Weekes, 2004a), makes possible the detection of high energy photons from GRBs with redshift z smaller than 0.3–0.5.

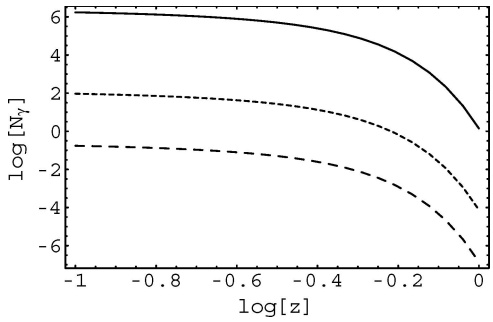


Figure 2. Variation of the photon number N_γ, for a $E_\gamma = 1$ TeV photon energy, as a function of the redshift z (in a logarithmic scale) for different high energy TeV gamma-ray production models: proton synchrotron radiation ($\beta = -0.5$) (solid curve), electron inverse Compton scattering emission in internal shocks ($\beta = 0.11$) (dotted curve) and gamma ray emission via inverse electron Compton scattering in external forward shocks ($\beta = 0.5$) (dashed curve). The optical depth for pair production is calculated by considering the lower limit for the extra-galactic infrared field density. The assumed collection area of the detector is of the order $A_{\rm col} = 5 \times 10^8$ cm^2.

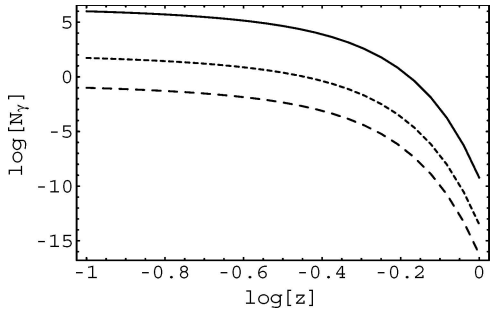


Figure 3. Variation of the photon number N_γ, for a $E_\gamma = 1$ TeV photon energy, as a function of the redshift z (in a logarithmic scale) for different high energy TeV gamma-ray production models: proton synchrotron radiation ($\beta = -0.5$) (solid curve), electron inverse Compton scattering emission in internal shocks ($\beta = 0.11$) (dotted curve) and gamma ray emission via inverse electron Compton scattering in external forward shocks ($\beta = 0.5$) (dashed curve). The optical depth for pair production is calculated by considering the upper limit for the extra-galactic infrared field density. The collection area of the detector is of the order $A_{\rm col} = 5 \times 10^8$ cm^2.

3. Photon Delay in Multi-Dimensional Universes

The energy-dependence of the speed of light of the photon due to the presence of an extra-dimension is given by Harko and Cheng (2004)

$$c = c_0\left[1 + \varepsilon\left(\frac{E}{E_K}\right)^{\beta}\right], \tag{3}$$

where we denoted $E_K = c^4\Delta v/G$, with $\Delta v = v - v^0$ describing the variation of the size of the fifth dimension between the moments of the emission and detection of a photon. $\varepsilon = \pm 1$ is a constant, related to the sign of the fifth dimension.

In the case of isotropic homogeneous cosmological models with large non-compact extra-dimensions there is a non-zero contribution in the four-dimensional space-time (the brane) from the *five*-dimensional Weyl tensor from the bulk, expressed by a scalar term U, called dark radiation (Chen et al., 2002). The "dark radiation" term is a pure five-dimensional effect.

By taking into account the expressions for the variation of the speed of light we obtain the following general equation describing the time delay of two photons with different energies (Harko and Cheng, 2004):

$$\Delta t = H_0^{-1} f^{(\beta)}(E_1, E_2)\int_0^z \frac{(1+z)^{\beta-1}}{\sqrt{\Omega_\Lambda + \Omega_{\rm M}(1+z)^3 + \Omega_U(1+z)^4}}dz, \tag{4}$$

where $H_0 = 72$ km s^{-1} Mpc^{-1}, $\Omega_{\rm M} \approx 0.3$ and $\Omega_\Lambda \approx 0.7$ are the mass density parameter and the dark energy parameter, respectively. Ω_U is the dark radiation parameter and the function $f^{(\beta)}(E_1, E_2)$ describes the different physical models incorporating extra-dimensional and/or quantum gravitational effects. For $\beta = 1$ we have the linear model, with $f^{(1)}(E_1, E_2) = \Delta E/E_K^{(1)}$, where we denoted $\Delta E = E_1 - E_2$.

The linear model corresponds, from the point of view of the extra-dimensional interpretation, to an Einstein–Yang–Mills type model. A linear energy dependence of the difference of the photon velocities has also been considered in Ellis et al. (2003).

A quadratic model of the form $f^{(2)}(E_1, E_2) = (\Delta E/E_K^{(2)})^2$, can also be considered in quantum gravitational models, in which selection rules, such as rotational invariance, forbid first order terms (Ellis et al., 2003). The function $f^{(3)}(E_1, E_2) = (E_1^3 - E_2^3)/E_K^{(3)}$, corresponding to $\beta = 3$, describes the effect of a pure five-dimensional gravity on the propagation of light in four-dimensions. In the above equations we denoted by $E_K^{(\beta)}$, $\beta = 1, 2, 3$ the energy scales associated with the different types of extra-dimensional and/or quantum gravity mechanisms.

If the effects of extra-dimension do exist, then the detected time profiles between the KeV/MeV/GeV burst and the TeV burst should be very different. The comparison of the time profiles at the emitter and observer is presented in Figure 4.

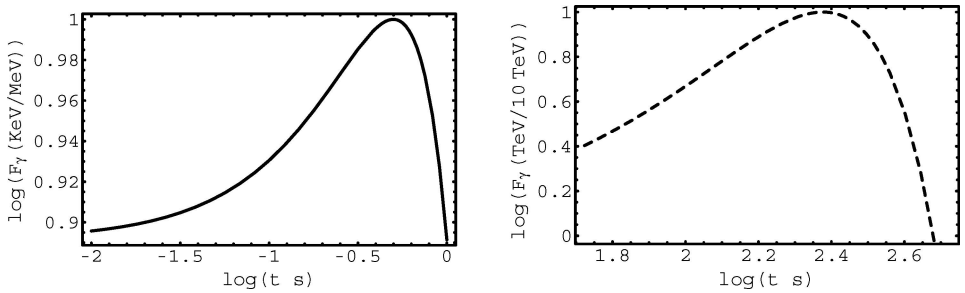


Figure 4. Comparison, in arbitrary units, of the initial KeV/MeV time profile of the GRB emission occurring at a redshift $z = 3$ (assumed to have a Gaussian form), with a duration of $\tau = 1$ s (solid curve), and the TeV time profile at the detector, modified due to the presence of multi-dimensional effects, for the linear model, with the fundamental energy scale $E_K = 1.2 \times 10^{19}$ GeV (dashed curve). For the mass and dark energy parameters we have used the values $\Omega_{\rm M} = 0.3$ and $\Omega_\Lambda = 0.7$, respectively.

4. Discussions and Final Remarks

By using Eq. (4) we can evaluate the extra-dimensional and/or quantum gravity energy scale, which follows from the time delay of the 18 GeV photon in GRB 940217 (Hurley et al., 1994). GRB 940217 is a very strong burst, with a total fluence above 20 keV of $(6.6 \pm 2.7) \times 10^{-4}$ erg cm^{-2} and a duration of $\sim$180 s in the BATSE range. After the low-energy emission has ended, an 18 GeV energy photon and 36 photons with 137 MeV energy have been recorded, after $\sim$5400 s following the low energy emission. Assuming that the photon originated at $z \sim 2$ and taking $\Delta t \approx 4500 \pm 800$ s, where we have also included the uncertainty in the moment of photon emission during the burst, we obtain for the linear energy scale the value $E_K^{(1)} \approx (1.75\text{–}2.51) \times 10^{15}$GeV.

This value is very close to the value $E_K^{(1)} \approx 6.9 \times 10^{15}$ GeV obtained by using a wavelet technique analysis of BATSE and OSSE data (Ellis et al., 2003). For the quadratic model energy scale we have $E_K^{(2)} \approx (1.77\text{–}2.12) \times 10^{8}$GeV.

In the case of quadratic quantum gravity corrections the corresponding energy scale, derived by using BATSE and OSSE data, is $E_K^{(2)} \geq 2.9 \times 10^6$ GeV (Ellis et al., 2003). For the pure Einstein gravity five-dimensional model we obtain $E_K^{(3)} \approx (8.28\text{–}9.34) \times 10^5$GeV.

From the point of view of multi-dimensional theories, the linear model could describe the effects on the propagation of light in Randall–Sundrum or Einstein–Yang–Mills type models (Harko and Cheng, 2004). The quadratic model is specific for quantum gravity effects, while the $\beta = 3$ case could describe the case of pure Einstein gravity in five dimensions. In all these cases the delay of the 18 GeV photon fixes the corresponding energy scales.

The remarkable concordance between the linear quantum gravity/extra-dimensional energy scale obtained from the present study of the time delay of

the 18 GeV photon in GRB 940217 and from the independent study of the BATSE and OSSE data (Ellis et al., 2003) strongly suggest that this time delay could be the signature of the extra-dimensions or/and quantum gravitational effects.

There are several proposed, satellite-based GRB research projects. SWIFT, a multi-wavelength GRB observatory will be launched in early 2004. It has the optimum capabilities in determining the origin of GRBs and their afterglows, providing redshifts for the bursts and multi-wavelength light curves. A wide-field gamma-ray camera will detect approximately 1000 GRBs in 3 years with a sensitivity five times fainter than the BATSE detector aboard Compton GRO. Sensitive narrow-field X-ray and UV/optical telescopes will be pointed at the burst location in 20 to 70 s by an autonomously controlled "swift" spacecraft. SWIFT will acquire high-precision locations for gamma ray bursts and will rapidly relay a 1-4 arcmin position estimate to the ground within 15 s (http://swift.gsfc.nasa.gov, 2003).

Another satellite-based experiment, the Gamma-ray Large Area Space Telescope (GLAST), a high energy (30 MeV–300 GeV) gamma-ray astronomy mission, is planned for launch at the end of 2006 (Weekes, 2004a; Weekes, 2004b). GLAST should detect more than 200 GRBs per year, with sensitivity to a few tens of GeV for a few bursts. GLAST could also detect the energy- and distance-dependent dispersion of (10 ms / GeV / Gpc), predicted by quantum gravity and multi-dimensional models within 1–2 years of observations (Harko and Cheng, 2004).

The possibility that the very high energy component of the gamma-ray bursts might be delayed makes the detection with the sensitive ground-based atmospheric telescopes more feasible. The time delay between the registration of the MeV burst and its notification to the ground-based observer can be as little as 10 s. The slew times for the large telescopes varies from 20 s to 5 min., but can be much less if the observing target for the telescope happens to be close to the gamma ray source direction. In principle the telescope can continue to monitor the source position for up to 8 h (depending on its elevation and the position of Sun and Moon) and on succeeding nights.

The sensitivity that can be achieved is, for the current Whipple 10-m telescope of the order of 8×10^{-8} ergs/cm^2 for a duration of the burst of 1 and 10 s, and of 2.4×10^{-7} ergs/cm^2 for a 100 s duration burst. For the proposed VERITAS array of telescopes (Weekes, 2004a) the minimum fluence is 10^{-8} ergs/cm^2 for 1 and 10 s bursts and 3×10^{-8} ergs/cm^2 for 100 s bursts.

These data can be regarded as representative of the present generation of operating telescopes and for those that will come on-line the next few years (CANGAROO III, HESS, MAGIC and VERITAS). Delayed gamma-ray bursts will be also dispersed, since the velocity of light is a function of energy; hence the energy resolution of the detectors will be critical. The minimum detectable fluence is limited by the duration of the burst. For short times the fluence is limited by the number of photons, since there is virtually no background (Weekes, 2004b).

Therefore, the detection of the time delay between Tev and GeV/MeV photons from GRBs could represent a new possibility for the study and understanding of some fundamental aspects of the physical laws governing our universe.

References

Chen, C.-M., Harko, T., Kao, W.F. and Mak, M.K.: 2002, *Nucl. Phys. B* **636**(1), 159.
Ellis, J., Farakos, K., Mavromatos, N.E., Mitsou, V. and Nanopoulos, D.V.: 2000, *Astrophys. J.* **535**(1), 139.
Ellis, J., Mavromatos, N.E., Nanopoulos, D.V. and Sakharov, A.S.: 2003, *A&A* **10**(11), 931.
Forgacs, P. and Horvath, Z.: 1979, *Gen. Relativity Gravit.*, **11**(3), 205.
Harko, T. and Cheng, K.S.: 2004, *Astrophys. J.* **611**, 633.
Horava, P. and Witten, E.: 1996, *Nuclear Physics B* **475**(1), 94.
Hurley, K. et al.: 1994, *Nature* **372**(1), 652.
Stecker, F.W., de Jager, O.C. and Salamon, M.H.: 1992, *Astrophys. J.* **390**(2), L49.
Wang, X.Y., Cheng, K.S., Dai, Z.G. and Lu, T.: 2004, *Astrophys. J.* **604**(1), 306.
Weekes, T.C.: 2004a, TeV Gamma-ray Observations and the Origin of Cosmic Rays. Plenary Talk at the 28th International Cosmic Ray Conference (Tsukuba, Japan), astro-ph/0312179.
Weekes, T.C.: 2004b, The next generation of ground-based TeV gamma-ray instruments and the identification of high-energy gamma-ray sources. In: K.S. Cheng and G.E. Romero (eds.) Cosmic γ-ray sources, Kluwer Academic Publishers, Dordrecht, 345.
Witten, E.: 1996, *Nucl. Phys. B*, **460**(2), 335.

SEARCH FOR TeV GAMMA-RAYS FROM 3EG J1234-1318 WITH THE CANGAROO-II TELESCOPE*

TAKAHIRO HATTORI and KYOSHI NISHIJIMA

Department of Physics, Tokai University, Hiratsuka, Kanagawa, Japan;
E-mail: hattori@tkikam.sp.u-tokai.ac.jp

(Received 4 June 2004; accepted 3 August 2004)

Abstract. We observed 3EG J1234-1318 with the CANGAROO-II telescope in March, 2002. This source is a steady unidentified EGRET gamma-ray source at high Galactic latitude which has been associated with a dynamically merging clusters of galaxies, and is therefore a candidate TeV source. TeV gamma-ray emission is also expected as a result of large-scale cosmological structure formation. We here report the resulting upper limit on the TeV gamma-ray emission from 3EG J1234-1318.

Keywords: gamma-rays, clusters of galaxies, 3EG J1234-1318

1. Introduction

Diffuse radio emission from clusters of galaxies is clearly due to synchrotron radiation by relativistic electrons (e.g., Giovannini et al., 1993; Giovannini and Feretti, 2000; Kempner and Sarazin, 2001), indicating the presence of non-thermal particles in these objects. The detections of power-law excesses at EUV (e.g., Lieu et al., 1999; Bowyer et al., 2001) and X-ray energies (e.g., Fusco-Femiano et al., 1999; Rephaeli et al., 1999; Kaastra et al., 1999; Fusco-Femiano et al., 2001) are also interpreted as arising from emission by non-thermal processes such as inverse Compton scattering.

Many numerical models for the dynamics of merging clusters of galaxies, based on the large-scale cosmological structure formation scenario, have been made and the level of emission from nonthermal particles predicted (Ricker and Sarazin, 2001; Miniati et al., 2001; Fujita and Sarazin, 2001; Petrosian, 2001; Berrington and Dermer, 2003; Fujita et al., 2003; Gabici and Blasi, 2003, 2004). Gamma-ray radiation from clusters of galaxies is also expected through the decay of neutral pions produced in the interaction of cosmic rays protons with the inter-cluster medium (Völk et al., 1996; Berezinski et al., 1997; Colafrancesco and Blasi, 1998; Völk and Atoyan, 1999) or in the annihilation of dark matter (Colafrancesco and Mele, 2001), or inverse Compton scattering of cosmic microwave background photons by highly relativistic electrons which are produced from thermal inter-cluster electrons through gravitationally induced shock waves during cluster mergers (Loeb and Waxman, 2000; Waxman and Loeb, 2000; Totani and Kitayama, 2000).

*For the CANGAROO Collaboration.

Astrophysics and Space Science **297:** 327–334, 2005.
© Springer 2005

Observationally, more than half of the discrete gamma-ray sources detected with the EGRET instrument have not yet been identified with known counterparts (Hartman et al., 1999). Nineteen of the approximately 170 unidentified sources are found at high Galactic latitudes, $|b| > 45^\circ$. Totani and Kitayama (2000) pointed out that seven sources at high Galactic latitudes that had been noted as being extended, or possibly due to multiple sources, in the third EGRET catalog were also classified as "steady" sources (Gehrels et al., 2000) which are therefore not likely to be AGNs. They also pointed out the number is consistent with the assumption that these seven sources may be dynamically forming clusters of galaxies emitting gamma-rays by high energy electrons accelerated in the shocks when they form. Kawasaki and Totani (2002) surveyed the galaxy clusters around these sources and found that five of the sources have one or two cluster groups/pairs within an angular separation of 1°. They claimed that merging clusters of galaxies are possible candidates for the origin of high Galactic latitude, steady, unidentified EGRET gamma-ray sources.

Although there are conflicting reports on the detection of high energy gamma-ray emission from clusters of galaxies (Colafrancesco, 2002; Scharf and Mukherjee, 2002; Reimer et al., 2003), Totani and Kitayama (2000) predicted the possibility of detecting TeV gamma-rays. In their model, which assumed a magnetic field strength of $B \sim 0.1\,\mu$G, and shock velocity of $V_{\rm shock} \sim 10^3\,{\rm km\,s^{-1}}$, the maximum electron energy can be as high as several tens of TeV, in which case cosmic microwave background photons can be up-scattered through inverse Compton scattering to gamma-ray energies up to several TeV. So there are good reasons for observing clusters of galaxies with ground based Cherenkov telescopes.

3EG J1234-1318 is one of the steady, high latitude EGRET unidentified sources for which a possible connection to galaxy clusters has been claimed (Kawasaki and Totani, 2002). In this paper, we report the results of a search for TeV gamma-rays from the direction of 3EG J1234-1318 made with CANGAROO-II ground-based Cherenkov telescope.

2. 3EG J1234-1318

3EG J1234-1318, centered on $(\alpha, \delta) = (12^{\rm h}34^{\rm m}02^{\rm s}.40, -13^\circ 18' 36'')$, has a relatively hard power law index of -2.09 ± 0.24 at EGRET energies. The flux above 100 MeV was reported to be $(7.3 \pm 1.7) \times 10^{-8}\,{\rm cm^{-2}\,s^{-1}}$.

Within the 95% confidence level error circle of the EGRET source is a rich structure including two galaxy clusters, Abell 1555 and Abell 1558 (see Figure 1). A close cluster group including Abell 1555 is also found, leading to the suggestion that this is a possible site for the merging of clusters of galaxies (Kawasaki and Totani, 2002). There are several radio sources associated with these clusters of galaxies (Condon et al., 1998), however there is no available information on these clusters at X-ray energies.

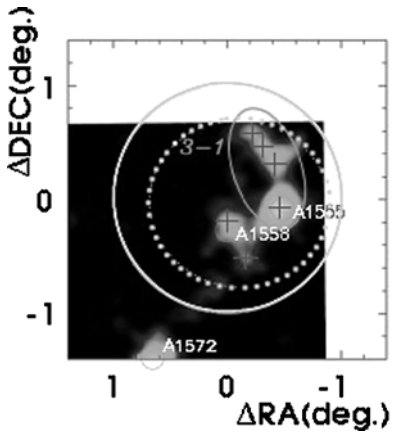


Figure 1. Richness map centered on 3EG J1234-1318 created by Kawasaki and Totani (2002) who examined an overdensity of clusters in the solid circle. The dotted ellipses denote the best-fit ellipse for 95% confidence region of the EGRET source and the plus signs denote the Abell-like cluster candidates. The close cluster group is shown as a solid ellipse.

3. Observations

We observed 3EG J1234-1318 with the CANGAROO-II 10 m atmospheric Cherenkov telescope located near Woomera, South Australia. As this is the first of the four 10 m telescopes in the CANGAROO-III array, hereafter we refer to it as T1. The imaging camera, consisting of an array of 552 photo-multiplier tubes (PMTs) with a pixel size of 0.115°, has a field of view of about 3°. The performance of the optical reflector system of the T1 is described in detail in Kawachi et al. (2001).

3EG J1234-1318 was observed from March 7 to 14, 2002 on clear moon-less nights. Observations were carried out using the long ON–OFF scan mode. Since the most probable position of the EGRET source and the clusters of galaxies are somewhat separated, the telescope tracked a point 0.23° northwest of the EGRET source for the ON source observations. Consequently, the EGRET source, Abell 1555, Abell 1558 and the center of merging clusters group are all within about 0.5° from the center of field of view. For the OFF source scans, the same range of altitude and azimuth as the ON source run was retraced for the background estimation. The total observation times are summarized in Table I.

4. Data Reduction and Analysis

Shower images are selected and cleaned using information on the number of photoelectrons and the timing of signals which are calibrated for each PMT using the data from nightly LED calibration runs. After excluding the data taken during cloudy

TABLE I
Total observation time and total effective observation time after passing all reduction procedures

	ON-source	OFF-source
Total observation time (h)	23.4	24.0
Effective observation time (h)	18.3	18.3

periods, we obtained a stable event rate of $\sim$2 Hz through our observation periods. The effective observation times finally obtained are summarized in Table I.

Image analysis using the so-called Hillas parameters (Hillas et al., 1985) are applied to the remaining shower data in order to discriminate the gamma-rays from the huge hadron background. Details of the data reduction and image analysis are given by Itoh et al. (2003).

From Monte Carlo simulations assuming power-law index of 2.09 for a point source and 1.0° extended source in turn, the background rejections after these reduction procedures were determined to be 96.7% for the point source and 93% for the extended source. The estimated energy thresholds are 700 GeV for a point source and 750 GeV for the extended source, respectively. The corresponding detection efficiencies of gamma-ray events are 42 and 37%.

5. Results

After all these image parameter cuts had been applied, the distributions of image orientation angle *alpha* were derived. Figure 2 shows the results for the directions of Abell 1555, Abell 1558, the center of proposed merging clusters, and the EGRET source position, respectively. In all figures, the left panel shows the result assuming a point source and the right panel shows the result for an extended source. We found no significant excess due to gamma-ray emission from any of all four directions.

Figure 3 shows a significance map over the field of view. The significance map was made from the distribution of detection significance at each point where the significance is obtained from *alpha* distribution based on the method of Li and Ma (1983) assuming each position in turn is a source position. There is no evidence of TeV gamma-ray sources existing in this field of view at a level detectable with our current sensitivity.

6. Discussion and Conclusions

At the sensitivity achieved with T1, there is no indication of TeV gamma-rays from 3EG J1234-1318. The 95% C.L. integral flux upper limits are obtained from the number of excess events at *alpha* less than 20° for a point source and less than

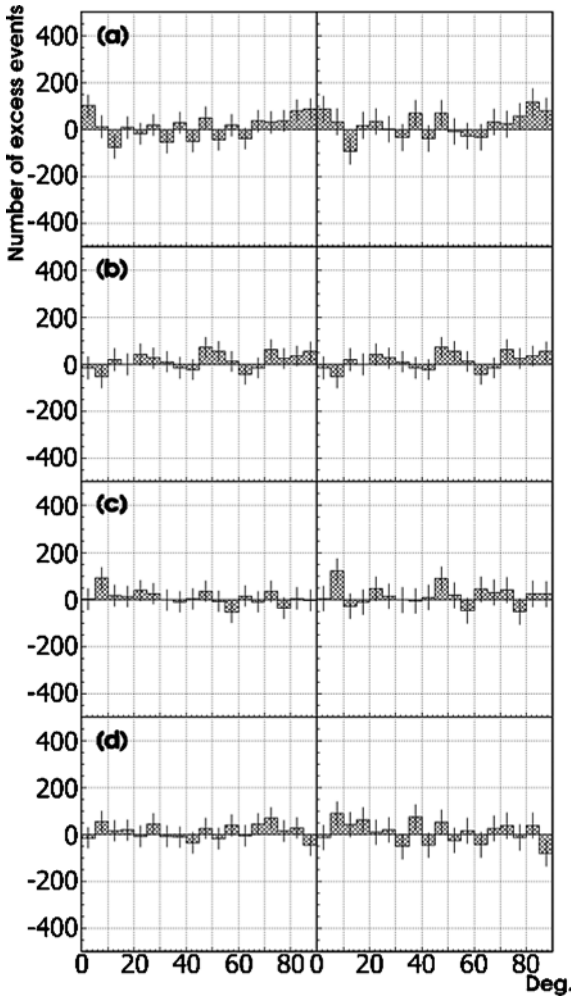


Figure 2. Alpha distributions, with OFF-source data subtracted from ON-source data, for the directions of (a) the EGRET source position, (b) Abell 1555, (c) Abell 1558, and (d) the center of the cluster group. The left panels are obtained with the assumption of a point source and the right panels assume an extended source.

30° for an extended source. The resulting upper limits are $8.3 \times 10^{-12}\,\mathrm{cm}^{-2}\,\mathrm{s}^{-1}$ above 700 GeV for a point source, and $2.1 \times 10^{-11}\,\mathrm{cm}^{-2}\,\mathrm{s}^{-1}$ above 750 GeV for a 1° extended source. The results are plotted in Figure 4 with the extrapolation from the EGRET flux with a power of -2.09 ± 0.24.

Assuming a point source, our result restricts the power-law spectral index to be less than -2.03 at 700 GeV if the spectrum extends to TeV energies. Theoretically, since synchrotron cooling is effective, the corresponding electron spectral index can be calculated to be less than -2.06, i.e., relatively steep, and is consistent

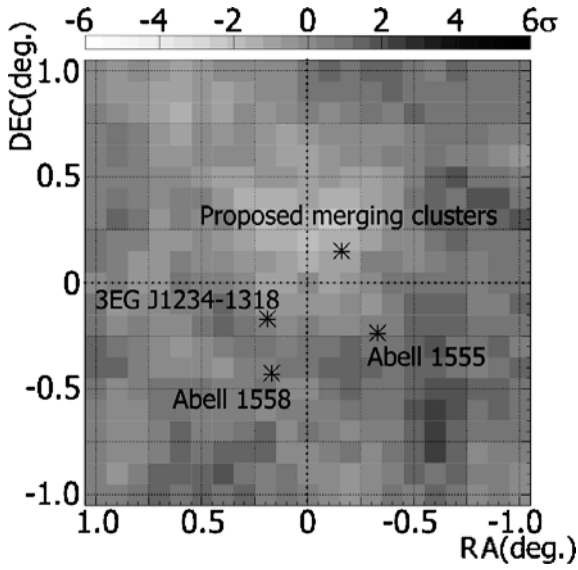


Figure 3. Significance map centered on the tracking point ($\alpha = 12^{\rm h}34^{\rm m}02^{\rm s}.40$, $\delta = -13^\circ 18' 36''$). Details are given in the text.

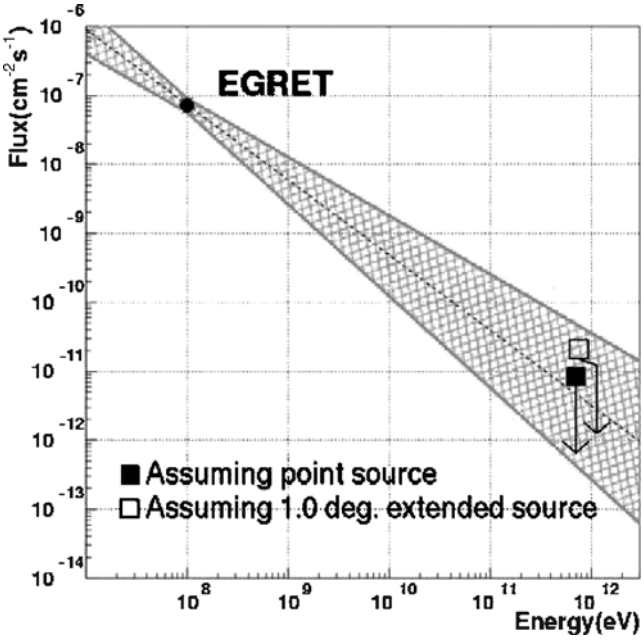


Figure 4. Flux upper limit with 95% C.L. for the direction of the 3EG1234-1318. The dotted line spectrum is extrapolated from the EGRET results. The hatched region inside the thick lines shows the error of the spectrum.

with the assumption of merging clusters of galaxies model. Alternatively, if we accept the gamma-ray merging cluster model with a harder electron spectral index, the non-detection of gamma-rays at 700 GeV approximately limits the strength of magnetic field to be less than ~ 0.1 μG from consideration of the maximum accelerated electron energy, assuming the velocity dispersion is roughly equal to the shock velocity of 10^3 km s^{-1}. However, unfortunately, sesitivity of T1 is not enough to give a significant limit.

Our result thus leaves open the question of an association between unidentified gamma-ray sources and cluster mergers. However, if electrons are accelerated to several tens of TeV by merger shocks, high-energy gamma-ray emissions from some of the clusters of galaxies may be detectable. Recently, ground-based Cherenkov telescopes of sensitivity have started operations. Clusters of galaxies are interesting targets for these telescopes.

Acknowledgements

We thank T. Totani for his useful comments on our observations and results. This research was supported by a Grant-in-Aid for scientific research of the Japanese MEXT, a Sasagawa Scientific Research Grant of the Japan Science Society, ARC Linkage Infrastructure Grant LE0238884, and Discovery Project Grant DP0345983.

References

Berezinski, V.S., Blasi, P. and Ptuskin, V.S.: 1997, *ApJ* **487**, 529.
Berrington, R.C. and Dermer, C.D.: 2003, *ApJ* **594**, 709.
Bowyer, S., Korpela, E. and Berghöfer, T.: 2001, *ApJ* **548**, L135.
Colafrancesco, S.: 2002, *A&A* **396**, 31.
Colafrancesco, S. and Blasi, P.: 1998, *Astropart. Phys.* **9**, 227.
Colafrancesco, S. and Mele, B.: 2001, *ApJ* **562**, 24.
Condon, J.J. et al.: 1998, *AJ* **115**, 1693.
Fujiata, Y., Takizawa, M. and Sarazin, C.L.: 2003, *ApJ* **584**, 190.
Fujita, Y. and Sarazin, C.L.: 2001, *ApJ* **563**, 660.
Fusco-Femiano, R. et al.: 1999, *ApJ* **513**, L21.
Fusco-Femiano, R. et al.: 2001, *ApJ* **552**, L97.
Gabici, S. and Blasi, P.: 2003, *ApJ* **583**, 695.
Gabici, S. and Blasi, P.: 2004, *Astropart. Phys.* **20**, 579.
Gehrels, N. et al.: 2000, *Nature* **404**, 363.
Giovannini, G. et al.: 1993, *ApJ* **406**, 399.
Giovannini, G. and Feretti, L.: 2000, *New Astron.* **5**, 335.
Hartman, R.C. et al.: 1999, *ApJS* **123**, 79.
Hillas, A.M.: 1985, in: *Proceedings of the 19th ICRC*, Vol. 3, p. 445.
Itoh, C. et al.: 2003, *A&A* **402**, 443.
Kaastra, J.S. et al.: 1999, *ApJ* **519**, L119.

Kawachi, A. et al.: 2001, *Astropart. Phys.* **14**, 261.
Kawasaki, W. and Totani, T.: 2002, *ApJ* **576**, 679.
Kempner, J.C. and Sarazin, C.L.: 2001, *ApJ* **548**, 639.
Lieu, R., Ip, W.-H., Axford, W.I. and Bonamente, M.: 1999, *ApJ* **510**, L25.
Li, T.-M. and Ma, Y.-Q.: 1983, *ApJ* **272**, 317.
Loeb, A. and Waxman, E.: 2000, *Nature* **405**, 156.
Miniati, F. et al.: 2001, *ApJ* **562**, 233.
Petrosian, V.: 2001, *ApJ* **557**, 560.
Reimer, O., Pohl, M., Sreekumar, P. and Mattox, J.R.: 2003, *ApJ* **588**, 155.
Rephaeli, Y., Gruber, D. and Blanco, P.: 2001, *ApJ* **511**, L21.
Ricker, P.M. and Sarazin, C.L.: 2001, *ApJ* **561**, 621.
Scharf, C.A. and Mukherjee, R.: 2002, *ApJ* **580**, 154.
Totani, T. and Kitayama, T.: 2000, *ApJ* **545**, 572.
Völk, H.J., Aharonian, F.A. and Breitschwerdt, D.: 1996, *Sp. Sci. Rev.* **75**, 279.
Völk, H.J. and Atoyan, A.M.: 1999, *Astropart. Phys.* **11**, 73.
Waxman, E. and Loeb, A.: 2000, *ApJ* **545**, L11.

MULTIWAVELENGTH STUDY OF TWO UNIDENTIFIED γ-RAY SOURCES

NICOLA LA PALOMBARA[1], PATRIZIA CARAVEO[1], ROBERTO MIGNANI[2], EVANTHIA HATZIMINAOGLOU[3], GIOVANNI F. BIGNAMI[4] and MISCHA SCHIRMER[5]

[1]*IASF/CNR – Sezione di Milano 'G.Occhialini', Via E.Bassini 15, I-20133 Milano, Italy; E-mail: nicola@mi.iasf.cnr.it*

[2]*European Southern Observatory, Karl Schwarzschild Strasse 2, D-85740 Garching, Germany*

[3]*Instituto de Astrofisica de Canarias, Via Lactea, E-38200 La Laguna-Tenerife, Spain*

[4]*CESR, 9 Avenue du colonel Roche, F-31028 Toulouse, France*

[5]*Isaac Newton Group of Telescopes, Edificio Mayantigo, Calle Alvarez Abreu 68, E-38700 Santa Cruz de la Palma, Spain*

(Received 4 June 2004; accepted 27 July 2004)

Abstract. Most counterparts of the identified low-latitude γ-ray sources are *isolated neutron stars* (INSs). Since INSs are characterized by an extremely high value of f_X/f_{opt}, a systematic X-ray/optical coverage of the fields of unidentified low-latitude γ-ray sources is the best way to unveil INS counterparts of unidentified sources. Since the low-latitude sources are heavily affected by the interstellar absorption in both the X-ray and optical bands, we decided to apply the above strategy to two middle-latitude *EGRET* sources, which could belong to a local galactic population: 3EG J0616-3310 and 3EG J1249-8330. Here we report on the global X-ray characterization of about 300 objects, on their candidate optical counterparts and on the preliminary results of their identification.

Keywords: stars: neutron, gamma rays: observations, X-rays: general, surveys, catalogs

1. X-ray Observations, Data Reduction and Source Detection

3EG J0616-3310 and 3EG J1249-8330 are two middle-latitude ($b \simeq -20^\circ$), still unidentified, *EGRET* sources (Figure 1). Since they have no candidate extra-galactic counterparts, we assumed that *isolated neutron stars* (INSs) are the most likely sources of the γ-ray emission. To this aim, we performed a multi-wavelength search of celestial objects with high (i.e. $\geq$1000) X-ray-to-optical flux ratios, according to an investigation strategy which was already successfully used for the identification of *Geminga* (Bignami and Caraveo, 1996) and of other *EGRET* sources (Mirabal and Halpern, 2001; Caraveo, 2001).

Both sources are positioned within error circles of $\sim$0.5° radius which corresponds roughly to the diameter of the *EPIC* field-of-view, the focal plane camera of the *XMM-Newton* Observatory. Each region was covered by four 10 ks *EPIC* pointings (Figure 2) and each of the eight pointings includes three data-sets for the *PN*, *MOS1* and *MOS2* cameras (Strüder et al., 2001; Turner et al., 2001), respectively.



Astrophysics and Space Science **297:** 335–344, 2005.
© Springer 2005

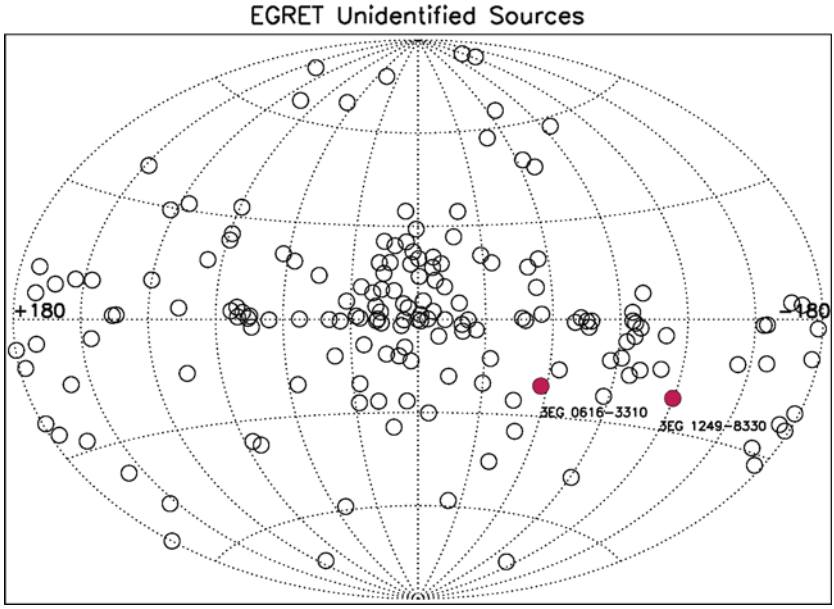


Figure 1. Sky distribution of the unidentified *EGRET* sources: the two filled circles show the celestial position of 3EG J0616-3310 and 3EG J1249-8330 (courtesy of S. Vercellone).

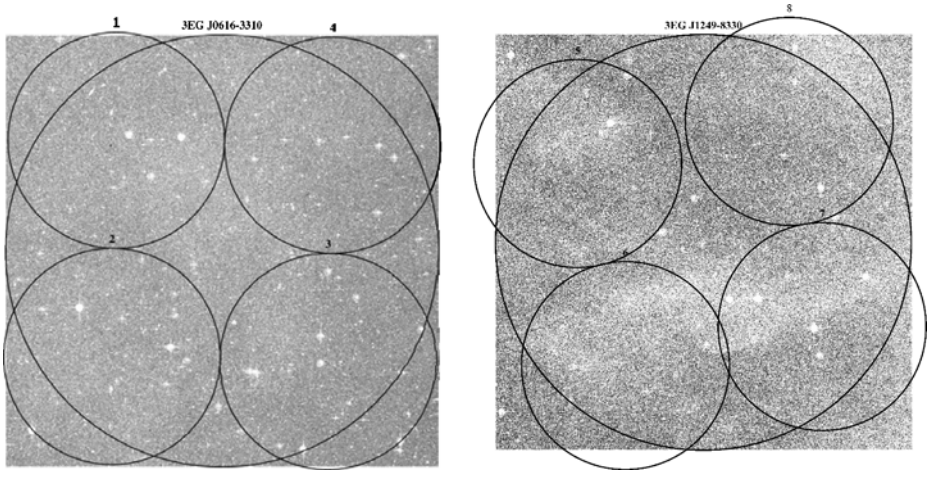


Figure 2. Optical image of the sky-area of 3EG J0616-3310 (left) and 3EG J1249-8330 (right), with the overlay of the γ-ray error–box (large circle) and the field–of–view covered by the four *XMM-EPIC* pointings (small circles).

All data-sets were independently processed with the standard *XMM-Newton Science Analysis System* (SAS).

After the standard processing pipeline, we performed the source detection in seven different energy ranges. Namely, we considered two coarse soft/hard bands

(0.5–2 and 2–10 keV) and a finer energy division (0.3–0.5, 0.5–1, 1–2, 2–4.5, 4.5–10 keV).

To increase the *signal-to-noise* (S/N) ratio and to reach fainter X-ray flux limits, we analyzed together the events from the three instruments, then we selected only the sources with a *detection likelihood* $L > 8.5$ in at least one of the predefined energy ranges. With this criterion we found a total of 146 sources in the 3EG J0616-3310 error circle and 148 sources in the 3EG J1249-8330 one (La Palombara et al., 2003).

2. X-ray Results

2.1. Full statistics

In Table I we report the number, as well as the percentage, of the sources detected in each energy range.

The number of detected sources within each field is strongly dependent on the selected energy band. More than 80% of all sources are detected in the range between 0.5 and 2 keV, with more than 50% of the total detected in the sub-range 1–2 keV. However, only very few sources are detected at very high or very low energies. It is also interesting to remark that the percentage of sources detected below 1 keV is lower for the 3EG J1249-8330 field than for the 3EG J0616-3310, whereas the number of sources is comparable at higher energies. Such a difference is very likely due to the column density of the interstellar gas, which is higher in the first field ($\sim 2.5 \times 10^{20}$ cm^{-2} and $\sim 10^{21}$ cm^{-2} for 3EG J0616-3310 and 3EG J1249-8330, respectively).

2.2. Source distribution over the count rates

Figure 3 shows the histogram of the source distribution over the logarithm of their *count rate* (CR) in three energy ranges for the whole error–circle of the two *EGRET*

TABLE I

X-ray sources detected in each energy range

Source range (keV)	3EG J0616-3310 $N(\%)$	3EG J1249-8330 $N(\%)$
0.5–2	119 (81.5)	119 (80.4)
2–10	41 (28.1)	42 (28.4)
0.3–0.5	28 (19.2)	14 (9.5)
0.5–1	73 (50)	43 (29.1)
1–2	81 (55.5)	77 (52)
2–4.5	47 (32.2)	36 (24.3)
4.5–10	4 (2.7)	8 (5.4)
Total	146	148

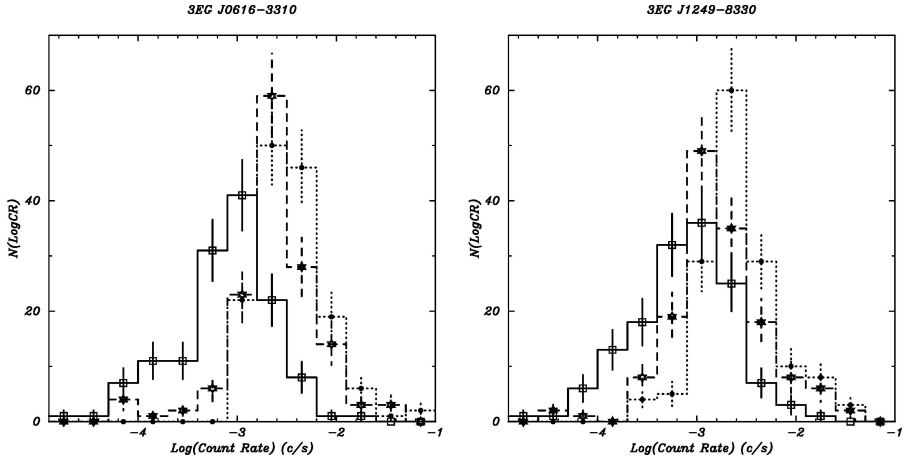


Figure 3. Histogram of the source distribution over the logarithm of their CR for the two whole error–circles of 3EG J0616-3310 (left) and 3EG J1249-8330 (right), in the energy ranges 0.3–10 keV (dotted line, filled circles), 0.3–2 keV (dashed line, small stars) and 2–10 keV (solid line, large squares).

fields. Note that in the full energy range (i.e. 0.3–10 keV) the distribution peak is around $\log \mathrm{CR} = -2.65$ (i.e. $\mathrm{CR} \simeq 2.2 \times 10^{-3}$ cts/s) for both error-circles. Since the number of detected sources for CR bin decreases below the peak CR, we assume that our sample becomes incomplete for lower CR values: therefore we consider the CR peak values as our completeness limit.

Moreover, we can see that, in the case of 3EG J0616-3310, the source distributions in the low and in the full enegy range are very similar, since the peak count rate below 2 keV is equal to or just below the full energy one; in the high energy range, however, the source distribution is very different and most of the detected sources have count rates below 10^{-3} cts/s. For 3EG J1249-8330, there is a larger difference between the full and the low energy ranges, perhaps due to the higher column density of the interstellar gas.

2.3. Source distribution over the Signal-to-Noise ratio

In Figure 4 we report the histogram of the source distribution as a function of the S/N ratio (in the whole energy range) for the two *EGRET* fields. The two distributions peak at 4.5 and 5.5 for, respectively, the 3EG J0616-3310 and the 3EG J1249-8330 sources. Moreover, in the case of the 3EG J0616-3310 sample, a significant fraction of the sources has a S/N ratio higher than 10; on the other hand, only one source of the 3EG J1249-8330 field has a very high (47.16) S/N ratio.

2.4. Source hardness ratios

The count statistics of the sources in our sample is very low (usually of the order of a few tens of photons) and therefore it is not possible to accumulate a significant

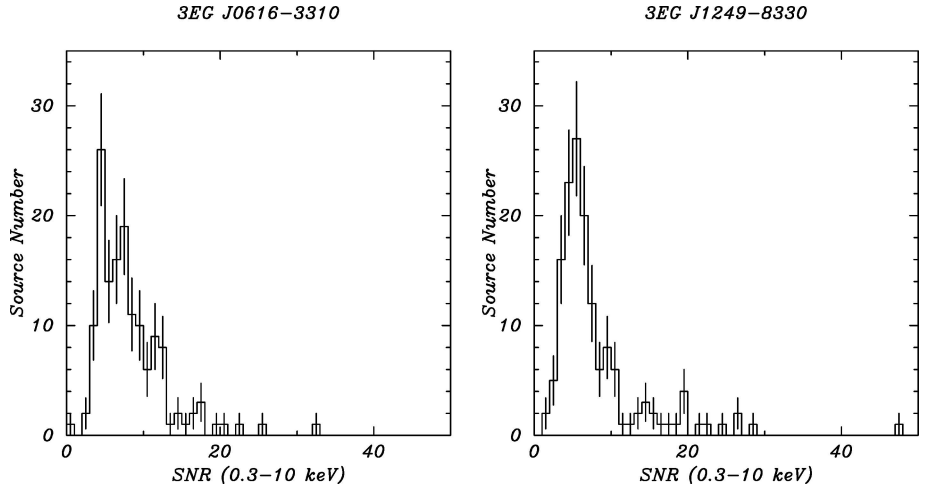


Figure 4. Histogram of the source distribution over their *S/N ratio* for 3EG J0616-3310 (left) and 3EG J1249-8330 (right).

spectrum and to perform a spectral fit. As an alternative, we used the CR in the seven energy ranges to calculate four different *hardness ratios* (HRs):

- HR1 = [CR(0.5–1) − CR(0.3–0.5)]/[CR(0.5–1) + CR(0.3–0.5)]
- HR2 = [CR(1–2) − CR(0.5–1)]/[CR(1–2) + CR(0.5–1)]
- HR3 = [CR(2–4.5) − CR(0.5–2)]/[CR(2–4.5) + CR(0.5–2)]
- HR4 = [CR(4.5–10) − CR(2–4.5)]/[CR(4.5–10) + CR(2–4.5)]

Figure 5 illustrates the histograms of the number of detected sources as a function of the single HRs. From a global point of view, we found that most of the sources have HR1 > 0, $-0.2 <$ HR2 $< +0.4$, HR3 < 0 and HR4 $\simeq -1$. These results suggest that our source population is characterized, on average, by rather soft spectra, with the count distributions peaking between 0.5 and 2 keV. In the majority of cases, the CR is higher in the 1–2 keV range than in the 0.5–1 keV one, while several sources show a significant CR up to 4.5 keV but only very few of them have a very soft or a very hard spectrum.

We also performed simulations to estimate the expected HRs for different spectral models. For comparison, the results are shown as vertical bars in the Figure 5. It is possible to see that the measured HR values are compatible with a rather wide range of both temperatures and photon indexes, thus suggesting that we are sampling a variety of types of serendipitous sources. Such a result is not surprising, since the two areas observed are at medium galactic latitude and therefore should contain both galactic and extragalactic X-ray sources. Making use of the results of

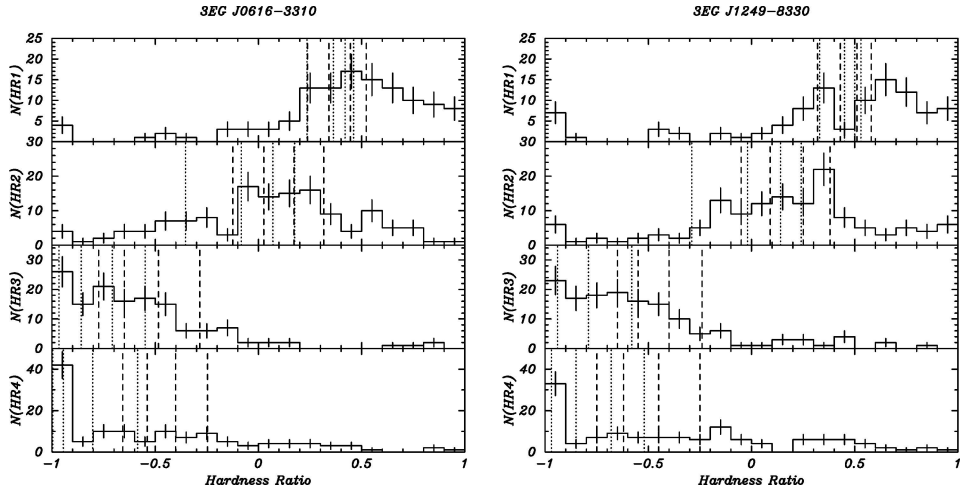


Figure 5. Histogram of the source distribution over their HRs for 3EG J0616-3310 (left) and 3EG J1249-8330 (right). Dotted bars indicate the expected HRs for thermal *bremsstrahlung* spectra with kT = 0.5, 1, 2 and 5 keV (from left to right). Dashed bars indicate the expected HRs for power–law spectra with $\alpha = 1$, 1.5, 2 and 2.5 (from right to left).

the simulations, we could tentatively assign to each source its most likely spectral parameters, both in the form of temperature and photon-index.

2.5. THE LOG(N)–LOG(S) SOURCE DISTRIBUTION

In order to evaluate the source fluxes, we considered the total count rate of each source in the 0.3–10 keV energy range and assumed a template *power-law* spectrum with photon–index $\alpha = 1.7$. As far as the hydrogen column density $n_{\rm H}$, we considered the estimated mean total galactic value for each of the eight EPIC pointings. To compute the corresponding count-rate-to-flux conversion factor (*CF*) for the eight individual pointings, we considered separately the three *EPIC* focal plane cameras and carefully combined both their *CFs* and their effective exposure times.

Figure 6 shows the cumulative Log(N)–Log(S) distributions of the sources detected in the two energy ranges 0.5–2 keV and 2–10 keV. For comparison, it shows also the lower and upper limits of the same distributions as measured at high galactic latitude, where only extragalactic sources should be observed (Baldi et al., 2002). It is interesting to note that in the soft energy band the source density is higher than at high latitudes. This indicates a significant excess of galactic sources. The same is not true in the hard energy range, where the source distribution is in good agreement with the high-latitude one, implying that galactic sources provide a negligible contribution at high energies.

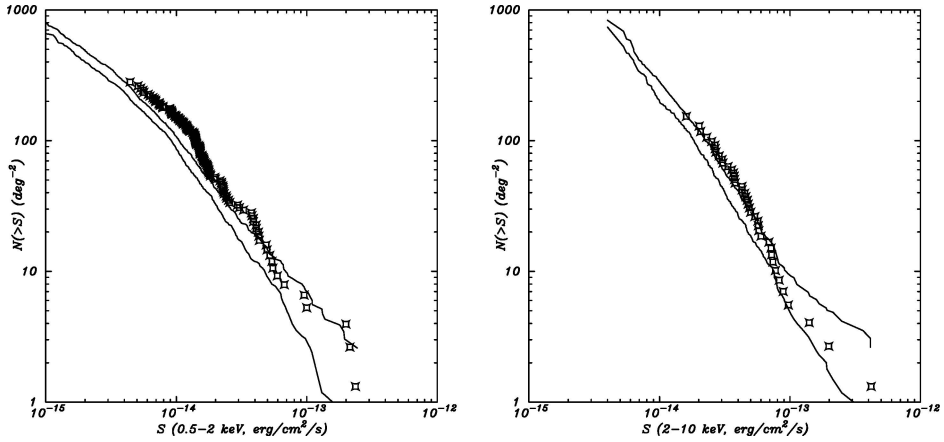


Figure 6. Cumulative Log(N)–Log(S) distribution of the detected sources in the soft (0.5–2 keV, left) and hard (2–10 keV, right) energy ranges. In both the diagrams the two solid lines are the lower and upper limits of the high-latitude Log(N)–Log(S).

3. The Optical Analysis

3.1. Search for optical counterparts

In order to search for possible optical counterparts of our X-ray sources, we cross-correlated their coordinates with the position of the sources of two optical/infrared catalogues: GSC2.2 (http://www–gsss.stsci.edu) and 2MASS (http://pegasus.phast.umass.edu). We found that only for very few cases an X-ray source could be clearly associated with a single optical object: we used the celestial positions of these optical sources to perform the astrometric correction of all the X-ray source coordinates, which turned out to be always lower than $2''$. Therefore, we assigned a conservative value of $5''$ to our X-ray error circle radii.

Firstly, we considered the X-ray sources of all the eight pointings and selected, as possible optical counterparts, all the GSC2.2 and 2MASS sources within their error circles. For some X-ray sources we found more than one candidate, while for several sources we found no counterpart within $5''$. Such a result does not come as a surprise. The GSC2.2 catalogue has a Bj limiting magnitude $\simeq$22.5 in the IIIaJ passband. Taking into account both the completeness limit of the X-ray source detection and the typical $f_{\rm X}/f_{\rm opt}$ ranges of the various classes of X-ray sources (Section 3.2), we estimated that the faintest counterparts should have V $\simeq$ 22 for stars and $V \geq 25$ for other classes of celestial objects. We therefore expect not to be able to detect the optical counterparts for several X-ray sources, for which we assume a limiting magnitude Bj = 22.5.

To reach deeper limiting magnitudes we used the *wide field imager* of the MPG/ESO 2.2 m telescope at La Silla. Three of the four *EPIC* pointings of 3EG

J0616-3310 (i.e. the pointings 2, 3 and 4 of Figure 2) were observed down to $V \simeq 25.5$ (see Schirmer et al., 2003 for the description of the data processing). Since our optical data should provide reliable counterparts for a large fraction of our X-ray sources, we analysed them separately. Even in this case, however, we found no counterpart within 5″ for a few X-ray sources, for which we assumed a limiting magnitude $V = 25.5$.

3.2. Source characterization and identification

Based on the available X-ray and optical data, we performed a preliminary characterization of all the X-ray sources in our sample.

From the X-ray point-of-view, we considered both the detection bands yielding significant detection and, based on them, the reliable HRs of each source; then we compared these parameters with the results of our numerical simulations. In this way we were able to constrain the possible range of values for each source spectral parameter, be it temperature or photon-index, yielding a rough indication on the source type.

From the magnitudes of the selected counterparts (Bj for the GSC2.2 data and V for the WFI ones), we obtained the corresponding optical fluxes and, then, the *X-ray-to-optical* flux ratios. In order to use this parameter for the source characterization, we had to select a 'reference f_X/f_{opt} classification scheme'. To this aim, we considered the results of the *Hamburg–RASS* optical identification program (Zickgraf et al., 2003), which provides the typical ranges of values of the f_X/f_{opt} ratio for each class of celestial sources. They were obtained using a different X-ray energy range (0.1–2.4 keV instead of 0.3–10 keV), different spectral models (specific for each class of sources instead of a fixed power-law) and, in the case of the WFI data, a different optical filter (Johnson V instead of SERC Bj). Therefore we had to adapt the *Hamburg-RASS* results to the parameters used in our work (Chieregato, 2004). Moreover, for a few of the WFI counterparts we had already a suggested classification, based on the photometric data (Hatziminaoglou et al., 2000).

Based on the above procedure, we could divide our X-ray sources in three sets of data:

- *Classified sources*, which have a single optical counterpart and whose X-ray and optical parameters agrees to provide a reliable classification.
- *Sources with candidate counterparts*, which have either more than one optical counterpart or a single one but whose X-ray and optical parameters do not yield a unique classification.
- *Sources without candidate optical counterparts* within a 5″ radius.

Table II shows the number of sources for the three cases, together with the total number of possible counterparts: there we have considered the two *EGRET* fields separately; moreover, we have also distinguished between pointings which are covered by the GSC2.2 data only (1, 5–8) and pointings which are covered by

TABLE II
Results of the cross-correlation of the X-ray sources with the optical data

EGRET field	3EG J0616-3310		3EG J1249-8330
EPIC pointings	1	2–4	5–8
Total number of X-ray sources	50	96	148
Classified X-ray sources	13 (26%)	24 (25%)	22 (15%)
X-ray sources with candidate counterparts	10 (20%)	55 (57%)	32 (22%)
Total number of candidate optical counterparts	26	126	61
X-ray sources without candidate counterparts	27 (54%)	17 (18%)	94 (63%)

the WFI data too (2–4). In the latter case there is a much lower percentage of X-ray sources without candidate counterparts, in comparison with the former one; on the other hand, both the percentage of X-ray sources with candidate counterparts and the total number of candidate counterparts is very high. These results are due to the deeper optical coverage (see previous section). This means that the missing counterparts are fainter than $V \simeq 25.5$ and Bj $\simeq 22.5$ for, respectively, pointings 2–4 and pointings 1, 5–8.

Figure 7 shows the $f_{\rm X}/f_{\rm opt}$ values as a function of the X-ray fluxes for all the X-ray sources of our sample, both with and without optical counterparts (for sources without optical counterpart lower limits have been computed). The plot

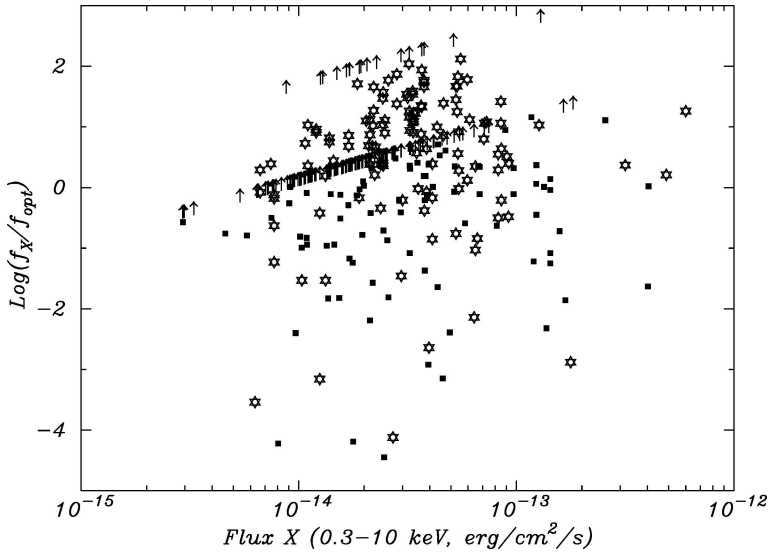


Figure 7. X-ray-to-optical flux ratio for the detected X-ray sources of our sample. Squares and stars refer to *GSC2.2* and *WFI* counterparts, respectively. X-ray sources without optical counterparts (for which upper limits have been used) are indicated with arrows.

shows that there is a large spread in the f_X/f_{opt} ratios at all values of the X-ray fluxes.

– When we consider only the sources with a candidate counterpart, we note that the maximum f_X/f_{opt} ratios are rather low: $\simeq$15 for the sources with only a GSC2.2 counterpart and $\simeq$130 for the sources with a WFI counterpart. These values are compatible with extragalactic identifications (AGN or cluster of galaxies) but not with an INS one.
– When we include also the sources without optical counterpart we estimated the flux ratios based on the limiting magnitudes (Bj $\simeq$ 22.5 or $V \simeq$ 25.5) and obtained *lower limits* to the f_X/f_{opt} values. They range between 0.4 and 25 for the GSC2.2 limit and between 45 and $\simeq$700 for the WFI limit: this last value is very interesting, since it approaches the expected X-ray-to-optical flux ratio for an INS ($\sim$1000).

4. Conclusions and Perspectives

Thanks to the *XMM-EPIC* observations, we have detected about 150 X-ray sources in both the error-circle of 3EG J1249-8330 and 3EG J0616-3310. Using survey optical data to search for counterparts within 5″, we had a success rate of $\sim$40%, leaving $\sim$60% of the X-ray sources unidentified down to a limiting magnitude Bj $\simeq$ 22.5. Ad hoc optical observations changed completely the scenario, since we observed a candidate counterpart brighter than $V \simeq$ 25.5 for other 80% of the X-ray sources. The estimated lower limits of the X-ray-to-optical flux ratios of the remaining sources are rather high and some of them potentially in agreement with the expected value for an INSs. Therefore, this sample of sources is very promising in order to find the counterpart of the two unidentified EGRET sources and will be the object of further, deeper investigations.

References

Baldi, A., Molendi, S., Comastri, A., Fiore, F., Matt, G. and Vignali, C.: 2002, *ApJ* **564**, 190.
Bignami, G.F. and Caraveo, P.A.: 1996, *Ann. Rev. Astron. Astrophys.* **34**, 331.
Caraveo, P.A.: 2001, Gamma-Ray Astrophysics, AIP Proceedings, Baltimore, MD, April 4–6, 2001, Vol. 587, p. 641, astro-ph/0107370.
Chieregato, M., et al.: 2004, *A&A* submitted.
Hatziminaoglou, E., Mathez, G. and Pello, R.: 2000, *A&A* **359**, 9.
La Palombara, N., Bignami, G.F., Caraveo, P., De Luca, A., Mereghetti, S. and Mignani, R.: 2003, *Recent Res. Dev. Astron. & Astrophys.* **1**, 739.
Mirabal, N. and Halpern, J.P.: 2001, *ApJ* **547**, L137.
Schirmer, M., et al.: 2003, *A&A* **407**, 869.
Strüder, L., et al.: 2001, *A&A* **365**, L18.
Turner, M.J.L., et al.: 2001, *A&A* **365**, L27.
Zickgraf, F.J., Engels, D., Hagen, H.-J., Reimers, D. and Voges, W.: 2003, *A&A* **406**, 535.

A NEW TeV SOURCE CONFIRMED IN WHIPPLE ARCHIVAL DATA: TeV J2032+41

M.J. LANG[1], D.A. CARTER-LEWIS[2], D.J. FEGAN[3], S.J. FEGAN[4], A.M. HILLAS[5], R.C. LAMB[6], M. PUNCH[7], P.T. REYNOLDS[8] and T.C. WEEKES[4]

[1]*Department of Physics, National University of Ireland, Galway, Ireland*
[2]*Department of Physics and Astronomy, Iowa State University, Ames, IA, USA*
[3]*Department of Experimental Physics, University College, Belfield, Dublin, Ireland*
[4]*Fred Lawrence Whipple Observatory, Harvard-Smithsonian CfA, Amado, AZ, USA*
[5]*Department of Physics and Astronomy, University of Leeds, Leeds, UK*
[6]*Space Radiation Laboratory, California Institute of Technology, Pasadena, CA, USA*
[7]*Physique Corpusculaire et Cosmologie, Collège de France, Place Marcelin Berthelot, Paris Cedex, France*
[8]*Department of Applied Physics and Instrumentation, Cork Institute of Technology, Bishopstown, Cork, Ireland; E-mail: tweekes@cfa.harvard.edu*

(Received 10 August 2004; accepted 28 August 2004)

Abstract. A re-analysis of data near Cygnus X-3 in 1989–1990 using the Whipple Observatory atmospheric Cherenkov imaging telescope confirms the existence of the TeV J2032 + 4130 source first reported at a conference by the Crimean Astrophysical Observatory and confirmed independently by the HEGRA Collaboration in a referred publication. The significance of the Whipple observations at the a priori HEGRA position is 3.3σ. The peak signal was found at RA = 20 h 32 m, Dec = $+41^\circ 33'$. This is 0.6° north of Cygnus X-3. The flux level (12% of the level of the Crab Nebula) is intermediate between that reported by the Crimean (100%) and HEGRA (3%) groups.

Keywords: gamma rays, observations, unidentified sources

1. Introduction

The region around Cygnus X-3 continues to be the subject of interest for TeV gamma-ray astronomers. The increasing sensitivity of the ground-based atmospheric Cherenkov imaging gamma-ray telescopes and the ability to make two-dimensional maps of the field of view encompassed by the cameras makes possible serendipitous detection of TeV gamma-ray sources in the vicinity of candidate objects or in the control regions commonly used in making such observations. Regions of the sky that include the Galactic Plane are particularly attractive for such searches. Early indications that Cygnus X-3 might be a TeV source (Vladimirsky et al., 1973), led to a concentration of observations in that crowded region of the sky. Recent observations have not confirmed emission from Cygnus X-3 but a two-dimensional study by the Crimean group of observations taken in 1993 suggested the existence of new source offset by 0.7° from Cygnus X-3 (Neshpor et al., 1995). The signal



Astrophysics and Space Science **297:** 345–351, 2005.
© Springer 2005

was at the 6σ level before taking trial factors into account. The observations were made over a six-week period and correspond to a flux of 3×10^{-11} photons cm^{-2} s^{-1} above an energy of 1 TeV; this is strong source at approximately the level of the Crab Nebula, the strongest known steady source in the sky. The coordinates of the new source were right ascension = 20 h 32 m and declination = $+41^{\circ}37'$. The uncertainty in the source position was estimated as 0.2°. Subsequent observations by the Crimean group in the following years did not confirm the emission at this high level (Fomin, private communication) and hence the result was not published in a refereed journal.

In a series of observations by the HEGRA group (Aharonian et al., 2002), the source was independently and serendipitously detected in observations of Cygnus X-3 and the EGRET unidentified source, GeV J2035 + 4214 (Lamb and Macomb, 1997). Both sets of observations encompassed the position of the putative Crimean source. HEGRA reported a detection based on 113 hours of observation over a three-year observing campaign (1999–2001 inclusive) at the 4.6σ post-trial level of significance. This large database was expanded to 279 h with additional observations taken in 2002 and the statistical significance was increased to the 7σ level (Rowell et al., 2003). The source location was determined to be right ascension (J2000) = 20 h 31 m 57.0 s, declination (J2000) = $+41^{\circ}29'56.8''$ with statistical and systematic uncertainties $\approx$ a few minutes of arc. This position is consistent with that of the Crimean source. However the flux level was only about 3% of the Crab flux ($F(> 1\text{TeV}) = (5.9 \pm 3.1) \times 10^{-13}$ photons cm^{-2} s^{-1}) and the differential spectral index was hard (-1.9). The source was reported to be extended ($6.2'$) with a point source hypothesis rejected at the 3σ level. This is a complicated region of the Galactic Plane with three EGRET sources nearby but not obviously related. The source lies close to the edge of the dense OB association, Cygnus OB2.

Following these reports we were motivated to re-analyze data taken on Cygnus X-3 with the Whipple telescope at an earlier epoch and at a somewhat lower energy threshold to search for evidence of this source. In this report we present the results of a preliminary analysis; a more complete report can be found elsewhere (Lang et al., 2004).

2. Observations

Cygnus X-3 was observed using the Whipple Observatory 10 m imaging telescope during the epoch 1988–1990 (O'Flaherty et al., 1992). The observations were carried out in the ON/OFF tracking mode, with Cygnus X-3 located at the center of the field of view. In this mode the telescope tracks the object for 38 min, recording an ON scan. Then during a 2 min interval the telescope is slewed to a position 40 min later in right ascension and records a comparison OFF scan over the same range of zenith and azimuth angles. At that time the telescope was equipped with a 109-pixel camera, consisting of 91 phototubes of diameter 2.9 cm (with a pixel separation of 0.25°), surrounded by an outer ring of 18 phototubes with a diameter of 5 cm (with

TABLE I
Summary of data

Year	No. of data pairs	Duration (h)	N (on)	N (off)	S (σ)
1989	43	26.8	367,783	368,508	−0.8
1990	40	23.5	280,759	280,904	−0.2
Total	83	50.4	648,542	649,412	−0.8

a pixel separation of 0.5°), (Cawley et al., 1990). The field of view of the camera was 3.5° which includes the reported location of TeV J2032 + 4130. The signal in each phototube was amplified and converted to a digital value in which each digital count represented a signal of 1.15 photoelectrons. The camera was triggered when the signal in 2 out of the inner 91 phototubes exceeded a threshold of about 40 digital counts. Moment-fitting parameters were used to characterise the shape and orientation of each recorded Cherenkov image. Gamma-ray-like events were selected on the basis of their shape and orientation defined in a single parameter, azimuthal width (*azwidth*) (Vacanti et al., 1991). During the season 1988–1989 this instrument was used to detect steady TeV emission from the Crab Nebula at the 20σ level. No evidence was found by O'Flaherty et al. (1992) for steady, modulated, or pulsed emission from Cygnus X-3.

Table I summarises the database used in this analysis.

In this re-analysis a small amount of the original data recorded in 1988 was omitted due to the elevated levels of electronic noise present. Slightly more data for the years 1989 and 1990 was included. This initial selection of data was made prior to the search for gamma-ray sources. The average elevation of the observations was about 70°. The statistical significance (S) of any excess of events seen in the ON region is calculated using the combined uncertainty in the ON and OFF event numbers (Li and Ma, 1983). There is no evidence for an excess of events from Cygnus X-3 in the unselected (raw) data.

3. Analysis

As the Cherenkov imaging technique has evolved, a more effective set of gamma-ray image criteria known as *supercuts* has been developed, which separately utilises the shape and orientation information in the image. The Crab database of 1988–1989 was used to optimise the parameters in *supercuts* (Punch et al., 1991) and the criteria were subsequently applied to observations of the Crab Nebula from 1989 to 1990 and 1990 to 1991 seasons giving significant improvements in sensitivity (Lang et al., 1991). *Supercuts* was then adopted as the standard analysis technique for observations with this camera (Reynolds et al., 1993), and, with minor modifications, has remained the standard selection method for subsequent higher resolution

TABLE II
Supercuts selection criteria

Trigger	2 phototubes $>$ 40 digital counts
Shape	$0.51^\circ < \textit{distance} < 1.1^\circ$
	$0.073^\circ < \textit{width} < 0.15^\circ$
	$0.16^\circ < \textit{length} < 0.30^\circ$
Orientation	$0.51^\circ < \textit{distance} < 1.1^\circ$
	$\textit{Alpha} < 15^\circ$

instruments. The *supercuts* selection criteria are listed in Table II. A standard *supercuts* analysis of the database was made in which the image *distance* and *alpha* parameters were calculated relative to the source position reported by Aharonian et al. (2002). It was assumed that the optic axis of the camera was centered on Cygnus X-3. After de-rotation of the field of view by the parallactic angle, this location is displaced from the center of the field of view by 0.09° in the x-axis (corresponding to right ascension) and by 0.54° in the y-axis (corresponding to declination). The results are listed in Table III. There is a 3.3σ excess present at this location. As this is an a priori search location there are no trial factors to be included and the presence of a weak TeV source is confirmed.

The two-dimensional search technique was previously applied to the Crab Nebula database of 1988–1989 by Akerlof et al. (1991). The field of view was divided using a Cartesian grid system covering an interval of $\pm 1.0^\circ$ in both the right ascension and declination directions. The grid step size was 0.1°, giving a total of 441 mesh points. An *azwidth*-type analysis was carried out at each mesh point and the Crab Nebula signal appeared as an approximately two-dimensional Gaussian function with a circular probable error of radius 0.21°. This is the gamma-ray point spread function (PSF) of the instrument. A similar analysis was carried out for observations in which the Crab Nebula was deliberately offset by 0.4° and 1.0° from the centre of the field of view. In each case a signal was detected. The efficiency of the telescope (measured in $\sigma\ \mathrm{h}^{-1}$) was undiminished when the source was offset by 0.4° and was reduced to 45% for the offset of 1.0°. At each offset the source location reconstructed from the shower images agreed with the tracking location

TABLE III
Results for HEGRA location

	N (on)	N (off)	N(on) $-$ N (off)	S
Shape	12,333	12,446	-113	-0.72
Orientation	42,607	42,692	-85	-0.29
Shape + Orientation	2031	1824	$+207$	$+3.33$

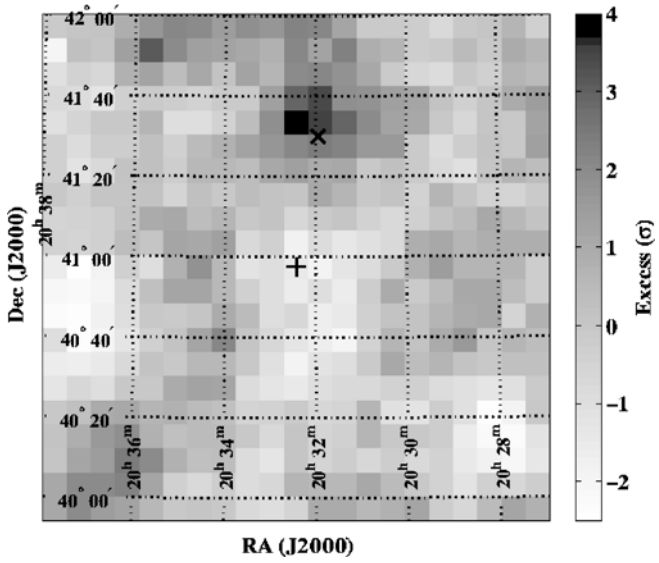


Figure 1. Sky map of the excess significance (σ) in a $2^\circ \times 2^\circ$ region centred on Cygnus X-3 (marked with a +). The HEGRA position for TeV J2032 + 4130 is marked with an ×.

to within approximately 0.03°, with the dominant error attributed to the telescope angle encoders and drive system.

We applied this two-dimensional analysis to the Cygnus X-3 database, where events were selected using the *supercuts* criteria at the 441 mesh points. Figure 1 is a sky map of the ON minus OFF signal over the grid. The significance of the pre-trial peak signal is 4.0σ, corresponding to an excess of 242 events. The peak occurs at the grid point 0.0° in the Right Ascension direction and +0.6° in declination, (RA_{J2000} = 20 h 32 m, Dec_{J2000} = +41°33′). which is compatible with both the Crimean and HEGRA positions. As a conservative estimate of the number of trial factors introduced by searching "near" the HEGRA position we have used the value 7, which corresponds to a search over one quarter of the field of view. This reduces the significance of the peak to 3.5σ. If a linear fall-off in sensitivity with displacement over the interval of 0.4° to 0.6° from the center of the field of view is assumed, the gamma-ray rate corresponds to 12% of the Crab flux, $(5.6 \pm 1.6_{stat} \pm 0.8_{sys}) \times 10^{-12}$ photons cm^{-2} s^{-1}, above the peak energy response of 0.6 TeV. The systematic error is representative of the uncertainty in the off-center sensitivity of the telescope.

There is no evidence that the signal is variable over the two years of observation. Given the gamma-ray PSF value and the weak nature of the signal, we are unable to determine the angular size of the source.

Although the signal is too weak to allow the determination of an energy spectrum we have investigated the effect of raising the energy threshold in software. The

TABLE IV
Peak signal results selected by image *size* (pre-trials)

	N (on)	*N* (off)	*N* (on)-*N* (off)	*S*
Size $\leq$ 600 dc	1574	1405	169	+3.10
Size $>$ 600 dc	395	322	73	+2.73

image parameter *size* measures the total number of photoelectrons in a Cherenkov image, and therefore the gamma-ray energy. Table IV lists the results when the data is selected on the basis of image *size*. The cutoff point of 600 digital counts corresponds to a doubling of the peak energy response to about 1.2 TeV. It would appear that the signal is not confined to low energy events.

4. Discussion

TeV J2032 + 4130 is located within the crowded Cygnus region of the Galactic Plane and hence it has no shortage of possible candidate identifications. The region is dominated by the very strong OB association, Cygnus OB2 and this was the first identification suggested (Aharonian et al., 2002). At a distance of 1.7 kpc, this implies a luminosity in the range 10^{32-34} erg which is a small fraction of the total energy estimated for the OB association. The apparent finite size of the TeV source would favour this identification.

An extensive study of the source region by Butt et al. (2003) using the Chandra and VLA telescopes was made to examine the hypothesis that the large scale shocks and turbulence induced by multiple interacting stellar winds from the young stars in the OB association might accelerate the hadronic component of the cosmic radiation and cause the emission of gamma rays. It was assumed that the TeV source was extended and steady. This work has been extended by Torres et al. (2004) who predict that this may be a strong source of TeV neutrinos.

An alternative approach was taken by Mukherjee et al. (2003) who associated TeV J2032 + 4130 with the nearby EGRET unidentified source 3EG J2033 + 4118 and assumed the TeV source to be variable and point-like. They suggested an identification with the brightest X-ray source in the field, which is variable and has a featureless spectrum suggestive of a BL Lac. This was suggested to be a "proton blazar" which would be notable for having little radio emission. Nolan et al. (2003) report the EGRET source to be non-variable.

Other possible identifications include an unusual supernova remnant caused by a supernova some tens of thousands of years ago (Bednarek, 2003) and the jet from the nearby microquasar, Cygnus X-3 (Aharonian et al., 2002). If the latter explanation was to be verified it would be an interesting final chapter to the long saga of Cygnus X-3 observations. The Whipple detection of a relatively weak signal

at a somewhat lower peak energy and at an earlier epoch is significant in that it suggests that the source is variable and hence aids in its identification with candidate objects. The detection is not deep enough to improve the positional information or to better define the energy spectrum. Also it is not possible to determine the angular size of the source which, like the other TeV sources detected by these experiments, is consistent with a point source. However the average flux detected in 1989–1990 (12% of the Crab) is clearly well above that seen as the average flux over a four-year period by the HEGRA group (3% of the Crab) in 1999–2002 and well below that seen over a six week period in 1993 by the Crimean experiment (approximately the level of the Crab). More sensitive observations by VERITAS, MAGIC and GLAST over the full energy range will probably be needed to unambiguously unravel the nature of the source.

Acknowledgements

The contributions of M.F. Cawley, K.S. O'Flaherty and G. Vacanti to the observational programme, and to the development of the original analysis software, are gratefully acknowledged.

References

Aharonian, F. et al.: 2002, *A&A* **393**, L37.
Akerlof, C.W. et al.: 1991, *ApJ* **377**, L97.
Bednarek, W.: 2003, *MNRAS* **345**, 847.
Butt, Y.M. et al.: 2003, *ApJ* **597**, 494.
Cawley, F.M. et al.: 1990, *Exp. Astron.* **1**, 173.
Lamb, R.C. and Macomb, D.: 1997, *ApJ* **488**, 872.
Lang, M.J. et al.: 1991, in: *Proceedings of the 22nd ICRC*, Dublin, Vol. 1, p. 204.
Lang, M.J. et al.: 2004, *A&A* **423**, 415.
Li, T.P. and Ma, Y.Q.: 1983, *ApJ* **272**, 317.
Mukherjee, R. et al.: 2003, *ApJ* **589**, 487.
Neshpor, Y.I. et al.: 1995, in: *Proceedings of the 25th ICRC*, Rome, Vol. 2, p. 385.
Nolan, P.L. et al.: 2003, *ApJ* **597**, 615.
O'Flaherty, K.S. et al.: 1992, *ApJ* **396**, 674.
Punch, M. et al.: 1991, in: *Proceedings of the 22nd ICRC*, Dublin, Vol. 1, p. 464.
Reynolds, P.T. et al.: 1993, *ApJ* **404**, 206.
Rowell, G. et al.: 2003, in: *Proceedings of the 28th ICRC*, Tsukuba, Vol. 4, p. 2345.
Torres, D.F., Domingo-Santamaria, E. and Romero, G.E.: 2004, *ApJ* **601**, L75.
Vacanti, G. et al.: 1991, *ApJ* **377**, 467.
Vladimirsky, B.M., Stepanian, A.A. and Fomin, V.P.: 1973, in: *Proceedings of the 13th ICRC*, Denver, Vol. 1, p. 456.

THE PROMPT ULTRAVIOLET/SOFT X-RAY EMISSION OF GRBs

ZHUO LI and LI-MING SONG

Particle Astrophysics Center, Institute of High Energy Physics, Chinese Academy of Sciences, Beijing, China; E-mail: lizhuo@mail.ihep.ac.cn

(Received 1 June 2004; accepted 15 July 2004)

Abstract. We discuss the prompt emission of gamma-ray bursts (GRBs), allowing for $\gamma\gamma$ pair production and synchrotron self-absorption. The observed hard spectra suggest heavy pair-loading in GRBs. The re-emission of the generated pairs results in the energy transmission from high-energy gamma-rays to long-wavelength radiation. Due to strong self-absorption, the synchrotron radiation by pairs is in optically thick regime. Thus, the re-emission would appear as a thermal-like spectral bump in the extreme-ultraviolet/soft X-ray band, other than the peak from the main burst. The confirmation of the thermal-like feature and the double-peak structure by future satellites, such as *Swift*, would indicate that the dominant radiation mechanism in GRBs is synchrotron rather than inverse-Compton radiation.

Keywords: gamma-rays: bursts, radiation mechanisms: nonthermal, relativity

1. Introduction

In the past few years, a standard model of gamma-ray burst (GRB) afterglows was well established, in which the ambient medium of GRBs are shock-heated by relativistic expanding blast-waves and give rise to synchrotron/inverse-Compton (IC) emission (Mészáros, 2002). However, the prompt emission of GRBs is believed to be irrelevant to ambient medium, and its radiation mechanism is still poorly known so far.

The recent definite proof of GRB 030329 associated with a type Ib/c supernova confirmed, as long suspected, that GRBs, at least the long class, originate from explosions of massive stars in distant galaxies (Stanek et al., 2003; Hjorth et al., 2003). Since GRBs are events occurring on stars, the emission region may be compact, and the huge energy release will lead to the formation of $e^{\pm}$, γ fireballs, exhibiting thermal-like spectra. But the GRB spectra are non-thermal and hard, with a significant fraction of the energy above the $e^{\pm}$ pair formation energy threshold. For a photon with tens of MeV to escape freely, avoiding $\gamma\gamma$ interactions, the fireball must be ultra-relativistic expanding, with $\Gamma \gtrsim 100$ (Lithwick and Sari, 2001, and references therein). The afterglow studies has also confirmed the presence of ultra-relativistic motion. However, if the intrinsic emission, before leaking out from fireball, includes radiation with even higher energy, say, beyond GeV, these radiation still suffers $\gamma\gamma$ absorption, leading to pair loading in GRBs. In the context of relativistic fireball model, Li et al. (2003, hereafter L03) found that, in a wide range

Astrophysics and Space Science **297:** 353–360, 2005.
© Springer 2005

of model parameters, the resulting pairs may dominate those electrons associated with fireball baryons. The presence of abundant pairs would affect the behaviors of the early afterglow from reverse shocks (L03), and may also emit particular signals in the bursting phase.

We discuss here the prompt GRB emission, with emphasis on the re-emission by the secondary $e^{\pm}$ pairs. If the energy density in the emission region is dominated by magnetic field, the pairs would re-emit mainly by synchrotron radiation, rather than IC process (e.g., Pilla and Loeb, 1998). Due to strong self-absorption, the pair emission appears as a thermal-like bump in the GRB spectrum. (Fan and Wei, 2004 have also studied the pair emission, but with less stress on the self-absorption effect.) This is of significant interest, since the detection of this feature would infer that synchrotron mechanism plays a dominant role in GRBs.

2. Pair Loading in GRB Fireballs

Let us consider a GRB central engine that produces a relativistic wind outflow, with an isotropic energy E, a bulk Lorentz factor Γ and a width Δ. We assume the isotropic geometry, which is valid even for a jetted GRB as long as the Lorentz factor $\Gamma > 1/\theta_{\rm jet}$, with $\theta_{\rm jet}$ the jet opening angle. The energy carried in the outflow may be composed of two components, the bulk kinetic energy of baryons (E_k) and the energy of magnetic field (E_B). The ratio between them can be defined as $\sigma \equiv E_B/E_k$ (e.g., Zhang and Mészáros, 2002). These energies are carried from the central engine to some radius R where GRB emission arises. As in L03, the emission site can be constrained by the non-thermal spectra and rapid varying light curves of GRBs, leading to typical value of $R \sim 10^{14}$ cm for $\Gamma \sim 300$. The width of outflow is $\Delta \lesssim 10^{12}$ cm for a wind lasting for a duration of $T \lesssim 100$ s. Thus the emission region can be usually regarded as a thin shell, with $\Delta \ll R$.

In the kinetic-energy dominated model, i.e., $\sigma < 1$, the bulk kinetic energy is dissipated by internal shock waves within the unsteady outflow, where the magnetic field strength B is in the equipartition value $B \sim (8\pi U_\gamma)^{1/2} = 10^4 L_{\gamma,51}^{1/2} \Gamma_{300}^{-1} R_{14}^{-1}$ G, with $L_\gamma = 10^{51} L_{\gamma,51}$ ergs s^{-1} the GRB luminosity, $\Gamma_{300} = \Gamma/300$ and $R_{14} = R/10^{14}$ cm. Here the equipartition mean the energy stored in the magnetic field, protons and electrons (and hence the released radiation) are comparable. In the magnetic-energy dominated model, the magnetic field strength could be much larger than the above equipartition value. Thus, we here assume that in general the radiation-to-magnetic energy ratio in emission region is $Y \equiv U_\gamma/U_B < 1$, and the magnetic field is scaled as $B = 10^4 B_4$ G in the following.

Due to the large luminosity and hard spectrum of a GRB, any intrinsic high energy gamma-rays produced in the GRB emission region could be absorbed for pair production. As in L03, the cut-off energy, above which the photons suffer strong absorption, and the number of produced pairs can be estimated from the observed GRB spectra. The observed photon spectra of GRBs can be approximated by a

broken power-law, with a high-energy portion of the form $dN_\gamma/d\epsilon \propto \epsilon^{-\beta}$ for $\epsilon > \epsilon_{\rm p}$, where $\epsilon_{\rm p} \sim m_e c^2$ is the energy at the broken point and the index $\beta \sim 2$–3. The number of the produced secondary pairs is equal to the absorbed photons above $\epsilon_{\rm cut}$. Assuming the intrinsic spectrum above $\epsilon_{\rm cut}$ follows the same power law below $\epsilon_{\rm cut}$, we calculate the pair number as $N_\pm = N_\gamma(>\epsilon_{\rm cut}) \simeq (E_\gamma/\epsilon_{\rm p})(\epsilon_{\rm cut}/\epsilon_{\rm p})^{-(\beta-1)}$. Since the timescale of $\gamma\gamma$ collisions (comoving frame), $t'_{\gamma\gamma} \simeq [(\sigma_T/5)n'_\gamma c]^{-1} = 0.2\Gamma_{300}R_{14}^2 L_{\gamma,51}^{-1}$ s, is usually shorter than the dynamic time (comoving frame), $t'_{\rm dyn} \simeq R/\Gamma c = 10 R_{14}\Gamma_{300}^{-1}$ s, the resulting pairs remain inside the outflow.

As in L03, $\epsilon_{\rm cut}$ should be defined by the photon energy at which the optical depth for $\gamma\gamma$ absorption equals unity, $\tau_{\gamma\gamma}(\epsilon) = 1$, where the optical depth can be given by a simplified expression under the thin-shell assumption of the emission region, $\tau_{\gamma\gamma}(\epsilon) = (11/180)\sigma_T N_\gamma(>\epsilon)/4\pi R^2$ (Lithwick and Sari, 2001). Furthermore, the observed cutoff energy must be larger than $\Gamma m_e c^2$. Therefore, we obtain

$$\epsilon_{\rm cut} = \max\left[0.3\left(\frac{R_{14}^2}{E_{\gamma,52}\epsilon_0^{\beta-2}}\right)^{1/(\beta-1)}\Gamma_{300}^2;\quad 0.2\Gamma_{300}\right]{\rm GeV}, \tag{1}$$

where $\epsilon_0 = \epsilon_{\rm p}/m_e c^2$, and hereinafter the numerical coefficient corresponds to $\beta = 2.4$. It can be seen that the detection of the cutoff energy can help to constrain the parameters Γ and R. EGRET had ever detected prompt GeV emission in several GRBs, without obvious attenuation (e.g., GRB 930131; Sommer et al., 1994). We expect that the future satellite *GLAST*, which works at the energy range from 10 MeV up to more than 300 GeV, could observe such a cutoff at multi-GeV.[1] With $\epsilon_{\rm GeV} = \epsilon_{\rm cut}/1\,{\rm GeV}$, the pair number is written as

$$N_\pm \simeq 3\times 10^{53} E_{\gamma,52}\epsilon_{\rm GeV}^{-(\beta-1)}\epsilon_0^{\beta-2}. \tag{2}$$

For comparison, the number of baryonic electrons in the fireball is $N_{\rm b} = E/(1+\sigma)\Gamma m_{\rm p}c^2 = 2\times 10^{52} E_{52}\Gamma_{300}^{-1}(1+\sigma)^{-1}$, with $E_{52} = E/10^{52}$ ergs. So pairs become the dominant component. The baryonic electrons are expected to be responsible for the prompt hard X-ray emission, whilst the pairs may give rise to low energy emission, discussed in the following section.

3. Extreme-Ultraviolet Bump in the Prompt Emission

The initial energy distribution of the generated pairs follows the form of the photon spectrum, i.e., $dn_\pm/d\gamma_e \propto \gamma_e^{-\beta}$ for $\gamma_e > \gamma_\pm$, where $\gamma_\pm$ corresponds to the cutoff energy, $\gamma_\pm = \epsilon_{\rm cut}/2\Gamma m_e c^2 \simeq 3.3\epsilon_{\rm GeV}\Gamma_{300}^{-1}$. These pairs will cool down by synchrotron rather than IC radiation in the $Y \lesssim 1$ condition here. Because of the strong magnetic field in the emission region, the synchrotron-cooling timescale of pairs, $t'_{\rm syn} = 8B_4^{-2}\gamma_\pm^{-1}$ s, is shorter than the fireball dynamical time, implying that

the pairs are always fast cooling. We show later that the pair annihilation time scale is shorter than the system dynamical time and also than the pair-cooling timescale, so pair annihilation is negligible.

For these fast cooling pairs, their energies are emitted quickly. As a result, the energy above $\epsilon_{\rm cut}$ in the intrinsic spectrum re-arises as the pair emission. The luminosity of the pair emission is given by

$$L_{\pm} \simeq \frac{\beta-1}{\beta-2}\frac{N_{\pm}\epsilon_{\rm cut}}{T} \simeq 2\times 10^{50} L_{\gamma,51}\left(\frac{\epsilon_0}{\epsilon_{\rm GeV}}\right)^{\beta-2} {\rm ergs\,s^{-1}}, \quad (3)$$

with $L_\gamma = E_\gamma/T = 10^{51} L_{\gamma,51}\,{\rm ergs\,s^{-1}}$ the GRB luminosity, and the characteristic synchrotron frequency is

$$\nu_{\pm} = 0.9\times 10^{14}\Gamma_{300}^{-1}\epsilon_{\rm GeV}^{2} B_4 {\rm Hz}. \quad (4)$$

If we assume $Y \ll 1$, the synchrotron radiation plays a dominant role of pair cooling, rather than IC process. In this condition, the luminosity $L_\pm$ will peak at frequency $\nu_\pm$. Thus a very intense optical flash will emerge accompanying the prompt gamma-rays if neglecting the self-absorption. However, as shown in the following, the self-absorption is strong in such low energy range, with the absorption frequency $\nu_{\rm a} \gg \nu_\pm$, i.e., most of the pair emission occurs in the optically thick regime. Similar to the case of reverse flash in the condition of $\nu_{\rm c} < \nu_{\rm m} < \nu_{\rm a}$, which is discussed by Kobayashi et al. (2004), a thermal-like bump will arise in the low energy range of a GRB spectrum.

The self-absorption suppresses the emission below absorption frequency $\nu_{\rm a}$, and the suppressed emission energy is redistributed again among the pairs, preventing the pairs cool down immediately. So, the pairs and the radiation obtain a mechanism to exchange their energies. The final result is that the initial injected pair energy is redistributed among pairs and radiation, leading to a bump in the spectrum. The emission in the hard X-ray band is not in the optically thick regime, and is not involved in the energy redistribution. In the GRB duration T, the pair energy is radiated around $\nu_{\rm a}$, where the flux is given by $F_{\nu_{\rm a}} \simeq L_\pm/4\pi D_L^2 \nu_{\rm a}$, with D_L the GRB luminosity distance. We follow the simple way by Sari and Piran (1999) to estimate the maximal flux as a blackbody with the pair temperature, $F_{\nu_{\rm a},{\rm bb}} \approx \pi(R_\perp/D_L)^2(2\nu_{\rm a}^2/c^2)kT_\pm$, where $R_\perp \simeq R/\Gamma$ is the observed size of the fireball, the pair temperature is $kT_\pm \simeq \Gamma\gamma_a m_e c^2/3$, and γ_a is the pair Lorentz factor that corresponds to $\nu_{\rm a}$ and is given by $(2\pi m_e c\nu_{\rm a}/\Gamma eB)^{1/2}$. Equating $F_{\nu_{\rm a},{\rm bb}} \simeq F_{\nu_{\rm a}}$ yields the self-absorption frequency

$$\nu_{\rm a} \simeq 1\times 10^{16} L_{\pm,50}^{2/7}\Gamma_{300}^{3/7} R_{14}^{-4/7} B_4^{1/7} {\rm Hz}, \quad (5)$$

which is in the extreme-ultraviolet (EUV) band in the source frame. Since $\nu_{\rm a} \gg \nu_\pm$, most of the emission is absorbed and re-distributed, giving rise to a black-body like

bump in the GRB spectrum, with peak frequency around $\nu_{\rm a}$ (Eq. 5) and luminosity $L_{\pm}$ (Eq. 3).

Notice that $\nu_{\rm a}$ is insensitive to all the parameters (Eq. 5), and would be fixed in the 10–100 eV range (in source frame) for various GRBs. However, Gou et al. (2004) had pointed out that between the Lyman-α frequency corresponding to the source frame and $\sim$0.2 keV, the GRB flux will be strongly subject to intergalactic and galactic absorption. Hence only the optical/UV or soft X-ray emission is expected for observation. Below $\nu_{\rm a}$ the spectrum behaves as $F_{\nu<\nu_{\rm a}} = F_{\nu_{\rm a}}(\nu/\nu_{\rm a})^2$, then the observed pair emission at 1 eV is

$$F_{\nu}^{\rm ob}(1\,{\rm eV}) \simeq 0.9\frac{L_{\gamma,51}(1+z)^3}{D_{28}^2\nu_{a,16}^3}\left(\frac{\epsilon_0}{\epsilon_{\rm GeV}}\right)^{\beta-2}{\rm mJy}, \tag{6}$$

where $\nu_{a,16} = \nu_{\rm a}/10^{16}$ Hz, and we have obviously shown the dependence on redshift z. Whereas in the band above $\nu_{\rm a}$, the emission is in optically thin regime and still exhibits the form radiated by the initial pairs, $F_{\nu>\nu_{\rm a}} = F_{\nu_{\pm}}(\nu/\nu_{\pm})^{-\beta/2}$, where $F_{\nu_{\pm}} \simeq L_{\pm}/4\pi D_L^2\nu_{\pm}$. If observed at 1 keV, the flux contributed by pairs is then

$$F_{\nu}^{\rm ob}(1\,{\rm keV}) \simeq 3\times10^{-8}\frac{L_{\gamma,51}}{D_{28}^2}\left[\frac{\epsilon_0^2 B_4}{\Gamma_{300}(1+z)}\right]^{(\beta-2)/2}{\rm ergs\,cm^{-2}s^{-1}keV^{-1}}. \tag{7}$$

This calculation is valid until at a high enough frequency where the emission is dominated by the main peak of the GRB. These prompt optical/UV and X-ray emission are expected to be observed by the UVOT and XRT detectors, respectively, on board the up-coming *Swift* satellite.

Finally, we estimate the annihilation rate of $e^{\pm}$ pairs. The comoving-frame annihilation timescale of the pairs in the thermal-like bump, with the comoving-frame temperature $\gamma_{\rm a}m_{\rm e}c^2$, is $t'_{\rm ann} \simeq (\sigma_{\rm ann}n_{\pm}c)^{-1}$, where $\sigma_{\rm ann} \simeq (3\sigma_T/8\gamma_{\rm a})(\ln 2\gamma_{\rm a} - 1)$ is the annihilation cross section, and the pair number density is given by $n_{\pm} \approx n_{\gamma}(>\epsilon_{\rm cut}) \simeq L_{\pm}/4\pi R^2\Gamma c\epsilon_{\rm cut}$. In the calculation here, the baryonic electrons are neglected. The annihilation fraction of pairs, $f_{\rm ann}$, can be estimated by $t'^{-1}_{\rm ann}$ times the comoving-frame dynamical timescale $t'_{\rm dyn}$, $f_{\rm ann} \sim 0.08(L_{\pm,51}/\Gamma_{300}^3R_{14})(10/\gamma_{\pm}\gamma_a)$. Since $f_{\rm ann} \ll 1$, most produced pairs will survive from annihilations and, as suggested by L03, be carried into the reverse shock later on, leading to a pair-rich reverse flash peaking at wavelengths longer than the optical band.

Though some pairs really annihilate into photons with energy $\epsilon_{\rm line} \simeq \Gamma\gamma_{\rm a}m_{\rm e}c^2$, no line feature would appear in the GRB spectrum. If $\epsilon_{\rm line} > \epsilon_{\rm cut}$, the photons would turn into pairs again. Otherwise, since the line luminosity $L_{\rm line} \sim f_{\rm ann}L_{\pm} < L_{\pm} \sim L_{\gamma}(>\epsilon_{\rm cut}) < L_{\gamma}(>\epsilon_{\rm line})$, the line flux is too low to stick out from the high-energy spectrum of the GRB.

As a result, the intrinsic high-energy emission in the GRB spectrum is absorbed and then transferred to a thermal-like bump in the EUV band, as shown in Figure 1.

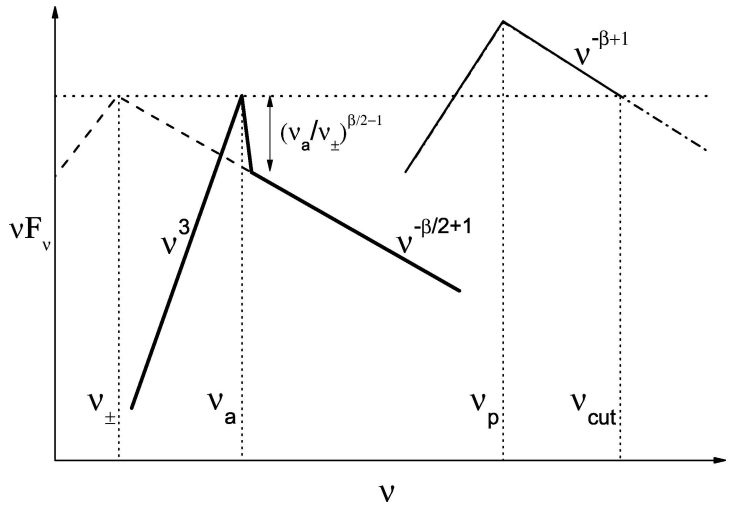


Figure 1. The schematic diagram of the νF_ν spectrum of the GRB prompt emission. Note that $\nu_{\rm p} = \epsilon_{\rm p}/h$ and $\nu_{\rm cut} = \epsilon_{\rm cut}/h$. The *thin solid* line shows the GRB emission with cutoff above $\nu_{\rm cut}$ due to $\gamma\gamma$ pair production, while the *dashed-dotted* line is the intrinsic spectrum without cutoff. The synchrotron radiation by the resulting pairs is shown by the *thick solid* or *dashed* lines, corresponding to with or without self-absorption, respectively. The maximum around $\nu_{\rm a}$ would appear as a thermal-like peak.

Since these features are expected to arise if $Y \ll 1$, the observation would provide a constraint on the magnetization parameter and the radiation mechanism in GRBs.

4. Summary and Discussion on Observation

We study the prompt GRB emission, taking into account the $\gamma\gamma$ pair production and synchrotron self-absorption. In context of relativistic fireball model, and based on the observed characteristics of GRB emission, we find that the resulting pairs usually dominate the baryonic electrons. The pairs will give rise to further emission by synchrotron radiation in the strong magnetic field, which is also responsible for the prompt hard X-ray emission. However, the pair emission occurs in the optically thick regime due to strong self-absorption, leading to a thermal-like spectral bump in the extreme UV/soft X-ray band, other than the peak in the hard X-ray band. The pair annihilation rate is estimated to be negligible, and hence no obvious annihilation lines appear in GRBs.

Some primary hypotheses have been taken in our calculation. First, we assume that the emission region is transparent for Compton scattering, even though the secondary pairs increase significantly the total optical depth. For typical parameter values this assumption is protected. However, if X-ray flashes (XRFs) are optically

thick due to pair formation, as suggested by Mészáros et al. (2002), our calculation using Eq. (2) may underestimate the pair-loading in XRFs, which may need detailed works of numerical simulation. Secondly, we assume strong magnetic field, $Y < 1$, in the emission region. If $Y > 1$, the pairs lose most energy by IC scattering the GRB photons, and the IC photons are not self-absorbed again since beyond the optically thick regime, hence no effective energy exchange between pairs and photons is established and the bump disappears. Therefore, once UV/soft X-ray bumps are detected this will infer $Y < 1$ and that it is synchrotron rather than IC radiation that gives rise to the sub-MeV emission of GRBs.

After a GRB, the subsequent fireball-medium interaction will also lead to very early emission in UV/optical band due to a reverse shock sweeping up the fireball material, which may confuse the observation. However, the reverse-shock emission is different in their spectral shape, with the α-slope ($F_\nu \propto \nu^\alpha$) order of $(5/2, \sim -1/2)$ or $(1/3, \sim -1/2)$ for pair-rich or pair-poor reverse shock, respectively (L03). Comparing with $\alpha \sim 2$ for pair emission in UV/optical band, this can be easily distinguished by observation.

It is further discussed in Li and Song (2004) that the recent observation of a dust halo around GRB 031203, which infers a spectral peak of the prompt burst emission in the soft X-ray band, seems to be consistent with the predicted double-peak structure. The peak of the bump is always subject to strong absorption, but we can diagnose it by the spectral slopes in the the UV/Optical and soft X-ray band. It is of particular interest that for high-redshift GRBs, from Eq. (6) and $D_L(z) \propto (1+z)[1 - 1.25/(1+z)^{1/2}]$ for $z \gtrsim 3$ (analytical fits of Pen 1999, with $\Omega_{\rm tot} = 1$ and $\Omega_{\rm m} = 0.3$), the UV flux scales with z faster than $\propto (1+z)$. Therefore UVOT may even be encouraged to detect the prompt emission from high-z GRBs.

Acknowledgements

Z. Li thank R. F. Shen and L. J. Gou for valuable comments. This work was supported by the National 973 Project and the Special Funds for Major State Basic Research Projects.

Note

1. Though the cosmic infrared background can also absorb high energy gamma-rays from cosmological GRBs, this external attenuation affects only gamma-rays higher than hundreds of GeV (e.g., Salamon and Stecker, 1998).

References

Fan, Y.Z. and Wei, D.M.: 2004, *MNRAS* **351**, 292.
Gou, L.J. et al.: 2004, *ApJ* **604**, 508.

Hjorth, J. et al.: 2003, *Nature* **423**, 847.
Kobayashi, S., Mészáros, P. and Zhang, B.: 2004, *ApJ* **601**, L13.
Li, Z., Dai, Z.G., Lu, T. and Song, L.M.: 2003, *ApJ* **599**, 380(L03).
Li, Z. and Song, L.M.: 2004, *ApJ* **608**, L17.
Lithwick, Y. and Sari, R.: 2001, *ApJ* **555**, 540.
Mészáros, P.: 2002, *ARA&A* **40**, 137.
Mészáros, P. et al.: 2002, *ApJ* **578**, 812.
Pen, U.-L.: 1999, *ApJS* **120**, 49.
Pilla, R. and Loeb, A.: 1998, *ApJ* **494**, L167.
Salamon, M.H. and Stecker, F.W.: 1998, *ApJ* **493**, 547.
Sari, R. and Piran, T.: 1999, *ApJ* **520**, 641.
Sommer, M. et al.: 1994, *ApJ* **422**, L63.
Stanek, K.Z. et al.: 2003, *ApJ* **591**, L17.
Zhang, B. and Mészáros, P.: 2002, *ApJ* **581**, 1236.

PERIODICITY SEARCH IN THE X-RAY DATA OF RX J0007.0+7302

LUPIN C.-C. LIN and HSIANG-KUANG CHANG

Department of Physics and Institute of Astronomy, National Tsing Hua University, Hsinchu, Taiwan; E-mail: lupin@crab0.phys.nthu.edu.tw

(Received 4 June 2004; accepted 29 June 2004)

Abstract. Some unidentified EGRET sources have been reported to have probable X-ray counterparts. Periodicities in the X-ray data of those sources, if found, may help to strengthen the identification and to reveal their nature. We performed a detailed search of periodicities with a photon-counting method, the H-test, in the XMM and ASCA data of RX J0007.0+7302, which is the most probable X-ray counterpart to the EGRET source 3EG J0010+7309. Although no periods with enough significance were found, a possible one, at 0.1275433±0.0000001 s (MJD 52327.03399), is quite intriguing based on results of cross-checking the two data sets. We suggest future analysis with other data to search the vicinity of this period.

Keywords: stars: individual (RX J0007.0+7302, 3EG J0010+7309), stars: neutron

1. Introduction

The nature of the gamma-ray source 3EG J0010+7309 (the 3rd EGRET catalogue, Hartman et al., 1999) remains unknown since its discovery by ERGET in early 1990s (in the 1st EGRET catalogue, GRO J0004+73: Fichtel et al., 1994; in the 2nd EGRET catalogue, 2EG J0008+7307: Thompson et al., 1995). Just like other members of the unidentified EGRET sources, the key to the understanding of their nature is their identification in other energy bands. The X-ray source RX J0007.0+7302, located near the center of the supernova remnant CTA 1, was proposed to be the counterpart to 3EG J0010+7309 (Slane et al., 1997; Brazier et al., 1998) based on the position coincidence and their consistency of being neutron stars. This connection was further strengthened by the spectral continuity from X-ray to gamma-ray bands (Slane et al., 2004). However, to firmly establish this identification, a conclusive evidence is a common period, presumably of the stellar rotation, in different energy bands. If such a period can be found, not only the identification is confirmed, but also its nature can be understood in the framework of gamma-ray pulsar theory. There are other similar proposals of identifying unidentified EGRET sources to neutron-star-like X-ray sources, such as 3EG J1835+5918 to RX J1836.2+5925 (Reimer et al., 2001; Halpern et al., 2002) and 3EG J2020+4017 to RX J2020.2+4026 (Brazier et al., 1996; Uchiyama et al., 2002).

These sources are also candidates of radio-quiet neutron stars. If they are confirmed to be gamma-ray pulsars, they will join the Geminga pulsar to form a class



© Springer 2005

of radio-quiet rotation-powered pulsars. Their spin-down behavior may help us to understand why they are radio-quiet and why other radio-quiet isolated neutron stars do not emit gamma-rays at a detectable level.

In this paper we report the results of a periodicity search in the ASCA and XMM data of RX J0007.0+7302. Timing analysis has been performed with these two data sets separately, both using the fast Fourier transform without any detection (Slane et al., 1997, 2004). We applied a photon-counting method, the H-test (De Jager et al., 1989), in our analysis with trial periods at steps of a small fraction of the corresponding Fourier width over the period range 0.1–1000 s. Several tempting features were found from cross-checking the ASCA and XMM data sets. Based on the inferred characteristic age and spin-down power, we suggest the one at 0.1275433 ± 0.0000001 s (MJD 52327.03399) be the most likely one.

2. Data Analysis and Results

The XMM data of RX J0007.0+7302 that we used in the analysis is the one from the 40-ks observation performed on 2002 February 21. Since our purpose was periodicity search, only the data obtained with the pn detector in the small window mode, whose time resolution is about 6 ms, was employed. Standard selection procedure was conducted using the science analysis system (SAS) package. We picked events within a $10''$-radius circle centered at (J2000) RA $= 00^{\rm h}07^{\rm m}02^{\rm s}.2$, DEC $= +73^\circ03'07''$ (Slane et al., 2004). Events were further restricted in the energy band of 0.2–12 keV. The resultant total number of photons is 1106 and the exposure time is about 28 ks. The solar system barycentric time correction was performed to yield an event time list for analysis.

The ASCA data we used is GIS data from the observation on 1996 January 25. Time resolutions of that data are about 4 ms for the medium bit rate one and about 15 ms for the high bit rate one. In the archival screened data, which have been processed with standard screening criteria, RX J0007.0+7302 is buried in the diffuse X-ray emission of CTA 1. We therefore selected photons within a circle of a smaller radius, $1'.5$, centered at (J2000) RA $= 00^{\rm h}07^{\rm m}01^{\rm s}.1$, DEC $= +73^\circ03'07'$, which was inferred from interpolating between the XMM (Slane et al., 2004) and the ROSAT positions (Brazier et al., 1998; Seward et al., 1995). Photons in 0.5–10 keV were selected. The resultant exposure time is about 44 ks for both GIS2 and GIS3 data, and the total number of photons is 377 for GIS2 and 443 for GIS3. Barycentric time correction was performed with the task timeconv in the HEASOFT package. In the following analysis, data of GIS2 and GIS3, and of high and medium bit rate, are all combined together into a single time list.

Upon the two lists (from XMM and ASCA) of photon arrival times, we conducted a complete search with the H-test over the period range 0.1–1000 s, in the sense that trial periods were separated at a small fraction of the corresponding Fourier width, $P^2/2T$, where P is the trial period and T is the total time span

TABLE I

Trial periods at which the H value is larger than about 35

XMM period (s)	H value	r.p.	ASCA period (s)	H value	r.p.
0.11200955	37.9	9.04×10^{-7}	0.108139845	42.6	2.49×10^{-7}
0.13397840	36.0	1.57×10^{-6}	0.126403815	43.7	1.87×10^{-7}
0.14692094	39.8	5.27×10^{-7}	0.127512095	39.4	5.92×10^{-7}
0.17767572	33.9	2.91×10^{-6}	0.14237634	37.8	9.22×10^{-7}
0.4368722	39.5	5.76×10^{-7}	0.28658588	36.6	1.32×10^{-6}
0.8765945	34.9	2.16×10^{-6}	0.8096734	37.8	9.33×10^{-7}

Periods are reported with digits accurate to about one tenth of corresponding Fourier widths The random probability (r.p.) is for one single trial only. The total number of trials is not taken into account.

of the data (40 ks for XMM, 83 ks for ASCA). The total number of independent trials in this period range is about 8×10^5 for XMM and 1.66×10^6 for ASCA respectively.

Since we have performed such a complete search with a huge number of trials, it is rather difficult to find signatures of periodicities with enough significance. For example, the highest value of the H-statistics found in our search, 43.7, is in the ASCA data at the trial period 0.126403815 s. (As in Table I, trial periods are reported with digits accurate to about one tenth of their corresponding Fourier width. This should not be understood as the uncertainty level of a possible period, which can be determined, for example, from the χ^2 value in the epoch-folding method (Leahy, 1987).) The random probability for such an H value is 1.87×10^{-7} for a single trial. When taking into account the total number of trials, it will not be significant at all. The first result of our search, therefore, was that no signatures of periodicities were found in the XMM and ASCA data of RX J0007.0+7302.

However, tempting features may be found if one cross-checks both data sets. We first picked all the features with the H value higher than about 35, which corresponds to a random probability of 10^{-6}. Twelve such trial periods are listed in Table I; six from XMM and six from ASCA. Unfortunately, none of the twelve can be considered as relevant to any one from the other data set, since their difference implies too large a period derivative, which in turn would give too small a characteristic age less than a few hundred years. The age of the supernova remnant CTA 1 was estimated to be about 10,000 years (Sieber et al., 1981; Slane et al., 2004).

From the above twelve periods we further looked for their possible counterparts in the other data set based on two criteria: (1) only periods at which the H value is larger than 25 were considered and (2) the implied characteristic age is larger than 1000 years. Six such combinations were found and are listed in Table II. The period uncertainty is estimated based on the χ^2 value describing the deviation of its

TABLE II

Tentative counterpart periods in the ASCA and XMM data

Item	ASCA period (s)		XMM period (s)		$\dot{P}$ (10^{-13} s^{-1})
P1	0.11195598(3)	29.7	0.11200955(7)	37.9	2.794(4)
P2	0.12640382(4)	43.7	0.12662308(9)	28.1	11.436(5)
P3	0.12751210(4)	39.4	0.1275433(1)	29.7	1.625(6)
P4	0.13374106(5)	33.8	0.1339784(1)	36.0	12.379(6)
P5	0.2865859(3)	36.6	0.2869217(5)	25.2	17.52(3)
P6	0.4365495(7)	32.4	0.4368722(8)	39.5	16.83(6)

Numbers in parentheses are the 1-σ statistical uncertainties in the last digit. Numbers following each period are the associated H values. The $\dot{P}$ is derived from the two periods. The ASCA periods are at epoch MJD 50107.83546 and XMM at MJD 52327.03399.

folded pulse profile from a flat distribution with the prescription in Leahy (1987), $\sigma_P/\Delta P = 0.71(\chi_r^2 - 1)^{-0.63}$, where $\Delta P = P^2/2T$ is the Fourier width.

We have also compared their pulse profiles to study their similarity. Pulse profiles were folded at corresponding periods with 20 bins. A χ^2-test was applied to assess the probability of the two counterpart profiles being consistent with each other (e.g. Press et al. 1992). An arbitrary shift in phase was allowed since the uncertainty in keeping the phase for such a six-year time span was already much larger than one period. These results together with inferred characteristic ages and spin-down powers are listed in Table III. The two sets of pulse profiles with higher significance of similarity are plotted in Figures 1 and 2.

TABLE III

Properties of the six tentative counterpart periods

				Similarity test	
Item	XMM period (s)	τ_c (yr)	$\dot{E}$ (erg s^{-1})	χ^2	r.p.
P1	0.11200955(7)	6350	7.85×10^{36}	38.6	0.75%
P2	0.12662308(9)	1750	2.224×10^{37}	34.8	2.11%
P3	0.1275433(1)	12430	3.09×10^{36}	26.0	16.78%
P4	0.1339784(1)	1710	2.032×10^{37}	31.3	5.35%
P5	0.2869217(5)	2590	2.93×10^{36}	27.0	13.66%
P6	0.4368722(8)	4110	7.97×10^{35}	35.2	1.90%

$\tau_c = P/2\dot{P}$ is the characteristic age, $\dot{E}$ is the estimated spin-down power, and the χ^2 value is for the similarity test of the ASCA and XMM pulse profiles. r.p. is the corresponding random probability of the χ^2-test. The XMM periods are at epoch MJD 52327.03399. The 1-σ uncertainty level in τ_c and $\dot{E}$ propagating from that in P and $\dot{P}$ is to the last significant digit.

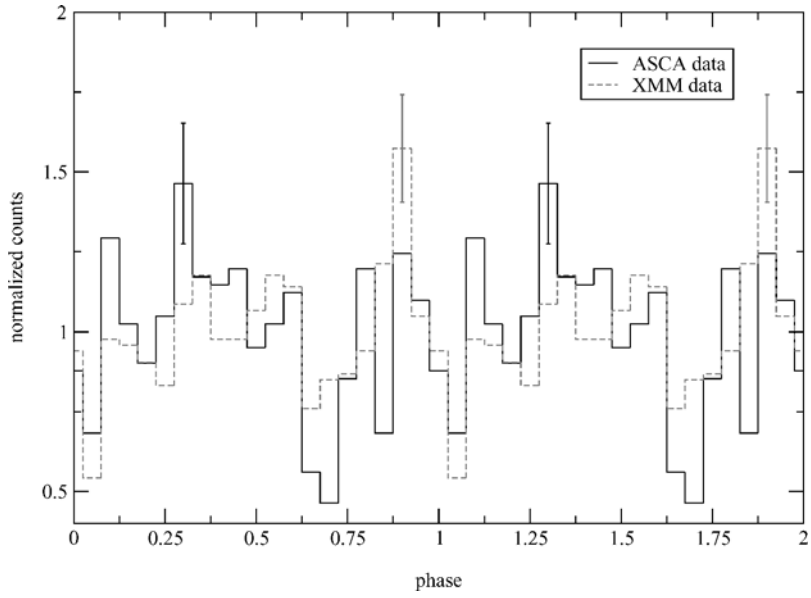


Figure 1. Pulse profiles of ASCA data folded at 0.127512095 s and XMM data at 0.127543255 s. It corresponds to item P3 in Tables II and III.

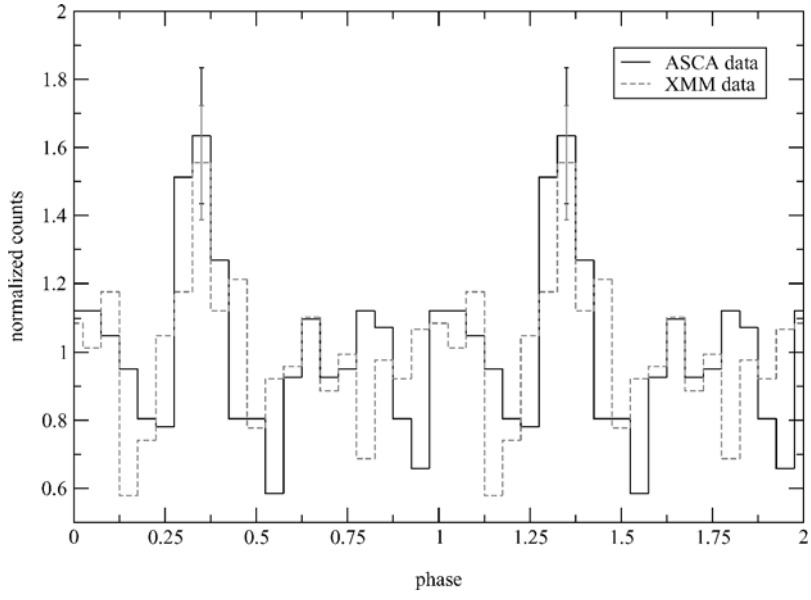


Figure 2. Pulse profiles of ASCA data folded at 0.286585876 s and XMM data at 0.286921721 s. It corresponds to item P5 in Tables II and III.

3. Discussion

We have performed a complete search for periodicities over the period range of 0.1–1000 s with the H-test. From cross-checking the ASCA and XMM data, Some tempting periods were found. The ASCA observation was on MJD 50107.83546 (the mid-point of the whole observation) and XMM on MJD 52327.03399. The characteristic age and estimated spin-down power $\dot{E} = 4\pi^2 I \dot{P}/P^3$, where I is taken as 10^{45} g cm^2, for all these cases are listed in Table III.

Item P3 in Table III deserves particular attention. Its characteristic age is close to that estimated in the literature (Sieber et al., 1981; Slane et al., 2004), its spin-down power is similar to that of the Vela pulsar and PSR B1706-44, which also have a similar characteristic age, and its ASCA and XMM pulse profiles show significant similarity (Figure 1). The spin-down power of RX J0007.0+7302 was estimated to be 1.7×10^{36} erg s^{-1} in Slane et al. (1997), based on an empirical relationship between the X-ray luminosity (0.2–4 keV) of the pulsar-powered plerion (plus the pulsar itself) and the pulsar spin-down power, $\log L_X = 1.39 \log \dot{E} - 16.6$ (Seward & Wang 1988). On the other hand, using another empirical relationship between the photon spectral index of the nonthermal X-ray emission from a pulsar and its spin-down power, $\Gamma = 2.08 - 0.029 \dot{E}_{40}^{-1/2}$ (Gotthelf 2003), with the photon index Γ being 1.5 (Slane et al. 2004), we obtain an estimate of $\dot{E} \approx 2.5 \times 10^{37}$ erg s^{-1}. All the inferred spin-down powers in Table III, except item P6, are between these two empirical estimates.

We note that, for gamma-ray pulsars, younger ones tend to have stronger spin-down powers. For example, the two young gamma-ray pulsars, the Crab pulsar and PSR B1509-58, with a characteristic age of $10^{3.1}$ and $10^{3.2}$ years have spin-down powers of $10^{38.7}$ and $10^{37.3}$ erg s^{-1}, respectively. The Vela pulsar, PSR B1706-44 and PSR B1951+32 have a characteristic age of 10^4–10^5 years and spin-down power of a few times 10^{36} erg s^{-1}. In line of this consideration, items P5 and P6 seem unfavored. But item P5 has noticeable similarity between its ASCA and XMM profiles (Figure 2). The characteristic age and spin-down power in items P2 and P4 are both very similar to that of PSR B1509-58. Furthermore, the supernova remnant G320.4-1.2 (MSH 15-52), which is believed to be associated with PSR B1509-58, is also estimated to be much older than the characteristic age of PSR B1509-58 (Seward and Harnden, 1982; Seward et al. 1983; van den Bergh and Kamper, 1984). However, the significance level of the similarity between the ASCA and XMM pulse profiles is not high for these two cases. The spin-down property of item P1 is just between the young gamma-ray pulsars and the middle-aged ones. The similarity of its pulse profiles seems low.

The gamma-ray emission of 3EG J0010+7309 peaks at 1–2 GeV (in terms of power per decade) and drops off beyond 2 GeV (Brazier et al., 1998). If it is a gamma-ray pulsar, it would be more Vela-like than Crab-like. It again supports the period in item P3 being the most probable one. We suggest future timing analysis

to search periodicities around these period candidates, particularly around the one in item P3.

Acknowledgements

This work was supported by the National Science Council of the Republic of China through grant NSC 92-2112-M-007-024.

References

Brazier, K.T.S., Kanbach, G., Carramiñana, A., Guichard, J. and Merck, M.: 1996, *MNRAS* **281**, 1033.
Brazier, K.T.S., Reimer, O., Kanbach, G. and Carramiñana, A.: 1998, *MNRAS* **295**, 819.
De Jager, O.C., Swanepoel, J.W.H. and Raubenheimer, B.C.: 1989, *A&A* **221**, 180.
Fichtel, C.E., et al.: 1994, *ApJS* **94**, 551.
Gotthelf, E.V.: 2003, *ApJ* **591**, 361.
Halpern, J.P., Gotthelf, E.V., Mirabal, N. and Camilo, F.: 2002, *ApJ* **573**, L41.
Hartman, R.C., et al.: 1999, *ApJS* **123**, 79.
Leahy, D.A.: 1987, *A&A* **180**, 275.
Press, W.H., Teukolsky, S.A., Vetterling, W.T. and Flannery, B.P.: 1992, *Numerical Recipes in C*, Cambridge University Press, Cambridge, p. 623.
Reimer, O., Brazier, K.T.S., Carramiñana, A., Kanbach, G., Nolan, P.L. and Thompson, D.J.: 2001, *MNRAS* **324**, 772.
Seward, F.D. and Harnden, F.R.: 1982, *ApJ* **256**, L45.
Seward, F.D., Harnden, F.R., Murdin, P. and Clark, D.H.: 1983, *ApJ* **267**, 698.
Seward, F.D., Schmidt, B. and Slane, P.: 1995, *ApJ* **453**, 284.
Seward, F.D. and Wang, Z.-R.: 1988, *ApJ* **332**, 199.
Sieber, W., Salter, C.J. and Mayer, C.J.: 1981, *A&A* **101**, 393.
Slane, P., Seward, F.D., Bendiera, R., Torii, K. and Tsunemi, H.: 1997, *ApJ* **485**, 221.
Slane, P. , Zimmerman, E.R., Hughes, J.P., Seward, F.D., Gaensler, B.M. and Clarke, M.J.: 2004, *ApJ* **601**, 1045.
Thompson, D.J., et al.: 1995, *ApJS* **101**, 259.
Uchiyama, Y., Takahashi, T., Aharonian, F.A. and Mattox, J.R.: 2002, *ApJ* **571**, 866.
van den Bergh, S. and Kamper, K.W.: 1984, *ApJ* **280**, L51.

THE KLEIN–NISHINA EFFECTS IN BLAZAR JETS

R. MODERSKI and M. SIKORA

Copernicus Astronomical Center, Bartycka, Warszawa, Poland; E-mail: moderski@camk.edu.pl

(Received 4 June 2004; accepted 23 July 2004)

Abstract. Blazars are the only (with one or two exceptions) extragalactic objects which were detected and identified at gamma-ray energies so far. It is suspected that most of the unidentified gamma-ray sources may be the blazars as well. Because the entire electromagnetic spectrum of these objects is dominated by non-thermal radiation from relativistically moving jets, the effects such as the Klein–Nishina regime in the Compton scattering may play a major role in shaping some parts of the blazar spectrum. Within the framework of external radiation Compton model, we present how these effect influence the spectra of blazars for which the production of gamma rays is dominated by Comptonization of external radiation.

Keywords: galaxies: active, galaxies: jets, gamma rays: theory, radiation mechanisms: non-thermal

1. Introduction

Most of the extragalactic gamma-ray sources are blazars – active galactic nuclei with relativistic jets pointing toward us. Spectrum of these objects consists of two broad components (von Montigny et al., 1995). The low-energy component is Doppler-boosted synchrotron radiation, while the high-energy one is produced by inverse-Compton process. Temporal behavior of blazars suggests that both component are produced co-spatially by the same population of relativistic electrons. In such a case the Klein–Nishina effects may significantly influence the observed radiation. Indeed, it was suggested that the Klein–Nishina effects may be responsible for the unexpectedly large spectral breaks observed in some blazars in MeV range (Georganopoulos et al., 2001). In this paper we analyze the influence of the Klein–Nishina effect not only on the produced radiation, but also on the electron distribution end its evolution during a blazar flare.

This article is organized as follows: in Section 2 we present our theoretical model. Section 3 contains our results, and we discuss the results in Section 4.

2. Model

Our model is an enhancement of the approach of Moderski et al. (2003). The non-thermal flare is produced during the collision of two inhomogeneities of the same mass traveling down the conical jet with different, constant velocities. Such



Astrophysics and Space Science **297:** 369–376, 2005.
© Springer 2005

collision produces shocks in which electrons are accelerated to relativistic energies. Because these shocks themselves are at most mildly relativistic (Sikora et al., 2001) we approximate the active region by thin shell.

2.1. Electron evolution

We follow the evolution of electron distribution, $N(\gamma, t')$ within the shell. This evolution is described by the equation (Blumenthal and Gould, 1970)

$$\frac{\partial N(\gamma, t')}{\partial t'} + \frac{\partial}{\partial \gamma}[\dot{\gamma} N(\gamma, t')] + N(\gamma, t') \int_1^{\gamma} C(\gamma, \gamma')\, d\gamma' - \int_{\gamma}^{\infty} N(\gamma', t') C(\gamma', \gamma)\, d\gamma' = Q, \tag{1}$$

where Q is the electron injection function, γ is the random electron Lorentz factor, $dt' = dt/\Gamma$ is the proper time, and Γ is the Lorentz factor of the bulk motion of a shell. $\dot{\gamma}$ is electron cooling rate from processes other than Compton cooling, which are assumed to operate in the non Klein–Nishina regime. $C(\gamma, \gamma')$ is the rate per unit time of Compton scattering from the Lorentz factor γ to γ', which for monochromatic external photons can be written as (Jones, 1968; Zdziarski, 1988; Coppi and Blandford, 1990).

$$C(\gamma, \gamma') = n \frac{3\sigma_{\mathrm{T}} c}{4\gamma^2 \alpha_0}[s + (2 - s)x - 2x^2 + 2x \ln x], \tag{2}$$

where α_0 is the energy, in units of $m_{\mathrm{e}}c^2$, of external photons with the density n (both quantities measured in a jet frame), and

$$s \equiv \frac{1}{2}\left(\frac{\gamma}{\gamma'} + \frac{\gamma'}{\gamma}\right), \qquad x \equiv \frac{\gamma - \gamma'}{4\gamma\gamma'\alpha_0}. \tag{3}$$

Kinetically allowed range of γ' is found from the condition $x < 1$. Note also that $C(\gamma, \gamma - \alpha)$ is the distribution of the up-scattered photons with energies α (Zdziarski, 1988).

Further on we assume that Compton scattering does not cause electrons to loose large fraction of their energy. This is justified providing that $4\alpha_0\gamma \leq 1$. In such a case integrals in Eq. (1) can be approximated by continuous energy losses

$$N(\gamma, t') \int_1^{\gamma} d\gamma' C(\gamma, \gamma') - \int_{\gamma}^{\infty} d\gamma' N(\gamma', t') C(\gamma', \gamma) = \frac{\partial}{\partial \gamma}[\dot{\gamma}_c N(\gamma, t')]. \tag{4}$$

This is similar to approach taken by Kusunose et al. (2003) in their analysis of 3C 279.

Thus the electron evolution Eq (1) takes the form

$$\frac{\partial N(\gamma, t')}{\partial t'} + \frac{\partial}{\partial \gamma}[(\dot{\gamma} + \dot{\gamma}_c) N(\gamma, t')] = Q. \tag{5}$$

Within the thin shell approximation, the time derivatives can be replaced with derivatives over the radial distance r. Using a relation $r = \beta_\Gamma c \Gamma dt'$, where $\beta_\Gamma = \sqrt{\Gamma^2 - 1}/\Gamma$, we obtain

$$\frac{\partial N(\gamma, r)}{\partial r} + \frac{\partial}{\partial \gamma}\left[N(\gamma, r) \frac{d\gamma}{dr} \right] = \frac{Q}{c \beta_\Gamma \Gamma}. \tag{6}$$

2.2. Electron cooling rates

For simplicity we consider only synchrotron and external Compton radiation as processes contributing to the energy losses of electrons. Thus we neglect adiabatic cooling and Comptonization of synchrotron radiation. Synchrotron cooling works at a rate (Rybicki and Lightman, 1979)

$$\dot{\gamma}_S = -\frac{4}{3} \frac{\sigma_\mathrm{T}}{m_\mathrm{e} c} u'_B \gamma^2, \tag{7}$$

where $u'_B = B'^2/8\pi$ is the magnetic energy density in a jet frame.

Total Compton cooling rate can be calculated from (2) and is given by (Jones, 1965, 1968)

$$\dot{\gamma}_c = \int_0^\gamma (\gamma' - \gamma) C(\gamma, \gamma')\, d\gamma' = \frac{4}{3} \frac{\sigma_\mathrm{T}}{m_\mathrm{e} c} u'_\mathrm{ext} \gamma^2 \frac{9 g(b)}{b^3}, \tag{8}$$

where $b = 4\gamma\alpha_0$, $u'_\mathrm{ext} = n\alpha_0 m_\mathrm{e} c^2$ is the external radiation density as measured in a jet frame, and

$$g(b) = \left(\frac{1}{2} b + 6 + \frac{6}{b} \right) \ln(1 + b) - \left(\frac{11}{12} b^3 + 6b^2 + 9b + 4 \right) \frac{1}{(1 + b)^2} - 2 + 2\mathrm{Li}_2(-b). \tag{9}$$

In the Thomson limit $b \to 0$, $g(b)/b^3 \to 1/9$ and we recover the usual formula

$$\dot{\gamma}_c = -\frac{4}{3} \frac{\sigma_\mathrm{T}}{m_\mathrm{e} c} u'_\mathrm{ext} \gamma^2, \tag{10}$$

while in the extreme Klein–Nishina regime we have

$$\dot{\gamma}_c = -\frac{4}{3} \frac{\sigma_\mathrm{T}}{m_\mathrm{e} c} u'_\mathrm{ext} \gamma^2 \frac{9}{2b^2} \left(\ln b - \frac{11}{6} \right). \tag{11}$$

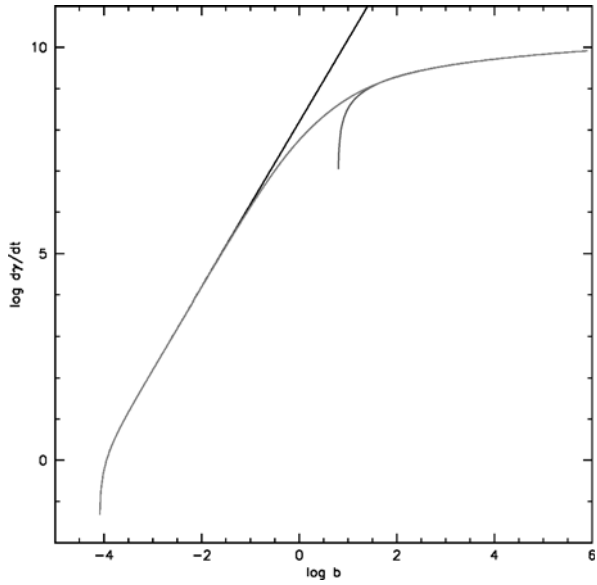


Figure 1. Electron cooling rate due to Compton scattering, $\dot{\gamma}_c$ as a function of the parameter $b \equiv 4\alpha_0\gamma$. Red curve shows the exact formula (8), while the black curve represents approximation of the Thomson limit (10) and the blue one the extreme Klein–Nishina limit (11).

A comparison of the exact formula (8) with its approximations (10) and (11) is presented in Figure 1.

2.3. INTRINSIC LUMINOSITIES

Synchrotron emission is calculated similar to Spada et al. (2001). First the synchrotron emissivity is used (Crusius and Schlickeiser, 1986; Chiaberge and Ghisellini, 1999)

$$j_S(\gamma, \nu) = \frac{3\sqrt{3}}{\pi}\frac{\sigma_T c}{\nu_B}u'_B \times t^2\left\{K_{4/3}(t)K_{1/3}(t) - \frac{3}{5}t\left[K^2_{4/3}(t) - K^2_{1/3}(t)\right]\right\}, \quad (12)$$

where $t \equiv \nu/(3\gamma^2\nu_B)$ and K is modified Bessel function.

Then we use synchrotron cross-section (Ghisellini and Svensson, 1991),

$$\sigma_S(\gamma, \nu) = \frac{8\sqrt{3}\pi^2}{15}\frac{e}{B'}\frac{t}{\gamma^5}\left[K^2_{4/3}(t) - K^2_{1/3}(t)\right], \quad (13)$$

to calculate a synchrotron absorption optical depth τ_S

$$\tau_S = \Delta R \int \sigma_S(\gamma, \nu)N(\gamma, r)\, d\gamma. \quad (14)$$

Finally the synchrotron luminosity is calculated according to the radiation transfer equation

$$L'_{\rm S}(\nu, r) = 4\pi V \frac{1 - {\rm e}^{-\tau_{\rm S}}}{\tau_{\rm S}} \int j_{\rm S}(\gamma, \nu) N(\gamma, r)\, d\gamma. \tag{15}$$

The Compton radiation is calculated with the use of (2)

$$L'_{C}(\nu, r) = \alpha \int C(\gamma, \gamma - \alpha) N(\gamma, r)\, d\gamma. \tag{16}$$

2.4. Observed spectra

The observed spectrum is calculated according to procedure described in detail by Moderski et al. (2003). We only mention here that this algorithm includes the effects of jet geometry, light travel and the Doppler boosting of the radiation.

3. Results

We use the numerical code *BLAZAR* (Moderski et al., 2003) to calculate the electron evolution and the spectra and compare the results to these obtained when only Thomson approximation is used. In all simulations we used the following parameters (see Moderski et al., 2003 for details): electrons are injected as a single power law with index $\alpha_\Gamma = -2$ with energies from $\gamma_{\rm min} = 1$ to $\gamma_{\rm max} = 10^6$; injection starts at the distance $r_0 = 2.0 \times 10^{17}$ cm and ends at $2r_0$; magnetic field $B' = 1$G and is constant; external radiation field with energy $h\nu = 10\,$eV have energy density 0.05 erg/cm^3; jet has opening angle $\theta_{\rm j} = 0.1$ and is observed along the jet axis.

Figure 2 presents the averaged electron distribution during the flare. The cooling break is clearly visible at around $\gamma = 10$ (see Blazejowski et al. (2000) for discussion). Below the cooling break the shape of the distribution differs significantly when the full Klein–Nishina cross-section is included. In Thomson approximation electron distribution follows the power-law shape with the index $\alpha_\Gamma - 1$. In the Klein–Nishina regime the distribution has a huge bump caused by inefficient cooling at high energies. This cooling effect can easily be deduced from the Figure 1.

Figure 3 shows the Compton component of the blazar spectrum, averaged over the flare. The decline in the cross section in the Klein–Nishina regime is totally compensated by the enhanced number of high energy electrons contributing to the spectrum. For comparison we show also the spectrum from single power-law electron distribution as calculated by Georganopoulos et al. (2001). We can easily see that in this case the difference is significant.

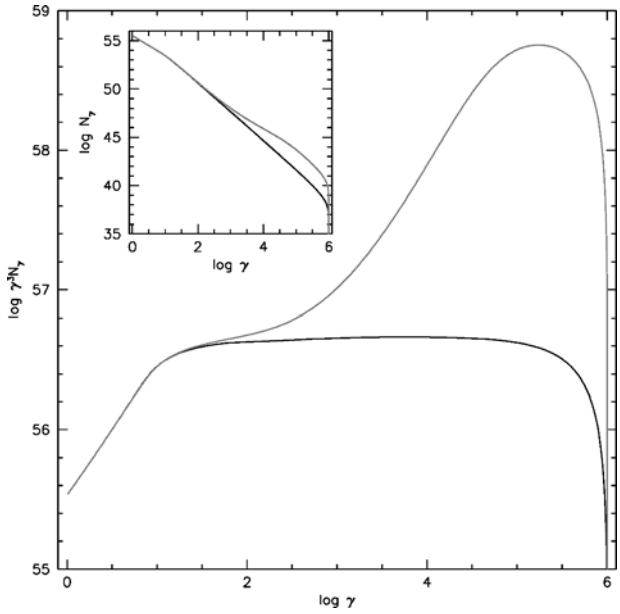


Figure 2. Averaged electron distribution during the blazar flare. Black curve shows the distribution in the Thomson approximation, while red curve includes the Klein–Nishina effects. Inset shows the distribution $N(\gamma)$ vs. γ, while the main picture shows $\gamma^3 N(\gamma)$ to enhance the differences at high energies.

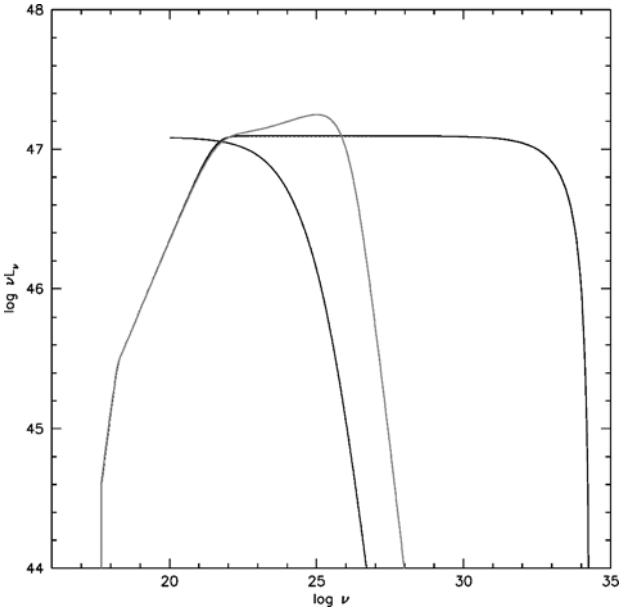


Figure 3. Averaged high-energy component of the spectrum. Thick black line shows the spectrum in the Thomson approximation, when red line uses full Klein–Nishina cross-section. Thin line represents the spectrum from a single, power-law distribution of electrons with index $\alpha_\Gamma = -3$ in the Klein–Nishina regime.

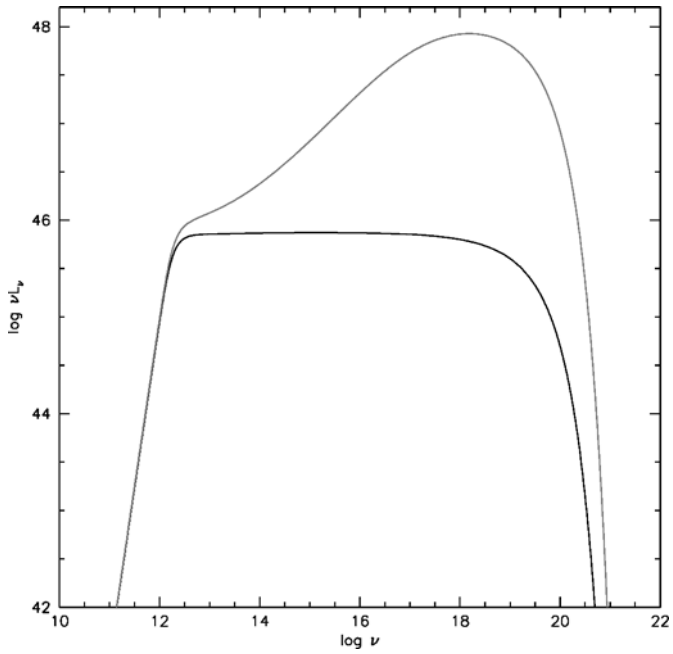


Figure 4. Averaged low-energy component of the spectrum. Thick black line shows the spectrum in the Thomson approximation, when red line uses full Klein–Nishina cross-section.

Figure 4 shows the averaged low-energy component of the blazar spectrum. Here the bump caused by increased number of high-energy electrons is also visible.

4. Summary

It was suggested (Georganopoulos et al., 2001) that the GeV emission of blazars is significantly modified by the Klein–Nishina effects, the spectrum being softer than that calculated in the Thomson limit. This conclusion was based on the calculations performed for a single power-law electron distribution. However, the Klein–Nishina effects affect not only emitted radiation but also underlying electron distribution. Decreased cooling of high-energy electrons causes their number to increase, which compensates for the lower scattering rate. The net effect is that the high-energy component of the spectrum remains almost the same as in the Thomson approximation.

Although the increased number of high-energy electrons is not "visible" in high-energy component of the spectrum it significantly changes the low-energy component. The change is so large that it may put severe constraints on any blazar model.

Past high-energy missions were not able to find any cut-offs in the blazar spectrum, so the importance of the Klein–Nishina effects is difficult to establish

observationally. For better results we will have to wait until first observations of the GLAST satellite.

Acknowledgements

This research was partially supported by Polish KBN grants 5 P03D 002 21 and PBZ 054/P03/2001.

References

Blumenthal, G.R. and Gould, R.J.: 1970, *Rev. Mod. Phys.* **42**, 237.
Blazejowski, M., Sikora M., Madejski, G.M. and Moderski, R.: 2000, *ApJ* **545**, 107.
Chiaberge, M. and Ghisellini, G.: 1999, *MNRAS* **306**, 551.
Coppi, P.S. and Blandford, R.D.: 1990, *MNRAS* **245**, 453.
Crusius, A. and Schlickeiser, R.: 1986, *A&A* **164**, L16.
Georganopoulos, M., Kirk, J.G. and Mastichiadis, A.: 2001, *ApJ* **561**, 111.
Ghisellini, G. and Svensson, R.: 1991, *MNRAS* **252**, 313.
Jones, F.C.: 1965, *Phys. Rev.* **137**, 1306.
Jones, F.C.: 1968, *Phys. Rev.* **167**, 1159.
Kusunose, M., Takahara, F. and Kato, T.: 2003, *ApJ* **592**, L5.
Moderski, R., Sikora, M. and Blazejowski, M.: 2003, *A&A* **406**, 855.
Rybicki, G. and Lightman, A.P.: 1979, *Radiative Processes in Astrophysics*, Wiley, New York.
Sikora, M., Blazejowski, M., Begelman, M.C. and Moderski, R.: 2001, *ApJ* **554**, 1.
Spada, M., Ghisellini, G., Lazzati, D. and Celotti, A.: 2001, *MNRAS* , **325**, 1559.
von Montigny, C., Bertsch, D.L., Chiang, J. et al.: 1995, *ApJ* **440**, 525.
Zdziarski, A.A.: 1988, *ApJ* **335**, 786.

DETECTIVITY OF UNIDENTIFIED EGRET SOURCES AS GAMMA-RAY PULSARS WITH THE MAGIC TELESCOPE

R. ORDUÑA[1], C. BAIXERAS[1], A. CARRAMIÑANA[2] and V. FONSECA[3], for the MAGIC COLLABORATION[4]

[1]*Physics Department, Universitat Autónoma de Barcelona, Barcelona, Spain; E-mail: raul.orduna@uab.es*

[2]*Instituto Nacional de Astrofisica, Óptica y Electrónica, Luis Enrique Erro, 1, Tonantzintla, Puebla, México, Spain*

[3]*Physics Department, Universidad Complutense de Madrid, Madrid, Spain*

[4]*Updated collaborator list at http://hegra1.mppmu.de/MAGICWeb/collaborators.html*

(Received 4 June 2004; accepted 23 August 2004)

Abstract. Most of the unidentified gamma ray sources detected near the Galactic plane by EGRET aboard CGRO are expected to be gamma ray pulsars. We present a study about the detectability and identification of some unidentified EGRET sources with the MAGIC telescope. We list some unidentified gamma ray sources from the third EGRET catalogue to be detected with MAGIC taking into account some important conditions such as the variability parameter of the source, spectral index, inclusion in the GeV catalogue (*ApJ* **488**, 1997, p. 872) and possible associations with known X-ray/radio sources located within the error box of the unidentified gamma ray source. We show the required observation time of these gamma ray pulsar candidates to be detected by MAGIC telescope considering reasonable values of cut-off energy. To be more realistic, we have chosen the zenith angle corresponding to the source culmination in the simulation of the effective area A since the observation time is function of the effective area. In addition to this study, it is very important to consider the extrapolated EGRET flux at MAGIC energies above 30 GeV of the gamma ray pulsar candidates taking the MAGIC sensitivity.

Keywords: pulsars, unidentified gamma-ray sources, cherenkov telescopes

1. Introduction

The EGRET telescope opened loud pulsars, which are almost certainly present among the large number of unidentified sources contained in the 3EG catalog. Other types of gamma-ray sources are certain to be present in the 3EG catalog, where (Gehrels, 2000) showed evidence of at least two separate Galactic populations. So, while isolated pulsars and radio-loud blazars are the dominant types of known gamma-rays sources, objects like supernova remnants (SNRs), microquasars, X-ray pulsars and binary pulsars have been proposed as counterparts for unidentified EGRET sources. The second generation of ground based γ-ray telescopes, able to detect gamma-ray photons of energies closer to the EGRET- and GLAST- energy range, should be able to provide fresh information to



© Springer 2005

these questions, like the association between pulsars and unidentified gamma-ray sources.

MAGIC (Major Atmospheric Gamma-ray Imaging Cherenkov Telescope) is a second generation gamma-ray telescope, with its large reflective area of 234 m^2 and high quantum efficiency photomultipliers and it is designed to capture γ-rays in the $\geq$30 GeV domain. In this paper, we present the estimated detection time for a selected number of EGRET pulsed gamma-ray sources. To calculate the source required observation time we have used Monte Carlo simulations corresponding to the culmination of each source or we have taken into account the minimum zenith angle of the source during the night. These Monte Carlo simulations are the current estimate of the telescope performance and no use of the gamma/hadron separation methods has been made.

2. The Unidentified EGRET Gamma-Ray Sources

Selected list showed that the brighter sources are located at low Galactic latitudes, while dimmer sources are concentrated as a large halo around the Galactic center (Gehrels, 2000). Furthermore, (Grenier, in press) showed the presence of four different populations, taking into account variability and source distribution models. The low-latitude gamma-ray sources are most probably young objects, like gamma-ray pulsars, although studies have also shown formidable evidence in favour of the association between EGRET sources, SNRs and star forming regions. Studies point to a significant number of Population I objects in the parent population of the low-latitude gamma-ray souces, like the correlation analysis with bright giant HII regions performed by (Romero, 2001). The work presented here addresses pulsars hidden among the unidentified gamma-ray sources, which are more likely to be in the group of bright sources, with estimated luminosities around 10^{34}–10^{36} erg/s, at low latitudes, $|b| < 5^{\circ}$. These unidentified sources have characteristics similar to those of gamma-ray pulsars.

3. Detection of Pulsed Emission by the MAGIC Telescope

The pulsar cutoffs for conservative polar cap models scale as (Nell and de Jager, 1991)

$$\frac{dN_\gamma}{dE} = K\left(\frac{E}{E_\mathrm{n}}\right)^{-\Gamma} \exp\left(-\left(\frac{E}{E_\mathrm{o}}\right)^{\beta}\right) \tag{1}$$

where β is the strength of the cutoff. The most conservative estimate for the detection sensitivity is to take $\beta > 1$, consistent with magnetic pair production above the polar cap, whereas a value of $\beta < 1$ will yield a very optimistic detection rate.

The expected rate of triggers of pulsed Cherenkov showers is obtained from the convolution of the collection area $A(E)$ and the differential spectra given in the Eq. (2):

$$R_{\mathrm{p}} = \int A(E)\left(\frac{dN_{\gamma}}{dE}\right)dE \tag{2}$$

The expression of the collection area $A(E)$ has been fitted from our simulations:

$$A(E) = \frac{aE^{b}}{\left(e + \left(\frac{E}{c}\right)^{d}\right)} \tag{3}$$

where a, b, c, d and e are the fit parameters. In order to be conservative in our estimations, we assume a typical polar cap scenario, with $\beta = 2$. According to the EGRET limit, we chose a cutoff energy $E_{\mathrm{o}} = 30$ GeV for the selected unidentified gamma-ray sources. We have fixed the normalising energy E_{n} at 1 GeV so that K is the monochromatic flux at 1 GeV, and Γ is the spectral index of the source above 100 MeV given in the Third EGRET Catalogue (Hartman et al., 1999).

The required observation time is given by $T = x^2(R_{\mathrm{p}} + R_{\mathrm{b}})/R_{\mathrm{p}}^2$, where R_{p} is the rate of pulsed γ-ray photons coming from the source calculated in the Eq. (2), R_{b} is the rate of background, including protons, Helium and muons and x is the significance of the detection. In our studies, we estimate $R_{\mathrm{b}} = 250$ Hz and $x = 5\sigma$.

4. The Selected Unidentified EGRET Sources

The chosen unidentified EGRET sources are compatible with the pulsar hypothesis. All of them should comply with the following criteria: 1) to be observable from La Palma, with lat $= 28.8^{\circ}$, 2) to have an spectral index within the range $\Gamma \approx 1.4$–2.3, typical for pulsar spectra, 3) to have a variability parameter δ compatible with gamma-ray pulsars, we have used the variability model proposed by (Nolan et al., 2003) 4) to have a high value of $\dot{E}/d^2$ of the associated radio pulsars, where $\dot{E}$ is the spin down luminosity and d the distance, 5) to have an unidentified EGRET source associated to a known pulsar, 6) to be listed in the Lamb and Macomb GeV catalogue, 7) to consider the possibility to detect unpulsed high energy emission from the pulsar wind nebulae associated to some unidentified EGRET sources.

As shown in Table I, where l is the galactic longitude in degrees, b is the galactic latitude in degrees, F is the extrapolated flux above 30 GeV (Petry, 2001) given in 10^{-10} cm^{-2} s^{-1}, δ is the variability parameter (Nolan et al., 2003) and Γ is the spectral index above 100 MeV. All the sources selected are low-latitude ones, except the mid-latitude sources 3EG J0010+7309 and 3EG J1835+5918, and four out of the six gamma-ray bright EGRET pulsars have wind nebula, further supportive evidence exists for most of the objects selected here.

TABLE I
The selected unidentified EGRET sources and its different parameters

3EG	GeV	l	b	F	δ	Γ	Pulsar associations
J0010+7309	J0008+7304	119.92	10.54	7.87	0.26	1.85	No
J1835+5918	J1835+5921	88.74	25.07	45.0	0.15	1.69	No
J1837−0606	J1837−0610	25.86	0.40	15.0	0.00	1.82	Yes
J1856+0114	J1856+0115	34.60	−0.54	12.6	0.71	1.93	Yes
J2020+4017	J2020+4023	78.05	2.08	12.6	0.06	2.08	No
J2021+3716	J2020+3658	75.58	0.33	21.8	0.36	1.86	Yes
J2227+6122	J2227+6101	106.53	3.18	1.06	0.20	2.24	Yes

TABLE II
Pulsar associations and the gamma-ray efficiency

3EG	PSR	$L_\gamma/\dot{E}$ (≥100 MeV)	$\log\dot{E}/D^2$ (erg s^{-1} kpc^{-2})
J1837−0606	J1837−0604	0.08	0.88
J1856+0114	J1856+0113	0.08	3.7
J2021+3716	J2021+3651	0.18	0.24
J2227+6122	J2229+6114	0.04	2.37

Table I contains the four EGRET sources selected which are positionally coincident with some radio pulsars, 3EG J1837-0606, 3EG J1856+0114, 3EG J2021+3716 and 3EG J2227+6122 have pulsar associations within their EGRET error boxes, the associated pulsars are shown in the Table II, but with pulsations not been found in the gamma-ray data. 3EG J1856+0114, 3EG J2021+3716 and 3EG J2227+6122 have pulsar wind nebulae (PWN's), which might be significant gamma-ray sources by themselves, while 3EG J1837−0606 does not have a nebula associated. γ-radiation above 200 GeV could be detected from the pulsar wind nebulae, although the unpulsed component of the pulsar itself cannot be excluded considering that the γ-ray nebula is the result of inverse Compton scattering of the electrons injected by the pulsar into the surrounding interstellar medium (ISM) of low magnetic field (Aharonian, 1997). The TeV fluxes can be estimated assuming that the γ-rays are produced in the X-ray nebula. Taking into account that the energy fluxes of many X-ray nebulae are between 10^{-12} and 10^{-11} erg cm^{-2} s^{-1} while the flux sensitivity of the MAGIC telescope is 10^{-10} cm^{-2} s^{-1} at 30 GeV, that opens an interesting line in the discovery of the X-ray nebulae around many radio pulsars since if the origin of these X-ray nebulae is via synchrotron emission, it would imply the existence of the accompanying γ-ray nebulae due to IC scattering of the relativistic electrons.

The three EGRET sources selected with no coincident known radio pulsar, 3EG J0010+7309, 3EG J2020+4017 and 3EG J1835+5918, might be related to radio-quiet pulsars. (Brazier et al., 1998) and (Slane et al., 2004) have studied the X-ray remnant CTA-1, coincident with 3EG J0010+7309, a nebula with a pulsar-like point source. 3EG J2020+4017, the brightest of the non variable unidentified EGRET sources, also has a X-ray nebula, the γ-Cygni supernova remnant.

3EG J0010+7309 and 3EG J2020+4017 show a hard Geminga-like spectra (Mirabal et al., 2001) and (Halpern et al., 2002), large gamma to X-ray flux ratios and no pulsed emission is known up to now. One principal hypothesis about these two sources is that they might be radio-quite Geminga class objects. Their variability is quite consistent with the identified pulsars. On the one hand, the low expected cut off energy, around 3–5 GeV, is the only objection to be detected by MAGIC telescope, on the other hand, the position of 3EG J2020+4017 is coincident with the γ-Cyg SNR, so that, it is a good gamma-ray pulsar candidate.

3EG J1835+5918 is an intriguing γ-ray pulsar candidate. The γ-rays properties of this source are very similar to those of Geminga and other EGRET pulsars, its soft X-ray flux is at least 50 times fainter that of Geminga and similar EGRET pulsars (Mirabal et al., 2000). Some gamma-ray studies show that if 3EG J1835+5918 is a pulsar, it must be either older or more distant than Geminga and may be a highly beamed gamma-ray transmitter.

However, it is important to know that four of the EGRET pulsars are known to have wind nebulae. We cannot forget that all these unidentified EGRET sources have been detected at GeV range (Lamb and Macomb, 1997), this fact is quite important to be considered in the detection capability of the telescope.

5. The Required Observation Time

We have calculated the estimated minimum required observation time from the effective area simulating gamma-ray showers at the culmination zenith angles for each unidentified source. The culmination angle is calculated from the following equation:

$$\theta_{\min} = |\mathrm{dec} - \mathrm{lat}| \tag{4}$$

where dec is the declination of the source and lat is the geographic latitude of the telescope (lat $= 28.8^{\circ}$). In Table III we show the used values to calculate the observation time for two threshold energy values (10 and 30 GeV).

In the Table III we have calculated the required observation time taking into account a threshold energy of about 30 and 10 GeV. During the first operation stage of the telescope, the expected threshold energy is estimated to be about of 30 GeV, in a second operation stage of the telescope, thanks to the new high quantum efficiency PMT's, the new threshold energy is expected to be not lower than 10 GeV.

TABLE III
Observation times for 10 and 30 GeV

3EG	K (10^{-8}cm^{-2}s^{-1}GeV^{-1})	$\theta_{\min}(^\circ)$	T(h) $E_{\rm thr} = 10$ GeV	T(h) $E_{\rm thr} = 30$ GeV
J0010+7309	5.2	44.3	33	135
J1835+5918	9	30.5	0.6	7
J1837−0606	5.5	35	3.1	50
J1856+0114	7.4	27.5	4.1	58
J2020+4017	11	11.5	3.7	90
J2021+3716	11.5	8.5	0.9	17.5
J2227+6122	4.8	32.5	65	1300

On the one hand, 3EG J1835+5918 and 3EG J2021+3716 are the sources that require the minimum observation time of all the listed sources, on the other hand, 3EG J0010+7309 and 3EG J2227+6122 require a large observation time to be detected, however, the pulsed emission of these sources could be detected during some nights considering a low energy threshold of the telescope. 3EG J1837−0606, 3EG J1856+0114 and 3EG J2020+4017 could be detected with an observation time of about 50, 58 and 90 h, respectively at 30 GeV. These observation times can be much lower taking into account 10 GeV threshold energy.

6. Conclusions

3EG J1835+5918 seems to be the most promising candidate out of the seven unidentified sources since we will need only 30 min or 7 h to detect it considering 10 and 30 GeV threshold energy respectively. The following better candidate for the MAGIC response is 3EG J2021+3716, the 10th bright source in the GeV domain with pulsar wind nebulae, with a detection time of 1 h or 17.5 h for 10 or 30 GeV, respectively. This source has a low zenith angle, therefore, it could be easily detected during one night, while 3EG J1835+5918 has the culmination angle at 30.5° what increases the required observation time for a detection (Fonseca et al., 2003).

References

Aharonian, F.A., Atoyan, A.M. and Kifune, T.: 1997, *MNRAS* **291**, 162.
Brazier, K.T.S. et al.: 1998, *MNRAS* **295**, 819.
Fonseca, V. et al.: 2003, Predicted sensitivity of the MAGIC telescope for gamma-ray pulsars, ICRC, 28th International Cosmic Ray Conference, Tsukuba, Japan.
Gehrels, N.: 2000, *Nature* **404**, 363.
Grenier, I.A.: in press, Cosmic Gamma-Ray Sources, Kluwer Academic Publishers, Dordrecht.
Halpern, J.P. et al.: 2002, *ApJS* **573**, L41.

Hartman, R.C. et al.: 1999, *ApJS* **123**, 79.
Lamb, R.C. and Macomb, D.J.: 1997, *ApJ* **488**, 872.
Mirabal, N. et al.: 2000, *ApJ* **541**, 180.
Mirabal, N. et al.: 2001, *ApJ* **547**, L137.
Nell, H.I. and de Jager, O.C.: 1991, *A&SS* **230**, 299.
Nolan, P.L. et al.: in press, *ApJ*.
Petry, D.: 2001, Astro-ph, 0101496.
Romero, G.E.: 2001, Kluwer Academic Publishers, Dordrecht, p. 65.
Slane, P. et al.: 2004, *ApJ* **601**, 1045.

ON THE NATURE OF THE UNIDENTIFIED X-RAY/γ-RAY SOURCES IGR J18027–1455 AND IGR J21247+5058

J.A. COMBI[1,2], M. RIBÓ[3] and I.F. MIRABEL[3,4]

[1]*Departamento de Física (EPS), Universidad de Jaén, Campus Las Lagunillas, Jaén, Spain; E-mail: jcombi@ujaen.es*

[2]*Instituto Argentino de Radioastronomía (IAR), Villa Elisa, Argentina*

[3]*Service d'Astrophysique, CEA Saclay, Gif-sur-Yvette, France*

[4]*Instituto de Astronomía y Física del Espacio (IAFE), Buenos Aires, Argentina*

(Received 4 June 2004; accepted 30 July 2004)

Abstract. We present a multiwavelength study of the environment of the unidentified X-ray/γ-ray sources IGR J18027–1455 and IGR J21247 + 5058, recently discovered by the IBIS/ISGRI instrument, onboard the INTEGRAL satellite. The main properties of the sources found inside their position error circles, give us clues about the nature of these high-energy sources.

Keywords: X-ray:galaxies, radio continuum: galaxies, infrared: galaxies

1. Introduction

Since it began to operate in November 2002 until the time of writing (about 18 months), the IBIS/ISGRI instrument onboard the INTEGRAL satellite (Winkler et al., 2003) has discovered up to 40 unidentified X-ray/γ-ray sources in the energy range from 20–100 keV (a regularly updated list is kept in http://isdc.unige.ch/~rodrigue/html/igrsources.html). These sources can be high- or low-mass X-ray binaries (not detected previously due to the absence of hard X-ray surveys), isolated pulsars, clusters of galaxies or AGNs, among other objects. New observations along the electromagnetic spectrum are necessary to discern their nature.

In this work, we present a multiwavelength study of the fields containing the unidentified INTEGRAL sources IGR J18027−1455 and IGR J21247+5058 (Walter et al., 2004), as earlier done in Combi et al. (2004) and in Ribó et al. (2004) but using here the new positions and information reported by Bird et al. (2004). Based on the properties of the sources found at other frequencies inside the error circles in position of the IGR sources, we suggest possible origins for both high-energy sources.

2. The IGR J18027–1455 Field

The source IGR J18027−1455 was detected with a significance of 8.9σ in the energy range from 20–100 keV during 769 ksec of observations conducted

Astrophysics and Space Science **297:** 385–391, 2005.
© Springer 2005

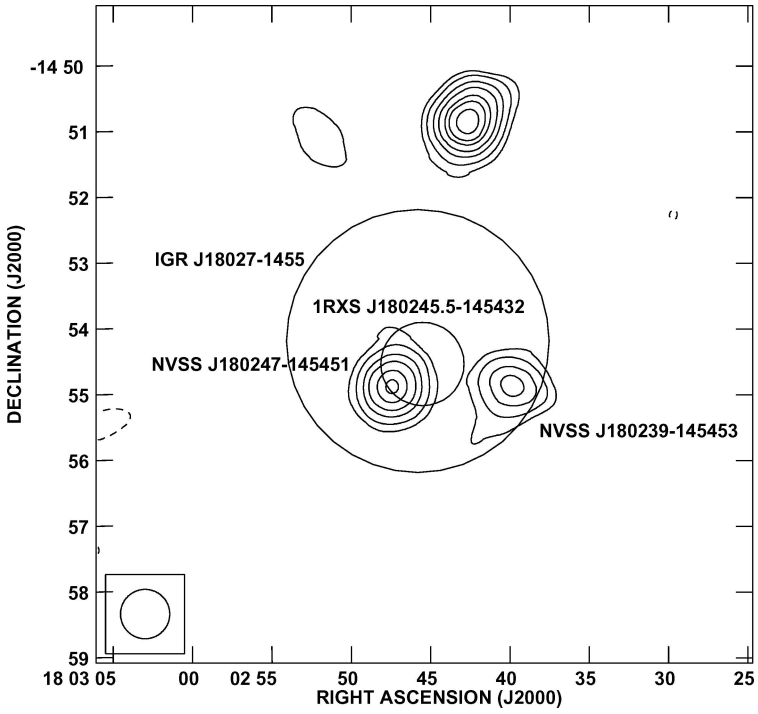


Figure 1. Image of the NVSS data obtained with the VLA at 1.4 GHz on 13 October 1997 around IGR J18027−1455. The image size is $10' \times 10'$. Contours represent −3, 3, 5, 8, 11, 15, 18, and 22 times the rms noise level of 0.5 mJy per beam. The circle in the bottom left corner represents the 45 arcsec of full width at half maximum (FWHM) of the convolving beam. Two NVSS sources fall inside the 90% error circle in position of IGR J18027−1455, and one of them is within the 2σ uncertainty error circle of a ROSAT source.

within the INTEGRAL/IBIS survey of the Galactic plane (Bird et al., 2004). The obtained fluxes compared to the Crab are $F_{(20\text{–}40\ \mathrm{keV})} = 2.6 \pm 0.2$ mCrab and $F_{(40\text{–}100\ \mathrm{keV})} = 3.0 \pm 0.4$ mCrab. Within its 2 arcmin-radius position error circle (at 90% confidence or 1.6σ uncertainty), centered at $(\alpha, \delta)_{\mathrm{J2000.0}} = (18^{\mathrm{h}}02^{\mathrm{m}}45\overset{\mathrm{s}}{.}8, -14^{\circ}54'11'')$, we have found two weak point-like radio sources in the 1.4 GHz NRAO VLA Sky Survey (NVSS, Condon et al., 1998) maps (see Figure 1). The first one, the source NVSS J180239–145453, has an estimated position of $(\alpha, \delta)_{\mathrm{J2000.0}} = (18^{\mathrm{h}}02^{\mathrm{m}}39\overset{\mathrm{s}}{.}94 \pm 0\overset{\mathrm{s}}{.}25, -14^{\circ}54'53\overset{''}{.}6 \pm 3\overset{''}{.}3)$ (1σ uncertainties), has a flux density of 6.9 ± 0.6 mJy and has no near-infrared (NIR) counterpart in the 2MASS catalog (Cutri et al., 2003).

The second one, NVSS J180247–145451, has an estimated position of $(\alpha, \delta)_{\mathrm{J2000.0}} = (18^{\mathrm{h}}02^{\mathrm{m}}47\overset{\mathrm{s}}{.}37 \pm 0\overset{\mathrm{s}}{.}13, -14^{\circ}54'51\overset{''}{.}6 \pm 2\overset{''}{.}2)$, a flux density of 10.5 ± 0.6 mJy, and lies inside and near the edge of the 2σ position error circle of the faint ROSAT X-ray source 1RXS J180245.5–145432 (Voges et al., 2000), which is well within the IBIS/ISGRI error circle. Inside the 2σ position error ellipse of this

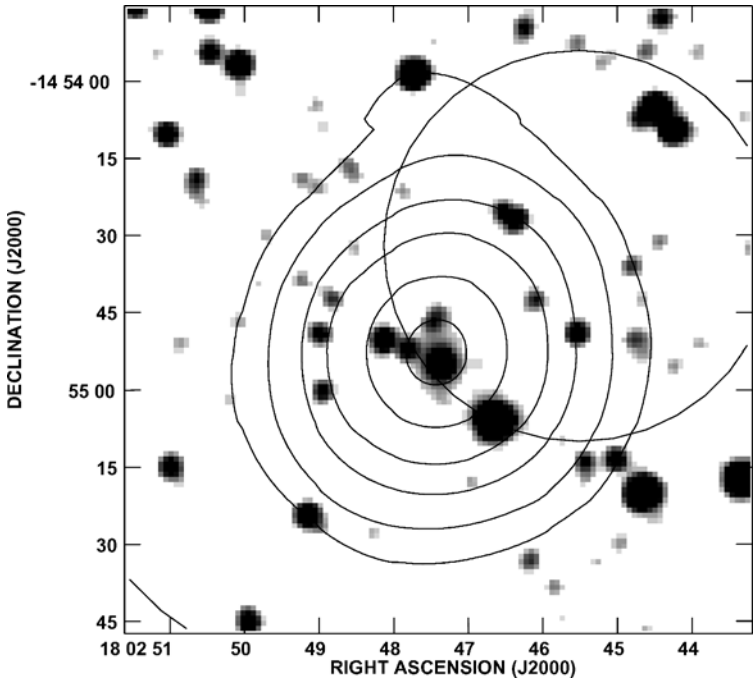


Figure 2. Enlargement of a $2' \times 2'$ region of Figure 1 around NVSS J180247−145451, where we plot in greyscale the 2MASS K_s-band image. The extended NIR source 2MASXi J1802473−145454 is clearly visible in a position compatible with the peak of the radio source.

radio source, it is located an extended NIR source, 2MASXi J1802473−145454 (see Figure 2), which has coordinates $(\alpha, \delta)_{\rm J2000.0} = (18^{\rm h}02^{\rm m}47\overset{\rm s}{.}370 \pm 0\overset{\rm s}{.}002, -14^\circ 54' 54\overset{''}{.}76 \pm 0\overset{''}{.}03)$ and magnitudes $J = 13.18 \pm 0.07$, $H = 12.02 \pm 0.09$, $K_{\rm s} = 10.94 \pm 0.04$. The optical counterpart of this NIR source has average magnitudes $B = 19.3 \pm 1.0$, $R = 14.9 \pm 0.8$ and $I = 13.8 \pm 0.5$ in the USNO-B1.0 catalog (Monet et al., 2003). The photometry of the NIR/optical counterpart is not consistent with a stellar spectrum. Optical and X-ray observations are planned to confirm the extragalactic nature of the source and to study its spectrum at softer X-rays.

3. The IGR J21247+5058 Field

This source was detected with a significance of 6.5σ in the energy range from 20–100 keV during only 70 ksec of observations conducted within the same INTEGRAL/IBIS survey of the Galactic plane (Bird et al., 2004). The obtained fluxes compared to the Crab are $F_{(20\text{–}40\ \rm keV)} = 5.4 \pm 0.7$ mCrab and $F_{(40\text{–}100\ \rm keV)} = 9.3 \pm 1.4$ mCrab. Inside its 2 arcmin-radius position error circle (at 90% confidence or 1.6σ uncertainty), centered at $(\alpha, \delta)_{\rm J2000.0} = (21^{\rm h}24^{\rm m}42\overset{\rm s}{.}0, +50^\circ 58' 48'')$ is located

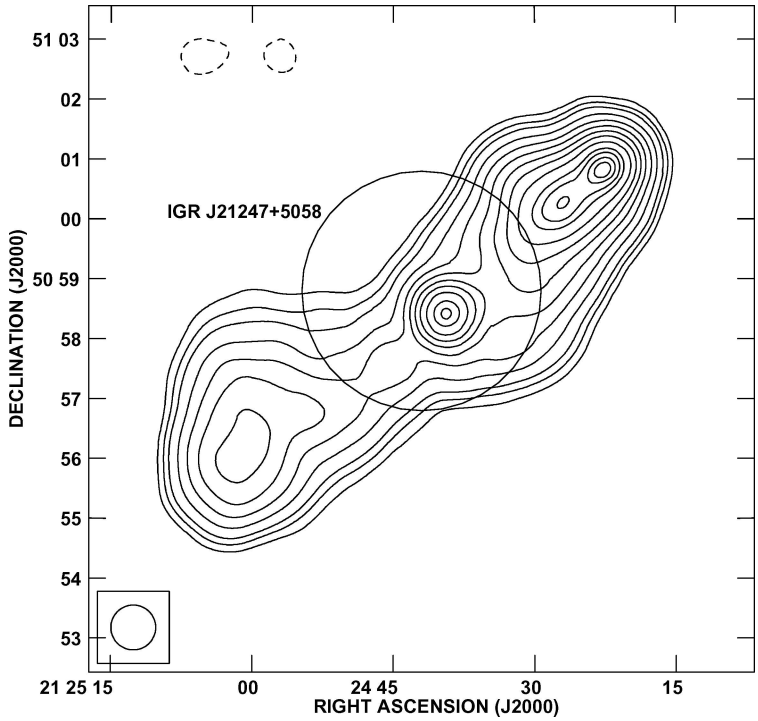


Figure 3. Image of the NVSS data obtained with the VLA at 1.4 GHz on 3 April 1995 around IGR J21247+5058. The image size is $10' \times 10'$. The core of the radio source 4C 50.55 is well within the 90% uncertainty error circle of the IGR source. Contours are -3, 3, 6, 10, 20, 35, 55, 80, 110, 150, 200, 230, 260 and 280 times the rms noise level of 1 mJy per beam. The circle in the bottom left corner represents the $45''$ FWHM of the convolving beam.

the core of the bright radio source 4C 50.55 (see Figure 3), also known as GPSR 93.3194+0.394, KR2, NRAO 659 or BG 2122+50, among other names.

The core has a flat radio spectrum with a peak flux density of 237 mJy per beam at 1.4 GHz. It is at the center of an elongated structure of 10×3 arcmin (see Figure 3) that ends in two large radio lobes having peak flux densities of 288 mJy per beam (NW) and 92 mJy per beam (SE), and spectral indices $\alpha \sim -0.6$ (where $S_\nu \propto \nu^{+\alpha}$), compatible with optically thin synchrotron radiation (Mantovani et al., 1982). The morphology of 4C 50.55 is typical of a radio galaxy, and the comparison among published radio data shows no significant changes in flux and morphology during the last 30 years (see, e.g. Fanti et al., 1981). These properties are consistent with an extragalactic source, although, to our knowledge, no conclusive optical counterpart of a galaxy host has ever been reported, probably due to its location close to the Galactic plane ($l = +93.32^\circ$, $b = +0.39^\circ$).

The estimated position of the radio core from the NVSS map and data in the literature is $(\alpha, \delta)_{\mathrm{J2000.0}} = (21^{\mathrm{h}}24^{\mathrm{m}}39\overset{\mathrm{s}}{.}35 \pm 0\overset{\mathrm{s}}{.}03, +50^\circ 58' 25\overset{''}{.}8 \pm 0\overset{''}{.}2)$

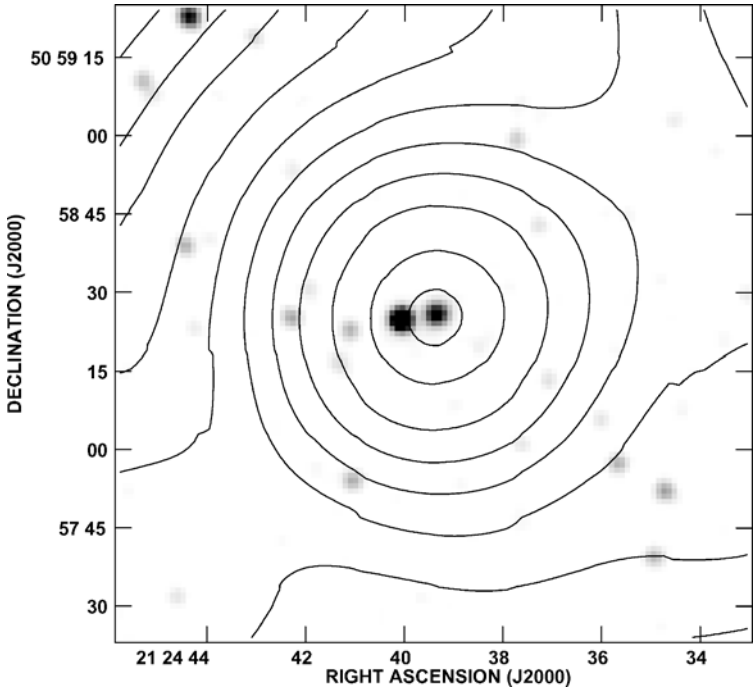


Figure 4. Enlargement of a $2' \times 2'$ region of Figure 3 around the core of 4C 50.55, where we plot in greyscale the 2MASS K_s-band image showing the proposed NIR counterpart, coincident with the radio peak.

(68% or 1σ uncertainty). Coincident with this position there is the NIR source 2MASS J21243932+5058259 (see Figure 4), with coordinates $(\alpha, \delta)_{J2000.0} = (21^h24^m39^s.328 \pm 0^s.003, +50°58'25''.93 \pm 0''.03)$ (68% or 1σ), and magnitudes $J = 13.27 \pm 0.04$, $H = 12.38 \pm 0.06$, $K_s = 11.37 \pm 0.04$. The optical counterpart of this NIR source has average magnitudes $B = 16.9 \pm 0.2$ and $R = 15.1 \pm 0.2$ in the USNO-B1.0 catalog (Monet et al., 2003). The photometry of the NIR/optical counterpart is not consistent with a stellar spectrum. There is no catalogued ROSAT or EGRET source coincident with IGR J21247+5058. Optical and X-ray observations are planned to confirm the extragalactic nature of the source and to study its spectrum at softer X-rays.

4. Further Comments

We have presented a multiwavelength study of the emission towards the direction of two recently discovered INTEGRAL sources, namely IGR J18027−1455 and IGR J21247+5058. Inside the position error box of the first one, we have found the radio source NVSS J180247−145451, compatible with the soft X-ray source 1RXS

J180245.5−145432, and having the extended source 2MASXi J1802473−145454 as NIR counterpart. We suggest that all these sources are likely associated with the counterpart of the hard X-ray source. The photometry of the NIR/optical source does not agree with a stellar spectrum, hence this object seems to be of extragalactic nature. This is supported by the extended appearance of the NIR counterpart. In the second case, we have found that the core of an extended radio source, which ends in two large radio lobes, lies well within the position error circle of the INTEGRAL source. The morphology of this extended source is typical of a radio galaxy. Coincident with the position of the radio core is a 2MASS source, with an optical counterpart not compatible with a stellar spectrum.

If the X-ray emission of IGR J21247+5058 comes indeed from a radio galaxy, then it should originate in the core and/or in the first section of the jet, where synchrotron or inverse Compton emission processes dominate (Harris and Krawczynski, 2002). This source could be a similar case to 3C 273 (Marshall et al., 2001), where the detected X-rays fade along the jet. Evidence supporting this possibility was also presented by Harris et al. (2002) for the radio galaxy M84. In this object, these authors found an excess of X-ray emission, or knots, aligned with one of the radio jets. These knots lie at $\sim$300 pc from the core and they are coincident with enhanced radio emission (see their Figure 1), suggesting that the X-rays are produced by a synchrotron mechanism.

Recently, Bassani et al. (2004), have presented a study of extragalactic sources detected by INTEGRAL during its first year of operation. Among them, 10 are active galaxies and one is a cluster of galaxies. If the extragalactic nature of the sources studied here is confirmed, then many of the unidentified INTEGRAL sources detected untill now could increase considerably the number of extragalactic objects shining in the hard X-ray domain.

Finally, it is interesting to note that there is no catalogued EGRET source coincident with these sources. Multiwavelength observations are currently in progress to unveil the nature of these high-energy sources.

Acknowledgements

We acknowledge Josep Martí for useful discussions. J.A.C. is a researcher of the programme *Ramón y Cajal* funded by the Spanish Ministry of Science and Technology and the University of Jaén, and was also supported by CONICET (under grant PEI 6384/03). M.R. acknowledges support by a Marie Curie Fellowship of the European Community programme Improving Human Potential under contract number HPMF-CT-2002-02053, and partial support by DGI of the Ministerio de Ciencia y Tecnología (Spain) under grant AYA2001-3092, as well as partial support by the European Regional Development Fund (ERDF/FEDER). This research has made use of the NASA's Astrophysics Data System Abstract Service, of the SIMBAD database, operated at CDS, Strasbourg, France, and of the NASA/IPAC

Extragalactic Database (NED) which is operated by the Jet Propulsion Laboratory, California Institute of Technology, under contract with the National Aeronautics and Space Administration. The Digitized Sky Survey was produced at the Space Telescope Science Institute under U.S. Government grant NAG W-2166. This publication makes use of data products from the Two Micron All Sky Survey, which is a joint project of the University of Massachusetts and the Infrared Processing and Analysis Center/California Institute of Technology, funded by the National Aeronautics and Space Administration and the National Science Foundation.

References

Bassani, L., Malizia, A., Stephen, J. B. et al.: 2004, in: Proceedings of The 5th INTEGRAL Workshop: The Integral Universe, ESA SP-552, 139 [arXiv:astro-ph/0404442].

Bird, A.J., Barlow, E.J., Bassani, L. et al.: 2004, *ApJ* **607**, L33.

Combi, J.A., Ribó, M. and Mirabel, I.F. 2004, *ATel* 246.

Condon, J.J., Cotton, W.D., Greisen, E.W. et al.: 1998, *AJ* **115**, 1693.

Cutri, R.M., Skrutskie, M.F., van Dyk, S. et al.: 2003, VizieR Online Data Catalog, II/246 (http://cdsweb.u-strasbg.fr/viz-bin/Cat?II/246).

Fanti, C., Mantovani, F. and Tomasi, P.: 1981, *A&AS* **43**, 1.

Harris, D.E. and Krawczynski, H.: 2002, *ApJ* **565**, 244.

Harris, D.E., Finoguenov, A., Bridle, A.H., Hardcastle, M.J. and Laing, R.: 2002, *ApJ* **580**, 110.

Mantovani, F., Nanni, M., Salter, C.J. and Tomasi, P.: 1982, *A&A* **105**, 176.

Marshall, H.L., Harris, D.E., Grimes, J.P. et al.: 2001, *ApJ* **549**, L167.

Monet, D.G., Levine, S.E., Canzian, B. et al.: 2003, *AJ* **125**, 984 (http://cdsweb.u-strasbg.fr/viz-bin/Cat?I/284).

Ribó, M., Combi, J.A. and Mirabel, I.F.: 2004, *ATel* 235.

Voges, W., Aschenbach, B., Boller, Th. et al.: 2000, VizieR Online Data Catalog, IX/29 (http://cdsweb.u-strasbg.fr/viz-bin/Cat?IX/29).

Walter, R., Bodaghee, A., Barlow, E. et al.: 2004, *ATel* 229.

Winkler, C., Courvoisier, T.J.-L., Di Cocco, G. et al.: 2003, *A&A* **411**, L1.

STATUS OF THE CONNECTION BETWEEN UNIDENTIFIED EGRET SOURCES AND SUPERNOVA REMNANTS: THE CASE OF CTA 1

DIEGO F. TORRES[1], THOMAS M. DAME[2] and GUSTAVO E. ROMERO[3]

[1]*Lawrence Livermore Laboratory, 7000 East Avenue L-413, Livermore, CA 94550, USA; E-mail: dtorres@igpp.ucllnl.org*

[2]*Harvard-Smithsonian Center for Astrophysics, 60 Garden Street, Cambridge, MA 02138, USA*

[3]*Instituto Argentino de Radioastronomía, C.C.5, 1894 Villa Elisa, Buenos Aires, Argentina*

(Received 4 June 2004; accepted 28 July 2004)

Abstract. In this paper we briefly comment on the observational status of the possible physical association between unidentified EGRET sources and supernova remnants (SNRs) in our Galaxy. We draw upon recent results presented in the review by Torres et al. (2003), concerning molecular gas in the vicinity of all 19 SNRs found to be positionally coincident with EGRET sources at low Galactic latitudes. In addition, we present new results regarding the supernova remnant CTA 1. Our findings disfavor the possibility of a physical connection with the nearby (in projection) EGRET source. There remains possible, however, that the compact object produced in the supernova explosion be related with the observed γ-ray flux.

Keywords: supernova remnants, gamma rays: observations, interstellar medium

1. A Brief Overview of the EGRET – SNR Connection

We have recently presented a case-by-case analysis of the positional correlation between unidentified EGRET sources and supernova remnants (SNRs, Torres et al., 2003). There are 19 EGRET sources at low Galactic latitudes ($|b| < 10^{\circ}$) in spatial correlation with, mostly shell-type, SNRs. The Poisson probability for the 19 coincidences to be a chance effect is 1.05×10^{-5}, i.e., there is an *a priori* 0.99998 probability that at least one of the positional associations is physical. This expected chance association was computed using a numerical code described by Romero et al. (1999) and Sigl et al. (2001). With the aim to identify the most plausible candidates for an EGRET – SNR connection, we have analyzed, among other things, the variability status of the EGRET sources and the potential contribution from known radio pulsars to the high energy flux (Torres et al., 2003).

To understand the origin of all the unidentified detections, their variability status is of paramount importance (Nolan, 2003; Torres et al., 2001). Classic known models for γ-ray sources in our Galaxy, like a SNR – molecular cloud interaction (e.g. Aharonian and Atoyan, 1996), would produce non-variable detections during the timescale of EGRET observations. To classify the variability status we take into account both indices quoted in the literature, Torres et al.'s (2001) I and



Astrophysics and Space Science **297:** 393–398, 2005.
© Springer 2005

Tompkins' τ. They are different in nature, although results have proven to be statistically correlated (Torres et al., 2001). The index I is a relative classification of variability with respect to the pulsar population. Sources with $I > 2.5$ are more than 3σ away from the statistical variability of pulsars. Similarly, sources for which τ is at least 0.6, are also more than 3σ away from the mean value of the τ upper limit for pulsars, and are thus classified as variable. For comparison, note that the mean value of τ (I) for known AGNs is 0.9 (3.3). We find that most EGRET sources in positional coincidence with SNRs, and certainly those which represent the best cases for a physical association, are non-variable.

In order to unambiguously identify a pulsar as the origin of the γ-rays from an EGRET source, γ-ray pulsations must be detected at the pulsar period. However, the γ-fluxes are generally very low, and nearly contemporaneous radio/X-ray and γ-ray observations are required to fold the few available photons with the correct ephemeris. Because this is no longer possible owing to the demise of the Compton Gamma-Ray Observatory, new candidate associations must mostly be judged by comparison with the properties of the six known EGRET pulsars and those of the known best candidates. We have done so for every known radio pulsar found to be coincident with these 19 EGRET sources, and have isolated several interesting candidates for an EGRET source – pulsar connection. These are mostly found with young pulsars pertaining to the recently released Parkes Multibeam Survey (see, e.g. Torres et al., 2001; Torres and Nuza, 2003). This scenario, then, is a competing one to the EGRET – SNR connection and has to be taken into account in judging the plausibility of the latter.

The need of a case-by-case analysis is then clearly established. Several cases for a physical association, based on the analysis of γ-ray data, the molecular environment of the SNR, and the analysis of any coincident pulsar (if any), have been isolated and reviewed in Torres et al. (2003). Among the most notable cases for such a physical association are G347.3-0.5, W66, W28 and IC443. The first of these, providing probably the best evidence to date for a hadronic origin of the γ-ray source detected by EGRET, has received much attention recently (Butt et al., 2001, 2002; Enomoto, 2002; Uchiyama et al., 2002). In addition, the case-by-case analysis shows that it is at least plausible, in contrast to expectations, that EGRET has detected distant (more than 6 kpc) SNRs. There are five coinciding pairs of 3EG sources and SNRs for which the latter apparently lie at such high values of distance (disregarding those related with SNRs spatially close to the galactic center). For all these cases, we have uncovered the existence of nearby, large, in some cases giant, molecular clouds that could enhance the GeV signal through pion decay. It is possible that the physical relationship between the 3EG source and the coincident SNR could provide for these pairs a substantial part of the GeV emission observed. This does not preclude, however, composite origins for the total amount of the radiation detected, since some of these cases present other plausible scenarios (e.g. energetic pulsars in the EGRET field). AGILE observations, in advance of GLAST, would greatly elucidate the origin for these 3EG sources, since even a factor of 2

of improvement in spatial resolution would be enough to reject the EGRET – SNR connection.

In what follows we attempt to briefly analyze, similarly to what was done in the case-by-case analysis of Torres et al. (2003), the pair CTA 1/3EG J0010+7309, a supernova remnant lying at relatively high Galactic latitudes, and for which there has been little analysis on their CO environment.

2. CTA 1: General Features

CTA 1 is a shell-type SNR, but its shell is incomplete and broken-out towards the NW. This breakout phenomenon may be caused by more rapid expansion of the blast wave shock into a lower density region toward the NW. HI observations supported this interpretation (Pineault et al., 1993, 1997). The latter papers place the SNR at 1.4 ± 0.3 kpc, the kinematic distance corresponding to the systemic velocity of a partial HI shell (-16 km/s) that the authors find to the NW. However, it is to be noticed that the systemic (unperturbed) velocity of a partially expanding shell might be subject to a great uncertainty.

Since CTA 1 is located at a relatively high latitude ($b = 10^\circ$) and it is nearby, it has a large angular size (90 arcmin), little foreground or background confusion, and it can be observed at exceptionally high linear resolution. The age of the SNR was estimated to be 10^4 yr by Pineault et al. (1993), but it could be younger by a factor of 2 (Slane et al., 1997). CTA 1 was subject of intense observational campaigns in the past years. There have been both ROSAT and ASCA X-ray observations (Seward et al., 1995; Slane et al., 1997), as well as optical, infrared and radio studies (see Pineault et al., 1997 and Brazier et al., 1998 for a review).

CTA 1 belongs to the class of composite SNRs (SNRs with central pulsar wind nebulae), which show a shell-type morphology in the radio band and are center-filled in X-rays. Five point sources were detected with ROSAT, one of which was found to coincide with the EGRET source (at the time of the analysis, 2EG J0008+7307), see Figure 3 of Brazier et al. (1998). ASCA data suggested that this source, named RX J0007.0+7302, has a non-thermal spectrum, and gave support to the idea that it is the pulsar left from the supernova explosion (Slane et al., 1997). Recent observations by Slane et al. (2004), using XMM, confirm that the X-ray spectrum of the source is consistent with that of a neutron star and is well described by a power law with the addition of a soft thermal component that may correspond to emission from hot polar cap regions or to cooling emission from a light-element atmosphere over the entire star. An extrapolation of the non-thermal spectrum of RX J0007.0+7302 to γ-ray energies would yield a flux consistent with that of EGRET source 3EG J0010+7309, supporting the proposition that these sources could be related. A Chandra image of the central X-ray source RX J0007.0+7303 (Halpern et al., 2004) reveals a point source, a compact nebula, and a bent jet, all of which are characteristic of energetic, rotation-powered pulsars.

Optical observations were carried out by Brazier et al. (1998), with a 2.12-m telescope, but no object was found within the positional error box of the X-ray source. This allowed an upper limit to be set on the optical magnitude of any counterpart to the putative pulsar. Halpern et al. (2004) also obtained upper limits in the optical at the position of the point source, corresponding to an X-ray-to-optical flux ratio larger than 100. Neither a VLA image at 1425 MHz nor a deep pulsar search at 820 MHz using the NRAO Green Bank Telescope, revealed a radio pulsar counterpart

The γ-ray source 3EG J0010+7309 is non-variable under the I and τ schemes, and has a hard spectral index of 1.85 ± 0.10, compatible with those of the Vela pulsar. This source was also detected in the Second EGRET Catalog, but with a shifted position which made it coincide with a nearby AGN – which was at the time proposed as a possible counterpart (Nolan et al., 1996). This AGN is not coincident with the 3EG source and can not be considered a plausible counterpart any longer. Based on positional coincidence, on the hard spectral index, and on physical similarities between the Vela pulsar and RX J0007.0+7302, Brazier et al. (1998) proposed that the 3EG source and this X-ray source were related. For an assumed 1 sr beaming, the observed 100–2000 MeV flux corresponds to a luminosity of 4×10^{33} erg s^{-1}, compatible with other γ-ray pulsar detections. A competing explanation to the γ-ray pulsar would be given if a massive and dense molecular cloud is found to be interacting with, or being overtaken by, the supernova remnant shock. The molecular environment of CTA 1 is analyzed below to further assess this possibility.

As can be noted from the figure, the EGRET source seems too far from the SNR nearest rim. However, if some SNRs interact, as expected, with nearby massive clouds producing enhanced γ-ray emission through hadronic/Bremsstrahlung interactions, cases in which there is just a marginal coincidence between the SNRs and the centers of the EGRET sources should be also considered, since the peak γ-ray emissivity will likely be biased towards the adjacent cloud.

3. CTA 1: Molecular Environment

As discussed in Dame et al. (1987), much of the local (closer than Perseus Arm) CO emission in the second quadrant of the Galaxy bifurcates into 2 velocity components, one centered near -12 km/s and the other close to 0 km/s. Dame et al. (1987) argue that the "-12 km/s clouds" are probably associated with a string of OB associations at 800 to 1000 pc from Earth. The clouds with velocities near 0 km/s were associated with the so-called "Lindblad Ring" at 300 pc. The long thin cloud partially overlapping CTA 1 (see Figure 1) has a mean velocity of ~ -3 km/s, suggesting that it is part of the Lindblad Ring population. In fact, these clouds appear to be part of a very large loop of local clouds (all in the range -5 to 0 km/s).

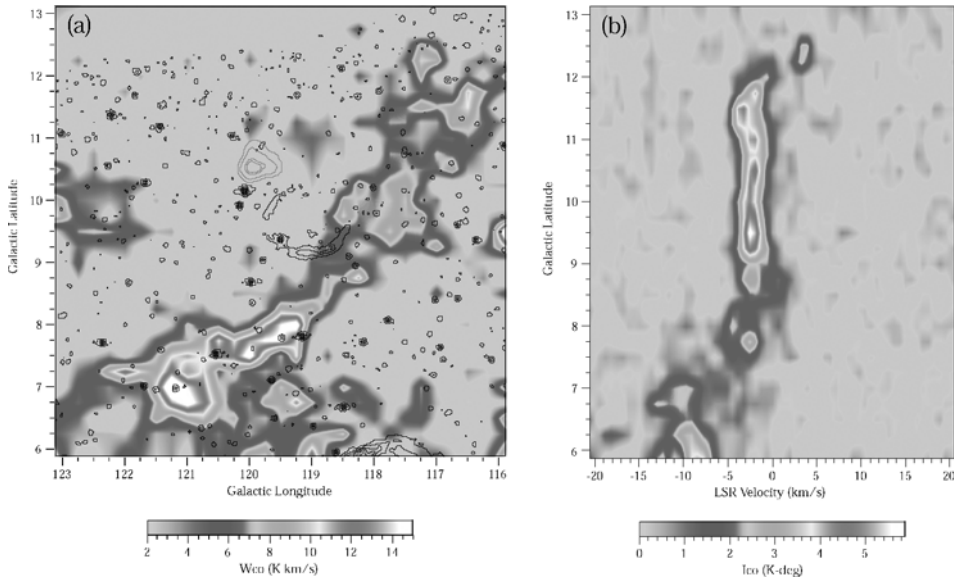


Figure 1. Molecular gas in the direction of the SNR CTA 1. (a) The false-color map is CO integrated over the velocity range −15 to +5 km/s. The black contours are 4.85 GHz intensity from the survey of Condon et al. (1994), which show CTA 1 as a semi-circular feature near the center of the map. The red (lighter) contours are the 50, 68, 95, and 99% confidence contours for the unidentified gamma ray source 3EG J0010+7309. (b) A CO latitude-velocity map integrated from 116° to 120° in Galactic longitude.

Grenier et al. (1989) proposed that this loop surrounds a 4×10^4 yr old Type I SNR 300 pc away. Thus, the velocity of the cloud near to CTA 1 suggests that it is part of this larger system, lying at only ∼300 pc.

The total H_2 mass (calculated from CO data) of the long thin cloud near CTA1 (in the region $l = 116°$ to $120°$, $b = 8°$ to $13°$, $v = -15$ to 5 km/s) is 4900 $M_\odot$, assuming a distance of 300 pc. However, there is no evidence of interaction between the remnant and the cloud (what is consistent with the different most plausible distances to each of these objects). Figure 1b attached, for example, shows a latitude – velocity map integrated over the longitude extent of the cloud. There is little indication of accelerated gas at the latitude/velocity of the remnant, $b = 9°$ to $10°$ and ~ -15 km/s, respectively. The cloud may well be, then, in the foreground, and unrelated to CTA 1. In addition to this, there is no CO emission detected within the contours of the 3EG source, which also argues against a hadronic origin of the γ-ray source.

Pineault et al.'s (1993) systemic velocity of −16 km/s for the HI shell is reasonable close to that of the "−12 km/s clouds," which in turn are probably associated with the OB associations Cep OB2, Cep OB3, Cep OB4, and Per OB3 at ∼800 pc. This might be suggesting that the latter is the most likely distance for

CTA 1, although it remains uncertain. In any case, it seems that CTA 1 and 3EG J0010+7309 might be physically related only through the compact object left by the supernova explosion (probably RX J0007.0+7302). A better localization of the γ-ray source with AGILE and GLAST will certainly test this suggestion. For the moment, our CO analysis shows that a molecular cloud origin of the γ-ray source 3EG J0010+7309 (for instance, through hadronic processes similar to the case of G347.3-0.5 proposed by Butt et al., 2001) is untenable.

Acknowledgments

The work of DFT was performed under the auspices of the U.S. Department of Energy (NNSA) by University of California Lawrence Livermore National Laboratory under contract No. W-7405-Eng-48. G.E.R. was supported by CONICET (under grant PIP N°0430/98), ANPCT (PICT 03-04881), as well as by Fundación Antorchas. We thank P. Slane for comments.

References

Brazier, K.T.S., Reimer, O., Kanbach, G. and Carramiñana, A.: 1998, *MNRAS* **295**, 819.
Butt, Y., et al.: 2001, *ApJ* **562**, L167.
Butt, Y. et al.: 2002, *Nature* **418**, 499.
Condon, J.J. et al.: 1994, *AJ* **107**, 1829.
Dame, T.M. et al.: 1987, *ApJ* **322**, 706.
Enomoto, R. et al.: 2002, *Nature* **416**, 823.
Grenier, I. et al.: 1989, *ApJ* **347**, 231.
Halpern, J.P., Gotthelf, E.V., Camilo, F., Helfand, D.J. and Ransom, S.M.: 2004, astro-ph/0404312.
Nolan, P.L. et al.: 1996, *ApJ* **459**, 100.
Nolan, P.L., Tompkins, W.F., Grenier, I.A. and Michelson, P.F.: 2003, *ApJ* **597**, 615.
Pineault, S. et al.: 1993, *AJ* **105**, 1060.
Pineault, S. et al.: 1997, *A&A* **324**, 1152.
Romero, G.E., Benaglia, P. and Torres, D.F.: 1999, *A&A* **348**, 868.
Seward, F.D., Schmidt, B. and Slane, P.: 1995, *ApJ* **453**, 284.
Sigl, G. et al.: 2001, *Phys. Rev.* **D63**, 081302.
Slane, P., Zimmerman, E.R., Hughes, J.P., Seward, F.D., Gaensler, B.M. and Clarke, M.J.: 2004, *ApJ* **601**, 1045.
Slane, P. et al.: 1997, *ApJ* **485**, 221.
Torres, D.F., Butt, Y.M. and Camilo, F.: 2001, *ApJ* **560**, L155.
Torres, D.F. and Nuza, S.E.: 2003, *ApJ* **583**, L25.
Torres, D.F., Pessah M.E. and Romero, G.E.: 2001, *Astronomische Nach.* **322**, 223.
Torres, D.F. et al.: 2001, *A&A* **370**, 468.
Torres, D.F. et al.: 2003, *Phys. Rep.* **382**, 303.
Uchiyama, Y., Takahashi, T. and Aharonian, F.A.: 2002, *PASJ* **54**, L73.

SPECTRAL CONSTRAINTS FOR MILLISECOND PULSARS DUE TO GENERAL RELATIVISTIC FRAME DRAGGING

C. VENTER and O.C. DE JAGER

Unit for Space Physics, North-West University, Potchefstroom Campus, Potchefstroom, South Africa; E-mail: fskcv@puk.ac.za

(Received 5 July 2004; accepted 12 August 2004)

Abstract. We develop a numerical code for simulating the magnetospheres of millisecond pulsars, which are expected to have unscreened electric potentials due to the lack of magnetic pair production. We incorporate General Relativistic (GR) expressions for the electric field and charge density and include curvature radiation (CR) due to primary electrons accelerated above the stellar surface, whereas inverse Compton scattering (ICS) of thermal X-ray photons by these electrons are neglected as a second-order effect. We apply the model to PSR J0437-4715, a prime candidate for testing the GR-Electrodynamic theory, and find that the curvature radiation spectrum cuts off at energies below 15 GeV, which are well below the threshold of the H.E.S.S. telescope, whereas Classical Electrodynamics predict a much higher cutoff near 100 GeV, which should be visible for H.E.S.S., if standard assumed Classical Electrodynamics apply. GR theory also predicts a relatively narrow pulse ($2\phi_L \sim 0.2$ phase width) centered on the magnetic axis, which sets the beaming solid angle to $\sim$0.5 sr per polar cap (PC) for a magnetic inclination angle of 35° relative to the spin axis, given an observer which sweeps close to the magnetic axis. We also find that EGRET observations above 100 MeV of this pulsar constrain the polar magnetic field strength to $B_{\rm pc} < 4 \times 10^8$ G for a pulsar radius of 10 km and moment of inertia of 10^{45} g cm^2. The field strength constraint becomes even tighter for a larger radius and moment of inertia. Furthermore, a reanalysis of the full EGRET data set of this pulsar, assuming the predicted pulse shape and position, should lead to even tighter constraints on neutron star and GR parameters, up to the point where the GR-derived potential and polar cap current may be questioned.

Keywords: stars: neutron, pulsars: individual (PSR J0437-4715)

1. Introduction

It has been noted by several authors (e.g. Muslimov and Harding, 1997; Dyks et al., 2001) that General Relativistic (GR) frame dragging in rotating neutron stars is a first-order effect, which has to be included in a self-consistent model of pulsar magnetospheric structure and associated radiation, and transport processes. Many efforts were directed towards this end.

Usov (1983) was the first to suggest that the low magnetic field strengths of millisecond pulsars allow gamma-rays up to at least 100 GeV to escape magnetic pair production. Subsequent evaluation (Harding et al., 2002 [HMZ02]) have shown that most millisecond pulsars have unscreened electric fields due to the low optical depths of primary curvature gamma-rays for magnetic pair production in such



Astrophysics and Space Science **297:** 399–407, 2005.
© Springer 2005

low-B pulsar magnetospheres. Radiation reaction limited curvature gamma-rays up to about 100 GeV from millisecond pulsars were predicted (Bulik et al., 2000; HMZ02), making nearby millisecond pulsars such as PSR J0437-4715 (Johnston et al., 1993) attractive targets for ground-based gamma-ray groups (Bulik et al., 2000; Venter, 2004). The unscreened case offers a test for fundamental GR electrodynamical derivations of the polar cap current and potential, without having to invoke additional modifications such as pair formation fronts (Harding and Muslimov, 1998) with associated slot gaps (Muslimov and Harding, 2003) to explain most observations of canonical (high-B) pulsars.

The assumption that no screening takes place was indeed validated *a posteriori* and is also supported by the fact that PSR J0437-4715 has a relatively low spindown power, inhibiting magnetic pair production (HMZ02). This means that the value of the GR-derived parallel electric field may be used with confidence (see Section 2.1). Secondly, several important parameters, most notably the mass and distance (Van Straten et al., 2001), are known to a high degree of accuracy (see Figure 1 for a list of parameters used). Thirdly, PSR J0437-4715 is one of the closest pulsars to Earth, lying at a distance of 139 ± 3 pc (Van Straten et al., 2001). PSR J0437-4715 may therefore be expected to be much brighter and more easily observable than other millisecond pulsars. Lastly, observations show that the radio and X-ray beams virtually coincide, implying that the observer's line of site cuts the PC near the magnetic axis, providing certainty about geometric constraints. In fact, Manchester and Johnston

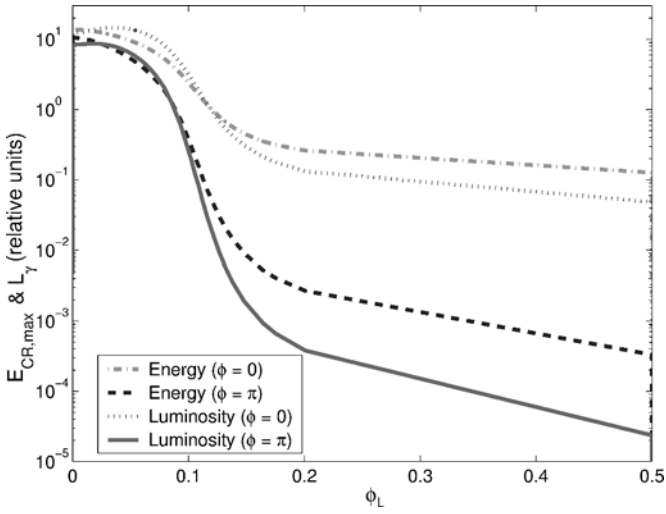


Figure 1. Maximum CR photon energy and photon luminosity (in relative units) vs. observer pulse phase for half a rotation period (with phase zero corresponding to the radio pulse maximum) for PSR J0437-4715, for magnetic azimuthal angle $\phi = 0$ and $\phi = \pi$ as indicated in the legend. The following parameters were assumed (Bulik et al., 2000; Van Straten et al., 2001; Zavlin et al., 2002): $P = 5.76 \times 10^{-3}$ s (period), $B_{pc} = 7.4 \times 10^8$ G, $R = 1.6 \times 10^6$ cm (stellar radius), $I = 3 \times 10^{45}$ g cm^2 (moment of inertia), $M = 1.58\ M_{sun}$ and $\chi = 35^\circ$.

(1995) infer a minimum observer angle of 5° with respect to the magnetic axis. The observer, therefore, sweeps through the approximate center of the polar cap.

The effect of GR constraints on millisecond pulsar (MSP) spectral cutoffs is investigated in this paper by simulating (using a finite element approach) radiative and transport processes that occur in a pulsar magnetosphere. One of the most interesting predictions from Muslimov and Harding (1997) is that the primary electron luminosity was predicted to be equal to a quadratic function of the compactness parameter $\kappa = \epsilon I/MR^2$ (with $\epsilon = 2GM/Rc^2$) of the neutron star, times the spin-down power ($\dot{E}_{\rm rot} = I\Omega\dot{\Omega}$, with Ω the angular speed and $\dot{\Omega}$ its time derivative) of the pulsar, giving (assuming that the magnetic and spin axes are aligned):

$$L^{|\chi=0}_{\rm prim,max} \sim \frac{3}{4}\kappa(1-\kappa)\dot{E}_{\rm rot}. \tag{1}$$

2. The Model

Standard classical expressions were employed for the dipole magnetic field and radius of curvature $\rho_{\rm c}$ of an oblique pulsar with magnetic moment μ inclined at an angle $\chi = 35°$ relative to the spin axis (Manchester and Johnston, 1995). GR corrections to these quantities were assumed to be of second order and were therefore not employed. The effect of relativistic frame dragging on the charge density, potential and hence the magnitude of $E_{||}$ (the electric field component parallel to the magnetic field) are however of first order and had to be carefully modelled as prescribed by Harding and Muslimov (1998) for the unscreened case.

2.1. The unscreened electric field

Since the optical depths for magnetic pair production for different regions above the PC are insignificantly small, we use the electric field expressions for the case when there is no screening, i.e. when no upper pair formation front (PFF) forms (Muslimov and Tsygan, 1992; Muslimov and Harding, 1997; Harding and Muslimov, 1998). For the 'near case', we use Eq. (51) of Muslimov and Tsygan (1992), which is equivalent to Eq. (64) of Muslimov and Harding (1997). For the 'far case', we use Eq. (14) of Harding and Muslimov (1998). For purposes of comparison, the 'classic' function of Bulik et al. (2000) as defined in their Eq. (2) was also investigated.

2.2. Radiative and transport processes

The change in the energy of a primary electron is given (when only the dominating CR component is considered, neglecting ICS and synchrotron radiation) by

$$\frac{dE}{dt} = e\beta_r c E_{||} - \frac{2}{3}\left(\frac{e^2 c}{\rho_{\rm c}^2}\right)\gamma^4, \tag{2}$$

with e the electron charge, ρ_c the curvature radius, $\beta_r = v_e/c$ the normalised electron speed (as a function of the radial coordinate r), $E_{||}$ the electric field component parallel to the magnetic field lines and γ the Lorentz factor. The photon energy is set equal to the characteristic CR energy in units of $m_e c^2$ (Luo et al., 2000):

$$\epsilon_\gamma \approx \epsilon_c = \frac{3}{2}\left(\frac{\lambda_c}{\rho_c}\right)\gamma^3, \tag{3}$$

with $\lambda_c = \hbar/m_e c \approx 3.86 \times 10^{-11}$ cm the Compton wavelength. The maximum CR cutoff energy is obtained by inserting a neutron star radius of $R_6 = R/10^6$ cm $= 1.6$ and moment of inertia of $I_{45} = I/10^{45}$ g cm^2 ~ 3 (e.g., HMZ02) for a mass of $M = 1.58\ M_{\rm sun}$ derived from the Shapiro delays (Van Straten et al., 2001). This corresponds to a compactness parameter of $\kappa = 0.11$. We also assume a polar cap field strength corrected for kinematic effects (as assumed by Bulik et al. (2000)) of $B_8 = B_{\rm pc}/10^8$ G $= 7.4$. The relative altitude (radial distance) for maximum CR energy is obtained as $\eta = r/R \sim 1.46$ corresponding to a normalized field line colatitude of $\xi = \theta/\Theta_0 = 0.1$ (with Θ_0 the polar angle of the last closed magnetic field line at the stellar surface) and field line radius of curvature of $\rho_c \sim 6.6 \times 10^7$ cm, while the magnetic azimuth $\phi = 0$ results in a maximum GR potential. Note again that $\chi = 35^\circ$ as derived from radio observations. The analytical expression for the maximum gamma-ray energy is obtained by combining the equation of the 'far' electric field with Eqs. (2) and (3), giving

$$\epsilon_{\gamma,\max} = \left(\frac{3}{2}\right)^{7/4}\lambda_c\left(\frac{\beta_r E_{||}}{e}\right)^{3/4}_{\rm max}\rho_c^{1/2} < 15\ {\rm GeV}. \tag{4}$$

3. Results

3.1. Energy spectra and fluxes

Since the electrons become relativistic for r slightly larger than R (stellar radius), the bolometric luminosity of a single polar cap will be given by (Muslimov and Harding, 1997)

$$L_{\rm prim} = \alpha c \int |\rho_e|\Phi\, dS, \tag{5}$$

with Φ the electric potential and dS the element of spherical surface cut by the last open field lines at radial distance r. Integrating over ξ and ϕ, and letting $\eta \to \infty$,

we obtain (Venter, 2004)

$$L_{\mathrm{prim,max}} = L^{|\chi=0}_{\mathrm{prim,max}} \left\{ \cos^2 \chi + \left(\frac{3\Theta_0 H(1)[\pi/2 - \Theta_0 H(1)]}{16\kappa(1-\kappa)} \right) \sin^2 \chi \right\}, \quad (6)$$

providing we adopt a value of $\Theta(\eta) = \pi/2$ for distances $\eta > c/\Omega R$ (see Eq. (6) of Harding and Muslimov (1998)). This result reduces back to Eq. (1) when χ is set equal to zero.

A value of $\chi = 35^\circ$ implies that the maximum efficiency of conversion of pulsar spindown power into particle luminosity is about 7% for PSR J0437-4715, for each PC. We also obtained the bolometric photon luminosity over the total polar cap *via* a finite element (particle tracing) approach and integrating numerically over all energies and field lines from the surface to the light cylinder

$$L_\gamma = \int_0^{\Theta_0} \int_0^{2\pi} \left(\dot{N}(\phi, \theta) \int_{r=R}^{r=c/\Omega} P_\gamma(\phi, \theta, r(t))\, dt \right) d\phi\, d\theta. \quad (7)$$

Here P_γ is the CR photon power integrated over frequency, $\dot{N} = \rho_e c dS/e$ the number of particles ejected per second from a PC surface patch dS centered at (ϕ, θ), and ρ_e the charge density. Since we cannot start with an initial velocity equal to c (i.e. infinite Lorentz factor), we assumed values close to c and found convergent photon luminosities of 6–7% (of the spindown power) corresponding to injection velocities of $0.9c$ and $0.99999c$, respectively (also depending on the assumed magnetic field strength, stellar radius and moment of inertia). This agrees closely with our analytical expression for the total electron luminosity of 7% – i.e. almost all particle luminosity is converted to photon luminosity as expected for strong radiation reaction. It should however also be noted that the fundamental expression for $E_{||}$ (unscreened) changes sign along ~40% of the field lines originating at the polar cap (see Figure 3).

We expect the system to reach a steady state as a result of the redistribution of charges along field lines corresponding to electric field reversals. These field lines are then expected to become equipotential lines, or, a reduced current for this region may develop, resulting in the suppression of particle acceleration along them. This justifies our neglect of these field lines (for which field reversals occur) when calculating the pulse profile, bolometric photon luminosity, and observer time-averaged integral flux.

For the classical case, the efficiency of converting spindown power into photon luminosity is ~90%, but this factor is highly uncertain due to the large uncertainty in electric potential for the classical case.

The differential photon power $dL_\gamma(E)/dE$ is obtained by inserting the ratio of the indicator function $I(E, E + dE)$ and the selected energy bin width dE in the integrand of Eq. (7). This allows us to compare the expected integral photon flux with EGRET (Fierro et al., 1995) above 100 MeV and 1 GeV, as well as proposed H.E.S.S. observations of this pulsar (Venter, 2004). Note that the imaging threshold

energy of H.E.S.S. is $\sim$100 GeV (Hofmann, 2001), although a non-imaging "pulsar trigger" for timing studies down to $\gtrsim$30 GeV can be employed for pulsar studies with H.E.S.S. (de Jager et al., 2001).

Since most of the power is radiated into a cone with half emission angle θ_B (the polar tangential angle at the emission point of the maximum CR energy), we can express the instantaneous polar cap averaged flux at a distance $d = 139$ pc to Earth as

$$F_\gamma^{\rm PC}(>E) = \frac{1}{\Delta\Omega d^2}\int_E^\infty \frac{1}{E'}\left(\frac{dL(E')}{dE'}\right)dE'. \tag{8}$$

The beaming solid angle is selected to correspond to energies above $E = 100$ MeV, giving

$$\Delta\Omega(>E) = 2\pi(1-\cos\theta_B) \sim 0.5 \text{ sr} \tag{9}$$

per polar cap, resulting in a phase-averaged photon flux (as would be seen on a DC skymap) for a single polar cap corresponding to

$$\bar{F}_\gamma(>E) = 2\phi_L F_\gamma^{\rm PC}, \tag{10}$$

with $2\phi_L \sim 0.2$ the pulse width corresponding to the bulk of this emission (see Figure 1). The stated values of $\Delta\Omega(>E)$ and $2\phi_L$ correspond within 20% to the range of values found for the range of assumed values of the polar cap magnetic field strengths, radii and moments of inertia. Only one polar cap is expected to be seen, given the relative orientations of the magnetic axis and observer line-of-sight to the spin axis. The radial coordinate at the position of maximum CR energy $\eta_{\rm m}$, as well as $2\phi_L/\Delta\Omega$, are independent of the choice of injection velocities up to $\sim 0.9999c$.

Figure 1 shows the pulse profile for an observer sweeping at an inclination angle of 40° relative to the spin axis, while the magnetic axis is tilted by an angle of $\chi = 35°$ relative to the spin axis (Manchester and Johnston, 1995). Only half a period is shown, with phase zero ($\phi_L = 0$) corresponding to the closest approach with respect to the magnetic axis, at which the observer is at an angle of $40° - \chi \sim 5°$ relative to the magnetic axis.

A value of $2\phi_L/\Delta\Omega = 0.4$ was used throughout (see Figure 2). The energy spectrum dL/dE is quite hard, resulting in a hard time-averaged photon flux $\bar{F}_\gamma(>E)$, as shown in Figure 2 for two values of the polar cap magnetic field strength and two (R, I) combinations indicated on the figure. It is clear that the EGRET upper limit at 100 MeV is most constraining, resulting in an upper limit of $B_8 < 4$ for $R_6 = I_{45} = 1$, but $B_8 < 1$ for $R_6 = 1.6$, $I_{45} = 3$.

Strong radiation reaction near the pulsar surface, combined with further (weak) acceleration towards the light cylinder, result in a total residual electron power of $\sim 0.05\dot{E}_{\rm rot}$ at the light cylinder.

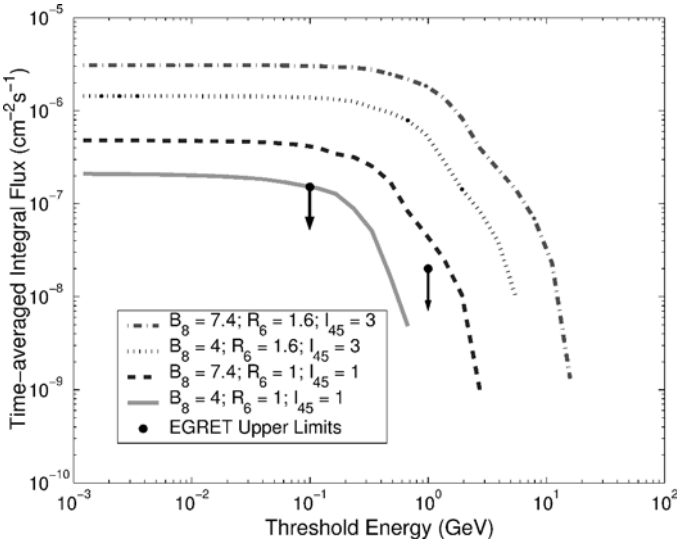


Figure 2. Observer time-averaged integral flux vs. threshold energy for different polar cap magnetic field strengths ($B_8 = B_{\rm pc}/10^8$ G), stellar radii ($R_6 = R/10^6$ cm) and moments of inertia ($I_{45} = I/10^{45}$ g cm^2) as indicated in the legend. These results are invariant (within 10%) for injection speeds corresponding to the range $0.9 < \beta_0 < 0.99999$ and $2\phi_L/\Delta\Omega = 0.4$. The EGRET upper limits are also indicated.

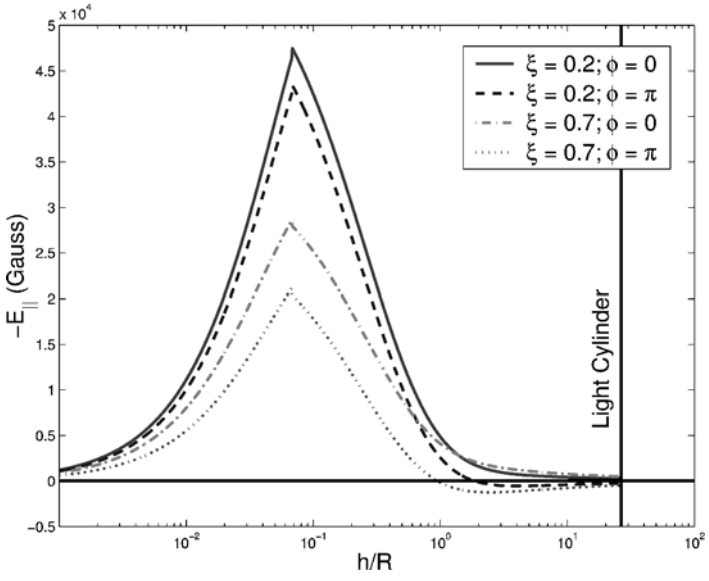


Figure 3. Electric field component parallel to the magnetic field vs. scaled height above the stellar surface for $B_8 = 4$, $R_6 = 1$, and $I_{45} = 1$. Note the sign reversal for $\phi = \pi$.

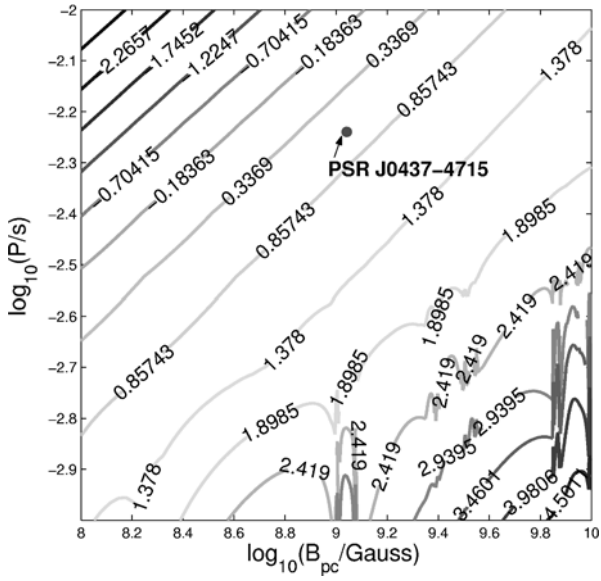


Figure 4. Contour plot of the maximum CR photon energy (labelled as $\log_{10}(E_{\rm CR}^{\rm max}/1\ {\rm GeV})$) vs. $\log_{10}(P/{\rm s})$ and $\log_{10}(B_{\rm pc}/{\rm Gauss})$. No magnetic pair production is expected to take place for the parameter ranges shown in the figure. We used $R_6 = 1$, $\chi = 45^\circ$ and $M = 1.4 M_{\rm sun}$. (It seems as though the model has some numerical instability at smaller periods and larger magnetic fields).

3.2. Spectral cutoffs for millisecond pulsars due to GR frame dragging

The maximum CR energies for millisecond pulsars were calculated from the finite element approach described earlier and plotted as contours in Figure 4. The period range corresponds to 0.001–0.01 s, whereas polar cap field strengths of 10^8–10^{10} G were selected.

The position of PSR J0437-4715 is also indicated on the figure (corresponding to an energy near 4 GeV for the assumed parameters indicated in the figure caption). The highest energies correspond to the smallest periods and largest field strengths, where screening may start to take place according to the model of HMZ02. Most millisecond pulsars are however expected to have unscreened magnetospheres, for which the earlier results apply.

4. Conclusions

CR cutoff energies for millisecond pulsars such as PSR J0437-4715 were predicted to be in the range 50–100 GeV by HMZ02 and Bulik et al. (2000), making proposals for ground-based telescopes with imaging thresholds near 100 GeV (e.g. H.E.S.S. (Hofmann, 2001) and CANGAROO (Yoshida et al., 2002)) attractive. From the present GR theory it appears as though these telescopes may not be able to see the

spectral tail corresponding to the intense primary CR component, since the hard primary CR spectrum does not extend to energies above ∼20 GeV, as verified by both analytical and numerical (finite element) approaches. An inverse Compton component resulting from TeV electrons scattering the UV/soft X-ray photons from the surface of PSR J0437-4715 may however still be detectable, although this prediction by Bulik et al. (2000) should be re-evaluated within a GR electrodynamical framework.

Even the EGRET upper limit above 100 MeV appears to be constraining: the polar cap field strength should be less than 4×10^8 G, with the exact limit depending on the equation of state. Furthermore, Fierro et al. (1995) analysed EGRET data up to 1995, whereas the full EGRET data set of this pulsar (including observations beyond 1995) should be reanalysed, using the additional *a priori* information of testing for a 20% duty cycle in phase with the radio pulse, which should lead to even more constraining flux upper limits than those presented here.

Future refinements should include incorporation of the GR-corrected magnetic field (or even multipoles instead of a dipole – see Navarro et al. (1997)), the GR curvature radius, making more appropriate assumptions concerning the primary electrons' initial velocities (Sakai and Shibata, 2003) and treating the field reversals properly. Also, cuts through the PC made by the observer should be modelled in detail, instead of using averaged values for the solid angle and duty cycle.

References

Bulik, T., Rudak, B. and Dyks, J.: 2000, *MNRAS* **317**, 97.

de Jager, O.C., Konopelko, A., Raubenheimer, B.C. and Visser, B.: 2001, *Am. Inst. Phys.* **558**, 613.

Dyks, J., Rudak, B. and Bulik, T.: 2001, Proceedings of the 4th Integral Workshop, A. Gimenez, V. Reglero and C. Winkler (ESA SP-459, Noordwyk) (eds.), p. 191.

Fierro, J.M., et al.: 1995, *ApJ* **447**, 807.

Harding, A.K. and Muslimov, A.G.: 1998, *ApJ* **508**, 328

Harding, A.K., Muslimov, A.G. and Zhang, B.: 2002, *ApJ* **576**, 366 (HMZ02).

Hofmann, W.: 2001, Proceedings of the 27th ICRC, Hamburg, vol. OG2.5, p. 2785.

Johnston, S., et al.: 1993, *Nature* **361**, 613.

Luo, Q., Shibata, S. and Melrose, D.B.: 2000, *MNRAS* **318**, 943.

Manchester, R.N. and Johnston, S.: 1995, *ApJ* **441**, L65.

Muslimov, A.G. and Harding, A.K.: 1997, *ApJ* **485**, 735.

Muslimov, A.G. and Harding, A.K.: 2003, *ApJ* **588**, 430.

Muslimov, A.G. and Tsygan, A.I.: 1992, *MNRAS* **255**, 61.

Navarro, J., Manchester, R.N., Sandhu, J.S., Kulkarni, S.R. and Bailes, M.: 1997, *ApJ* **486**, 1019.

Sakai, N. and Shibata, S.: 2003, *ApJ* **584**, 427.

Usov, V.V.: 1983, *Nature* **305**, 409.

Van Straten, W., Bailes, M., Britton, M.C., Kulkarni, S.R., Anderson, S.B., Manchester, R.N. and Sarkissian, J.: 2001, *Nature* **412**, 158.

Venter, C.: 2004, *M.Sc. thesis*, North-West University, Potchefstroom, unpublished.

Yoshida, T., Yoshikoshi, T. and Yuki, A.: 2002, *Astropart. Phys.* **16**, 235.

Zavlin, V.E., Pavlov, G.G., Sanwal, D., Manchester, R.N., Trümper, J., Halpern, J.P. and Becker, W.: 2002, *ApJ* **569**, 894.

A MULTIWAVELENGTH INVESTIGATION OF UNIDENTIFIED EGRET SOURCES

P. WALLACE[1], S. BLOOM[2] and M. LEWIS[1,3]

[1]*Berry College, Mount Berry, GA, U.S.A.; E-mail: pwallace@berry.edu*
[2]*Hampden-Sydney College, Hampden-Sydney, VA, U.S.A.; E-mail: sbloom@hsc.edu*
[3]*Present address: Dartmouth College, Hanover, NH, U.S.A.;*
E-mail: matthew.s.lewis@dartmouth.edu

(Received 30 June 2004; accepted 27 July 2004)

Abstract. Statistical studies indicate that the 271 point sources of high-energy gamma rays belong to two groups: a galactic population and an isotropic extragalactic population. Many unidentified extragalactic sources are certainly blazars, and it is the intention of this work to uncover gamma-ray blazars missed by previous attempts. Until recently, searches for blazar counterparts to unidentified EGRET sources have focused on finding AGN that have 5-GHz radio flux densities S_5 near or above 1 Jy. However, the recent blazar identification of 3EG J2006-2321 ($S_5 = 260$ mJy) and other work suggest that careful studies of weaker flat-spectrum sources may be fruitful. In this spirit, error circles of four high-latitude unidentified EGRET sources have been searched for 5-GHz sources. The gamma-ray sources are 3EG J1133+0033, 3EG J1212+2304, 3EG J1222+2315, and 3EG J1227+4302. Within the error contours of each of the four sources are found six radio candidates; by observing the positions of the radio sources with the 0.81-m Tenagra II telescope it is determined that 14 of these 24 radio sources have optical counterparts with $R < 22$. Eight of these from two different EGRET sources have been observed in the B, V, and R bands in more than one epoch and the analysis of these data is ongoing. Any sources that are found to be variable will be the objects of multi-epoch polarimetry studies.

Keywords: techniques: photometry galaxies: active gamma rays: observations

1. Introduction

With the exception of the LMC, blazars constitute all identified high-energy gamma-ray sources with galactic latitude $|b| > 30^\circ$; in this region there are 30 unidentified sources (Hartman et al., 1999). Galaxy clusters may be responsible for a very small number of unidentified EGRET sources at high latitudes (Colafrancesco et al., 2001) but any high-energy gamma-ray emission from such clusters probably falls below EGRET's sensitivity (Reimer et al., 2003). It is also possible that the Galactic halo houses some of the persistent EGRET sources (Grenier et al., 2001), but to date this is only a conjecture. It remains that the only identified gamma-ray sources above 30° galactic latitude are blazars with flat-spectrum radio counterparts, and we suggest that there are others among the 30 unidentified sources with $|b| > 30^\circ$.



Astrophysics and Space Science **297:** 409–414, 2005.
© Springer 2005

The present article describes an effort to single out those high-latitude gamma-ray sources that are most likely to be blazars, and to suggest plausible optical and radio counterparts for them. Using NED, we have searched within the 95% confidence contours of four EGRET sources for 5-GHz radio sources; 24 such radio sources were found, and fields centered on these radio sources were subsequently observed with the 0.81-m Tenagra II telescope at Tenagra Observatory, with the goal of determining plausible optical counterparts to the radio sources, and thus to the gamma-ray sources. The R-magnitudes of these sources are determined using IRAF, and follow-up photometry has been performed on those for which optical counterparts were found.

Our working assumption is that these four gamma-ray sources are blazars, and it is our goal to determine their most probable radio and optical counterparts. In cases where no plausible counterparts are found, it may be that the source is not a blazar, but a new class of high-energy gamma-ray source. This work complements that of Sowards–Emmerd et al. (2003; hereafter SRM 2003), in which detailed spectroscopic information was compiled for a large number of northern gamma-ray counterpart sources and in which a number of plausible identifications were reported. Only one of the four present sources (J1133+0033) is found to have a compelling counterpart in SRM 2003. In addition, two of our sources (J1212+2304 and J1222+2315) are listed in SRM 2003 as having no plausible blazar counterpart at all. This work also complements that of Bloom et al. (2004), who has performed similar work on a different set of high-latitude unidentified sources.

2. Selection of Gamma-Ray and Radio Sources

It is impractical to search the error boxes of all the unidentified sources for variable optical counterparts to 5-GHz radio sources. We therefore restrict our source sample in several ways. First, we look only at high Galactic latitudes, as sources with $|b| > 30^\circ$ have low sky densities and are least susceptible to source confusion. Also, high-latitude EGRET sources are least likely to be of Galactic origin. Further, we look to those gamma-ray sources that display some evidence of being variable. We use the variability statistics τ and I, described in Torres et al. (2001). The τ statistic takes into account 145 marginal sources not listed in Hartman et al. (1999); the maximum likelihood fluxes of all 416 sources are then re-computed. From these data, each source was assigned a value of τ, which is defined as $\tau = \sigma/\mu$, where σ is the standard deviation of the individual viewing period fluxes and μ is their mean value. In this scheme one must pay attention not only to τ itself but to its error bars; we consider a source to be variable if its 68% lower limit is equal or greater than unity. An assumption of the I-statistic is that on the time scales under consideration (weeks to years) pulsars are not variable. I is then defined as $\mu_{\rm source}/\mu_{\rm pulsars}$, where $\mu = 100 \times \sigma \times F - 1$; F is a weighted mean of the individual EGRET fluxes

for $E > 100$ MeV and σ is their standard deviation. So for pulsars, $I = 1$; we consider a source to be variable if $I > 4$, corresponding to $>6\sigma$ above pulsar "variability".

For an EGRET source to be included in this study, we require that at least τ or I indicate that the source is variable. This restriction is meant to act as blunt instrument and is intended only to help us avoid those sources that show no evidence whatsoever of variability. (Also, it is important to realize that for these dim sources all means of determining gamma-ray variability are subject to significant uncertainties.) Cutting out sources with far southerly declinations leaves us with 12 candidates. Four of these have been searched for radio sources and optical counterparts have been sought.

Each of the four 95% error boxes contain six 5-GHz radio sources that satisfy the flowing criteria (1) the flux density at this frequency is roughly 50 mJy or greater (this is near the limit of the Parkes and Green Bank 5-GHz surveys); (2) the spectral index α, where $F_\nu \propto \nu^\alpha$, between 1.4 and 5 GHz is greater than about -1.0; (3) the position is known to an uncertainty of about $5''$; (4) the radio source is well-separated from nearby sources (within astrometric uncertainty), and (5) the source's optical counterpart (if any) is not extended. In this way we have restricted our candidates to those with radio features like those of the population of EGRET blazars. In some cases one or two of these requirements was relaxed if the radio source fell particularly close to the gamma-ray centroid, or if other indicators were particularly favorable for a blazar identification. These radio sources, with their NED-resolved names, 5-GHz flux densities S_5, radio spectral index α, and angular separation from the EGRET centroid are listed in Table I. The listing is by increasing RA of the EGRET sources and then by increasing angular separation. The spectral indexes are determined by finding S at frequencies of 1.4 and 5 GHz; in those cases where there is no known 1.4 GHz counterpart, no α is given.

3. Optical Observations

Optical observations of all 24 radio positions were made with the Tenagra 0.81-m telescope in Nogales, Arizona during 2003 April and May. Those with known V magnitudes were observed for 300 or 600 s, depending on their brightness. Those with unknown magnitudes were observed for 1500 s each; the Tenagra 0.81-m reaches $R \sim 21$ in this time under good sky conditions. In addition, Landolt standard stars (Landolt, 1992) and faint calibration stars from the Hamburg Quasar Monitoring program (e.g., Borgeest and Shramm, 1994) were observed nightly to determine the photometric scale and atmospheric absorption. The data were reduced using the standard packages of the Image Reduction and Analysis Facility (IRAF). After the astrometric plate solutions were produced using Mira software and the USNO-A2.0 catalog, it was determined that 14 of the 24 had

TABLE I
Properties of radio candidates

γ-ray Src #	γ-ray Src name	NED-Resolved Name	S_5 (mJy)	α	Ang Sep (arcmin)
1.	3EG J1133+0033	PKS B1130+008	352	−0.2	4.4
		PMN J1132+0033	252	−0.2	6.5
		LBQS 1130+003	194	–	21.2
		PMN J1133+0059	122	−0.3	26.1
		4C −00.45	451	−0.8	67.1
		87GB 112551.8+005033	74	−0.5	68.7
2.	3EG J1212+2304	4C +23.29	210	−0.9	48.7
		87GB 120653.1+225922	39	–	50.7
		4C +24.25	67	−0.9	53.5
		MG2 J121626+2335	73	−0.8	59.6
		87GB 121037.6+221200	42	–	69.4
		MG2 J120941+2220	112	−0.8	80.2?
3.	3EG J1222+2315	MG2 J122209+2311	109	−0.9	6.0
		MG2 J122402+2238	99	−0.1	42.0
		4C +22.35	179	−1.1	47.6
		4C +23.30	123	−1.1	49.4
		87GB 122307.4+240021	44	−0.7	52.1
		MG2 122443+2359	98	−1.0	52.9
4.	3EG J1227+4302	B3 1224+428	53	−1.3	29.9
		B3 1224+439	161	−0.1	38.6
		B3 1222+438	235	−0.4	40.6
		B3 1225+442	124	−0.9	58.7
		B3 1219+438	30	−1.1	62.1
		3C 272	360	−1.2	62.6

high-confidence optical counterparts (radio and optical sources within 2 s of arc).

4. Current Results and Future Direction

Results from initial R-band photometry of the optical candidates, performed from 8–22 May 2003 at Tenagra Observatory, are given in Table II. ID's are from this work and from SRM 2003. Multi-epoch photometry in the B, V, and R bands for J1133+0033 and J1212+2304 was performed at Tenagra from January–March 2004 and is currently being reduced and analyzed. In northern spring 2005 the remaining optical sources will be monitored for color and variability; those sources

TABLE II
Results of initial optical photometry

γ-ray Src #	NED-Resolved Radio Name	NED mag	Exposure (s)	Observed R mag	σ_R
1.	PKS B1130+008	18.5	300	16.99	0.06
	PMN J1132+0033	–	1500	–	–
	LBQS 1130+003	18.7	300	–	–
	PMN J1133+0059	–	1500	19.87	0.30
	4C −00.45	16.5	300	15.94	0.01
	87GB 112551.8+005033	–	1500	18.43	0.13
2.	4C +23.29	17.5	300	17.06	0.15
	87GB 120653.1+225922	–	1500	20.08	0.14
	4C +24.25	–	1500	–	–
	MG2 J121626+2335	–	1500	18.25	0.17
	87GB 121037.6+221200	–	1500	19.15	0.41
	MG2 J120941+1220	–	1500	–	–
3.	MG2 J122209+2311	–	1500	17.71	0.04
	MG2 122402+2238	–	1500	–	–
	4C +22.35	18.5	300	17.92	0.12
	4C +23.30	–	1500	–	–
	87GB 122307.4+240021	–	1500	–	–
	MG2 122443	–	1500	–	–
4.	B3 1224+428	–	1500	–	–
	B3 1224+439	–	1500	18.89	0.11
	B3 1222+438	20.4	600	20.00	0.55
	B3 1225+442	18.2	300	18.64	0.25
	B3 1219+438	–	1500	–	–
	3C 272	–	1500	20.08	0.50

that show evidence of variability will be considered for optical polarimetry; any sources which show variability in flux and polarization will be considered the best candidates for association with gamma-ray blazars.

Acknowledgements

PMW thanks J. P. Halpern for spectroscopy on PKS 1130+008 & PKS B1130+009. Also, thanks to Michael Schwartz and Paulo Holvorcem at Tenagra Observatories. This research has made use of the NASA/IPAC Extragalactic Database (NED) which is operated by the Jet Propulsion Laboratory, California Institute of Technology, under contract with the National Aeronautics and Space Administration.

References

Bloom, S.D. et al.: 2001, *Proc. Gam 2001, AIP* **587**, 648.
Bloom, S.D. et al.: 2004, *AJ* **128**, 56.
Borgeest, U. and Shramm, K.: 1994, *A&A* **284**, 764B.
Hartman, R.C. et al.: 1999, *ApJS* **123**, 79.
Landolt, A.U.: 1992, *AJ* **104**, 340.
Reimer, O. et al.: 2003, *ApJ* **588**, 155.
Sowards-Emmerd, D. et al.: 2003, *ApJ* **590**, 109.
Torres, D. et al.: 2001, *AN* **322**, 223.
Wallace, P.M. et al.: 2002, *ApJ* **569**, 36.

X-RAY LINES IN GAMMA-RAY BURSTS AND CERENKOV LINE MECHANISM

WEI WANG

National Astronomical Observatories, Chinese Academy of Sciences, Beijing 100012, China;
Department of Physics, University of Hong Kong, Pokfulam Road, Hong Kong;
E-mail: wwang@bohr.physics.hku.hk

(Received 4 June 2004; accepted 17 July 2004)

Abstract. X-ray emission and absorption features are of great importance in our understanding the nature and environment of gamma-ray bursts (GRBs). So far, iron emission lines have been detected in at least four GRB afterglows. In this paper, the observational properties and physical constraints on materials surrounding GRB sources are reviewed, and several classes of theoretical models are also discussed. We will specially concentrate on the Cerenkov line mechanism, in which the broad iron lines are expected, and a small mass of Fe is required to produce the large line luminosity. In addition, our interpretation can favor the recent jet unified model for different classes of gamma-ray bursts with a standard energy reservoir.

Keywords: gamma-rays: bursts, X-rays, lines, radiation mechanism: nonthermal

1. X-ray Lines in Gamma-Ray Bursts

The detection of X-ray emission lines and absorption features in the GRB afterglows provides a powerful tool to probe the environments around GRB sources, and then probably gives us clues to the nature of the progenitors. Moreover, the identification of X-ray lines by the high spectral resolution detectors could directly provide the redshift information for GRBs.

Recent GRB observational reports have shown the emission line features in the X-ray afterglows of at least four GRBs (GRB 970508, Piro et al., 1999; GRB 970828, Yoshida et al., 1999; GRB 991216, Piro et al., 2000; GRB 000214, Antonelli et al., 2000). These lines generally last half day to several days, with large line width and very high line luminosity. The properties of the detected emission lines in GRBs are summarized in Table I. The X-ray prompt emission is also detected in GRB 990712 with BeppoSAX (Frontera et al., 2001), which could be interpreted as either a line profile with centroid energy of 4.5 keV or a blackbody spectrum with the temperature ~ 1.3 keV, so we will not discuss it further in this paper. According to the variability and very large flux and equivalent width, we can estimate that there are large iron masses of 0.01-1.0$M_{\odot}$ in the emission region a size of $\sim 10^{15-16}$ cm if these lines are supposed to be produced by fluorescence or recombination. So much Fe would come from the surrounding medium rather



Astrophysics and Space Science **297:** 415–422, 2005.
© Springer 2005

TABLE I
The properties of X-ray emission lines in GRBs

GRB	Detector	z	Line energy (keV)	Width (keV)	Intensity (10^{-5} ph cm^{-2}s^{-1})	Line luminosity (erg s^{-1})	Reference
970508	BeppoSAX	0.835	3.4	$\leq$0.5	5.0	2.7×10^{44}	1, 2
970828	ASCA	0.957	5.04	0.31	1.9	1.1×10^{44}	3, 4
991216	Chandra	1.02	3.49	0.23	3.2	4.0×10^{44}	5, 6
			4.4	1.0	3.8	4.8×10^{44}	5
000214	BeppoSAX	0.47	4.7	0.2	0.9	4.0×10^{43}	7

Here the cosmological model $(\Omega_{\rm M}, \Omega_\Lambda, h) = (1/3, 2/3, 0.7)$ is taken, the redshift of GRB 000214 is determined only based on Fe $K\alpha$ emission identification. Two lines is discovered in GRB 991216, generally, one is identified as the fluorescent line, the other as the recombination.
References: 1. Piro et al., 1999; 2. Metzger et al., 1997; 3. Yoshida et al., 1999; 4. Djorgovski et al., 2001; 5. Piro et al., 2000; 6. Vreeswijk et al., 2000; 7. Antonelli et al., 2000.

than GRB progenitors themselves, because it will involve the famous problem of baryon contamination.

A large number of irons in the close environment of GRBs imply the mental enriched process before GRBs occur. Then there exists a very dense medium surrounding the GRB progenitor, so we expect that the absorption features should be detected too. Up to now, only a discovery of a transient absorption edge in X-ray spectrum of GRB 990705 (Amati et al., 2000) has been reported. The absorption feature shows that the iron abundance is about 75 times higher than the solar value. Other ion emission lines were also detected in GRB 011211 by an XMM-Newton observation (Reeves et al., 2002). The X-ray spectrum reveals evidence for emission lines of Mg, Si, S, Ar, Ca and possible Ni. The line identification show the redshift $z = 1.88 \pm 0.06$, differing significantly from the known GRB redshift $z = 2.140 \pm 0.001$ by the spectroscopy of the optical afterglow (Holland et al., 2002), implying an outflow velocity for the line emitting material of $v = 25800$ km s^{-1} or $v/c = 0.086$. Additional evidence for the presence of ion lines were also suggested for two XMM-Newton spectra of GRB 001025A and GRB 010220 (Watson et al., 2002). These ion lines are attributed to the emission from the ionized optically thin plasma, indicating that thermal emission from light elements may be common in the early X-ray afterglows. And metal enrichments may occur preceding the GRB events.

2. Model Constraints From Observations

The iron line observations show constraints on the theoretical models: (1) If the iron lines are produced by fluorescence or recombination, we require that the compact regions ($\sim10^{15-16}$ cm) contain $0.01 - 1 M_\odot$ Fe with the electron density larger than 10^{10} cm^{-2}, but must be optically thin to electron scattering (size problem). (2) So

much iron (corresponding to several solar mass material) cannot be produced by burst itself because of the famous problem of baryon contamination. These irons should come from the surrounding medium. Furthermore, iron-rich medium may be not consistent with the normal interstellar medium even in the dense region of stellar formation. (3) If we interpret the line width as due to the velocity of a supernova remnant, their sizes allow us to estimate the age of SNR which turn out to be tens of days, while at this time, cobalt nuclei would dominate and the line would be produced mainly by cobalt not iron (kinematic problem).

A large mass of Fe around the progenitor really produces a challenge to the present GRB models. And the problem also focuses on how the torus of iron-rich material formed. Mészáros and Rees (1998) have shown that the circumburst environment created by the stellar wind before the hypernova (Paczyński, 1998). While, this scenario may not produce so high luminosity Fe lines. Recently, Dado et al. (2003) argued that the line detected are not the real iron lines but the strongly Doppler-blueshift Lyα line emissions by jets of highly relativistic cannonballs produced by a supernova. At present, there are mainly two classes of model put forward to explain the lines: the geometry dominated and engine dominated models, and the key difference is the reason for the observed duration of the line emission.

In the geometry dominated models, the line emission duration is due to light travel time effect. Since the lines appear in the timescale of 1 day, the emission size estimated is about 10^{16} cm. A favorable situation is expected in the supranova (Vietri and Stella, 1998), where a GRB is preceded by a supernova explosion for several months to years with ejection of an iron-rich massive shell. In this scenario, high density in excess of $10^{10}\,\mathrm{cm}^{-3}$ may be expected, and Fe absorption features of strength comparable to these in emission should be also be detected. While, in the engine dominated models, the emission material, at a typical emission size about 10^{13} cm, can be pre-GRB ejecta or the expanding envelope of a supergiant GRB progenitor (Rees and Mészáros, 2000; Mészáros and Rees, 2001). They have argued that the strong line emission can be attributed to the interaction of a continuing post-burst relativistic outflow from the central decaying magnatar with the progenitor stellar envelope at distance less a light hour, and only a small mass Fe is required.

3. Cerenkov Line Mechanism

We have proposed a new mechanism Cerenkov line emission for the lines in X-ray afterglows. (Wang et al., 2002). As we know, Cerenkov radiation is produced when the particle velocity exceeds the light speed in the medium. Furthermore, You and Chen (1980) argued that for relativistic electrons moving through a dense gas, the Cerenkov effect will produce peculiar atomic/molecular emission lines: Cerenkov lines. They also extended the work to the X-ray band, such as Fe K_α lines (You et al., 2000). Cerenkov line emission has following remarkable features (see Figure 1):

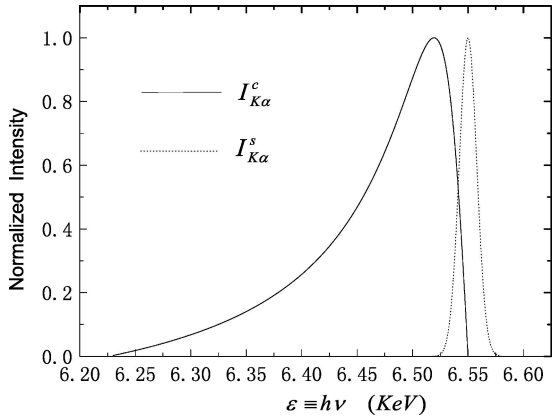


Figure 1. The calculated profile of Cerenkov line $I^{c}_{K_\alpha} \sim \varepsilon$ of iron ion Fe^{+21} in optically thick case, where $\varepsilon \equiv h\nu$ is the energy of line photon. The Cerenkov line-profile is broad, asymmetric, and redshifted. The profile of a normal line by spontaneous transition $I^{s}_{K_\alpha} \sim \varepsilon$ is also plotted for the comparison.

broad, asymmetrical, Cerenkov redshift and polarized if relativistic electrons have an anisotropic velocity distribution.

Here, we emphasize the special importance of the Cerenkov redshift which markedly strengthens the emergent intensity of the Cerenkov emission line. For an optically thick dense gas, the emergent line is determined both by the emission and absorption. The absorption mechanisms for the normal line and Cerenkov line are extremely different. The intensity of normal line, $I^{\rm n}$ is greatly weakened by the strong resonant absorption $k_{\rm lu}(\nu_{\rm lu})$ (the subscripts u and l denote the upper and lower-levels) due to the fact that the normal line is located exactly at the position of the intrinsic frequency $\nu_{\rm lu}$ where $k_{\rm lu}$ is very large. In the extreme case of a very dense gas, the emergent flux has the continuum with a black body spectrum, and the normal line disappeared, $I^{\rm n} \sim 0$. However, the Cerenkov line, located at $\nu < \nu_{\rm lu}$ due to the redshift, can avoid the resonant absorption because of $k_{\rm lu}(\nu < \nu_{\rm lu}) \to 0$ (see the special dispersion relations at a wavelength shown in Figure 2). The main absorption mechanism which affects the intensity of Cerenkov line is the photoionization absorption $k_{\rm bf}$ which is very small compared with $k_{\rm lu}$. Thus the Cerenkov line photons can easily escape from deep inside a dense gas cloud, causing a strong emergent line flux, only if the density of relativistic electrons $N_{\rm e}$ is high enough. In other words, the dense gas appears to be more transparent for the Cerenkov line than normal line, which makes it possible for the Cerenkov line mechanism to dominate over the normal line mechanisms when the gas is very dense and there exist abundant relativistic electrons in the emission region.

In the astrophysical processes of GRBs, a large amount of relativistic electrons and dense gas regions could exist. For the long burst afterglows localized so far,

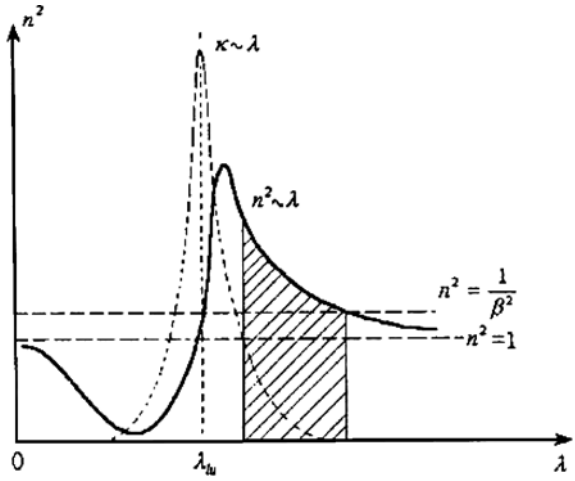


Figure 2. The relations between refractive index n^2 which is proportional to emissivity and wavelength λ, and between extinction coefficient κ and λ. The Cerenkov radiation survives in the shaded narrow region.

the host galaxies show signs of star formation activity, where the high-density environment is expected. Recent broadband observations of the afterglows of GRB 000926 (Piro et al., 2001) and statistical analysis (Reichart and Price, 2002) imply the evidence for a fireball in a dense medium. When the ultra-relativistic blast waves interact with the dense regions, very strong Cerenkov line emission in X-ray band would be observed, and Cerenkov mechanism may dominate in the case of the optically thick gases. Importantly, broad line features are naturally explained in our model (see Figure 1).

The total intensity of Cerenkov line is (You et al., 2000)

$$I^{\mathrm{c}} = Y\left[\ln(1+X^2) + 2\left(1 - \frac{\arctan X}{X}\right)\right], \tag{1}$$

where $Y \equiv \frac{N_{\mathrm{e}}}{2}\frac{C_1}{k_{\mathrm{bf}}}$, and $X \equiv \sqrt{\frac{k_{\mathrm{bf}}}{C_2}}\, y_{\mathrm{lim}}$, N_{e} is the relativistic electron density, $y_{\mathrm{lim}} = C_0\gamma_0^2$, γ_{c} is the electron Lorentz factor, and

$$\begin{aligned} C_0 &= 1.05 \times 10^{-76}\varepsilon_{\mathrm{lu}}^{-4} A_{\mathrm{ul}} g_u N_{\mathrm{Fe}} \frac{S_l}{g_l}, \\ C_1 &= 5.77 \times 10^{-53}\varepsilon_{\mathrm{lu}}^{-2} A_{\mathrm{ul}} g_u N_{\mathrm{Fe}} \frac{S_l}{g_l}, \\ C_2 &= 1.75 \times 10^{-87}\varepsilon_{\mathrm{lu}}^{-4} \Gamma_{\mathrm{lu}} A_{\mathrm{ul}} g_u N_{\mathrm{Fe}} \frac{S_l}{g_l}, \\ k_{\mathrm{bf}} &= 8.4 \times 10^{-46}\varepsilon_{\mathrm{lu}}^{-3} N_{\mathrm{Fe}} S_2. \end{aligned} \tag{2}$$

The damping constant $\Gamma_{\rm lu}$ is related to Einstein's coefficient $A_{\rm ul}$, g_u is the statistical weights. For Fe $K\alpha$ line, $\varepsilon_{\rm lu} = 6.4$ keV, only levels $l = 1$, $u = 2$ are considered, and $S_1 = g_1 = 2$, $g_2 = 8$, and $S_2 \sim 5$ for the GRB afterglow.

In the optically thick gas, we have found $X \gg 1$, then we can simplify the formulae of Cerenkov line intensity as $I^{\rm c} \simeq 2Y(\ln X - 1)$ (Wang et al., 2002). And we only take the main contribution $2Y$ in our following estimation, so

$$I^{\rm c} \sim \frac{C_1}{k_{\rm bf}} N_{\rm e} \sim 1.12 \times 10^{-7} \varepsilon_{12} A_{21} N_{\rm e}. \tag{3}$$

For the optically thick case, the outward flux per unit area and per unit time $\pi F \approx \pi I^{\rm c}$. Assuming that there exist a lot of spherical clouds with dense gas that is distributed homogeneously in the circumburst environment, the cloud radius and number are R, $N_{\rm c}$, respectively, an isotropic fireball interacts with these clouds. Therefore, the total line luminosity from the clouds is $L^{\rm c} = 4\pi^2 R^2 N_{\rm c} I^{\rm c}$. Defining a covering factor $C \equiv N_{\rm c}\pi R^2/4\pi D^2$, where D is the distance between the clouds and burst center, then

$$L^{\rm c} = 16\pi^2 C D^2 I^{\rm c} \sim 8.2 \times 10^{32} C_{0.1} D_{16}^2 N_{\rm e} {\rm erg\ s^{-1}}, \tag{4}$$

where we have taken $A_{21} = 4.6 \times 10^{14} {\rm s^{-1}}$ and the characteristic scales $C \sim 0.1$, $D \sim 10^{16}$ cm. From Eq. (4), we can clearly see that the total line luminosity by the Cerenkov mechanism is strongly dependent on the electron density rather than the iron abundance. Thus, we propose that some classes of GRB models predict the presence of a very high relativistic electron density, therefore the ultra-strong iron lines in the X-ray afterglows can be explained probably without additional request for initial and external conditions of iron-rich torus.

We also could estimate the relativistic electron density required for X-ray lines from four GRB afterglows. Take the cosmological model with $H_0 = 70$ km s^{-1} Mpc^{-1}, $\Omega_0 = 1/3$, $\Omega_\Lambda = 2/3$, and let $C_{0.1} = D_{16} = 1$, we find that the electron densities $N_{\rm e}] \sim 10^{10}$–10^{11} cm^{-3} are similar to the one estimated by other models. We first simply estimate the relativistic electron density from the fireball, $N_{\rm e} \sim E/4\pi D^2 \Delta_{\rm D} \gamma m_{\rm p} c^2$, and taking the isotropic energy $E \sim 10^{53}$ erg, $\gamma \sim 100$, $\Delta_{\rm D} \sim \gamma cT$ (T is the duration $\sim$10 s), we obtained the density $N_{\rm e} \sim 10^8\,{\rm cm^{-3}}$, which will be lower than our requirement in the model. So we think the relativistic electrons should come from other processes. We here propose that the electrons would be produced by a pulsar wind from the central millisecond magnetar (Thompson, 1994) or e^+e^- outflow from the Kerr black hole with magnetized torus (MacFadyen and Woosley, 1999) as the delayed injection after GRB events. Our interpretation is similar to that of Rees and Mészáros (2000), but we consider the e^+e^- outflow instead of electromagnetic flux. The luminosity is required as high as $L \sim 4\pi D^2 N_{\rm e} c \gamma_{\rm e} m_{\rm e} c^2 \sim 10^{48}$ erg s^{-1}, where we take $N_{\rm e} \sim 10^{10}\,{\rm cm^{-3}}$, $\gamma_{\rm e} \sim 10$ at the distance of 10^{16} cm. The luminosity could be satisfied by the central compact

objects with the acceptable parameters such as very strong magnetic field. Because the scattering cross section of relativistic electrons will be near to the zero due to the Klein-Nishina formula at the very high frequency(due to the Doppler effect), we need not worry about the electron scattering process will greatly affect the line profile and intensity.

Furthermore, we also have considered the optically thin case for the Cerenkov line emission mechanism (Wang, 2003). In this case, The emission intensity will be dependent on both the electron density and iron abundance (in a form $\propto X^2Y$). Meanwhile, the computations show that only a small mass of iron about $10^{-6}M_{\odot}$ is needed to produce the high line luminosity within the emission region of $\sim 10^{16}$ cm, so a normal homogeneous medium around the GRB progenitor could meet the requirement.

Finally, the research and development of thirty years on gamma ray bursts more and more make the astronomers believe that there probably exists a unified picture for gamma ray bursts. Recently, some researchers proposed the jet unified models of short and long gamma-ray bursts, X-ray rich gamma-ray bursts, and X-ray flashes (Lamb et al., 2004; Yamazaki et al., 2004). The jet models assume the different classes of gamma-ray bursts have a standard total energy within a range of 10^{50}–10^{51} erg (Frail et al., 2001). However, the standard energy is much lower than the total energy limit determined from the X-ray emission lines, $\sim 10^{52}$ erg (Ghisellini et al., 2002). Since based on the fluorescence or recombination, the line radiation is isotropic, and the burst energy cannot be lower than the X-ray afterglow energy, so the inconsistency still exists. But the Cerenkov line mechanism has not the problem and could make the jet unified picture more convincible, because the Cerenkov line intensity can be independent of the prompt energy of gamma-ray bursts, and if the relativistic electrons distribute not in the homogeneous direction, the Cerenkov line emissions are not isotropic too, the "beaming" effect will decreases the total X-ray afterglow energy to the same order of the standard energy reservoir.

References

Amati, L. et al.: 2000, *Science* **290**, 953.
Antonelli, L.A. et al.: 2000, *ApJ* **545**, L39.
Dado, S., Dar, A. and De Rújula, A.: 2003, *ApJ* **585**, 890.
Djorgovski, S.G. et al.: 2001, *ApJ* **562**, 654.
Frail, D.A. et al.: 2001, *ApJ* **562**, L55.
Frontera, F. et al.: 2001, *ApJ* **550**, L47.
Ghisellini, G. et al.: 2002, *A&A* **389**, L33.
Holland, S. et al.: 2002, *AJ* **124**, 639.
Lamb, D.Q., Donaghy, T.Q. and Graziani, C.: 2004, *New Astronomy Reviews* **48**, 459.
MacFadyen, A. and Woosley, S.E.: 1999, *ApJ* **524**, 262.
Mészáros, P. and Rees, M.J.: 1998, *MNRAS* **299**, L10.
Mészáros, P. and Rees, M.J.: 2001, *ApJ* **556**, L37.

Metzger, M.R. et al.: 1997, *Nature* **387**, 878.
Paczyński, B.: 1998, *ApJ* **494**, L45.
Piro, L. et al.: 1999, *ApJ* **514**, L73.
Piro, L. et al.: 2000, *Science* **290**, 955.
Piro, L. et al.: 2001, *ApJ* **558**, 442.
Rees, M.J. and Mészáros, P.: 2000, *ApJ* **545**, L73.
Reeves, J.N. et al.: 2002, *Nature* **416**, 512.
Reichart, D.E. and Price, P.A.: 2002, *ApJ* **565**, 174.
Thompson, C. 1994, *MNRAS* **270**, 480.
Vietri, M. and Stella, L.: 1998, *ApJ* **507**, L45.
Vreeswijk, P.M. et al.: 2000, GCN notice 496.
Wang, W., Zhao, Y. and You, J.H.: 2002, *ApJ* **576**, L37.
Wang, W.: 2003, the Master's Thesis, Chinese Academy of Sciences.
Watson, D. et al.: 2002, *A&A* **393**, L1.
Yamazaki, R., Ioka, K. and Nakamura, T.: 2004, *ApJ* **607**, L103.
Yoshida, A. et al.: 1999, *A&AS* **138**, 433.
You, J.H. and Cheng, F.H.: 1980, *Acta Phys. Sinica* **29**, 927.
You, J.H. et al.: 2000, *A&A* **362**, 762.

LINE EMISSION FROM CONICAL JETS AROUND ROTATING BLACK HOLES

YE-FEI YUAN[1], BO LI[1] and JIAN-MIN WANG[2]

[1]*Center for Astrophysics, University of Science and Technology of China, Hefei, Anhui 230026, Peoples Republic of China; E-mail: yfyuan@ustc.edu.cn*

[2]*Laboratory for Cosmic Ray and High Energy Astrophysics, Institute of High Energy Physics, Chinese Academy of Sciences, Beijing 100039, Peoples Republic of China*

(Received 4 June 2004; accepted 14 July 2004)

Abstract. Some observations indicate the presence of Doppler-shifted emission lines in the X-ray spectra of black hole candidates and active galactic nuclei. Motivated by which, we studied the observed profile of emission lines from relativistic outflows around black holes in great detail, but jets are simply treated as pencil beams. It was found that the observed line emission shows a doubly peaked profile at large viewing angles for extreme Kerr black holes. In this work, we study the observed profile of an emission line from a more realistic, cone-shaped jet, and we find that an intrinsically narrow line is basically singly peaked, which is different from our previous results. Therefore, we conclude that the double peaks in our previous results is due to the simplified assumption on the geometrical structure of jets. This finding emphasizes the difference between the observed line profile in the jet case and those in the disc case in which there are generally double peaks in the observed spectra.

Keywords: black holes, jets, X-ray

1. Introduction

Blueshifted and extremely strong X-ray emission lines have been detected recently in both active galactic nucleus (AGNs) and stellar black hole candidates (BHCs). Yaqoob et al. (1998) reported the detection of an emission line at 1.6 KeV in the rest frame (with EW = 60 eV) in PKS 0637–75 from an *ASCA* observation, which was interpreted as blueshifted O VII line. Later on, a highly blueshifted Fe K emission line at $\sim 17.0 \pm 0.5$ KeV in the rest frame with EW $= 300 \pm 200$ eV was discovered in PKS 2149–306 from *ASCA* data (Yaqoob et al., 1999). More recently, a strong X-ray emission line in CXOCDFS J033225.3–274219 which was identified as a type 1 AGNs has also been detected from a *Chandra* observation (Wang et al., 2003). The line observed at $\sim$16.2 KeV with EW = 11.5 KeV in the rest frame was suggested as the Doppler-blueshifted Fe K emission line. Blueshifted emission lines have also been observed in stellar BHCs. Migliari et al. (2002) were successful in spatially isolating and extracting X-ray spectra of the two jets of SS 433 from the *Chandra* data. They reported the presence of two Doppler-shifted iron emission



Astrophysics and Space Science **297:** 423–430, 2005.
© Springer 2005

lines at ∼7.3 KeV for the approaching jet and ∼6.4 KeV for the receding jet. Another possible detection of two emission lines at ∼5.7 and 7.7 KeV in BHC 4U 1630–47 was also reported (Cui et al., 2000). But it is still unclear whether both lines arise from a single iron emission line that is Doppler redshifted and blueshifted in a bipolar outflow.

The origin of the relativistic outflow in black hole systems are still mysterious to us, which barriers our understanding of the mechanism of the line emission from the jets. Yaqoob et al. (1999) suggested that Fe-K line photons originating in an accretion disk and Compton scattering off a leptonic jet aligned along the disk axis can account for the emission line. Because this model failed in explaining the large equivalent width of the line in CXOCDFS J033225.3–274219, Wang et al. (2003) argued that the lines originate from the outflow itself, probably an inner X-ray jet. The observations on SS 433 also supported this idea.

Motivated by the *ASCA* observations, we studied the observed profile of an emission line from relativistic outflows around a Kerr black hole in great detail, but the jets were simply treated as pencil beams (Wang et al., 2000, hereafter Paper I). In this paper, we generalize our previous work and study the line emission from more realistic, cone-shaped jets. Even if the jets are collimated as pencil beams, the possible precession of the jets makes the observed results the same as those from the conical jets if the observational integration time is longer than the precession cycle.

2. The Model

It is believed that jets might originate in rotating black holes or neutron stars, although the concrete mechanism for jet production is still unclear. Therefore, the space-time of such systems should be described by the Kerr metric containing two parameters, the mass of the compact object M and its angular momentum per unit mass a.

So far, there have been lots of works on the profile of an emission line from an accretion disc around a rotating black hole (Fabian et al., 2000; Reynolds and Nowak, 2003 and references therein). The key step in these investigations is to calculate the trajectories of the emitting photons. Basically two main approaches have been considered. One is the method of direct integration in which the trajectories of photons are followed from the disc to the observer at infinity and the other is the so-called ray tracing method in which the trajectories of photons are followed reversely from the photographic plate to the disc (see Fanton et al., 1997 for more detail). The latter is much more efficient than the previous one because only those photon trajectories that reach the observer are considered. Cadez et al. (1998) improved the ray tracing approach by introducing Jacobian elliptic functions to determine the trajectories of photons analytically and therefore, efficiently. The Cadez et al.'s analytic method has the advantage that it is not necessary to deal

with the turning points in both the θ-integral and radial integrals of the photo trajectories specifically. In our previous work on the line emission from jets, Cadez's analytic ray tracing method is used. We continue to use this elegant method in this work.

Here we summarize briefly the main physics in our calculations first. There are three constants of motion for test particles in the Kerr metric: the energy at infinity $E = -p_t$, the azimuthal angular momentum at infinity $L_z = p_\phi$, and the Carter constant $Q = p_\theta^2 - a^2E^2\cos^2\theta + L_z^2\cot^2\theta$, which stems from the separability of the equations of motion (Carter, 1968). A recent discussion on the meaning of Q can be found in de Felice and Preti (1999). Since the photon trajectory does not depend on its energy E, it is determined by two dimensionless constants: $\lambda = L_z/E$, $q = Q/E^2$. The two impact parameters of a photon in the photographic plate can be expressed as

$$\alpha = -\frac{\lambda}{\sin\theta_{\rm obs}}, \tag{1}$$

$$\beta = \pm(q + a^2\cos^2\theta_{\rm obs} - \lambda^2\cot^2\theta_{\rm obs})^{1/2}, \tag{2}$$

where the sign of β is related to $(dr/d\theta)_{\rm obs}$ (Bardeen and Cunningham, 1973) and $\theta_{\rm obs}$ is the angular coordinate of the observer at infinity. Given λ and q, the trajectory of the photon originating from $(r_{\rm em}, \theta_{\rm em})$ can be obtained according to the following equation:

$$\int_{r_{\rm em}}^{\infty} \frac{dr}{\sqrt{R(r,\lambda,q)}} = \int_{\theta_{\rm em}}^{\theta_{\rm obs}} \frac{d\theta}{\sqrt{\Theta(r,\lambda,q)}} = P, \tag{3}$$

where

$$R(r,\lambda,q) = r^4 + (a^2 - \lambda^2 - q)r^2 + 2[q + (\lambda - a)^2]r - a^2q, \tag{4}$$

$$\Theta(r,\lambda,q) = [q + (a\cos\theta)^2 - (\lambda\cot\theta)^2], \tag{5}$$

and P is value of the integrals along the geodesics. Due to the azimuthal symmetry of the metric, the ϕ motion is neglected. It is evident that as $P \to 0$, then $r_{\rm em} \to \infty$ and $\theta_{\rm em} \to \theta_{\rm obs}$. To guarantee the existence of the above integrals, $R(r,\lambda,q) \geq 0$, $\Theta(r,\lambda,q) \geq 0$ along the trajectory. The so-called turning points in r (radial turning points) or θ (azimuthal turning points) which are the roots of $R(r,\lambda,q)$ or $\Theta(r,\lambda,q)$ play the key role in determining the trajectories. For these photons which can reach infinity, there is only one turning point $r_{\rm min}$, the maximal real root of $R(r,\lambda,q)$, but the minimal radius where the photon can reach.

It is noticed that both the θ and r-integrals can be expressed in terms of Jacobian elliptic integrals of the first kind (Chandrasekhar, 1983). The radial integral is more complex than the θ-integral, fortunately, Cadez et al. (1998) obtained the obvious expressions for the radial integral in terms of the elliptic functions. Different

number of the real roots in $R = 0$ gives the different concrete expressions for the r-integral.

Let us summarize the procedures how to determine the trajectory of a photon numerically in the light of the ray tracing method:

(i) Specify a, $\theta_{\rm jet}$, $\theta_{\rm obs}$;
(ii) Choose a pair of α and β, equivalently, fix the values of λ, q which satisfy $\Theta \geq 0$;
(iii) Calculate the integral P from the θ-integral, there might be more than one value of P, which depends on whether there are turning points (Cadez et al., 1998);
(iv) Calculate the maximal value of the r-integral,

$$P^r_{\rm max} = 2\int_{r_{\rm min}}^{\infty} \frac{dr}{\sqrt{R}}. \tag{6}$$

If $p < p^r_{\rm max}$, $r_{\rm em}$ can be determined from the r-integral in Eq. (3) by using Cadez et al. (1998)'s method. If not, that means the photon with chosen α and β can not reach the infinity, then, go to step (ii) for choosing a new pair of α and β.

From above procedures, finally we obtain the radius of the emitter $r_{\rm e} = r_{\rm e}(\alpha, \beta)$.

The next step is to calculate the shift of the photon energy g which is defined as a ratio of the observed energy to the emitted energy,

$$g \equiv E_{\rm obs}/E_{\rm em} = u^{\mu}_{\rm obs} p_{\mu} / u^{\mu}_{\rm em} p_{\mu}. \tag{7}$$

The function g is related to the redshift z as $g = 1/(1+z)$. The momentum of the photon p_{μ} in the Kerr metric has the components,

$$(p_t, p_r, p_\theta, p_\phi) = \left(-E, \pm E\sqrt{R}/\Delta, \pm E\sqrt{\Theta}, E\lambda\right), \tag{8}$$

where $\Delta = r^2 - 2r + a^2$. Meanwhile the four-velocity of the emitter moving along jets is $u^{\mu} = (u^t, u^r, 0, 0)$, and that of the observer at infinity $u^{\mu}_{\rm obs} = (1, 0, 0, 0)$. Therefore, we have

$$g = u^t \pm u^r \sqrt{R}/\Delta, \tag{9}$$

where the sign of the second term on the left is related to $(dr/d\theta)_{\rm obs}$, as in Eq. (2).

Finally, assuming the emitted flux of the line is isotropic and monochromatic in the rest frame of the emitters, the total observed flux with the frequency $\nu_{\rm obs}$ is given by,

$$F_{\rm obs}(\nu_{\rm obs}) = \int_{\rm image} \epsilon(r) g^4 \delta(\nu_{\rm obs} - g\nu_{\rm em})\, d\Xi, \tag{10}$$

where $\epsilon(r)$ is the emissivity function of the jets, for simplicity we assume a power law for $\epsilon(r)$, i.e., $\epsilon(r) = Kr^{-m}$ as in our previous work (Wang et al., 2000), here K and m are constants. In Eq. (10), $d\Xi = d\alpha d\beta/d^2$ is the solid angle subtended by the disc in the observer's sky and the integral extends over the whole emitting region, here d is the distance between the source and the observer. In the following numerical calculations, the jet image in the (α, β) plane is divided into enough numbers of grids, the observed flux in a pixel $(\alpha, \beta) - (\alpha + \Delta\alpha, \beta + \Delta\beta)$ is given by,

$$F(r_{\rm e}(\alpha, \beta), \nu_{\rm obs}) = \frac{K}{d^2 \nu_{\rm em}} r_e^{-m}(\alpha, \beta) g^4(\alpha, \beta) \left(\frac{\Delta\alpha \Delta\beta}{\Delta\nu_{\rm obs}} \right), \tag{11}$$

where $\Delta\nu_{\rm obs}$ is the difference of the observed frequencies in the range of the pixel. Rearranging the observed flux versus the observed frequency results in the line profile we need.

3. Numerical Results

In the following calculations, we assume that the jets move symmetrically along the spin axis of black holes with the half opening angle $\theta_{\rm jet}$. The inner radius is taken as the marginally stable radius $r_{\rm ms}$, and the outer radius $r_{\rm out} = 500\, r_{\rm g}$, here $r_{\rm g}$ is the gravitational radius. Because of the following two reasons, as a first step, we do not consider the line emission from a receding jet. The first reason is that due to the Doppler effects, basically the luminosity of a receding jet is several orders lower than that of an approaching one, so it is much more difficult to observe the profiles of line emission from receding jets. The other is that it was shown in our previous paper, the profile of a line emission from a receding jet is not sensitive to $\theta_{\rm obs}$. Therefore, it can be predicted that the line profile might be very similar in the case of conical and cylindrical jets. Using the techniques of determining the photon trajectories, the image of a jet in the photographic plates, (α, β)-space, is shown in Figure 1.

To determine the observed line profile, the dynamics of jets should be specified. As in our previous work, the jets are assumed to move radially with a constant Lorentz factor Γ. So the velocity components of the emitter can be expressed in terms of the metric and Γ. From Eq. (11), the observed line profiles can be obtained. Figures 2–3 show the line profiles of emission lines from approaching jets with different opening angles and viewing angles. It is clearly shown in Figure 2 that the intrinsically narrow lines are broadened due the combination of the effects of special and general relativity, but there are basically only one peak in the line profile, which is different from those in disc case in which double peaks are frequently observed in the previous theoretical investigations, one of which is named as the red wing whose peak value is weaken by the strong gravitational field.

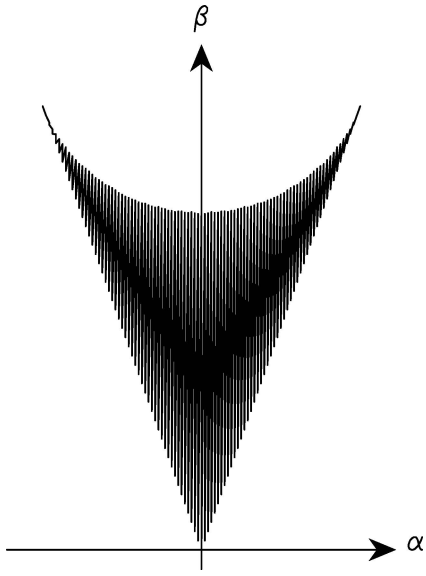


Figure 1. Image of an approaching jet along the spin axis of a extreme black hole as seen by an observer at infinity. The half opening angle of the jet is taken as $\theta_{\rm jet} = 5^0$, and the viewing angle $\theta_{\rm obs} = 15^0$ to the spin axis, the spin of the hole $a = 0.998$.

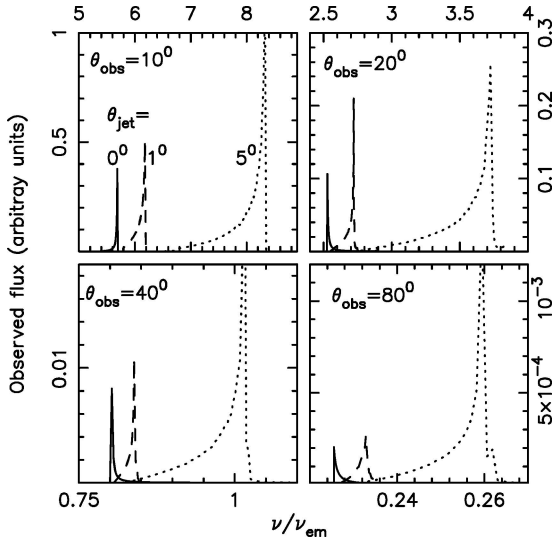


Figure 2. The observed profile (in arbitrary units) of an emission line from a relativistic jets by an observer at infinity. The parameters of the model are as follows: the jet moves with a constant Lorentz factor $\Gamma = 5$, the index of the emissivity laws is $m = 0.5$, the spin of the hole is a $= 0.998$, the inner radius $r_{\rm inner} = r_{\rm ms}$ and the outer radius $r_{\rm out} = 500\, r_{\rm g}$.

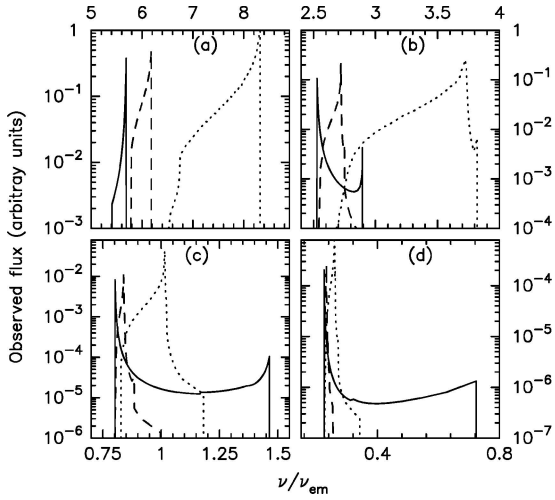


Figure 3. The same as Figure 2, but the observed flux are rescaled logarithmically.

4. Discussions

Motivated by the observations, we studied the observed profile of an emission line from relativistic outflows around rotating black holes. It was found that the observed line emission shows a doubly peaked profile at large viewing angles for extreme Kerr black holes. From the qualitatively analysis and numerical calculations, it was known that the peak I at lower frequencies is from the outer region, while the peak II at the high frequencies is from the inner region of jets (Paper I).

In this work, we generalize our previous work and study the line emission from more realistic, cone-shaped jets, and we find that an intrinsically narrow line is basically singly peaked, the peak II of Paper I has disappeared or weakened significantly. This result is quite different from the previous results in Paper I and emphasizes the difference between the results in the jet case and those in the disc case in which double peaks are frequently observed in the previous theoretical investigations (Fabian et al., 1989; Laor, 1991). In our opinion, the weakening or disappearance of the peak II of Paper I is due to the geometrical effect. Roughly speaking, the differential emitting area of the jets is proportional to its radius, therefore, the innermost the position of the region of emission the fewer the photons emitted.

Acknowledgements

We would like to thank the discussions with Dr Rob Fender and Dr Xiang-Yu Wang on the line emission from SS 433. This work is partially supported by the

Special Funds for Major State Research Projects, and the National Natural Science Foundation (10233030). J.M.W. thanks the support from Alexander von Humboldt Foundation, the Hundred Talent Program of Chinese Academy of Sciences, and the Special Funds for Major State Basic Research Projects and NSFC.

References

Bardeen, C.T. and Cunningham, J.M.: 1973, *Astrophys. J.* **183**, 237.
Cadez, A., Fanton, C. and Calvani, M.: 1998, *New Astron.* **3**, 647.
Carter, B.: 1968, *Phys. Rev.* **174**, 1559.
Chandrasekhar, S.: 1983, The Mathematical Theory of Black Holes, Research supported by NSF. Oxford/New York, Clarendon Press/Oxford University Press (International Series of Monographs on Physics. Vol. 69), p. 663.
Cui, W., Chen, W. and Zhang, S.N.: 2000, *Astrophys. J.* **529**, 952.
de Felice, F. and Preti, G.: 1999, *Class. Quant. Grav.* **16**, 2929.
Fabian, A.C., Iwasawa, K., Reynolds, C.S. and Young, A.J.: 2000, *PASP* **112**, 1145.
Fabian, A.C., Rees, M.J., Stella, L. and White, N.E.: 1989, *MNRAS* **238**, 729.
Fanton, C., Calvani, M., de Felice, F. and Cadez, A.: 1997, *PASJ* **49**, 159.
Laor, A.: 1991, *Astrophys. J.* **376**, 90.
Migliari, S., Fender, R. and Méndez, M.: 2002, *Science* **297**, 1673.
Reynolds, C.S. and Nowak, M.A.: 2003, *Phys. Rep.* **377**, 389.
Wang, J., Yaqoob, T., Szokoly, G., Gilli, R., Kewley, L., Mainieri, V., Nonino, M., Rosati, P., Tozzi, P., Zheng, W., Zirm, A. and Norman, C.: 2003, *Astrophys. J. Lett.* **590**, L87.
Wang, J., Zhou, Y., Yuan, Y., Cao, X. and Wu, M.: 2000, *Astrophys. J.* **544**, 381. (Paper I).
Yaqoob, T., George, I.M., Nandra, K., Turner, T.J., Zobair, S. and Serlemitsos, P.J.: 1999, *Astrophys. J. Lett.* **525**, L9.
Yaqoob, T., George, I.M., Turner, T.J., Nandra, K., Ptak, A. and Serlemitsos, P.J.: 1998, *Astrophys. J. Lett.* **505**, L87.

A SURVEY OF UNIDENTIFIED EGRET SOURCES AT TeV ENERGIES

S.J. FEGAN, T.C. WEEKES and THE VERITAS COLLABORATION
Fred Lawrence Whipple Observatory, Harvard-Smithsonian CfA, Amado, AZ, USA;
E-mail: tweekes@cfa.harvard.edu

(Received 13 August 2004; accepted 14 July 2004)

Abstract. The Whipple Observatory 10 m γ-ray telescope has been used to survey the error boxes of 24 EGRET unidentified sources in an attempt to find counterparts at energies of 350 GeV and above. In no case is a statistically significant signal found in the EGRET error box which implies that, at least for this sample, the γ-ray spectra of these sources steepen between 100 MeV and 350 GeV.

Keywords: gamma rays: observations, sources: unidentified

1. Introduction

One of the significant legacies of the EGRET mission on the Compton Gamma Ray Observatory was the large number of detected sources for which no obvious counterpart was found at longer wavelengths and whose nature therefore remains elusive (Lamb and Macomb, 1997; Hartman et al., 1999; Macomb and Lamb, 1999).

Atmospheric Čerenkov imaging telescopes are ideally suited to the study of unidentified EGRET sources since the fields of view of typical Čerenkov cameras are considerably larger than the EGRET error boxes. Although these telescopes have optimum sensitivity for sources in the center of the field of view, i.e., on the optical axis, sensitive search techniques have been developed to search for sources that are not on the axis (Akerlof et al., 1991; Lessard et al., 2001). For the Whipple telescope, the flux sensitivity at 1.0° off axis is ∼50% of that on axis (Fegan et al., 2001). The telescope has been shown to have flux sensitivity even outside the geometrical field of view of the camera.

The detection of a TeV γ-ray signal from an unidentified EGRET source would expand our knowledge of the source and increase the possibility that the source might be identified. The angular resolution of Čerenkov telescopes operating above 350 GeV is significantly better than EGRET; better source location leads to a reduced error box and increases the chances of identification with a known source. In addition, detection of an EGRET source at TeV energies would allow for the much better determination of the energy spectrum of the source and this would help to classify it. Because ground-based instruments offer the possibility for long-term monitoring, the variability of the source (if any) can be measured, independent of the mission constraints that pertain to space telescopes. Also the very large


Astrophysics and Space Science **297:** 431–438, 2005.
© Springer 2005

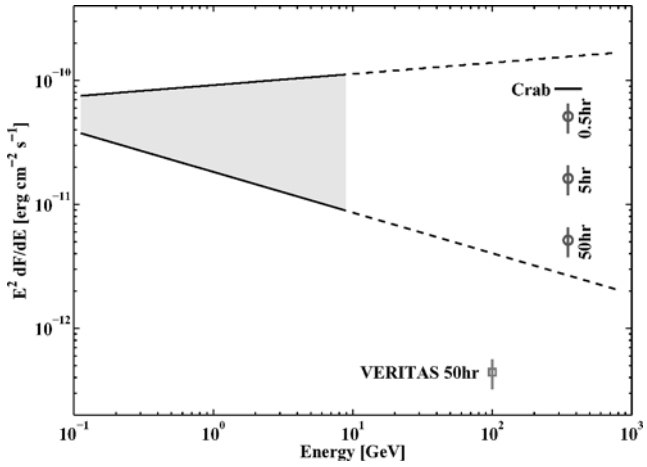


Figure 1. Comparison of upper limit on source luminosity derivable through observations at Whipple with the extrapolated luminosity of a "mean" 100 MeV source. Upper limits for 0.5, 5 and 50 h observations are shown, assuming a Crab-like spectrum. The hypothetical 100 MeV source has an integral flux spectrum given by the mean flux and spectral index from 3EG sources chosen for this survey: $I(>E) = (30.9 \pm 4.1) \times 10^{-8}(E/100MeV)^{-1.12\pm0.21}$ cm^{-2}s^{-1}. The upper-limits are derived by assuming that the VHE emission is from a source with a spectral index similar to that of the Crab Nebula in this energy regime, i.e. $\Gamma \approx 2.5$. The point marked as *VERITAS* 50 hr indicates the limits which can be derived from 50 h of observations with a ground-based array such as VERITAS or HESS.

collection area of the ground-based telescope permits short-term variations to be detected.

The Whipple instrument has a detection sensitivity of ≈30% of the flux of the Crab in 5 h of observation (for a detection at the 4 σ level). The potential of such ground-based observations is illustrated in Figure 1 where the upper limit that can be placed on the source flux above 350 GeV from observations with various durations is shown relative to a hypothetical EGRET source.

The source list surveyed includes 24 sources from both the EGRET and GeV catalogs; their distribution in the sky relative to the Galactic equator and the Gould Belt is shown in Figure 2.

2. Technique

Cosmic gamma rays at energies greater than 300 GeV are detected at ground-level by the Čerenkov radiation given off by the atmosphere caused by the passage of the electromagnetic cascade. The Čerenkov images from the γ-ray initiated cascades from a point source can be distinguished the more numerous images resulting from the cascades initiated by charged hadrons in the cosmic radiation by the shape and orientation of the images. The images are recorded in fast cameras made of arrays of photomultipliers in the focal plane of large optical reflectors. The γ-ray

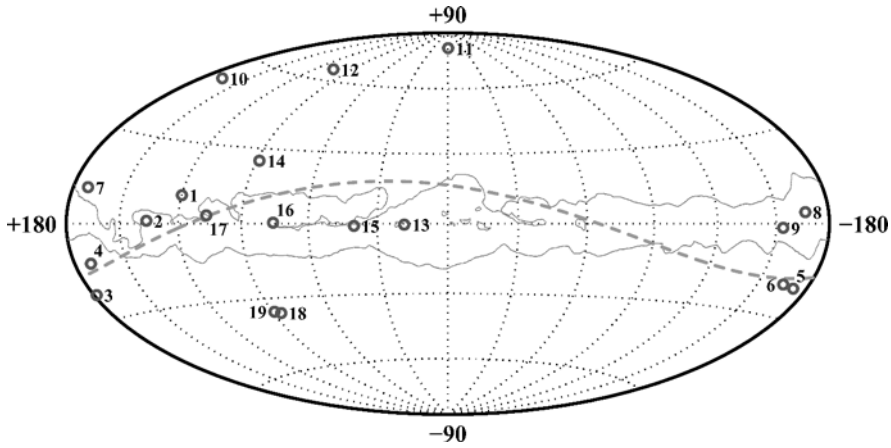


Figure 2. The unidentified EGRET sources considered in this survey, plotted in Galactic coordinates. The outline of the Milky Way, from optical observations and the Gould Belt (dashed line) are also depicted for comparison.

observations reported here were made with the GRANITE-III camera (Finley et al., 1999) on the Whipple Observatory 10 m aperture optical reflector (Cawley et al., 1990) which is located on the 2.3 km level of Mount Hopkins in southern Arizona, USA. This is a mature camera-telescope configuration that has been in regular use since 1999; a number of important detections have been reported (Horan et al., 2002; Krennrich et al., 2002; Holder et al., 2003; Kosack et al., 2004).

The high resolution GRANITE-III camera (Finley et al., 1999) is equipped with 379 photomultipliers that each subtend an angle on the sky of 0.12°; the camera has a total field of view of 2.6°. The outputs of these PMTs are connected through 50 m of coaxial cable to amplifiers in the camera control room.

3. Observations and Analysis

Data for this survey were taken from 1999 to 2003 as part of the routine observing program of the Whipple Observatory. Significant changes were made to the telescope during the summer and fall of 2001 when a new technique was applied to the alignment of mirror facets.

Observations with the instrument are made in one of two modes, termed ON/OFF and Tracking modes, which have significantly different approaches to background estimation. When operating in the ON/OFF mode, two separate 28 min scans (ON and OFF) are made. The ON scan is taken while tracking the sky with the candidate object at the center of the field of view and gives an estimate of the γ-ray flux combined with the background rate. The OFF scan is taken in the absence of the candidate object to give an independent estimate of the background rate. The ON

and OFF scans are taken such that they are separated by 30 min in time and track locations in the sky separated by 30 min in Right Ascension. When operating in the Tracking mode, a single scan is taken tracking the candidate object. An estimate of the background is inferred from the number of events present in the scan, which are not consistent with having originated from the candidate source location. The ON/OFF mode can be used to test the hypothesis that the γ-ray emission is occurring from any location within the field of view of the instrument. This is the case for a candidate source whose location is not known *a priori*, such as unidentified sources with large error-box locations and for sources whose emission is expected to be extended, such as SNR. Hence the bulk of the observations taken in this survey were made in the ON/OFF mode.

The power of the atmospheric Čerenkov imaging technique depends on the data analysis algorithms which are used to separate candidate γ-ray images from the background of images from cosmic ray initiated air shower, local muons and night-sky noise fluctuations. In general, these algorithms are based on Monte Carlo simulations and optimized using a standard candle such as the Crab Nebula. One of the simplest, most effective, single telescope, point-source analysis techniques, dubbed "Supercuts", was developed for data taken at the Whipple 10 m telescope (Punch et al., 1992). Data selection is based on a set of strict criteria applied to a set of parameters, which are calculated for each image. The selection cuts are optimized to preferentially select γ-ray-induced events over background events. This technique typically keeps 50% of γ-ray events and discards >99% of background events, significantly improving the signal-to-noise (S/N) ratio. For a bright source such as the Crab Nebula, a S/N ratio corresponding to a $\approx$3–4σ rejection of the null hypothesis that no source is present (with an event rate large enough that Gaussian statistics apply) can be achieved in 30 min of observations. This point-source analysis technique has been adapted to sources whose location is not well defined and to extended sources.

When Whipple data from an unidentified EGRET source are analyzed, a map of *a priori* significance is produced and the EGRET 95% contour level overlaid. The area of the region inside the contour is used to calculate an equivalent number of independent bins. This value is then used to calculate a significance level which is equivalent to the accepted Gaussian 4σ confidence level.

4. Results

The results of the observations are summarized in Table I, which gives the upper limits (at the 99% confidence level) for a source anywhere within the EGRET 95% confidence region. Where identifications have been suggested, the upper limit for the candidate is presented elsewhere (Fegan et al., 2004). Significance maps for excess TeV γ-ray like events from the Whipple observation of the two unidentified sources 3EG J1337+5029 and 3EG J2227+6122 are shown in Figures 3 and 4, respectively.

TABLE I
Upper limits for unidentified EGRET fields

Source name	Coordinates		Extent	Upper limit
	α_{2000}	δ_{2000}	[deg × deg]	[10^{-11} cm^{-2} s^{-1}]
3EG J0010+7309	$00^h09^m36.6^s$	$+73°10'57.4''$	0.25 × 0.22	2.2
3EG J0241+6103	$02^h41^m31.3^s$	$+61°04'12.3''$	0.21 × 0.15	2.2
3EG J0423+1707	$04^h23^m56.5^s$	$+16°56'27.4''$	0.88 × 0.65	6.6
3EG J0433+2908	$04^h33^m35.1^s$	$+29°07'42.2''$	0.19 × 0.16	1.6
3EG J0450+1105	$22^h15^m06.5^s$	$+31°28'55.7''$	0.65 × 0.61	5.0
3EG J0613+4201	$06^h14^m20.6^s$	$+41°59'51''$	0.66 × 0.46	4.3
3EG J0628+1847	$06^h28^m36.1^s$	$+18°50'35''$	0.66 × 0.49	4.1
3EG J0634+0521	$06^h34^m39.9^s$	$+05°28'21''$	0.85 × 0.50	5.3
3EG J0631+0642	$06^h31^m39.4^s$	$+06°41'42''$	0.55 × 0.39	6.0
GeV J0633+0645	$06^h33^m08.8^s$	$+06°45'49''$	0.42 × 0.42	4.9
3EG J1009+4855	$10^h09^m59.3^s$	$+48°50'30''$	1.12 × 0.80	4.6
3EG J1323+2200	$13^h23^m20.1^s$	$+22°02'52''$	0.52 × 0.43	3.1
3EG J1337+5029	$13^h38^m00.8^s$	$+50°25'57''$	0.77 × 0.66	5.9
3EG J1826−1302	$18^h26^m01.0^s$	$-13°05'28''$	0.55 × 0.39	4.2
3EG J1823−1314	$18^h23^m24.7^s$	$-13°14'32''$	0.33 × 0.23	3.2
GeV J1825−1310	$18^h25^m14.3^s$	$-13°10'19''$	0.32 × 0.32	4.2
3EG J1835+5918	$18^h35^m24.9^s$	$+59°19'15.3''$	0.16 × 0.13	3.8
GeV J1907+0557	$19^h07^m40.4^s$	$+05°57'14''$	0.38 × 0.28	3.0
GeV J2020+3658	$20^h20^m45.1^s$	$+36°58'50''$	0.28 × 0.21	3.7
3EG J2021+3716	$20^h21^m19.9^s$	$+37°15'12''$	0.35 × 0.26	3.7
3EG J2016+3657	$20^h16^m34.1^s$	$+36°52'22''$	0.68 × 0.44	5.8
3EG J2227+6122	$22^h27^m20.8^s$	$+61°23'28.9''$	0.50 × 0.41	4.1
GeV J2227+6101	$22^h27^m45.9^s$	$+61°01'22.7''$	0.54 × 0.54	3.5
3EG J2248+1745	$22^h48^m54.3^s$	$+17°47'09.5''$	1.13 × 0.78	5.2

The upper limit on the integral γ-ray flux above an energy 350 GeV is at the 99% confidence level.

Multiwavelength observations have proved to be the most powerful tool available to investigate the origin of the high-energy emission from the unidentified EGRET sources. For a number of such sources, x-ray, radio and optical observations have narrowed the list of scientifically viable, potential candidates. In some cases, such observations have ruled out all but one candidate. This survey was undertaken in the hope that VHE emission would be detected from one of the sources chosen, and that the higher spatial resolution achievable with the ground-based technique would allow the source of the γ-ray emission to be identified. There is significant overlap between the VHE source catalog (Horan and Weekes, 2004) and the EGRET sources; 7 of the 18 credible VHE sources were also seen by EGRET at some level.

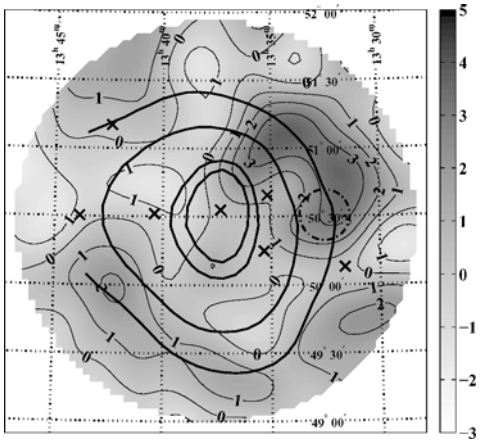


Figure 3. Significance of excess γ-like events detected from the region of 3EG J1337+5029 (light solid lines). The 3EG likelihood contours are shown as heavy lines, the cluster of galaxies, A1758 is shown as a dot-dashed circle, and the various other sources in the field as "X" marks.

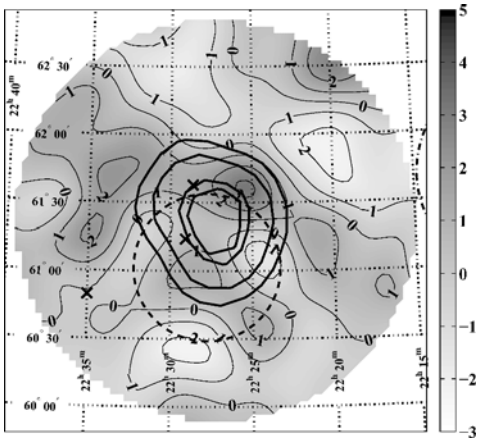


Figure 4. Significance of excess γ-ray-like events, detected from the region of 3EG J2227+6122 (light solid lines). The 3EG likelihood contours are shown as heavy lines. The GeV source location is indicated by the heavy dashed line and the nearby OB association as a dot-dashed line, which barely overlaps the region, to the west.

Of the two categories of sources unambiguously identified by EGRET, blazars and pulsars, detections of eight BL Lac type blazars have been claimed at TeV energies. No pulsars have been directly detected by ground-based instruments, but some EGRET pulsars are associated with PWN which like the Crab may be visible to VHE γ-ray instruments.

In total, results from VHE observations of 24 EGRET sources are reported, more than 10% of the unidentified source population. The observations yielded

an average of 5 h of data from each source. When the survey was initiated, little was known about many of the observed sources, outside of what was published in the 3EG catalog. Since that time, our understanding of these sources has advanced considerably, both through work on the population as a whole and through multiwavelength observations of individual sources. Of particular note in the first category are the calculation of source variability by Nolan et al. (2003) and the systematic correlation of the sources with radio sources (Mattox et al., 2001) and SNR, OB-associations and massive stars (Romero et al., 1999). That so many of the sources chosen here now have potential associations is a testament to the ongoing interest in multiwavelength observations of these sources, e.g. Kaaret et al. (1999); Mukherjee et al. (2000); Roberts et al. (2001).

Based on the number of observations made (i.e. the number of sources surveyed and the number of independent bins in each two-dimensional image) it cannot be claimed that VHE γ-ray emission was detected from any of the sources, at a significant level. Two of these sources, 3EG J1337+5029 and 3EG J2227+6122, have excesses with sufficiently low chance probability that they would be considered as suggestive of γ-ray emission, if the observations are taken in isolation from the rest of the survey. In the case of J1337+5029, the location of the VHE excess corresponds to the location of a cluster, Abell 1758. If the excess is the result of γ-ray emission from the cluster, it would represent a new class of VHE emission and it would be the most distant source of VHE emission to date (at $z = 0.279$, considerably more distant than H1426+428, the most distant VHE blazar, at $z = 0.129$) and have important implications for the density of the inter-galactic infra-red radiation field (IIRF). The location of the VHE excess in the case of J2227+6122 does not correspond to any of the suggested associations for the EGRET source. To confirm (or refute) any emission, independent follow-up observations will be made. The excesses correspond to fluxes of 0.40 and 0.33 of the integral Crab Nebula flux, at energies > 350 GeV, respectively. At this level, a 5–10 h exposure on each source will be sufficient for confirmation.

The next generation of ground-based instruments, such as VERITAS, HESS, CANGAROO-III and MAGIC, will be more than an order of magnitude more sensitive than the Whipple 10 m instrument (Figure 1). They will be most sensitive to γ-rays at approximately $\sim$100 GeV, with some sensitivity even below this energy. A survey of EGRET sources with these instruments should have considerable success in detecting γ-ray emission.

References

Akerlof, C.W. et al.: 1991, *ApJ* **377**, L97.

Cawley, F.M. et al.: 1990, in: *Proceedings of the 21st International Cosmic Ray Conference*, Vol. 4(OG), p. 224.

Fegan, S.J. et al.: 2001, in: Proceedings of the AIP Conference 587: Gamma 2001: Gamma-Ray Astrophysics, pp. 296.

Fegan, S.F. et al.: 2004, in preparation.
Finley, J.P. et al.: 1999, in: Dingus, Salamon, and Kieda (eds.), *Proceedings of the AIP Conference Workshop on GeV-TeV Gamma Ray Astrophysics, Towards a Major Atmospheric Cherenkov Detector VI*, Vol. 301.
Hartman, R.C. et al.: 1999, *ApJS* **123**, 79.
Holder, J. et al.: 2003, *ApJ* **583**, L9.
Horan, D. et al.: 2002, *ApJ* **571**, 753.
Horan, D. and Weekes, T.C.: 2004, in: S. Swordy and L. Fortson (eds.), *New Astronomy Review, Proceedings of the Second VERITAS Symposium on TeV Astrophysics of Extragalactic Sources*, Vol. 48, pp. 527.
Kaaret, P., Piraino, S., Halpern, J. and Eracleous, M.: 1999, *ApJ* **523**, 197.
Kosack, K. et al.: 2004, *ApJ* **608**, L97.
Krennrich, F. et al.: 2002, *ApJ* **575**, L9.
Lamb, R.C. and Macomb, D.J.: 1997, *ApJ* **488**, 872.
Lessard, R.W., Buckley, J.H., Connaughton, V. and Le Bohec, S.: 2001, *A&A* **15**, 1.
Lessard, R.W. et al.: 1999, in: Dingus, Salamon and Kieda (eds.), *Proceedings of the 26th International Cosmic Ray Conference*, Vol. 3, p. 488.
Macomb, D.J. and Lamb, R.C.: 1999, in: Dingus, Salamon and Kieda (eds.), *Proceedings of the 26th International Cosmic Ray Conference*, Vol. 4, p. 107.
Mattox, J.R., Hartman, R.C. and Reimer, O.: 2001, *ApJS* **135**, 155.
Mukherjee, R., Gotthelf, E.V., Halpern, J. and Tavani, M.: 2000, *ApJ* **542**, 740.
Nolan, P.L. et al.: 2003, *ApJ* **597**, 615.
Punch, M. et al.: 1992, *Nature* **358**, 477.
Roberts, M.S.E., Romani, R.W. and Kawai, N.: 2001, *ApJS* **133**, 451.
Romero, G.E., Benaglia, P. and Torres, D.F.: 1999, *A&A* **348**, 868.